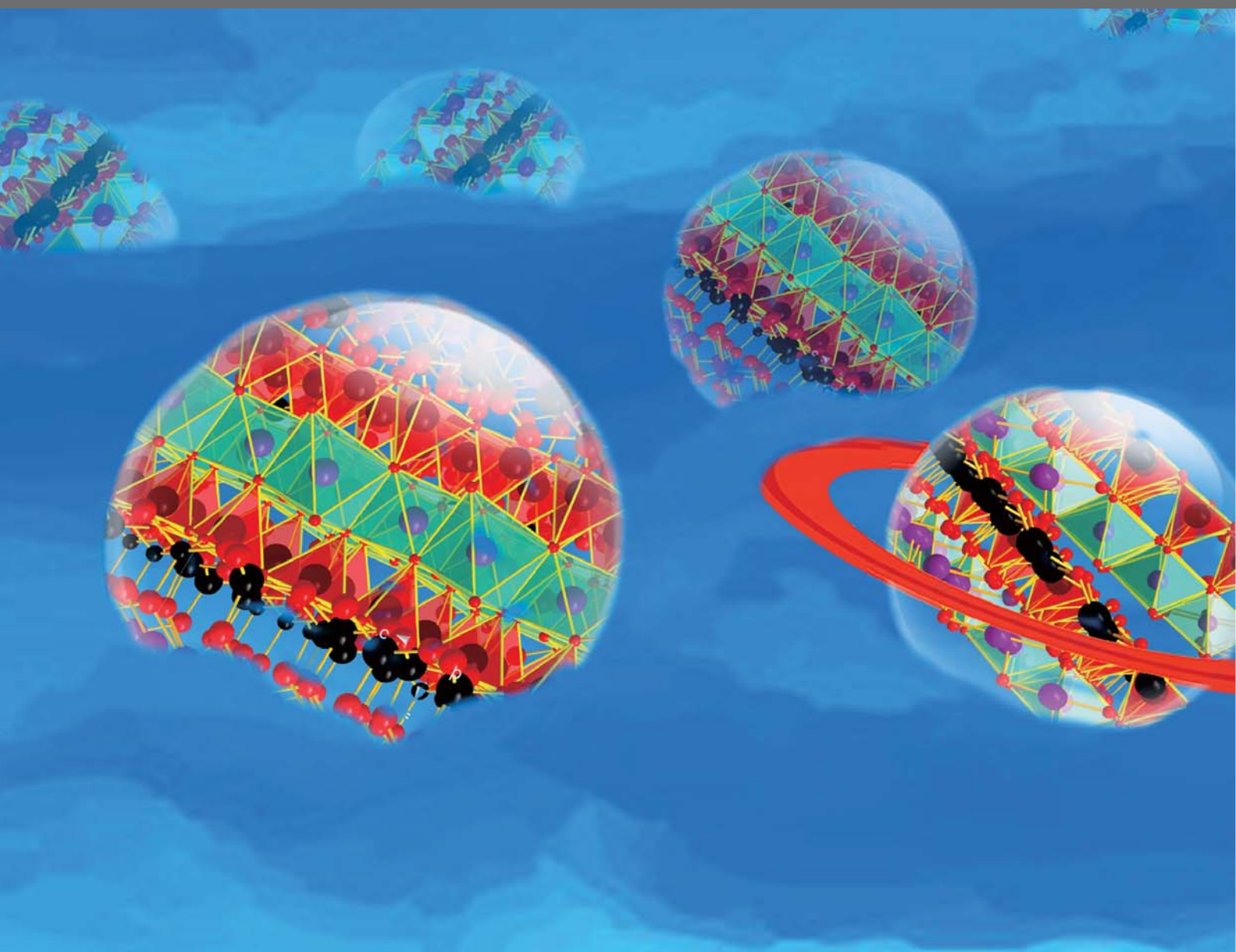


NOVEL APPROACHES TO DESIGN ECO-FRIENDLY MATERIALS BASED ON NATURAL NANOMATERIALS

EDITED BY: Aiqin Wang, Wenbo Wang, Hongfei Cheng and Chunhui Zhou
PUBLISHED IN: Frontiers in Chemistry





frontiers

Frontiers Copyright Statement

© Copyright 2007-2019 Frontiers Media SA. All rights reserved.

All content included on this site, such as text, graphics, logos, button icons, images, video/audio clips, downloads, data compilations and software, is the property of or is licensed to Frontiers Media SA ("Frontiers") or its licensees and/or subcontractors. The copyright in the text of individual articles is the property of their respective authors, subject to a license granted to Frontiers.

The compilation of articles constituting this e-book, wherever published, as well as the compilation of all other content on this site, is the exclusive property of Frontiers. For the conditions for downloading and copying of e-books from Frontiers' website, please see the Terms for Website Use. If purchasing Frontiers e-books from other websites or sources, the conditions of the website concerned apply.

Images and graphics not forming part of user-contributed materials may not be downloaded or copied without permission.

Individual articles may be downloaded and reproduced in accordance with the principles of the CC-BY licence subject to any copyright or other notices. They may not be re-sold as an e-book.

As author or other contributor you grant a CC-BY licence to others to reproduce your articles, including any graphics and third-party materials supplied by you, in accordance with the Conditions for Website Use and subject to any copyright notices which you include in connection with your articles and materials.

All copyright, and all rights therein, are protected by national and international copyright laws.

The above represents a summary only. For the full conditions see the Conditions for Authors and the Conditions for Website Use.

ISSN 1664-8714
ISBN 978-2-88945-912-4
DOI 10.3389/978-2-88945-912-4

About Frontiers

Frontiers is more than just an open-access publisher of scholarly articles: it is a pioneering approach to the world of academia, radically improving the way scholarly research is managed. The grand vision of Frontiers is a world where all people have an equal opportunity to seek, share and generate knowledge. Frontiers provides immediate and permanent online open access to all its publications, but this alone is not enough to realize our grand goals.

Frontiers Journal Series

The Frontiers Journal Series is a multi-tier and interdisciplinary set of open-access, online journals, promising a paradigm shift from the current review, selection and dissemination processes in academic publishing. All Frontiers journals are driven by researchers for researchers; therefore, they constitute a service to the scholarly community. At the same time, the Frontiers Journal Series operates on a revolutionary invention, the tiered publishing system, initially addressing specific communities of scholars, and gradually climbing up to broader public understanding, thus serving the interests of the lay society, too.

Dedication to Quality

Each Frontiers article is a landmark of the highest quality, thanks to genuinely collaborative interactions between authors and review editors, who include some of the world's best academicians. Research must be certified by peers before entering a stream of knowledge that may eventually reach the public - and shape society; therefore, Frontiers only applies the most rigorous and unbiased reviews.

Frontiers revolutionizes research publishing by freely delivering the most outstanding research, evaluated with no bias from both the academic and social point of view. By applying the most advanced information technologies, Frontiers is catapulting scholarly publishing into a new generation.

What are Frontiers Research Topics?

Frontiers Research Topics are very popular trademarks of the Frontiers Journals Series: they are collections of at least ten articles, all centered on a particular subject. With their unique mix of varied contributions from Original Research to Review Articles, Frontiers Research Topics unify the most influential researchers, the latest key findings and historical advances in a hot research area! Find out more on how to host your own Frontiers Research Topic or contribute to one as an author by contacting the Frontiers Editorial Office: researchtopics@frontiersin.org

NOVEL APPROACHES TO DESIGN ECO-FRIENDLY MATERIALS BASED ON NATURAL NANOMATERIALS

Topic Editors:

Aiqin Wang, Lanzhou Institute of Chemical Physics (CAS), China

Wenbo Wang, Lanzhou Institute of Chemical Physics (CAS), China

Hongfei Cheng, Chang'an University, China

Chunhui Zhou, Zhejiang University of Technology, Qing Yang Institute for Industrial Minerals, China

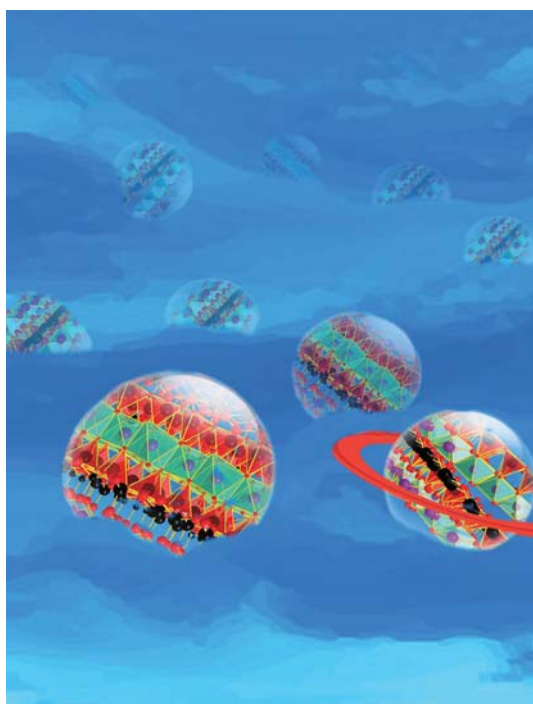


Image: designed by Prof. Wenbo Wang and Dr. Xiaowen Wang, and drawn by Dr. Xiaowen Wang.

Naturally available nanomaterials or those synthesized from natural resources become “new favorite” of material world due to their advantages of low cost, safety and environmental friendliness. They are honored as future “green materials” and widely used in fabricating various functional materials. Naturally available materials have been playing an increasingly important role in many fields such as environmental remediation, separation, catalysis, and polymer composites. This book collects latest research results on the new composites for environmental application, focusing on the study of fabricating functional composites using natural clay minerals. Naturally available materials or solid waste or minerals are good precursors for producing adsorbents. Composites based on sub-bituminous coal, lignite, and a blend of coal and *Irvingia gabonensis* seed shells, the Cl-type Mg-Al hydrotalcite (Cl-LDH), the hydroxyapatite decorated with carbon nanotube and Zirconium (Zr)-containing

silica residue purification (ZSR-P) were proved to have good adsorption capability to Cd(II) and Pb(II) ions, antibiotic molecules, Cd(II), and fluoride, respectively. The nano-Mg(OH)₂ loaded carbon cloth showed good separation effect for Eu(III), and the sodium-modified clinoptilolite showed good separation effect for CH₄/N₂ from coal bed gas. Also, natural nanoclay is an effective precursor for the preparation of inorganic-inorganic or organic-inorganic nano-hybrid materials. Using nano-kaolinite as a carrier, the inorganic-inorganic hybrid cobalt blue pigment with excellent color and stability can be obtained by surface co-precipitation and in-situ calcination crystallization process. The intercalation of 7-amino-4-methylcoumarin (AMC) molecules into the interlayer space of montmorillonite (MMT) can effectively inhibit fluorescence quenching and improve the detection effectiveness of Cr(VI) in water. The interlayer space of kaolinite can accommodate organic molecules to form an organic-inorganic hybrid composite. Natural clay minerals are also effective carriers for catalysts. Er³⁺:CeO₂/palygorskite nanocomposites prepared by a facile precipitation method showed excellent desulfurization rate under visible light irradiation. The zero-valent iron-loaded nanoclays composite catalysts can degrade efficiently Rhodamine 6G (Rh 6G) under microwave irradiation. In addition, the polymer composites have been developed using natural palygorskite, montmorillonite nanosheets or silica nanoparticles as inorganic components, which are potential to be used in many fields such as packing, biomedicine, or rubber. With the increasing attention to clay minerals, research methods for the microstructure of clay minerals continue to receive attention. It is no doubt that natural materials have got a booming attention from researchers in mineralogy, materials science, chemistry, energy, biomedicine and other fields due to their advantages. However, there is still a long way to go to substitute traditional synthetic nanomaterials with natural ones, and there are still theoretical and technological limitation in the design and synthesis of new materials from natural materials. Related theoretical research and technological development require continuous exploration by researchers. This book has collected some recent advances in related research, and hopes to play a role in attracting more attention to the construction of functional materials from natural raw materials. It is also believed that through the unremitting efforts of all researchers, the dream of green materials and green preparation processes can be realized.

Citation: Wang, A., Wang, W., Cheng, H., Zhou, C., eds. (2019). *Novel Approaches to Design Eco-friendly Materials Based on Natural Nanomaterials*. Lausanne: Frontiers Media. doi: 10.3389/978-2-88945-912-4

Table of Contents

SECTION I

ADSORPTION/SEPARATION MATERIALS BASED ON NATURAL NANOMATERIALS

- 06** *Preparation and Evaluation of Adsorbents From Coal and Irvingia gabonensis Seed Shell for the Removal of Cd(II) and Pb(II) Ions From Aqueous Solutions*
Mercy A. Ezeokonkwo, Okechukwu F. Ofor and Julius U. Ani
- 20** *The Interactions Between Three Typical PPCPs and LDH*
Erwei Li, Libing Liao, Guocheng Lv, Zhaohui Li, Chengxue Yang and Yanan Lu
- 29** *Enhanced Defluoridation Capacity From Aqueous Media via Hydroxyapatite Decorated With Carbon Nanotube*
Qingzi Tang, Tongdan Duan, Peng Li, Ping Zhang and Daishe Wu
- 38** *Adsorption Properties and Mechanism of Cd²⁺ in Water by Zr-Containing Silica Residue Purification*
Wanting Chen, Han Zhang, Yu Liang, Hao Ding and Sijia Sun
- 49** *Carbon Cloth Supported Nano-Mg(OH)₂ for the Enrichment and Recovery of Rare Earth Element Eu(III) From Aqueous Solution*
Yinong Li, Chen Tian, Weizhen Liu, Si Xu, Yunyun Xu, Rongxin Cui and Zhang Lin
- 58** *Separation of CH₄/N₂ of Low Concentrations From Coal Bed Gas by Sodium-Modified Clinoptilolite*
Xiaofei Hao, Zhen Li, Hongjie Hu, Xueqin Liu and Yanqiu Huang
- 67** *Synthesis and Microwave Absorbing Properties of Porous One-Dimensional Nickel Sulfide Nanostructures*
Min Lu, Qian Wu, Xiao-Hui Guan, Wei Xu, Hao-Yue Zhang, Xin Di, Guang-Sheng Wang and Shao-Hua Dong

SECTION II

HYBRID MATERIALS BASED ON NATURAL NANOMATERIALS

- 75** *CoAl₂O₄/Kaoline Hybrid Pigment Prepared via Solid-Phase Method for Anticorrosion Application*
Anjie Zhang, Bin Mu, Xiaowen Wang and Aiqin Wang
- 89** *Formation and Coloring Mechanism of Typical Aluminosilicate Clay Minerals for CoAl₂O₄ Hybrid Pigment Preparation*
Anjie Zhang, Bin Mu, Xiaowen Wang, Lixin Wen and Aiqin Wang
- 100** *Fabrication of an AMC/MMT Fluorescence Composite for its Detection of Cr(VI) in Water*
Yanke Wei, Lefu Mei, Rui Li, Meng Liu, Guocheng Lv, Jianle Weng, Libing Liao, Zhaohui Li and Lin Lu
- 107** *Molecular Structure and Decomposition Kinetics of Kaolinite/Alkylamine Intercalation Compounds*
Yi Zhou, Qinghe Liu, Peijie Xu, Hongfei Cheng and Qinfu Liu

SECTION III

CATALYSIS MATERIALS BASED ON NATURAL NANOMATERIALS

117 *Z-Scheme Photocatalyst Constructed by Natural Attapulgite and Upconversion Rare Earth Materials for Desulfurization*

Fengqin Wu, Xiazhang Li, Haiguang Zhang, Shixiang Zuo and Chao Yao

126 *Enhanced Degradation of Rh 6G by Zero Valent Iron Loaded on Two Typical Clay Minerals With Different Structures Under Microwave Irradiation*

Wenxiu Rao, Guocheng Lv, Danyu Wang and Libing Liao

SECTION IV

POLYMER COMPOSITES

133 *Effect of Natural Nanostructured Rods and Platelets on Mechanical and Water Resistance Properties of Alginate-Based Nanocomposites*

Dajian Huang, Zhuo Zhang, Zonghong Ma and Qiling Quan

143 *Novel Design of Eco-Friendly Super Elastomer Materials With Optimized Hard Segments Micro-Structure: Toward Next-Generation High-Performance Tires*

Xuan Qin, Jiadong Wang, Bingyong Han, Bo Wang, Lixin Mao and Liqun Zhang

SECTION V

STRUCTURE CHARACTERISTICS

152 *Rietveld Structure Refinement of Cu-Trien Exchanged Nontronites*

Xiaoli Wang and Libing Liao



Preparation and Evaluation of Adsorbents from Coal and *Irvingia gabonensis* Seed Shell for the Removal of Cd(II) and Pb(II) Ions from Aqueous Solutions

Mercy A. Ezeokonkwo, Okechukwu F. Ofor and Julius U. Ani*

Department of Pure and Industrial Chemistry, University of Nigeria, Nsukka, Nigeria

OPEN ACCESS

Edited by:

Hongfei Cheng,
China University of Mining and
Technology, China

Reviewed by:

Zhanjie Xu,
Tianjin University, China
Biswanath Dutta,
University of Connecticut,
United States

*Correspondence:

Julius U. Ani
julius.ani@unn.edu.ng

Specialty section:

This article was submitted to
Green and Environmental Chemistry,
a section of the journal
Frontiers in Chemistry

Received: 25 October 2017

Accepted: 22 December 2017

Published: 26 January 2018

Citation:

Ezeokonkwo MA, Ofor OF and Ani JU
(2018) Preparation and Evaluation of
Adsorbents from Coal and *Irvingia
gabonensis* Seed Shell for the
Removal of Cd(II) and Pb(II) Ions from
Aqueous Solutions.
Front. Chem. 5:132.
doi: 10.3389/fchem.2017.00132

Cd(II) and Pb(II) ions removal using adsorbents prepared from sub-bituminous coal, lignite, and a blend of coal and *Irvingia gabonensis* seed shells was investigated. Fourier transform infrared, scanning electron microscope and X-ray fluorescence analyses implicated hydroxyl, carbonyl, Al₂O₃, and SiO₂ as being responsible for attaching the metal ions on the porous adsorbents. The optimum adsorption of carbonized lignite for the uptake of Cd(II) and Pb(II) ions from aqueous media were 80.93 and 87.85%, respectively. Batch adsorption was done by effect of adsorbent dosage, pH, contact time, temperature, particle size, and initial concentration. Equilibrium for the removal of Pb(II) and Cd(II) was established within 100 and 120 min respectively. Blending the lignite-derived adsorbent with *I. gabonensis* seed shell improved the performance significantly. More improvement was observed on modification of the blend using NaOH and H₃PO₄. Pb(II) was preferentially adsorbed than Cd(II) in all cases. Adsorption of Cd(II) and Pb(II) ions followed Langmuir isotherm. The adsorption kinetics was best described by pseudo-second order model. The potential for using a blend of coal and agricultural byproduct (*I. gabonensis* seed shell) was found a viable alternative for removal of toxic heavy metals from aqueous solutions.

Keywords: lignite, adsorption, *Irvingia gabonensis*, isotherm, kinetics

INTRODUCTION

The accumulation of toxic heavy metals in industrial wastewater effluents has become a great challenge in less developed countries such as Nigeria, as these effluents are indiscriminately discharged into water bodies or on land (Weber et al., 1991). Wastewater effluents generated in some chemical process industries contain cadmium, lead, copper, zinc, nickel, and chromium (Argun and Dursun, 2008), which if contained above a given concentration are hazardous and has the propensity of leading to fatal health challenges. In addition, these elements, unlike most pollutants are not ecologically degradable rather they undergo a universal ecological cycle in which soil and water are the main pathways (Nwokonkwo, 2008). High levels of heavy metals in soils could result in uptake by local and agronomic plants and leaching to ground and surface waters.

Sewage sludge application causes related problems like rise in injurious level of the heavy metal concentration in edible crops (Nwajei, 2005). Cadmium (II) can enter the food chain

via plant uptake (Nwajei, 2005). Natural waters are contaminated by lead through several activities in industries, which include battery, paint, metal plating, smelting, textiles, and plastics, amongst others (Opeolu et al., 2008). All foods contain varying amounts of lead and cadmium. Concentrations of lead and selenium in plants may produce subsequent toxic effects (Nwajei, 2005). Cadmium and lead are among the most highly toxic metals commonly found in most industrial wastewater. Lead has been implicated as one of the three highly harmful heavy metals, which exhibit latent prolonged negative effect on human health; thereby resulting in a number of diseases such as hepatitis, anaemia, nephritic syndrome, and encephalopathy (Deng et al., 2006). It can also lead to brain and bone damage (Mishra, 2014). Cadmium on the other hand endangers human health as it can cause so many health disorder including kidney damage, diarrhea, itai—ita disease, mucous membrane destruction, bone damage, and vomiting. It also influences the formation of progesterone and testosterone (Johannes et al., 2006). These and many other health problems associated with lead and cadmium prompted the choice of lead and cadmium in this study. There is need for the concentration of heavy metals in industrial effluents to be controlled within tolerable levels (Meena et al., 2008) before being discharged into sewage systems, water ways, or on land to avoid ecological pollution.

Several technologies are available in literature for the removal of heavy metals from industrial wastewater (Anand et al., 1985; Kim et al., 1985; Murphy and Erkey, 1997; Monser and Adhoum, 2002; Erdem et al., 2004; Golder et al., 2007; Lin et al., 2008; Yuan et al., 2008), which include coagulation/flocculation, adsorption, reverse osmosis, and biological treatment. Of all these techniques, adsorption is the most efficient and versatile for removal of heavy metal. (Agarwal et al., 2006). Most of the other methods are non-selective and not very effective in the face of low metal concentration in the effluent (Mishra, 2014). According to Kurniawan et al. (2006), adsorption can be defined as “a mass transfer process by which a substance is transferred from the liquid phase to the surface of a solid, and becomes bound by physical and/or chemical interaction.” Adsorption occurs by transport of adsorbates from the bulk fluid to the adjoining fluid-adsorbent interface by film diffusion of adsorbates through the laminar boundary layer surrounding the adsorbent particle. This is followed by surface reaction of the adsorbate reactants to the internal surface of the porous adsorbent to form adsorbed products (Nabi et al., 2015). Several works on the adsorption of heavy metals using activated carbon prepared from various low-cost precursors have been reported (Kumar, 2006). In addition, the potential of coal and coal fly ash as adsorbents has been investigated (Gangoli et al., 1975; Grover and Narayanaswamy, 1982; Yadera et al., 1987; Moreno-Castilla et al., 1994; Martyniuk and Wieckowska, 1997; Menkiti and Onukwuli, 2011). Various research works have similarly been conducted on the use of blended adsorbents for wastewater effluent treatment (Panday et al., 1984; Nordiana and Siti, 2013). Nordiana and Siti (2013) reported that a blend of activated charcoal and peanut shell was more efficient in adsorbing lead ions from aqueous solution than the individual adsorbents. Wang and Xing (2002) also reported that phosphate-modified goethite improved both

cadmium adsorption and adsorption process. Earlier studies have shown that adsorption efficiency increases with increase in carbonization temperature as well as the modification of the adsorbent with activating agents such as nitric acid (Kareem and Adisa, 2002), potassium permanganate (Muhammad et al., 2011), hydrochloric acid (Bada and Potgieter-Vermaak, 2008; Muhammad et al., 2011), hydrogen peroxide (Muhammad et al., 2011), and potassium hydroxide (Evboumwan et al., 2013).

Despite the fact, that much work has been done on adsorption of heavy metals, there is still need for further exploitation of this area (Mishra, 2014). The use of cost effective, readily available, and ecologically friendly materials should be encouraged. There is need for low cost adsorbents with improved adsorption capacity and having little or no harmful effect to the ecosystem or environment. To this end, the focus of heavy metal adsorption studies, as demonstrated in this work, has shifted to the sourcing of adsorbents from natural products that are readily available such as coal, and some environmentally friendly agricultural byproducts namely ogbono (*Irvingia gabonensis*) seed shell, coconut shell, palm kernel shell, walnut shell, and almond shell (Golder et al., 2007). Coal is formed after long time of degradation of plant material in the ground. Coal is classified as lignite, sub-bituminous, bituminous, and anthracite depending (in that order) on the age of degradation of the plant matter that formed the coal, and the carbon content. According to statistical survey, there are proven coal reserves in the following parts of Nigeria: Anambra coal basin, covering 1.5 million hectares; Benue district (Omkpa-Ezimo), 175,000 hectares; Kogi district, 225,000 hectares; Enugu district, 270,000 hectares; Inyi deposit, south of Enugu city; the Afikpo deposit, Lafia Obi deposit, the Gombe deposit, and the Asaba lignite deposit (Odesola et al., 2013). Coal has many industrial applications which include electricity generation, metallurgical extraction of metals, and chemicals production. Little has been reported on the use of Nigerian coal for the preparation of adsorbent (Ani et al., 2012).

This study aims at evaluating the adsorption potential of different types of coal namely lignite and sub-bituminous coal, and *Irvingia gabonensis* seed shell (IGSS), for cadmium and lead removal. The objectives include finding a simpler and more versatile method for surface modification of coal to improve its morphology and surface area for increased adsorption rate.

MATERIALS AND METHODS

Reagents and Instruments

Analytical grade of all the chemicals and reagents were used.

The instruments used include Mettler Toledo Seven compact pH meter, atomic absorption spectrometer (Buck Scientific, Model 210 VGP), Fourier transform infrared spectrophotometer (Model IRTracer-100 Shimadzu, Japan), electron scanning microscope (PHENOM PROX TESCAN, The Netherlands), and X-Ray fluorescence (Oxford Instruments, England). Others are heat treatment furnace (Kohaszati Gyarepito Vallat Budapest, type KCO-120), air-drying oven (BTOV 1423), Cisa cedacteria industrial electromagnetic Shaker (Model BA200N), digital water bath (Model DK600), Ohaus weighing balance (Model PA213), and a multifunctional oscillator.

Sampling/Sample Preparation

Lignite was obtained from Garinmaiganga mine in Gombe State, sub-bituminous coal from Okaba mine in Kogi State; *Irvingia gabonensis* seed shells were obtained from Obe in Nkanu-west local government area of Enugu State, all in Nigeria. The samples were thoroughly washed, to remove extraneous materials such as dirt, sand and other impurities, and subsequently dried, and milled to fine particle sizes. They were then carbonized separately in a muffle furnace (Kohaszati Gyarepito Vallat Budapest, type KCO-120) at different temperatures.

Preparation of Adsorbate Solution

The stock solutions of Cd(II) and Pb(II) ions of concentrations 1000 mg/L each were obtained by dissolving 2.03 g cadmium chloride, ($\text{CdCl}_2 \cdot 2\frac{1}{2}\text{H}_2\text{O}$) and 1.6 g lead nitrate, [$\text{Pb}(\text{NO}_3)_2$], respectively with distilled water in a 1000 mL standard flask and made up to mark. The solutions were then diluted to desired working concentrations with distilled water.

Preparation of Adsorbents

The adsorbents were prepared by carbonization of the raw materials. For the first stage of the experiments, lignite, and sub-bituminous coal were carbonized at 800°C. This was done by measuring 700 g each of the coals into separate clay pots. The pots were covered, with the edges between the pots and their lids sealed with clay to prevent penetration of air. The samples were put in a muffle furnace and carbonized at 800°C for 2 h, following the method of Scientific Equipment Development Institute (SEDI), Enugu, Nigeria. Lignite, being the sample that had better adsorption efficiency was used in the determination of the effect of batch adsorption parameters, and was carbonized at different temperatures (400–1100°C) for the determination of the effects of carbonization temperature.

Modification Using *Irvingia gabonensis* Seed Shell

Lignite carbonized at 400°C, which gave the optimum percent yield of 75%, was blended with IGSS biomass in equal proportion. The mixing of the seed shell with lignite was made to find out if blending coal with agricultural byproduct would improve adsorption performance.

Chemical Modification of Adsorbents

The adsorbents from lignite and its IGSS blend were chemically modified with 0.1 M of both NaOH and H_3PO_4 following the method of Argun and Dursun (2006). Twenty five grams of adsorbent was measured, washed severally with distilled water to remove particles sticking to the surface and any particle that could be soluble in water. The adsorbent was oven-dried at 85°C for 2 h. The sample was placed in a 500 mL conical flask containing 250 mL of the modifying reagent. It was then agitated at 200 rpm in a multifunctional oscillator for 4 h, left overnight and filtered to separate the adsorbent. The adsorbent was washed severally with distilled water to attain neutral pH. Finally, it was oven-dried at 85°C for 2 h and stored for use.

Characterization of Adsorbent

X-Ray Fluorescence Analysis

The X-Ray Fluorescence (XRF) characterization was performed to determine the chemical compositions of the raw materials.

Fourier Transform Infrared Analysis

Fourier transform infrared (FTIR) spectroscopic analysis was performed to give the vibration frequencies of the adsorbents lattice, which result from stretching of bending modes of the functional groups present in the activated carbon. The samples were examined in the range 400–4000 cm^{-1} . The analysis was done using KBr as background material.

Scanning Electron Microscopy

The morphology of the prepared adsorbents was studied by use of scanning electron microscope (SEM). Little amounts of the prepared adsorbent samples were first put on a circular disc-like structure in the scanning electron microscope. Specific tapes were used to attach the samples to the surface of the disc. The disc was then positioned in the electron chamber, and the electron gun releases a beam of electrons used for the scanning. As the electrons interact with the atoms, images of the surface topography is produced, and viewed on a monitor. In order to obtain a more quality image and appropriate clarity, the magnification of the scan was adjusted. The specific magnifications images were later saved.

Adsorption Experiments

Four grams of the adsorbents prepared separately from lignite, sub-bituminous coal, and IGSS-coal blend were introduced separately to 100 mL of 300 mg/L metal ion solution in a conical flask and agitated on the multifunctional oscillator set at 200 rpm for 2 h at room temperature. After adsorption was completed, the solution was filtered using Whatman No. 1 filter paper. The residual metal ion concentrations of the solution were determined by atomic absorption spectrophotometer. The adsorption capacity and efficiency were calculated using Equations (1, 2), respectively:

$$q_e = \frac{(C_i - C_e)V}{m} \quad (1)$$

$$\% \text{Adsorption} = \frac{C_i - C_t}{C_i} \times 100 \quad (2)$$

Where q_e is the amount of metal adsorbed at equilibrium (mg/g), m is the mass of adsorbent (g),

C_i and C_e are the initial and equilibrium concentrations of the metal ions (mg/L), while C_t is the concentration at time t (minutes).

Comparative adsorption experiment was carried out using adsorbents from lignite and sub-bituminous coal. Dosage of adsorbent from lignite was varied in the range 5–40 g/L to determine its effect on adsorption of the metal ions. The effect of pH on the adsorption was carried out by adjusting the metal solution pH from 4 to 10, using 0.1 M HCl and 0.1 M H_3PO_4 .

The effect of contact time on adsorption was determined by varying time of the process in the range 20–120 min. To study

the effect of temperature the flask was agitated at a temperature that is within the range of 30–65°C.

Carbonized unmodified lignite was used for adsorption at different particle sizes (250, 355, 500, 710, 850, and 1400 μm) to determine effect of particle size. The effect of initial metal ion concentration was determined by varying the adsorbate concentration from 100 to 350 mg/L.

RESULTS AND DISCUSSION

XRF, SEM, and FTIR Techniques

X-Ray Fluorescence Characterization

The XRF characterization was performed to obtain the chemical compositions of the raw materials (lignite, sub-bituminous coal, and *Irvingia gabonensis* seed shell). These are as given in **Table 1**. It could be observed that Al_2O_3 and SiO_2 are the key constituents of these materials. Fe_2O_3 is present in considerable amount, while Na_2O , MgO , P_2O_5 , K_2O , CaO , and TiO_2 are present in trace quantities. Hence Al_2O_3 , SiO_2 , and Fe_2O_3 might have contributed in the removal of Cd(II) and Pb(II) ions from the simulated waste water.

Scanning Electron Microscopy

The SEM images of the experimental adsorbents are shown in **Figure 1**. The adsorbents have irregular and porous surface structure, which is a characteristic of a potential adsorbent. The porous structure is an indication that physical adsorption has serious effect on the removal of the lead and cadmium ions from aqueous solution (Vafakhah et al., 2014). It is evident that the carbon particles have wide range of pore sizes. There appears to be accumulated deposits in the pores of the spent adsorbents probably due to adsorption of the metal ions onto the pores on the surface of the adsorbents.

Analyses of the FTIR Spectra

FTIR spectrum of carbonized unmodified lignite (CUL) is shown in **Figure 2A**. The figure indicates the presence of majorly carbonyl and hydroxyl groups, which constitute important adsorption centres. By comparing the FTIR spectrum of CUL and spent CUL (**Figures 2A,B**), changes in peaks were observed.

These changes may be due to interaction between the functional groups and metal ions because of adsorption or chemical reaction. The sharp peaks at 3567, 3676, 3690, 3751, 3649, 3821, 3712, 3736, 3858, and 3904 cm^{-1} were due to O-H stretching vibrations in alcohols and phenols. Whereas, the peaks at 3587, 3619, and 3629 cm^{-1} are assigned to oximes O-H stretching vibrations. There is absorption band at 2923 cm^{-1} present in the CUL, which can be attributed to the presence of aliphatic CH_3 . This band was observed in the spent CUL at 2950 cm^{-1} (**Figure 2B**). A peak is also observed at 2860 cm^{-1} in the CUL. The corresponding peak is observed at 2858 cm^{-1} in the spent CUL. These peaks are assigned to the aliphatic CH_2 group. The peaks 1734 and 1772 cm^{-1} are assigned to C=O stretching vibrations of aldehydes and ketones. The peak at 1697 is assigned to C=O stretching vibrations in α -amino acids whereas the peak at 1684 is due to the C=O stretching vibrations in α , β -unsaturated acids.

Most of these peaks are not seen in the FTIR spectra of the spent carbonized lignite used to remove cadmium (**Figure 2B**) and lead (**Figure 2C**). The reason for this could be the interaction between the functional groups and metal ions as a result of adsorption. This is an indication that binding of metal ions on the adsorbent took place.

The infrared spectrum of *Irvingia gabonensis* seed shell lignite blend (IGSSLB) is shown in **Figure 2D**. Analyses of FTIR spectra of IGSSLB revealed a sharp and high intensity at 2923 cm^{-1} ascribed to C-H stretching vibration of alkanes in the compound. The peak range that centres around 2362–1376 cm^{-1} characterize: O-H, N-H, and C-H stretching vibrations. Absorption signal at 722 cm^{-1} reveal the presence of aromatic C-H out of plane bend, skeletal C-C vibrations. The frequencies and the proposed assignments of vibrations are based on previous assignments.

Effect of Process Parameters on Batch

Adsorption

Effect of Carbonization Temperature

Figure 3A shows the effect of the carbonization temperature of unmodified lignite on Cd(II) and Pb(II) adsorption from aqueous solutions. The adsorption of both Cd(II) and Pb(II) ions by CUL increased with increase in carbonization temperature until the adsorption reached 100%. This can be as a result of the increased adsorption properties of the adsorbents at higher temperatures as more volatile matter is released at the higher temperatures allowing for the creation of more pores unto which more metal ions are adsorbed. The Cd(II) adsorption was more gradual before peaking at 100%. Ozer et al. (1998) has reported a similar trend for the adsorption of cadmium on activated carbon from sugar beet pulp. Also, **Figure 3A** shows that Pb(II) ions adsorption was faster to reach the peak of 100% and remained constant. Thus, it was shown that Pb(II) was more preferentially adsorbed than Cd(II). Similar result has been reported by Kongsuwan et al. (2006).

Effect of Adsorbent Dosage and Contact Time

The dependence of Cd(II) and Pb(II) adsorption on adsorbent dosage was determined by varying the amount of adsorbents

TABLE 1 | XRF Results of lignite, sub-bituminous coal, and *Irvingia gabonensis* seed shell.

Chemical constituent	Raw material composition (Wt %)		
	Lignite	SBC	IGSS
Na_2O	1.979	2.835	2.842
MgO	2.235	1.164	1.726
Al_2O_3	19.475	19.686	20.374
SiO_2	17.408	17.467	11.520
P_2O_5	1.100	1.105	1.681
K_2O	0.266	0.285	3.000
CaO	4.704	0.665	2.356
TiO_2	0.773	0.852	0.596
Fe_2O_3	6.278	5.986	6.503

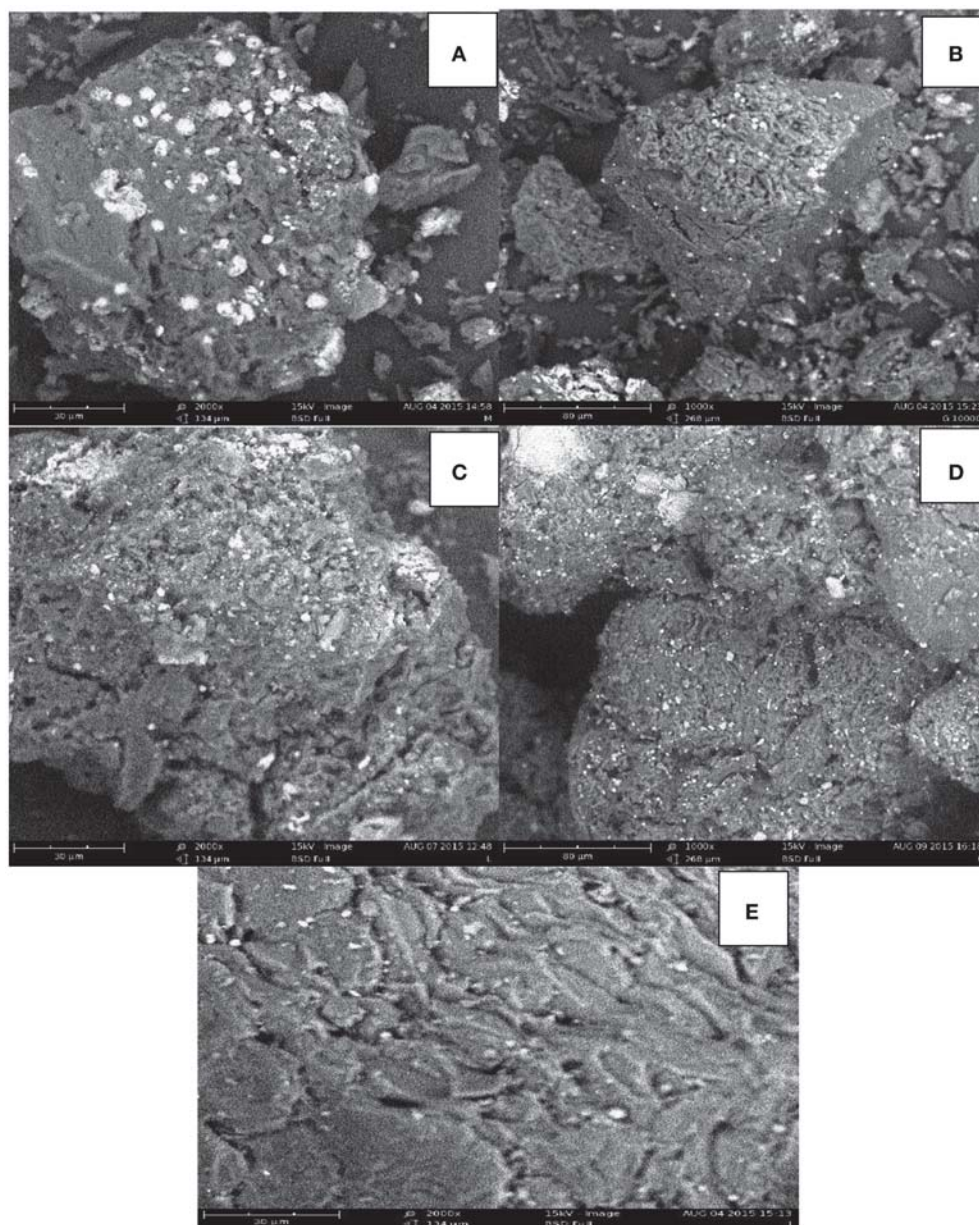
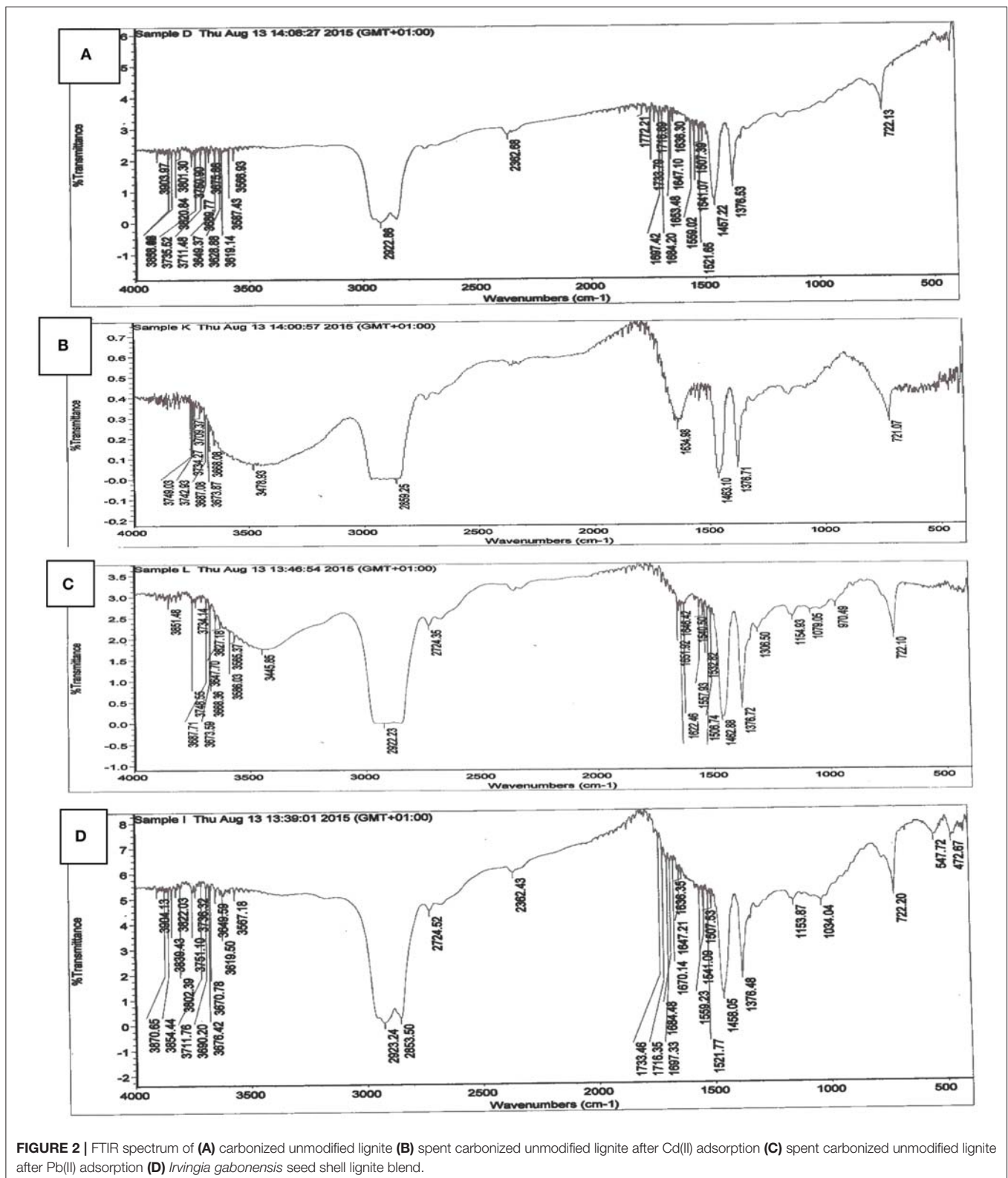


FIGURE 1 | SEM images of (A) carbonized unmodified sub-bituminous coal (B) carbonized unmodified lignite (C) spent carbonized unmodified lignite after Cd(II) adsorption (D) spent carbonized unmodified lignite after Pb(II) adsorption (E) *Irvingia gabonensis* seed shell lignite blend.

from 5 to 40 g/L, while keeping other parameters constant. **Figure 3B** shows the adsorption of Cd(II) and Pb(II) efficiencies for the different dosages used. It can be observed that in general, adsorption efficiencies of the adsorbent increased with increase in dosage. The percentage removal of Pb(II) increased from 99.87% at adsorbent dosage of 5 g/L to 100% at adsorbent dosage of 20 g/L, and remained constant till 40 g/L adsorbent dosage. For Cd(II), percentage adsorption increased from 74.17% at 5 g/L to 99.70% at 40 g/L. The increased adsorption pattern for both metal ions could be attributed to higher number of available adsorption sites as dosage increases. This agrees with

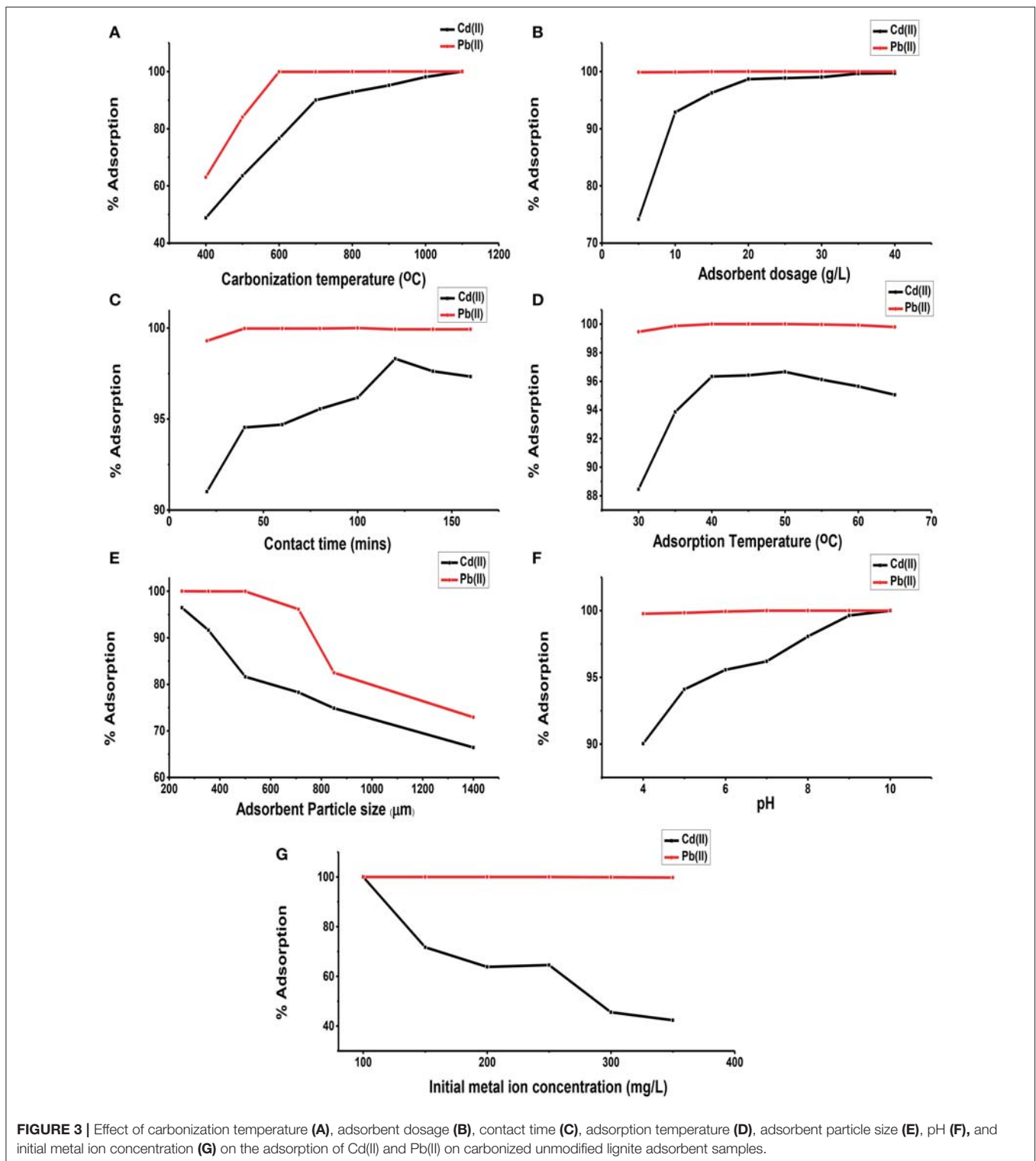
the observations by Kumar et al. (2012) and Gala and Sanak-Rydlewska (2011).

In order to determine the time required for equilibrium adsorption of metal ions, the effect of contact time on the adsorption of Cd(II) and Pb(II) ions from aqueous solution on the surface of CUL was investigated over a period of time. In all the cases, increased adsorption of metals with increasing contact time was observed until equilibrium, after which there was slight decrease in efficiency, as shown in **Figure 3C**. For Cd(II) ion, equilibrium was reached at 120 min at 98.31%. Afterwards the adsorption efficiencies decreased to



97.63 and 97.33% at 140 and 160 min respectively. However, for the Pb(II) ion, adsorption increased from 99.30 to 99.97% at the early stage, remained constant until peaking at 100 min

at 100% before dropping to 99.93% at 120 min and then remaining constant. This phenomenon can be due to the fact that, initially, all the active sites on the CUL were



vacant and were used for initial adsorption; subsequently, as time increased, the adsorption rate of metal ions became constant at equilibrium due to saturation of active sites in agreement with a work reported elsewhere (Meitei and Prasad, 2013).

Effect of Adsorption Temperature

Figure 3D shows the effect of solution temperature on the adsorption of Cd(II) and Pb(II) ions on carbonized unmodified lignite. As shown in Figure 3D, efficiency of Cd(II) increased from 88.45% at 30°C to 96.67% at 50°C. Beyond 50°C, it

decreased. The same trend was observed in the adsorption of Pb(II) on CUL. Similar results have been reported elsewhere (García-Rosales and Colín-Cruz, 2010; Park et al., 2010; Giri et al., 2012). The increase in adsorption of Cd(II) and Pb(II) ions on carbonized unmodified lignite with the increase in temperature showed that the adsorption process is endothermic, which may be due to the higher rate of diffusion of the cations onto the adsorbent's particle surface at moderately higher temperatures. The high surface diffusion is due to the higher random motion of the adsorbates, resulting from the rise in thermal energy. As the temperatures were increased beyond the optimum values [50°C for Cd(II) and 40°C for Pb(II)], the adsorbent surface might decompose leading to reduced adsorption capacity as explained by Nabi et al. (2015). **Table 2** gives the thermodynamic data (plot not shown) of the adsorption of Cd(II) by carbonized unmodified lignite. The Gibbs free energy change (ΔG) increased with increase in temperature. The positive values of the enthalpy change (ΔH) and (ΔG) indicate that the process is endothermic and thermodynamically non-spontaneous. The value of ΔH (**Table 2**) is +1027.78 J/mol indicating chemical adsorption. The reason that the adsorption process involves a decrease in entropy might be because a molecule in solution has more freedom of motion than one that is attached to a surface which implies decreased disorderliness on the adsorbent surface.

Effect of Adsorbent Particle Size

The influence of particle size of CUL on the adsorption of Cd(II) and Pb(II) ions from aqueous solution is shown in **Figure 3E**. For Cd, adsorption efficiency was highest (96.43%) at 250 μm , being the least particle size, while the lowest efficiency (66.43%) was recorded at 1400 μm , being the largest particle size. Also for Pb, at 250 μm adsorption efficiency was 100%, while at 1400 μm , it became 72.92%. A close observation of the results shows that efficiency is inversely related to particle size. As the particle size decreased, both surface area and adsorption efficiency of the adsorbent increased. Therefore, a decrease in adsorption with increasing particle size is due to a decrease in the surface area of the adsorbent, consistent with results reported by other authors (Badmus et al., 2007; Ozer et al., 2007; Kannan and Veemaraj, 2010; Banerjee et al., 2012; Kelly-Vargas et al., 2012; Barka et al., 2013).

TABLE 2 | Thermodynamic data for adsorption of Cd(II) by carbonized unmodified lignite.

Temperature (K)	ΔG (J/mol)
303	4,318.36
308	4,372.66
313	4,426.96
318	4,481.26
323	4,535.56
328	4,589.86
333	4,644.16
338	4,698.46
ΔH (J/mol)	$-\Delta S$ (J/mol K)
1027.78	10.86

Effect of Adsorption Solution pH

The pH of the solution has a considerable effect on the removal of heavy metals from aqueous solutions, because the surface charge of the adsorbent and the degree of ionization and speciation of the adsorbate are controlled by pH (Park et al., 2010). **Figure 3F** shows the effect of pH on the adsorption of Cd(II) and Pb(II) ions. The adsorption of Cd(II) was from under 90% while that of Pb(II) ions was from above 99%. The optimum adsorption for Cd(II) was at pH 10 while that of Pb(II) was at pH 6.5. However, percentage adsorption increased as pH increased. This could be attributed to the fact that as the pH of solution increases, the adsorptive removal of cationic metals increases, whereas that of anions decreases. At lower pH, the overall surface charge of the adsorbent may be positive. The H^+ ions competed effectively with the Cd(II) and Pb(II) ions, causing a decrease in adsorption capacity. When pH values were increased, the CUL surface became increasingly negatively charged, which favoured the removal of metal ions as a result of electrostatic interaction. This is similar to the observations made by Njoku et al. (2011) and Taha et al. (2011).

The differential removal of the two ions may be attributed to the difference in their ionic radius. It has been shown that the smaller the ionic radius or area, the greater is its tendency to be hydrolyzed leading to reduced sorption (Horsfall and Spiff, 2005).

Effect of Initial Metal Ion Concentration and Adsorbent Modification

Figure 3G shows that increase in the initial metal concentration led to a decrease in removal efficiency. There was 100% removal of Pb(II) ions at concentrations 100–250 mg/L, whereas at concentrations 300 and 350 mg/L adsorption of 99.83 and 99.76% were respectively obtained. However, in the adsorption of Cd(II), there was a proportionate decrease in removal efficiency as the initial metal concentrations were increased. This observation could be due to the saturation of adsorption sites on CUL surface. This is in agreement with the results reported by previous workers (Boota et al., 2009; Kannan and Veemaraj, 2010; Sahmoune et al., 2011; Taha et al., 2011; Kumar et al., 2012). By applying 300 mg/L initial concentration (C_i) of the metal ions (Cd and Pb) adsorption, 100% removal was recorded for each. However, when the concentrations were increased to 400 mg/L for ions (Cd and Pb), 80.93 and 87.85% removal were respectively obtained. Thus, carbonized unmodified lignite is a potentially good adsorbent for the removal of Cd and Pb ions from aqueous solution. Adsorption of Cd(II) and Pb(II) ions on adsorbent from lignite and sub-bituminous coal were compared at initial metals [Cd(II) and Pb(II)] concentration of 1000 mg/L. The adsorption for Pb(II) was 192 mg/L (19.2%) and 294.90 mg/L (29.49%) on sub-bituminous coal and lignite respectively. On the other hand, amount adsorbed for Cd(II) was 142.85 mg/L (14.29%) and 268.00 (26.80%) on sub-bituminous coal and lignite respectively. It could be observed that the amount adsorbed for all was not up to 300 mg/L. As a result, 300 mg/L was chosen as the working concentration for subsequent experiments, lignite on the other hand was used having more adsorption capacity than sub-bituminous coal.

Blends of coal were prepared by mixing lignite carbonized at 400°C with *Irvingia gabonensis* seed shell, NaOH and H₃PO₄ in order to achieve improved adsorption efficiency. **Table 2** presents how various modifications of the carbonized lignite affected the adsorption efficiencies of the adsorbent. Upon modification of the CUL, the performance was significantly improved. For example, in Cd(II) adsorption, the sodium hydroxide and phosphoric acid modified lignite (SHML and PAML) increased adsorption efficiencies from 48.8 to 64.17% and 63.70% respectively. The Pb(II) adsorption was similarly enhanced due to the chemical modification (using NaOH and H₃PO₄) of the adsorbents.

In a work, Argun and Dursun (2006) made similar observations. There was also a similar trend of increased adsorption efficiencies with the blended derivatives namely *Irvingia gabonensis* seed shell lignite blend (IGSSLB), phosphoric acid modified *Irvingia gabonensis* seed shell lignite blend (PAMIGSSLB) and sodium hydroxide modified *Irvingia gabonensis* seed shell lignite blend (SHMIGSSLB) as given in **Table 3**. However, adsorbents modified with NaOH had better efficiencies than those modified with H₃PO₄. Highest efficiency was obtained with sodium hydroxide modified SHMIGSSLB.

Adsorption Isotherm Studies

Some routinely used adsorption isotherm models were applied to describe the adsorption mechanism involving carbonized unmodified lignite. The experimental data at 25°C were fitted into the following linear adsorption isotherm equations representing the selected isotherm models:

$$\left(\frac{C_e}{q_e}\right) = \left(\frac{1}{K_L q_m}\right) + \left(\frac{C_e}{q_m}\right) \quad (3)$$

$$\ln q_e = \ln K_f + \frac{1}{n} \ln C_e \quad (4)$$

$$q_e = B_T \ln A_T + B_T \ln C_e \quad (5)$$

where Equations (3–5) represent Langmuir, Freundlich, and Temkin adsorption isotherms. Symbols contained in the adsorption isotherm equations are: the maximum monolayer adsorption capacity (q_m), and adsorption constants (K_L , K_f , B_T , A_T , and $1/n$).

The equilibrium isotherm parameters for this study were obtained from the slopes and intercepts of Equations (3–5) generated from their respective plots (**Figure 4**) and given in **Table 4**. The values of the maximum monolayer adsorption capacity of the adsorbent (q_m) and the Langmuir adsorption equilibrium constant (K_L) can be determined from the intercept and slope respectively of the linear plot of $\left(\frac{C_e}{q_e}\right)$ vs. C_e . The Linearized Langmuir adsorption isotherm was developed with slope, intercept and regression coefficients equal 0.268, 1.660, and 0.984 respectively for Cd(II), and 1.696, -0.018, and 1.000 respectively for Pb(II). The Langmuir constants were calculated from intercept and slope [$q_m = 3.731$ (mg/g) (Cd), 0.590 (mg/g) (Pb) and $K_L = 0.162$ L/mg (Cd), -94.162 L/mg (Pb)].

The values of K_f [Freundlich constant related to adsorption (mg/g)] and $1/n$ (Freundlich constant related to the intensity of adsorption) can be determined from the intercept and slope, respectively, of linear plot of $\ln q_e$ vs. $\ln C_e$. The linearized Freundlich adsorption isotherm was developed with slope, intercept and regression coefficients equal to 0.074, 0.884, and 0.613 respectively for Cd(II), and 0.917, 1.509, and 0.300 respectively for Pb(II). The Freundlich constants were calculated from intercept and slope [$K_f = 7.656$ L/g (Cd), 32.285 L/g (Pb), and $1/n = 0.074$ (Cd), 0.197 (Pb)]. Freundlich constant $1/n$ was < 1 in both Cd and Pb adsorption, indicating that the adsorbent surface is heterogeneous.

The values of B_T [constant related to the heat of adsorption (mg/g)] and A_T [Temkin isotherm constant (L/g)] can be determined from the intercept and slope, respectively, of linear plot of q_e vs. $\ln C_e$. The linearized Temkin adsorption isotherm was developed with slope, intercept, and regression coefficients equal 0.225, 2.396, and 0.559 respectively for Cd(II), and 4.855, 4.908, and 0.334 respectively for Pb(II). The Temkin constants were calculated from intercept and slope [$B_T = 0.225$ mg/g (Cd), 4.885 mg/g (Pb), and $A_T = 4.46 \times 10^{10}$ L/g (Cd), 10.255 L/g (Pb)].

Because the regression coefficients (R^2) for the Langmuir, Freundlich, and Temkin isotherms are (Cd): 0.984, 0.613, and 0.559, and (Pb): 0.992, 0.300, and 0.334 respectively, it appears that the Langmuir isotherm correlates the adsorption data better than the other isotherms. This phenomenon suggests that the adsorption process may be attributed to a monolayer adsorption. The R_L (Langmuir isotherm separation factor) values obtained for Cd(II) and Pb(II) ions respectively, are 1.7×10^{-2} and 3.03

TABLE 3 | Effect of adsorbent modification on Cd(II) and Pb(II) Adsorption [C_i of Cd(II) and Pb(II) = 300 mg/L].

Sample	C_e (mg/L)		q_e (mg/g)		% Adsorption		Surface area (m ² /g)	
	Cd	Pb	Cd	Pb	Cd	Pb	Cd	Pb
CUL (400°C)	153.60	111.0	3.66	4.73	48.80	63.00	805.80	865.80
PAML	108.90	47.0	4.78	6.33	63.79	84.30	857.30	887.30
SHML	107.50	46.2	4.81	6.35	64.17	84.60	888.90	888.90
IG SSLB	106.30	45.5	4.84	6.36	64.57	84.83	889.40	888.10
PAMIGSSLB	82.90	10.3	5.43	7.24	72.37	96.57	893.90	890.50
SHMIGSSLB	80.00	10.0	5.50	7.25	73.33	96.67	895.70	891.90

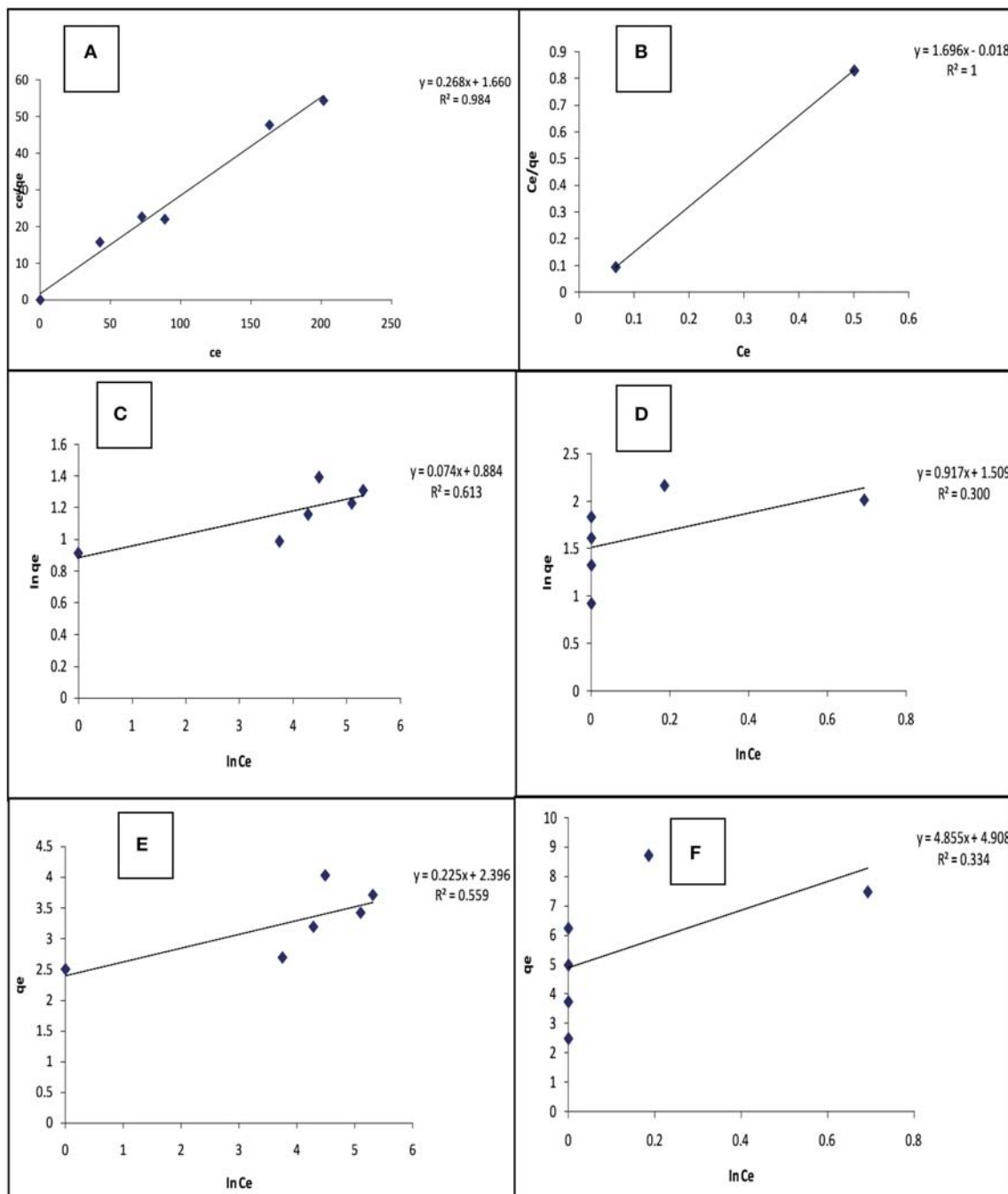


FIGURE 4 | Langmuir (A,B); Freundlich (C,D); and Temkin (E,F) isotherms for the adsorption of Cd(II) and Pb(II) respectively, on carbonized unmodified lignite at 25°C.

$\times 10^{-5}$ suggesting that the adsorption of the metals unto the adsorbent surface was favourable ($0 < R_L < 1$). (Jumina et al., 2007) defined R_L as:

$$R_L = 1/(1 + KC_o) \quad (6)$$

where K is the adsorption constant and C_o is the initial concentration of adsorbate (g/L). Further, the lower the value of R_L is indicative of a more favourable adsorption.

Adsorption Kinetics

Adsorption kinetics study was performed by varying time of the process for Cd(II) and Pb(II) ions removal using carbonized unmodified lignite, in the range 20–120 min. In all the cases, increased adsorption of metals with increasing contact time was observed until equilibrium, after which there was slight decrease in efficiency, as shown in **Figure 3C**. The adsorption got to equilibrium because at

TABLE 4 | Adsorption isotherm data for carbonized unmodified lignite at 25°C.

Isotherm Model	Cd(II)	Pb(II)
LANGMUIR		
q_m (mg/g)	3.731	0.590
K_L (L/mg)	0.162	-94.162
R^2	0.984	0.992
R_L	0.017	0.0000303
FREUNDLICH		
K_f (L/g)	7.656	32.285
$1/n$	0.074	0.197
R^2	0.613	0.300
TEMKIN		
A_T (L/g)	4.46×10^{10}	10.255
B_T (mg/g)	0.225	4.855
R^2	0.559	0.334

that point the metals could not be removed anymore by the adsorbent.

The kinetic data obtained for the adsorption of Cd(II) and Pb(II) ions are fitted by pseudo first-order kinetic model, pseudo second-order kinetic model, and intra-particle diffusion model represented by Equations (6–8), respectively.

$$\ln(q_e - q_t) = \ln q_e - k_1 t \quad (7)$$

$$\frac{t}{q_t} = \frac{1}{k_2 q_e^2} + \frac{t}{q_e} \quad (8)$$

$$q_t = k_i t^{0.5} + I \quad (9)$$

The adsorption kinetic parameters for the present study were obtained from the slopes and intercepts of Equations (6–8)

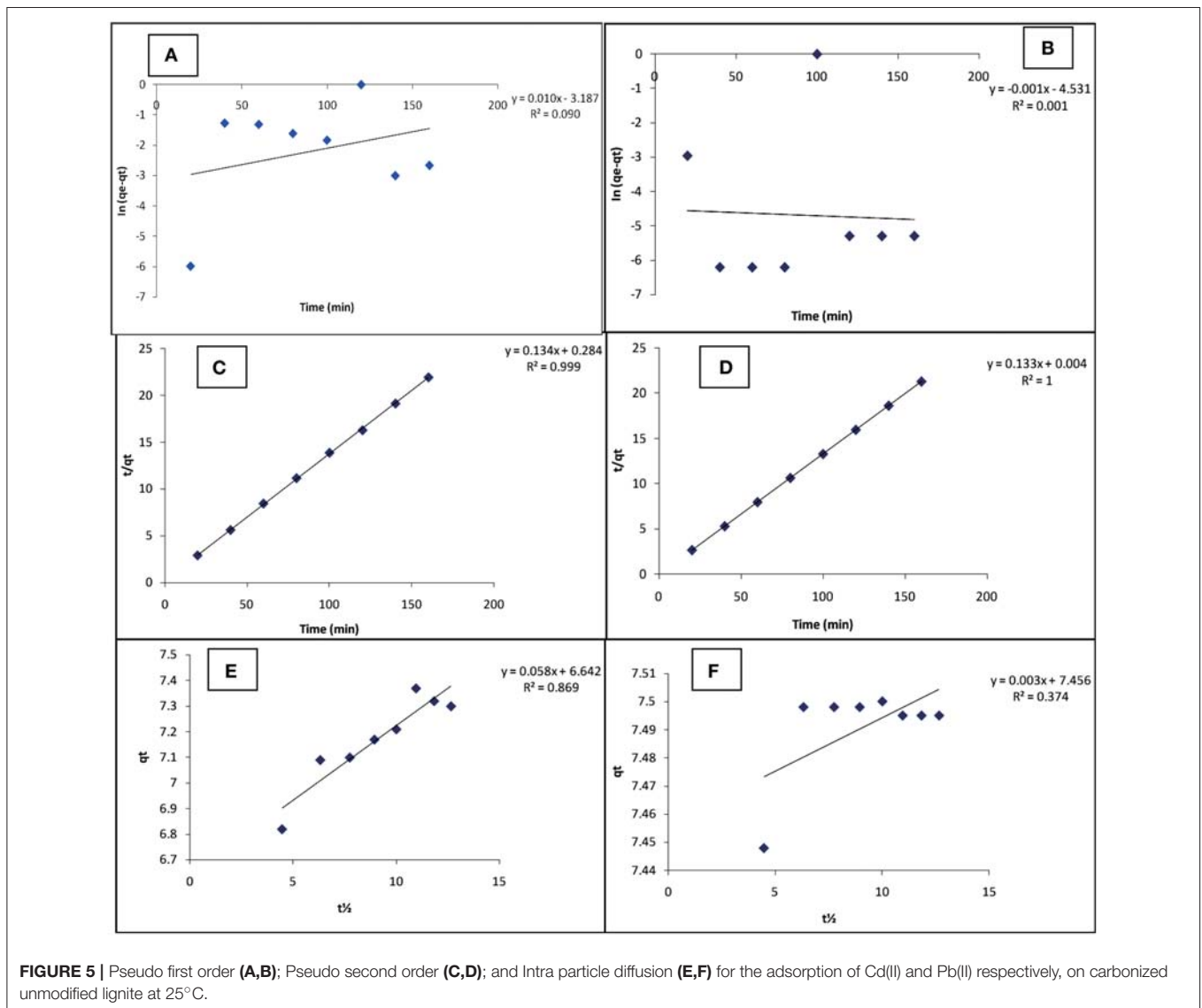


FIGURE 5 | Pseudo first order (A,B); Pseudo second order (C,D); and Intra particle diffusion (E,F) for the adsorption of Cd(II) and Pb(II) respectively, on carbonized unmodified lignite at 25°C.

TABLE 5 | Chemical kinetic data of carbonized unmodified lignite at 25°C.

Model/Parameters	Cd(II)	Pb(II)
PFO		
$q_{e,cal.}$ (mg/g)	6.5×10^{-4}	2.94×10^{-5}
k_1 (/min)	2.303×10^{-2}	-2.3×10^{-3}
R^2	0.090	0.001
$q_{e,exp.}$ (mg/g)	7.37	7.50
PSO		
$q_{e,cal.}$ (mg/g)	7.46	7.52
k_2 (g/mg min)	6.33×10^{-2}	4.42
R^2	0.999	1
$q_{e,exp.}$ (mg/g)	7.37	7.50
IPD		
K_d (mg/g min ^{1/2})	0.058	0.003
C	6.642	7.456
R^2	0.869	0.374

generated from their respective plots (Figure 5) and given in Table 5. The values of the calculated equilibrium adsorption capacity (q_e) and the rate constant for pseudo first-order model (k_1) can be determined from the intercept and slope respectively of the linear plot of $\ln(q_e - q_t)$ vs. t (min). The pseudo first-order kinetic model was developed with slope, intercept and regression coefficients equal 0.010, -3.187, and 0.090 respectively for Cd(II), and -0.001, -4.531, and 0.001 respectively for Pb(II). The pseudo first-order parameters were calculated from intercept and slope [$q_e = 6.5 \times 10^{-4}$ (mg/g) (Cd), 2.94×10^{-4} (mg/g) (Pb) and $k_1 = 2.303 \times 10^{-2}$ /min (Cd), -2.300×10^{-3} /min (Pb)].

The values of the calculated equilibrium adsorption capacity (q_e) and the rate constant for pseudo second-order model (k_2) can be determined from the intercept and slope respectively of the linear plot of $\frac{t}{q_t}$ vs. t (min). The pseudo second-order kinetic model was developed with slope, intercept and regression coefficients equal 0.134, 0.284, and 0.999 respectively for Cd(II), and 0.133, 0.004, and 1.000 respectively for Pb(II). The pseudo second-order parameters were calculated from intercept and slope [$q_e = 7.46$ (mg/g) (Cd), 7.52 (mg/g) (Pb), and $k_2 = 6.33 \times 10^{-2}$ g/mg min (Cd), 4.42 g/mg min (Pb)].

The regression coefficient (R^2) values of the adsorption process (Table 4) indicated better agreement with the pseudo-second order (PSO) model [0.999 (Cd) and 1.000 (Pb)] than the pseudo-first order (PFO) model [0.090 (Cd), 0.001 (Pb)], for the metal ions removal. In addition, the calculated equilibrium adsorption capacity ($q_{e,cal.}$) values for both metals [7.46 (mg/g) (Cd) and 7.52 (mg/g) (Pb)] are quite close to the experimental equilibrium adsorption capacity ($q_{e,exp.}$) values (7.37 (mg/g) (Cd) and 7.50 (mg/g) (Pb)) in the pseudo-second order model, suggesting that adsorption followed the pseudo-second order model. The calculated q_e [6.5×10^{-4} (mg/g) (Cd) and 2.94×10^{-5} (mg/g) (Pb)] and the experimental q_e values are wide apart in the pseudo-first order model. The rate constant (k_2) values for PSO are significantly higher than those (k_1 values) for PFO which further supports that the adsorption favours the pseudo second-order kinetic model.

The kinetic data was further analyzed with the intra-particle diffusion (IPD) model. A linear plot of q_t vs. $t^{1/2}$ was used

to obtain the constants K_d and C. Intra-particle diffusion is the sole rate-controlling step if the plot is linear and passes through the origin ($C=0$). The R^2 value obtained for the two metal ions indicates the existence of an intra-particle diffusion mechanism, more in Cd(II) ion (0.869) removal than in Pb(II) ion (0.374) adsorption, although it is not the sole rate-controlling step ($C \neq 0$). Occurrence of the intercept C shows the existence of a boundary layer effect, indicating a surface phenomenon such as mass transfer or liquid film diffusion in the adsorption process.

CONCLUSIONS

In this work, lignite and sub-bituminous coal with blends and modifications were explored as precursors for the removal of toxic pollutants from wastewater effluents. Lignite was found to be more efficient than sub-bituminous coal in the adsorption of Cd(II) and Pb(II) from aqueous media. The carbonized unmodified lignite was found to perform optimally at pH 10, contact time 120 min, adsorption temperature 50°C, adsorbent particle size of 250 μ m and dosage of 40 g/L. FTIR showed that hydroxyl and carbonyl groups may be the major functional groups responsible for the binding of the metal ions on the prepared adsorbents. X-ray refractive fluorescence showed that Al_2O_3 and SiO_2 were the major constituents of the prepared adsorbents. Lignite and *Irvingia gabonensis* seed shell performed better when modified with NaOH and H_3PO_4 . For Cd(II) adsorption efficiency, the sodium hydroxide and phosphoric acid modified lignite (SHML and PAML) improved efficiencies were from 48.8% (lignite) to 64.17% and 63.70% respectively. Similar improvements were observed with Pb(II) ions from 63% (lignite) to 84.30% and 84.60% respectively. The analysis of the adsorption isotherms for Cd(II) and Pb(II) show the R^2 to be 0.984 and 0.992 favouring the Langmuir isotherm and thus a monolayer adsorption for both metals. The kinetics of adsorption was better described by pseudo-second order than pseudo-first order model.

AUTHOR CONTRIBUTIONS

ME organized the research problem on the effect of coal ranks and coal biomass blends on the removal of cadmium and lead from aqueous solution and made some scientific inputs on interpretation of the results, and participated in writing the manuscript. OO conducted the experimental work on the preparation of the adsorbent and batch adsorption tests, and participated in writing the manuscript. JA conceived theoretical inputs on process parameters affecting batch adsorption of cadmium (II) and lead (II) ions from aqueous solution, and participated in writing the manuscript.

ACKNOWLEDGMENTS

The laboratory assistance given by some technical staff of Projects Development Institute, Enugu, Nigeria is hereby acknowledged. We thank Mr. I. O. Obi of Energy Centre Research and Development, University of Nigeria, Nsukka, for contributing in the collection of some useful data and proofreading the manuscript.

REFERENCES

- Agarwal, G. S., Bhuptawat, H. K., and Chaudhari, S. (2006). Biosorption of aqueous chromium (VI) by *Tamarindus indica* seeds. *Bioresour. Technol.* 97, 949–956. doi: 10.1016/j.biortech.2005.04.030
- Anand, P., Etzel, J. E., and Friedlaender, F. J. (1985). Heavy-metals removal by high gradient magnetic separation. *IEEE Trans. Magn.* 21, 2062–2064. doi: 10.1109/TMAG.1985.1064013
- Ani, J. U., Nnaji, N. J., Okoye, C. O., and Onukwuli, O. D. (2012). Factorial analyses, equilibrium studies, kinetics and thermodynamics of the removal of suspended particles from an industrial effluent on coal based activated carbon. *Int. J. Chem. Sci.* 10, 1765–1784.
- Argun, M. E., and Dursun, S. (2006). Removal of heavy metal using chemically modified adsorbents. *J. Int. Environ. Appl. Sci.* 1, 27–40.
- Argun, M. E., and Dursun, S. (2008). A new approach to modification of natural adsorbent for heavy metal adsorption. *Bioresour. Technol.* 99, 2516–2527. doi: 10.1016/j.biortech.2007.04.037
- Bada, S. O., and Potgieter-Vermaak, S. (2008). Evaluation and treatment of coal fly ash for adsorption application. *Leonardo El J. Pract. Technol.* 12, 37–48.
- Badmus, M. A., Audu, T. O., and Anyata, B. U. (2007). Removal of lead ion from industrial wastewaters by activated carbon prepared from periwinkle shells. *Turkish J. Eng. Environ. Sci.* 31, 251–263.
- Banerjee, K., Ramesh, S. T., Nidheesh, P. V., and Bharathi, K. S. (2012). A novel agricultural waste adsorbent, water melon shell for the removal of copper from aqueous solutions. *Iran. J. Energy Environ.* 3, 143–156.
- Barka, N., Abdennour, M., El-Makhfoute, M., and Qourzal, S. (2013). Biosorption characteristics of cadmium and lead onto eco-friendly dried cactus cladodes. *J. Environ. Chem. Eng.* 1, 144–149. doi: 10.1016/j.jece.2013.04.008
- Boota, R., Bhatti, H. N., and Hanif, M. A. (2009). Removal of Cu(II) and Zn(II) using lignocellulosic fiber derived from *Citrus reticulata* (Kinnow) waste biomass. *Sep Pur Technol.* 44, 4000–4022. doi: 10.1080/01496390903183196
- Deng, L., Su, H., Wang, X., and Zhu, X. (2006). Biosorption of copper (II) and lead (II) from aqueous solutions by non-living green algae *Cladophora fascicularis*: equilibrium, kinetics and environmental effects. *Adsorption* 2, 267–277. doi: 10.1007/s10450-006-0503-y
- Erdem, E., Karapinar, N., and Donat, R. (2004). The removal of heavy metal cations by natural zeolites. *J. Colloid Interface Sci.* 280, 309–314. doi: 10.1016/j.jcis.2004.08.028
- Evbuomwan, B. O., Abutu, A. S., and Ezeh, C. P. (2013). The effect of carbonisation temperature on some physiochemical properties of bamboo based activated carbon by potassium hydroxide (KOH) activated. *Greener J. Phys. Sci.* 3, 187–191.
- Gala, A., and Sanak-Rydlowska, S. A. (2011). Comparison of Pb (II) sorption from aqueous solutions on walnut shells and plum stones. *Pol. J. Environ. Stud.* 20, 877–883.
- Gangoli, N., Markey, P. C., and Thodos, G. (1975). “Removal of heavy metal ions from aqueous solution with fly ash,” in *Paper Presented at: Second National Conference on Complete Water Reuse* (Chicago, IL).
- García-Rosales, G., and Colín-Cruz, A. (2010). Biosorption of lead by maize (*Zea mays*) stalk sponge. *J. Environ. Manage.* 91, 2079–2086. doi: 10.1016/j.jenvman.2010.06.004
- Giri, A. K., Patel, R., and Mandal, S. (2012). Removal of Cr (VI) from aqueous solution by *Eichhorniacrassipes* root biomass-derived activated carbon. *Chem. Eng. J.* 185–186, 71–81. doi: 10.1016/j.jece.2012.01.025
- Golder, A. K., Chanda, A. K., Samanta, A. N., and Ray, S. (2007). Removal of Cr (VI) from aqueous solution: electro coagulation vs chemical coagulation. *Sep Pur Tech.* 42, 2177–2193. doi: 10.1080/01496390701446464
- Grover, M., and Narayanaswamy, M. S. (1982). Removal of hexavalent chromium by adsorption on fly ash. *J. Inst. Eng.* 63, 36–39.
- Horsfall, M., and Spiff, A. L. (2005). Effect of ion concentration on the biosorption of Pb²⁺ and Cd²⁺ by *Caladium bicolor* (wild cocoyam). *Afr. J. Biotechnol.* 4, 19–196.
- Johannes, F. S., Grosse-Siestrup, C., Esche, V., Brandenburg, P., Reich, A., and Groneberg, D. A. (2006). The toxicity of cadmium and resulting hazards for human health. *J. Occup. Med. Toxicol.* 1, 1–6. doi: 10.1186/1745-6673-1-1
- Jumina, R., Eko, S., Brajna, P., Ika, H., and Dwi, S. (2007). Adsorption Characteristics of Pb(II) and Cr(III) onto C-4-Methoxyphenylcalix[4]resorcinane in Batch and Fixed Bed Column Systems. *J. Chinese Chem. Soc.* 54, 1167–1178. doi: 10.1002/jccs.200700167
- Kannan, N., and Veemaraj, T. (2010). Batch adsorption dynamics and equilibrium studies for the removal of Cd (II) ions from aqueous solution using jack fruit seed and commercial activated carbons – a comparative study. *Electron. J. Environ. Agric. Food Chem.* 9, 327–336.
- Kareem, S. A., and Adisa, A. I. (2002). Effect of carbonisation temperature on activated carbon adsorption properties in aqueous media. *Nigeria J. Appl. Sci.* 17, 1302–1308.
- Kelly-Vargas, K., Cerro-Lopez, M., Reyna-Tellez, S., Bandala, E. R., and Sanchez-Salas, J. L. (2012). Biosorption of heavy metals in polluted water using different waste fruit cortex. *Phys. Chem. Earth* 37, 26–29. doi: 10.1016/j.pce.2011.03.006
- Kim, H., Baek, K., Kim, B. K., Shin, H. J., and Yang, J. W. (1985). Removal characteristics of metal cations and their mixtures using micellar-enhanced ultrafiltration. *Korean J. Chem. Eng.* 25, 232–258.
- Kongsuwan, A., Patnukao, P., and Pavasant, P. (2006). “Removal of metal ion from synthetic waste water by activated carbon from *Eucalyptus camaldulensis* dehn bark,” in *Conference Paper on Sustainable Energy and Environment* (Bangkok), 1–9.
- Kumar, P. S., Ramalingam, S., Sathyaselvabala, V., Kirupha, S. D., Murugesan, A., and Sivanesan, S. (2012). Removal of Cd (II) from aqueous solution by agricultural waste cashew nut shell. *Korean J. Chem. Eng.* 29, 756–768. doi: 10.1007/s11814-011-0259-2
- Kumar, U. (2006). Agricultural products and by-products as a low cost adsorbent for heavy metal removal from water and wastewater: a review. *Acad. J.* 1, 33–37.
- Kurniawan, T. A., Chan, G. Y., Lo, W. H., and Babel, S. (2006). Physico-chemical treatment techniques for wastewater laden with heavy metals. *Chem. Eng. J.* 118, 83–98. doi: 10.1016/j.jcej.2006.01.015
- Lin, L. C., Li, J. K., and Juang, R. S. (2008). Removal of Cu(II) and Ni(II) from aqueous solutions using batch and fixed-bed ion exchange processes. *Desalination* 225, 249–259. doi: 10.1016/j.desal.2007.03.017
- Martyniuk, H., and Wieckowska, J. (1997). The effect of coal rank and carbonization temperature on SO₂ adsorption properties of coal chars. *Fuel* 76, 563–565. doi: 10.1016/S0016-2361(97)00076-8
- Meena, A. K., Kadivelu, K., Mishra, G. K., Rajagopal, C., and Nagar, P. N. (2008). Adsorptive removal of heavy metals from aqueous solution by treated sawdust (*Acacia arabica*). *J. Hazard Mater.* 150, 604–611. doi: 10.1016/j.jhazmat.2007.05.030
- Meitei, M. D., and Prasad, M. N. (2013). Pb(II) and Cd(II) biosorption on *Spirodela polyhiza* Scheleiden biomass. *J. Environ. Chem. Eng.* 1, 200–207. doi: 10.1016/j.jece.2013.04.016
- Menkiti, M. C., and Onukwuli, O. D. (2011). Studies on dye removal from aqueous media using activated coal and clay: an adsorption approach. *N. Y. Sci. J.* 4, 91–95.
- Mishra, S. P. (2014). Adsorption–desorption of heavy metal ions. *Curr. Sci.* 107, 601–612.
- Monser, L., and Adhoom, N. (2002). Modified activated carbon for the removal of copper, zinc, chromium and Cyanide from wastewater. *Sep Pur Tech.* 26, 137–146. doi: 10.1016/S1383-5866(01)00155-1
- Moreno-Castilla, C., Rivera-Utrilla, J., Lopez-Ramon, M. V., and Carrasco-Marin, F. (1994). Adsorption of some substituted phenols on activated carbons from a bituminous coal. *Carbon* 33, 845–851. doi: 10.1016/0008-6223(94)00182-Y
- Muhammad, I., Khalid, S., Imtiaz, A., Muhammad, S., and Muhammad, I. K. (2011). Physicochemical characteristics and Maleic Acids Adsorption Capacity of Lakhra Coal (Pakistan). *J. Chem. Soc. Pak.* 33, 360–363.
- Murphy, J. M., and Erkey, C. (1997). Thermodynamics of extraction of copper (II) from aqueous solutions by chelation in supercritical carbon dioxide. *Environ. Sci. Technol.* 31, 1674–1679. doi: 10.1021/es960519o
- Nabi, S. A., Bushra, R., Naushad, M., and Kahn, A. M. (2015). Synthesis, characterization and analytical applications of a new cation exchange material poly-o-toluidine stannic molybdate for the separation of toxic metal ions. *Chem. Eng. J.* 165, 529–536. doi: 10.1016/j.jcej.2010.09.064
- Njoku, V. O., Ayuk, A. A., Ejike, E. E., Oguzie, E. E., Duru, C. E., and Bello, O. S. (2011). Cocoa pod husk as a low cost biosorbent for the removal of Pb(II) and Cu(II) from aqueous solutions. *Aust. J. Basic Appl. Sci.* 5, 101–110.

- Nordiana, S. M., and Siti, Z. A. (2013). Adsorption of lead in aqueous solution by a mixture of activated charcoal and peanut shell. *World J. Sci. Tech. Res.* 1, 102–109.
- Nwajei, G. E. (2005). Trace metals in mushroom from urban and rural areas in Delta State of Nigeria. *J. Chem. Soc. Nig.* 30, 1–4.
- Nwokonkwo, D. C. (2008). Heavy metal pollution of soils: a case study of Obio/Akpor area in Niger Delta. *J. Chem. Soc. Nig.* 33, 17–20.
- Odesola, I. F., Eneje, S., and Temilola, O. (2013). Coal development in Nigeria: prospects and challenges. *Int. J. Eng. Appl. Sci.* 4, 64–73.
- Opeolu, B. O., Bamgbose, O., Arowolo, T. A., and Adetunji, M. T. (2008). Sorption of lead (II) from aqueous solutions using chemically modified and unmodified *Dioscorea alata* (Yam) and *Manihot esculenta* (Cassava) peels. *J. Chem. Soc. Nig.* 2, 1–10.
- Ozer, A., Tanyildizi, M. S., and Tumen, F. (1998). Study of cadmium adsorption from aqueous solution on activated carbon from sugar beet pulp. *Environ. Technol.* 19, 1119–1125. doi: 10.1080/09593331908616770
- Ozer, D., Dursun, G., and Ozer, A. (2007). Methylene blue adsorption from aqueous solution by dehydrated peanut hull. *J. Hazard Mater.* 144, 171–179. doi: 10.1016/j.jhazmat.2006.09.092
- Panday, K. K., Presad, G., and Singh, V. N. (1984). Removal of Cr(VI) from aqueous solutions by adsorption on fly ash-woolastonite. *J. Chem. Tech. Biotechnol.* 34A, 367–374.
- Park, D., Yun, Y., and Park, J. M. (2010). The past, present, and future trends of biosorption. *Biotechnol. Bioprocess. Eng.* 15, 86–102. doi: 10.1007/s12257-009-0199-4
- Sahmoune, M. N., Louhab, K., and Boukhar, A. (2011). Advanced biosorbents materials for removal of chromium from water and wastewaters. *Environ. Prog. Sustain.* 30, 284–293. doi: 10.1002/ep.10473
- Taha, G. M., Arifien, A. E., and El-Nahas, S. (2011). Removal efficiency of potato peels as a new biosorbent material for uptake of Pb(II), Cd(II) and Zn(II) from the aqueous solutions. *J. Solid Waste Technol. Manage.* 37, 128–140. doi: 10.5276/JSWTM.2011.128
- Vafakhah, S., Bahrololoom, M. E., Bazarganlari, R., and Saeedikhani, M. (2014). Removal of copper ions from electroplating effluent solutions with native corn cob and corn stalk and chemically modified corn stalk. *J. Environ. Chem. Eng.* 2, 356–361. doi: 10.1016/j.jece.2014.01.005
- Wang, K., and Xing, B. (2002). Adsorption and desorption of Cd by goethite pretreated with phosphate. *Chemosphere* 48, 665–670. doi: 10.1016/S0045-6535(02)00167-4
- Weber, W. J., Jr, McGinley, P. M., and Katz, L. E. (1991). Sorption phenomena in sub-surface systems: concepts, models and effects on contaminant fate and transport. *Water Res.* 25, 499–528. doi: 10.1016/0043-1354(91)90125-A
- Yadera, K. P., Tyagi, B. S., Panday, K. K., and Singh, V. N. (1987). Fly ash for the treatment of Cd(II)-rich effluents. *Environ. Technol. Lett.* 8, 225–234. doi: 10.1080/09593338709384482
- Yuan, X. Z., Meng, Y., Zeng, G. M., Fang, Y., and Shi, J. G. (2008). Evaluation of tea-derived biosurfactant on removing heavy metal ions from dilute wastewater by ion flotation. *Colloids Surf. A Physicochem. Eng. Aspects* 317, 256–261. doi: 10.1016/j.colsurfa.2007.10.024

Conflict of Interest Statement: The authors declare that the research was conducted in the absence of any commercial or financial relationships that could be construed as a potential conflict of interest.

Copyright © 2018 Ezeokonkwo, Ofor and Ani. This is an open-access article distributed under the terms of the Creative Commons Attribution License (CC BY). The use, distribution or reproduction in other forums is permitted, provided the original author(s) and the copyright owner are credited and that the original publication in this journal is cited, in accordance with accepted academic practice. No use, distribution or reproduction is permitted which does not comply with these terms.



The Interactions Between Three Typical PPCPs and LDH

Erwei Li¹, Libing Liao^{1*}, Guocheng Lv^{1*}, Zhaohui Li², Chengxue Yang¹ and Yanan Lu¹

¹ Beijing Key Laboratory of Materials Utilization of Nonmetallic Minerals and Solid Wastes, National Laboratory of Mineral Materials, School of Materials Science and Technology, China University of Geosciences, Beijing, China, ² Geosciences Department, University of Wisconsin–Parkside, Kenosha, WI, United States

OPEN ACCESS

Edited by:

Aiqin Wang,
Lanzhou Institute of Chemical Physics
(CAS), China

Reviewed by:

Wenbo Wang,
Lanzhou Institute of Chemical Physics
(CAS), China
Hui-Fang Cui,
Zhengzhou University, China
Runliang Zhu,
Guangzhou Institute of Geochemistry
(CAS), China

*Correspondence:

Libing Liao
clayl@cugb.edu.cn
Guocheng Lv
guochenglv@cugb.edu.cn

Specialty section:

This article was submitted to
Green and Environmental Chemistry,
a section of the journal
Frontiers in Chemistry

Received: 10 November 2017

Accepted: 19 January 2018

Published: 05 March 2018

Citation:

Li E, Liao L, Lv G, Li Z, Yang C and
Lu Y (2018) The Interactions Between
Three Typical PPCPs and LDH.
Front. Chem. 6:16.
doi: 10.3389/fchem.2018.00016

With a layered structure, layered double hydroxide (LDH) has potential applications in remediation of anionic contaminants, which has been a hot topic for recent years. In this study, a Cl type Mg-Al hydrotalcite (Cl-LDH) was prepared by a co-precipitation method. The adsorption process of three pharmaceuticals and personal care products (PPCPs) [tetracycline (TC), diclofenac sodium (DF), chloramphenicol (CAP)] by Cl-LDH was investigated by X-ray diffraction (XRD), Zeta potential, dynamic light scattering (DLS), BET, Fourier transform infrared (FTIR) spectroscopy, and molecular dynamics simulation. The results showed that the adsorption equilibrium of TC and DF could be reached in 120 min, and the maximum adsorption capacity of the TC and DF were 1.85 and 0.95 mmol/g, respectively. The isothermal adsorption model of TC was fitted with the Freundlich adsorption model, and the isothermal adsorption model of DF was fitted with the Langmuir adsorption model. The adsorption dynamics of TC and DF followed the pseudo-second-order model. The adsorption mechanisms of the three PPCPs into Cl-LDH were different based on the experimental results and molecular dynamics simulation. The TC adsorption on Cl-LDH was accompanied by the electrostatic interactions between the negative charge of TC and the positive charge of Cl-LDH. The uptake of DF was attributed to anion exchange and electrostatic interaction. Cl-LDH does not adsorb CAP due to no electrostatic interaction. The molecular dynamic simulation further confirmed different configurations of three selected PPCPs, which were ultimately responsible for the uptake of PPCPs on Cl-LDH.

Keywords: Cl-LDH, PPCPs, adsorption, electrostatic interaction, anion exchange

INTRODUCTION

For the past decades, a wide range of pharmaceutical and personal care products (PPCPs) have been repeatedly observed in natural waters all over the world (Richardson et al., 2005; Nakada et al., 2007; Sui et al., 2015). Owing to their bioaccumulation and biological activity, possible impacts of PPCPs on the human health and ecological safety have received a lot of concerns (Suárez et al., 2008; Sun et al., 2016). Due to the high demands of PPCPs in curing diseases and sustaining economic development in agriculture and livestock farming, the global production of PPCPs was over 1×10^6 tons in 1993, and the production keep increasing. Among PPCPs, Tetracycline (TC) was reported as the most widely used in animal feed. However, the majority of used TC was hard to be metabolized by animals or human beings, resulting in a considerable amounts as high as 80–90% of initial value or its metabolites being released to the external environment

(Ahmadi et al., 2017). The environmental concentrations of TC was about 1.12 $\mu\text{g/L}$ (Jie and Shuhe, 2015). Another widely used non-steroidal anti-inflammatory drug was Diclofenac sodium (DF), which had potential threats in municipal wastewaters and surface waters (Huang et al., 2017). The environmental concentrations of DF could reach 28.4 $\mu\text{g/L}$ (Qi et al., 2015). As a broad-spectrum antibiotic, chloramphenicol (CAP) was widely used in both animal and human medicine. Nevertheless, CAP had severe side-effects on humans, such as bone marrow suppression, aplastic anemia acute leukemia, “gray baby syndrome” etc. (Sai et al., in press). Therefore, environmental pollution caused by abuse of PPCPs is becoming more and more serious. In order to eliminate the potential risk of the PPCPs, it is necessary to get rid of the PPCPs in natural waters. Accordingly, many methods have been developed to remove the PPCPs, such as physical (Kim and Tanaka, 2009), chemical (Huber et al., 2005), and biological treatments (Suarez et al., 2010).

Adsorption is an old, simple yet effective method. Eco-friendly adsorbents that adsorption process could remove hazardous chemicals efficiently without special facilities and unknown byproducts has been successfully utilized for the removal of antibiotics from aqueous solutions. Adsorbents for antibiotics removal, such as silicate (Sun et al., 2017), clay minerals (Lv et al., 2017), mesoporous materials (Zhang et al., 2015; Li et al., 2017), and layered double hydroxides (LDHs) (Monash and Pugazhenthii, 2014) have been extensively studied. LDHs constitute an important class of layered materials, which have potential applications in remediation of anionic contaminants (Prasanna and Vishnu Kamath, 2008). The chemical formula can be typically expressed as “[M(II)_{1-x}M(III)_x(OH)₂]^{x+}(Aⁿ⁻)_{x/n}•mH₂O,” in which the M(II) and M(III) are divalent and trivalent cations, represented by Mg²⁺ and Al³⁺ or many other transition metal cations (Jobbágy and Regazzoni, 2011; Peng et al., 2015). Aⁿ⁻ stands for an interlayer anion with a negative charge n, and m represents the number of interlayer water molecules. The value of x has a range of 0.17 and 0.33. Many anions or anionic complexes (both organic and inorganic) can be incorporated into the crystal structure of LDHs. The LDHs can be abbreviated as [M^{II}-M^{III}-A], where M^{II} can be occupied by Zn²⁺, Mg²⁺, Cu²⁺, Mn²⁺, and Ca²⁺ ions; M^{III} stands for Al³⁺, Cr³⁺, Fe³⁺, and Ga³⁺; Aⁿ⁻ refers to Cl⁻, NO₃⁻, CO₃²⁻, and SO₄²⁻ (Liao et al., 2012). Due to their high anionic exchange capacities, especially, the anions are mainly extracted through ionic exchange with anions in the interlayer of LDHs. On the other hand, adsorption performance of the LDHs is affected by the surface properties of the LDHs (surface area, micropore surface area, and pore size distribution). LDHs have been considered as one of the most promising adsorbents for removing antibiotics. Thus, Cl-LDH could be a useful adsorbent to remove PPCPs.

In this study, we synthesized Cl-LDH by co-precipitated method and applied them as adsorbents for the removal of the three PPCPs (TC, DF, and CAP) from aqueous solution; to investigate the effect of pH, adsorbents time and PPCPs concentration; to discuss the adsorbent mechanism of PPCPs on Cl-LDH by theoretical calculations. In addition, the molecular dynamics simulation was also carried out to reveal

the configuration of PPCPs in the interlayer space and the interactions between PPCPs and the layer structure of Cl-LDH, which helped to understand the adsorption mechanism of Cl-LDH. The purpose of this paper was to explore the possibility of using Cl-LDH for the removal of TC and DF and develop eco-friendly adsorbents.

METHODS AND EXPERIMENT

Preparation of Mg-Al-Cl LDH

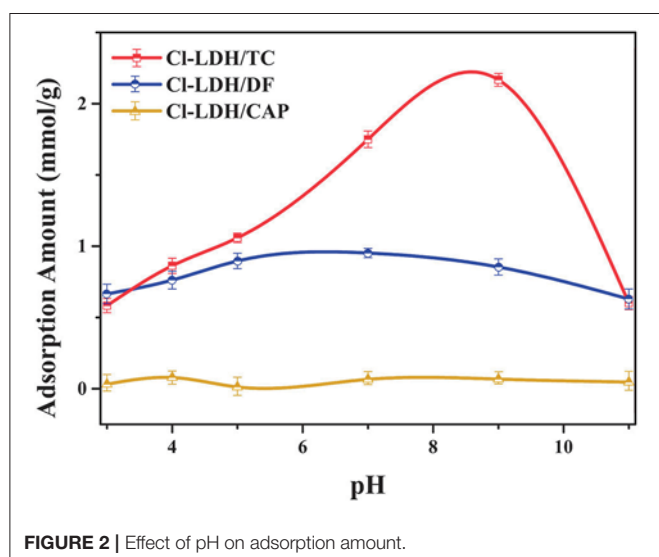
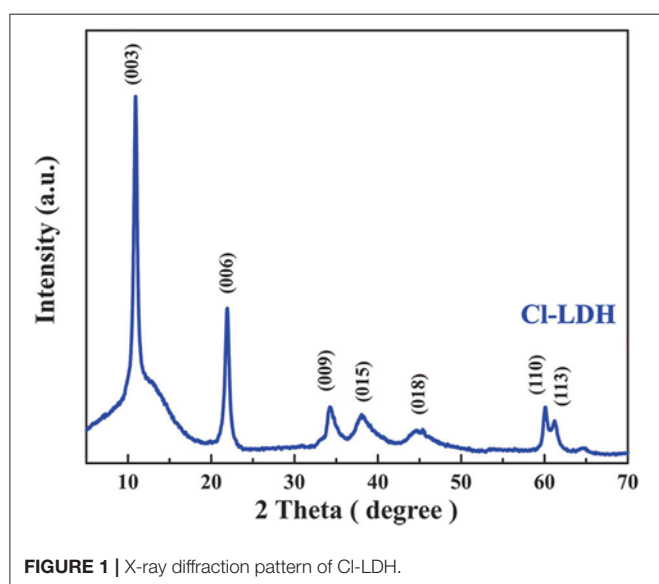
All reagents used in this study were of analytical grade and used without further purification. The Cl-LDH was synthesized through a co-precipitated method based on a previous study (Vreysen and Maes, 2008; Yue et al., 2017). Stoichiometric ratio of MgCl₂•6H₂O (24.396 g, 0.12 mol) (Beijing Chemical Works, AR) and AlCl₃•9H₂O (7.2429 g, 0.03 mol) (Beijing Chemical Works, AR) were dissolved in 150 mL deionized water, marked as solution A. NaOH (12.0 g, 0.3 mol) (Beijing Chemical Works, AR) and NaCl (1.7532 g, 0.03 mol) (Beijing Chemical Works, AR) were dissolved in 150 mL boiled deionized water to form solution B. Solution A and solution B were added dropwise using a burette at a rate of two drops per second into a three-necked flask simultaneously, and the mixture was stirred to be homogeneous and the pH-value was kept around 10. The slurry was aged for 12 h at 70°C. After being centrifuged, the precipitate was collected and washed with deionized water for several times, and then LDHs sample was obtained after drying at 110°C for 24 h. During the entire process of the experiment, an inert atmosphere of N₂ was used to prevent the influence of carbonate ions.

Adsorption Experiments

0.015 g Cl-LDH and 25 mL PPCPs (pH = 7) solution were mixed in a 50 mL centrifuge tube for all batch studies. For the isotherm study, the initial concentrations of TC (Shanghai Yiji Industrial Co., AR), DF (Chizhou Kelon Import and Export Co., AR), and CAP (Shenzhen Shijin Valley Technology Co., AR) solutions varied from 0.03 to 3.0 mmol/L. The kinetic study of PPCPs (pH = 7) was conducted at initial concentrations of 2.4 mmol/L for all the three PPCPs. For the pH study, same initial concentrations of PPCPs solutions with different pH-values (3, 4, 5, 7, 9, 11) were prepared to investigate the effect of pH on the adsorption characteristics of PPCPs. The mixtures were shaken in a water bath (CHA-S) with a speed of 150 rpm at room temperature for 24 h except for the kinetic study in which mixtures were shaken from 1 to 1,440 min. After that, the mixtures were centrifuged by high speed centrifuge (TG18K-1, DongWang instrument) at 4,500 rpm for 5 min. Then, the supernatant solutions were analyzed using the UV/VIS spectrophotometer (T6 New Century) to determine the equilibrium PPCPs concentration. PPCPs removal was identified by the difference between the initial and final solution concentrations. All batch experiment was run in duplicates.

Methods of Analyses

The structures of the samples were analyzed using a Rigaku D/Max-IIIa X-ray diffraction analyses diffractometer (XRD) with Ni-filtered CuK α radiation at 30 kV and 20 mA. Samples were

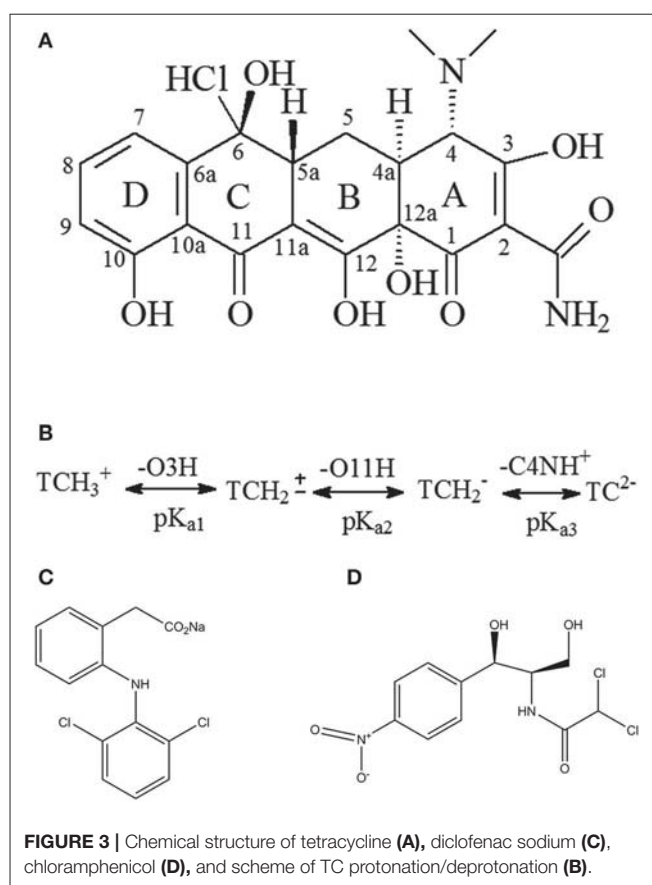


scanned from 3 to 70° (2θ) at 8°/min with a scanning step of 0.01°/step. A 1° divergent slit and scatter slit and 0.3 mm receiving slit were used.

Fourier transform infrared (FTIR) spectra were collected on a Nicolet-560 spectrometer (Thermal Nicolet Co., USA) from 400 to 4,000 cm⁻¹ with a nominal resolution of 4 cm⁻¹. For each spectrum 16 runs were collected and averaged. The hydrotalcite samples for FTIR measurement were prepared by adding approximately 1 wt% of the sample powder to dry KBr powder, and the mixture was pressed into tablet.

The equilibrium PPCPs concentrations were analyzed by a UV/VIS spectrophotometer (T6 New Century). The optimum wavelength of TC, DF, and CAP were 357, 276, and 278 nm, respectively.

Analyzer dynamic light scattering (DLS) and Zeta-potential of the material were studied on zeta-potential (ELSZ-1000,



Otsuka Electronics Co., Ltd., Japan). The BET specific surface area was determined by surface area analyzer (ASAP 2020HD, Micromeritics Instrument Corporation, USA).

RESULTS AND DISCUSSION

Characterization of Cl-LDH

Figure 1 showed the XRD pattern of the as-prepared Cl-LDH sample. It was apparently that a series of symmetric (00*l*) peaks at lower 2θ-values of Cl-LDH could be well-indexed to clay minerals containing layered structure LDHs. The main strong peak neared 2θ = 11.3°, corresponding to *d* = 0.7852 nm, and the other sharp peak neared 2θ = 22.7°, corresponding to *d* = 0.3920 nm, were attributed to basal reflections. The sharpness and intensity of the peaks indicated a highly crystalline structure of Cl-LDH. The typical *d* (003)-value of Cl-LDH was 0.7852 nm, which agreed well with the values reported by other researchers in the literature (Özgümüş et al., 2013; Peng et al., 2015).

The zeta potential of Cl-LDH was 36.2 mV, indicating that Cl-LDH had a good dispersity in water (Liu et al., 2017; Li et al., 2018). The DLS method resembled the size distribution of Cl-LDH in the range of 200–620 nm. The SEM image (Figure S1) of as prepared Cl-LDH reproved the size distribution of LDH as well. The BET surface of Cl-LDH was 34.85 m²/g, indicating that Cl-LDH had a strong adsorption ability.

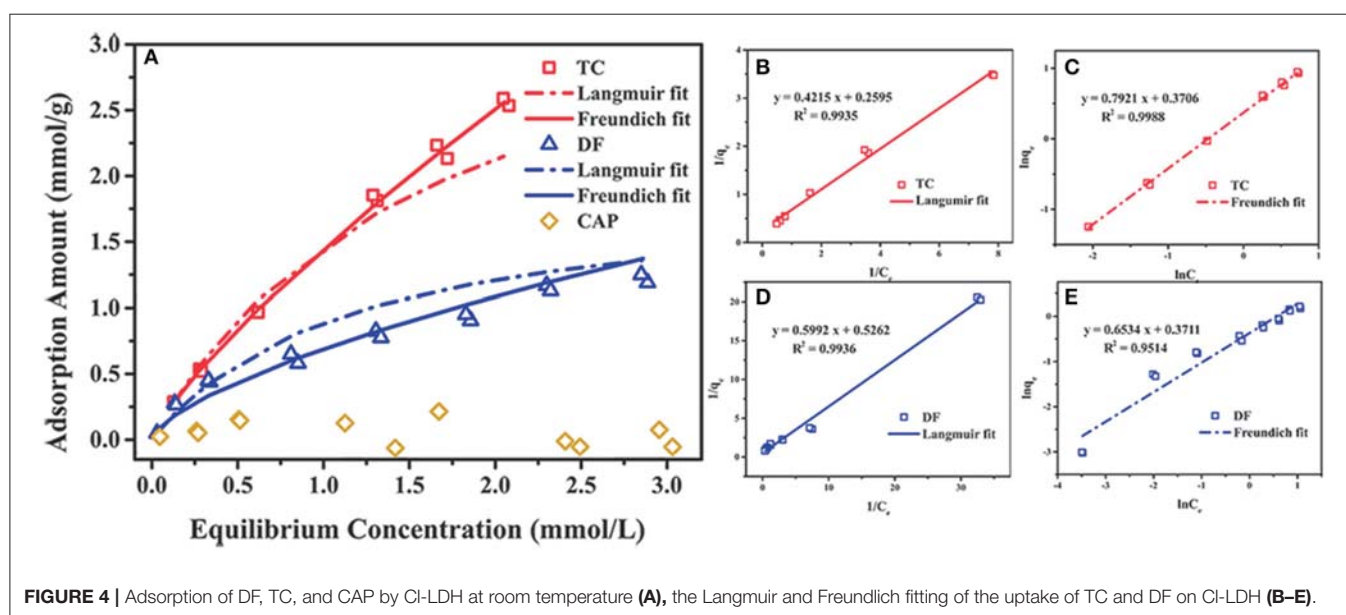


FIGURE 4 | Adsorption of DF, TC, and CAP by Cl-LDH at room temperature (A), the Langmuir and Freundlich fitting of the uptake of TC and DF on Cl-LDH (B-E).

TABLE 1 | Langmuir and Freundlich parameters for the TC and DF onto Cl-LDH.

Adsorbent	Langmuir equation			Freundlich equation		
	q_m (mmol/g)	K_L (L/mmol)	R^2	K_F ($\text{mol}^{1-1/n} \text{L}^{1/n}$ g^{-1})	n	R^2
TC	1.85	1.19	0.993	1.05	1.38	0.999
DF	0.95	1.14	0.996	1.53	0.69	0.983

Effect of pH

The pH of the solution should be considered to be an important factor affecting the adsorbate process due to its impact on the degree of ionization of pollutant species and the surface charge of the adsorbent (Figure 2). When $\text{pH} < \text{pH}_{\text{PZC}}$, the surface of Cl-LDH ($\text{pH} < 9.6$) was positively charged due to isomorphic substitution of Mg^{2+} ions by Al^{3+} ions. The zeta potential value of Cl-LDH was 36.2 mV which was measured at pH around 7, suggesting positively charged surfaces. TC was a yellow crystalline substance with a molecular weight of 480.9 g/mol, and the structure of TC was given in Figure 3A. In aqueous solutions three different groups of the molecule could undergo protonation–deprotonation reactions according to varying pH of solution. As shown in Figure 3B, three values of the dissociation constants ($\text{pK}_{\text{a}1} \approx 3.4$; $\text{pK}_{\text{a}2} \approx 7.5$; $\text{pK}_{\text{a}3} \approx 9.3$) had been determined experimentally that corresponds to existence of the protonated (TCH_3^+), neutral zwitterionic (TCH_2^\pm), monoanionic (TCH^-), and dianionic (TC^{2-}) forms of TC (Sassman and Lee, 2005; Soori et al., 2016). It could be easily seen that the bigger the pH-value was, the more amount of anionic species was. When the pH-value of equilibrium solution was < 9 , the adsorption amount of TC increased quickly with increasing pH. The maximum adsorption amount of TC was 2.16 mmol/L when $\text{pH} = 9$, which was attributed to the electrostatic interactions between

the negative charge of TC and the positive charge of Cl-LDH. Whereas when $\text{pH} > \text{pH}_{\text{PZC}}$, namely, $\text{pH} > 9.6$ for Cl-LDH, the surface charge of Cl-LDH became negative and repulsive to the negatively charged TC species, which caused the result that the adsorption amount decreased with the increasing of pH.

The adsorption capacity at pH-values lower than the pK_a (4.2) of DF was smaller than that at pH of 5.0, because DF was in the form of neutral molecules ($-\text{COOH}$) (Liu et al., 2017; Sun et al., 2017) and the structure of DF was given in Figure 3C. On increasing the pH from 5.0 to 9.0, the adsorption capacity reached maximum and kept constant due to DF in the form of anions ($-\text{COO}^-$) at $\text{pH} > \text{pK}_a$, finally decreased at $\text{pH} > 9.0$. The zeta potential of the Cl-LDH indicated that there was a positive surface charge on Cl-LDH at $\text{pH} < 9.6$, but surface positive charge decreased at $\text{pH} > 9.6$. This increases the electrostatic attraction between the negatively charged DF and Cl-LDH, which results in increased adsorption at $\text{pH} < 9.6$. Correspondingly the electrostatic attraction decreases due to the decrease of surface positive charge of Cl-LDH from 9.6 to 11 resulting in the decreased adsorption. The results suggested that the electrostatic interactions between anionic DF and cationic Cl-LDH could be the main driving forces for adsorption.

For CAP that the structure of CAP was given in Figure 3D, no uptake was observed on Cl-LDH. In the water solution, CAP molecule existed as a cation and was positively, so Cl-LDH had no electrostatic interaction with CAP.

Cl-LDH Sorption Isotherm

The adsorption isotherms of Cl-LDH on different initial concentrations of TC, DF, and CAP were shown in Figure 4A. With increasing concentrations, the adsorption amount of TC increased rapidly. When the initial concentration was 2.4 mmol/L (the equilibrium concentration of 1.3 mmol/L),

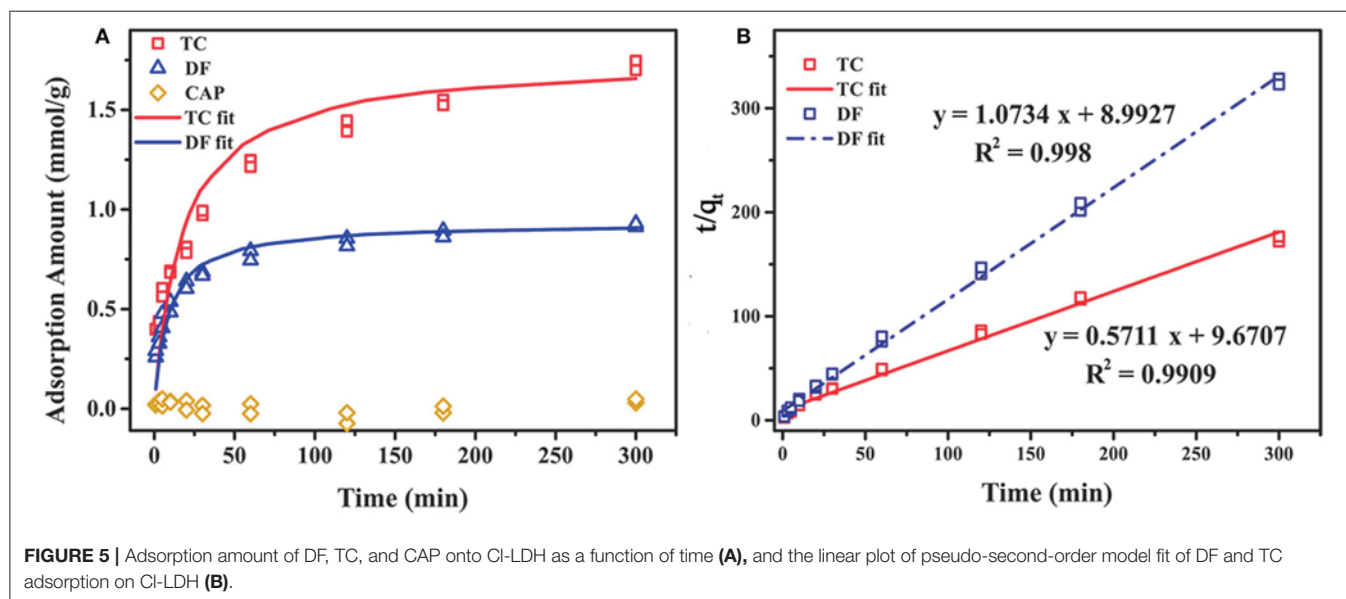


FIGURE 5 | Adsorption amount of DF, TC, and CAP onto Cl-LDH as a function of time (A), and the linear plot of pseudo-second-order model fit of DF and TC adsorption on Cl-LDH (B).

TABLE 2 | Pseudo-second-order model constants for the TC and DF adsorption on Cl-LDH.

Adsorbent	TC			DF		
	K_2 ($\text{g}\cdot\text{mmol}^{-1}$ $\cdot\text{min}^{-1}$)	q_e (mmol/g)	R^2	K_2 ($\text{g}\cdot\text{mmol}^{-1}$ $\cdot\text{min}^{-1}$)	q_e (mmol/g)	R^2
Cl-LDH	0.03	1.75	0.991	0.13	0.93	0.998

the adsorption amount reached 1.82 mmol/g. And when the equilibrium concentration was 1.85 mmol/L (the initial concentration of 2.4 mmol/L), the maximum adsorption amount of DF reached saturation about 0.95 mmol/g. The adsorption amount of CAP on Cl-LDH had no obvious change with the increase of initial concentration, and when the equilibrium concentration was 2.39 mmol/L (the initial concentration 2.4 mmol/L), the maximum adsorption amount was only 0.02 mmol/g.

The uptake of TC and DF on Cl-LDH were fitted using both Langmuir and Freundlich sorption models. The Langmuir model assumed that the uptake of specific homogeneous surface by monolayer sorption without interaction between adsorbed ions, which could be written by the following equation (Huang et al., 2016):

$$\frac{1}{q_e} = \frac{1}{q_{max}k_l C_e} + \frac{1}{q_{max}}$$

in which q_e (mmol/g) and q_{max} (mmol/g) were the amount of adsorbed TC and DF at equilibrium time and the maximum theoretical adsorption capacity, respectively. C_e (mmol/L) stood for the equilibrium solution concentration, and K_l (L/mmol) referred to the adsorption equilibrium parameter. The

parameters q_{max} and K_l could be obtained from the intercept and the slope of a plot of $1/q_e$ against C_e .

The Freundlich equation was developed empirically, with no theoretical basis. It was useful for describing the sorption of ions by chemical adsorption and surface precipitation reactions. This model, which was appropriate for heterogeneous systems, could be expressed by the following equation:

$$q_e = K_F C_e^{1/n}$$

where K_F and $1/n$ were characteristic parameters related to the sorption capacity and sorption intensity of the system, respectively. The values of K_F and $1/n$ were calculated from a linear plot of $\ln q_e$ against $\ln C_e$.

Figures 4B–E illustrated the Langmuir and Freundlich fitting of the uptake of TC and DF on Cl-LDH, and the adsorption isotherm parameters for TC and DF were summarized in Table 1. It was obvious that the Langmuir fitting had a bigger R^2 -value than Freundlich fitting, indicating the DF adsorption onto the surface of the Cl-LDH was monolayer, in contrast to TC adsorption onto the surface of the Cl-LDH was multilayer. The fitted TC and DF maximum sorption capacities were 1.85 and 0.95 mmol/g, respectively. Gao et al. (2012) reported the maximum adsorption capacity that the removal of TC by graphene oxide is 0.65 mmol/g, and Li et al. (2010) reported the maximum adsorption capacity for TC by smectite is 0.40 mmol/g. Meanwhile, the complete different behavior between TC and DF uptake may reflected totally different mechanisms of their uptake on Cl-LDH the same experimental condition.

Cl-LDH Sorption Kinetics

The effect of contact time on the adsorption amount of Cl-LDH at room temperature was investigated, and the adsorption capacity of DF, TC, and CAP onto Cl-LDH as a function of

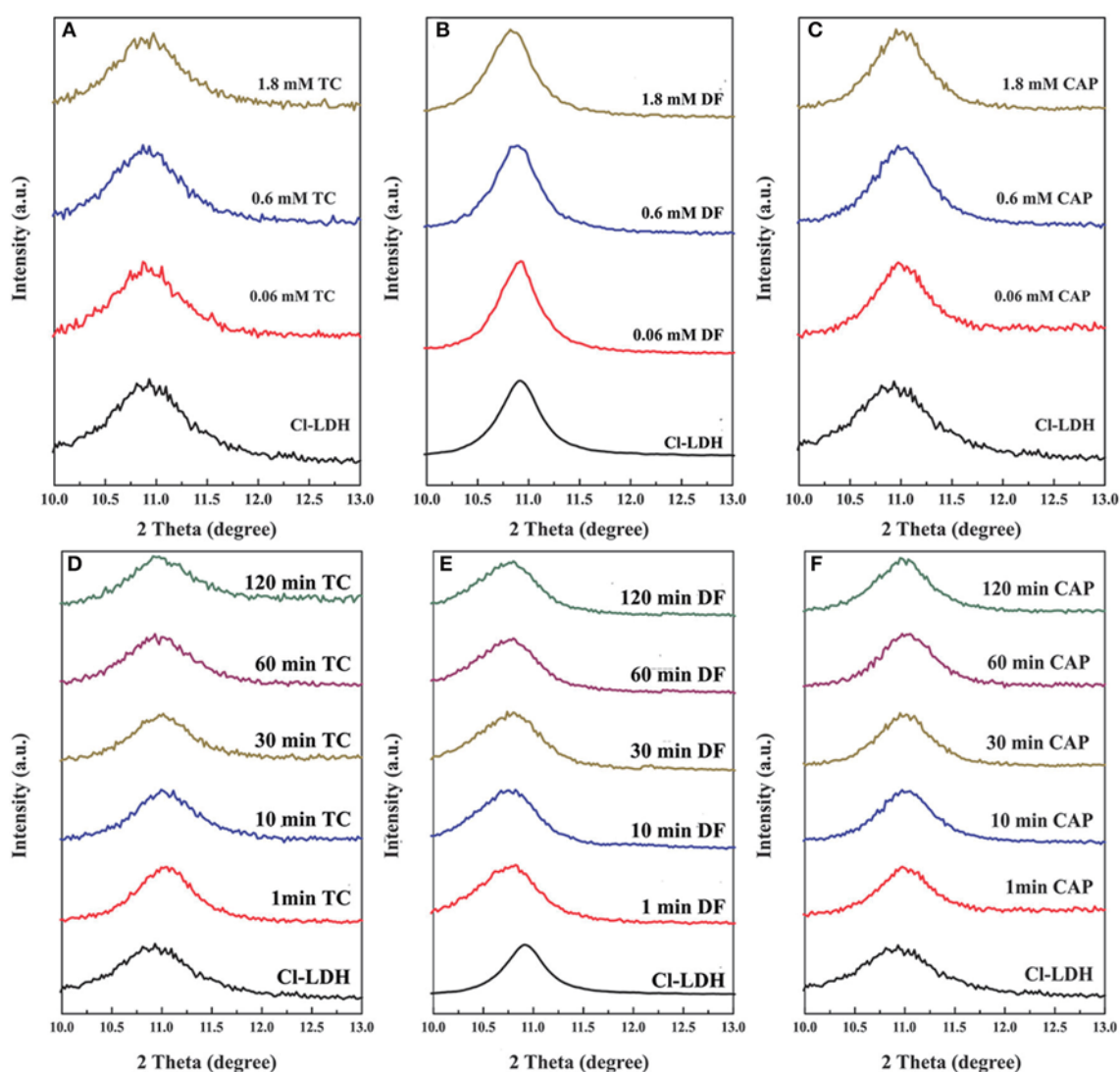


FIGURE 6 | X-ray diffraction pattern of Cl-LDH before and after adsorption of TC, DF, and CAP. **(A–C)** Patterns of Cl-LDH after TC, DF, and CAP adsorption with different initial concentrations, respectively. **(D–F)** XRD patterns of Cl-LDH after TC, DF, and CAP adsorption at different reaction time, respectively.

time was depicted in **Figure 5**. With the increasing reaction time, the adsorption amount of TC and DF increased gradually then reaches saturation, while adsorption amount of CAP was small and showed no obvious change. The rate of TC and DF uptake was rapid in the first 60 min, where adsorption amount were 1.24 and 0.74 mmol/g for TC and DF, respectively. After that, the adsorption amount was reached in 120 min, with the maximum adsorption amount of 1.72 and 0.91 mmol/g for TC and DF, respectively. At the initial stage, the high adsorption rate might be attributed to abundant vacant active sites on Cl-LDH surfaces available for adsorption. With a gradual reducing quantity of active sites, the electrostatic repulsive force played the leading role in the TC and DF loading on Cl-LDH. Thus, the adsorption of TC and DF slowed down, and finally the adsorption equilibrium was established.

In order to understand the mechanism of adsorption and evaluate the TC and DF adsorption performance of Cl-LDH adsorbent, the pseudo-first-order kinetic, and pseudo-second-order kinetic models were applied to analyze the dynamics adsorption experimental data. The kinetic models were expressed as follows (Ho and Mckay, 1998; Fu et al., 2015):

The pseudo-first-order kinetic model:

$$\log(q_e - q_t) = \log q_e - \frac{k_1}{2.303} t$$

The pseudo-second-order kinetic model:

$$\frac{t}{q_t} = \frac{t}{q_e} + \frac{1}{k_2 q_e^2}$$

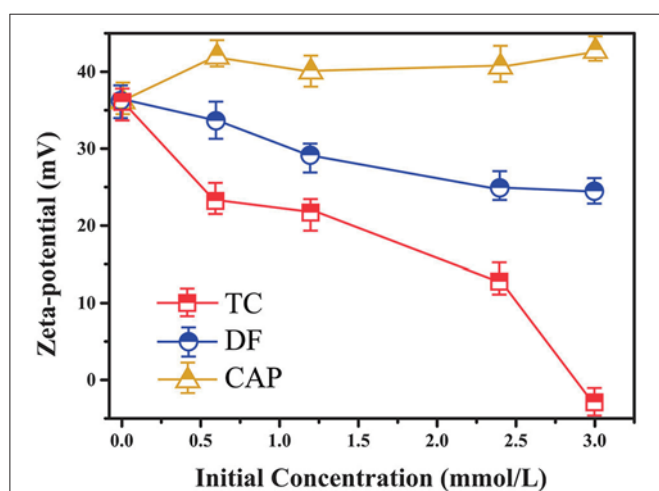


FIGURE 7 | Zeta potential of Cl-LDH after TC, DF, and CAP adsorption.

where k_1 (min^{-1}) and k_2 ($\text{g}\cdot\text{mol}^{-1}\cdot\text{min}^{-1}$) were the pseudo-first-order equilibrium rate constant and the pseudo-second-order equilibrium rate constant, respectively; q_1 and q_2 ($\text{mmol}\cdot\text{g}^{-1}$) were the TC and DF adsorption amount at equilibrium; q_t ($\text{mmol}\cdot\text{g}^{-1}$) was the amount of the TC and DF adsorbed at time t .

The experimental data could be well fitted with the pseudo-second-order model. The values of q_e and k_2 could be calculated from the interception and slope of the linear equation of t/q_t against t (Figure 5). The parameters of pseudo-second-order kinetic for TC and DF were summarized in Table 2.

The adsorption capacities of TC and DF in the kinetic study were 1.75 and 0.93 mmol/g, respectively. The result was in good accordance with the results obtained from the experiment data (1.72 and 0.91 mmol/g for TC and DF). The effect of the contact time on the desorption of extent of TC and DF was also discussed in Supplementary Information.

XRD Analyses

The XRD patterns of Cl-LDH samples before and after adsorption of TC, DF, and CAP were shown in Figure 6. Spacing values of (003) remained approximately the same, indicating that anion exchange, especially exchanged with interlayer anion did not account for the high loading efficiency of TC. So the sorption of TC on Cl-LDH were all on the external surfaces. The d_{003} peak of Cl-LDH shifted toward smaller angle after the adsorption of DF, of different initial concentrations and different reaction time, as revealed by Figures 6B,E, suggesting the adsorption of DF was based on intercalation of Cl-LDH. Besides, no newly-appeared or no shift in peak was observed in CAP experiment, (Figures 6C,F) which meant the adsorption of CAP was mainly on the external surfaces of Cl-LDH or Cl-LDH tended not to adsorb CAP. The results of molecular simulation (Figure S2) was in good agreement with the XRD results.

Zeta Potential Determination

Zeta potential was an indicator for the surface charge as well as the surface hydrophobicity, and the zeta potential of Cl-LDH

before and after adsorption was illustrated by Figure 7. The Cl-LDH had a zeta potential of 36.2 mV ($\text{pH} = 7$), indicating positively charged surfaces. As the initial concentrations went up, there was a significant decrease of zeta potential during the adsorption of TC onto Cl-LDH, which was caused by the electrostatic attraction between TC and Cl-LDH. It agreed well with the results from XRD analysis of TC/Cl-LDH. The adsorption of TC onto Cl-LDH was a process of charge neutralization on the external faces. The zeta potential of DF/Cl-LDH showed a smaller decrease compared with TC/LDH. Combined with the result from XRD analysis, the adsorption of DF might probably be consisted of two parts: electrostatic attraction on the surface and intercalation into Cl-LDH layers. Nevertheless, the zeta potential of CAP/Cl-LDH remained almost the same after adsorption despite the increase of the initial concentrations, which proved that the adsorption of CAP onto Cl-LDH tended to be poor.

FTIR Analyses

The FTIR spectra of Cl-LDH samples before and after adsorption of TC, DF, and CAP were shown in Figure 8. In the spectra of Cl-LDH adsorbed TC, the broad peak located in the region of 3,100–3,400 cm^{-1} related to O–H stretching vibrations. The fingerprint peaks of TC range from 1,600 to 750 cm^{-1} emerge on the FTIR spectra of Cl-LDH after adsorption, which indicated that the TC had been effectively adsorbed on Cl-LDH. The band at 1,581.45 cm^{-1} , which could be attributed (C=C) vibration in aromatic rings. The band at 1,328.21 cm^{-1} was due to the C–O stretching vibration of phenol group, as shown in Figure 8A. The DF phases primarily appeared in four characteristic bands: the peak at 1,669 cm^{-1} was due to the C=O stretching vibration, the peak of 1,448 cm^{-1} referred to the flexural vibration of the CH_2 , the peak of 1,301 cm^{-1} was attributed to the C–N extension, and the peak of 478 cm^{-1} corresponded to the C–Cl stretching vibration, as shown in Figure 8B. For CAP-adsorbed Cl-LDH, there showed no obvious characteristic vibration peak of CAP. It suggested CAP could not be adsorbed by Cl-LDH, as shown in Figure 8C.

CONCLUSIONS

An Cl-LDH was synthesized, characterized, and examined for removal of the three chosen PPCPs (TC, DF, and CAP) from aqueous solution. According to XRD pattern, the prepared adsorbent had a typical LDH nanostructure. TC sorption on Cl-LDH followed the Freundlich type isotherm, and DF sorption on Cl-LDH followed the Langmuir type isotherm. The TC and DF sorption by Cl-LDH fitted the pseudo-second-order model well. The novel adsorbent shown a high adsorption capacity of TC and DF (1.82 and 0.95 mmol/g). The adsorption mechanism of PPCPs into Cl-LDH were proved to be different. The TC adsorption on Cl-LDH was accompanied by the electrostatic interactions between the negative charge of TC and the positive charge of Cl-LDH. The uptake of DF was attributed to negative exchange and electrostatic interaction. Cl-LDH did not adsorb CAP due to no electrostatic interaction. The molecular dynamic simulation further confirmed different configurations of three selected

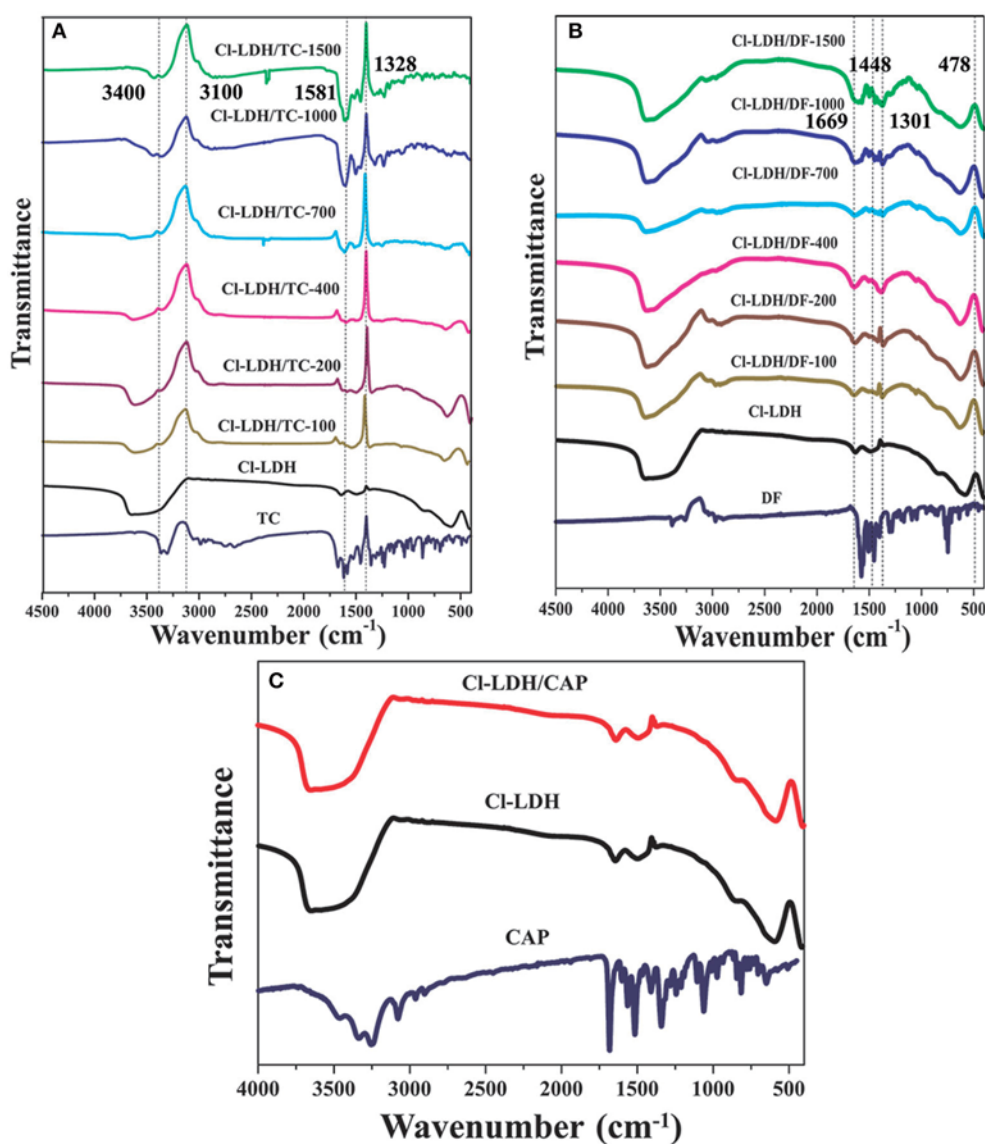


FIGURE 8 | FTIR spectra of CL-LDH after adsorption of TC (A), DF (B), and CAP (C).

PPCPs were ultimately responsible for the uptake of PPCPs on CI-LDH. The overall results of the present study suggested the efficient use of CI-LDH for the removal of TC and DF from the aqueous solution.

AUTHOR CONTRIBUTIONS

GL and LL designed the experiments. EL and CY carried out the experiments and analyzed the data. YL carried out the experiments. All authors discussed the results, EL, GL, and ZL wrote the paper. The manuscript has been reviewed and approved by all authors.

FUNDING

This present work was supported by the National Natural Science Foundations of China (Grant No. 51604248), the Fundamental Research Funds for the Central Universities (Grant No. 2652017338 and 2652017380).

SUPPLEMENTARY MATERIAL

The Supplementary Material for this article can be found online at: <https://www.frontiersin.org/articles/10.3389/fchem.2018.00016/full#supplementary-material>

REFERENCES

- Ahmadi, M., Ramezani Motlagh, H., Jaafarzadeh, N., Mostoufi, A., Saeedi, R., Barzegar, G., et al. (2017). Enhanced photocatalytic degradation of tetracycline and real pharmaceutical wastewater using MWCNT/TiO₂ nano-composite. *J. Environ. Manage.* 186, 55–63. doi: 10.1016/j.jenvman.2016.09.088
- Fu, J., Chen, Z., Wang, M., Liu, S., Zhang, J., Zhang, J., et al. (2015). Adsorption of methylene blue by a high-efficiency adsorbent (polydopamine microspheres): kinetics, isotherm, thermodynamics and mechanism analysis. *Chem. Eng. J.* 259, 53–61. doi: 10.1016/j.cej.2014.07.101
- Gao, Y., Li, Y., Zhang, L., Huang, H., Hu, J., Shah, S. M., et al. (2012). Adsorption and removal of tetracycline antibiotics from aqueous solution by graphene oxide. *J. Colloid Interface Sci.* 368, 540–546. doi: 10.1016/j.jcis.2011.11.015
- Ho, Y. S., and McKay, G. (1998). Kinetic models for the sorption of dye from aqueous solution by wood. *Process Saf. Environ.* 76, 183–191. doi: 10.1205/095758298529326
- Huang, Q., Deng, S., Shan, D., Wang, Y., Wang, B., Huang, J., et al. (2017). Enhanced adsorption of diclofenac sodium on the carbon nanotubes-polytetrafluoroethylene electrode and subsequent degradation by electro-peroxide treatment. *J. Colloid Interface Sci.* 488, 142–148. doi: 10.1016/j.jcis.2016.11.001
- Huang, X., Liu, Y., Liu, S., Tan, X., Ding, Y., Zeng, G., et al. (2016). Effective removal of Cr(VI) using β -cyclodextrin-chitosan modified biochars with adsorption/reduction bifunctional roles. *RSC Adv.* 6, 94–104. doi: 10.1039/C5RA22886G
- Huber, M. M., Korhonen, S., Ternes, T. A., and von Gunten, U. (2005). Oxidation of pharmaceuticals during water treatment with chlorine dioxide. *Water Res.* 39, 3607–3617. doi: 10.1016/j.watres.2005.05.040
- Jie, Z., and Shu, W. (2015). The distribution and eco toxicology of tetracycline in soil and water environment and its degradation: a review. *Acta Ecol. Sin.* 35, 2819–2825. doi: 10.5846/stxb201306111662
- Jobbágy, M., and Regazzoni, A. E. (2011). Dissolution of nano-size Mg–Al–Cl hydrotalcite in aqueous media. *Appl. Clay Sci.* 51, 366–369. doi: 10.1016/j.clay.2010.11.027
- Kim, I., and Tanaka, H. (2009). Photodegradation characteristics of PPCPs in water with UV treatment. *Environ. Int.* 35, 793–802. doi: 10.1016/j.envint.2009.01.003
- Li, B., Ma, J., Zhou, L., and Qiu, Y. (2017). Magnetic microsphere to remove tetracycline from water: adsorption, H₂O₂ oxidation and regeneration. *Chem. Eng. J.* 330, 191–201. doi: 10.1016/j.cej.2017.07.054
- Li, L., Qi, G., Wang, B., Yue, D., Wang, Y., and Sato, T. (2018). Fulvic acid anchored layered double hydroxides: a multifunctional composite adsorbent for the removal of anionic dye and toxic metal. *J. Hazard. Mater.* 343, 19–28. doi: 10.1016/j.jhazmat.2017.09.006
- Li, Z., Chang, P. H., Jean, J. S., Jiang, W. T., and Wang, C. J. (2010). Interaction between tetracycline and smectite in aqueous solution. *J. Colloid Interface Sci.* 341, 311–319. doi: 10.1016/j.jcis.2009.09.054
- Liao, L., Zhao, N., and Xia, Z. (2012). Hydrothermal synthesis of Mg–Al layered double hydroxides (LDHs) from natural brucite and Al(OH)₃. *Mater. Res. Bull.* 47, 3897–3901. doi: 10.1016/j.materresbull.2012.07.007
- Liu, T., Xie, Z., Zhang, Y., Fan, J., and Liu, Q. (2017). Preparation of cationic polymeric nanoparticles as an effective adsorbent for removing diclofenac sodium from water. *RSC Adv.* 7, 38279–38286. doi: 10.1039/C7RA06730E
- Lv, G., Li, Z., Elliott, L., Schmidt, M. J., MacWilliams, M. P., and Zhang, B. (2017). Impact of tetracycline-clay interactions on bacterial growth. *J. Hazard. Mater.* doi: 10.1016/j.jhazmat.2017.09.029. [Epub ahead of print].
- Monash, P., and Pugazhenth, G. (2014). Utilization of calcined Ni–Al layered double hydroxide (LDH) as an adsorbent for removal of methyl orange dye from aqueous solution. *Environ. Prog. Sustain.* 33, 154–159. doi: 10.1002/ep.11771
- Nakada, N., Shinohara, H., Murata, A., Kiri, K., Managaki, S., Sato, N., et al. (2007). Removal of selected pharmaceuticals and personal care products (PPCPs) and endocrine-disrupting chemicals (EDCs) during sand filtration and ozonation at a municipal sewage treatment plant. *Water Res.* 41, 4373–4382. doi: 10.1016/j.watres.2007.06.038
- Özgümüş, S., Gök, M. K., Bal, A., and Güçlü, G. (2013). Study on novel exfoliated polyampholyte nanocomposite hydrogels based on acrylic monomers and Mg–Al–Cl layered double hydroxide: synthesis and characterization. *Chem. Eng. J.* 223, 277–286. doi: 10.1016/j.cej.2013.02.098
- Peng, C., Yu, J., Zhao, Z., Fu, J., Zhao, M., Wang, W., et al. (2015). Preparation and properties of a layered double hydroxide deicing additive for asphalt mixture. *Cold Reg. Sci. Technol.* 110, 70–76. doi: 10.1016/j.coldregions.2014.11.013
- Prasanna, S. V., and Vishnu Kamath, P. (2008). Chromate uptake characteristics of the pristine layered double hydroxides of Mg with Al. *Solid State Sci.* 10, 260–266. doi: 10.1016/j.solidstatesciences.2007.09.023
- Qi, M., Zhihao, Z., Xiuwen, C., Pu, W., and Huiling, L. (2015). Research progress in the pollution situation and treatment methods for diclofenac in water. *Shandong Chem. Indus.* 44, 66–68. doi: 10.19319/j.cnki.issn.1008-021x.2015.16.026
- Richardson, B. J., Lam, P. K., and Martin, M. (2005). Emerging chemicals of concern: pharmaceuticals and personal care products (PPCPs) in Asia, with particular reference to Southern China. *Mar. Pollut. Bull.* 50, 913–920. doi: 10.1016/j.marpolbul.2005.06.034
- Sai, N., Wu, Y., Sun, Z., Yu, G., and Huang, G. (in press). A novel photonic sensor for the detection of chloramphenicol. *Arab. J. Chem.* doi: 10.1016/j.arabjc.2016.06.015
- Sassman, S. A., and Lee, L. S. (2005). Sorption of Three Tetracyclines by Several Soils: assessing the role of pH and cation exchange. *Environ. Sci. Technol.* 39, 7452–7459. doi: 10.1021/es0480217
- Soori, M. M., Ghahramani, E., Kazemian, H., Al-Musawi, T. J., and Zarrabi, M. (2016). Intercalation of tetracycline in nano sheet layered double hydroxide: an insight into UV/VIS spectra analysis. *J. Taiwan Inst. Chem. Eng.* 63, 271–285. doi: 10.1016/j.jtice.2016.03.015
- Suárez, S., Carballa, M., Omil, F., and Lema, J. M. (2008). How are pharmaceutical and personal care products (PPCPs) removed from urban wastewaters? *Rev. Environ. Sci. Biol.* 7, 125–138. doi: 10.1007/s11157-008-9130-2
- Suarez, S., Lema, J. M., and Omil, F. (2010). Removal of pharmaceutical and personal care products (PPCPs) under nitrifying and denitrifying conditions. *Water Res.* 44, 3214–3224. doi: 10.1016/j.watres.2010.02.040
- Sui, Q., Cao, X., Lu, S., Zhao, W., Qiu, Z., and Yu, G. (2015). Occurrence, sources and fate of pharmaceuticals and personal care products in the groundwater: a review. *Emerg. Contam.* 1, 14–24. doi: 10.1016/j.emcon.2015.07.001
- Sun, K., Shi, Y., Wang, X., Rasmussen, J., Li, Z., and Zhu, J. (2017). Organokaolin for the uptake of pharmaceuticals diclofenac and chloramphenicol from water. *Chem. Eng. J.* 330, 1128–1136. doi: 10.1016/j.cej.2017.08.057
- Sun, Q., Li, Y., Li, M., Ashfaq, M., Lv, M., Wang, H., et al. (2016). PPCPs in Jiulong river estuary (China): spatiotemporal distributions, fate, and their use as chemical markers of wastewater. *Chemosphere* 150, 596–604. doi: 10.1016/j.chemosphere.2016.02.036
- Vreysen, S., and Maes, A. (2008). Adsorption mechanism of humic and fulvic acid onto Mg/Al layered double hydroxides. *Appl. Clay Sci.* 38, 237–249. doi: 10.1016/j.clay.2007.02.010
- Yue, X., Liu, W., Chen, Z., and Lin, Z. (2017). Simultaneous removal of Cu(II) and Cr(VI) by Mg–Al–Cl layered double hydroxide and mechanism insight. *J. Environ. Sci.* 53, 16–26. doi: 10.1016/j.jes.2016.01.015
- Zhang, Z., Liu, H., Wu, L., Lan, H., and Qu, J. (2015). Preparation of amino-Fe(III) functionalized mesoporous silica for synergistic adsorption of tetracycline and copper. *Chemosphere* 138, 625–632. doi: 10.1016/j.chemosphere.2015.07.014

Conflict of Interest Statement: The authors declare that the research was conducted in the absence of any commercial or financial relationships that could be construed as a potential conflict of interest.

The reviewer WW, and handling Editor declared their shared affiliation.

Copyright © 2018 Li, Liao, Lv, Li, Yang and Lu. This is an open-access article distributed under the terms of the Creative Commons Attribution License (CC BY). The use, distribution or reproduction in other forums is permitted, provided the original author(s) and the copyright owner are credited and that the original publication in this journal is cited, in accordance with accepted academic practice. No use, distribution or reproduction is permitted which does not comply with these terms.



Enhanced Defluoridation Capacity From Aqueous Media via Hydroxyapatite Decorated With Carbon Nanotube

Qingzi Tang¹, Tongdan Duan¹, Peng Li², Ping Zhang^{1,2*} and Daishe Wu^{1*}

¹ Key Laboratory of Poyang Lake Environment and Resource Utilization, School of Environmental and Chemical Engineering, Ministry of Education, Nanchang University, Nanchang, China, ² Australian Institute for Bioengineering and Nanotechnology, The University of Queensland, Brisbane, QLD, Australia

OPEN ACCESS

Edited by:

Hongfei Cheng,
China University of Mining and
Technology, China

Reviewed by:

Jie Lei,
Fudan University, China
Runliang Zhu,
Guangzhou Institute of Geochemistry
(CAS), China

Nito Angelo Debacher,
Universidade Federal de Santa
Catarina, Brazil

*Correspondence:

Ping Zhang
zhangping@ncu.edu.cn
Daishe Wu
dswu@ncu.edu.cn

Specialty section:

This article was submitted to
Green and Sustainable Chemistry,
a section of the journal
Frontiers in Chemistry

Received: 13 February 2018

Accepted: 20 March 2018

Published: 11 April 2018

Citation:

Tang Q, Duan T, Li P, Zhang P and
Wu D (2018) Enhanced Defluoridation
Capacity From Aqueous Media via
Hydroxyapatite Decorated With
Carbon Nanotube.
Front. Chem. 6:104.
doi: 10.3389/fchem.2018.00104

In this work, the potential of a novel hydroxyapatite decorated with carbon nanotube composite (CNT-HAP) for fluoride removal was investigated. The synthesized CNT-HAP composite was systematically characterized by X-ray diffraction (XRD), Fourier Transform infrared spectroscopy (FTIR), scanning electron microscope (SEM) and Brunauer–Emmett–Teller (BET). Batch adsorption experiments were conducted to investigate the defluorination capacity of CNT-HAP. The CNT-HAP composite has a maximum adsorption capacity of 11.05 mg·g⁻¹ for fluoride, and the isothermal adsorption data were fitted by the Freundlich model to calculate the thermodynamic parameters. Thermodynamic analysis implies that the adsorption of fluoride on CNT-HAP is a spontaneous process. Furthermore, the adsorption of fluoride follows pseudo-second-order model. The effects of solution pH, co-existing anions and reaction temperature on defluorination efficiency were examined to optimize the operation conditions for fluoride adsorption. It is found that the optimized pH-value for fluoride removal by CNT-HAP composite is 6. In addition, among five common anions studied in this work, the presence of HCO₃⁻ and PO₄³⁻ could considerably affect the fluoride removal by CNT-HAP in aqueous media. Finally, the underlying mechanism for the fluoride removal by CNT-HAP is analyzed, and an anion exchange process is proposed.

Keywords: fluoride removal, hydroxyapatite decorated with carbon nanotube (CNT-HAP), ion-exchanged, hydroxyl anions, removal mechanism

INTRODUCTION

Fluoride is an essential element for both human and animals. However, it may be useful or harmful to human bodies, depending on its concentration in drinking water and total ingested amount (Chen et al., 2012; Sharma et al., 2017). It is recommended by World Health Organization (WHO) that the most appropriate concentration of fluoride in drinking water is 0.5–1.5 mg·L⁻¹, exceeding which people could have dental and / or skeletal fluorosis such as softening of bones, mottling of teeth and neurological damage (Liu et al., 2015; Zhang L. E. et al., 2017). Unfortunately, the concentration of fluoride has been found to be as high as 30 mg·L⁻¹ in the drinking water of about 25 countries across the world, including India, Mexico and China (Amini et al., 2008). And the fluoride pollution in drinking water is even worse and worse. (Jagtap et al., 2012; Roy and Dass, 2013). Therefore, it is necessary to remove the excess fluoride from drinking water.

Currently, there are several methods available for defluorination, such as chemical precipitation (Xin et al., 2016; Huang et al., 2017), membrane filtration (Zhang J. et al., 2017), electrolysis (Schaefer et al., 2017), ion exchange (Popat et al., 1994; Jamhour, 2005), and adsorption (Rehman et al., 2015; Lin et al., 2016). Among the above-mentioned methods, adsorption is a most attractive option owing to its low cost, high efficiency, and good flexibility (Mohan et al., 2017). Hydroxyapatite [$\text{Ca}_{10}(\text{PO}_4)_6(\text{OH})_2$, HAP] is a natural mineral with abundance in bone and skeletal tissues. It has been demonstrated to be a promising candidate adsorbent for fluoride removal because of its easy synthesis, high recyclability, and good biocompatibility (Beladi et al., 2017; Lei et al., 2017). Jiménez-Reyes et al. reported that the defluorination capacity of HAP was 4.7 mg of fluoride/g of adsorbent in the pH range of 5.0–7.3 (Jiménez-Reyes and Solache-Ríos, 2010). Sundaram et al. prepared the HAP / chitosan nanocomposite for fluoride removal with a defluorination capacity of 1.56 $\text{mg}\cdot\text{g}^{-1}$ (Gao et al., 2009). There are two factors contributing to the removal of fluoride by HAP: ion exchange and electrostatic interaction (He et al., 2015). In this process, fluorapatite [$\text{Ca}_5(\text{PO}_4)_3\text{F}$] or mixed fluorinated HAP [$\text{Ca}_5(\text{PO}_4)_3(\text{OH}\cdot\text{F})$] which are thermodynamically more stable are formed.

However, the practical application of HAP in fluoride removal from drinking water is still limited by its low defluorination capacity. It has been well established that adsorbents with high surface areas and active sites density can be fabricated by tailoring the morphology and pore size (Chen et al., 2016). Moreover, adsorbents with hierarchically meso- and /or macroporous networks enable the fast diffusion of guest molecules in the channels, thus facilitating their access to active sites. Among various kinds of materials, carbon nanotubes (CNT) are particularly attractive because they not only have the characteristics mentioned above, but also can act as adsorbents for fluoride removal. For example, Li et al. (2003) reported use of aligned CNT to remove fluoride, and an adsorption capacity of 4.5 $\text{mg}\cdot\text{g}^{-1}$ was achieved in the aqueous solution with the fluoride concentration of 15 $\text{mg}\cdot\text{L}^{-1}$.

In a very recently study, Neelgund et al. (Neelgund and Oki, 2016) found that CNT could improve the photothermal efficiency (PTE) of HAP, and HAP could also overcome the poor dispersion of CNT. In this work, we proposed the combination of HAP with CNT for fluoride removal from aqueous media. To the best of our knowledge, there are few study on such a subject. The major objectives of our work are: (1) to characterize CNT-HAP composite by XRD, FTIR, SEM, and TGA; (2) to compare the defluorination performance between HAP and CNT-HAP composite; (3) to optimize the operation conditions for fluoride removal; (4) to disclose the underlying mechanism of fluoride removal.

EXPERIMENTAL SECTION

Materials

All the chemicals were purchased from Tianjin Damao Chemicals Co. Ltd., (China), and used directly without further purification. The water used in this work was in ultrapure grade.

Preparation of CNT-HAP Composite

CNT-HAP composite was synthesized by co-precipitation. The pH of aqueous solutions of $\text{Ca}(\text{NO}_3)_2$ (0.25 $\text{mol}\cdot\text{L}^{-1}$) and $(\text{NH}_4)_2\text{HPO}_4$ (0.3 $\text{mol}\cdot\text{L}^{-1}$) ($\text{Ca}/\text{P} = 1.67$) were adjusted to 10.0 by $\text{NH}_3\cdot\text{H}_2\text{O}$. The CNT (5 wt%) was functionalized by HNO_3 , and then added into the aqueous solution of $\text{Ca}(\text{NO}_3)_2$. The solution was ultrasonicated until a homogeneous solution was formed (A). The aqueous solution of $(\text{NH}_4)_2\text{HPO}_4$ was dripped slowly into the solution A under vigorous stirring for 1 h at 45°C to generate precipitates. Afterwards, the pH of solution was adjusted to 10.0 by $\text{NH}_3\cdot\text{H}_2\text{O}$. The mixture was aged for 24 h at room temperature to form colloids. The colloids were centrifuged, washed with ultrapure water for several times, milled with ethanol, dried at 80°C, and finally calcined at 200°C for 2 h to give CNT-HAP composite.

Materials Characterizations

The phase composition and crystal structure of CNT-HAP composite were characterized by an X-ray powder diffractometer (XRD, D8 ADVANCE X), using $\text{Cu K}\alpha$ (40 kV, 40 mA) radiation in the scanning range of 10–80°. The chemical structure was characterized by a Fourier transform infrared spectrometer (FTIR, Nicolet 5700,) in the wavenumber range of 400–4,000 cm^{-1} . The elemental composition was examined by an X-ray photoelectron spectroscopy (XPS, Axis Ultra DLD), using $\text{Al K}\alpha$ radiation. The morphology was examined by a scanning electron microscope (SEM, JSM 6701F) at the accelerating voltage of 5 kV. The specific surface area was calculated by Brunauer-Emmett-Teller (BET) equation from the N_2 adsorption-desorption isotherms determined by a porosity analyser (JW-BK132F). The pH-values were determined by a pH electrode (pH SJ-4A). The concentrations of fluoride in aqueous solutions were determined by ion chromatography (IC, ICS-1100).

Adsorption Experiments

The adsorption experiments were performed by the batch method to investigate the effects of different parameters (e.g., temperature, reaction time, pH and co-existing ions) on fluoride removal by CNT-HAP. In a typical run, 0.01 g of CNT-HAP was mixed with 20 mL of aqueous solution containing fluoride, and the mixture was stirred at the rate of 180 rpm and temperature of 25°C for 24 h to achieve the adsorption equilibrium.

RESULTS AND DISCUSSION

X-Ray Diffraction

The XRD patterns of HAP, CNT and CNT-HAP composite are presented in **Figure 1**. The diffraction peaks of HAP could be indexed to hexagon-phased HAP with considerable intensities at 26, 33, 34, 35, and 40° (JCPDS file 09-0432). In comparison with the diffraction patterns of HAP, those of CNT-HAP are very similar, indicating the successful incorporation of HAP into the matrices of CNT. However, it is worth noting that the diffraction patterns of CNT could hardly be observed in those of CNT-HAP composite, which should be attributed to the overlap of the major diffraction peaks of CNT and HAP at 26°. On the other hand, if CNT was directly wrapped by as-synthesized

HAP, the characteristic peaks of CNT can also not be observed in the diffraction patterns of CNT-HAP composite. This could also elucidate successful synthesis of CNT-HAP. In addition, the sharp and symmetric diffraction peaks confirm good crystallinity of synthesized CNT-HAP composite.

Infrared Spectroscopy

The FT-IR spectra of HAP, CNT and CNT-HAP are shown in **Figure 2**. The broad peaks at 3,150–3,550 cm^{-1} are assigned to the O-H vibration (Xu et al., 2013). The bands at 1,030–1,040, 600–610, and 550–570 cm^{-1} are associated with the stretching vibration of phosphate, confirming the presence of HAP in CNT-HAP composite. Besides those peaks associated with HAP, the C-H stretching vibration appears at 2,800–3,000 cm^{-1} while the C-H bending vibration is observed at 1,370–1,400 cm^{-1} (Zhang et al., 2012). The peaks at 1,630–1,640 cm^{-1} are attributed to the C = O stretching vibration. All these characteristic peaks can also be found in the acidified CNT, confirming the pliable phase composition of CNT-HAP composite, which is in accordance with the results concluded from XRD patterns.

Scanning Electron Microscopy

The SEM images of CNT, HAP and CNT-HAP are presented in **Figure 3**. HAP displays faint lamellar morphology and compact internal structure, while CNT-HAP displays legible lamellar morphology because the introduction of CNT is beneficial for the nucleation and crystallization of HAP. The vertical growth of HAP along CNT implies that CNT-HAP has higher specific surface area than HAP. In **Figure 3c**, the characteristic tubular structure cannot be observed in CNT-HAP, suggesting that CNT is wrapped by HAP on the surface, which is consistent with the results concluded from XRD patterns. The SEM images prove the successful synthesis of CNT-HAP and the assembly of HAP on the surface of CNT.

Adsorption Isotherms

The adsorption isotherms of fluoride on HAP and CNT-HAP at 25, 35, and 45°C were determined, as shown in **Figure 4**. The adsorbed amounts of fluoride by HAP and CNT-HAP both increase rapidly at low fluoride concentrations, and the increasing trend gradually fades out at high fluoride concentrations. With the increase of temperature, the adsorbed amounts of fluoride increase continuously. The maximum adsorption capacity (q_m) of fluoride on CNT-HAP at 25°C is 11.05 $\text{mg}\cdot\text{g}^{-1}$, being higher than pristine HAP and other HAP-based materials reported in the literature (**Table 1**; Gao et al., 2009; Sairam Sundaram et al., 2009; Jiménez-Reyes and Solache-Ríos, 2010; Liu et al., 2010; Kanno et al., 2014; Prabhu and Meenakshi, 2014; He et al., 2017; Nigri et al., 2017; Zúñiga-Muro et al., 2017).

To better understand the adsorption behavior of fluoride, the Langmuir and Freundlich models were used to correlate the adsorption data. The Langmuir model (Equation 1) applicable for monolayer adsorption process (Li et al., 2012; Reynel-Avila et al., 2016).

$$q_e = \frac{q_m k_L c_e}{1 + k_L c_e} \quad (1)$$

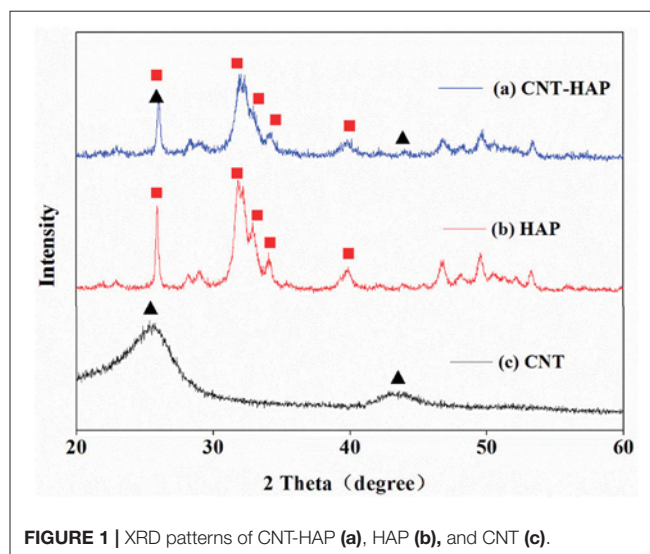


FIGURE 1 | XRD patterns of CNT-HAP (a), HAP (b), and CNT (c).

TABLE 1 | Comparison of fluoride adsorption capacities of pristine HAP and various HAP-based materials.

Adsorbents	Adsorption capacities ($\text{mg}\cdot\text{g}^{-1}$)	C_{initial} ($\text{mg}\cdot\text{L}^{-1}$)	pH	References
HAP powder	4.7	20	7.0	Jiménez-Reyes and Solache-Ríos, 2010
Nano-HAP/Chitin	3.0	10	7.0	Sairam Sundaram et al., 2009
Al-HAP adsorption membrane	7.15	10	7.0	He et al., 2017
HAP-coated-limestone	9.3	50	7.0	Kanno et al., 2014
Synthetic nano-HAP	4.8	80	5.0–6.0	Gao et al., 2009
DTAB-HAP powder	3.436	10	7.0	Prabhu and Meenakshi, 2014
Nano-HAP/Chitosan	1.56	10	7.0	Sairam Sundarama, 2008
Synthetic siderite	1.775	3–20	4.0–9.0	Liu et al., 2010
bone char	4.81	10	7.2–7.7	Nigri et al., 2017
cerium-containing bone char	13.6	10	7.0	Zúñiga-Muro et al., 2017

Where q_e ($\text{mg}\cdot\text{g}^{-1}$) is the adsorbed amount of fluoride at equilibrium; C_e ($\text{mg}\cdot\text{L}^{-1}$) is the concentration of fluoride in supernatant solution at equilibrium; q_m ($\text{mg}\cdot\text{g}^{-1}$) represents the maximum adsorption capacity; and k_L ($\text{L}\cdot\text{mg}^{-1}$) represents the adsorption equilibrium constant. The Freundlich model (Equation 2) is applicable for the description of adsorption data on heterogeneous surfaces at low to intermediate concentrations (Mahmoud et al., 2016).

$$q_e = k_F C_e^{\frac{1}{n}} \quad (2)$$

Where k_F ($\text{mg}^{1-n}\cdot\text{L}^n\cdot\text{g}^{-1}$) is the adsorption capacity when the equilibrium concentration of ion equals to 1; and n is the dependent degree of adsorption capacity on equilibrium concentration, with the value of 1~10. The fitted parameters for

two adsorption models as well as the correlation coefficients (R^2) are shown in **Table 2**. According to the values of R^2 and fitted curves shown in **Figure 4**, it is obvious that the Langmuir model is better for describing the adsorption behavior of fluoride on HAP, implying that the adsorption energy is constant and the adsorption capacity is limited by the amounts of active sites. In contrast, the Freundlich model is better for describing the adsorption behavior of fluoride on CNT-HAP, implying that the adsorption of fluoride is subjected to multi-layer and physical-chemical adsorption.

Adsorption Thermodynamic Analysis

The thermodynamic parameters such as Gibbs free energy change (ΔG°), adsorption enthalpy (ΔH°) and adsorption entropy (ΔS°) could be calculated from the adsorption data according to eqs. 3~6 (Luo et al., 2015; Wang et al., 2015; Singh and Anil Kumar, 2016).

$$\Delta G^\circ = -RT \ln K_d \quad (3)$$

$$\Delta S^\circ = - \left(\frac{\partial \Delta G^\circ}{\partial T} \right)_P \quad (4)$$

$$\Delta H^\circ = \Delta G^\circ + T \Delta S^\circ \quad (5)$$

$$\ln K = \Delta S^\circ / R - \Delta H^\circ / RT \quad (6)$$

Where R is the gas constant ($8.314 \text{ J}\cdot\text{mol}^{-1}\cdot\text{K}^{-1}$); T is the absolute temperature (K); and K_d is the adsorption equilibrium constant. As shown in **Table 3**, the negative values of ΔG° indicate that the adsorption process of fluoride is spontaneous. The much lower values of ΔG° for fluoride adsorption on CNT-HAP than on HAP at the same temperature suggests the easier adsorption of fluoride on CNT-HAP than on HAP. The positive value of ΔS° elucidate that the organization of fluoride ions on the surface of adsorbents is more random than in the aqueous solutions. The positive values of ΔH° suggest that the adsorption of fluoride on HAP and CNT-HAP is endothermic.

Adsorption Kinetics

The adsorbed amounts of fluoride were plotted vs. adsorption time to examine the adsorption kinetics, as shown in **Figure 2**. The amounts of fluoride adsorbed by HAP and CNT-HAP rapidly increase in the first 2 h. Then the adsorption rate slows down

and reaches equilibrium at 240 and 300 min, respectively. The adsorption kinetic data were fitted by pseudo-first-order model (Equation 7), and pseudo-second-order model (Equation 8), respectively (Naowanat et al., 2016; Subbaiah and Kim, 2016; Sun et al., 2017).

$$q_t = q_e \left(1 - e^{-k_1 t} \right) \quad (7)$$

$$q_t = \frac{q_e^2 k_2 t}{1 + q_e k_2 t} \quad (8)$$

Where k_1 (min^{-1}); k_2 ($\text{g}\cdot\text{mg}^{-1}\cdot\text{h}^{-1}$) are the pseudo-first-order and the pseudo-second-order rate constant, respectively; q_t ($\text{mg}\cdot\text{g}^{-1}$) is the adsorbed amount of fluoride on adsorbents at time t (min); q_e ($\text{mg}\cdot\text{g}^{-1}$) is the equilibrium adsorption capacity. The nonlinear fitting for q_t vs. t is presented in **Figure 5**. All the fitted kinetic kinetic parameters as well as the correlation coefficients (R^2) are listed in **Table 4**. Obviously, the kinetic data of fluoride adsorption on HAP and CNT-HAP are well fitted to the pseudo-second-order model, indicating that the fluoride removal processes are subjected to chemical reaction (Tadjarodi et al., 2016), which determines the overall adsorption rate.

TABLE 3 | The thermodynamic parameters of fluoride adsorption on HAP and CNT-HAP composite.

Adsorbents	T ($^\circ\text{C}$)	ΔG° ($\text{kJ}\cdot\text{mol}^{-1}$)	ΔH° ($\text{kJ}\cdot\text{mol}^{-1}$)	ΔS° ($\text{J}\cdot\text{mol}^{-1}\cdot\text{K}^{-1}$)	$\ln K_d$
CNT-HAP	25	-16.53			6.67
CNT-HAP	35	-17.78	20.68	124.38	6.94
CNT-HAP	45	-19.03			7.19
HAP	25	-15.54	19.80	118.72	6.27
HAP	35	-16.81			6.56
HAP	45	-17.90			6.77

TABLE 2 | Fitted Langmuir and Freundlich model parameters for fluoride adsorption on HAP and CNT-HAP composite at different temperatures.

Samples	Temperatures ($^\circ\text{C}$)	Langmuir model			Freundlich model		
		$q_m / (\text{mg}\cdot\text{g}^{-1})$	$K_L / (\text{L}\cdot\text{mg}^{-1})$	R^2	k_F	n	R^2
HAP	25	5.01	0.55	0.9772	2.63	6.56	0.8932
HAP	35	6.25	0.50	0.9493	3.07	5.88	0.9136
HAP	45	6.81	1.08	0.9479	4.07	7.77	0.8933
CNT-HAP	25	11.05	0.18	0.9142	3.57	3.96	0.9735
CNT-HAP	35	13.57	0.17	0.9075	4.26	3.88	0.9695
CNT-HAP	45	16.78	0.17	0.8835	5.08	3.74	0.9831

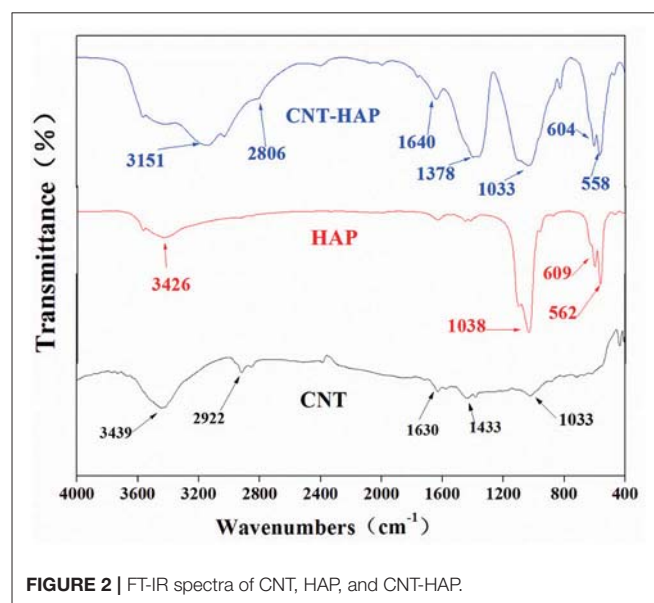


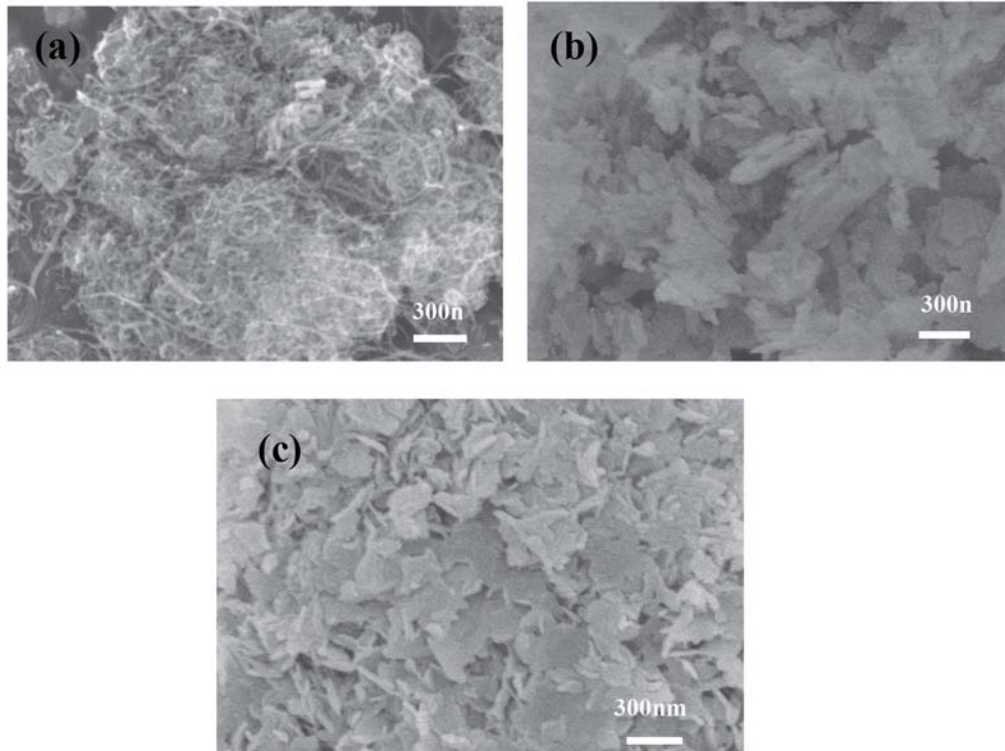
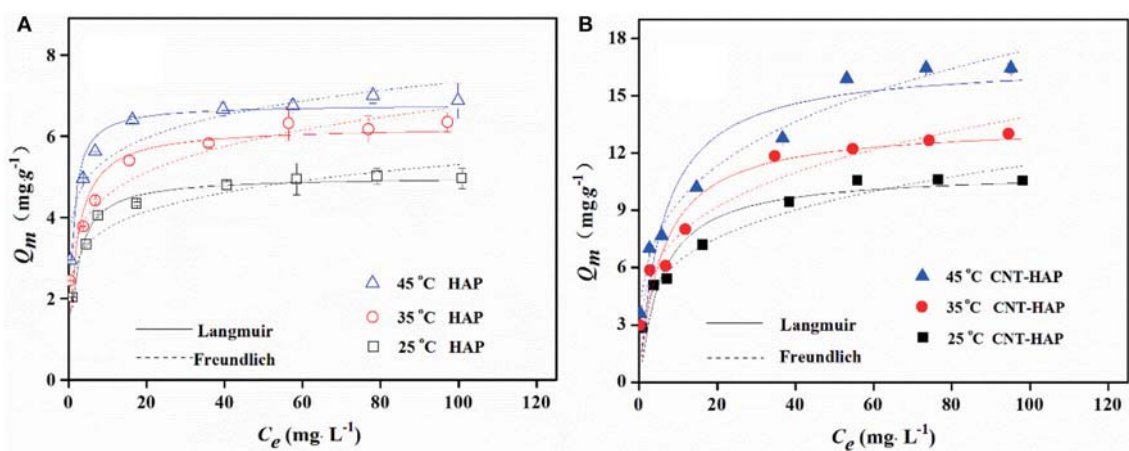
FIGURE 2 | FT-IR spectra of CNT, HAP, and CNT-HAP.

TABLE 4 | Fitted kinetic parameters for fluoride adsorption on HAP and CNT-HAP composite.

Samples	Pseudo first-order			Pseudo second-order		
	$k_1 / (\text{min}^{-1})$	$q_e / (\text{mg}\cdot\text{g}^{-1})$	R^2	$k_2 / (\text{g}\cdot\text{mg}^{-1}\cdot\text{min}^{-1})$	$q_e / (\text{mg}\cdot\text{g}^{-1})$	R^2
HAP	0.22	4.73	0.9204	0.09	4.85	0.9827
CNT-HAP	0.20	5.70	0.3956	0.05	5.97	0.8277

Effects of Solution pH and Co-existing Anions

The adsorption of fluoride on HAP and CNT-HAP from aqueous solutions with different pH values ranging from 3.0 to 10.0 was investigated (Figure 6A). Obviously, the CNT-HAP composite exhibits considerably higher adsorption capacities for fluoride than HAP, thereby displaying great potential application in defluorination from aqueous media. As for the effect of solution

**FIGURE 3** | SEM images of CNT (a), HAP (b), and CNT-HAP (c).**FIGURE 4** | Adsorption isotherms of fluoride on HAP (A) and CNT-HAP (B) at three different temperatures (adsorbents dosage: $0.5\text{ g}\cdot\text{L}^{-1}$, pH: 7.0).

pH, the fluoride adsorption capacities first increase in the pH range of 3.0–6.0, but then decrease in the pH range of 6.0–10.0. Therefore, the optimal pH-value for fluoride removal is 6.0. Under such a weakly acidic condition, the surface of CNT-HAP and HAP would be protonated, thus increase the density of active sites on the surface (Jiménez-Reyes and Solache-Ríos, 2010; Nie et al., 2012). In contrast, the surface of CNT-HAP and HAP would be saturated with negative charges under alkaline condition, which restrains the diffusion of fluoride ions on the surface, thus resulting in lower adsorption capacities. Our results are consistent with some other works, which reported the high fluoride removal efficiency in acidic media owing to the attraction of fluoride anion to the positively charged adsorbents surface, and

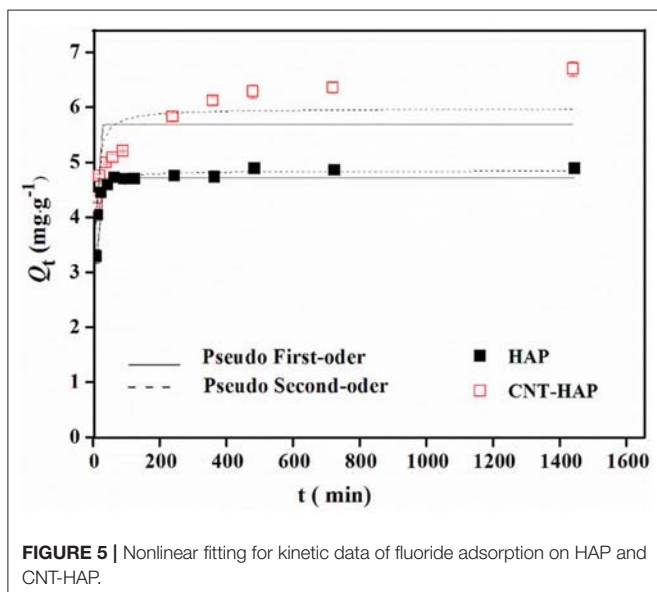


FIGURE 5 | Nonlinear fitting for kinetic data of fluoride adsorption on HAP and CNT-HAP.

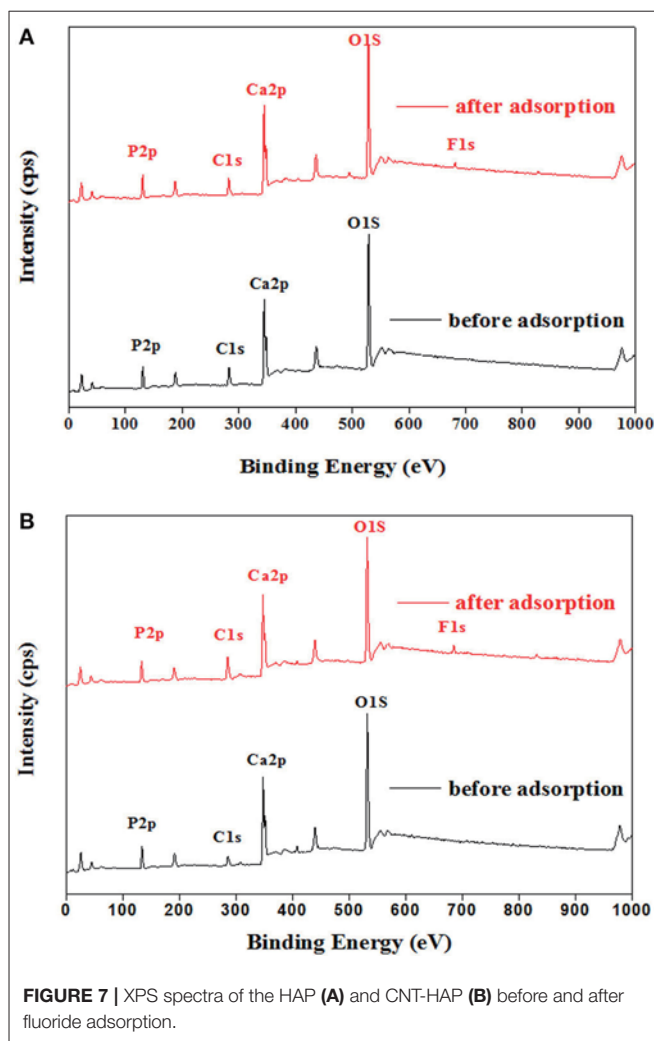


FIGURE 7 | XPS spectra of the HAP (A) and CNT-HAP (B) before and after fluoride adsorption.

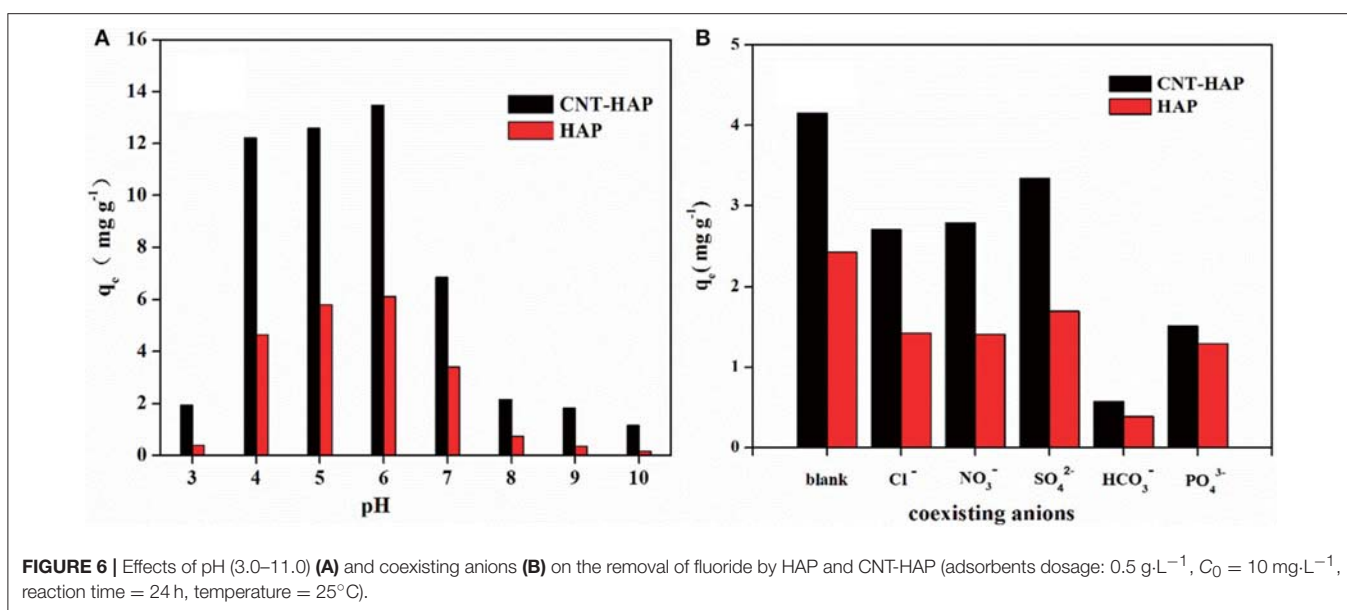
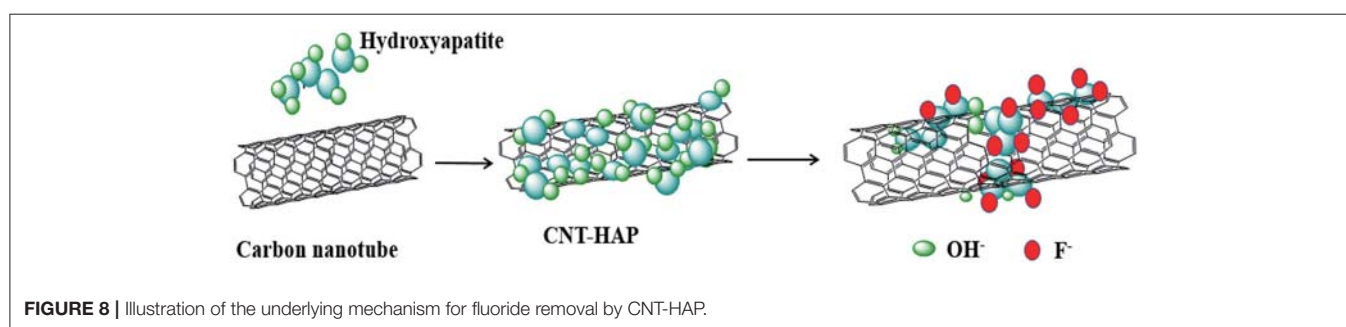


FIGURE 6 | Effects of pH (3.0–11.0) (A) and coexisting anions (B) on the removal of fluoride by HAP and CNT-HAP (adsorbents dosage: 0.5 g L^{-1} , $C_0 = 10 \text{ mg L}^{-1}$, reaction time = 24 h, temperature = 25°C).



the low fluoride removal efficiency in alkaline media due to the repulsion of fluoride anion from the negatively charge adsorbents surface.

In addition, the removal of fluoride in the presence of five co-existing anions (Cl^- , NO_3^- , HCO_3^- , SO_4^{2-} , and PO_4^{3-}) were investigated, and results are shown in **Figure 6B**. As can be seen, the introduction of Cl^- , NO_3^- , and SO_4^{2-} have slightly negative effect on the fluoride removal efficiency, while the introduction of HCO_3^- and PO_4^{3-} has significantly negative impact. This phenomenon can be explained by the charge/radius (Z/r , \AA^{-1}) of these anions. In our case, the order of Z/r values of some common anions is PO_4^{3-} ($3/2.38$) > SO_4^{2-} ($2/2.30$) > F^- ($1/1.33$) > OH^- ($1/1.37$) > HCO_3^- ($1/1.56$) > NO_3^- ($1/1.79$) > Cl^- ($1/1.81$) (Yang et al., 2014). Clearly, the Z/r value of PO_4^{3-} is the largest among these anions, suggesting that PO_4^{3-} could easily form bond with Ca^{2+} in competition with F^- , and reduce the fluoride adsorption capacities (Nie et al., 2012). The Z/r value of HCO_3^- ($1/1.56$) is similar to that of OH^- ($1/1.37$), as a result, it could replace the OH^- in HAP, which subsequently influence the fluoride adsorption capacities. SO_4^{2-} , though with high Z/r value as well, has only slight effect on the fluoride adsorption capacities because of its large ionic radii (2.30 \AA). Cl^- and NO_3^- also have only slight influence on the fluoride adsorption capacities because of they have lower ability for binding with the active sites on adsorbents than F^- (Mohanty et al., 2005).

Brunauer-Emmett-Teller Analysis

The BET surface area of CNT-HAP composite was determined to be $70.94 \text{ m}^2 \cdot \text{g}^{-1}$, being much larger than CNT and HAP (32.60 and $20.78 \text{ m}^2 \cdot \text{g}^{-1}$), which is consistent with the results concluded from SEM images. The enhancement of specific surface area in CNT-HAP composite can be explained by the vertical growth of HAP on the surface of CNT, although they are not assembled compactly. Consequently, the CNT-HAP composite exhibits improved internal density.

Generally, the fluoride removal by HAP is subjected to ion exchange, during which the original hydroxyl anions attached to HAP are replaced by fluoride anions (Chen et al., 2016). To examine the reaction mechanism for fluoride adsorption on CNT-HAP, the XPS spectra of HAP and CNT-HAP before and after fluoride adsorption were collected and shown in **Figure 7**. As shown in **Figure 7A**, the F 1s signal locating at 680 eV can be observed in the XPS spectra of HAP after fluoride adsorption, indicating that fluoride is binding to the surface of HAP. In the XPS spectra shown in **Figure 7B**, the F 1s signal locating at 680 eV

also appears after fluoride adsorption on CNT-HAP, which is similar to the case of fluoride adsorption on HAP. Therefore, we confirm that the fluoride removal by CNT-HAP is also subjected to anion exchange mechanism.

Based on the results obtained, the underlying mechanism for fluoride removal by CNT-HAP is proposed and depicted in **Figure 8**. First, the HAP is doped with CNT via co-precipitation method to produce CNT-HAP composite. The HAP is mainly loaded on the surface of CNT, and the CNT-HAP composite is of large surface area. Then the hydroxyl anions in HAP adsorb fluoride via ion exchange. The hydroxyl ion in solution will increase the pH of the bath solution during the experiments, thus the reaction was suitable to occur in a weakly acidic condition, which was consistent with the result showed above. In summary, it is suggested that the significantly enhance fluoride removal efficiency of CNT-HAP is attributed to the cooperative effect of surface hydroxyl anions in HAP and large surface area of CNT.

CONCLUSION

The hydroxyapatite decorated with carbon nanotube was prepared and used as an effective adsorbent for fluoride removal. The adsorption of fluoride on CNT-HAP could be well described by the Freundlich model. The nature of the adsorption process is spontaneous and endothermic. The kinetics of adsorption follows pseudo-second-order. The defluorination capacity can be significantly affected by the solution pH and co-existing anions. Combining the results from XRD, FTIR, SEM, BET, and XPS analysis, it is demonstrated that the adsorption mechanism follows an anion exchange process. The efficiency of fluoride removal by CNT-HAP is greatly enhanced in relative to the pristine HAP, because the introduction of CNT can enlarge the specific surface area of HAP, thereby affording more surface hydroxyl anions to be replaced by fluoride.

AUTHOR CONTRIBUTIONS

QT: Performed the experiments and the data analyses and wrote the manuscript; TD: Helped performed the experiments and analyze the data; PL: Revised the manuscript; PZ: Coordinated and supervised the research activities that are being described in the manuscript, and DW: Contributed to the conception of this study.

ACKNOWLEDGMENTS

We would like to thank the support of Analysis and Test Center of Nanchang University for infrastructure and morphology characterizations. We would like to thank Dr. Kuan Huang (Nanchang University) for suggestions contributing to

the final script. This project is financially supported by National Nature Science Foundation of China No. 21467014, No. 21767018, Postdoctoral Science Foundation of China No. 2017M612164 and the Natural Science Foundation for Distinguished Young Scholars of Jiangxi Province No. 20171BCB23017.

REFERENCES

- Amini, M., Mueller, K., Abbaspour, K. C., Rosenberg, T., Afyuni, M., Møller, K. N., et al. (2008). Statistical modeling of global geogenic fluoride contamination in groundwaters. *Environ. Sci. Technol.* 42, 3662–3668. doi: 10.1021/es071958y
- Beladi, F., Saber-Samandari, S., and Saber-Samandari, S. (2017). Cellular compatibility of nanocomposite scaffolds based on hydroxyapatite entrapped in cellulose network for bone repair. *Mater. Sci. Eng. C Mater. Biol. Appl.* 75, 385–392. doi: 10.1016/j.msec.2017.02.040
- Chen, L., He, S., He, B.-Y., Wang, T.-J., Su, C.-L., Zhang, C., et al. (2012). Synthesis of iron-doped titanium oxide nanoadsorbent and its adsorption characteristics for fluoride in drinking water. *Ind. Eng. Chem. Res.* 51, 13150–13156. doi: 10.1021/ie300102v
- Chen, L., Zhang, K.-S., He, J.-Y., Xu, W.-H., Huang, X.-J., and Liu, J.-H. (2016). Enhanced fluoride removal from water by sulfate-doped hydroxyapatite hierarchical hollow microspheres. *Chem. Eng. J.* 285, 616–624. doi: 10.1016/j.cej.2015.10.036
- Gao, S., Cui, J., and Wei, Z. (2009). Study on the fluoride adsorption of various apatite materials. *J. Fluorine Chem.* 130, 1035–1041. doi: 10.1016/j.jfluchem.2009.09.004
- He, J., Zhang, K., Wu, S., Cai, X., Chen, K., Li, Y., et al. (2015). Performance of novel hydroxyapatite nanowires in treatment of fluoride contaminated water. *J. Hazard. Mater.* 303, 119–130. doi: 10.1016/j.jhazmat.2015.10.028
- He, J., Chen, K., Cai, X., Li, Y., Wang, C., Zhang, K., et al. (2017). A biocompatible and novel-defined Al-HAP adsorption membrane for highly effective removal of fluoride from drinking water. *J. Colloid Interface Sci.* 490, 97–107. doi: 10.1016/j.jcis.2016.11.009
- Huang, H., Liu, J., Zhang, P., Zhang, D., and Gao, F. (2017). Investigation on the simultaneous removal of fluoride, ammonia nitrogen and phosphate from semiconductor wastewater using chemical precipitation. *Chem. Eng. J.* 307, 696–706. doi: 10.1016/j.cej.2016.08.134
- Jagtap, S., Yenkie, M. K., Labhsetwar, N., and Rayalu, S. (2012). Fluoride in drinking water and defluoridation of water. *Chem. Rev.* 112, 2454–2466. doi: 10.1021/cr2002855
- Jamhour, R. M. A. Q. (2005). New inorganic ion-exchange material for the selective removal of fluoride from potable water using ion-selective electrode. *A J. Environ. Sci.* 1, 1–4. doi: 10.3844/ajessp.2005.1.4
- Jiménez-Reyes, M., and Solache-Ríos, M. (2010). Sorption behavior of fluoride ions from aqueous solutions by hydroxyapatite. *J. Hazard. Mater.* 180, 297–302. doi: 10.1016/j.jhazmat.2010.04.030
- Kanno, C. M., Sanders, R. L., Flynn, S. M., Lessard, G., and Myneni, S. C. (2014). Novel apatite-based sorbent for defluoridation: synthesis and sorption characteristics of nano-micro-crystalline hydroxyapatite-coated-limestone. *Environ. Sci. Technol.* 48, 5798–5807. doi: 10.1021/es405135r
- Lei, Y., Xu, Z., Ke, Q., Yin, W., Chen, Y., Zhang, C., et al. (2017). Strontium hydroxyapatite/chitosan nanohybrid scaffolds with enhanced osteoinductivity for bone tissue engineering. *Mat. Sci. Eng. C Mater.* 72, 134–142. doi: 10.1016/j.msec.2016.11.063
- Li, J., Wang, S., Zhang, X., Wei, J., Xu, C., and Luan, Z. (2003). Adsorption of fluoride from water by aligned carbon nanotubes. *Mater. Res. Bull.* 38, 469–476. doi: 10.1016/S0025-5408(02)01063-2
- Li, J., Zhang, S., Chen, C., Zhao, G., Yang, X., Li, J., et al. (2012). Removal of Cu(II) and fulvic acid by graphene oxide nanosheets decorated with Fe₃O₄ nanoparticles. *ACS Appl. Mater. Interf.* 4, 4991–5000. doi: 10.1021/am301358b
- Lin, K.-Y. A., Liu, Y.-T., and Chen, S.-Y. (2016). Adsorption of fluoride to UiO-66-NH₂ in water: stability, kinetic, isotherm and thermodynamic studies. *J. Colloid. Interf. Sci.* 461, 79–87. doi: 10.1016/j.jcis.2015.08.061
- Liu, G., Ye, Q., Chen, W., Zhao, Z., Li, L., and Lin, P. (2015). Study of the relationship between the lifestyle of residents residing in fluorosis endemic areas and adult skeletal fluorosis. *Environ. Toxicol. Phar.* 40, 326–332. doi: 10.1016/j.etap.2015.06.022
- Liu, Q., Guo, H., and Shan, Y. (2010). Adsorption of fluoride on synthetic siderite from aqueous solution. *J. Fluorine Chem.* 131, 635–641. doi: 10.1016/j.jfluchem.2010.02.006
- Luo, J., Luo, X., Crittenden, J., Qu, J., Bai, Y., Peng, Y., et al. (2015). Removal of antimonite (Sb(III)) and antimonate (Sb(V)) from aqueous solution using carbon nanofibers that are decorated with Zirconium Oxide (ZrO₂). *Environ. Sci. Technol.* 49, 11115–11124. doi: 10.1021/acs.est.5b02903
- Mahmoud, M. E., Nabil, G. M., El-Mallah, N. M., Bassiouny, H. I., Kumar, S., and Abdel-Fattah, T. M. (2016). Kinetics, isotherm, and thermodynamic studies of the adsorption of reactive red 195 A dye from water by modified Switchgrass Biochar adsorbent. *J. Ind. Eng. Chem.* 37, 156–167. doi: 10.1016/j.jiec.2016.03.020
- Mohan, S., Singh, D. K., Kumar, V., and Hasan, S. H. (2017). Effective removal of Fluoride ions by rGO/ZrO₂ nanocomposite from aqueous solution: fixed bed column adsorption modelling and its adsorption mechanism. *J. Fluorine Chem.* 194, 40–50. doi: 10.1016/j.jfluchem.2016.12.014
- Mohanty, K., Jha, M., Meikap, B. C., and Biswas, M. N. (2005). Removal of chromium (VI) from dilute aqueous solutions by activated carbon developed from Terminalia arjuna nuts activated with zinc chloride. *Chem. Eng. Sci.* 60, 3049–3059. doi: 10.1016/j.ces.2004.12.049
- Naowanat, N., Thouchprasitchai, N., and Pongstabodee, S. (2016). Adsorption of emulsified oil from metalworking fluid on activated bleaching earth-chitosan-SDS composites: optimization, kinetics, isotherms. *J. Environ. Manage.* 169, 103–115. doi: 10.1016/j.jenvman.2015.12.024
- Neelgund, G. M., and Oki, A. R. (2016). Influence of carbon nanotubes and graphene nanosheets on photothermal effect of hydroxyapatite. *J. Colloid Interf. Sci.* 484, 135–145. doi: 10.1016/j.jcis.2016.07.078
- Nie, Y., Hu, C., and Kong, C. (2012). Enhanced fluoride adsorption using Al (III) modified calcium hydroxyapatite. *J. Hazard. Mater.* 233–234, 194–199. doi: 10.1016/j.jhazmat.2012.07.020
- Nigri, E. M., Bhatnagar, A., and Rocha, S. D. F. (2017). Thermal regeneration process of bone char used in the fluoride removal from aqueous solution. *J. Clean Prod.* 142, 3558–3570. doi: 10.1016/j.jclepro.2016.10.112
- Popat, K. M., Anand, P. S., and Dasare, B. D. (1994). Selective removal of fluoride ions from water by the aluminium form of the aminomethylphosphonic acid-type ion exchanger. *React. Polym.* 23, 23–32. doi: 10.1016/0923-1137(94)90107-4
- Prabhu, S. M., and Meenakshi, S. (2014). Synthesis of surface coated hydroxyapatite powders for fluoride removal from aqueous solution. *Powder Technol.* 268, 306–315. doi: 10.1016/j.powtec.2014.08.041
- Rehman, M. A., Yusoff, I., and Alias, Y. (2015). Fluoride adsorption by doped and un-doped magnetic ferrites CuCexFe_{2-x}O₄: preparation, characterization, optimization and modeling for effectual remediation technologies. *J. Hazard. Mater.* 299, 316–324. doi: 10.1016/j.jhazmat.2015.06.030
- Reynel-Avila, H. E., Mendoza-Castillo, D. I., and Bonilla-Petriciolet, A. (2016). Relevance of anionic dye properties on water decolorization performance using bone char: adsorption kinetics, isotherms and breakthrough curves. *J. Mol. Liq.* 219, 425–434. doi: 10.1016/j.molliq.2016.03.051
- Roy, S., and Dass, G. (2013). Fluoride contamination in drinking water—a review. *Resour. Environ.* 3, 53–58. doi: 10.5923/jr.20130303.02
- Sairam Sundaram, C., Viswanathan, N., and Meenakshi, S. (2009). Fluoride sorption by nano-hydroxyapatite/chitin composite. *J. Hazard. Mater.* 172, 147–151. doi: 10.1016/j.jhazmat.2009.06.152

- Sairam Sundaram, C., Viswanathan, N., Meenakshi, S. (2008). Uptake of fluoride by nano-hydroxyapatite/chitosan, a bioinorganic composite. *Bioresour. Technol.* 99, 8226–8230. doi: 10.1016/j.biortech.2008.03.012
- Schaefer, C. E., Andaya, C., Burant, A., Condee, C. W., Urriaga, A., Strathmann, T. J., et al. (2017). Electrochemical treatment of perfluorooctanoic acid and perfluorooctane sulfonate: insights into mechanisms and application to groundwater treatment. *Chem. Eng. J.* 317, 424–432. doi: 10.1016/j.cej.2017.02.107
- Sharma, M., Mondal, D., Singh, N., Upadhyay, K., Rawat, A., Devkar, R. V., et al. (2017). Seaweed-derived nontoxic functionalized graphene sheets as sustainable materials for the efficient removal of fluoride from high fluoride containing drinking water. *ACS Sustainable Chem. Eng.* 5, 3488–3498. doi: 10.1021/acssuschemeng.7b00198
- Singh, V. K., and Anil Kumar, E. (2016). Measurement and analysis of adsorption isotherms of CO₂ on activated carbon. *Appl. Therm. Eng.* 97, 77–86. doi: 10.1016/j.applthermaleng.2015.10.052
- Subbaiah, M. V., and Kim, D. S. (2016). Adsorption of methyl orange from aqueous solution by aminated pumpkin seed powder: kinetics, isotherms, and thermodynamic studies. *Ecotoxicol. Environ. Saf.* 128, 109–117. doi: 10.1016/j.ecoenv.2016.02.016
- Sun, M., Zhang, P., Wu, D., and Frost, R. L. (2017). Novel approach to fabricate organo-LDH hybrid by the intercalation of sodium hexadecyl sulfate into tricalcium aluminate. *Appl. Clay Sci.* 140, 25–30. doi: 10.1016/j.clay.2017.01.026
- Tadjarodi, A., Moazen Ferdowsi, S., Zare-Dorabei, R., and Barzin, A. (2016). Highly efficient ultrasonic-assisted removal of Hg(II) ions on graphene oxide modified with 2-pyridinecarboxaldehyde thiosemicarbazone: Adsorption isotherms and kinetics studies. *Ultrason. Sonochem.* 33, 118–128. doi: 10.1016/j.ultrsonch.2016.04.030
- Wang, T., Zhang, P., Wu, D., Sun, M., Deng, Y., and Frost, R. L. (2015). Effective removal of zinc (II) from aqueous solutions by tricalcium aluminate (C(3)A). *J. Colloid Interface Sci.* 443, 65–71. doi: 10.1016/j.jcis.2014.11.046
- Xin, S., Guo, X., Hao, H., and Yong, L. (2016). Crystallization kinetics modeling for fluoride removal from steam ammonia wastewater by chemical precipitation. *Ciesc J.* 67, 1357–1367. doi: 10.11949/j.issn.0438-1157.20151079
- Xu, W., Wang, J., Wang, L., Sheng, G., Liu, J., Yu, H., et al. (2013). Enhanced arsenic removal from water by hierarchically porous CeO₂-ZrO₂ nanospheres: role of surface- and structure-dependent properties. *J. Hazard. Mater.* 260, 498–507. doi: 10.1016/j.jhazmat.2013.06.010
- Yang, C., Gao, L., Wang, Y., Tian, X., and Komarneni, S. (2014). Fluoride removal by ordered and disordered mesoporous aluminas. *Microporous Mesoporous Mater.* 197, 156–163. doi: 10.1016/j.micromeso.2014.06.010
- Zhang, J., Chen, N., Su, P., Li, M., and Feng, C. (2017). Fluoride removal from aqueous solution by Zirconium-Chitosan/Graphene Oxide Membrane. *React. Funct. Polym.* 114, 127–135. doi: 10.1016/j.reactfunctpolym.2017.03.008
- Zhang, L. E., Huang, D., Yang, J., Wei, X., Qin, J., Ou, S., et al. (2017). Probabilistic risk assessment of Chinese residents' exposure to fluoride in improved drinking water in endemic fluorosis areas. *Environ. Pollut.* 222, 118–125. doi: 10.1016/j.envpol.2016.12.074
- Zhang, P., Qian, G., Xu, Z. P., Shi, H., Ruan, X., Yang, J., et al. (2012). Effective adsorption of sodium dodecylsulfate (SDS) by hydrocalumite (CaAl-LDH-Cl) induced by self-dissolution and re-precipitation mechanism. *J. Colloid Interface Sci.* 367, 264–271. doi: 10.1016/j.jcis.2011.10.036
- Zúñiga-Muro, N. M., Bonilla-Petriciolet, A., Mendoza-Castillo, D. I., Reynel-Ávila, H. E., and Tapia-Picazo, J. C. (2017). Fluoride adsorption properties of cerium-containing bone char. *J. Fluorine Chem.* 197, 63–73. doi: 10.1016/j.jfluchem.2017.03.004

Conflict of Interest Statement: The authors declare that the research was conducted in the absence of any commercial or financial relationships that could be construed as a potential conflict of interest.

Copyright © 2018 Tang, Duan, Li, Zhang and Wu. This is an open-access article distributed under the terms of the Creative Commons Attribution License (CC BY). The use, distribution or reproduction in other forums is permitted, provided the original author(s) and the copyright owner are credited and that the original publication in this journal is cited, in accordance with accepted academic practice. No use, distribution or reproduction is permitted which does not comply with these terms.



Adsorption Properties and Mechanism of Cd²⁺ in Water by Zr-containing Silica Residue Purification

Wanting Chen¹, Han Zhang¹, Yu Liang², Hao Ding^{1*} and Sijia Sun¹

¹ Beijing Key Laboratory of Materials Utilization of Nonmetallic Minerals and Solid Wastes, National Laboratory of Mineral Materials, School of Materials Science and Technology, China University of Geosciences, Beijing, China, ² School of Materials Science and Technology, Shenyang University of Chemical Technology, Shenyang, China

Zirconium (Zr)-containing silica residue purification (ZSR-P) discharged from industrial production of ZrOCl₂ was used as an adsorbent, and CdCl₂ solution was used as the simulated wastewater containing cadmium ions (Cd²⁺). The properties and mechanisms of ZSR-P absorbing Cd²⁺ were studied. The results showed that ZSR-P had a good effect on the adsorption and removal of Cd²⁺ in water. The adsorption time, initial concentration of Cd²⁺, and pH of the solution had a significant effect on the adsorption behavior, whilst the pH value had the greatest effect amongst them. Under optimal conditions, the amount of Cd²⁺ adsorbed by ZSR-P was 43.1 mg/g. The isothermal adsorption conformed to the Langmuir adsorption model, and the adsorption kinetics conformed to the secondary adsorption rate model. In ZSR-P-Cd, Cd²⁺ was uniformly distributed on the surface of SiO₂ particles and in the pores formed by the accumulation of particles. Adsorption of Cd²⁺ by ZSR-P was achieved through the reaction between Si-OH on the surface of SiO₂ and Cd²⁺ hydroxyl compounds.

Keywords: Zr-containing silica residue purification, adsorption, Cd²⁺, kinetic model, isothermal models

OPEN ACCESS

Edited by:

Wenbo Wang,
Lanzhou Institute of Chemical Physics
(CAS), China

Reviewed by:

Jianxi Zhu,
Guangzhou Institute of Geochemistry
(CAS), China
Shiyong Sun,
Southwest University of Science and
Technology, China

*Correspondence:

Hao Ding
dinghao113@126.com

Specialty section:

This article was submitted to
Green and Sustainable Chemistry,
a section of the journal
Frontiers in Chemistry

Received: 27 July 2018

Accepted: 29 October 2018

Published: 23 November 2018

Citation:

Chen W, Zhang H, Liang Y, Ding H
and Sun S (2018) Adsorption
Properties and Mechanism of Cd²⁺ in
Water by Zr-containing Silica Residue
Purification. *Front. Chem.* 6:556.
doi: 10.3389/fchem.2018.00556

INTRODUCTION

In recent decades, especially in some developing countries, the world economy has been growing rapidly. The process of industrialization, agricultural economy, and urbanization have been speeding up, which results in heavy metal pollution in water due to mining, metal smelting process, electroplating, and pesticide and fertilizer abuse. The excess emissions of sewage have become more critical than ever (Sekhar et al., 2004; Srivastava and Majumder, 2008; Fu and Wang, 2011; Huang et al., 2014). Heavy metal ions are the main water pollutants. They are easy, biologically enriched and hard to degrade and have high toxicity and stable chemical property, so their damage is extremely serious (Sha et al., 2010). Cadmium ion (Cd²⁺) is one of the most hazardous ions among these heavy metal ions. It has a strong chemical activity in the environment and can easily migrate into the food chain and endanger human health (Solenkova et al., 2014; Venza et al., 2014). Chronic exposure to Cd could cause great damage to cardiovascular system, nervous system, and livers of mammals and humans and may lead to renal failure and ultimately death (Romero-Gonzalez et al., 2001). For this reason, international regulatory agencies have issued wastewater standards for the discharge of various heavy metal ions, including Cd, to limit their entry into surface water and municipal sewers. However, due to the high cost of compliance with pollution control legislation, some small businesses cannot afford it. Therefore, some efficient, convenient, and cost effective processes need to be found for removing heavy metal ions from wastewater.

Currently, there are many available methods to remove heavy metals from the environment (Basci et al., 2004; Dabrowski et al., 2004; Ho and Ofomaja, 2006; Janin et al., 2009; Soylak et al., 2010), including oxidation reduction, chemical precipitation, ion exchange, membrane separation and adsorption, etc. Amongst these methods, oxidation reduction and chemical precipitation are traditional methods which cause some issues such as the large amount of chemical reagents, a secondary source of pollution to the environment, and poor treatment of low-concentration wastewater. Although the methods of ion exchange and membrane separation are effective, the processing scale is small and both the investment cost and operation cost are high. In contrast, the adsorption method, which is highly efficient and simple, suitable for renewable use and is applicable for low-concentration wastewater, requires low investment. Therefore, it is an attractive method with a vital potential for further development. At present, in addition to some nonmetallic minerals, the adsorbents used to treat the wastewater containing heavy metal ions also include activated carbon, humic acid adsorbents, macromolecule materials, biomaterials, and industrial solid wastes (Wong et al., 2003; Sprynskyy et al., 2006; Fan et al., 2007; Veli and Alyüz, 2007; Mohammad-Khah and Ansari, 2009). Bhattacharyya and Gupta (2008), Zhu et al. (2009), and Hong-Ping et al. (2001) studied the adsorption behavior of Cd²⁺ by using montmorillonite and kaolinite with the adsorption method and found that the adsorption capacity of different minerals for Cd²⁺ was different. However, since the surface area of the mineral material is not high, the amount of adsorption is reduced; therefore, a large amount of the adsorbent is required for the operation, which may cause a certain proportion of resources to be wasted. Bayat (2002) used fly ash as an adsorbent to adsorb Zn²⁺ and Cd²⁺ in wastewater. Because of its porous honeycomb structure and large surface area in the internal structure, it has a good adsorption capacity for various metal ions in wastewater. The unmodified fly ash needs to be chemically modified in order to improve its adsorption performance as the small number of functional groups contained on the surface invisibly increases the processing cost of the adsorption process, thus complicating it. The adsorption capacity of the modified fly ash can be compared with that of activated carbon, and the cost is only one third of the activated carbon.

Recently, more attention has been paid to low-cost adsorbents that can be used to replace carbonaceous and mineral materials. Industrial solid waste has become a hot adsorbent material because of its dual advantages in cost and technology. Zirconium (Zr)-containing silica residue is the solid gelatinous waste during industrial acid reaction process in the production of zirconium oxychloride (ZrOCl₂) from zirconite as the raw material. It is a loose-type gel. The main solid components of the gel are amorphous SiO₂ and a small amount of unreacted zirconite, crystalline NaCl, and other impurities. The main liquid components are water, some dissolved substances such as hydrochloric acid (HCl), ZrOCl₂, Na⁺, Cl⁻, and Fe³⁺, Zr⁴⁺, etc. In addition, the Zr-containing silica residue is purified to obtain Zr-containing silica residue purification (ZSR-P), which is mainly composed of amorphous SiO₂. It is expected to be an excellent adsorbent for the treatment of heavy metal ions in

the water by means of the surface charge properties of SiO₂, the characteristics of functional groups, and the pore channels formed by the accumulation of particles. This work undoubtedly has a positive significance for recycling solid waste and reducing the cost of wastewater treatment. However, very few reports have been made on the adsorption behavior and the thermodynamics of heavy metal ions by ZSR-P.

In this work, the adsorption behavior of Cd²⁺ from an aqueous solution using ZSR-P was studied by a set of experiments at various conditions, including temperature, adsorption time, initial concentration of Cd²⁺, and initial pH value. In order to identify the possible mechanisms involved in Cd²⁺ binding by ZSR-P, some characterization methods such as Fourier transform infrared spectrometer (FTIR) and X-ray photoelectron spectroscopy (XPS) were performed along with the analysis.

EXPERIMENTS

Raw Materials, Reagents, and Instruments

Zirconium-containing silica residue purification was obtained by purifying Zr-containing silica residue using a physical method. The Zr-containing silica residue raw material was produced by Henan Baililian Chemical Co. Ltd., Henan, China. The purification process involved the following steps. (1) The Zr-containing silica residue and water were added to a dispersing machine at a solid-liquid ratio of 7% to be crushed and mixed to form a uniform slurry. (2) The mixed slurry was pre-ground by an ultrafine grinder at 1,200 r/min. After 10 min, the alumina grinding balls were added to the mixed slurry at a ball ratio of 15:1. The grinding time was 35 min. (3) The mixed slurry containing the grinding balls was sieved to obtain the slurry. (4) The mixed slurry was separated by centrifugation, and each group of samples was centrifuged three times in order to obtain a gel of high purity containing amorphous silica. (5) The gel obtained after centrifugation was dried to finally obtain ZSR-P (Zhang et al., 2011). Additionally, ZSR-P had a specific surface area of 680.08 m²/g, and the pore diameter was 3.83 nm. The main chemical components before and after purification are shown in **Table 1**. The X-ray diffraction (XRD) analysis of ZSR-P is shown in **Figure 1**. It can be seen that a broad characteristic peak appears at a diffraction angle (2θ) of 20–25°, indicating that ZSR-P contains a large amount of amorphous phase components. In addition, there are no characteristic peaks of other impurities in the XRD pattern. So, combining with chemical analysis results (SiO₂ content of 94.63%), it suggests that the main component of ZSR-P should be amorphous SiO₂. Obviously, the properties of amorphous SiO₂ determine the performance of ZSR-P.

The CdCl₂ solution was used as the simulated wastewater containing Cd²⁺. A certain amount of solid CdCl₂ was weighed and added into distilled water, followed by stirring and dissolving to prepare the CdCl₂ solution with different Cd²⁺ contents. An NaOH solution of 0.1 mol/L or HCl of 0.1 mol/L was used for pH adjustment. All chemicals used were of analytical reagent grade and were obtained from Beijing Chemical Works, China.

The main test equipments used are described as follows. The adsorption reaction of ZSR-P on heavy metal simulated wastewater under different conditions was carried out by

using a SHZ-82 Thermostatic Bath Oscillator (Beijing Guohua Technology Group Ltd., Beijing, China). In addition, pH-3C (Inesa Analytical Instrument Co., Ltd, Shanghai, China) was used to adjust the pH of the reaction solution. Prodigy Inductively Coupled Plasma Atomic Emission Spectrometry (Leeman Labs INC., USA) was used to test the residual heavy metal ion content after the adsorption reaction. The potential of the surface before and after the adsorption of heavy metals by the adsorbent was tested by using a Zetasizer Nano ZS Potentiometer (Malvern Panalytical, UK). The structural characteristics of mesoporous materials were characterized by a specific surface area and porosity analyzer (BET, Quadrasorb Si-MP, Quantachrome, USA). The characterization was mainly at liquid nitrogen temperature (77K), and the relative pressure was $P/P_0 = 0\sim 0.35$. The particle size, surface morphology, and elemental content distribution of ZSR-P were determined by using a scanning

electronic microscope combined with an energy dispersive X-ray detector (SEM-EDX, Hitachi High-Technologies Corporation, Tokyo, Japan). The particle size of the sample material and the comparative sample was observed using a FEI Tecnai G²F30 Field transmission electron microscope (TEM; acceleration voltage of 300 kV). The XRD analyses were conducted on a Rigaku D/max-rA (12 KW) X-ray powder diffractometer (XRD, D/MAX-2000, Rigaku Corporation, Tokyo, Japan) to determine the mineral composition operated with Cu K α radiation at 40 kV and 100 mA and with a scanning speed of 0.5° (2 θ)/min. A Fourier transform infrared spectroscopy (FTIR, Perkin Elmer, Shanghai, China) was used to evaluate the distribution of functional groups on the surface between different materials. The XPS (Kratos Axis Ultra, UK) was used to characterize the surface composition and the combination state of the elements of ZSR-P before and after adsorption. Binding energies were referenced to the C1s peak at 284.8 eV. The oxide content and the elemental composition of the samples were analyzed by X-ray fluorescence (XRF) spectroscopy (S4-Explorer, Brukeraxs, Germany).

TABLE 1 | Comparison XRF of ZSR-P before and after purification.

ZSR		ZSR-P	
Analyte	Result (%)	Analyte	Result (%)
SiO ₂	81.8407	SiO ₂	92.7501
ZrO ₂	10.0438	ZrO ₂	4.7031
Cl	4.5786	Cl	1.2328
Na ₂ O	1.2677	Al ₂ O ₃	0.6939
CaO	0.4332	HfO ₂	0.2300
HfO ₂	0.3437	Na ₂ O	0.0951
Fe ₂ O ₃	0.3437	TiO ₂	0.0879
TiO ₂	0.3208	Fe ₂ O ₃	0.0733
Al ₂ O ₃	0.2688	Cr ₂ O ₃	0.0545
SO ₃	0.2032	K ₂ O	0.0411
MgO	0.1429	ThO ₂	0.0288
Y ₂ O ₃	0.0809	NbO	0.0094
Cr ₂ O ₃	0.0650		
ThO ₂	0.0396		
K ₂ O	0.0272		

Adsorption Experiments

The 100 ml Cd²⁺ solution with a known concentration was weighed and transferred into a 250 mL Erlenmeyer flask, regulating the pH value and adding a certain amount of ZSR-P into the suspension. The suspension was shaken for a certain period of time and then centrifuged to obtain a precipitate and a supernatant liquid, which were the ZSR-P products adsorbing Cd²⁺ (ZSR-P-Cd) and the Cd²⁺ removed from the solution, respectively. The Cd²⁺ content in the supernatant can be measured to evaluate the adsorption effect.

Characterization and Evaluation Method

(1) Calculation of adsorption amount

Inductively coupled plasma atomic emission spectrometry (ICP-AES) was used to determine the Cd²⁺ concentration of the supernatant after adsorption. The adsorption amount of Cd²⁺ by ZSR-P was calculated by the following formula:

$$q = \frac{(C_0 - C)V}{m}, \quad (1)$$

where C_0 and C are the initial concentration and residual concentration of Cd²⁺ in the solution, respectively, which are also called the concentrations before and after adsorption by ZSR-P (mg/L); q is the adsorption capacity of Cd²⁺ adsorbed by ZSR-P (mg/g); V is the solution volume (L); and m is the quality of ZSR-P added (g).

(2) Surface hydroxyl test

An amount of 2 g of the sample to be tested was weighed and placed in a 200 mL beaker, adding 75 mL of NaCl solution, which had a quality score of 0.2; 25 mL of absolute ethanol was added to the mixture, and then the mixture was stirred evenly with a magnetic stirrer. After adjusting the pH of the solution to 4 by using 0.1 mol/L NaOH or 0.1 mol/L HCl, 0.1 mol/L NaOH was added to raise the pH of the solution to 9 slowly and the pH value was kept unchanged for 20 s. The volume of NaOH used was recorded, and the

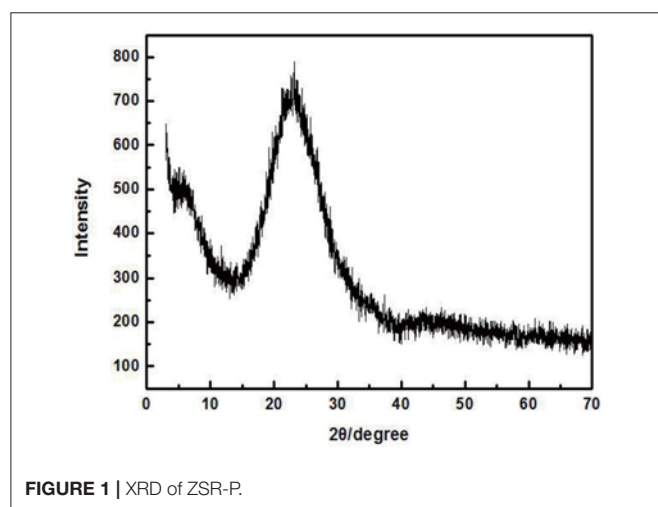


FIGURE 1 | XRD of ZSR-P.

number of hydroxyl groups N per square nanometer of the sample was calculated according to the following formula:

$$N = \frac{CVN_A \times 10^{-3}}{Sm}, \quad (2)$$

where C is the concentration of the NaOH solution (mol/L); V is the volume (L) of the NaOH solution; N_A is Avogadro's constant; S is the specific surface area of the sample (m²/g); and m is the mass of the sample (g).

RESULTS AND DISCUSSION

Study on Adsorption Properties

Effect of Temperature

The Cd²⁺ solution with a concentration of 100 mg/L (actual measured value was 94.97 mg/L by ICP-AES) was adjusted to an initial pH of 8. Later, 3 g/L of ZSR-P was added and heated to a certain temperature; the thermal insulation oscillation time was 10 min. **Figure 2** shows the effect of solution temperature on the adsorption of Cd²⁺ by ZSR-P. It can be seen that as the temperature rose from 25°C (room temperature) to 45°C, the amount of Cd²⁺ adsorbed by ZSR-P remained unchanged. When the temperature rose to 65°C, the adsorption amount increased slightly, indicating that temperature had little effect on the adsorption of Cd²⁺ by ZSR-P. According to the test results, considering the cost and operation conveniences for the treatment of the actual wastewater, the adsorption of the Cd²⁺ solution should be carried out at a temperature of 25°C, which is the normal temperature.

Adsorption Kinetics

The effect of the adsorption time on the adsorption of Cd²⁺ by ZSR-P is shown in **Figure 3**. The concentration of the Cd²⁺ solution used was 100 mg/L (actual measured value was 106.87 mg/L by ICP-AES), initial pH was 8, temperature was 25°C, and

ZSR-P dosage was 3 g/L. It can be seen from **Figure 3** that ZSR-P showed a fast adsorption behavior when the adsorption time was between 0 and 3 min. The adsorption time exceeded 3 min, and the adsorption capacity increased slowly and reached an equilibrium value at 7 min; the value was 22 mg/g. It showed that ZSR-P had a good effect on Cd²⁺ adsorption, and the effect of Cd²⁺ removal from the water was obvious.

According to the adsorption data of Cd²⁺ by ZSR-P in **Figure 3**, fitting was performed according to Lagergren quasi-first-order kinetic model and quasi-second-order kinetic model. The equations of the two models are as follows:

$$\text{Quasi - first - order kinetic model : } \log(Q_e - Qt) = \log Q_e - \frac{K_1}{2.303} \bullet t \quad (3)$$

$$\text{Quasi - second - order kinetic model : } \frac{t}{Qt} = \frac{1}{2K_2 \bullet Q_e^2} + \frac{t}{Q_e} \quad (4)$$

In the formula, Q_e is the quality (mg/g) of Cd²⁺ adsorbed by ZSR-P in solution during adsorption equilibrium; Q_t is the quality (mg/g) of Cd²⁺ adsorbed by ZSR-P in solution at adsorption time t ; and K_1 and K_2 are empirical factors.

Table 2 shows the parameters of the fitted kinetic equations. **Figure 4** compares the fitting curves and the distribution of the experimental data points. According to the quasi-first-order kinetic model, the correlation coefficient R^2 was only 0.035, indicating a low level of fitting degree. According to the quasi-second-order kinetic model, R^2 was as high as 0.999, indicating a high fitting degree. Obviously, the adsorption of Cd²⁺ by ZSR-P conformed to the pseudo-second-order kinetic model, and it also indicated that this adsorption was the surface adsorption reaction control process (Ho et al., 2000).

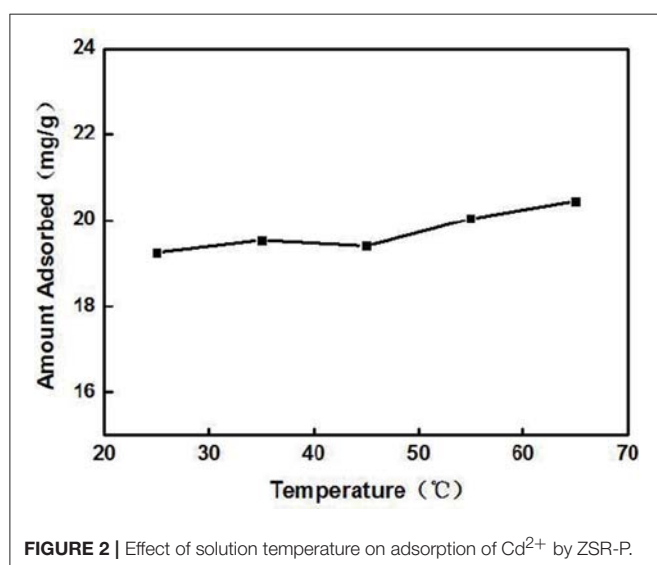


FIGURE 2 | Effect of solution temperature on adsorption of Cd²⁺ by ZSR-P.

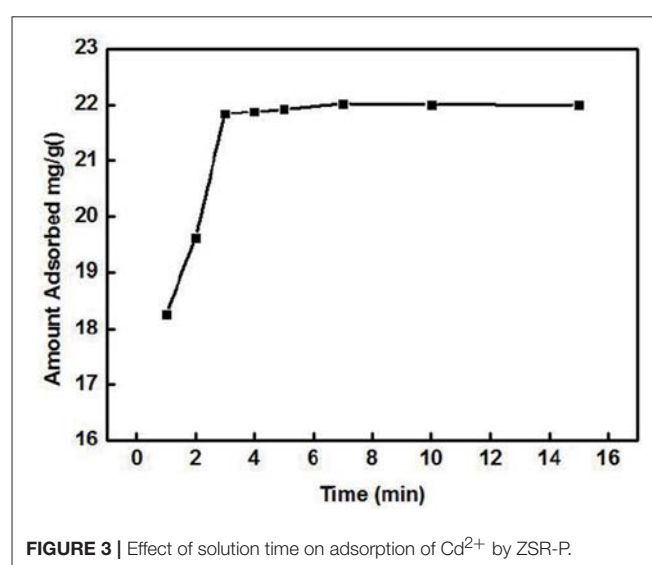


FIGURE 3 | Effect of solution time on adsorption of Cd²⁺ by ZSR-P.

Equilibrium Isotherms

Figure 5 shows the relationship between Cd²⁺ residual concentration (equilibrium concentration) in the solution and Cd²⁺ adsorption amount under the conditions of solution temperature 25°C, pH 8, ZSR-P dosage 3g/L, and adsorption time 15 min (In order to ensure that the adsorption reaction of Cd²⁺ by ZSR-P was fully balanced, the adsorption time was increased to 15 min), which is called the adsorption isotherm. It can be seen that with the increase in the concentration of Cd²⁺, the adsorption amount of Cd²⁺ by ZSR-P continued to increase until the concentration of Cd²⁺ was more than 80 mg/L; the stable value of the adsorption amount was 28 mg/g. According to the data in **Figure 5**, the isotherm of Cd²⁺ adsorbed by ZSR-P can be model-regressed. The Langmuir and Freundlich adsorption isothermal models commonly used are as follows.

Langmuir equation:

$$\frac{C_e}{Q_e} = \frac{1}{K_L Q_m} + \frac{C_e}{Q_m} \quad (5)$$

Freundlich equation:

$$\ln Q_e = \ln K_f + \frac{1}{n} \ln C_e \quad (6)$$

In the formula, C_e is the equilibrium concentration (mg/L) of Cd²⁺ adsorbed by ZSR-P in solution, Q_e is the adsorption amount (mg/g), Q_m is the saturated adsorption amount (mg/g), and K_L , K_f , and n are all empirical coefficients.

The data in **Figure 5** were processed and model-fitted to obtain the adsorption isotherm equations described by the

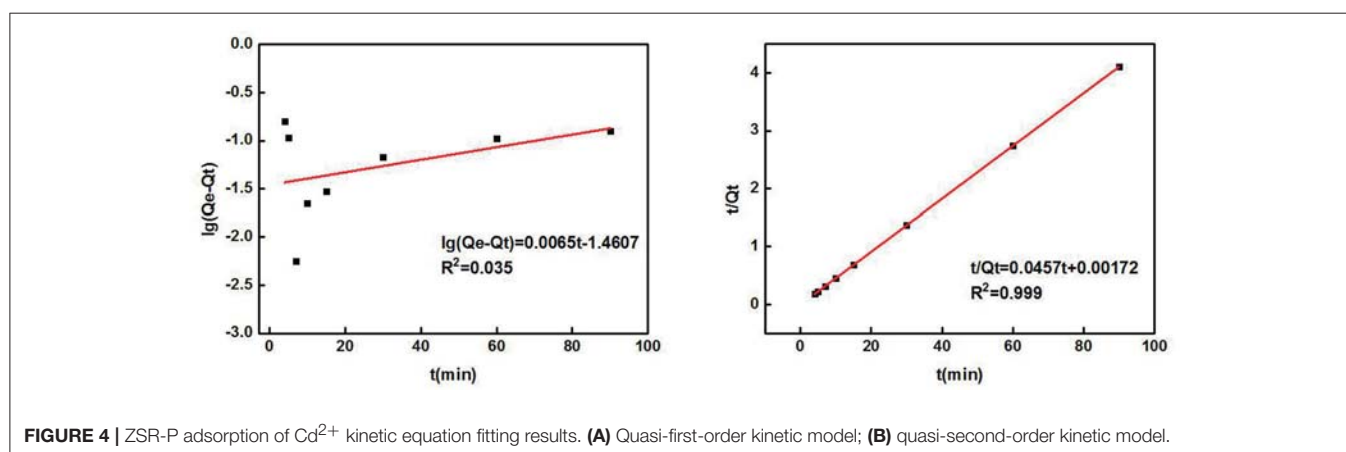
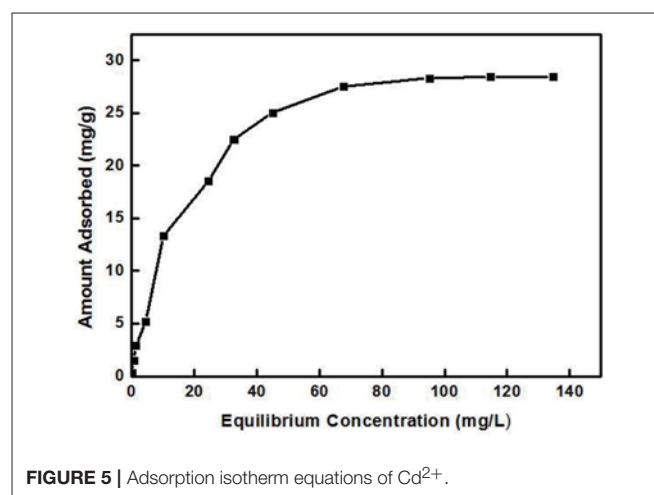
TABLE 2 | ZSR-P adsorption kinetic parameters of Cd²⁺.

Quasi-first-order kinetic model			Quasi-second-order kinetic model		
Q _e (mg/g)	K ₁	R ²	Q _e (mg/g)	K ₂	R ²
28.89	0.015	0.035	21.88	0.607	0.999

Langmuir and Freundlich models, as shown in **Table 3** and **Figure 6**. It can be seen that the correlation constants R^2 of the fitted Langmuir and Freundlich adsorption models were 0.994 and 0.85, respectively, indicating that the Langmuir model can better describe the adsorption isothermal behavior on Cd²⁺ by ZSR-P. The above results indicated that the adsorption of Cd²⁺ by ZSR-P was a monolayer adsorption, which indicated that the adsorption site was a single layer arrangement. The adsorption constant K_L was 0.058 (the value was small), indicating that the adsorption sites have a strong affinity (Langmuir, 2015).

Effect of pH

A 3 g/L solution of ZSR-P was added to the Cd²⁺ solution with different pH values under the conditions of solution Cd²⁺ concentration of 100 mg/L (actual measured value was 108.39 mg/L by ICP-AES) and temperature of 25°C, and then it was oscillated for 10 min to perform adsorption. **Figure 7** shows the effect of solution pH on adsorption. From **Figure 7**, it can be seen that the solution pH had a great influence on the adsorption of Cd²⁺ by ZSR-P. When pH value was less than 6, the adsorption



amount of Cd²⁺ was less than 10 mg/g, indicating that when pH was low, the adsorption of Cd²⁺ by ZSR-P was poor. When the pH was higher than 7, the adsorption amount increased greatly, and the maximum value was reached at pH 9, which was 43.1 mg/g. It showed that increasing the pH of the Cd²⁺ solution can greatly enhance the adsorption of Cd²⁺ by ZSR-P. The main reason was that Cd²⁺ was prone to hydrolysis at a higher pH, while ZSR-P has a stronger affinity to Cd²⁺ hydrolysate than free Cd²⁺ (Bayat, 2002). Obviously, the pH value of the solution was crucial for the adsorption of Cd²⁺ by ZSR-P.

TABLE 3 | Results of the fitting models of Cd²⁺ adsorption by ZSR-P.

Langmuir model			Freundlich model		
Q _m	K _L	R ²	n	K _f	R ²
33.33	0.058	0.994	2.22	3.78	0.85

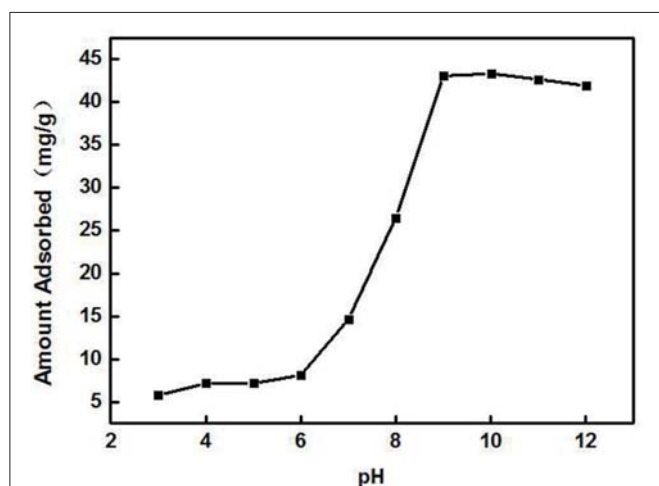


FIGURE 7 | Effect of pH on the adsorption of Cd²⁺ by ZSR-P.

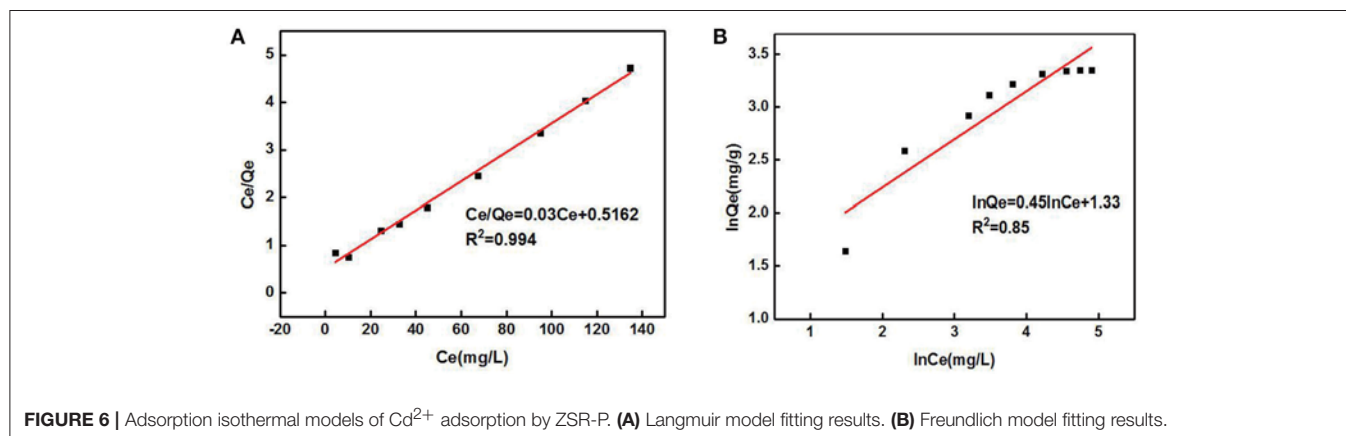


FIGURE 6 | Adsorption isothermal models of Cd²⁺ adsorption by ZSR-P. (A) Langmuir model fitting results. (B) Freundlich model fitting results.

ADSORPTION MECHANISM

Analysis of Adsorption Position

Figure 8 shows the SEM images and the surface distribution of the elements, such as O, Si, Zr, and Cd, of ZSR-P raw material and adsorbed Cd²⁺ product (ZSR-P-Cd). **Table 4** shows the energy spectrum analysis (EDX) values of each element on the surface. It can be seen that there was no Cd in the ZSR-P raw material while there was a large amount of Cd in ZSR-P-Cd, which was consistent with the test results of the adsorption amount of Cd²⁺. The distribution area of Cd was consistent with the position of ZSR-P particles in the SEM images, indicating that Cd²⁺ was uniformly adsorbed on the surface of SiO₂ particles in ZSR-P.

Figure 9 shows the TEM images of ZSR-P and ZSR-P-Cd. It can be clearly seen from **Figure 9A** that ZSR-P is mainly composed of aggregates formed by combining primary particles with sizes of about 20 nm. The small particles adhere to each other, and large aggregates of particles were formed. Due to the small particle size of the primary particles, ZSR-P had a large specific surface area, which was consistent with the test results. The large amount of hydroxyl groups present on the surface may provide a large number of adsorption and reaction binding sites for Cd²⁺. **Figure 9B** shows the TEM images of ZSR-P-Cd. It can be seen that the aggregated shape of ZSR-P-Cd particles was consistent with that of ZSR-P, indicating that no new substances were produced in the adsorption reaction. It was inferred that Cd²⁺ was adsorbed on the surface of ZSR-P and binding occurs between their interfaces.

Adsorbent Properties

Changes of Zeta Potential

The zeta potential is the difference between the shear plane of the solid-liquid relative movement and the potential inside the solution. The magnitude and the positive and negative values are determined by the solid surface properties, the Stern layer of the solid-liquid interface, the properties of the medium, and the concentration and nature of the ions in the solvation layer, which can reflect the difference in surface properties of ZSR-P before and after the adsorption of Cd²⁺ (Moreno-Castilla

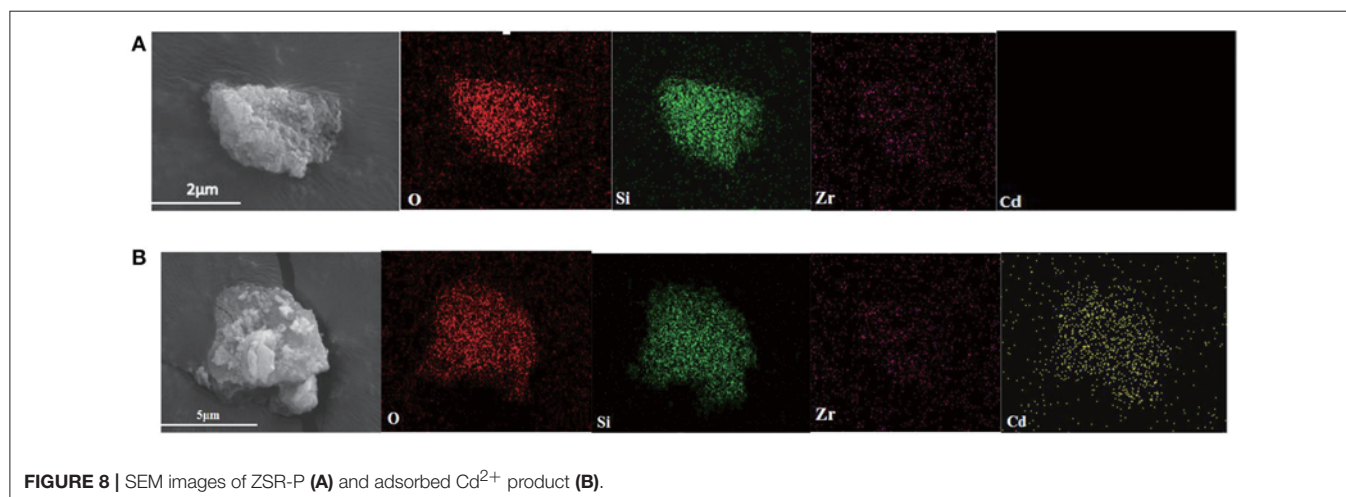
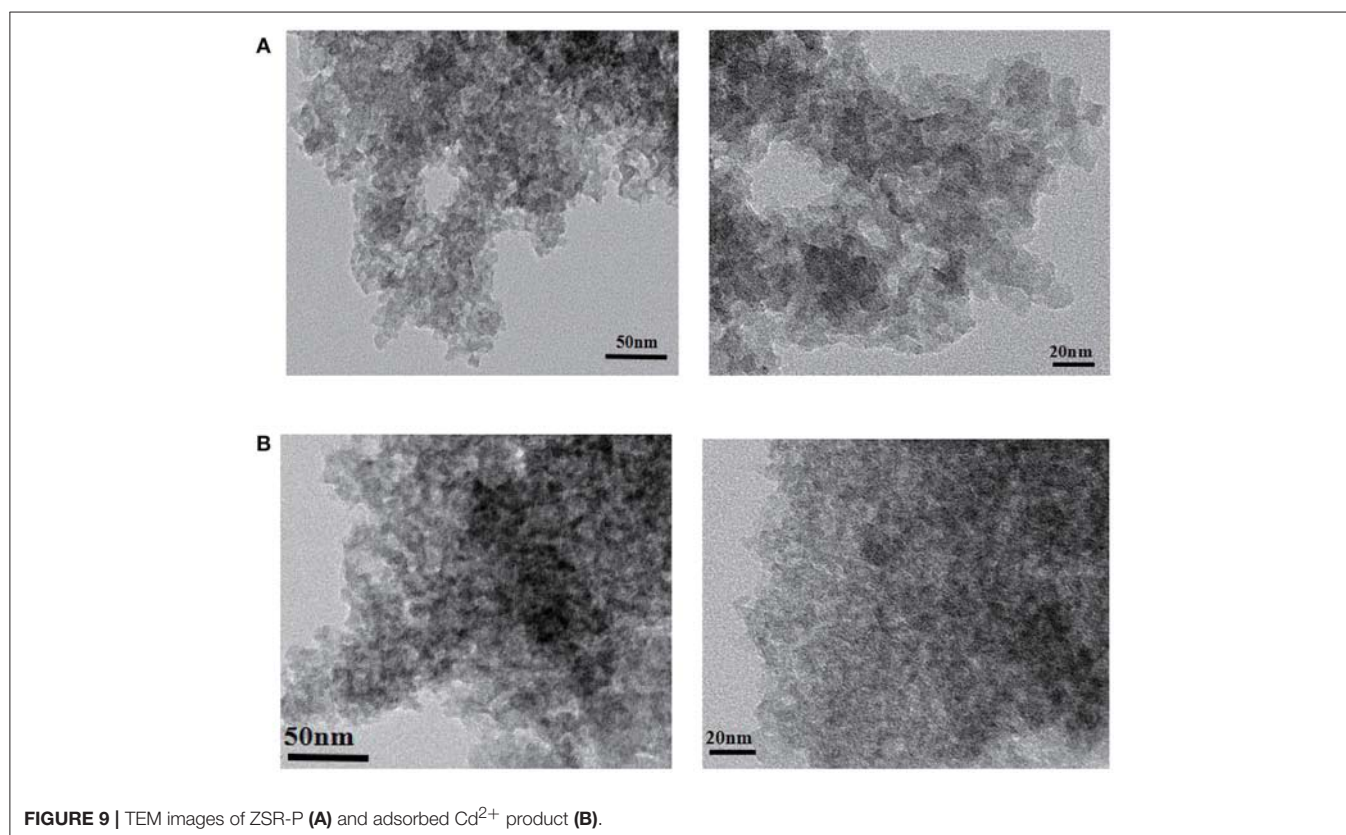


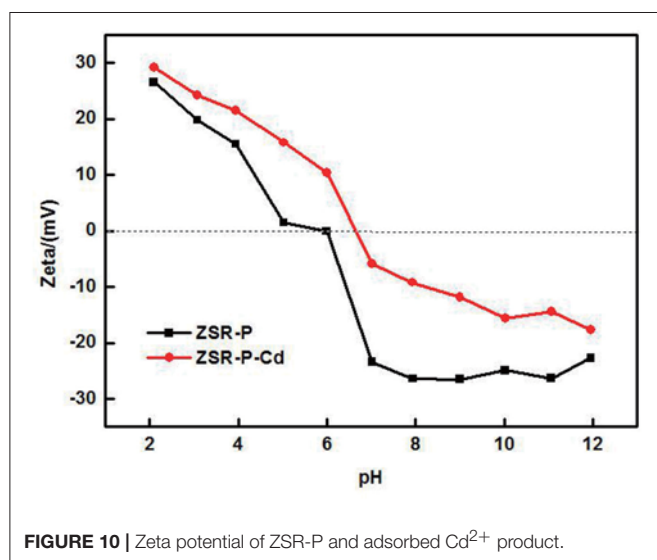
TABLE 4 | Elemental analysis of ZSR-P and adsorbed Cd²⁺ product.

Sample	O		Si		Zr		Cd	
	Atom fraction	Weight fraction	Atom fraction	Weight fraction	Atom fraction	Weight fraction	Atom fraction	Weight fraction
ZSR-P	78.42	59.17	17.47	23.14	4.11	17.69	0	0
ZSR-P-Cd	76.90	54.64	18.10	22.58	2.32	9.41	2.68	13.37



et al., 2000, 2001). **Figure 10** shows the surface zeta potential values of ZSR-P raw materials and adsorbed Cd²⁺ products (ZSR-P-Cd) at different pH conditions. It can be seen that the zeta potential of the surface before and after the adsorption of Cd²⁺ by ZSR-P in the water system decreased with the increase in the pH value. When pH was less than 5.92, the zeta potential of the ZSR-P surface was positive, which indicated that the surface charge of ZSR-P was positive, and the counter ion of the Stern layer in the solution was negative. As the pH increased, the H⁺ ions in the solution gradually decreased, and the OH⁻ ions in the Stern layer and the diffusion layer of the ZSR-P surface gradually increased. The zeta potential of the ZSR-P surface was negative, and the absolute value gradually increased. When ZSR-P adsorbed Cd²⁺, the point of zero charge of ZSR-P-Cd shifted to the right to pH 6.7, indicating that more cations were adsorbed on the surface of the particles. When the pH was less than 6.7, the surface charge value of ZSR-P-Cd was larger than that of ZSR-P under the same pH condition. When the pH was greater than 6.7, the absolute surface charge value of ZSR-P-Cd was smaller than that of ZSR-P at the same pH.

Using the surface hydroxyl test method in formula (2), the surface hydroxyl groups before and after adsorption of Cd²⁺ by ZSR-P were 1.39/nm² and 1.06/nm², respectively. Therefore, it can be seen from the changes in surface zeta potential and hydroxyl density that under the same pH condition, the number of hydroxyl groups on the surface of the product after adsorption of Cd²⁺ were much smaller than that on the surface of ZSR-P. This indicates that when Cd²⁺ was added to the solution, ZSR-P was surrounded by a large number of cations in the solution, and the large amount of hydroxyl groups on the surface became the main binding site of the adsorption reaction; therefore, Cd²⁺ ions occupy the surface of the ZSR-P particles and the pores formed by the accumulation of particles.

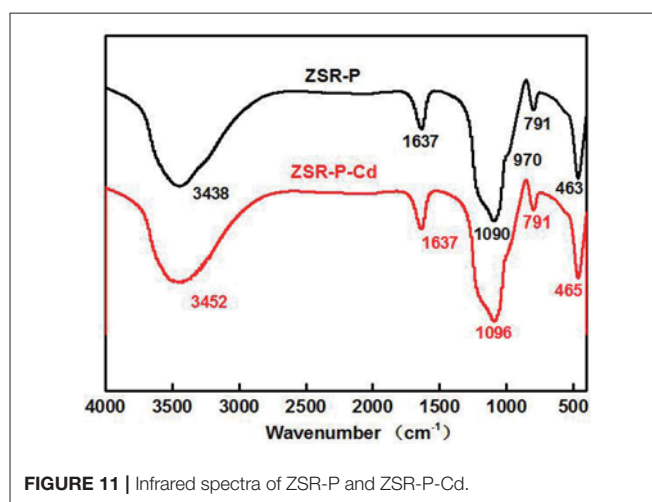


Fourier Transform Infrared (FTIR) Spectroscopy

Figure 11 is the infrared spectra of ZSR-P and its adsorbed Cd²⁺ product (ZSR-P-Cd). In the infrared spectrum of ZSR-P, the peak at 3,438 cm⁻¹ was OH stretching of water; 1,637 cm⁻¹ was OH deformation of water; the strong absorption band caused by Si-O stretching appeared at 1,090 cm⁻¹ and 791 cm⁻¹; the peak at 970 cm⁻¹ belonged to Si-OH stretching; and the peak at 463 cm⁻¹ was Si-O-Si deformation, reflecting the characteristics of amorphous SiO₂ in ZSR-P. The peaks located at 1,637 cm and 3,438 cm were attributed by the abundant hydroxyl groups, which existing on the large specific surface area, absorb the surrounding water molecules. The comparison showed that the above absorption peaks appeared in the spectrum of ZSR-P adsorbed Cd²⁺ product except for the absorption peak at 970 cm⁻¹, and the peaks at 1,090 cm⁻¹ were slightly moved to 1,096 cm⁻¹. It was speculated that the Si-O stretching (Da-Qing et al., 2000) formed on the surface of SiO₂ hydrolyzed to form -SiOH (Bogdan et al., 1996) and combined with Cd²⁺ (d'espinoise de la Caillerie et al., 1997). The disappearance of the Si-OH stretching at 970 cm⁻¹ was presumed to be due to the dehydroxylation reaction on the surface of ZSR-P after the adsorption of Cd²⁺.

XPS Analysis

X-ray photoelectron spectroscopy analysis of ZSR-P and ZSR-P-Cd was performed, and the results are shown in **Figure 12**. The results show that the peaks of O, Si, and Zr appeared in the ZSR-P spectrum, reflecting the characteristics of ZSR-P being a component of SiO₂ and a small quantity of Zr-containing impurities. However, the peak of Cd3d_{5/2} appeared in the XPS of ZSR-P-Cd, and its binding energy was 405.72eV, indicating that Cd²⁺ was adsorbed on the surface of SiO₂, which was consistent with the results of SEM. In addition, the binding energies of Si2s and Si2p in the XPS of ZSR-P were 153.64 and 102.83 eV, respectively. While their binding energies in the XPS of ZSR-P-Cd were 154.07 and 103.04 eV, respectively. The larger binding energy value indicated that the chemical environment of Si had changed after the adsorption of Cd²⁺, which was consistent with



the results of Si-OH on the SiO_2 surface and Cd^{2+} hydrate reactions.

Adsorption Model

Based on the above analysis of the properties and mechanisms of ZSR-P adsorbing Cd^{2+} , an interaction model reflecting this property, mechanism, and process was established and shown in Figure 13.

CONCLUSIONS

- (1) Zirconium-containing silica residue purification is mainly composed of aggregates of amorphous SiO_2 nanoparticles. It has an excellent adsorption and removal effect on Cd^{2+} in water. The pH value of the solution, Cd^{2+} concentration, and adsorption time have a significant effect on the removal effect. In addition, ZSR-P, at a dosage of 3 mg/L, was added to

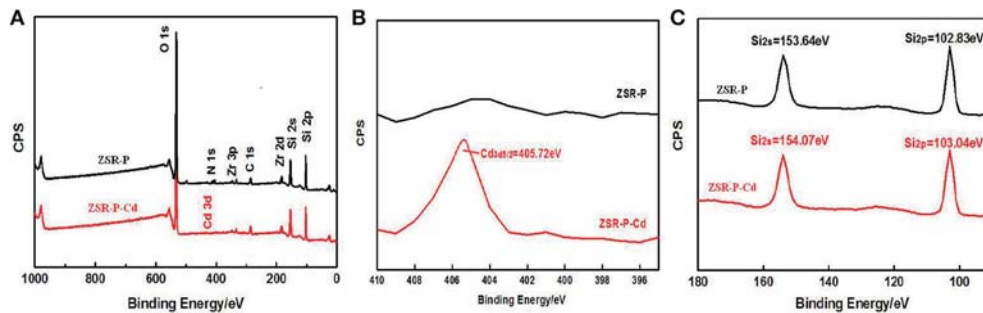


FIGURE 12 | XPS of ZSR-P and ZSR-P-Cd. (A) The XPS full spectrum of ZSR-P and ZSR-P-Cd. (B) The Cd 3d spectrum of ZSR-P-Cd. (C) The Si 2s and Si 2p spectra of ZSR-P and ZSR-P-Cd.

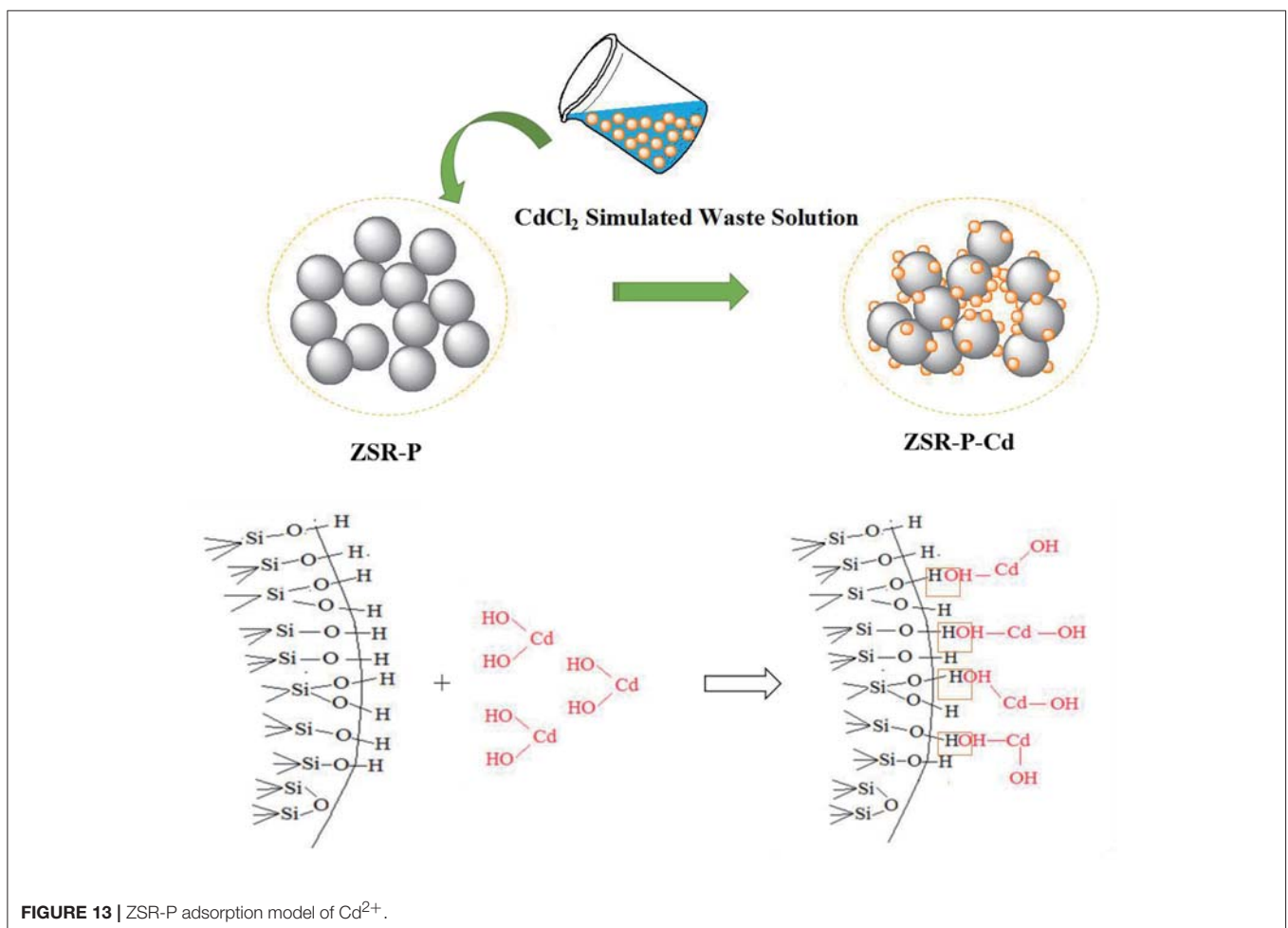


FIGURE 13 | ZSR-P adsorption model of Cd^{2+} .

an aqueous solution, which had a Cd²⁺ concentration of 100 mg/L and pH 9, and then the mixture was shaken for 10 min; subsequently, the adsorption reached an equilibrium. The adsorption amount of Cd²⁺ by ZSR-P is 43.1 mg/g.

- (2) The isothermal adsorption of Cd²⁺ by ZSR-P is in accordance with the Langmuir adsorption model, consistent with the adsorption characteristics of general microporous materials. The adsorption kinetics equation of ZSR-P for Cd²⁺ conforms to the second-order model for adsorption rate.
- (3) The removal of Cd²⁺ in aqueous solution by ZSR-P is mainly based on the adsorption between them. In addition, Cd²⁺ is uniformly distributed on the surface of SiO₂ particles and in the pores formed by the accumulation of particles in ZSR-P-Cd. Adsorption between SiO₂ and Cd²⁺ is achieved by the

reaction between Si-OH on the surface of SiO₂ and Cd²⁺ hydroxyl compounds.

AUTHOR CONTRIBUTIONS

WC, HZ, HD, and SS conceived and designed the experiments. WC, HZ, and YL performed the experiments. WC and SS analyzed the data. HZ, YL, and SS contributed reagents. WC wrote the manuscript. YL retouched the document.

ACKNOWLEDGMENTS

The authors are thankful to the School of Materials Science and Technology, China University of Geoscience (Beijing), China for providing laboratory facilities.

REFERENCES

- Basci, N., Kocadagistan, E., and Kocadagistan, B. (2004). Biosorption of copper (ii) from aqueous solutions by wheat shell. *Desalination* 164, 135–140. doi: 10.1016/S0011-9164(04)00172-9
- Bayat, B. (2002). Combined removal of zinc (ii) and cadmium (ii) from aqueous solutions by adsorption onto high-calcium turkish fly ash. *Water. Air. Soil. Poll.* 136, 69–92. doi: 10.1023/A:1015296032528
- Bhattacharyya, K. G., and Gupta, S. S. (2008). Adsorption of a few heavy metals on natural and modified kaolinite and montmorillonite: a review. *Adv. Colloid. Interfac.* 140, 114–131. doi: 10.1016/j.cis.2007.12.008
- Bogdan, A., Kulmala, M., Gorbunov, B., and Kruppa, A. (1996). Nmr study of phase transitions in pure water and binary H₂O/HNO₃ films adsorbed on surface of pyrogenic silica. *J. Colloid. Interf. Sci.* 177, 79–87. doi: 10.1006/jcis.1996.0008
- Dabrowski, A., Hubicki, Z., Podkościelny, P., and Robens, E. (2004). Selective removal of the heavy metal ions from waters and industrial wastewaters by ion-exchange method. *Chemosphere* 56, 91–106. doi: 10.1016/j.chemosphere.2004.03.006
- Da-Qing, W. U., Diao, G. Y., Wei, J. F., and Yuan, P. (2000). Surface function groups and surface reactions of minerals. *Geol. J. China Univ.* 6, 225–226. doi: 10.16108/j.issn1006-7493.2000.02.019
- d'espinoise de la Caillerie J. B., Aimeur, M. R., Kortobi, Y. E., and Legrand, A. P. (1997). Water adsorption on pyrogenic silica followed by 1h mas nmr. *J. Colloid. Interf. Sci.* 194, 434–439. doi: 10.1006/jcis.1997.5126
- Fan, Z., Yu, B., Yue, Z., Wang, T., Xian, W., Liu, Z., et al. (2007). Preparation of porous chitosan gel beads for copper(ii) ion adsorption. *J. Hazard. Mater.* 147, 67–73. doi: 10.1016/j.jhazmat.2006.12.045
- Fu, F., and Wang, Q. (2011). Removal of heavy metal ions from wastewaters: a review. *J. Environ. Manage.* 92, 407–418. doi: 10.1016/j.jenvman.2010.11.011
- Ho, Y. S., Ng, J. C. Y., and McKay, G. (2000). Kinetics of pollutant sorption by biosorbents: review. *Separ. Purif. Method.* 29, 189–232. doi: 10.1081/SPM-100100009
- Ho, Y. S., and Ofomaja, A. E. (2006). Kinetic studies of copper ion adsorption on palm kernel fibre. *J. Hazard. Mater.* 137, 1796–1802. doi: 10.1016/j.jhazmat.2006.05.023
- Hong-Ping, H. E., Guo, J. G., Zhu, J. X., and Yang, D. (2001). An experimental study of adsorption capacity of montmorillonite, kaolinite and illite for heavy metals. *Acta Petrologica Et Mineralogica.* 20, 573–578.
- Huang, J., Lei, P., Zeng, G., Li, X., Zhao, Y., Liu, L., et al. (2014). Evaluation of micellar enhanced ultrafiltration for removing methylene blue and cadmium ion simultaneously with mixed surfactants. *Sep. Purif. Technol.* 125, 83–89. doi: 10.1016/j.seppur.2014.01.020
- Janin, A., Zaviscka, F., Drogui, P., Blais, J. F., and Mercier, G. (2009). Selective recovery of metals in leachate from chromated copper arsenate treated wastes using electrochemical technology and chemical precipitation. *Hydrometallurgy* 96, 318–326. doi: 10.1016/j.hydromet.2008.12.002
- Langmuir, I. (2015). The adsorption of gases on plane surfaces of glass, mica and platinum. *J. Chem. Phys.* 40, 1361–1403. doi: 10.1021/ja02242a004
- Mohammad-Khah, A., and Ansari, R. (2009). Activated charcoal: preparation, characterization and applications: a review article. *Int. J. Chemtech. Res.* 1, 859–864.
- Moreno-Castilla, C., Carrasco-Mari, N. F., Parejo-Pérez, C., and Ramón, M. V. L. (2001). Dehydration of methanol to dimethyl ether catalyzed by oxidized activated carbons with varying surface acidic character. *Carbon.* 39, 869–875. doi: 10.1016/S0008-6223(00)00192-5
- Moreno-Castilla, C., López-Ramón, M. V., and Carrasco-Marín, F. (2000). Changes in surface chemistry of activated carbons by wet oxidation. *Carbon* 38, 1995–2001. doi: 10.1016/S0008-6223(00)00048-8
- Romero-Gonzalez, M. E., Williams, C. J., and Gardiner, P. H. (2001). Study of the mechanisms of cadmium biosorption by dealginated seaweed waste. *Environ. Sci. Technol.* 35, 3025–3030. doi: 10.1021/es991133r
- Sekhar, K. C., Chary, N. S., Kamala, C. T., Suman Raj D. S., and Sreenivasa Rao A. (2004). Fractionation studies and bioaccumulation of sediment-bound heavy metals in Kolleru lake by edible fish. *Environ. Int.* 29, 1001–1008. doi: 10.1016/S0160-4120(03)00094-1
- Sha, L., Guo, X. Y., Feng, N. C., and Tian, Q. H. (2010). Effective removal of heavy metals from aqueous solutions by orange peel xanthate. *T. Nonferr. Metal. So. C.* 20, 187–191. doi: 10.1016/S1003-6326(10)60037-4
- Solenkova, N. V., Newman, J. D., Berger, J. S., Thurston, G., Hochman, J. S., and Lamas, G. A. (2014). Metal pollutants and cardiovascular disease: mechanisms and consequences of exposure. *Am. Heart. J.* 168, 812–822. doi: 10.1016/j.ahj.2014.07.007
- Soylak, M., Unsal, Y. E., Kizil, N., and Aydin, A. (2010). Utilization of membrane filtration for preconcentration and determination of cu(ii) and pb(ii) in food, water and geological samples by atomic absorption spectrometry. *Food. Chem. Toxicol.* 48, 517–521. doi: 10.1016/j.fct.2009.11.005
- Sprynskyy, M., Buszewski, B., Terzyk, A. P., and Namieśnik, J. (2006). Study of the selection mechanism of heavy metal (Pb²⁺, Cu²⁺, Ni²⁺, and Cd²⁺) adsorption on clinoptilolite. *J. Colloid. Interf. Sci.* 304, 21–28. doi: 10.1016/j.jcis.2006.07.068
- Srivastava, N. K., and Majumder, C. B. (2008). Novel biofiltration methods for the treatment of heavy metals from industrial wastewater. *J. Hazard. Mater.* 151, 1–8. doi: 10.1016/j.jhazmat.2007.09.101

- Veli, S., and Alyüz, B. (2007). Adsorption of copper and zinc from aqueous solutions by using natural clay. *J. Hazard. Mater.* 149, 226–233. doi: 10.1016/j.jhazmat.2007.04.109
- Venza, M., Visalli, M., Biondo, C., Oteri, R., Agliano, F., Morabito, S., et al. (2014). Epigenetic effects of cadmium in cancer: focus on melanoma. *Curr. Genom.* 15, 420–435. doi: 10.2174/138920291506150106145932
- Wong, K. K., Lee, C. K., Low, K. S., and Haron, M. J. (2003). Removal of Cu and Pb by tartaric acid modified rice husk from aqueous solutions. *Chemosphere* 50, 23–28. doi: 10.1016/S0045-6535(02)00598-2
- Zhang, X. J., Ding, H., and Wang, B. K. (2011). Recycling and characterisation of amorphous silica from zr-containing silica residue. *Adv. Mater. Res.* 194–196, 2109–2114. doi: 10.4028/www.scientific.net/AMR.194-196.2109
- Zhu, X. P., Bai, D. K., Xi-Kun, L. I., Zeng, J. P., and Cao, S. Y. (2009). The adsorption behaviors of montmorillonite and some other clay minerals for cadmium. *Acta Petrologica Et Mineralogica.* 28, 643–648.

Conflict of Interest Statement: The authors declare that the research was conducted in the absence of any commercial or financial relationships that could be construed as a potential conflict of interest.

Copyright © 2018 Chen, Zhang, Liang, Ding and Sun. This is an open-access article distributed under the terms of the Creative Commons Attribution License (CC BY). The use, distribution or reproduction in other forums is permitted, provided the original author(s) and the copyright owner(s) are credited and that the original publication in this journal is cited, in accordance with accepted academic practice. No use, distribution or reproduction is permitted which does not comply with these terms.



Carbon Cloth Supported Nano-Mg(OH)₂ for the Enrichment and Recovery of Rare Earth Element Eu(III) From Aqueous Solution

Yinong Li, Chen Tian, Weizhen Liu*, Si Xu, Yunyun Xu, Rongxin Cui and Zhang Lin

The Key Laboratory of Pollution Control and Ecosystem Restoration in Industry Clusters (Ministry of Education), School of Environment and Energy, South China University of Technology, Guangzhou, China

OPEN ACCESS

Edited by:

Hongfei Cheng,
Chang'an University, China

Reviewed by:

Xuan Dou,
Northwestern University, United States
Ping Zhang,
Nanchang University, China

*Correspondence:

Weizhen Liu
weizhliu@scut.edu.cn

Specialty section:

This article was submitted to
Green and Sustainable Chemistry,
a section of the journal
Frontiers in Chemistry

Received: 09 February 2018

Accepted: 30 March 2018

Published: 18 April 2018

Citation:

Li Y, Tian C, Liu W, Xu S, Xu Y, Cui R
and Lin Z (2018) Carbon Cloth
Supported Nano-Mg(OH)₂ for the
Enrichment and Recovery of Rare
Earth Element Eu(III) From Aqueous
Solution. *Front. Chem.* 6:118.
doi: 10.3389/fchem.2018.00118

Nano-Mg(OH)₂ is attracting great attention as adsorbent for pre-concentration and recovery of rare earth elements (REEs) from low-concentration solution, due to its superior removal efficiency for REEs and environmental friendliness. However, the nanoparticles also cause some severe problems during application, including aggregation, blockage in fixed-bed column, as well as the difficulties in separation and reuse. Herein, in order to avoid the mentioned problems, a carbon cloth (CC) supported nano-Mg(OH)₂ (nano-Mg(OH)₂@CC) was synthesized by electrodeposition. The X-ray diffraction and scanning electron microscopy analysis demonstrated that the interlaced nano-sheet of Mg(OH)₂ grew firmly and uniformly on the surface of carbon cloth fibers. Batch adsorption experiments of Eu(III) indicated that the nano-Mg(OH)₂@CC composite maintained the excellent adsorption performance of nano-Mg(OH)₂ toward Eu(III). After adsorption, the Eu containing composite was calcined under nitrogen atmosphere. The content of Eu₂O₃ in the calcined material was as high as 99.66%. Fixed-bed column experiments indicated that no blockage for Mg(OH)₂@CC composite was observed during the treatment, while the complete blockage of occurred to nano-Mg(OH)₂ at an effluent volume of 240 mL. Moreover, the removal efficiency of Mg(OH)₂@CC was still higher than 90% until 4,200 mL of effluent volume. This work provides a promising method for feasible application of nanoadsorbents in fixed-bed process to recycle low-concentration REEs from wastewater.

Keywords: Nano-Mg(OH)₂, carbon cloth, composite, rare earth, recovery

INTRODUCTION

Recent years, Rare earth elements (REEs) are considered to be irreplaceable critical dopants for advanced materials in high-tech applications (Alonso et al., 2012), such as luminescent (Zhang et al., 2018), catalysts (Li et al., 2017; Lin et al., 2017), permanent magnets (Mudryk et al., 2017), and sensor material (Willa et al., 2017), due to their special metallurgical, optical, and electronic properties (Dutta et al., 2016). With the development of the society and industry, the demand for the REEs is increasing all over the world (Dutta et al., 2016; Tansel, 2017). However, the REEs resource is in a serious shortage due to their low reserves and outputs from the natural minerals.

Therefore, in order to relieve the environmental burden and ease the potential supply crisis, many secondary resources for recycling REEs are developed, including discarded REEs-containing solid waste (Maroufi et al., 2017; Tansel, 2017) and industrial wastewater (Binnemans et al., 2013; Wilfong et al., 2017), etc. Nevertheless, the REE concentrations in most of the secondary resources are as low as hundreds of ppm (Binnemans et al., 2013, 2015), which makes their enrichment and separation extremely difficult.

In view of the above issues, adsorption is regarded as an effective technology for the pre-concentration and recovery of REEs, owing to its simplicity, easy handling, sludge-free operation, and cost effectiveness (Liu et al., 2017; Qi et al., 2017; Wilfong et al., 2017). Compared with other adsorbents, nano-Mg(OH)₂, an environmental-friendly material, exhibits rapid kinetics, and high efficiency (with a maximum adsorption capacity of 1,827 mg/g) toward a typical REE of Tb(III) at extremely low concentrations (Li et al., 2013). However, it should be pointed out that, like other nanoadsorbents, the small size of nano-Mg(OH)₂ also caused some issues and difficulties in separation and reuse, including mass transfer and excessive pressure drops when applied in fixed bed or any other flow-through systems (Zhao et al., 2011). Moreover, the release of nanoparticles into the environment is also a possible risk to ecosystems and human health. These drawbacks strongly hinder the application of nano-Mg(OH)₂ in the wastewater treatment (Zhao et al., 2011; Tesh and Scott, 2014).

An effective approach for overcoming the above bottlenecks is to fabricate nano-Mg(OH)₂ onto supporting materials of larger size (Zhao et al., 2011; Tesh and Scott, 2014; Chen et al., 2016). The resultant nanocomposite is expected to retain the inherent properties of nano-Mg(OH)₂, while the supporting material would provide higher mechanical strength and improve the dispersity of nano-Mg(OH)₂ (Chen et al., 2016). In the previous study, common supporting materials include natural polymers (e.g., Chitosan, alginate; Xiao et al., 2015; Zhang L. et al., 2015; Kwon et al., 2016), inorganic materials (He et al., 2011; Chen et al., 2017), synthetic macromolecule materials (Chen et al., 2016; Yu et al., 2016; Zhang et al., 2017), and some carbon materials (e.g., graphene, carbon nanotubes, carbon cloth; Dimpe et al., 2017; Kumar et al., 2017; Tian et al., 2017; Xu et al., 2017). Despite plenty of supporting materials can be alternates for nanomaterials, very few of them were used to support nano-Mg(OH)₂. Jia et al. (2014) reported that the nanofibrous membrane of PA6@Mg(OH)₂, which was fabricated by electrospinning technique combined with hydrothermal strategy, exhibited preferable removal ability to Cr(VI). Xie et al. (2014) developed a novel modified diatomite adsorbent modified by dispersed magnesium oxide nanoflake for the remediation of eutrophic lakes by removing excess PO₄⁴⁻. Li et al. (2011) synthesized a Mg(OH)₂@reduced graphene oxide composite using *in-situ* chemical deposition method. The composite exhibited excellent adsorption effect to methylene blue. In the above studies, nano-Mg(OH)₂ was loaded onto the surface of carriers by coprecipitation or hydrothermal method, which still caused some drawbacks such as complicated

operation, poor controllability, and low synthesis efficiency of nano-Mg(OH)₂.

Compared with the above methods, electrodeposition is a rapid, simple, and low-cost method without high-temperature treatment to fabricate the nano-composites (Lv et al., 2011; Liu T. et al., 2015). Currently, carbon cloth (CC) has been considered to be an ideal candidate for supporting materials by electrodeposition, owing to the following three advantages: (1) CC has abundant functional group, which can fasten the nanoparticles on its surface; (2) CC has excellent mechanical property, admirable resistance to the acid/alkali and environmental friendliness; (3) CC has superior electrical conductivity, which can control the morphology and the loading amount of nanoparticles during the synthesis. An et al. (2016) fabricated the honeycomb-shaped porous NiCo₂O₄ on electro-etched CC with strong adhesion by electrodeposition. The composites as a bind-free electrode display fast kinetics and superior electrochemical behavior controlled by the surface reaction. Fan et al. (2016) reported a highly flexible electrode synthesized by a facile *in-situ* electrodeposition of MnO₂ and polypyrrole on CC. The composite showed superior electrochemical performance.

In this work, a nanocomposite was synthesized by electrodepositing Mg(OH)₂ nanoparticles onto carbon cloth. Adsorption performance of the nano-Mg(OH)₂@CC composite to Eu(III), a typical species of REE, was investigated via batch adsorption experiments. The properties of nano-Mg(OH)₂@CC nanocomposites before and after adsorption were characterized by X-ray diffraction (XRD), scanning electron microscope (SEM), energy dispersive spectroscopy (EDS), and inductively coupled plasma(ICP). Furthermore, fixed-bed adsorption experiments were conducted to assess the enrichment of Eu(III) and the recovery of nano-Mg(OH)₂@CC for the treatment of effluent containing the Eu(III).

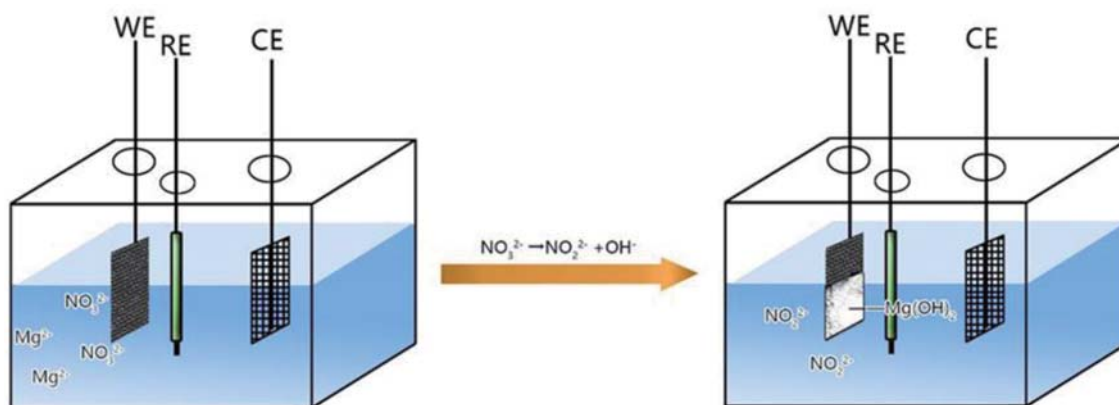
EXPERIMENTAL SECTION

Reagents and Materials

All solutions were prepared using deionized water. Europium chloride hexahydrate (EuCl₃·6H₂O) was obtained from Aladdin (China). Magnesium sulfate (MgSO₄·7H₂O), magnesium nitrate [Mg(NO₃)₂·6H₂O] and sodium hydroxide (NaOH) were obtained from Sinopharm Chemical Reagent Co. Ltd. (Shanghai, China). All of the chemicals were analytical grade and used without further purification. Carbon cloth was obtained from PHYCHEMi Co. Ltd. (Taiwan, China).

Preparation of Adsorbents

Flowerlike nano-Mg(OH)₂ was prepared at room temperature (25°C) by precipitation from NaOH and MgSO₄·7H₂O solutions according to the method described in our previous study (Liu M. et al., 2015). The fabrication of Mg(OH)₂@CC nanocomposite is illustrated in **Scheme 1**. In a typical process, a piece of commercial carbon cloth was washed by acetone, methanol, and isopropanol under sonication for 30 min to remove any contaminants on the surface. After drying in the oven, the piece of carbon cloth was cut into small rectangle piece of



SCHEME 1 | Schematic diagram showing the process for the engineering growth of the interlaced nano-sheet Mg(OH)₂ on the surface of carbon cloth.

2 × 1 cm and used as the working electrodes. However, only half of the CC was soaked into the electrolyte to make Mg(OH)₂ only grow in an area of 1 × 1 cm. The electrodeposition of Mg(OH)₂ on CC was conducted in a three-electrode system with a static potential of −1.5 V, soaking in Mg(NO₃)₂·6H₂O aqueous solution of 1 mol/L. The counter and reference electrode utilized in the electrodeposition is platinum (Pt) net electrode and SCE electrode, respectively. After electrodeposition, the CC was rinsed by DI water and dried in a vacuum oven. Generally, the loading content of Mg(OH)₂ on CC can be controlled by the electrodeposition time. Therefore, different electrodeposition times were conducted to optimize the preparation condition. Finally, the Mg(OH)₂@CC nanocomposite prepared in optimal condition was used in the following study.

Batch Adsorption Experiments

A stock solution of Eu(III) at a concentration of 1,000 mg/L was prepared using sodium Eu(III) (EuCl₃·6H₂O; AR). A series of 500 mL glasses of the solution were added to 200 mL of 10, 40, 70, 100, 130, 160 mg/L Eu(III) solutions and 14 mg Mg(OH)₂/CC or 14 mg flowerlike nano-Mg(OH)₂. The adsorbent quality used for analyzing the adsorption data of the two adsorbents are both in terms of the quality of magnesium hydroxide. The samples were shaken at 200 rpm at room temperature for 24 h to ensure the adsorption reaching equilibrium. The adsorption data were fitted using Langmuir (Equation 1) and Freundlich model (Equation 2). The Langmuir model expressed by the following equation:

$$\frac{C_e}{q_e} = \frac{C_e}{q_m} + \frac{1}{k_L q_m} \quad (1)$$

Where C_e (mg/L) and q_e (mg/g) are the solute concentration and adsorption capacity at equilibrium, respectively, and q_m (mg/g) and k_L (L/mg) are the maximum monolayer adsorption capacity and the binding energy of adsorption, respectively. The Freundlich adsorption model expressed by the following equation:

$$q_e = k_f C_e^{1/n} \quad (2)$$

Where k_f and n are the Freundlich constants measuring the adsorption capacity and the adsorption intensity, respectively.

Kinetic experiments were conducted by mixing certain amount of Mg(OH)₂@CC or flowerlike nano-Mg(OH)₂ into a 2,000 mL flask containing 100 mg/L Eu(III) solutions. For milli liter solution was sampled at various time intervals to determine the adsorption kinetics. The kinetic data were fitted by the pseudo-first-order (Equation 3) and pseudo-second-order equation (Equation 4):

$$q_t = q_e (1 - e^{-k_1 t}) \quad (3)$$

$$q_t = \frac{q_e^2 K_2 t}{1 + q_e K_2 t} \quad (4)$$

Where q_e (mg/g) is the adsorption capacity at equilibrium, q_t (mg/g) is the adsorption capacity at time t , and k_1 (min^{−1}) and k_2 (g/mg·min) are the rate constants of pseudo-first-order and pseudo-second-order kinetics, respectively. The rate constants k_1 and k_2 were determined by plotting $\log(q_e - q_t)$ vs. t and t/q_t vs. t , respectively.

Continuous Effluent System Experiments

Three grams nano-Mg(OH)₂ was put into the sealed polytetrafluoroethylene groove with two cores to prevent the loss of nano-Mg(OH)₂ (the inner groove size is 200 mm in length, 12 mm in width, 18 mm in height). The initial concentration of Eu(III) is 100 mg/L. The peristaltic pump was used to control the water inlet velocity, while the automatic collector was used for collecting samples at the same interval time. The flow rate is calculated by the volume of per unit time collected by the automatic collector. Figure S1a illustrates the above process in a simplified sequence flow diagram.

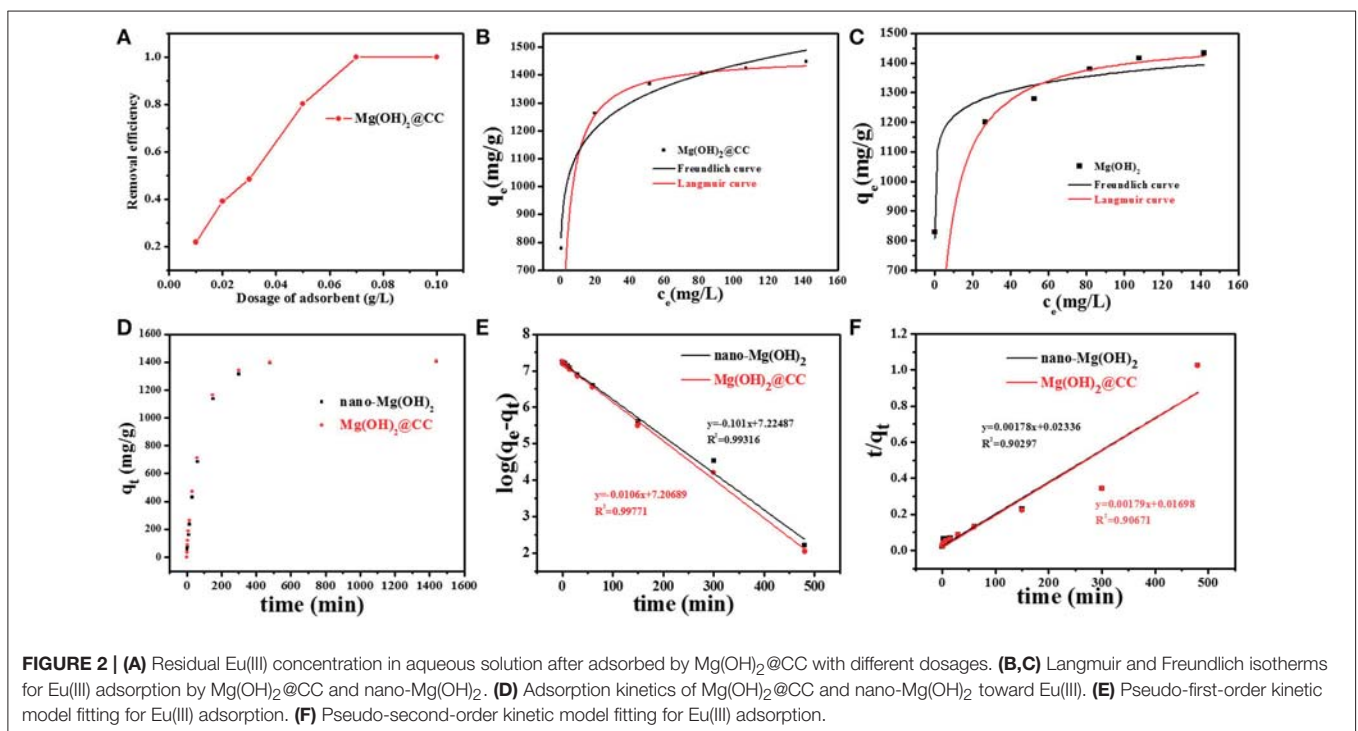
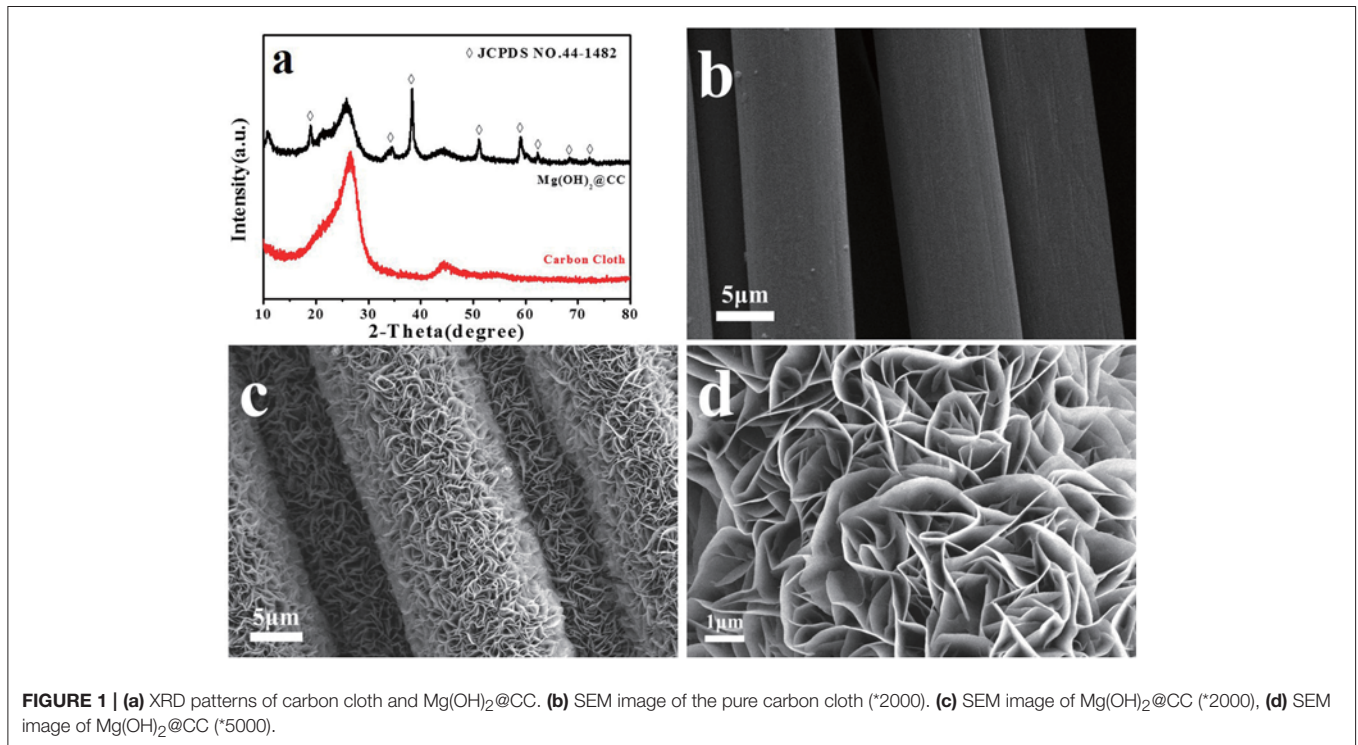
The composite loaded 3 g Mg(OH)₂ was put into the sealed polytetrafluoroethylene groove with two slots to fix the Mg(OH)₂@CC well into the groove (the inner groove size is 200 mm in length, 12 mm in width, 18 mm in height). The initial concentration of Eu(III) is 100 mg/L. The peristaltic pump was used to cycle 200 mL solution containing Eu(III) through

the groove for 10 h with constant flow rate. The solution was replaced by 200 mL of fresh Eu(III) solution every 10 h, while each of the 200 mL solution was considered as one cycle to test the treatment effect of the nanocomposite to Eu(III). During processing for 25 circulations, the residual solution of every cycle was collected to measure the Eu(III) concentration. Figure S1b

illustrates the above process in a simplified sequence flow diagram.

Characterization

XRD patterns were collected on a Bruker X-ray powder diffractometer (advance D8) with $\text{Cu-K}\alpha$ radiation. The tube

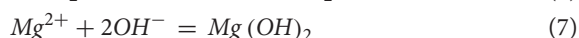
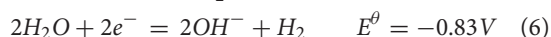
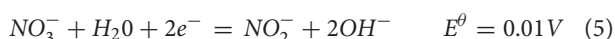


voltage was 40 kV and the tube current was 40 mA. Diffraction patterns were collected over $2\theta = 10^\circ\text{--}80^\circ$ at $1^\circ/\text{min}$. The step size of the scan was 0.02° . The morphology of the samples was observed using a JSM-7100F SEM with an Oxford INCA EDS. Eu(III) content in solution was determined by inductively coupled plasma optical emission spectrometry (ICP-OES).

RESULTS AND DISCUSSION

Mechanism Study

Mechanism of electrodeposition process is shown in **Scheme 1** and Equations (5–7):



Equations (5, 6) are the main electrode reaction equations of synthesizing nano-Mg(OH)₂ by electrodeposition. Briefly, when the electrochemical workstation is in running state, the cathode will continuously produce the OH[−] which combines with Mg²⁺ in solution, by electrolyzing NO₃[−] and H₂O. When the concentration product of OH[−] and Mg²⁺ reach the solubility product of Mg(OH)₂, Equation (7) occurs and the Mg(OH)₂ will adhere onto the surface of carbon cloth firmly.

Characterization of the Adsorbents

The XRD patterns of the carbon cloth and Mg(OH)₂@CC composite are shown in **Figure 1a**, both of which exhibit two strong peaks at $2\theta = 26.2$ and 44.4° . The two peaks are attributed to (002) and (101) planes of the carbon cloth, respectively (Zhang G. et al., 2015). For the Mg(OH)₂@CC composite, the characteristic diffraction peaks at $2\theta = 18.4, 32.9, 38.0, 50.9, 58.7, 62.2, 68.4, \text{ and } 72.1^\circ$ (except peaks derived from the carbon cloth) are well indexed to (001), (100), (011), (102), (110), (111), (103), and (201) phases of Mg(OH)₂, respectively (JCPDS NO.44-1482). **Figure S2** shows the SEM image of Mg(OH)₂@CC at different electrodeposition time. It can be found that with too short electrodeposition time, magnesium hydroxide on the surface of carbon cloth is very sparse. While with too long electrodeposition time, the magnesium hydroxide on the surface of carbon cloth will crack. Only with the appropriate electrodeposition time (around 10min), one layer of magnesium hydroxide is interlaced on the surface of the carbon cloth and attached strongly. **Figures 1b–d** show the typical morphologies of pure carbon cloth (*2000), Mg(OH)₂@CC (*2000), and Mg(OH)₂@CC (*5000), respectively. A low-magnification SEM image (**Figure 1b**) reveals that the fibers of the carbon cloth possess $\sim 10\ \mu\text{m}$ in diameter with a smooth surface. After the synthesis of Mg(OH)₂@CC composites via electrodeposition, it is noticed that the interlaced nano-sheets of Mg(OH)₂ are firmly and uniformly grown on the fibers with an average diameter of $15\ \mu\text{m}$ (**Figures 1c,d**). The above results collectively demonstrated the successful integration of the Mg(OH)₂@CC. In addition, the XRD patterns and SEM image of nano-Mg(OH)₂

shown in **Figure S3** indicated that the flower-like nano-Mg(OH)₂ was successfully synthesized similar to the reported literature.

Eu(III) Adsorption Isotherm and Kinetics

To confirm that the carbon cloth carrier in Mg(OH)₂@CC has no negative effect on the adsorption performance of nano-Mg(OH)₂, the adsorption effect of Mg(OH)₂@CC toward Eu(III) was compared with nano-Mg(OH)₂. **Figure 2A** shows that with an initial Eu(III) concentration of 100 mg/L (the concentration of REEs in the actual environment), Mg(OH)₂@CC could decrease the residual Eu(III) concentration in the solution with increasing adsorbent dosage. When the dosage of adsorbent increased to 0.07 g/L, the removal efficiency can reach 99%. Once exceed 0.07 g/L, the adsorbent will be excessive. Therefore, in the experiments of adsorption kinetics and adsorption thermodynamics, the dosage of adsorbent was 0.07 g/L.

The adsorption isotherm data of nano-Mg(OH)₂ and Mg(OH)₂@CC to Eu(III) were fitted by the Langmuir and Feriundlich models. The results and related parameters are shown in **Figures 2B,C** and **Table 1**. Obviously, no matter using nano-Mg(OH)₂ or Mg(OH)₂@CC, the adsorption capacities increase with the concentration of Eu(III), until it reaches equilibrium. Both of Langmuir and Feriundlich models can be used to describe the adsorption of the two adsorbents ($R^2 > 0.95$), while the R^2 value of Langmuir model is higher than of Feriundlich model. Therefore, Langmuir model is more suitable to describe the adsorption of two adsorbents to Eu(III) and the adsorption type of two materials to Eu(III) is chemical adsorption. The maximum adsorption capacities of nano-Mg(OH)₂ and Mg(OH)₂@CC calculated by Langmuir model were 1428.571 and 1436.781 mg/g, respectively (**Table 1**). Therefore, the loading Mg(OH)₂ on the carbon cloth will not affect the adsorption effect of Mg(OH)₂.

The adsorption kinetics data of nano-Mg(OH)₂ and Mg(OH)₂@CC composites to Eu(III) were fitted by the pseudo-first-order kinetic and the pseudo-second-order

TABLE 1 | Parameters of Langmuir and Freundlich isotherm for Eu(III) on Mg(OH)₂ and Mg(OH)₂@CC.

Eu(III)	Langmuir constant			Freundlich constant		
	R^2	q_m (mg/g)	k_L	R^2	K_F (mg/g)	n
Mg(OH) ₂	0.9995	1428.571	0.4375	0.9822	854.144	8.8261
Mg(OH) ₂ @CC	0.9976	1436.781	0.2692	0.9631	1091.709	20.6612

TABLE 2 | Kinetic parameters calculated from Pseudo-first order and Pseudo-second order kinetic models.

Eu(III)	Pseudo-first order			Pseudo-second order		
	R^2	k_1 (1/min)	q_e (mg/g)	R^2	k_2 (1/min)	q_e (mg/g)
Mg(OH) ₂	0.9938	0.0101	1373.201	0.9127	0.000138	555.56
Mg(OH) ₂ @CC	0.9979	0.0106	1348.705	0.9164	0.000191	555.56

kinetic model. The results and related parameters are shown in **Figures 2D,E** and **Table 2**. **Figure 2D** showed that the equilibrium adsorption capacity of the two materials varies with time. When the dosage of adsorbent was 0.07 g/L and the initial concentration Eu(III) was 100 mg/L, both of the two adsorbents could reach equilibrium in 400 min and the equilibrium adsorption capacities were around 1,400 mg/g. Therefore, loading Mg(OH)₂ on the carbon cloth will not affect its adsorption rate. The kinetic data of two adsorbents were fitted using the pseudo-first-order and pseudo-second-order models. The fitting results (**Table 2**) show that the kinetics of the two adsorbents were better described with pseudo-first-order model kinetics, which suggested that physical and chemical interactions may simultaneously contribute and control the uptake of Eu(III) onto the surface of Mg(OH)₂.

As a consequence, loading Mg(OH)₂ on the surface of carbon cloth has no negative effect on its adsorption performance. The main reason is that the electrodeposited Mg(OH)₂ is evenly distributed on the surface each carbon fiber. Since the carbon fibers are relatively independent, they have no coverage and interference to the active site of Mg(OH)₂, leading to enough active sites exposing for Eu(III) adsorption.

Material Characterization After Adsorption

To explore the adsorption mechanism, Mg(OH)₂@CC was exposed to Eu(III) solution with a high concentration. The morphology, distribution, and crystal phase of Mg(OH)₂@CC-Eu(III) were determined by SEM-EDS and XRD. The SEM

image showed that after adsorption, the original laminar structure of Mg(OH)₂@CC slightly bended, but still retained the interlacing laminar structure (**Figure 3a**). This is due to the ions interaction between Eu(III) and Mg(II) that changes the morphology (Li et al., 2013). The distribution map of corresponding elements (Eu, O, Mg) was recorded by SEM-EDS (**Figures 3b–d**). The thick purple areas in **Figure 3b** show that the Eu is evenly distributed on the carbon fiber surface, while the sparse blue areas shown in **Figure 3d** indicate the decrease of Mg(II) content after adsorption. To confirm the enrichment of Mg(OH)₂@CC to Eu(III), the adsorbed powder of Mg(OH)₂-Eu was collected from the surface of carbon cloth through mechanical methods and calcinated at 800°C without oxygen. The XRD patterns of the obtained powder shown in **Figure 4** can be well indexed as Europium Oxide phase (ICCD card no.00-034-0392). The corresponding ICP data are shown in **Table 3**. The content of europium in solid phase is 860,727 mg/kg, while the content of magnesium is only 21.3 mg/kg. According to ICP, SEM-EDS, and XRD data, it can be calculated that 99.66% of the obtained powder after calcination is europium oxide, while there is almost no magnesium oxide. Therefore, the Mg(OH)₂@CC can extract Eu(III) from solution to the surface of the nanocomposite, which can realize the enrichment and recovery of REEs.

Continuous System (Fixed Bed-Column)

To further investigate the practical application of Mg(OH)₂@CC, a fixed bed-column experiment was conducted to verify the

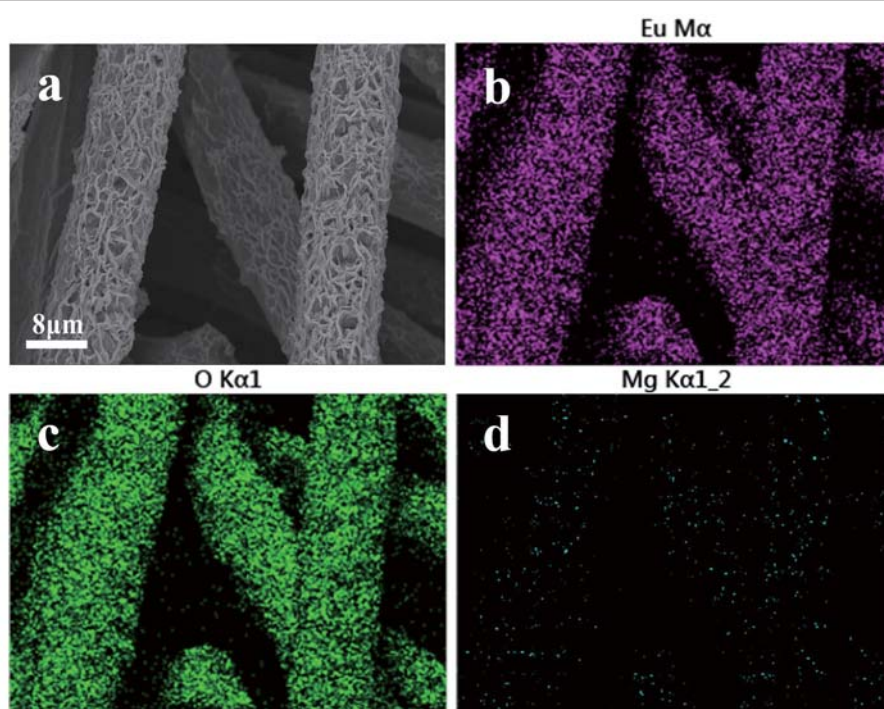


FIGURE 3 | (a) SEM image of Mg(OH)₂@CC-Eu after reacting with high concentration Eu(III) solution for 24 h. (b) Corresponding EDS elemental mapping images for Eu, (c) for O, (d) for Mg.

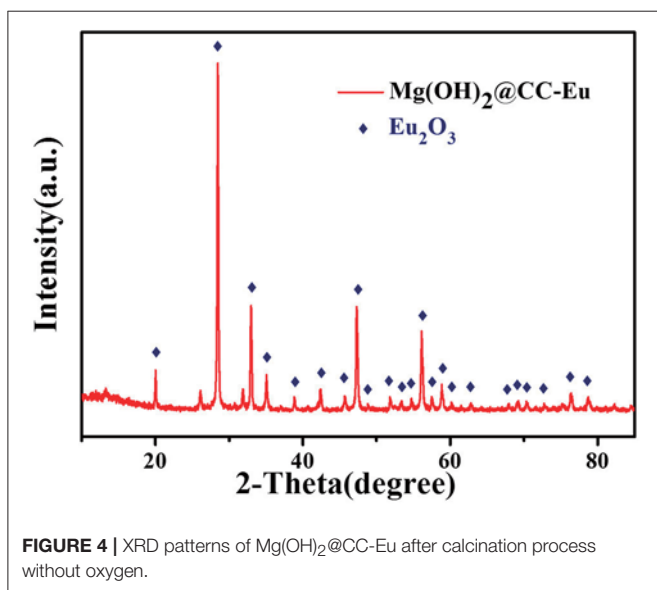


FIGURE 4 | XRD patterns of Mg(OH)₂@CC-Eu after calcination process without oxygen.

TABLE 3 | ICP data of the reacted powder.

Component	Mg	Eu	Eu ₂ O ₃
Conversion content	21.3 mg/kg	860, 727 mg/kg	996, 631 mg/kg

removal performance of Eu(III) by Mg(OH)₂@CC, taking nano-Mg(OH)₂ as comparison. As shown in **Figure 5**, with the same quality of Mg(OH)₂ and the initial Eu(III) concentration of 100 mg/L, the adsorption column performance of Mg(OH)₂@CC is much better than that of pure nano-Mg(OH)₂. It can be explained that the main adsorption mechanism of Mg(OH)₂@CC to Eu(III) includes two parts: (1) ion exchange of Eu(III) with magnesium hydroxide; (2) the enhanced dispersion of nano-Mg(OH)₂ by the surface function groups of carbon cloth. Under the two mechanisms, the treatment capacity of Mg(OH)₂@CC is as high as 4,200 mL (C/C_0 is <0.10), while the concentration of effluent Eu(III) decreases to the $\mu\text{g/L}$ level after treatment. Meanwhile, the effluent of Mg(OH)₂@CC can be processed at a steady flow rate. The curve of nano-Mg(OH)₂ toward Eu(III) uptake in fixed-bed columns is shown in the bottom left corner of **Figure 5A**, where there is a short black curve. The magnification of the short black curve is shown in **Figure 5B**. The effluent effect of nano-Mg(OH)₂ is superior (C/C_0 approaches 0.00). However, with the increase of effluent volume, the flow rate also decreases rapidly. When the effluent volume reaches 240 mL, the flow rate is close to zero. A possible explanation is that the agglomeration of the nanoparticles reduces the specific surface area of nano-Mg(OH)₂, and thus decreases the active sites for Eu(III) adsorption. Moreover, the agglomeration of nano-Mg(OH)₂ leads to the increase of particle size, which further causes blockage in fix-bed column. This problem will severely limit the development of nano-Mg(OH)₂ in practical application. Therefore, magnesium hydroxide plays an important role in the

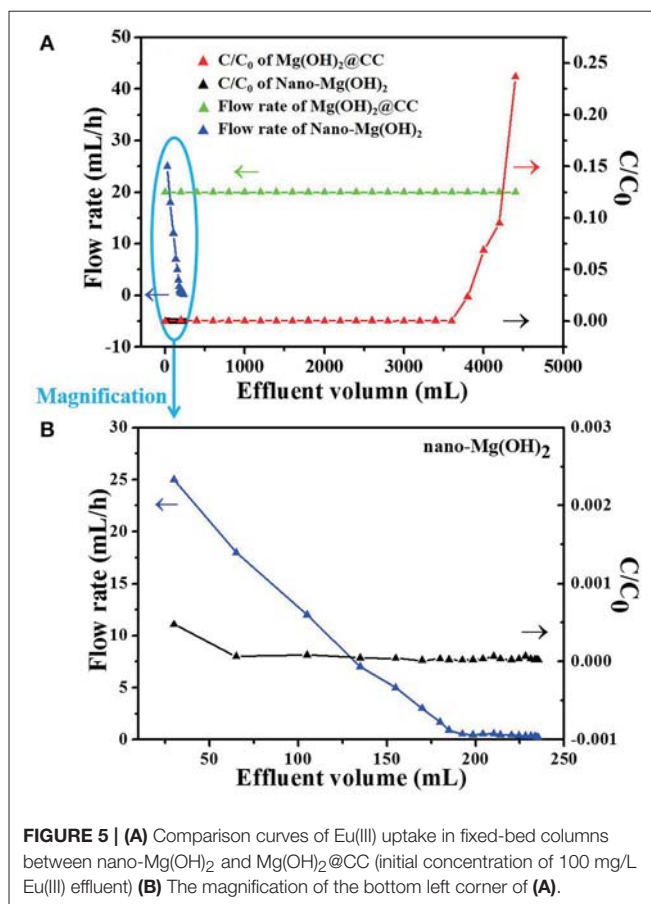


FIGURE 5 | (A) Comparison curves of Eu(III) uptake in fixed-bed columns between nano-Mg(OH)₂ and Mg(OH)₂@CC (initial concentration of 100 mg/L Eu(III) effluent) (B) The magnification of the bottom left corner of (A).

absorption of Eu(III) by Mg(OH)₂@CC, while the main effect of carbon cloth is to strengthen the dispersion of nano-Mg(OH)₂. The combination of nano-Mg(OH)₂ with carbon cloth would further improve the efficiency of nano-Mg(OH)₂ and prevent its loss.

CONCLUSIONS

In summary, a new nanocomposite Mg(OH)₂@CC was prepared by electrodeposition, and used to adsorb Eu(III) in fixed-bed. The morphology and phase analyses revealed that the interlaced Mg(OH)₂ nano-sheets are uniformly loaded on the carbon cloth fibers. The maximum adsorption capacity (1436.8 mg/g) and removal rate (95% within 300 min) of Mg(OH)₂@CC toward Eu(III) is close to those of nano-Mg(OH)₂, indicating that loading Mg(OH)₂ on the surface of carbon cloth has no negative effect on its adsorption performance. Moreover, up to 99.66% of Eu₂O₃ is found in the adsorbed powder, indicating Mg(OH)₂@CC could be an ideal candidate for the enrichment and recovery of Eu(III) from aqueous solution. In addition, Mg(OH)₂@CC exhibited great potential for Eu(III) removal in the fixed-bed compared with nano-Mg(OH)₂. Therefore, the excellent performance of Mg(OH)₂@CC suggests that loading nanoparticles on CC via electrodeposition is a promising

method to improve the application of nano-adsorption materials.

AUTHOR CONTRIBUTIONS

YL: Organized the research problem on carbon cloth supported nano-Mg(OH)₂ for the enrichment and recovery of Rare Earth Element Eu(III) from aqueous solution, and participated in writing the manuscript; CT: Synthesized Mg(OH)₂@CC and nano-Mg(OH)₂; SX: Conducted the batch adsorption experiments and the data fitting; YX: Conducted the characterization of the adsorbents before and after adsorption; RC: conducted the fixed bed experiment of two adsorbents; WL and ZL: Analyzed the mechanism of the carbon cloth on enhancing the adsorption ability of Mg(OH)₂@CC toward Eu(III) in fixed bed and participated in writing the manuscript.

REFERENCES

- Alonso, E., Sherman, A. M., Wallington, T. J., Everson, M. P., Field, F. R., Roth, R., et al. (2012). Evaluating rare earth element availability: a case with revolutionary demand from clean technologies. *Environ. Sci. Technol.* 46, 3406–3414. doi: 10.1021/es203518d
- An, Y., Hu, Z., Guo, B., An, N., Zhang, Y., Li, Z., et al. (2016). Electrodeposition of honeycomb-shaped NiCo₂O₄ on carbon cloth as binder-free electrode for asymmetric electrochemical capacitor with high energy density. *RSC Adv.* 6, 37562–37573. doi: 10.1039/C6RA04788B
- Binnemans, K., Jones, P. T., Blanpain, B., Van Gerven, T., and Pontikes, Y. (2015). Towards zero-waste valorisation of rare-earth-containing industrial process residues: a critical review. *J. Clean. Prod.* 99, 17–38. doi: 10.1016/j.jclepro.2015.02.089
- Binnemans, K., Jones, P. T., Blanpain, B., Van Gerven, T., Yang, Y., Walton, A., et al. (2013). Recycling of rare earths: a critical review. *J. Clean. Prod.* 51, 1–22. doi: 10.1016/j.jclepro.2012.12.037
- Chen, D., Zhu, H., Yang, S., Li, N., Xu, Q., Li, H., et al. (2016). Micro-nanocomposites in environmental management. *Adv. Mater. Weinheim.* 28, 10443–10458. doi: 10.1002/adma.201601486
- Chen, M., Wu, P., Yu, L., Liu, S., Ruan, B., Hu, H., et al. (2017). FeOOH-loaded MnO₂ nano-composite: an efficient emergency material for thallium pollution incident. *J. Environ. Manage.* 192, 31–38. doi: 10.1016/j.jenvman.2017.01.038
- Dimpe, K. M., Nyaba, L., Magoda, C., Ngila, J. C., and Nomngongo, P. N. (2017). Synthesis, modification, characterization and application of AC@Fe₂O₃@MnO₂ composite for ultrasound assisted dispersive solid phase microextraction of refractory metals in environmental samples. *Chem. Eng. J.* 308, 169–176. doi: 10.1016/j.cej.2016.09.079
- Dutta, T., Kim, K. H., Uchimiya, M., Kwon, E. E., Jeon, B. H., Deep, A., et al. (2016). Global demand for rare earth resources and strategies for green mining. *Environ. Res.* 150, 182–190. doi: 10.1016/j.envres.2016.05.052
- Fan, X., Wang, X., Li, G., Yu, A., and Chen, Z. (2016). High-performance flexible electrode based on electrodeposition of polypyrrole/MnO₂ on carbon cloth for supercapacitors. *J. Power Sources* 326, 357–364. doi: 10.1016/j.jpowsour.2016.05.047
- He, S., Zhao, Y., Wei, M., Evans, D. G., and Duan, X. (2011). Fabrication of hierarchical layered double hydroxide framework on aluminum foam as a structured adsorbent for water treatment. *Ind. Eng. Chem. Res.* 51, 285–291. doi: 10.1021/ie2015894
- Jia, B.-B., Wang, J.-N., Wu, J., and Li, C.-J. (2014). “Flower-Like” PA6@Mg(OH)₂ electrospun nanofibers with Cr (VI)-removal capacity. *Chem. Eng. J.* 254, 98–105. doi: 10.1016/j.cej.2014.05.005
- Kumar, V., Kim, K.-H., Park, J.-W., Hong, J., and Kumar, S. (2017). Graphene and its nanocomposites as a platform for environmental applications. *Chem. Eng. J.* 315, 210–232. doi: 10.1016/j.cej.2017.01.008
- Kwon, O. H., Kim, J. O., Cho, D. W., Kumar, R., Baek, S. H., Kurade, M. B., et al. (2016). Adsorption of As(III), As(V) and Cu(II) on zirconium oxide immobilized alginate beads in aqueous phase. *Chemosphere* 160, 126–133. doi: 10.1016/j.chemosphere.2016.06.074
- Li, B., Cao, H., and Yin, G. (2011). Mg(OH)₂@reduced graphene oxide composite for removal of dyes from water. *J. Mater. Chem.* 21, 13765–13768. doi: 10.1039/c1jm13368c
- Li, C. C., Rui, X., Wei, W., Chen, L., and Yu, Y. (2017). Component-customizable porous rare-earth-based colloidal spheres towards highly effective catalysts and bioimaging applications. *Chemistry* 23, 16242–16248. doi: 10.1002/chem.201702161
- Li, C., Zhuang, Z., Huang, F., Wu, Z., Hong, Y., and Lin, Z. (2013). Recycling rare earth elements from industrial wastewater with flowerlike nano-Mg(OH)₂. *ACS Appl. Mater. Interfaces* 5, 9719–9725. doi: 10.1021/am4027967
- Lin, F., Liu, Z., Wang, T., and Cui, D. (2017). Highly 2,3-selective polymerization of phenylallene and its derivatives with rare-earth metal catalysts: from amorphous to crystalline products. *Angew. Chem. Int. Ed. Engl.* 56, 14653–14657. doi: 10.1002/anie.201707601
- Liu, J., Huang, K., Wu, X.-H., and Liu, H. (2017). Enrichment of low concentration rare earths from leach solutions of ion-adsorption ores by bubbling organic liquid membrane extraction using N1923. *ACS Sustain. Chem. Eng.* 5, 8070–8078. doi: 10.1021/acssuschemeng.7b01682
- Liu, M., Wang, Y., Chen, L., Zhang, Y., and Lin, Z. (2015). Mg(OH)₂ supported nanoscale zero valent iron enhancing the removal of Pb(II) from aqueous solution. *ACS Appl. Mater. Interfaces* 7, 7961–7969. doi: 10.1021/am509184e
- Liu, T., Liang, Y., Liu, Q., Sun, X., He, Y., and Asiri, A. M. (2015). Electrodeposition of cobalt-sulfide nanosheets film as an efficient electrocatalyst for oxygen evolution reaction. *Electrochem. Commun.* 60, 92–96. doi: 10.1016/j.elecom.2015.08.011
- Lv, Y., Zhang, Z., Lai, Y., Li, J., and Liu, Y. (2011). Formation mechanism for planes (011) and (001) oriented Mg(OH)₂ films electrodeposited on SnO₂ coating glass. *CrystEngComm* 13, 3848–3851. doi: 10.1039/c0ce00728e
- Maroufi, S., Khayyam Nekouei, R., and Sahajwalla, V. (2017). Thermal isolation of rare earth oxides from Nd-Fe-B magnets using carbon from waste tyres. *ACS Sustain. Chem. Eng.* 5, 6201–6208. doi: 10.1021/acssuschemeng.7b01133
- Mudryk, Y., Paudyal, D., Liu, J., and Pecharsky, V. K. (2017). Enhancing magnetic functionality with scandium: breaking stereotypes in the design of rare earth materials. *Chem. Mater.* 29, 3962–3970. doi: 10.1021/acs.chemmater.7b00314
- Qi, X. H., Du, K. Z., Feng, M. L., Gao, Y. J., Huang, X. Y., and Kanatzidis, M. G. (2017). Layered A₂Sn₃S₇·1.25H₂O (A = Organic Cation) as efficient ion-exchanger for rare earth element recovery. *J. Am. Chem. Soc.* 139, 4314–4317. doi: 10.1021/jacs.7b00565
- Tansel, B. (2017). From electronic consumer products to e-wastes: global outlook, waste quantities, recycling challenges. *Environ. Int.* 98, 35–45. doi: 10.1016/j.envint.2016.10.002
- Tesh, S. J., and Scott, T. B. (2014). Nano-composites for water remediation: a review. *Adv. Mater. Weinheim.* 26, 6056–6068. doi: 10.1002/adma.201401376
- Tian, C., Zhao, J., Zhang, J., Chu, S., Dang, Z., Lin, Z., et al. (2017). Enhanced removal of roxarsone by Fe₃O₄@3D graphene nanocomposites:

ACKNOWLEDGMENTS

This work was supported by the National Natural Science Foundation of China (Grant No. 21607045 and 21477129), the Guangdong Innovative and Entrepreneurial Research Team Program (No. 2016ZT06N569), Guangzhou Science and Technology Project (No. 201804010189), and the Fundamental Research Funds for the Central Universities (No. 2015ZM157 and 2017PY009).

SUPPLEMENTARY MATERIAL

The Supplementary Material for this article can be found online at: <https://www.frontiersin.org/articles/10.3389/fchem.2018.00118/full#supplementary-material>

- synergistic adsorption and mechanism. *Environ. Sci. Nano* 4, 2134–2143. doi: 10.1039/C7EN00758B
- Wilfong, W. C., Kail, B. W., Bank, T. L., Howard, B. H., and Gray, M. L. (2017). Recovering rare earth elements from aqueous solution with porous amine-epoxy networks. *ACS Appl. Mater. Interfaces* 9, 18283–18294. doi: 10.1021/acsami.7b03859
- Willa, C., Schmid, A., Briand, D., Yuan, J., and Koziej, D. (2017). Lightweight, room-temperature CO₂ gas sensor based on rare-earth metal-free composites—an impedance study. *ACS Appl. Mater. Interfaces* 9, 25553–25558. doi: 10.1021/acsami.7b07379
- Xiao, G., Su, H., and Tan, T. (2015). Synthesis of core-shell bioaffinity chitosan-TiO₂ composite and its environmental applications. *J. Hazard. Mater.* 283, 888–896. doi: 10.1016/j.jhazmat.2014.10.047
- Xie, F., Wu, F., Liu, G., Mu, Y., Feng, C., Wang, H., et al. (2014). Removal of phosphate from eutrophic lakes through adsorption by *in situ* formation of magnesium hydroxide from diatomite. *Environ. Sci. Technol.* 48, 582–590. doi: 10.1021/es4037379
- Xu, W., Lan, R., Du, D., Humphreys, J., Walker, M., Wu, Z., et al. (2017). Directly growing hierarchical nickel-copper hydroxide nanowires on carbon fibre cloth for efficient electrooxidation of ammonia. *Appl. Catal. B Environ.* 218, 470–479. doi: 10.1016/j.apcatb.2017.07.005
- Yu, M., Li, W., Wang, Z., Zhang, B., Ma, H., Li, L., et al. (2016). Covalent immobilization of metal-organic frameworks onto the surface of nylon—a new approach to the functionalization and coloration of textiles. *Sci. Rep.* 6:22796. doi: 10.1038/srep22796
- Zhang, D., Zhao, Q., Zang, J., Lu, Y.-J., Dong, L., and Shan, C.-X. (2018). Luminescent hybrid materials based on nanodiamonds. *Carbon* 127, 170–176. doi: 10.1016/j.carbon.2017.11.009
- Zhang, G., Hou, S., Zhang, H., Zeng, W., Yan, F., Li, C. C., et al. (2015). High-performance and ultra-stable lithium-ion batteries based on MOF-derived ZnO@ZnO quantum dots/C core-shell nanorod arrays on a carbon cloth anode. *Adv. Mater. Weinheim.* 27, 2400–2405. doi: 10.1002/adma.201405222
- Zhang, L., Jing, X., Li, R., Liu, Q., Liu, J., Zhang, H., et al. (2015). Magnesium carbonate basic coating on cotton cloth as a novel adsorbent for the removal of uranium. *RSC Adv.* 5, 23144–23151. doi: 10.1039/C4RA16446F
- Zhang, X., Cheng, C., Qian, J., Lu, Z., Pan, S., and Pan, B. (2017). Highly efficient water decontamination by using sub-10 nm FeOOH confined within millimeter-sized mesoporous polystyrene beads. *Environ. Sci. Technol.* 51, 9210–9218. doi: 10.1021/acs.est.7b01608
- Zhao, X., Lv, L., Pan, B., Zhang, W., Zhang, S., and Zhang, Q. (2011). Polymer-supported nanocomposites for environmental application: a review. *Chem. Eng. J.* 170, 381–394. doi: 10.1016/j.cej.2011.02.071

Conflict of Interest Statement: The authors declare that the research was conducted in the absence of any commercial or financial relationships that could be construed as a potential conflict of interest.

Copyright © 2018 Li, Tian, Liu, Xu, Xu, Cui and Lin. This is an open-access article distributed under the terms of the Creative Commons Attribution License (CC BY). The use, distribution or reproduction in other forums is permitted, provided the original author(s) and the copyright owner are credited and that the original publication in this journal is cited, in accordance with accepted academic practice. No use, distribution or reproduction is permitted which does not comply with these terms.



Separation of CH₄/N₂ of Low Concentrations From Coal Bed Gas by Sodium-Modified Clinoptilolite

Xiaofei Hao^{1,2}, Zhen Li^{1*}, Hongjie Hu², Xueqin Liu¹ and Yanqiu Huang¹

¹ Faculty of Materials Science and Chemistry, China University of Geosciences, Wuhan, China, ² Zhengzhou Fulong Science and Technology of New Materials Co., Ltd., Zhengzhou Institute of Multipurpose Utilization of Mineral Resources, Chinese Academy of Geological Sciences, Zhengzhou, China

OPEN ACCESS

Edited by:

Wenbo Wang,
Lanzhou Institute of Chemical Physics
(CAS), China

Reviewed by:

Libing Liao,
China University of Geosciences,
China
Federica Valentini,
Dipartimento di Scienze e Tecnologie
Chimiche, Università di Roma Tor
Vergata, Italy
Xiaozhang Li,
Changzhou University, China

*Correspondence:

Zhen Li
zhenli1963@163.com

Specialty section:

This article was submitted to
Green and Sustainable Chemistry,
a section of the journal
Frontiers in Chemistry

Received: 29 June 2018

Accepted: 06 December 2018

Published: 18 December 2018

Citation:

Hao X, Li Z, Hu H, Liu X and Huang Y
(2018) Separation of CH₄/N₂ of Low
Concentrations From Coal Bed Gas
by Sodium-Modified Clinoptilolite.
Front. Chem. 6:633.
doi: 10.3389/fchem.2018.00633

Clinoptilolite is a widely distributed tectosilicate, mainly composed of Al₂O₃, SiO₂ with exchangeable cations such as Ca, K, Mg, and Na. In this research, raw clinoptilolite was ground, gravimetrically concentrated and ion-exchanged using different concentrations of NaCl solution. Then the modified clinoptilolite powder was formulated into particles as adsorbents. The adsorbents were applied to CH₄ separation in coal bed gas. The raw and modified clinoptilolites were characterized by X-ray diffraction (XRD), scanning electron microscope (SEM), transmission electron microscope (TEM), atomic emission spectrometer (ICP-AES), Fourier transform infrared spectrometer (FTIR), and Brunauer Emmett Teller (BET) specific surface area. The CH₄ absorptivity by raw and modified clinoptilolites was evaluated using pressure swing adsorption (PSA) to assess the CH₄ separation ability. The results indicated that the ion-exchanged clinoptilolite using 0.2 mol/L NaCl solution was found to be promising for the kinetic PSA separation of CH₄/N₂, giving a better absorptivity for CH₄ separation under different influence factors. Based on the simulated static experiments, it was indicated that both CH₄ and N₂ were capable of diffusing into clinoptilolite while N₂ adsorption by clinoptilolite was excellent. The experiment results also indicated that ion-exchanged clinoptilolite using a 0.2 mol/L NaCl solution was the optimal adsorbent for separating CH₄/N₂ at the low pressure condition. From the simulated dynamic experiments, the ion-exchanged clinoptilolite using a 0.2 mol/L NaCl solution as a potential sorbent in kinetic PSA processes for N₂/CH₄ separation, exhibited the best performance at 648 K under 0.2 MPa within 28 min, in comparison to the raw clinoptilolite and clinoptilolite under other modification conditions. In the next phase of research, the modified clinoptilolite will be tested for CH₄ separation in real coal bed gas.

Keywords: clinoptilolite, ion-exchange, nitrogen/methane separation, selectivity, low concentrations methane, pressure swing adsorption

INTRODUCTION

The coalbed gas is found in coal bed with a main composition of methane (CH₄), which was absorbed on the surface of the coal particles. Part of coal bed gas was dissociated or dissolved in the hydrocarbon gas in the coal pore and the water of coal bed, which is automatically stored up in the coal bed as the powerful complement to raw gas. CH₄ in the coal bed is a high quality gas fuel. Meanwhile, it is also one of detrimental gases influencing mining underground coal and an

important harmful source leading to atmospheric greenhouse effect. In China, there is up to 13 billion m³ CH₄ under the process of coal mine a year, which accounts for around one third of its emissions globally. On the other hand, the utilization ratio of CH₄ in the coal bed gas was only 35%, resulting in a huge CH₄ resource loss. We know that the greenhouse effect of CH₄ is 21 times to the CO₂ and power of CH₄ for damaging ozone (O₃) is 7 times to the CO₂. Thus, recycling coal bed gas is of great significance on both energy development and environmental protection. With improving consciousness of human on the coal mine safety and environmental protection, the exploitation of CH₄ in the coal bed has been attached great importance to the world in recent years.

The separation technology of CH₄ in the coal bed is not effective, which is one of the main reasons for low the utilization ratio. In the separation process of low concentration of coal bed gas, the physicochemical property of N₂ and CH₄ was similar (Perry et al., 1999; Johnson III, 2015). It led the recycle and separation technology to be a key common technology challenge. It was also one of the most important technological obstacles on gas development, energy saving and emission reduction (Bomberger et al., 1999; Cavenati et al., 2006; Tagliabue et al., 2009). At present, the common technologies were cryogenic distillation, pressure swing adsorption (PSA), membrane separation, hydration technology and dissolution-adsorption technology. The PSA separation method has become the mainstream technology for the purification of coal bed gas at small and medium scales, due to its advantages of low energy consumption, less investment equipment and high degree of automation (Arya et al., 2014; Yin et al., 2015). Its key challenge is the selection of adsorbents. The main adsorbents currently used are activated carbon (AC) (Zhou et al., 2002; Gu et al., 2015; Gao et al., 2017), carbon molecular sieve (CMS) (Fatehi et al., 1995; Cavenati et al., 2005; Grande et al., 2005), natural clinoptilolite (Aguilar-Armenta et al., 2001; Jayaraman et al., 2004, 2005), titanium silicon molecular sieve (Aguilar-Armenta et al., 2001; Jayaraman et al., 2004, 2005; Faghihian et al., 2008). The equilibrium adsorption capacity of CH₄ is higher than that of N₂ for AC. Although the separation coefficient is higher and the effect is better based on results from laboratory studies, it is still far away from industrial application. The main reason is that the preparation process of AC is complex and the cost is relatively high. And it obtains CH₄ product in vacuum desorption stage, the subsequent operation needs to be compressed, so the power cost is increased, and the economic effect is not obvious. The separation of CH₄ and N₂ by CMS is based on the kinetic effect. The diffusion rate of N₂ in the micropore is higher than CH₄. A large amount of N₂ is adsorbed into the pore and CH₄ remains outside the pore in a relatively short time. Therefore, the product CH₄ is obtained by the adsorption or sequestration of the PSA process, instead of the vacuum step. With the increase of adsorption time, the kinetically the effect becomes weaker, and the equilibrium effect will dominate, making CH₄ and N₂ separation difficult. Although CMS has achieved good results in the laboratory, it is mainly aimed at the coal bed gas with high concentration of CH₄ (CH₄ content >70%). However, there are few reports on the study of coal bed gas

with low concentrations. The natural clinoptilolite as a kind of PSA adsorbents is of great potential for application with the advantage of acid resistance, heat resistance, alkali resistance, stable structure, rich resources, and low price. They can show both equilibrium and kinetic effects. However, the adsorbent prepared from natural clinoptilolite are of different sodium contents and its application in low concentration coal bed gas (CH₄ < 30%) has not been reported.

Here we present a study of the adsorption isotherms of four adsorbents made from natural clinoptilolite with different sodium contents at 298 K. And the corresponding adsorption kinetics were measured at the same and different pressure using the feed gas containing 20% CH₄ and 80% N₂ at 298 K. This study will provide technical support for the implementation of industrialization.

MATERIALS AND METHODS

Materials

Clinoptilolite and All Agents

The raw clinoptilolite was collected from the south of the Liaoxi metallogenic belt in China. The adsorbents used were CH₄ (99.95%), N₂ (99.95%). The purging gas for adsorbent activation/regeneration was He (99.999%, pre-purified). All gases were provided by Praxair. The reagents, including NaCl, used in this research were of analytically pure and bought from Sinopharm Group Chemical Reagent Co., Ltd.

Clinoptilolite Pretreatment

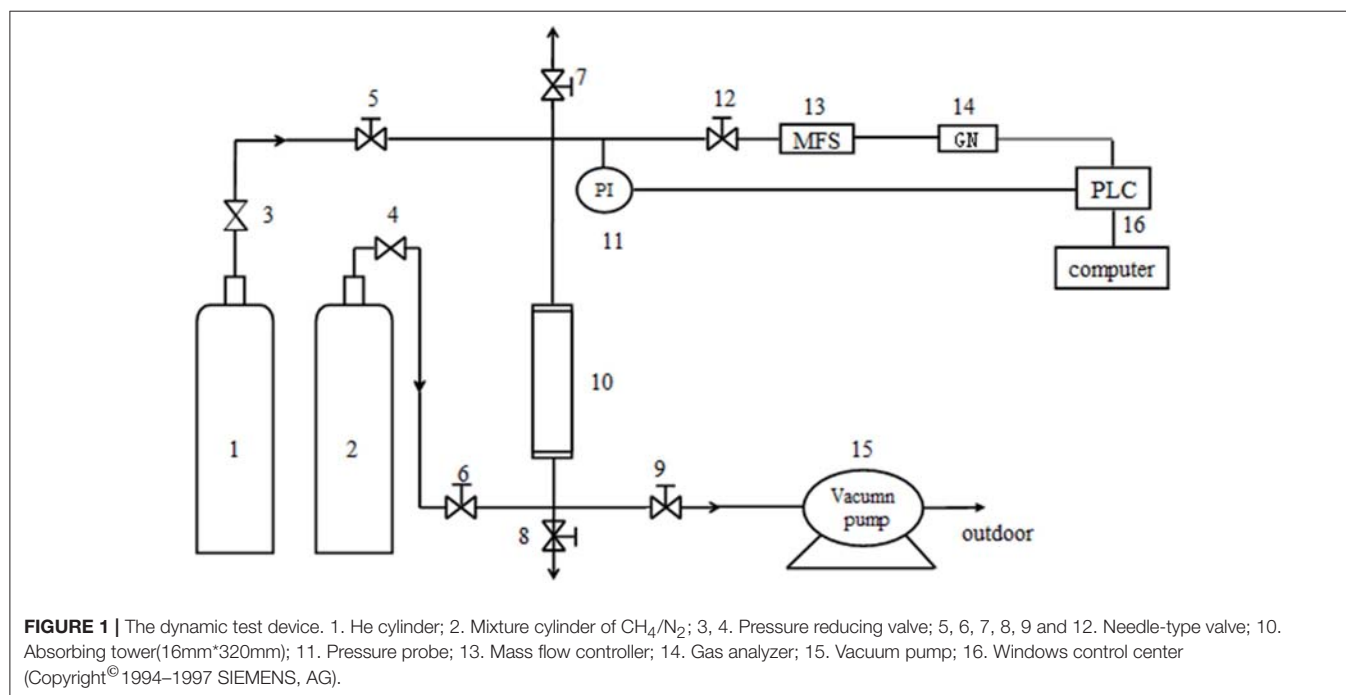
The raw clinoptilolite was ground by a ball grinder to a granular size <70 μm. Then the milled pulp with clinoptilolite powders was poured into a Falcon centrifuge to remove some heavy impurities. The purified clinoptilolite was dried at 105°C and stored in a desiccator. It was used as a raw material for the preparation of adsorbents.

Preparation of Modified Clinoptilolite

The processed clinoptilolite powders were mixed NaCl solutions at concentrations of 0.1, 0.2, 0.4, and 0.6 mol/L at a solid to liquid ratio of 1:20 for 2.5 h in Erlenmeyer flasks separately and covered with sealing films and maintained in a 90°C water bath. The mixture was centrifuged to separate the solids, then washed using deionized water until no Cl⁻. All ion-exchanged clinoptilolite samples were pressed into a round cake and calcined at 200°C (to dry the samples) for 2 h. And then they were crushed and sieved. Particles of 0.5–1.5 mm sizes were used as adsorbents.

Separation Experiment With CH₄/N₂

The gas mixture of CH₄ and N₂ was prepared by high-pure standard gas, and the ratio of CH₄/N₂ was 20/80%. The experimental device for adsorption was a single absorbing tower filled with raw and modified clinoptilolites (**Figure 1**). At first, the device was pressurized using high-pure standard He until the adsorption pressure was up to the setting pressure. Then the intake valve of He was closed and the intake valve of mixture gas was opened (it was the start time of data recording). In order to keep the pressure of absorbing tower reaching the experimental



value, it was adjusted by control valves (the flow value of gas was set to 50 mL/min). The outlet discharge was set using mass flow controller before the test. In the process of adsorption, the change of concentration of CH₄ was tested and recorded by a gas analyzer. The test was continued until the concentration of CH₄ was the same as the initial concentration of CH₄ in the mixture. The activation and regeneration of modified clinoptilolite was not begun until inverse vacuum was pumped for 10 min.

Pressure/Vacuum Swing Adsorption Experimental Program

A vacuum pressure swing adsorption (VPSA) cycle was devised to be experimented in the pilot-scale unit, which was the purpose of catching CH₄ from a dynamical mix of CH₄/N₂ simulated coal bed gas. The device, single-tower adsorption layer, was shown in **Figure 1**. Before test, the adsorbents were modified clinoptilolites which were activated in the vacuum rotation activation furnace for 6 h in 648 K. When the test began, the pressure of He and pressure of adsorption were both set at the certain pressure, and flow value of tower top was 60 mL/min. It needed to be emphasized that vacuum pumping treatment using vacuum pumps was initiated before the experiments.

Analytical Methods

The morphologies of purified clinoptilolite and modified clinoptilolite were observed with TEM (Tecnai G2 TF30) and SEM (Hitachi S-4800).

X-ray diffraction (Rigaku MiniFlex600) measurements were proceeded with copper CuK α 1 radiation ($\lambda = 1.5406 \text{ \AA}$), utilizing a voltage of 40 kV and a current of 15 mA. The divergence slit was 0.3 mm and data was gathered for 2θ scanned from 3° to 80° at $10^\circ/\text{min}$.

TABLE 1 | The chemical composition of clinoptilolites (wt%).

Composition (wt %)	Modified clinoptilolites				
	C-0	C-1	C-2	C-3	C-4
SiO ₂	66.99	68.49	68.48	68.08	68.09
Al ₂ O ₃	12.01	12.86	12.85	13.02	13.01
K ₂ O	1.63	1.65	1.62	1.61	1.59
Na ₂ O	0.65	1.94	2.45	3.30	3.68
CaO	3.80	3.09	2.73	2.14	1.89
MgO	1.29	1.26	1.20	1.08	1.01
Fe ₂ O ₃	1.37	1.47	1.48	1.50	1.60
TiO ₂	0.20	0.19	0.19	0.19	0.19

The chemical components of purified clinoptilolite and modified clinoptilolite samples were analyzed using an inductively coupled plasma atomic emission spectroscopy (ICP-AES, ICAP7400 THERMO Fisher). To obtain a more representative chemical composition of a sample, the analysis was done in triplicates per sample, and the element contents were averaged (**Table 1**).

Mid-infrared spectra were recorded using a Fourier transform infrared (FT-IR) spectrometer (Nicolet IS50) with a Smart Endurance™ single bounce diamond ATR cell. Spectra were acquired of $4,000\text{--}400 \text{ cm}^{-1}$ by the average of 64 scans with a resolution ratio of 4 cm^{-1} . A mirror speed of 0.6 cm/s was used.

The BET surface area was $57.84 \pm 0.20 \text{ m}^2/\text{g}$ measured by an ASAP 2020 instrument (Micromeritics, USA). N₂ (at 298 K) and CH₄ (at 298 K) adsorption were measured to determine the BET surface area and micropore size distribution.

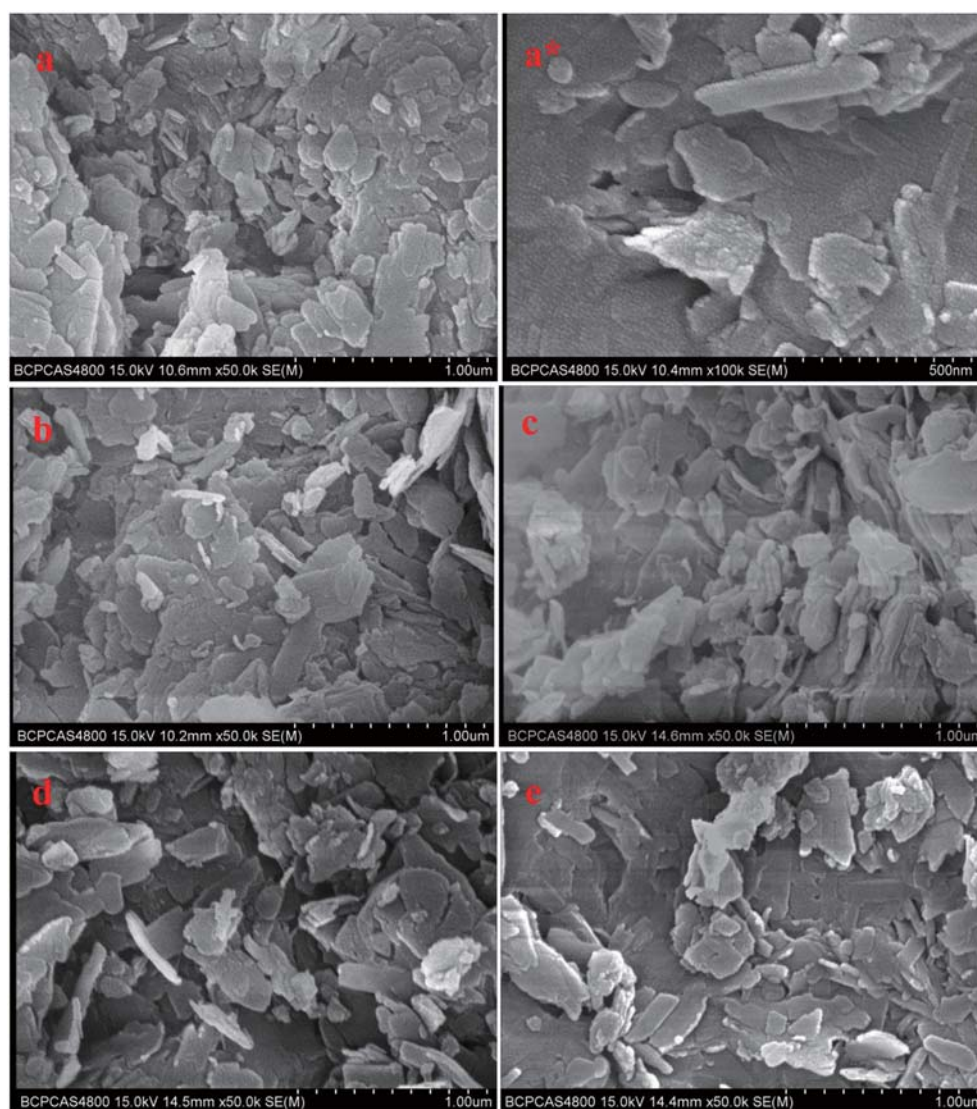


FIGURE 2 | SEM photographs of clinoptilolites: (a,a*) C-0, (b) C-1, (c) C-2, (d) C-3, (e) C-4.

RESULTS AND DISCUSSION

Characterization of Clinoptilolites

Figure 2 showed SEM photographs of unmodified and modified clinoptilolites. They didn't change significantly among them. In **Figure 2**, C-0, unmodified clinoptilolite, was purified clinoptilolite with no NaCl treatment. The modified clinoptilolites were depicted by C-1, C-2, C-3, and C-4, which were treated by 0.1, 0.2, 0.4, and 0.6 mol/L NaCl solution, respectively. These crystals are flaggy or schistose, which appears as parallel conjunctive aggregate. Individual crystals span is from hundreds of nanometers to several microns. A number of ordered small particles were also found on the crystals from **Figure 2a***.

In order to observe the internal microstructure of samples, TEM photographs of modified clinoptilolites were shown in

Figure 3. From **Figure 3**, inside of C-0 was large lamella stacking. However, inside of C-1, C-2, C-3, and C-4 were stacked with small lamella, in which the number of fissures produced by flake particles. This is because they are stirred on thin sheets during ion exchange, so more lamellar clinoptilolite is stripped, mainly concentrated at 100×300 nm, which also makes the exchange easier. The 131 faces of clinoptilolite can be seen in C-2 of photograph c*, whose crystal plane spacing is 3.98 Å, which have not seen in other published papers.

ICP-AES was adopted to analyze the ion change before and after modification (**table 1**). It is obviously that with the increasing of NaCl concentrations, the Na⁺ component increased from 0.65 to 3.68 wt% gradually. Meanwhile, the Ca²⁺ component decreased from 3.8 to 1.89 wt% apparently. In addition, other elements showed a random change with increased NaCl concentrations (such as Si, Al, K, Mg, Fe, and Ti). The

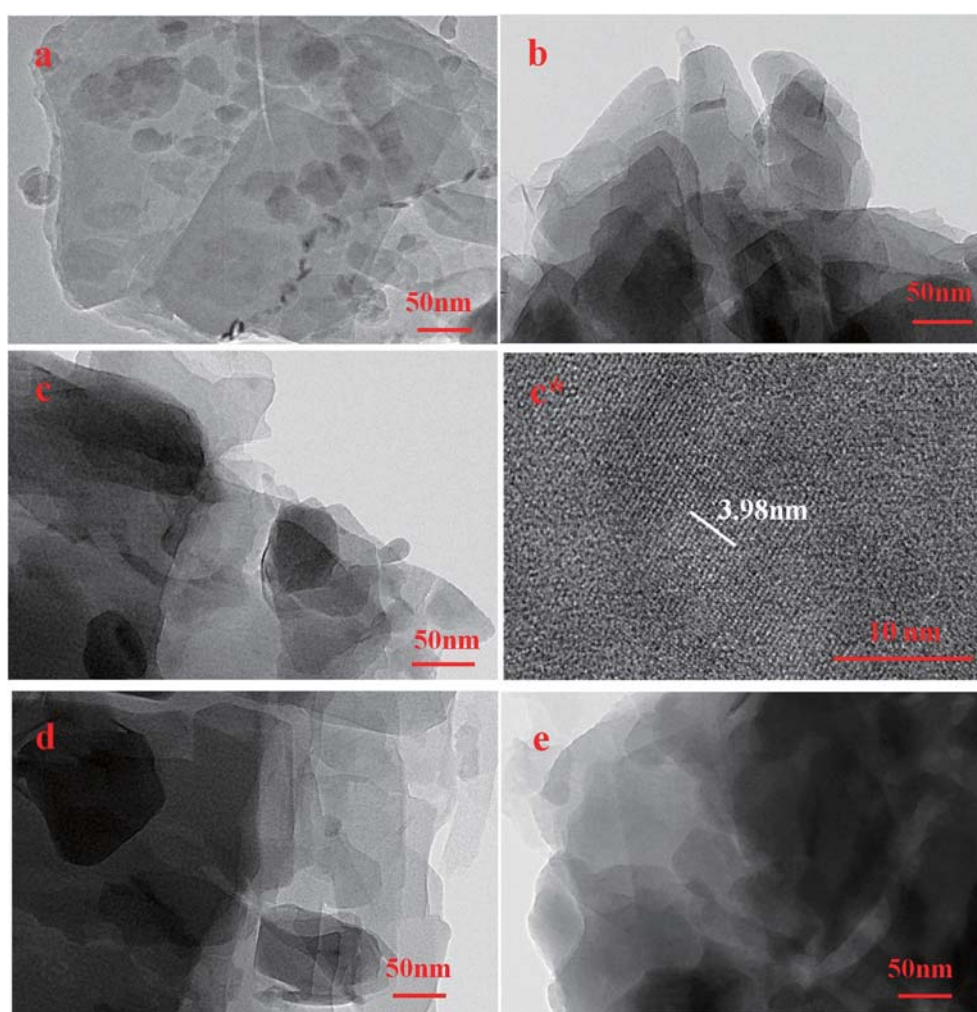


FIGURE 3 | TEM photographs of clinoptilolites: (a). C-0, (b). C-1, (c,c*). C-2, (d). C-3, (e). C-4.

phenomenon indicated that the ion exchange of Na⁺ for Ca²⁺ were carried out in clinoptilolite samples with NaCl solutions bath.

The XRD patterns were mainly used for confirmation the difference in all clinoptilolites without and with treatment using NaCl solution (**Figure 4**). The major mineral in all samples was clinoptilolite with minor amounts of quartz. All the lattice parameters were not observably influenced by the different contents of NaCl. We couldn't see the characteristic peak of NaCl in modified clinoptilolites, It showed that the Na⁺ entered the lattice, and we combined the chemical composition analysis in **Table 2**. So we know it was replaced with Ca²⁺. The obvious difference was the D value of the characteristic peak was smaller than modified clinoptilolites. It was because the exchange of different ions led to the change of lattice spacing.

The broad band at 620 cm⁻¹ in the clinoptilolites spectra were attributed to stretching vibrations related to Si-O tetrahedron structure (**Figure 5**). The characteristic peak of clinoptilolite without ion-exchange was weak. Furthermore, the vibration

absorption peak of Si-O-Si and Al-O-Si appears at 795 cm⁻¹. Compared with clinoptilolite without ion-exchange, some evident changes in characteristic absorption peaks were discovered. The characteristic peak at 985.46 cm⁻¹ deriving from Al-O vibrations shifted to 1043.32 cm⁻¹, caused a small amount of Al-O losing after ion-exchange. A small account of non-framework Al stuck in the unit cell was shifted by ion-exchange. And a small account of Al was shifted from framework because of Al-O-Si hydrolyzing in the clinoptilolites. Then cavities were formed leading to pore volume increasing. For modified clinoptilolites, the Si-O and/or Al-O out-of-plane bend occurred at 485 and 1,622 cm⁻¹. Thus, the intensity of Al-O out-of-plane bend in modified clinoptilolites was stronger than that of clinoptilolite. It was because ion-exchange caused a small amount of Al-O losing. The broad band at 2,328 cm⁻¹ mainly resulted from stretching vibrations of OH⁻ groups on modified clinoptilolites after ion-exchange. The broad band at 3,743 cm⁻¹ mainly resulted from stretching vibrations of O-H on modified clinoptilolites after ion-exchange.

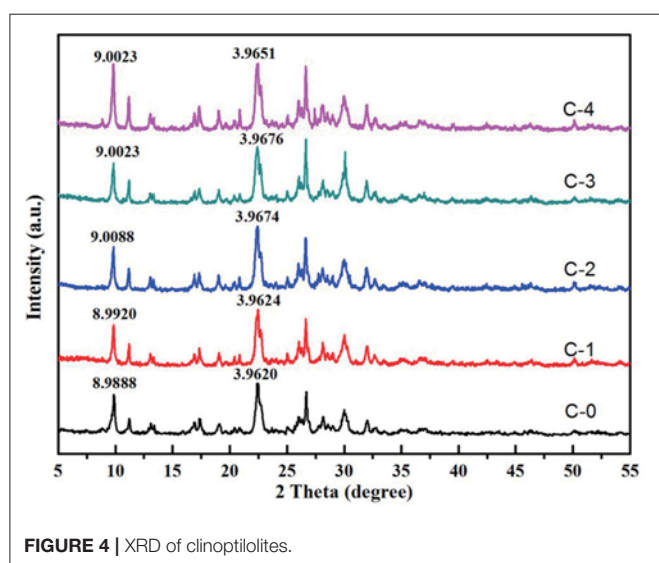


FIGURE 4 | XRD of clinoptilolites.

TABLE 2 | BET of modified clinoptilolites treated by NaCl of different concentrations with N₂ at 77 K.

	C-1	C-2	C-3	C-4
BET (m ² /g)	16.1	16.0	16.0	15.9
External surface area (m ² /g)	12.0	11.8	12.1	11.8
Micropore surface area (m ² /g)	4.0	4.2	3.9	4.1
Vp (m ³ /g)	0.068	0.065	0.062	0.073
D (nm)	16.8	16.2	15.5	17.7

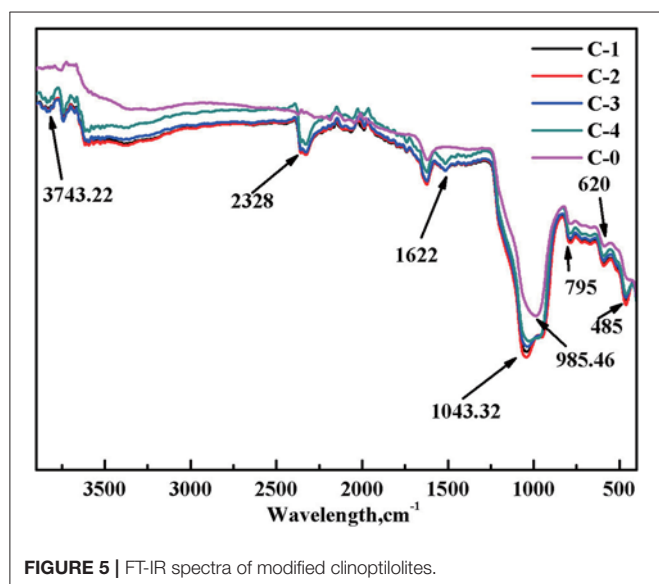


FIGURE 5 | FT-IR spectra of modified clinoptilolites.

The N₂ adsorption-desorption isotherms at 77 K with the four adsorbents were shown in Figure 6A. According to the

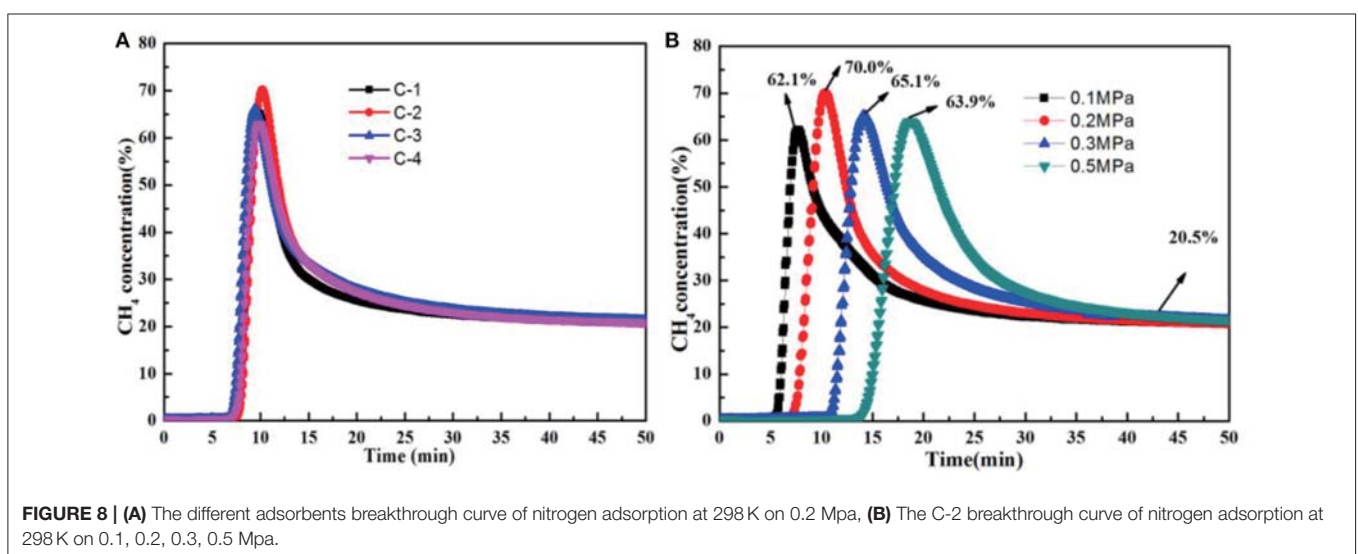
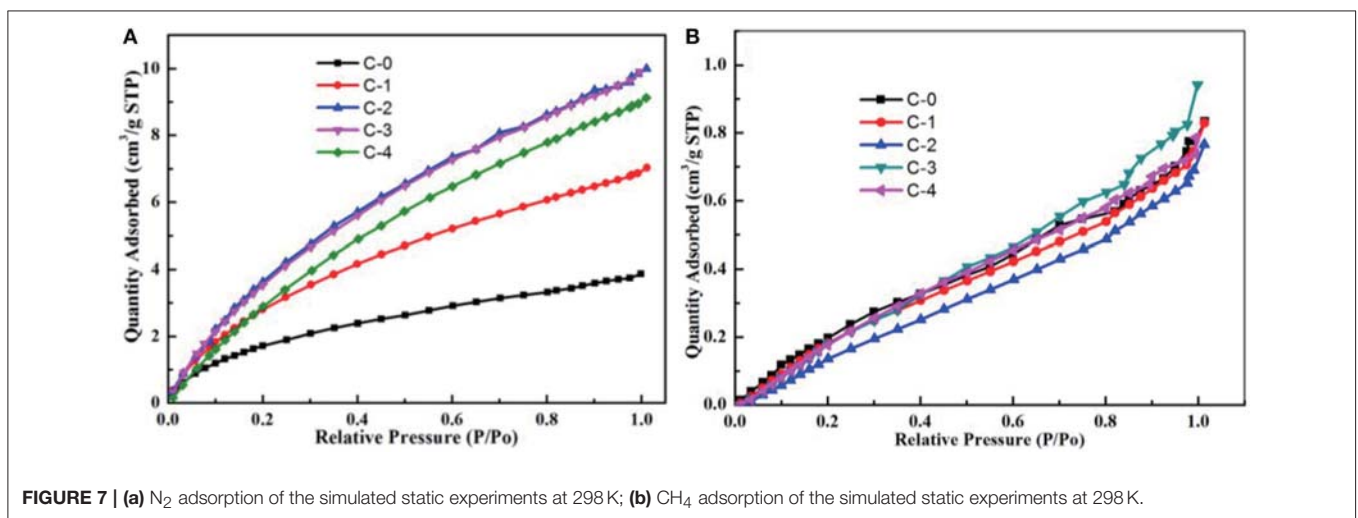
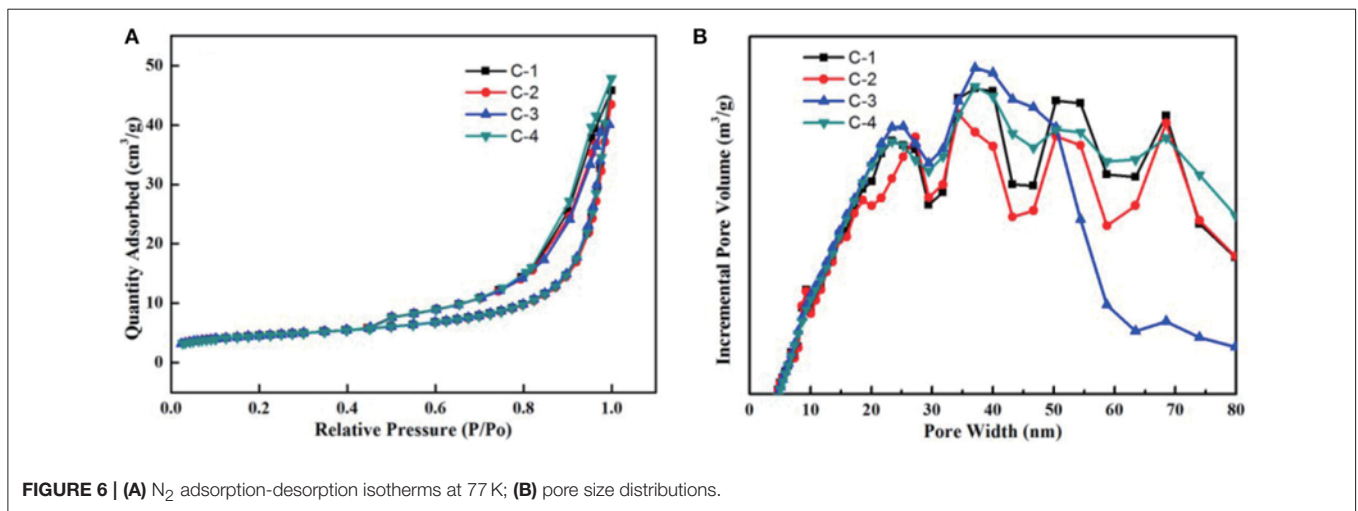
IUPAC classification, all curves were identified as type IV. The surface has mesopore and macropore, The curve of p/p_0 region of low relative pressure is convex up, in the higher p/p_0 region, the adsorbed material is condensed by capillary, the isotherm obtained by desorption does not coincide with the isotherm obtained by adsorption, and the desorption isotherm lags over the adsorption isotherm. So they present a hysteresis loop. It belongs to the class D loop. It is mainly due to the slit holes formed by sloping sheet stacking. In Figure 6B, we know most of the pores are between 5 and 80 nanometers, They have different pore structure by loading different contents of sodium ions. According to Table 2, we know that the internal surface area of C-2 adsorbents is the largest. With the increase of the loading of sodium ions, the micropore surface area of adsorbent increased first and then decreased. So the micropores are adjusted. At the beginning, the calcium ion was replaced by sodium ion, and the pore channel of clinoptilolite became smaller. When loading a certain amount, a large number of sodium ions loaded the surface of clinoptilolite and blocked some channels.

Simulated Experiments

To explore the separation capability of CH₄/N₂ on the modified clinoptilolites, the simulated static experiments were conducted using BET equipment, and the simulated dynamic experiments were conducted using the device of adsorption of single tower (Figure 1), in which pure N₂ and CH₄ gas were chosen as gas-supply.

CH₄ adsorption and N₂ adsorption of the simulated static experiments were shown in Figure 7. It should be noted that adsorption of the two molecules is competitive and thus the gas-supply in the simulated static experiments is high purity N₂ and high purity CH₄ at 298 K, separately. Before the adsorption experiment begun, The adsorbents were vacuum activated for 8 h at 370°. From Figure 7, there was obvious difference between quantity adsorbed of CH₄ and N₂ using clinoptilolites. At the same relative pressure condition, quantity adsorbed of N₂ on clinoptilolites was much more than that of CH₄. From Figure 7A, the quantity adsorbed of N₂ using clinoptilolites followed: C-3 = C-2 > C-4 > C-1 > C-0. From Figure 7B, the quantity adsorbed of CH₄ using clinoptilolites was as follows: C-3 > C-4 > C-0 > C-1 > C-2. Considering the contradiction between adsorption capability of clinoptilolites for CH₄ and N₂, it is obvious that the C-2 adsorbents static equilibrium separation coefficient is the larger than other three. It is the most potential adsorbent for separating CH₄/N₂.

Dynamic experiments had been done. The CH₄ volume concentration of product is obtained at 298 K on certain pressure when the feed gas is a mixture of CH₄ (20%) and N₂ gas (80%), as shown in Figure 8. Concentrated CH₄ could be obtained directly by using these adsorbents of C-1, C-2, C-3, C-4. In this experiment, before testing, the adsorbent was vacuum activated for 8 h at 648 K, and then the package was sealed for use. When the concentration of CH₄ of the top of the tower is 20%, it is put back to normal pressure, and a 30 min vacuum is activated and regenerated. The experiment was repeated three times, and the data are recorded in the third experiment. Figure 8A showed the



different adsorbents breakthrough curve of nitrogen adsorption at 298 K on 0.2 Mpa. In the dynamic adsorption curve, it showed that CH₄ concentration can be increased. C-1 is from 20 to 65.2%, C-2 is from 20 to 70.0%, C-3 is from 20 to 66.1%, C-4 is from 20 to 63.1%. Moreover, they can be continuously regenerated. So the adsorbent of C-2 is the best among these adsorbents, which is consistent with the static adsorption results. **Figure 8B** shows the C-2 breakthrough curve of nitrogen adsorption at 298 K on the different pressure. We can control residence time of raw gas in adsorbent by adjusting the pressure of carrier He gas. The residence time corresponding to 0.1, 0.2, 0.3, and 0.5 Mpa is 5, 7.5, 11, and 14 min, respectively. The peak value of CH₄ reaches 70.0% when the residence time is 7.5 min. The results show that the N₂ adsorption was bigger than CH₄ when the mixture of CH₄/N₂ were in the absorbing tower. The bigger the pressure, the longer the residence time. CH₄ adsorption was bigger than N₂ adsorption when they were adsorbed. The separation factors would decrease. So, It is very important to choose the suitable residence time.

From the above, it seemed that the C-2 shows the greatest performance at 648 K under 0.2 MPa within 50 min, in comparison to the other modified clinoptilolites, as a underlying sorbent in kinetic PSA processes for the N₂/CH₄ separation. The different concentrations of Na⁺ that were existed in its porous network as well as their distribution were the primary influence factor that specifies the adsorption and kinetic properties of the clinoptilolites. Thus, the ion-exchange with differences in the concentration of Na⁺ disturbed the Na⁺ distribution as well as the electrostatic field inside the clinoptilolite's pores affecting the adsorption property.

CONCLUSION

The material structure and CH₄/N₂ adsorbability of raw and Na⁺ ion-exchanged clinoptilolites have been examined in detail using PSA. The effect of adsorbent prepared by clinoptilolite with different sodium ion content on methane nitrogen separation is very different. The clinoptilolite adsorbents can be adjusted for

their pore channel by controlling the loaded amount of sodium ions.

The C-2 adsorbent prepared using 0.2 mol/L NaCl solutions was the most promising for the kinetic PSA separation of CH₄/N₂, giving the better adsorptivity and influence factors concerning the CH₄ separation.

From the simulated static experiments, it indicated that N₂ and CH₄ are both competent in diffusing into the clinoptilolites while N₂ adsorptions of clinoptilolites are more excellent. The pertinent results also indicated that adsorption capability of ion-exchanged clinoptilolite using 0.2 mol/L NaCl solutions was the optimal adsorbent for separating CH₄/N₂ at low pressure, considering the contradiction between adsorption capability of clinoptilolites for CH₄ and N₂.

According to the simulated dynamic experiments, the ion-exchanged clinoptilolite using 0.2 mol/L NaCl solutions exhibits the best performance at 648 K under 0.2 MPa within 50 min, in comparison to raw and other modified clinoptilolites, as a underlying sorbent in kinetic PSA processes for the N₂/CH₄ separation.

The ion-exchange with differences in the concentration of Na⁺ as well as the electrostatic field inside the clinoptilolite's pores affecting the adsorption property. Finally, further manipulation for CH₄ separation of the clinoptilolite is underway with coal bed gas as gas-supply.

AUTHOR CONTRIBUTIONS

XH and ZL conceived and designed the project. XH performed the experiments and wrote the manuscript. HH, XL, and YH analyzed the data.

FUNDING

The work was financially supported by the Special Fund for National/International Science and Technology Cooperation in China (Grant no. 2015DFR60640) and the Science and Technology Plan of Henan Province (No. 182102310031).

REFERENCES

- Aguilar-Armenta, G., Hernandez-Ramirez, G., Flores-Loyola, E., Ugarte-Castaneda, A., Silva-Gonzalez, R., Tabares-Munoz, C., et al. (2001). Adsorption kinetics of CO₂, O₂, N₂, and CH₄ in cation-exchanged clinoptilolite. *J. Phys. Chem. B* 105, 1313–1319. doi: 10.1021/jp9934331
- Arya, A., Divekar, S., Rawat, R., Gupta, P., Garg, M. O., Dasgupta, S., et al. (2014). Upgrading biogas at low pressure by vacuum swing adsorption. *Ind. Eng. Chem. Res.* 54, 404–413. doi: 10.1021/ie503243f
- Bomberger, D. C., Bomben, J. L., Amirbahman, A., and Asaro, M. (1999). *Nitrogen Removal From Natural Gas: Phase II*. Office of Scientific and Technical Information Technical Reports.
- Cavenati, S., Grande, C. A., and Rodrigues, A. E. (2005). Separation of methane and nitrogen by adsorption on carbon molecular sieve. *Separation Sci. Technol.* 40, 2721–2743. doi: 10.1080/01496390500287846
- Cavenati, S., Grande, C. A., and Rodrigues, A. E. (2006). Separation of CH₄/CO₂/N₂ mixtures by layered pressure swing adsorption for upgrade of natural gas. *Chem. Eng. Sci.* 61, 3893–3906. doi: 10.1016/j.ces.2006.01.023
- Faghihian, H., Talebi, M., and Pirouzi, M. (2008). Adsorption of nitrogen from natural gas by clinoptilolite. *J. Iran. Chem. Soc.* 5, 394–399. doi: 10.1007/BF03245993
- Fatehi, A. I., Loughlin, K. F., and Hassan, M. M. (1995). Separation of methane–nitrogen mixtures by pressure swing adsorption using a carbon molecular sieve. *Gas Separation Purification* 9, 199–204. doi: 10.1016/0950-4214(95)98227-C
- Gao, S., Ge, L., Rufford, T. E., and Zhu, Z. (2017). The preparation of activated carbon discs from tar pitch and coal powder for adsorption of CO₂, CH₄ and N₂. *Microporous Mesoporous Mater.* 238, 19–26. doi: 10.1016/j.micromeso.2016.08.004
- Grande, C. A., Cavenati, S., Da Silva, F. A., and Rodrigues, A. E. (2005). Carbon molecular sieves for hydrocarbon separations by adsorption. *Ind. Eng. Chem. Res.* 44, 7218–7227. doi: 10.1021/ie050376r

- Gu, M., Zhang, B., Qi, Z., Liu, Z., Duan, S., Du, X., et al. (2015). Effects of pore structure of granular activated carbons on CH₄ enrichment from CH₄/N₂ by vacuum pressure swing adsorption. *Separation Purification Technol.* 146, 213–218. doi: 10.1016/j.seppur.2015.03.051
- Jayaraman, A., Hernandez-Maldonado, A. J., Yang, R. T., Chinn, D., Munson, C. L., and Mohr, D. H. (2004). Clinoptilolites for nitrogen/methane separation. *Chem. Eng. Sci.* 59, 2407–2417. doi: 10.1016/j.ces.2003.10.030
- Jayaraman, A., Yang, R. T., Chinn, D., and Munson, C. L. (2005). Tailored clinoptilolites for nitrogen/methane separation. *Indus. Eng. Chem. Res.* 44, 5184–5192. doi: 10.1021/ie0492855
- Johnson III, R. D. (2015). *NIST Computational Chemistry Comparison And Benchmark Database*. NIST Standard Reference Database Number 101, Release 15b. 2011. Available online at: cccbdb.nist.gov
- Perry, R. H., Chilton, C. H., and Kirkpatrick, S. D. (1999). *Chemical Engineers Handbook*. New York, NY: McGraw-Hill.
- Tagliabue, M., Farrusseng, D., Valencia, S., Aguado, S., Ravon, U., Rizzo, C., et al. (2009). Natural gas treating by selective adsorption: material science and chemical engineering interplay. *Chem. Eng. J.* 155, 553–566. doi: 10.1016/j.ces.2009.09.010
- Yin, C., Sun, W., Yang, H., and Zhang, D. (2015). Optimization of three-bed VPSA system for biogas upgrading. *Chem. Eng. Sci.* 135, 100–108. doi: 10.1016/j.ces.2015.06.022
- Zhou, L., Guo, W. C., and Zhou, Y. P. (2002). A feasibility study of separating CH₄/N₂ by adsorption. *Chin. J. Chem. Eng.* 10, 558–561.

Conflict of Interest Statement: The authors declare that the research was conducted in the absence of any commercial or financial relationships that could be construed as a potential conflict of interest.

Copyright © 2018 Hao, Li, Hu, Liu and Huang. This is an open-access article distributed under the terms of the Creative Commons Attribution License (CC BY). The use, distribution or reproduction in other forums is permitted, provided the original author(s) and the copyright owner(s) are credited and that the original publication in this journal is cited, in accordance with accepted academic practice. No use, distribution or reproduction is permitted which does not comply with these terms.



Synthesis and Microwave Absorbing Properties of Porous One-Dimensional Nickel Sulfide Nanostructures

Min Lu¹, Qian Wu¹, Xiao-Hui Guan¹, Wei Xu², Hao-Yue Zhang², Xin Di³, Guang-Sheng Wang^{2*} and Shao-Hua Dong^{3*}

¹ School of Chemical Engineering, Northeast Electric Power University, Jilin, China, ² School of Chemistry, Beihang University, Beijing, China, ³ Pipeline Technology Research Center, China University of Petroleum–Beijing, Beijing, China

OPEN ACCESS

Edited by:

Wenbo Wang,
Lanzhou Institute of Chemical Physics
(CAS), China

Reviewed by:

Zheng Ren,
University of Connecticut,
United States
Aiwei Tang,
Beijing Jiaotong University, China

*Correspondence:

Guang-Sheng Wang
wanggs@buaa.edu.cn
Shao-Hua Dong
shdong@cup.edu.cn

Specialty section:

This article was submitted to
Green and Sustainable Chemistry,
a section of the journal
Frontiers in Chemistry

Received: 30 June 2018

Accepted: 20 August 2018

Published: 11 October 2018

Citation:

Lu M, Wu Q, Guan X-H, Xu W,
Zhang H-Y, Di X, Wang G-S and
Dong S-H (2018) Synthesis and
Microwave Absorbing Properties of
Porous One-Dimensional Nickel
Sulfide Nanostructures.
Front. Chem. 6:405.
doi: 10.3389/fchem.2018.00405

One-dimensional (1D) porous Ni_xS_y nanostructures have been successfully fabricated by two-step method consisting of solvothermal and subsequent annealing process. The suitable heat treatment temperature and reaction time play crucial roles in the final structure, morphology, as well as performance. The uniform and perfect porous Ni_xS_y nanostructures obtained at 310°C exhibit outstanding microwave absorption performances. A minimum reflection loss of −35.6 dB is achieved at 8.5 GHz, and the effective absorption bandwidth almost covers 14.5 GHz with the absorber thickness range of 2.0–5.0 mm. It can be supposed that this porous structure with rough surface which is favor for increasing the microwave multiple reflection and scattering, contributes a high-performance electromagnetic absorption.

Keywords: porous, nickel sulfide, one-dimensional, dielectric loss, microwave absorption

INTRODUCTION

Microwave absorber with strong capacity in absorption, low proportion in filler loading, thin thickness in coating, and wide bandwidth in absorption frequency, has aroused burgeoning research interest because of their great potential applications both in military and civil fields, including stealth technology, information security, electromagnetic interference shielding, and healthcare (Zhu et al., 2010; Zhao H. et al., 2014). As is well known that many factors such as morphology, geometry and structure, have vital impacts on determining the microwave absorption (MA) properties (He et al., 2013). Conventional microwave absorbers with different morphologies that have been divided into three classes are as follows: (1) one-dimensional nanostructures such as ZnO nanowires (Wang et al., 2014), Bi₃S₂ nanorods (Luo et al., 2014); (2) two-dimensional materials such as MoS₂ nanosheets (Ning et al., 2015), α-Fe₂O₃ flakes (Lv et al., 2015a); and (3) three-dimensional network structures, including Co₂₀Ni₈₀ hierarchical nanospheres (Liu et al., 2015), Ni chains nets (Liu et al., 2016), Fe₃O₄@carbon ordered arrays (Yuan et al., 2015) and so on. However, the aforementioned materials usually possess high density, thus leading to severe limitations to their practical applications in some specialized fields. In this regard, materials with characteristics of low density and special void spaces, such as yolk-shell structural microspheres (Liu et al., 2013; Yu et al., 2014; Qiang et al., 2016), foam composites (Zhang Y. et al., 2015; Zhao H. B. et al., 2016), as well as porous nanostructures (Yan et al., 2009; Zhou et al., 2010; Zhu et al., 2011), are highly beneficial to obtaining superior microwave absorption performance.

Considerable attention has been concentrated on the porous structure of MA materials owing to its fascinating characteristics. For example, Liu et al. fabricated porous carbon/Co composites, and the results suggested that the composites with large dielectric loss could achieve a minimum RL of -40 dB at 4.2 GHz with a coating thickness of 5 mm (Liu et al., 2008). Lv et al. synthesized Co/CoO porous 3-D flower nanostructure through annealing process at 400°C and found that the minimal reflection loss was up to -50 dB when the coating thickness was 3.5 mm (Lv et al., 2015b). Similarly, Wang et al. reported the formation of porous flower-like NiO decorated graphene, and the composites with a filler loading of 25 wt% exhibited highly MA performance (-59.6 dB) because of their special porous structures and numerous void spaces (Wang et al., 2017). Benefiting from the porous structure, the above-mentioned materials show superior electromagnetic wave absorption performance, which reveals that these porous materials are effective as MA materials.

Metal sulfides, as semiconductor materials, have been proven to have promising potential as an ideal microwave absorber on account of their typical dielectric loss mechanism (Zhang X. J. et al., 2017). Recent studies have suggested that metal sulfides including MoS_2 (Wang et al., 2015), CoS_2 (Zhang C. et al., 2017), CdS (Zhang et al., 2014), and CuS (He et al., 2014), as well as various phase of nickel sulfides (Zhou et al., 2010) can effectively absorb electromagnetic waves and attenuate them in the form of thermal energy. However, the microwave-absorbing properties of Ni_xS_y with special porous structure have not been reported previously. Based on the above study, we demonstrated the successful design and fabrication of porous one-dimensional Ni_xS_y nanomaterial through a facile solvothermal route together with annealing process. The MA properties of resultant composites were investigated in detail for the first time. As expected, the synthesized Ni_xS_y nanostructure exhibited excellent microwave absorption property confirming that this material can be used as high-performance microwave absorber.

MATERIALS AND METHODS

Preparation of Porous Ni_xS_y

Nickel nitrate hexahydrate ($\text{Ni}(\text{NO}_3)_2 \cdot 6\text{H}_2\text{O}$), elemental sulfur, ethylene glycol (EG), and ethylenediamine (EN) were purchased from Nanjing Chemical Reagent Co. All of the chemical reagents were analytical-grade purity and used without further purification.

Typically, nickel sulfide was synthesized by the reaction of $\text{Ni}(\text{NO}_3)_2 \cdot 6\text{H}_2\text{O}$, EN and sulfur powder in EG. At first, $\text{Ni}(\text{NO}_3)_2 \cdot 6\text{H}_2\text{O}$ (0.3489 g) was added to EG (135 mL) under strong magnetic stirring to form a light green homogeneous solution. Then the sulfur powder (0.0288 g) was dissolved in EN (15 mL) through ultrasonic treatment. Mix the two solutions together and put it into oil bath, maintained at 120°C for 6 h. After being cooled to room temperature, the resulting solid precursors were centrifuged, washed with alcohol to remove possible remnant, and finally dried in air at 60°C for 24 h. The dried precursors were treated at 310°C for 2 h with a heating rate of $2^{\circ}\text{C}/\text{min}$ under N_2 atmosphere to get the final Ni_xS_y products.

Preparation of Nickel Sulfide/PVDF Nanocomposites

The polyvinylidene fluoride (PVDF) was first dispersed in *N-N* dimethylformamide (20 mL) under magnetic stirring for 1 h. Then, the desired amount of nickel sulfide was added into the suspension. After ultrasonication for another 1 h, the mixture was poured onto a glass plate and dried at 80°C for 24 h. The samples for testing were also compacted into a cylindrical compact ($\Phi_{out} = 7.00$ mm and $\Phi_{in} = 3.04$ mm) by hot pressing at 210°C under 5 MPa (pressed for 15 min, followed by cooling to room temperature under the same pressure).

Instrumental Analyses

The X-ray diffraction (XRD) pattern of the nickel sulfide product was carried out on a Rigaku, Dmax2200 diffractometer equipped with a CuK α radiation source ($\lambda = 1.5416$ Å) in the range of $2\theta = 10$ – 80° . For the phase analysis. Further microstructural analyses were performed by using a FEI Quanta 250 field emission gun environmental scanning electron microscope (JSM-6700F microscope) at 15 kV. In brief, SEM samples were prepared by diluting the final products with alcohol by ultrasonic treatment and dropping it on the silicon slice. The relative permittivity (ϵ' , ϵ'') and permeability (μ' , μ'') values were measured using two-port vector network analyzer (Agilent E5071C) over the frequency of 2–18 GHz at room temperature, coupled with a coaxial wire setup. Finally, the reflection loss (RL, dB) value which presents the ratio of the total reflected microwave power against the incident microwave power can be calculated by using the following formulas (Abbas et al., 2006; Xu et al., 2018).

$$Z_{in} = \sqrt{\frac{\mu_r}{\epsilon_r}} \tanh \left[j \left(\frac{2f\pi d}{c} \right) \sqrt{\mu_r \epsilon_r} \right] \quad (1)$$

$$RL(\text{dB}) = 20 \log \left| \frac{Z_{in} - 1}{Z_{in} + 1} \right| \quad (2)$$

where Z_{in} is the normalized input characteristic impedance, f is the frequency of microwave, d is the thickness of the absorber. A lower RL value stands for a better MA performance.

RESULTS AND DISCUSSION

An illustration of the synthesis of the Ni_xS_y is shown in **Figure S1**. We first prepared the precursors of Ni_xS_y nanorods by a simple solvothermal method in a controlled way as described later. Then the collected dried precursors were transferred into a tube furnace and annealed at 310°C for 2 h under an N_2 atmosphere, which eventually led to the generation of the porous Ni_xS_y . It is well recognized that reaction parameters such as temperature, pressure, reaction time, type of solvent, and concentration of reagents, have a huge effect on the morphology of the products. In the present reaction system, Ethylene glycol and Ethylenediamine were applied as solvents for the precursors synthesis of Ni_xS_y , and the temperature as well as reaction time was tightly regulated so that the precursors at a well-defined state were obtained.

Figure 1 shows the representative SEM images of the precursors prepared at different temperature of 80, 100, 120, 140,

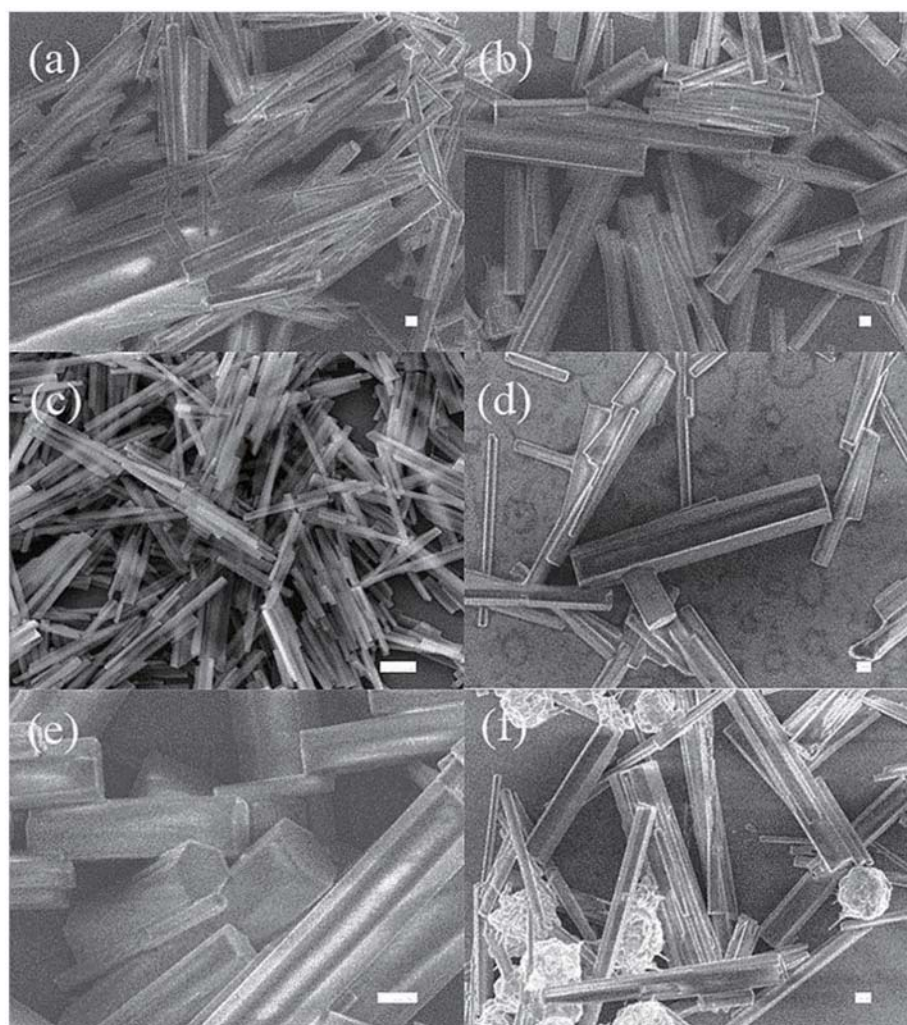


FIGURE 1 | SEM images of precursor of Ni_xS_y samples under different reaction temperatures: (a) 80, (b) 100, (c) 120, (d) 140, (e) 160, and (f) 180°C. (scale bar = 1 μm).

160, and 180°C, respectively. When the reaction is performed under the lower temperature (80 and 100°C), although one-dimensional structures of products can be formed, their thicknesses and lengths are varying greatly. On the contrary, when the temperature reaches 180°C, the 1D nanostructures are nonuniform, and a certain number of spherical impurities emerge. By comparing the morphology of the products under different temperature conditions, the best reaction temperature is determined. The products are well-defined nanorods with diameters of about 50 nm and lengths of several micrometers at the suitable reaction temperature of 120°C (Figure 1c). On the other hand, the stages of the growth process are monitored at 120°C by varying the reaction time from 2 to 10 h (Figure S2). It is interesting to find that reaction time does not change the overall morphology of the precursors. However, the yield of the products is very low within a short period of 2 h, indicating the slow reaction rate in such reaction system. Further increasing

the reaction time produce more products, while the diameter and structure of the nanorods remain stable.

To obtain porous 1D nanostructures, the precursors were annealed at different temperatures ranging from 280 to 330°C under the flowing nitrogen gas, and the final products are exhibited in Figure 2. It can be seen that the surfaces are actually becoming porous with annealing temperature, and the as-obtained Ni_xS_y retain the rods morphology with appropriate porosity when prepared at 310°C. Further increasing the annealing temperature will lead to 1D structural instability and collapse. The energy-dispersive X-ray spectroscopy (EDS) indicates that the obtained product is composed of Ni, S, C, N, and O elements, also demonstrating a very homogeneous elemental distribution (Figure 3). It is worth mentioning that the C, N, and O element signals originate from the incomplete decomposition of organic compositions of precursors during heat treatment. Meanwhile, the XRD results suggest that the

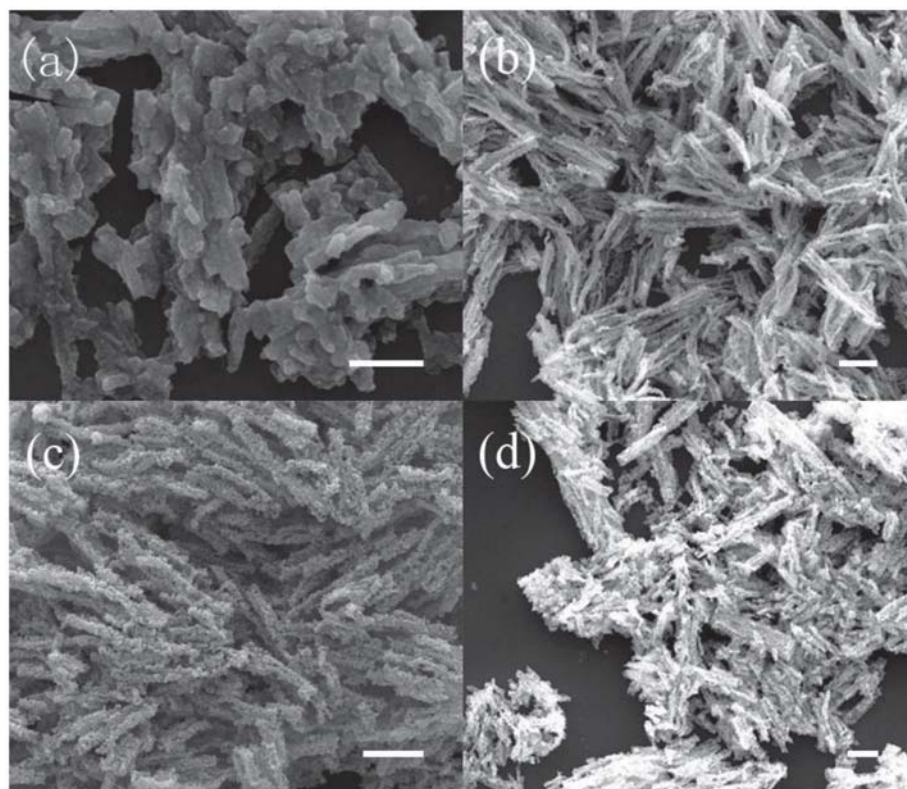


FIGURE 2 | SEM images of Ni_xS_y samples under different annealing temperatures: **(a)** 280, **(b)** 300, **(c)** 310, and **(d)** 330°C. (scale bar = 1 μm).

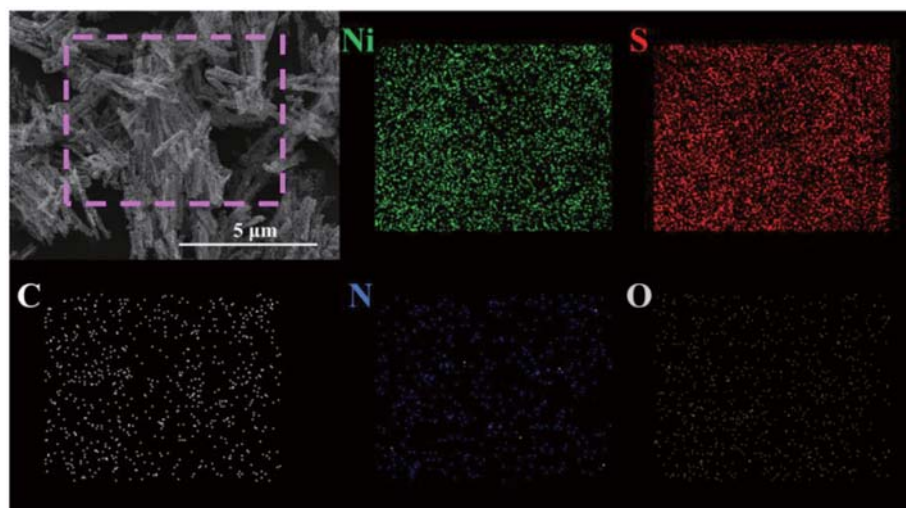


FIGURE 3 | FESEM image of the Ni_xS_y nanorods and corresponding elemental mapping images of Ni, S, C, N, and O.

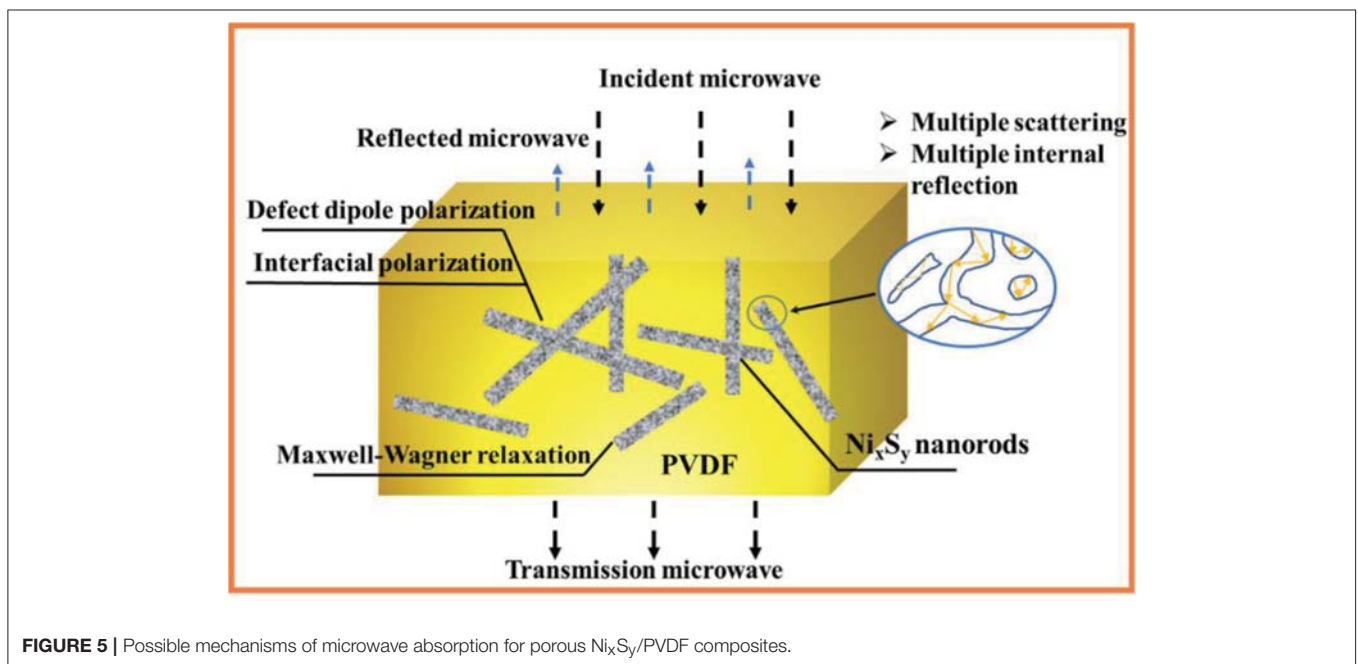
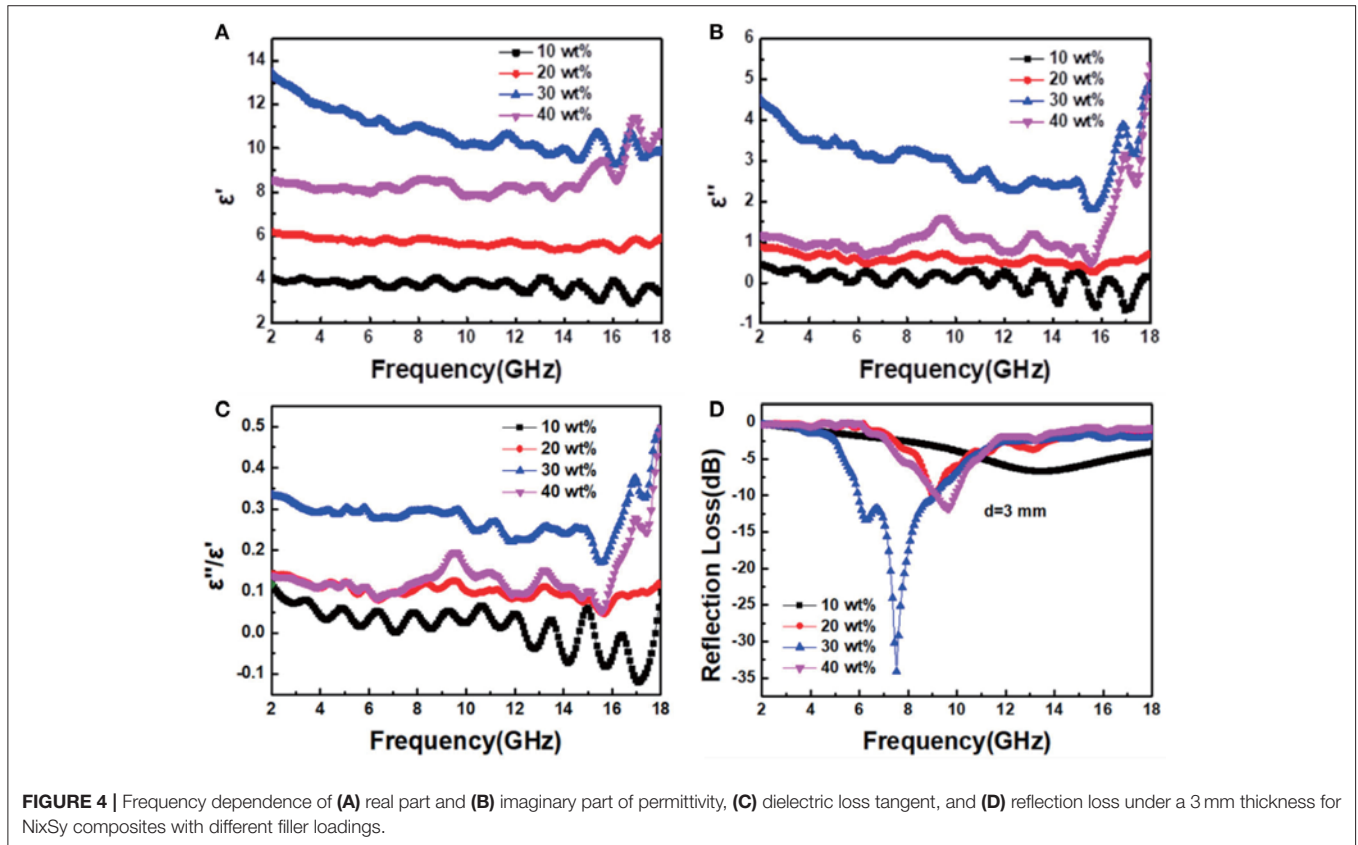
as-synthesized products are poorly crystallized, containing NiS_2 phase and Ni_7S_6 phase (**Figure S3**).

Figures 4A,B show the frequency dependence of the real part (ϵ') and imaginary part (ϵ'') of the complex permittivity for $\text{Ni}_x\text{S}_y/\text{PVDF}$ composites with 10, 20, 30, and 40 wt% filler

loadings in the frequency range of 2–18 GHz. Generally, the ϵ' is known to stand the storage capability of electromagnetic energy, and ϵ'' associated with various of polarization present the energy dissipation (Zhang X. et al., 2015; Zhao B. et al., 2016). As can be seen in **Figure 4**, with the increase of Ni_xS_y , the ϵ'

and ϵ'' values show a similar tendency. For nanohybrids with low concentration of filler (10 and 20 wt%), the values of ϵ' and ϵ'' are approximately equal to some certain constant in the whole frequency range ($\epsilon' = 4$, $\epsilon'' = 0.5$, and $\epsilon' = 6$, $\epsilon'' = 1$). With the

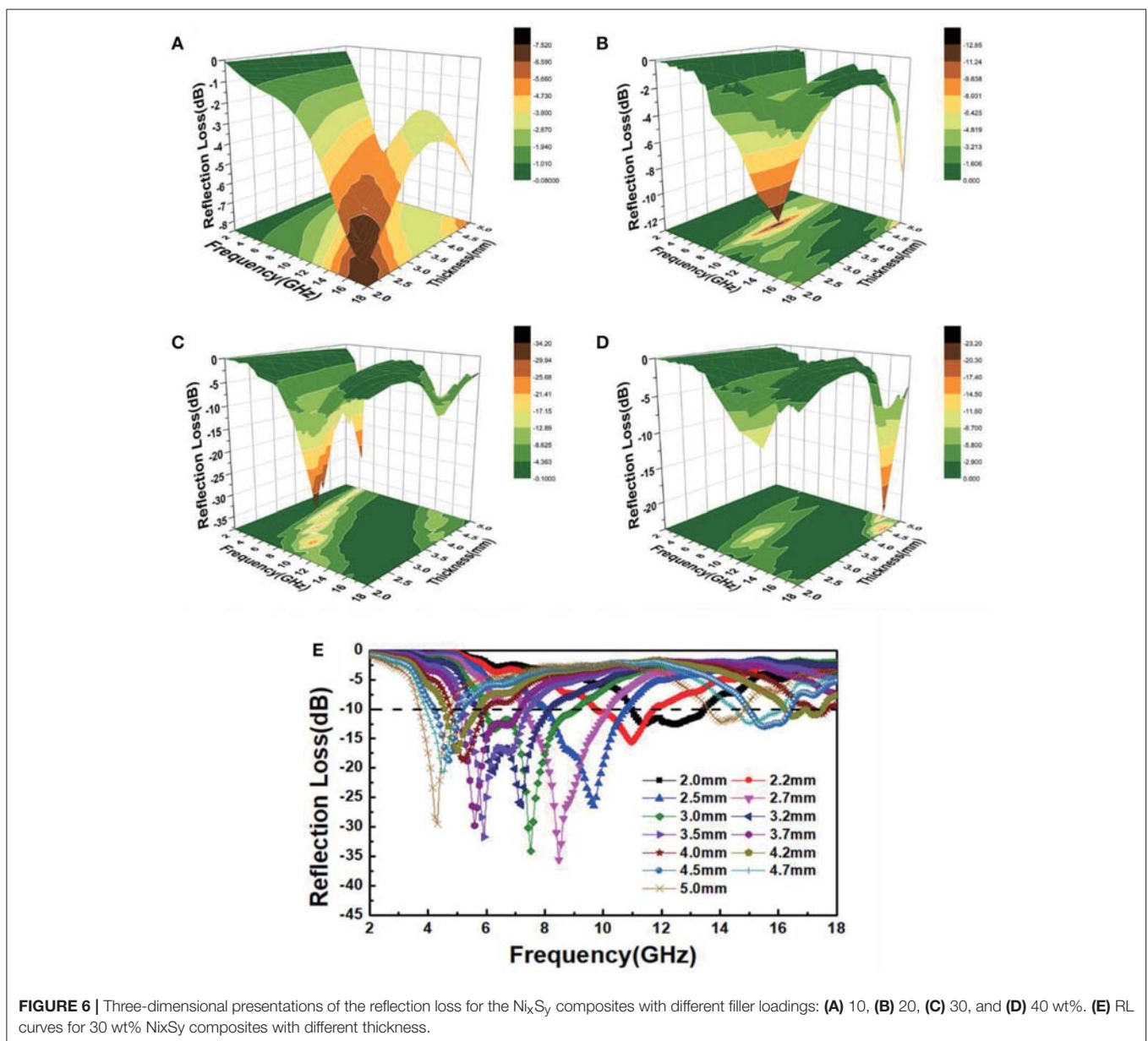
Ni_xS_y proportion increasing from 20 to 30 wt%, the ϵ' increases from 6 to 13 and the ϵ'' changes from 1 to 4.5 at 2 GHz. However, when the proportion of fillers is increased to 40 wt%, both the ϵ' and ϵ'' dramatically decrease, which is possibly due to the



fact that the higher concentration of Ni_xS_y in this nanohybrid may result in severe agglomeration. Similar phenomena could be observed in dielectric loss tangent ($\tan \delta_e = \epsilon''/\epsilon'$) which is universally applied to evaluate the dielectric loss capacity of the microwave absorber (Yang et al., 2017), shown in **Figure 4C**. It can be seen that the dielectric loss tangent increases with the Ni_xS_y proportion first, getting a maximum value of 0.35 with 30 wt% Ni_xS_y , and then decreases to a value of 0.1.

On the basis of the above analysis, it can be deduced that the nanohybrids with 30 wt% Ni_xS_y possess the best microwave absorption properties which is highly consistent with the test results, shown in **Figure 4D**. The minimum RL reaches -34 dB at 7.5 GHz with a thickness of 3 mm, indicating that 99.9% of incident electromagnetic wave is attenuated. Since

Ni_xS_y is a typical semiconductive material, various polarization, and related relaxation resulting in a strong dielectric loss are the dominant mechanism for microwave attenuation (Zhao et al., 2015). The dielectric loss of Ni_xS_y mainly originate from the defect dipole polarization, the interfacial polarization, and the electronic relaxation loss. First, the defect dipoles are generated by the charge unbalance around the sulfur vacancies in the Ni_xS_y lattice, while the interfacial polarizations come from the existence of plentiful interfaces between porous fillers and polymer matrix. Moreover, the porous structures of fillers with rough surfaces further induce the multiple reflection and scattering, resulting in more longer propagation path and greater energy loss (**Figure 5**). Second, the carbonation of precursors benefits electrical conduction, while the internal



doping with nitrogen favors electron transport thus further improving electrical conduction. Furthermore, the calcination also induces a structural disorder and defects into Ni_xS_y that frequently lead to an enhanced electrical activity. This calcination process results in significant electronic relaxation polarization, which would enhance the dielectric loss obviously.

Figures 6A–D shows three-dimensional presentations of calculated reflection loss for the Ni_xS_y/PVDF with different filler loadings. Clearly, the composite with 30 wt% Ni_xS_y has the best performance, and the RL values under different thickness are shown in **Figure 6E**. The minimal reflection loss of -35.6 dB is obtained at 8.5 GHz with a coating thickness of 2.7 mm and the effective bandwidth is about 3 GHz. Furthermore, the RLs exceeding -10 dB in the frequency range of 3.68–18 GHz are obtained for a variation in absorber thicknesses of 2.0–5.0 mm, demonstrating that this kind of materials has great potential for use as a microwave absorber. Meanwhile, there is an interesting phenomenon that with the increasing thickness of absorber the RL peaks shift to the lower-region frequency. This phenomenon is consistent with a so-called quarter-wavelength ($\lambda/4$) matching model (Deng and Han, 2007; Wang et al., 2011, 2013) which plays another significant role in electromagnetic attenuation. The model can be expressed as $t_m = n\lambda/4 = nc/4f_m\sqrt{|\mu_r||\epsilon_r|}$ ($n = 1, 3, 5$), where $|\mu_r|$ and $|\epsilon_r|$ are the moduli of μ_r and ϵ_r , respectively. Besides, when the thickness of absorber satisfies above equation, the curves corresponding to wavelengths of $\lambda/4$ (crescent shape) can be observed (seen in **Figure 6C**).

CONCLUSIONS

In summary, we have successfully demonstrated an approach for the large-scale production of 1D porous Ni_xS_y nanostructures via solvothermal synthesis together with an annealing process.

REFERENCES

- Abbas, S. M., Chandra, M., Verma, A., Chatterjee, R., and Goel, T. C. (2006). Complex permittivity and microwave absorption properties of a composite dielectric absorber. *Compos. A Appl. Sci. Manufact.* 37, 2148–2154. doi: 10.1016/j.compositesa.2005.11.006
- Deng, L. J., and Han, M. G. (2007). Microwave absorbing performances of multiwalled carbon nanotube composites with negative permeability. *Appl. Phys. Lett.* 91:023119. doi: 10.1063/1.2755875
- He, S., Lu, C., Wang, G. S., Wang, J. W., Guo, H. Y., and Guo, L. (2014). Synthesis and growth mechanism of white-fungus-like nickel sulfide microspheres and their application in polymer composites with enhanced microwave-absorption properties. *ChemPlusChem* 79, 569–576. doi: 10.1002/cplu.201300435
- He, S., Wang, G. S., Lu, C., Liu, J., Wen, B., Liu, H., et al. (2013). Enhanced wave absorption of nanocomposites based on the synthesized complex symmetrical CuS nanostructure and poly(vinylidene fluoride). *J. Mater. Chem. A* 1, 4685–4692. doi: 10.1039/c3ta00072a
- Liu, J., Cao, M. S., Luo, Q., Shi, H. L., Wang, W. Z., and Yuan, J. (2016). Electromagnetic property and tunable microwave absorption of 3D nets from nickel chains at elevated temperature. *ACS Appl. Mater. Interfaces* 8, 22615–22622. doi: 10.1021/acsami.6b05480
- Liu, J., Xu, J., Che, R., Chen, H., Liu, M., and Liu, Z. (2013). Hierarchical Fe₃O₄@TiO₂ yolk-shell microspheres with enhanced microwave-absorption properties. *Chem. A Eur. J.* 19, 6746–6752. doi: 10.1002/chem.201203557
- Liu, Q., Xu, X., Xia, W., Che, R., Chen, C., Cao, Q., et al. (2015). Dependency of magnetic microwave absorption on surface architecture of Co₂₀Ni₈₀ hierarchical structures studied by electron holography. *Nanoscale* 7, 1736–1743. doi: 10.1039/c4nr05547k
- Liu, Q. L., Zhang, D., and Fan, T. X. (2008). Electromagnetic wave absorption properties of porous carbon/Co nanocomposites. *Appl. Phys. Lett.* 93:013110. doi: 10.1063/1.2957035
- Luo, X., Wang, G. S., Guo, H. Y., Zhang, X. J., Cao, W. Q., Wei, Y. Z., et al. (2014). Enhanced wave-absorption properties of nanocomposites based on the synthesized Bi₂S₃ nanorods and polyvinylidene fluoride. *ChemPlusChem* 79, 1089–1095. doi: 10.1002/cplu.201402050
- Lv, H., Liang, X., Cheng, Y., Zhang, H., Tang, D., Zhang, B., et al. (2015a). Coin-like α -Fe₂O₃@CoFe₂O₄ core-shell composites with excellent electromagnetic absorption performance. *ACS Appl. Mater. Interfaces* 7, 4744–4750. doi: 10.1021/am508438s
- Lv, H., Liang, X., Ji, G., Zhang, H., and Du, Y. (2015b). Porous three-dimensional flower-like Co/CoO and its excellent electromagnetic absorption properties. *ACS Appl. Mater. Interfaces* 7, 9776–9783. doi: 10.1021/acsami.5b01654
- Ning, M. Q., Lu, M. M., Li, J. B., Chen, Z., Dou, Y. K., Wang, C. Z., et al. (2015). Two-dimensional nanosheets of MoS₂: a promising material with high dielectric properties and microwave absorption performance. *Nanoscale* 7:15734. doi: 10.1039/c5nr04670j
- Qiang, R., Du, Y., Wang, Y., Wang, N., Tian, C., Ma, J., et al. (2016). Rational design of yolk-shell C@C microspheres for the effective enhancement in microwave absorption. *Carbon* 98, 599–606. doi: 10.1016/j.carbon.2015.11.054

Through controlling the reaction temperature and time, products with uniform morphology are obtained. The results reveal that the interesting porous structure of Ni_xS_y might benefit the access of incident microwave and offer more active sites for multiple reflections and scattering, and thereby improve microwave absorbing performance. The minimum RL of -35.6 dB is achieved with a thickness of 2.7 mm at -35.6 dB GHz. The absorption bandwidth with RLs below -10 dB is up to 14.5 GHz when considering thicknesses of 2.0–5.0 mm. Combining the synergistic effect with intrinsic chemical properties and special structures, the Ni_xS_y nanorods are promising for utilization as MA materials in various fields, such as aeroplanes and spacecraft.

AUTHOR CONTRIBUTIONS

ML designed experiments, carried out experiments, analyzed experimental results, and wrote the manuscript. QW, WX, H-YZ, and XD helped experimental result. X-HG gave guidance on the revision of the experimental plan and manuscript. G-SW and S-HD funded experimental topics.

ACKNOWLEDGMENTS

This project was supported by the National Nature Science Foundation of China (No. 51472012), and the Fundamental Research Funds for the Central Universities.

SUPPLEMENTARY MATERIAL

The Supplementary Material for this article can be found online at: <https://www.frontiersin.org/articles/10.3389/fchem.2018.00405/full#supplementary-material>

- Wang, B., Wei, J., Yang, Y., Wang, T., and Li, F. (2011). Investigation on peak frequency of the microwave absorption for carbonyl iron/epoxy resin composite. *J. Magnet. Magnetic Mater.* 323, 1101–1103. doi: 10.1016/j.jmmm.2010.12.028
- Wang, G. S., Wu, Y. Y., Zhang, X. J., Li, Y., Guo, L., and Cao, M. S. (2014). Controllable synthesis of uniform ZnO nanorods and their enhanced dielectric and absorption properties. *J. Mater. Chem. A* 2, 8644–8651. doi: 10.1039/c4ta00485j
- Wang, L., Xing, H., Gao, S., Ji, X., and Shen, Z. (2017). Porous flower-like NiO/graphene composites with superior microwave absorption properties. *J. Mater. Chem. C* 5, 2005–2014. doi: 10.1039/c6tc05179k
- Wang, Y., Chen, D., Yin, X., Xu, P., Wu, F., and He, M. (2015). Hybrid of MoS₂ and reduced graphene oxide: a lightweight and broadband electromagnetic wave absorber. *ACS Appl. Mater. Interfaces* 7, 26226–26234. doi: 10.1021/acsami.5b08410
- Wang, Y., Wang, L., and Wu, H. (2013). Enhanced microwave absorption properties of α -Fe₂O₃-filled ordered mesoporous carbon nanorods. *Materials* 6, 1520–1529. doi: 10.3390/ma6041520
- Xu, W., Pan, Y. F., Wei, W., and Wang, G. S. (2018). Nanocomposites of oriented nickel chains with tunable magnetic properties for high-performance broadband microwave absorption. *ACS Appl. Nano Mater.* 1, 1116–1123. doi: 10.1021/acsnm.7b00293
- Yan, D., Cheng, S., Zhuo, R. F., Chen, J. T., Feng, J. J., Feng, H. T., et al. (2009). Nanoparticles and 3D sponge-like porous networks of manganese oxides and their microwave absorption properties. *Nanotechnology* 20:105706. doi: 10.1088/0957-4484/20/10/105706
- Yang, R., Wang, B., Xiang, J., Mu, C., Zhang, C., Wen, F., et al. (2017). Fabrication of NiCo₂-anchored graphene nanosheets by liquid-phase exfoliation for excellent microwave absorbers. *ACS Appl. Mater. Interfaces* 9, 12673–12679. doi: 10.1021/acsami.6b16144
- Yu, M., Liang, C., Liu, M., Liu, X., Yuan, K., Cao, H., et al. (2014). Yolk-shell Fe₃O₄@ZrO₂ prepared by a tunable polymer surfactant assisted sol-gel method for high temperature stable microwave absorption. *J. Mater. Chem. C* 2, 7275–7283. doi: 10.1039/c4tcQ1285b
- Yuan, K., Che, R., Cao, Q., Sun, Z., Yue, Q., and Deng, Y. (2015). Designed fabrication and characterization of three-dimensionally ordered arrays of core-shell magnetic mesoporous carbon microspheres. *ACS Appl. Mater. Interfaces* 7, 5312–5319. doi: 10.1021/am508683p
- Zhang, C., Wang, B., Xiang, J., Su, C., Mu, C., Wen, F., et al. (2017). Microwave absorption properties of CoS₂ nanocrystals embedded into reduced graphene oxide. *ACS Appl. Mater. Interfaces* 9, 28868–28875. doi: 10.1021/acsami.7b06982
- Zhang, D. D., Zhao, D. L., Zhang, J. M., and Bai, L. Z. (2014). Microwave absorbing property and complex permittivity and permeability of graphene-CdS nanocomposite. *J. Alloys Compounds* 589, 378–383. doi: 10.1016/j.jallcom.2013.11.195
- Zhang, X., Ji, G., Liu, W., Quan, B., Liang, X., Shang, C., et al. (2015). Thermal conversion of an Fe₃O₄@metal-organic framework: a new method for an efficient Fe-Co/nanoporous carbon microwave absorbing material. *Nanoscale* 7, 12932–12942. doi: 10.1039/c5nr03176a
- Zhang, X. J., Wang, S. W., Wang, G. S., Li, Z., Guo, A. P., Zhu, J. Q., et al. (2017). Facile synthesis of NiS₂@MoS₂ core-shell nanospheres for effective enhancement in microwave absorption. *RSC Adv.* 7, 22454–22460. doi: 10.1039/c7ra03260a
- Zhang, Y., Huang, Y., Zhang, T., Chang, H., Xiao, P., Chen, H., et al. (2015). Broadband and tunable high-performance microwave absorption of an ultralight and highly compressible graphene foam. *Adv. Mater.* 27, 2049–2053. doi: 10.1002/adma.201405788
- Zhao, B., Guo, X., Zhao, W., Deng, J., Shao, G., Fan, B., et al. (2016). Yolk-Shell Ni@SnO₂ composites with a designable interspace to improve the electromagnetic wave absorption properties. *ACS Appl. Mater. Interfaces* 8, 28917–28925. doi: 10.1021/acsami.6b10886
- Zhao, B., Shao, G., Fan, B., Zhao, W., Xie, Y., and Zhang, R. (2015). Facile preparation and enhanced microwave absorption properties of core-shell composite spheres composed of Ni cores and TiO₂ shells. *Phys. Chem. Chem. Phys.* 17, 8802–8810. doi: 10.1039/c4cp05632a
- Zhao, H., Li, Z., Zhang, N., Du, Y., Li, S., Shao, L., et al. (2014). γ -irradiation induced one-step synthesis of electromagnetic functionalized reduced graphene oxide-Ni nanocomposites. *RSC Adv.* 4, 30467–30470. doi: 10.1039/c4ra05477f
- Zhao, H. B., Fu, Z. B., Chen, H. B., Zhong, M. L., and Wang, C. Y. (2016). Excellent electromagnetic absorption capability of Ni/Carbon based conductive and magnetic foams synthesized via a green one pot route. *ACS Appl. Mater. Interfaces* 8, 1468–1477. doi: 10.1021/acsami.5b10805
- Zhou, J. H., He, J. P., Li, G. X., Wang, T., Sun, D., Ding, X. C., et al. (2010). Direct incorporation of magnetic constituents within ordered mesoporous carbon-silica nanocomposites for highly efficient electromagnetic wave absorbers. *J. Phys. Chem. C* 114, 7611–7617. doi: 10.1021/jp911030n
- Zhu, C. L., Zhang, M. L., Qiao, Y. J., Xiao, G., Zhang, F., and Chen, Y. J. (2010). Fe₃O₄/TiO₂ core/shell nanotubes: synthesis and magnetic and electromagnetic wave absorption characteristics. *J. Phys. Chem. C* 114, 16229–16235. doi: 10.1021/jp104445m
- Zhu, H. L., Bai, Y. J., Liu, R., Lun, N., Qi, Y. X., Han, F. D., et al. (2011). *In situ* synthesis of one-dimensional MWCNT/SiC porous nanocomposites with excellent microwave absorption properties. *J. Phys. Chem.* 21, 13581–13587. doi: 10.1039/c1jm11747e

Conflict of Interest Statement: The authors declare that the research was conducted in the absence of any commercial or financial relationships that could be construed as a potential conflict of interest.

Copyright © 2018 Lu, Wu, Guan, Xu, Zhang, Di, Wang and Dong. This is an open-access article distributed under the terms of the Creative Commons Attribution License (CC BY). The use, distribution or reproduction in other forums is permitted, provided the original author(s) and the copyright owner(s) are credited and that the original publication in this journal is cited, in accordance with accepted academic practice. No use, distribution or reproduction is permitted which does not comply with these terms.



CoAl₂O₄/Kaoline Hybrid Pigment Prepared via Solid-Phase Method for Anticorrosion Application

Anjie Zhang^{1,2}, Bin Mu^{1*}, Xiaowen Wang^{1,2} and Aiqin Wang^{1*}

¹ Key Laboratory of Clay Mineral Applied Research of Gansu Province, Center of Eco-material and Green Chemistry, Lanzhou Institute of Chemical Physics, Chinese Academy of Sciences, Lanzhou, China, ² Center of Materials Science and Optoelectronics Engineering, University of Chinese Academy of Sciences, Beijing, China

OPEN ACCESS

Edited by:

Pu-Xian Gao,
University of Connecticut,
United States

Reviewed by:

Na Tian,
China University of Geosciences,
China

Adimali Piyadasa,
Intel, United States

*Correspondence:

Bin Mu
mubin@licp.cas.cn
Aiqin Wang
aqwang@licp.cas.cn

Specialty section:

This article was submitted to
Green and Sustainable Chemistry,
a section of the journal
Frontiers in Chemistry

Received: 31 July 2018

Accepted: 09 November 2018

Published: 29 November 2018

Citation:

Zhang A, Mu B, Wang X and Wang A
(2018) CoAl₂O₄/Kaoline Hybrid
Pigment Prepared via Solid-Phase
Method for Anticorrosion Application.
Front. Chem. 6:586.
doi: 10.3389/fchem.2018.00586

In this study, kaoline is incorporated to prepare CoAl₂O₄/kaoline hybrid pigments via traditional solid-state reaction, and the introduction of kaoline decreases the preparation temperature for formation of spinel CoAl₂O₄, and reduces the production cost of cobalt blue as well. More importantly, kaoline may participate in the crystallization of spinel CoAl₂O₄ during calcining process, and the hybrid pigments prepared using 8.1% Co₃O₄ and 81.5% kaoline features bright blue and good chemical resistance. Due to the synergistic effect between the sheet-like kaoline and the loaded CoAl₂O₄, the as-prepared CoAl₂O₄/kaoline hybrid pigments can be incorporated into epoxy paint system to obtain the high-performance blue anticorrosion coating, especially for acetic acid-salt fog corrosion.

Keywords: CoAl₂O₄, hybrid pigments, kaoline, anticorrosion coating, acetic acid-salt fog

INTRODUCTION

It is well-known that corrosion of the metal materials is one of the common and key problems to industry applications, especially the high risk fields including aviation, ocean, and chemical industry, etc. (De Leon et al., 2012; Daham et al., 2014; Hao et al., 2017). The organic anticorrosion coating has been recognized as the most effective and economical method for metal protection (Vesely et al., 2010; Golru et al., 2015; Gu et al., 2015; Madhup et al., 2017). The anticorrosion mechanisms of the coatings usually include protection of barrier type, inhibition type protection and electrochemical protection (Al-Sabagh et al., 2017), and the organic anticorrosion coating is served as a physical barrier between corrosive electrolyte and steel substrate. However, the main disadvantage of the organic anticorrosion coating, especially epoxy system, is the creation of holes and defects over the film due to the high crosslink density.

Several approaches have been proposed to enhance the anticorrosion properties of organic anticorrosion coating. By contrast, incorporation of inorganic pigments is efficient and economical way (Kartsonakis et al., 2012; Montemor et al., 2012; Jeon et al., 2013; Naderi et al., 2014). It is conducive to improving the aesthetics (e.g., gloss, opacity, and color) and the mechanical properties of the film (El Saeed et al., 2012). However, the relevant application of some commercial available inorganic pigments is limited due to their disadvantages, such as poor adhesive force and optical transparency, weak abrasion and scratch resistance performance (Zhou et al., 2002; Cayton and Sawitowski, 2005; El-Wahab et al., 2009). Therefore, many attempts have been carried out to prepare high-performance pigments with good anticorrosion properties by designing lamellar-based nano-materials preventing water, oxygen, or ions from penetrating film (Kalendová et al., 2008; Ahmed et al., 2012; Ammar et al., 2016; Zhang et al., 2016).

Cobalt aluminate (cobalt blue, CoAl₂O₄) is a spinel type structure blue eco-friendly pigments with excellent thermal and chemical stability, and it has been widely used in the fields of ceramics, plastics, paint, rubber and glass (Jafari and Hassanzadeh-Tabriz, 2014; Álvarez-Docio et al., 2017; He et al., 2017; Yoneda et al., 2018). Therefore, cobalt blue may be expected to develop the high-performance anticorrosion coating, especially for acetic acid-salt fog corrosion. However, the agglomeration of CoAl₂O₄ nanoparticles is inevitable during preparation process, which goes against the dispersion of cobalt blue in coating substrate. In addition, the high-cost of cobalt blue also limits its wide application in anticorrosion coating (Tirsoaga et al., 2011; Dandapat and De, 2012; Zou and Zheng, 2016). In our previous work (Mu et al., 2015; Zhang A. J. et al., 2017), clay minerals were employed to fabricate the high-performance CoAl₂O₄ hybrid pigment with low-cost and perfect color properties. Kaoline (Kaol) is a 1:1 type layered silicate mineral with one tetrahedral sheet of silica (SiO₄) linked through oxygen atoms to one octahedral sheet of alumina (AlO₆) octahedral (Liu et al., 2016; Klopogge, 2017; Zhang S. L. et al., 2017). Owing to the advantages of excellent mechanical properties, thermal stability, high whiteness and unique flake-like morphology (Vesely et al., 2010; Ahmed et al., 2012; Qu et al., 2017), it is a promising candidate for preparation of cobalt blue hybrid pigment to design the color high-performance anticorrosion coating (Zhang et al., 2018a,b). However, the preparation process of co-precipitation usually involves in the discharge of the wastewater and lengthy steps including washing, solid-liquid separation and drying.

In this study, CoAl₂O₄/Kaol hybrid pigments were prepared by the traditional solid-state reaction after grinding the mixture of γ -Al₂O₃, Co₃O₄, and Kaol. The preparation conditions were systematically investigated including the grinding time, the calcining temperature and the added amount of Kaol. Furthermore, the formation and coloring mechanisms of CoAl₂O₄/Kaol hybrid pigments were also studied and discussed. In order to evaluate the anticorrosion application of the as-prepared hybrid pigment, it was incorporated into the epoxy paint system to obtain the blue anticorrosion coating, and then placed in acetic acid-salt spray testing chamber.

MATERIALS AND METHODS

Materials

Kaol was obtained from Longyan kaoline Development Co., Ltd., (FuJian, China), Kaol were firstly crushed and purified by 4% HCl (wt%), and then the solid were filtered by passing through a 200-mesh sieve to remove quartz sand, and the XRF (X-ray fluorescence) chemical compositions of Kaol were presented in **Table S1** (see ESI) before and after being treated by HCl. γ -Al₂O₃ (purity > 99.9%, particle size = 20 ~ 50 nm) and Co₃O₄ (purity > 99.9%, D50: 4 ~ 6 μ m) were obtained from Shanghai Reagent Factory (Shanghai, China).

Preparation of CoAl₂O₄/Kaol Hybrid Pigments

8.00 g of Kaol, 0.80 g of Co₃O₄ and 1.02 g of Al₂O₃ with a Co to Al mole ratio of 2:1 were mixed and grinded in a

TABLE 1 | Conditions for preparation of the samples.

Factors	Temperature/°C	Co ₃ O ₄ /g	Al ₂ O ₃ /g	Kaol/g	Grinding time (h)
Temperature	900	0.8	1.02	1	2
	1,000	0.8	1.02	1	2
	1,100	0.8	1.02	1	2
	1,200	0.8	1.02	1	2
Added amount of Kaol	1,100	0.8	1.02	0	2
	1,100	0.8	1.02	1	2
	1,100	0.8	1.02	2	2
	1,100	0.8	1.02	4	2
	1,100	0.8	1.02	6	2
	1,100	0.8	1.02	8	2
Grinding time	1,100	0.8	1.02	1	0.5
	1,100	0.8	1.02	1	1
	1,100	0.8	1.02	1	2
	1,100	0.8	1.02	1	4

mortar mill (CRINOER, MG100, China) for 2 h in anhydrous ethanol medium, and then the mixture was calcined to obtain CoAl₂O₄/Kaol hybrid pigments. The optimum preparation conditions were systematically investigated including the calcining temperatures (900, 1,000, 1,100, and 1,200°C), the grinding time (0.5, 1, 2, and 4 h) and the added amount of Kaol (0, 1, 2, 4, 6, and 8 g), as summarized in **Table 1**.

Characterization

The Fourier Transform infrared (FTIR) spectra were collected on a Thermo Nicolet NEXUS TM spectro photometer using KBr pellets. The morphology was observed using transmission electron microscopy (TEM, JEM-1200EX/S, JEOL). XRD test was conducted on X'pert PRO diffractometer with a scan step size of 0.02° per second. Raman spectra were tested using a Labram HR Evolution Raman spectrometer (Horiba). The chemical compositions were measured on a MiniPal 4 XRF spectrometer (PANalytical Co., Netherland). The anticorrosion performance was evaluated on a salt spray testing chamber (YWX-750, Nanjing Huanke experimental equipment Co. Ltd, China). The colorimetric values and reflectance spectra were measured on a Color-Eye automatic differential colorimeter (X-Rite, Ci 7800).

Stability Evaluation of CoAl₂O₄/Kaol Hybrid Pigments

In order to evaluate the environmental stability of CoAl₂O₄/Kaol hybrid pigment, it was sprayed onto glass substrate and dried in the open atmosphere after being ultrasonically dispersed into ethanol for 30 min. And then the glass plates were placed for 15 days in a UV Accelerated Weathering Tester (ZN-P, Xinlang, Shanghai, China) with eight UV-B (280-315 nm) bulbs (40 W) at 60°C under UV-B exposure with a radiation intensity of 320 W/m². The color properties were measured before and after being exposed in a UV accelerated weathering tester to evaluate UV irradiation stability.

The obtained sample plates were also immersed into 3M HCl, 3M NaOH, and ethanol at room temperature for 72 h to study the chemical stability of CoAl₂O₄/Kaol hybrid pigment, respectively. Unlike with above glass substrate, the hybrid pigments were sprayed onto ceramic substrate and then placed in a muffle furnace to be calcined at 1,000°C for 2 h to evaluate the thermal stability.

Anticorrosion Evaluation of the Blue Epoxy Coating

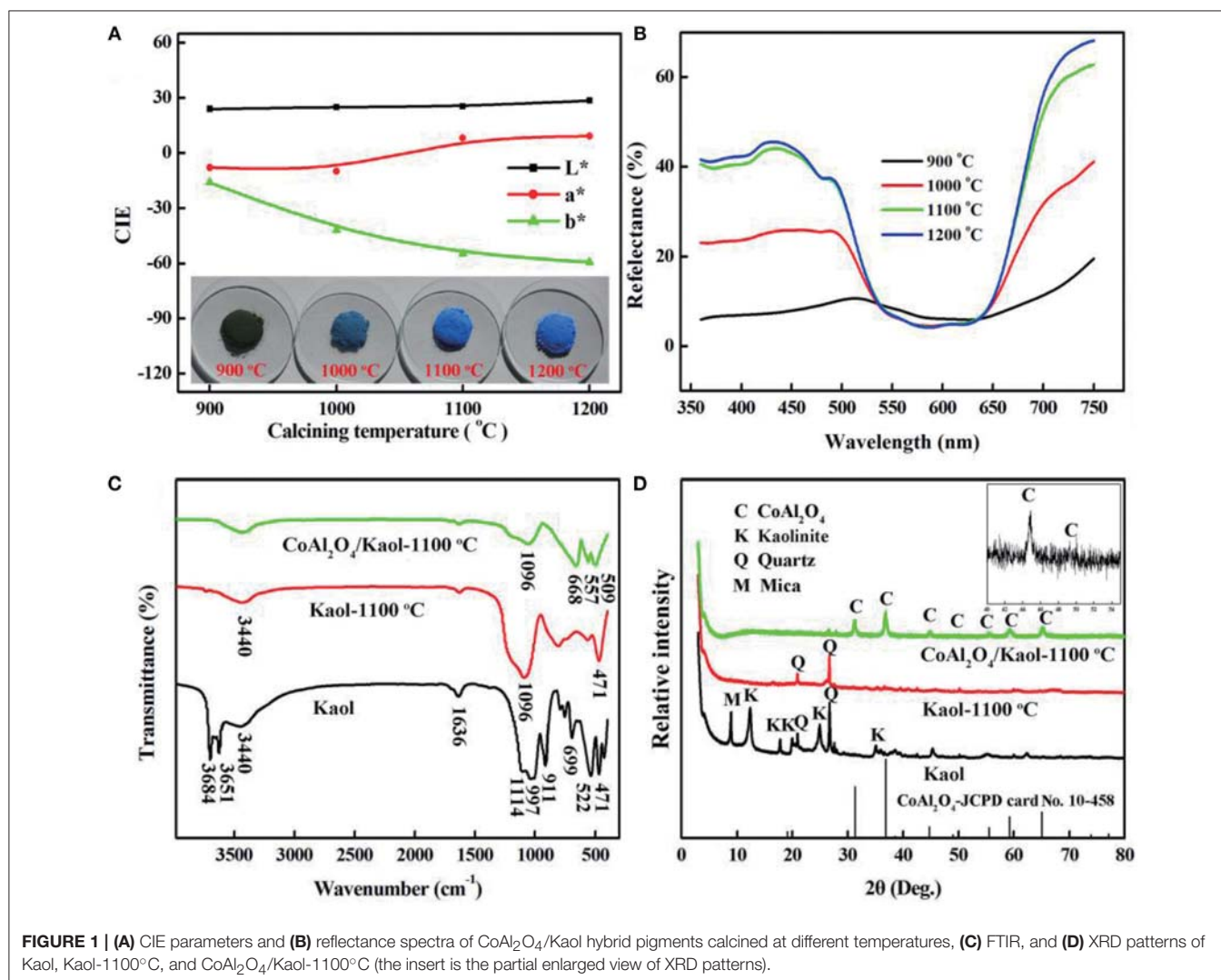
The anticorrosion coating was prepared by following procedures: Firstly, epoxy resin, 5 wt% CoAl₂O₄/Kaol hybrid pigment, dispersing agent, flattening agent, auxiliary solvents, talcum powder, ethyl acetate, and some grading beads added in a 500 mL stainless steel under high shear for 30 min (2,000 rpm), and then the antifoaming agent, wetting agent were added into the above mill base and stirred under low shear for 60 min (500 rpm). If the maximum pigment size was lower than 30 μm, the grinding was considered for meet the requirements, and then the viscosity of

the coating was adjusted by ethyl acetate to 20~30 s. And then it was sprayed onto steel plate substrate of size 15 cm × 10 cm × 0.1 cm and dried under the standard conditions (temperature: 25°C and humidity: 40%) for 7 days (the coating thickness: D = 50 ± 2 μm). The obtained sample plates were placed in salt spray testing chamber to evaluate the salt fog corrosion resistance performance (35°C, 100% humidity and 5.0 wt% NaCl solution). In addition, the obtained sample plates were also placed in acetic acid-salt spray testing chamber to evaluate the acetic acid-salt fog corrosion resistance performance (35°C, 100% humidity and 5.0 wt% NaCl solution, pH = 2.8 ~ 3.0).

RESULTS AND DISCUSSION

Preparation of CoAl₂O₄/Kaol Hybrid Pigments

The calcining temperature is an important factor to form spinel CoAl₂O₄ with perfect blue color (Yang et al., 2013), and thus the effect of calcining temperatures on the color



parameters of hybrid pigment was studied. **Figure 1a** gives the color parameters of CoAl₂O₄/Kaol hybrid pigments after being calcined at 900~1,200°C. The b^* value of hybrid pigments firstly decreases with the increase in the temperatures, and then it almost has no obvious change as the temperature is above 1,100°C. The values of L^* and a^* continuously increase with the increase in the calcining temperatures. With the increase in the calcining temperature from 900 to 1,100°C, the color of the hybrid pigments transforms from green to blue to bright blue, which is also consistent with the change of their color parameters. The blue color is derived from Co²⁺ in tetrahedral sites, while the green color is attributed to Co³⁺ in octahedral coordination (Álvarez-Docio et al., 2017). By contrast, the b^* value of hybrid pigments reaches the minimum value after being calcined at 1,100°C, suggesting that the optimum calcining temperature is 1,100°C. As shown in **Figure 1b**, the reflection bands and absorption bands are observed at 440~500 nm and at 550~650 nm, respectively, except for hybrid pigment prepared at 900°C. These bands are associated with the blue color of CoAl₂O₄ due to $^4A_2(F) \rightarrow ^4T_1(P)$ of the Co²⁺ $d-d$ transition in tetrahedral coordination (Tielens et al., 2006; Kurajica et al., 2012; Gomesan et al., 2015; Tahereh et al., 2016). And for the

hybrid pigment prepared at 900°C, the bands at 380 and 670 nm are indicative of the occurrence of octahedrally coordinated Co³⁺, and are ascribed to the $^1A_{1g} \rightarrow ^1T_{2g}$ and $^1A_{1g} \rightarrow ^1T_{1g}$ transitions of low spin Co³⁺ in octahedral symmetry (Brik et al., 2001; Herrero et al., 2007), the sample exhibits greenish hue annealed at low temperature, which is also in accordance with the digital photos of the hybrid pigment calcined at 900°C (Kurajica et al., 2012). In addition, the intensity of the reflection peaks also increases with the increase in the preparation temperatures until 1,100°C, and then it decreases as the calcining temperature reaches 1,200°C, which may be due to crystal phase and structural transformation of Kaol (Juneja et al., 2010; Yeo, 2011).

Figure S1a depicts the effect of grinding time on color parameters of hybrid pigment, the b^* value of CoAl₂O₄/Kaol hybrid pigments firstly decreases with the increase in the grinding time from 0.5 to 1 h, and no obvious change is observed with the continuous increasing grinding time. In order to ensure the reaction uniformity, the grinding time is selected to 2 h. **Figure S1b** exhibits the effect of the added amount of Kaol on color parameters. At the same calcining temperature (1,100°C), the L^* value of hybrid pigments gradually increases with increase

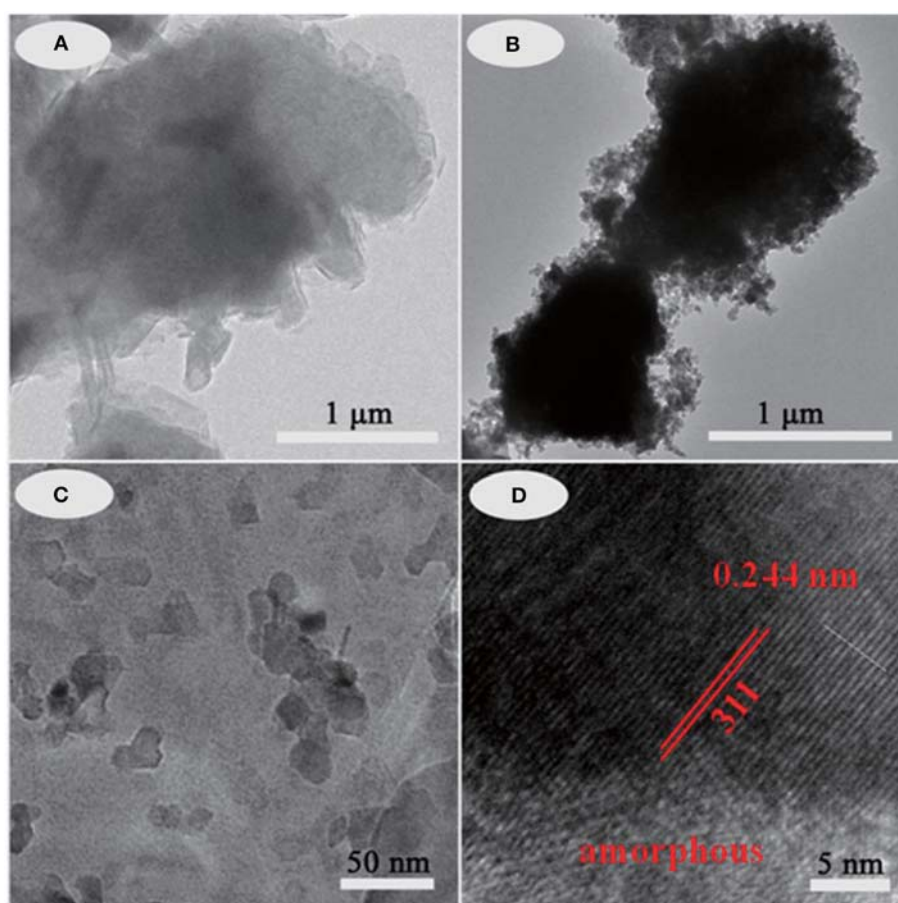


FIGURE 2 | TEM images of (A) Kaol and (B–D) CoAl₂O₄/Kaol-1100°C.

in the added amount of Kaol, while the a^* and b^* values of the sample containing Kaol of 35.5 wt% (1 g Kaol) reach maximum. Interestingly, CoAl₂O₄/Kaol hybrid pigments still exhibits good color properties ($L^* = 29.9$, $a^* = 2.01$, $b^* = -54.93$) as the added amount of Kaol is up to 81.5 wt% (8 g Kaol). However, the sample is atrovirens prepared without Kaol at 1,100°C, suggesting that the introduction the low-cost Kaol not only reduces the production cost of CoAl₂O₄, but also decreases the high temperature crystallization temperature for formation of spinel structure. During calcining process, Kaol (2SiO₂ · Al₂O₃ · 2H₂O) transforms into metakaolinite (2SiO₂ · Al₂O₃) at 400~600°C, and then it turns into SiAl₂O₅ and amorphous SiO₂ (>900°C), even amorphous SiO₂ and low-order crystalline α -Al₂O₃ at above 1,100°C (Ribeiro et al., 2005; Gilkes and Prakongkep, 2016). Because the mass transfer process is the rate controlling step during CoAl₂O₄ preparation (He and Becker, 1997), the uniform distribution Co₃O₄ and Al₂O₃ on the surface of Kaol after being grinded is in favor of reducing the mass transfer resistance, thus the incorporation of Kaol decreases the calcining temperature for formation of spinel CoAl₂O₄ (Wang et al., 2006; Gabrovska et al., 2014). Based on above results, the optimum conditions for preparing hybrid pigment with the prefect color are 1,100°C and 81.5 wt% of Kaol.

Characterization of CoAl₂O₄/Kaol Hybrid Pigment

Figure 1c presents FTIR spectra of Kaol, the calcined Kaol at 1,100°C and CoAl₂O₄/Kaol hybrid pigment, respectively. FTIR spectrum of Kaol exhibits the characteristic bands of Si-O-Si (at about 471, 522, 699, 1,032, and 1,114 cm⁻¹), Si-O-Al (at around 525, 750, and 795 cm⁻¹), Al-Al-OH (at around 522 and 911 cm⁻¹), -OH (at about 3,684, 3,684, 3,651, and 3,440 cm⁻¹), while the bending vibration of the inter-layer water is observed at 1,636 cm⁻¹ (Rekik et al., 2017; Sreelekshmi et al., 2017). After being calcined, these typical absorption bands disappear

compared with that of the raw Kaol, which is ascribed to the dehydroxylation and the crystal phase transition of Kaol during calcining process. In the case of FTIR spectrum of hybrid pigment, several new absorption bands appear at 668, 557, and 509 cm⁻¹, which can be attributed to the stretching vibration of Al-O of AlO₆ and Co-O of CoO₄, respectively (Zayat and Levy, 2000; Zhang A. J. et al., 2017), indicating the formation of CoAl₂O₄.

Figure 1d shows the XRD patterns of Kaol, the calcined Kaol at 1,100°C and CoAl₂O₄/Kaol hybrid pigment, respectively. It is clear that the associated minerals are quartz ($2\theta = 20.8^\circ$ and 26.7°) and mica ($2\theta = 8.9^\circ$) (Chhikara et al., 2015; Mymrin et al., 2017), and the typical characteristic peaks of kaolinite presents the well-defined reflections at $2\theta = 12^\circ$ and 25° . When Kaol was calcined at 1,100°C, only diffraction peaks of quartz are remained. For hybrid pigment, new diffraction peaks are observed at $2\theta = 31.1^\circ$, 36.8° , 44.8° , 49.0° , 55.5° , 59.2° and 65.2° , which correspond to (220), (311), (400), (331), (422), (511), and (440) planes of CoAl₂O₄ according to JCPD card No. 10-458, respectively (Xi et al., 2012; Zhu et al., 2015). In fact, CoO also reacts with silica derived from Kaol to form cobaltous silicate, but this reaction is considered to be a minor reaction since most of CoO react with Al₂O₃ because CoO has high affinity to Al₂O₃ (Ahmed et al., 2012).

Figure S2 shows Raman spectra of CoAl₂O₄ pigment without Kaol and CoAl₂O₄/Kaol hybrid pigment. CoAl₂O₄ pigment with a spinel structure usually exhibits five Raman active modes: A_{1g} (764 cm⁻¹), F_{2g} (644, 511, and 203 cm⁻¹) and E_g (413 cm⁻¹). Hybrid pigment also clearly presents the five expected Raman active modes at 760, 641, 510, 410, and 202 cm⁻¹, indicating that hybrid pigments is assigned to the spinel structure (Zha et al., 2016; Liu et al., 2017). Compared with the Raman spectrum of CoAl₂O₄, all modes of hybrid pigment shift to lower frequencies, and this red shift suggests that primary coordinative environments of tetrahedron and octahedron positions may change after incorporation of Kaol.

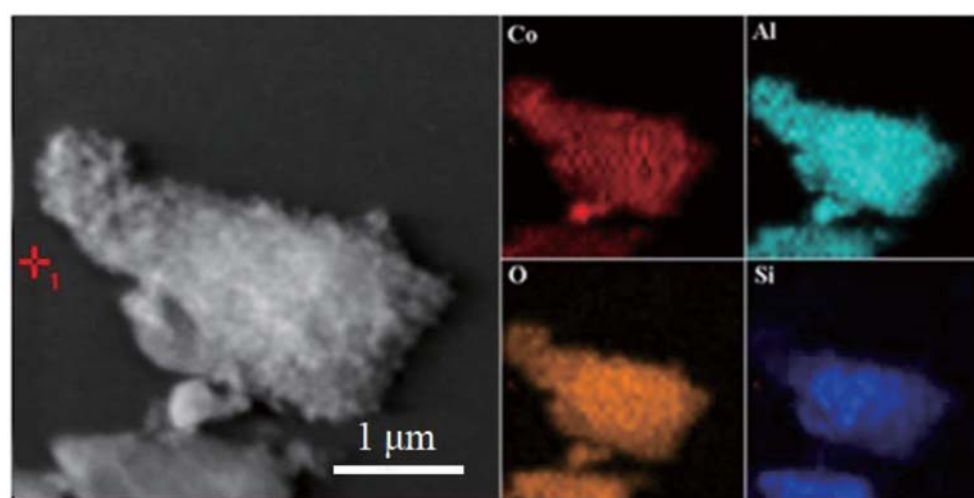


FIGURE 3 | TEM image and the corresponding element mapping of CoAl₂O₄/Kaol-1100°C.

The typical structures and the morphology evolution of the samples can be observed by TEM. As illustrated in **Figure 2a**, Kaol presents a typical lamellar structure with a smooth surface. After being calcined at 1,100°C (**Figure S3a**), the lamellar morphology remains well, which reveals that Kaol possesses the good thermal stability. With the introduction of CoAl₂O₄ nanoparticles, the surface of lamellar morphology becomes coarse (**Figures 2b,c**), and CoAl₂O₄ nanoparticles are uniformly distributed on the substrate surface with a diameter of 10~20 nm. Furthermore, no obvious aggregation is observed, thus it indicates that incorporation of Kaol effectively prevents from the aggregation and controls the size of CoAl₂O₄ nanoparticles. The selected area electron diffraction pattern of hybrid pigment also indicates the successful formation of spinel CoAl₂O₄ (**Figure S3b**) (Naderi et al., 2014; Zou and Zheng, 2016). **Figure 2d** gives an enlarged electron micrograph, and it provides a well-resolved lattice plane with an interplanar spacing of 0.244 nm, corresponding to (311) plane of the cubic *Fd3m* space group, which is identified on the basis of data of the standard CoAl₂O₄ database JCPD card No. 10-458 (Kim et al., 2012). Meanwhile, the micrograph also displays the coexistence of amorphous and crystalline phases, which is attributed to the amorphous SiO₂ derived from Kaol and spinel CoAl₂O₄, respectively (Cho and Kakihana, 1999). In addition, **Figure 3** illustrates the elemental mapping of hybrid

pigment, it is clear that hybrid pigment is mainly composed of Co, Al, O, and Si elements. Co element is uniformly distributed on the surface of lamellar substrates, suggesting that the generated CoAl₂O₄ is uniformly anchored on the surface of substrate.

Based on our previous studies, Kaol is not merely a carrier for loading of CoAl₂O₄ nanoparticles, Al₂O₃ as one of the main compositions of Kaol might participate in the high-temperature crystallization to form clay mineral doped spinel CoAl₂O₄. In order to confirm above inference, the sample was prepared using Co₃O₄ and Kaol without Al₂O₃ by the same procedure with CoAl₂O₄/Kaol hybrid pigments. As shown in **Figure 4** and **Table S2**, the color of the as-prepared pigment is blue, and the values of *L** and *a** decrease with the increase of the addition amount of Co₃O₄, but *b** firstly decrease with the increase of the added amount of Co₃O₄ to 13%, and then it begins to increase as Co₃O₄ reaches 16%. At this moment, the obtained pigment is dark-green color, which is mainly ascribed to the fact that the excess Co₃O₄ is not fully involved in the reaction and anchors on the pigment surface (Aguilar-Elguézabal et al., 2017). At the low addition amount of Co₃O₄ (4.8%), CoO derived from the thermal reduction of Co₃O₄ can react with Al₂O₃ derived from Kaol to form spinel CoAl₂O₄ at 1,100°C, which can be confirmed by their XRD patterns and FTIR spectra (**Figure S4**). Therefore, it can be safely concluded that Kaol may be served as

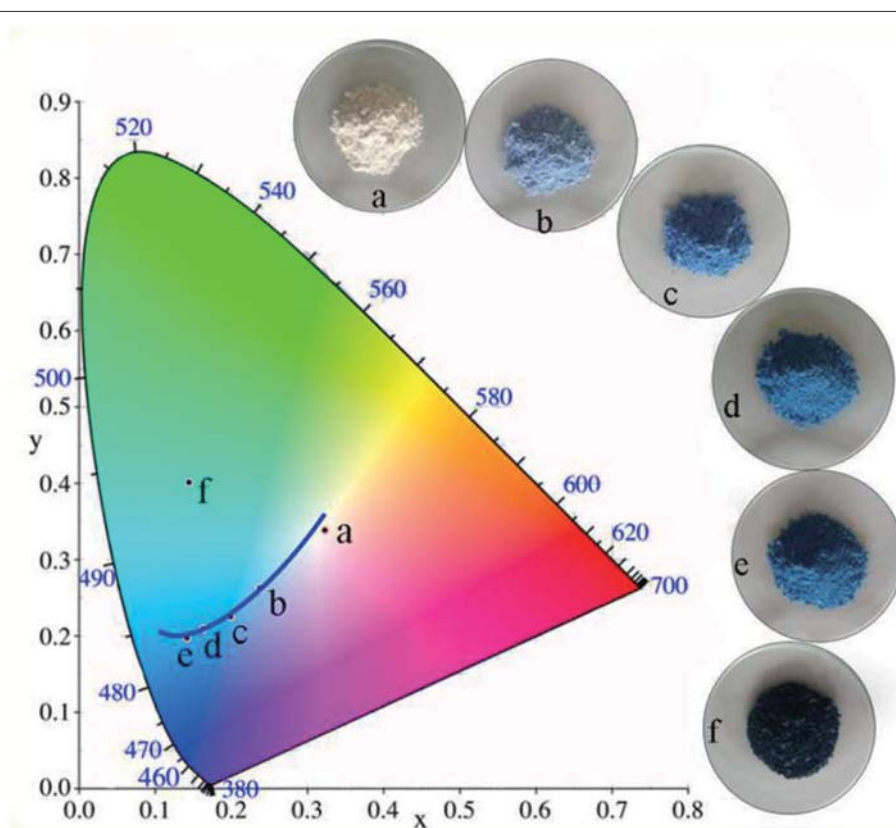


FIGURE 4 | Color coordinates of pigment prepared using the different addition of Co₃O₄ in the presence of 2 g Kaol without Al₂O₃ (a-0%, b-2.4%, c-4.8%, d-9.1%, e-13%, f-16.7%).

an aluminum source to take part in the crystallization process of CoAl₂O₄.

Possible Formation Mechanism of CoAl₂O₄/Kaol Hybrid Pigment

According to the above results, the as-prepared hybrid pigment exhibit good color performances at a low Co content compared with the commercial CoAl₂O₄ pigments even 7 wt%. The possible formation mechanism of CoAl₂O₄/Kaol hybrid pigments can be described as follows: Co₃O₄ and Al₂O₃ can be uniformly distributed on the surface of Kaol during grinding. With the increase of the calcining temperature (400~600°C), Kaol (2SiO₂·Al₂O₃·2H₂O) is turned into metakaolinite (2SiO₂·Al₂O₃). As the calcining temperature increases to 900°C, Co₃O₄ begins to thermally reduce into CoO, subsequently the increase in the calcining temperature results in the formation of spinel CoAl₂O₄ based on the reaction between CoO and Al₂O₃ on Kaol substrate accompanied with the crystal phase transition of Kaol to amorphous SiO₂ and low-order crystalline α-Al₂O₃. In this process, the uniform distribution of Co₃O₄ and Al₂O₃ may be expected to decrease the mass transfer resistance for formation of spinel CoAl₂O₄, which reduces the processing time and calcining temperature, while the traditional solid-phase method for preparation of CoAl₂O₄ spends the long time ranging from several hours to days at high temperature (>1,200°C) (Wang et al., 2006). Furthermore, α-Al₂O₃ from Kaol also simultaneously reacts with CoO during high-temperature crystallization, thus the generated CoAl₂O₄ and the calcined production of Kaol finally form a solid solution. The possible formation mechanism of CoAl₂O₄/Kaol hybrid pigment can be illustrated in Scheme 1.

Environmental Stability of CoAl₂O₄/Kaol Hybrid Pigments

As shown in Figure S5a, the reflectance spectra of hybrid pigments are nearly same before and after being exposed under UV light for 15 days, indicating the excellent stability of hybrid pigment to UV light. In addition, the color of the sample plates has no obvious difference before and after being immersed into HCl, NaOH and ethanol, suggesting the excellent resistance of

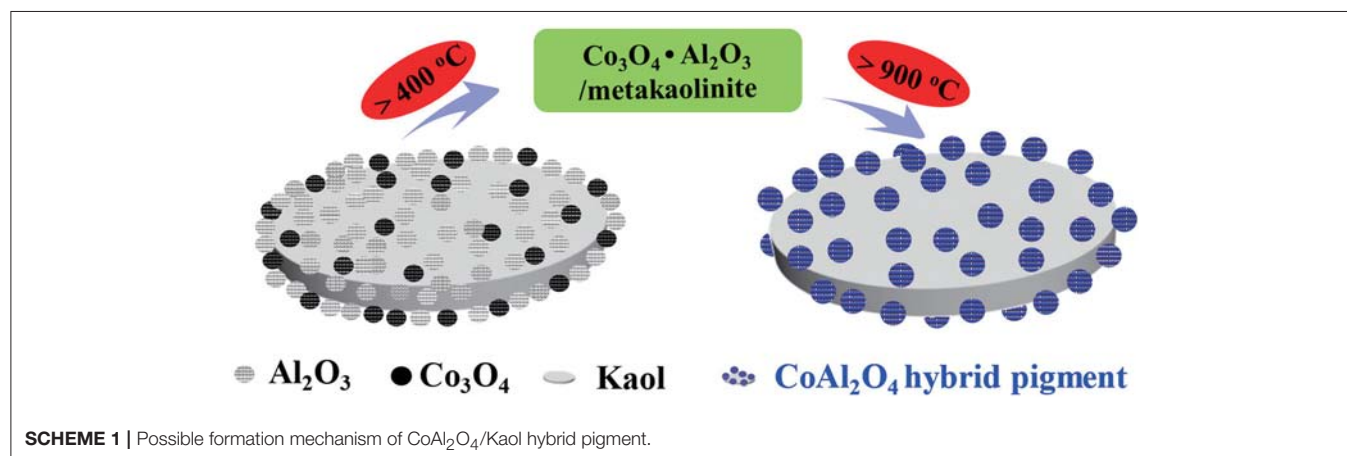
hybrid pigments to the corresponding reagents, which also can be confirmed from their color parameters (Table 2). Meanwhile, CoAl₂O₄/Kaol hybrid pigment presents the excellent thermal stability (Figures S5b,c).

In this study, the potential applications of the as-prepared hybrid pigment were also explored in this study. The thermal resistance coating were also prepared by following procedures: Firstly, 5 wt% CoAl₂O₄/Kaol hybrid pigment was dispersed into ethyl acetate and stirred under high shear for 30 min (2,000 rpm), and the above obtained mill base were added into commercial thermal resistance coating and stirred under low shear for 60 min (500 rpm). The viscosity of the coating was adjusted by ethyl acetate to 20~30 s. And then it was sprayed onto steel plate substrate of size 15 cm × 10 cm × 0.1 cm and dried under the standard conditions (temperature: 25°C and humidity: 40%) for 7 days (the coating thickness: D = 50 ± 2 μm). The obtained sample plates were shown in Figure S6c, it is clear that the surface of the sample plate is smooth after hybrid pigment (5 wt%) is added into the commercial thermal resistance coating, indicating hybrid pigment disperses well in the painting. Furthermore, the film containing hybrid pigments exhibits the similar color parameters (L* = 24.88, a* = 13.54, b* = -57.80) (Figure S6d) after being calcined at 800°C for 2 h. However, the steel plate coated the

TABLE 2 | Color parameters of the sample plates before and after being immersed into 3M HCl, 3M NaOH, and ethanol for 72 h, respectively.

Different medium	Color parameters		
	L*	a*	b*
Before immersion	43.68	-7.88	-59.33
3M HCl	42.86	-7.56	-59.38
3M NaOH	43.55	-7.63	-59.12
Ethanol	43.83	-7.92	-59.34

The Commission Internationale de l'Eclairage (CIE) 1976 L*, a*, b* colorimetric method was revised based on the Hunter L*a*b* (1958). And the parameters of L* is the lightness axis (0 for black and 100 for white). The parameters of a* (negative values for green and positive values for red) and b* (negative values for blue and positive values for yellow) denote the hue or color dimensions.



commercial thermal resistance coating (**Figure S6a**) is damaged heavily (**Figure S6b**). It indicates that the film containing hybrid pigment has a good thermal stability, and it can effectively protect steel plate substrate to avoid excessive damage. Meanwhile, this film also exhibited excellent fireproof properties, which can be illustrated by its fire test using a flame gun (800~1,000°C) (**Figure S6e**). It is found that this film has no obvious change after being placed on the fire for 30 s (**Movie S1** and **Figure S6f**), revealing that the hybrid pigment may be used as fireproof paint. In addition, the as-prepared hybrid pigment also can be used as a colored painting and artistic pigment (**Figures S7a,b**).

Anticorrosion Coating Application of Hybrid Pigments

Corrosion is a natural and gradual destruction process of metal materials resulting from chemical and/or electrochemical reaction with their environment, which leads to enormous losses to our lives, finances, etc. Therefore, corrosion engineering is the field to control and stop corrosion using various methods, especially surface coating protection technology, in which inorganic pigments (e.g., ZnO and TiO₂) are commonly incorporated to improve the anticorrosion properties of coating, and perhaps provide the color for coating (e.g., α -Fe₂O₃). Therefore, the as-prepared hybrid pigment is incorporated into the common epoxy anticorrosion coating to investigate its anticorrosion properties. As shown in **Figure 5**, the steel plate substrate suffers from an aggravating corrosion referred from the large-scale red rust without the epoxy anticorrosion coating (**Figure 5e**). After coating of epoxy anticorrosion coating, the corrosion of steel plate is slightly improved (**Figure 5f**). In

particular, this anticorrosion effect is obvious after introducing the commercial CoAl₂O₄ pigments (**Figure 5g**). With the incorporation of the as-prepared hybrid pigment, no obvious rust was found on the surface of coating (**Figure 5h**). It suggests that the introduction of hybrid pigment obviously improves the corrosion resistance of coating. This is mainly ascribed to the synergistic effect between the lamellar layered structure of Kaol and the excellent weatherability of CoAl₂O₄, which can prevent small molecules (H₂O and O₂) or ions from penetrating into the coating film. Thus, the relevant mechanisms of anticorrosion can be illustrated in **Scheme 2**.

Furthermore, the chemical stability of the anticorrosion coating film was also evaluated by immersing into 3M HCl, 3M NaOH, and ethanol at room temperature for 72 h, respectively.

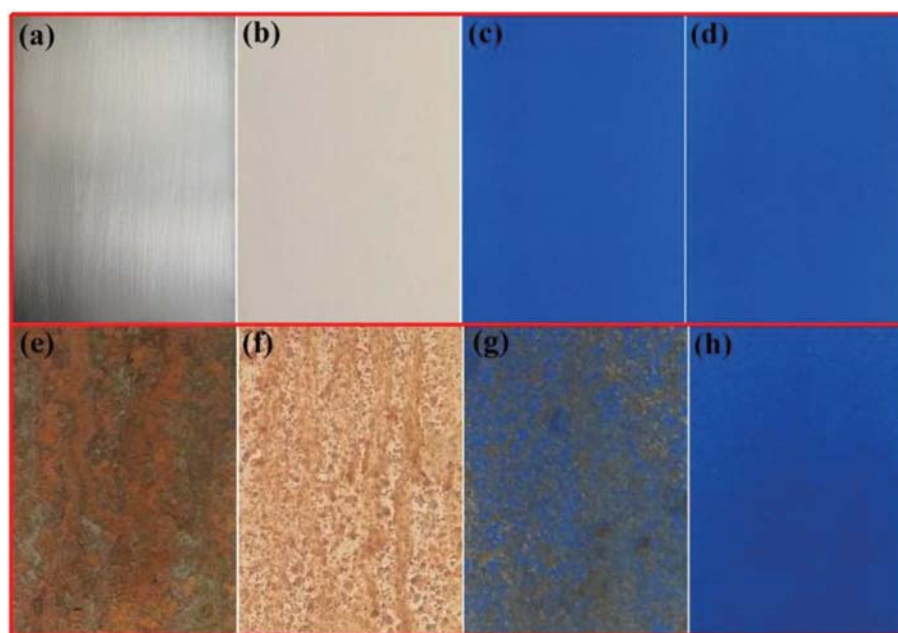
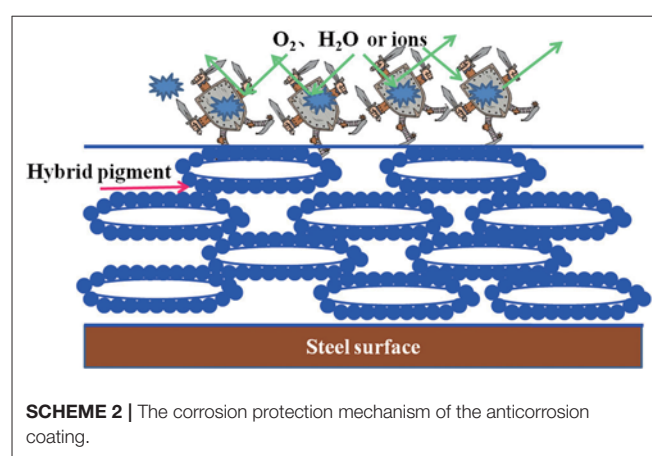


FIGURE 5 | Photographs of (a) steel substrate, (b) steel coated the paint without pigment, (c) steel coated the paint containing commercial CoAl₂O₄, (d) steel coated the paint containing hybrid pigment. (e–h) Their corresponding images after being exposed to salt spray test for 60 days, respectively.

The film has no obvious difference before and after being immersed, exhibiting the excellent resistance to HCl, NaOH, and ethanol (**Figure S8**). This is also confirmed by their color

TABLE 3 | Color parameters of the film before and after being immersed into 3M HCl, 3M NaOH and ethanol for 72 h, respectively.

Different medium	Color parameters		
	L*	a*	b*
Before immersion	25.11	13.97	-58.10
3M HCl	25.12	13.86	-58.05
3M NaOH	24.88	13.75	-57.88
Ethanol	25.13	13.88	-58.31

The Commission Internationale de l'Eclairage (CIE) 1976 L*, a*, b* colorimetric method was revised based on the Hunter L*a*b (1958). And the parameters of L* is the lightness axis (0 for black and 100 for white). The parameters of a* (negative values for green and positive values for red) and b* (negative values for blue and positive values for yellow) denote the hue or color dimensions.

parameters before and after being immersed in the corresponding reagents (**Table 3**). More importantly, the obtained sample plates were also immersed into 3.5 wt% saline water to study the salted water resistance test for 60 days. As shown in **Figure 6**, the surface of coating film without pigment is smooth and dense before immersing (**Figure 6a**). After adding of CoAl₂O₄ without Kaol, the film color seems darker compared with that of containing CoAl₂O₄/Kaol hybrid pigment (**Figures 6b,c**). As expected, the film without pigment is swelling, blistering, and rusty after immersed into saline water for 60 days (**Figure 6d**). Furthermore, the same phenomenon also is observed from the one containing CoAl₂O₄ (**Figure 6e**), but the situation is better than the former due to the good weatherability of CoAl₂O₄ to acid, salt, etc. Surprisingly, the film incorporating of CoAl₂O₄/Kaol hybrid pigment was perfect without any defects (**Figure 6f**). It suggests that the coating film exhibited the excellent salted water resistance, which may be ascribed to the synergistic effect of the lamellar layered structure of Kaol and the excellent weatherability of CoAl₂O₄.

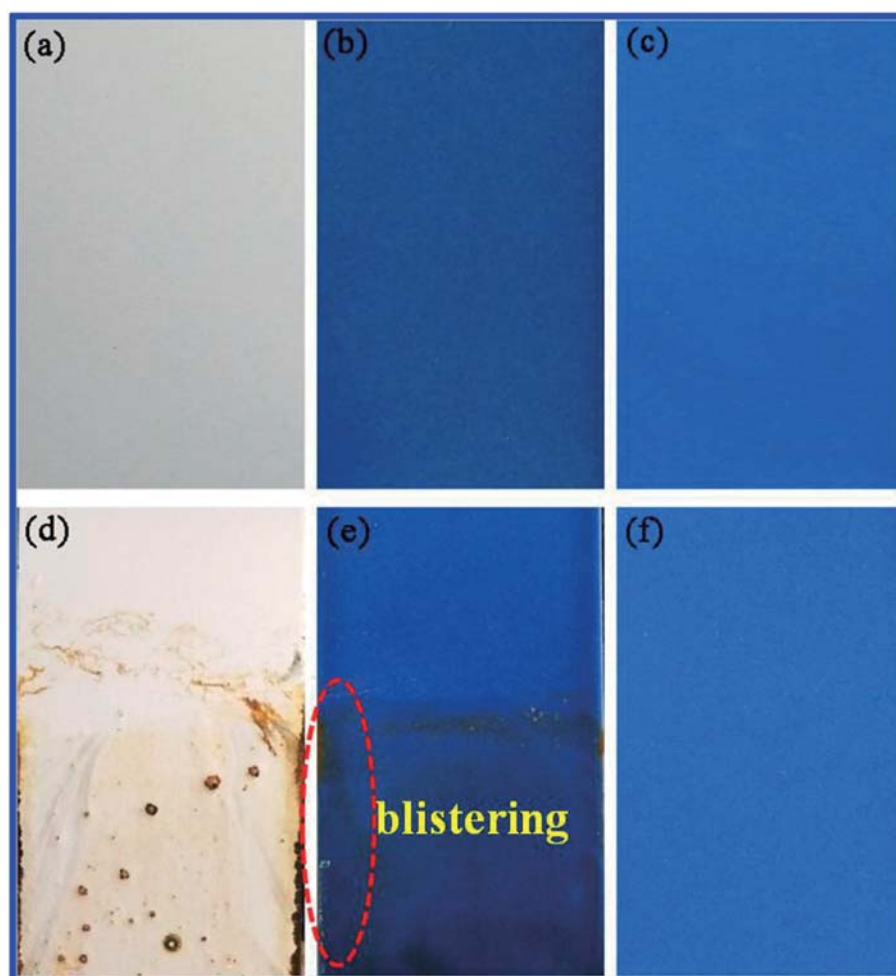


FIGURE 6 | Photographs of the film (a) without pigment, (b) containing CoAl₂O₄, and (c) hybrid pigment. (d-f) Their corresponding images after being exposed to 3.5% NaCl for 60 days, respectively.

Furthermore, the obtained sample plate containing hybrid pigment presents the better acid resistance than that of incorporating of ultramarine after contacting with 36.5 wt% HCl, which changes from blue to white due to its instability to acid (Figure S9). Therefore, the obtained sample plate was also placed in acetic acid-salt spray testing chamber to evaluate the acetic acid-salt fog corrosion resistance of the anticorrosion coating. As a control, the coatings containing Kaol, ZnO, Fe₂O₃ and CoAl₂O₄ calcined at 1,100°C are also investigated, and the components of paints were provided in Table S3. Firstly, the different amounts of the CoAl₂O₄/Kaol hybrid pigment were added into epoxy resin to determine the amounts of the hybrid pigment, and the results are shown in Figure S10. It is clear that the sample that containing 5 wt% CoAl₂O₄/Kaol hybrid pigment is bright blue, so the added amounts of the hybrid pigment is 5 wt%. And then the sample containing Kaol, ZnO, Fe₂O₃, and CoAl₂O₄ calcined at 1,100°C are shown in Figure 7, the corrosion of the films containing Fe₂O₃ (Figure 7f), CoAl₂O₄ calcined at 1,100°C (Figure 7g), and ZnO (Figure 7j) are very serious after be exposed in salt spray testing chamber 60 days. Interestingly, the corrosion of the sample containing

CoAl₂O₄/Kaol hybrid pigment (Figure 7h) and Kaol (Figure 7j) were negligible, especially the sample of hybrid pigment. It may be ascribed to the excellent acid resistance and lamellar layered structure of hybrid pigment and Kaol, respectively. In addition, Figure 8 gives the anticorrosion ability of the coatings containing CoAl₂O₄/Kaol hybrid pigments, ZnO, Fe₂O₃, CoAl₂O₄ calcined at 1,100°C and the one without pigment. Bode plots indicates that the addition of CoAl₂O₄/Kaol hybrid pigments in epoxy paint shows a significant improvement in the anticorrosion properties compared with the pure epoxy paint and others pigment. It also suggests the synergistic effect between the lamellar layered structure of Kaol and the excellent weatherability of CoAl₂O₄ is in favor of improving the resistance to salts, which also is superior to the reported works (Table 4).

Anti-corrosion of the anticorrosive film is commonly determined from electrochemical measurements such as corrosion potential (*E*_{corr}) and corrosion current (*I*_{corr}), and Electrochemical Impedance Spectroscopy (EIS) measurements were carried out with the use of an electrochemical working station (CHI660E) at open circuit potential. A three-electrode cell including the Ag/AgCl (3M KCl) reference electrode, the studied

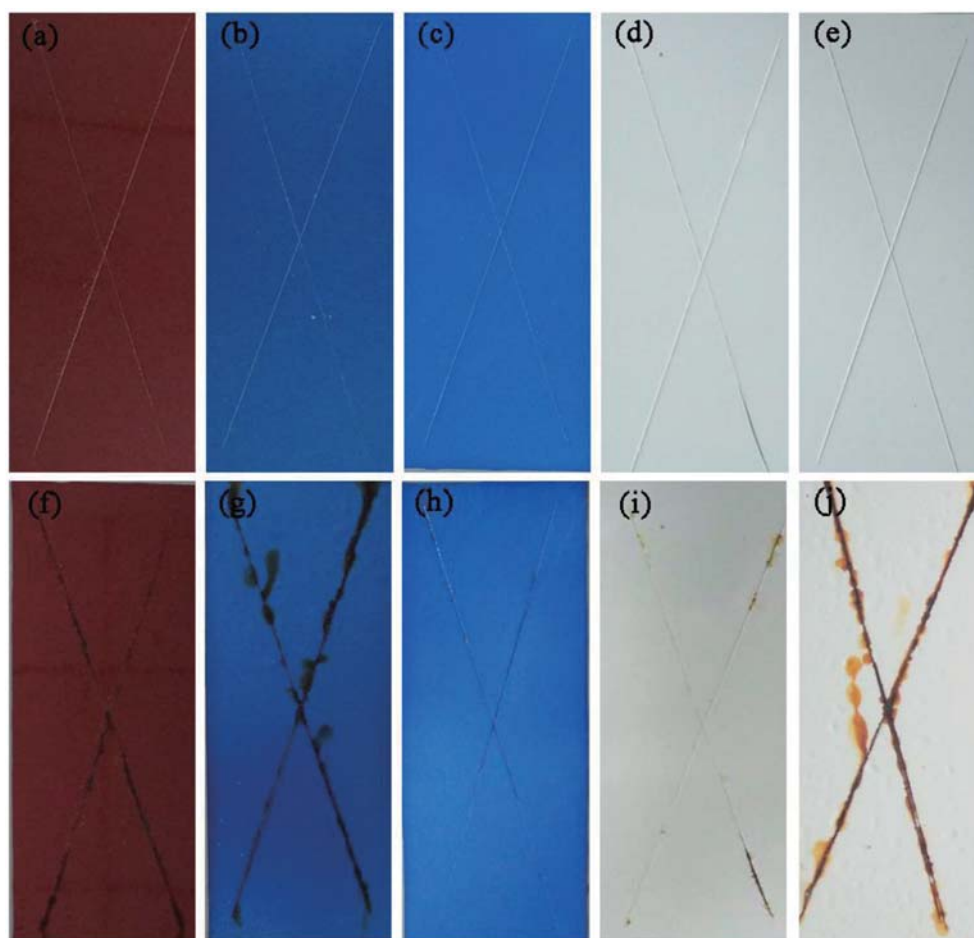


FIGURE 7 | Photographs of the film containing (a) Fe₂O₃, (b) CoAl₂O₄, (c) CoAl₂O₄/Kaol hybrid pigment, (d) Kaol, and (e) ZnO. (f–j) The corresponding images of the film after being exposed to acetic acid-salt spray for 60 days, respectively.

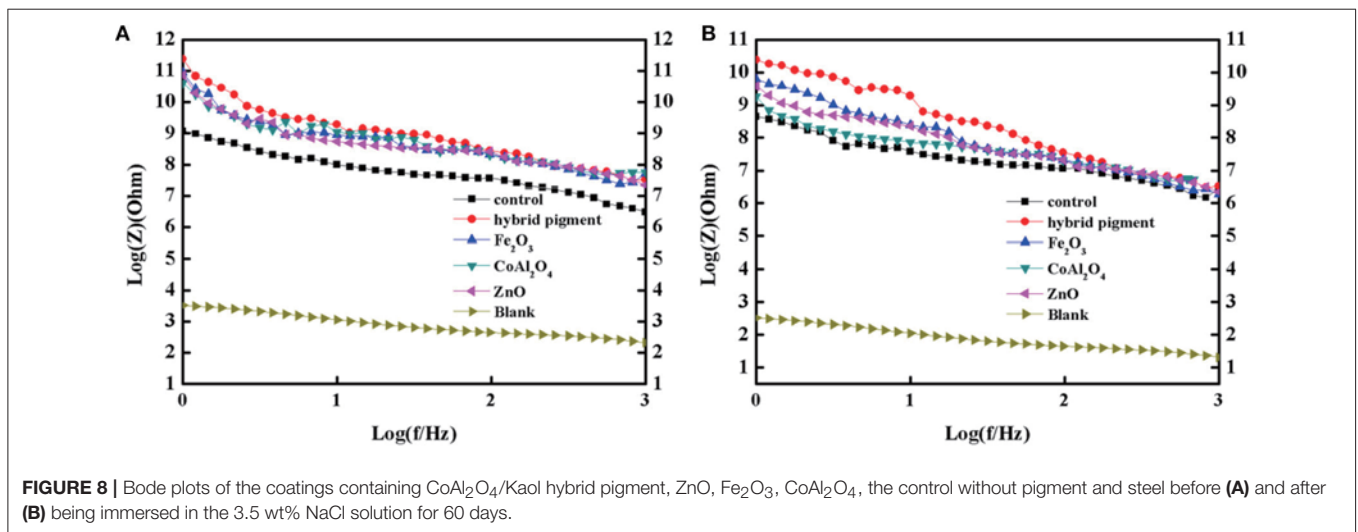
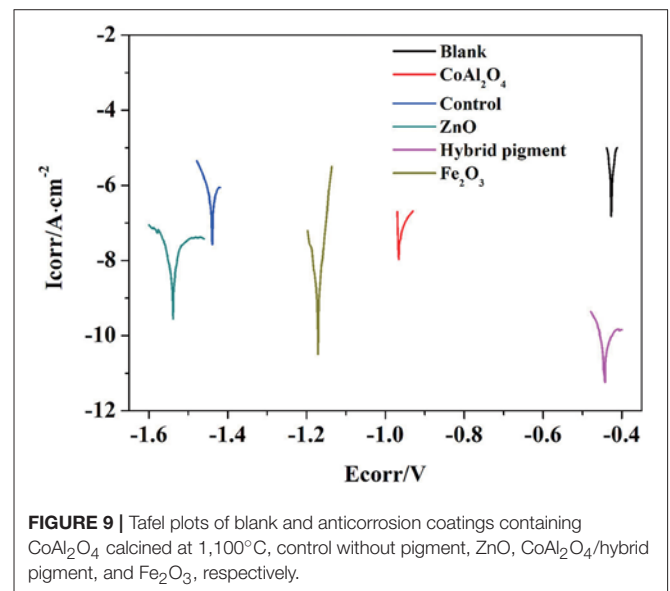


TABLE 4 | Comparison with the anticorrosion performance of the reported additives and hybrid pigment in epoxy anticorrosive coating.

Condition	Materials (added amount)	Time/h	References
Neutral salt spray test	H-BN decorated with Fe ₃ O ₄ (2%)	720	Zhang et al., 2016
Neutral salt spray test	Graphite nanoplatelets (0.5%)	750	Mohammadi et al., 2014
Neutral salt spray test	Zn (6%)	500	Bagherzadeh and Mousavinejad, 2012
Neutral salt spray test	ZnO/nano-Co:ZnO (6%)	168	Rostami et al., 2014
Neutral salt spray test	ZnO (6.5%)	720	Naderi et al., 2014
Neutral salt spray test	Ceramic nanocontainers (4%)	750	Kartsonakis et al., 2012
Neutral salt spray test	Hybrid pigments (5%)	1,440	This work
Acetic acid-salt spray test	Hybrid pigments (5%)	1,440	This work



sample as working electrode and the platinum counter electrode was used to run EIS tests. EIS measurements are studied in the frequency range from 100 kHz to 0.005 Hz with a perturbation of 5 mV, and the working electrode area was 1 cm². **Figure 9** shows the Tafel plots generated for the anticorrosion coating containing CoAl₂O₄/hybrid pigment, ZnO, Fe₂O₃, CoAl₂O₄ calcined at 1,100°C, control (without pigment) and blank immersed in 3.5 wt% NaCl solution about 30 min. And the Tafel curve parameters are given in **Table 5**. As shown in **Figure 9** and **Table 5**, the corrosion current of the control (without pigment) decreases from -1.52×10^{-7} A to -3.39×10^{-8} A compared with the blank, and the corrosion current obviously declines when the pigments were added into the anticorrosion coating. After incorporation of CoAl₂O₄/hybrid pigment, the

corrosion current decreases from -3.39×10^{-8} A to -5.75×10^{-12} A, while the corrosion potential increases from -1.439 V to -0.443 V. In fact, the anticorrosion ability of the coating is related to the chemical composition and microstructure. The lower of the corrosion current or the higher corrosion potential suggests the better of the anticorrosion ability (Liang et al., 2007; Chang et al., 2012). Therefore, the anticorrosion coatings containing CoAl₂O₄/hybrid pigment, ZnO, Fe₂O₃ present good anticorrosion ability, and CoAl₂O₄/hybrid pigment exhibits superior anticorrosion ability compared with than that of ZnO and Fe₂O₃, which is consistent with that of the Bode plots (**Figure 8**), implying that the addition of CoAl₂O₄/Kaol hybrid pigments in epoxy paint shows a significant improvement in the electrochemical corrosion properties compared with the pure epoxy paint and other pigments.

TABLE 5 | Tafel curve parameters of the anticorrosion coatings containing different pigments and blank sample.

Sample	Corrosion potential (E _{corr})/V	Corrosion current density (I _{corr})/A·cm ⁻²	Corrosion current (I)/A
Blank	-0.427	-6.82	-1.52 × 10 ⁻⁷
CoAl ₂ O ₄	-0.966	-7.96	-1.10 × 10 ⁻⁸
Fe ₂ O ₃	-1.171	-10.50	-3.16 × 10 ⁻¹¹
ZnO	-1.538	-9.55	-2.82 × 10 ⁻¹⁰
Control	-1.439	-7.57	-3.39 × 10 ⁻⁸
Hybrid pigment	-0.443	-11.24	-5.75 × 10 ⁻¹²

CONCLUSION

In conclusion, the low-cost bright blue CoAl₂O₄/Kaol hybrid pigments were successfully prepared by the traditional solid-state reaction. The introduction of Kaol not only reduces the Co consumption and the temperature for formation of spinel CoAl₂O₄, but also enhances the color properties of cobalt blue pigments with bright blue and high NIR reflectance, especially prepared using 8.1% Co₃O₄ and 81.5% Kaol. During preparation, Co₃O₄ and Al₂O₃ can be uniformly distributed on the surface of Kaol, which reduces the mass transfer resistance and prevents from the aggregation CoAl₂O₄ nanoparticles during high-temperature crystallization process. In addition, the Al₂O₃ originated from Kaol also may participate in the formation of spinel CoAl₂O₄ pigments. Due to the synergistic effect between the lamellar layered structure of Kaol and the excellent

weatherability of CoAl₂O₄, the anticorrosion coating containing hybrid pigments exhibited the excellent corrosion resistance toward the salt and acetic acid-salt system. Furthermore, the CoAl₂O₄/Kaol hybrid pigments prepared by traditional solid-phase method can be applied in thermal resistance coating, wall painting and artistic pigment.

AUTHOR CONTRIBUTIONS

AZ and XW contribute to the experiment process, samples characterization, data analysis, and paper preparation. BM and AW are mainly responsible for the design of experiment, data analysis, and paper revision.

ACKNOWLEDGMENTS

This work is supported by the Regional Key Project of the Science and Technology Service of the Chinese Academy of Sciences ([2016] No. 70), the Youth Innovation Promotion Association CAS (2017458), the Major Projects of the National Natural Science Foundation of Gansu, China (18JR4RA001), and The Funds for Creative Research Groups of Gansu, China (17JR5RA306).

SUPPLEMENTARY MATERIAL

The Supplementary Material for this article can be found online at: <https://www.frontiersin.org/articles/10.3389/fchem.2018.00586/full#supplementary-material>

REFERENCES

- Aguilar-Elguézabal, A., Román-Aguirre, M., De la Torre-Sáenz, L., Pizá-Ruiz, P., and Bocanegra-Bernal, M. (2017). Synthesis of CoAl₂O₄/Al₂O₃ nanoparticles for ceramic blue pigments. *Ceram. Int.* 43, 15254–15257. doi: 10.1016/j.ceramint.2017.08.062
- Ahmed, N. A., Abdel-Fatah, H. T. M., and Youssef, E. A. (2012). Corrosion studies on tailored Zn-Co aluminate/kaolin core-shell pigments in alkyd based paints. *Prog. Org. Coat.* 73, 76–87. doi: 10.1016/j.porgcoat.2011.09.003
- Al-Sabagh, A. M., Abdou, M. I., Migahed, M. A., Fadl, A. M., Farag, A. A., Mohammedy, M. M., et al. (2017). Influence of ilmenite ore particles as pigments on the anticorrosion and mechanical performance properties of polyamine cured epoxy for internal coating of gas transmission pipelines. *Egypt. J. Pet.* doi: 10.1016/j.ejpe.2017.07.005. [Epub ahead of print].
- Álvarez-Docio, C. M., Reinoso, J. J., Del Campo, A., and Fernández, J. F. (2017). 2D particles forming a nanostructured shell: a step forward cool NIR reflectivity for CoAl₂O₄ pigments. *Dyes Pigments* 137, 1–11. doi: 10.1016/j.dyepig.2016.09.061
- Ammar, S., Ramesh, K., Vengadaesvaran, B., Ramesh, S., and Arof, A. K. (2016). Amelioration of anticorrosion and hydrophobic properties of epoxy/pdms composite coatings containing Nano ZnO particles. *Prog. Org. Coat.* 92, 54–65. doi: 10.1016/j.porgcoat.2015.12.007
- Bagherzadeh, M. R., and Mousavinejad, T. (2012). Preparation and investigation of anticorrosion properties of the water-based epoxy-clay nanocoating modified by Na⁺-MMT and Cloisite 30B. *Prog. Org. Coat.* 74, 589–595. doi: 10.1016/j.porgcoat.2012.02.006
- Brik, Y., Kacimi, M., Ziyad, M., and Bozon-Verduraz, F. (2001). Titania-supported cobalt and cobalt-phosphorus catalysts: characterization and performances in ethane oxidative dehydrogenation. *J. Catal.* 202, 118–128. doi: 10.1006/jcat.2001.3262
- Cayton, H. R., and Sawitowski, T. (2005). The impact of nano-materials on coating technologies. *NSTI-Nanotech* 2, 83–85.
- Chang, C. H., Huang, T. C., Peng, C. W., Yeh, T. C., Lu, H. I., Hung, W. I., et al. (2012). Novel anticorrosion coatings prepared from polyaniline/graphene composites. *Carbon* 50, 5044–5051. doi: 10.1016/j.carbon.2012.06.043
- Chhikara, D., Kumar, M. S., and Srivatsa, K. M. K. (2015). On the synthesis of Zn/ZnO core-shell solid microspheres on quartz substrate by thermal evaporation technique. *Superlattice. Microstruct.* 82, 368–377. doi: 10.1016/j.spmi.2015.02.036
- Cho, W. S., and Kakhana, M. (1999). Crystallization of ceramic pigment CoAl₂O₄ nanocrystals from Co-Al metal organic precursor. *J. Alloy. Compd.* 287, 87–90. doi: 10.1016/S0925-8388(99)00059-6
- Daham, P. V., Gunawardana, S., Nguyen, T. T. M., Walmsley, J. C., and Venk, H. J. (2014). Initiation of metal dusting corrosion in conversion of natural gas to syngas studied under industrially relevant conditions. *Ind. Eng. Chem. Res.* 53, 1794–1803. doi: 10.1021/ie4024947
- Dandapat, A., and De, G. (2012). Host-mediated synthesis of cobalt aluminate/γ-alumina nanoflakes: a dispersible composite pigment with high catalytic activities. *ACS Appl. Mater. Inter.* 4, 228–234. doi: 10.1021/am201283c
- de Leon, A. C., Pernites, R. B., and Advincula, R. C. (2012). Superhydrophobic colloiddally textured polythiophene film as superior anticorrosion coating. *ACS Appl. Mater. Inter.* 4, 3169–3176. doi: 10.1021/am300513e
- El Saeed, A. M., El-Fattah, M. A., and Azzam, A. M. (2012). Synthesis of ZnO nanoparticles and studying its influence on the antimicrobial, anticorrosion and mechanical behavior of polyurethane composite for surface coating. *Dyes Pigments* 121, 282–289. doi: 10.1016/j.dyepig.2015.05.037
- El-Wahab, H. A., EL-Fattah, M. A., Abdou, M. I., and El-Hai, F. A. (2009). New anticorrosive coating compositions incorporated ilmenite ore. *Prog. Org. Coat.* 66, 242–247. doi: 10.1016/j.porgcoat.2009.07.010

- Gabrovska, M. V., Crisan, D., Stanica, N., and Kardjieva, R. (2014). Co-Al layered double hydroxides as precursors of ceramic pigment CoAl₂O₄. Part I: phase composition. *Rev. Roum. Chim.* 59, 445–450.
- Gilkes, R. J., and Prakongkep, N. (2016). How the unique properties of soil kaolin affect the fertility of tropical soils. *Appl. Clay Sci.* 131, 100–106. doi: 10.1016/j.clay.2016.01.007
- Golru, S. S., Attar, M. M., and Ramezanadeh, B. (2015). Effects of surface treatment of aluminium alloy 1050 on the adhesion and anticorrosion properties of the epoxy coating. *Appl. Surf. Sci.* 345, 360–368. doi: 10.1016/j.apsusc.2015.03.148
- Gomesan, Y. F., Medeiros, P. N., Bomioa, M. R. D., Santos, I. M. G., Paskocimasa, C. A., and Nascimento, R. M. (2015). Optimizing the synthesis of cobalt aluminate pigment using fractional factorial design. *Ceram. Int.* 41, 699–706. doi: 10.1016/j.ceramint.2014.08.125
- Gu, L., Liu, S., Zhao, H., and Yu, H. B. (2015). Facile preparation of water-dispersible graphene sheets stabilized by carboxylated oligoanilines and their anticorrosion coatings. *ACS Appl. Mater. Inter.* 7, 17641–17648. doi: 10.1021/acsami.5b05531
- Hao, L., Yan, T. T., Zhang, Y. M., Zhao, X. H., Lei, X. D., Xu, S. L., et al. (2017). Fabrication and anticorrosion properties of composite films of silica/layered double hydroxide. *Surf. Coat. Tech.* 326, 200–206. doi: 10.1016/j.surfcoat.2017.06.024
- He, T., and Becker, K. D. (1997). An optical in-situ study of a reacting spinel crystal. *Solid State Ionics* 101, 337–342. doi: 10.1016/S0167-2738(97)84050-7
- He, Y., Cao, Y., Liao, H. L., and Wang, J. A. (2017). Preparation of porous cobalt aluminate and its chromogenic mechanism. *Powder Technol.* 324, 95–101. doi: 10.1016/j.powtec.2017.08.056
- Herrero, M., Benito, P., Labajos, F. M., and Rives, V. (2007). Stabilization of Co²⁺ in layered double hydroxides (LDHs) by microwave-assisted ageing. *J. Solid State Chem.* 180, 873–884. doi: 10.1016/j.jssc.2006.12.011
- Jafari, M., and Hassanzadeh-Tabriz, S. A. (2014). Preparation of CoAl₂O₄ nanoblu pigment via polyacrylamide gel method. *Powder Technol.* 266, 236–239. doi: 10.1016/j.powtec.2014.06.018
- Jeon, H., Park, J., and Shon, M. (2013). Corrosion protection by epoxy coating containing multi-walled carbon nanotubes. *J. Ind. Eng. Chem.* 19, 849–853. doi: 10.1016/j.jiec.2012.10.030
- Juneja, A., Hegde, A., Lee, F. H., and Yeo, C. H. (2010). Centrifuge modelling of tunnel face reinforcement using forepoling. *Tunn. Undergr. Space Tech.* 25, 377–381. doi: 10.1016/j.tust.2010.01.013
- Kalendová, A., Sapurina, I., Stejskal, J., and Veselý, D. (2008). Anticorrosion properties of polyaniline-coated pigments in organic coatings. *Corros. Sci.* 50, 3549–3560. doi: 10.1016/j.corsci.2008.08.044
- Kartsonakis, I. A., Balaskas, A. C., Koumoulos, E. P., Charitidis, C. A., and Kordas, G. C. (2012). Incorporation of ceramic nanocontainers into epoxy coatings for the corrosion protection of hot dip galvanized steel. *Corros. Sci.* 57, 30–41. doi: 10.1016/j.corsci.2011.12.037
- Kim, J. H., Son, B. R., Yoon, D. H., Hwang, K. T., Noh, H. G., Cho, W. S., et al. (2012). Characterization of blue CoAl₂O₄ nano-pigment synthesized by ultrasonic hydrothermal method. *Ceram. Int.* 38, 5707–5712. doi: 10.1016/j.ceramint.2012.04.015
- Klopprogge, J. T. (2017). Chapter 6 - Raman spectroscopy of clay minerals. *Dev. Clay Sci.* 8, 150–199. doi: 10.1016/B978-0-08-100355-8.00006-0
- Kurajica, S., Popovic, J., Tkalec, E., Grzeta, B., and Mandic, V. (2012). The effect of annealing temperature on the structure and optical properties of sol-gel derived nanocrystalline cobalt aluminate spinel. *Mater. Chem. Phys.* 135, 587–593. doi: 10.1016/j.matchemphys.2012.05.030
- Liang, J., Hu, L. T., and Hao, J. C. (2007). Improvement of corrosion properties of microarc oxidation coating on magnesium alloy by optimizing current density parameters. *Appl. Surf. Sci.* 253, 6939–6945. doi: 10.1016/j.apsusc.2007.02.010
- Liu, Q. F., Li, X. G., and Cheng, H. F. (2016). Insight into the self-adaptive deformation of kaolinite layers into nanoscrolls. *Appl. Clay Sci.* 124–125, 175–182. doi: 10.1016/j.clay.2016.02.015
- Liu, Y., Jia, L. T., Hou, B., Sun, D. K., and Li, D. B. (2017). Cobalt aluminate-modified alumina as a carrier for cobalt in fischer-tropsch synthesis. *Appl. Catal. A: Gen. 530*, 30–36. doi: 10.1016/j.apcata.2016.11.014
- Madhup, M. K., Shah, N. K., and Parekh, N. R. (2017). Investigation and improvement of abrasion resistance, water vapor barrier and anticorrosion properties of mixed clay epoxy nanocomposite coating. *Prog. Org. Coat.* 102, 186–193. doi: 10.1016/j.porgcoat.2016.10.012
- Mohammadi, S., Taromi, F. A., Shariatpanahi, H., Neshati, J., and Hemmati, M. (2014). Electrochemical and anticorrosion behavior of functionalized graphite nanoplatelets epoxy coating. *J. Ind. Eng. Chem.* 20, 4124–4139. doi: 10.1016/j.jiec.2014.01.011
- Montemor, M. F., Snihiro, D. V., Taryb, M. G., Lamaka, S. V., Kartsonakis, I. A., and Balaskas, A. C. (2012). Evaluation of self-healing ability in protective coatings modified with combinations of layered double hydroxides and cerium molybdate nanocontainers filled with corrosion inhibitors. *Electrochim Acta* 60, 31–40. doi: 10.1016/j.electacta.2011.10.078
- Mu, B., Wang, Q., and Wang, A. Q. (2015). Effect of different clay minerals and calcination temperature on the morphology and color of clay/CoAl₂O₄ hybrid pigments. *RSC Adv.* 5, 102674–102681. doi: 10.1039/C5RA19955G
- Mymrin, V., Pedroso, A. M., Ponte, H. A., Ponte, M. J. J., Alekseeva, K., and Evaniki, D., et al. (2017). Thermal engineering method application for hazardous spent petrochemical catalyst neutralization. *Appl. Therm. Eng.* 110, 1428–1436. doi: 10.1016/j.applthermaleng.2016.09.077
- Naderi, R., Arman, S. Y., and Fouladvand, S. (2014). Investigation on the inhibition synergism of new generations of phosphate-based anticorrosion pigments. *Dyes Pigments* 105, 23–33. doi: 10.1016/j.dyepig.2014.01.015
- Qu, M. N., Liu, S. S., He, J. M., Feng, J., Yao, Y. L., Ma, X. R., et al. (2017). Fabrication of recyclable and durable superhydrophobic materials with wear/corrosion-resistance properties from kaolin and polyvinylchloride. *Appl. Surf. Sci.* 410, 299–307. doi: 10.1016/j.apsusc.2017.03.127
- Rekik, S. B., Gassara, S., Bouaziz, J., Deratani, A., and Baklouti, S. (2017). Development and characterization of porous membranes based on kaolin/chitosan composite. *Appl. Clay Sci.* 143, 1–9. doi: 10.1016/j.clay.2017.03.008
- Ribeiro, M. J., Tulyagavov, D. U., Ferreira, J. M., and Labrincha, J. A. (2005). High temperature mullite dissolution in ceramic bodies derived from al-rich sludge. *J. Eur. Ceram. Soc.* 25, 703–710. doi: 10.1016/j.jeurceramsoc.2004.03.028
- Rostami, M., Rasouli, S., Ramezanzadeh, B., and Askari, A. (2014). Electrochemical investigation of the properties of Co doped ZnO nanoparticle as a corrosion inhibitive pigment for modifying corrosion resistance of the epoxy coating. *Corros. Sci.* 88, 387–399. doi: 10.1016/j.corsci.2014.07.056
- Sreelekshmi, R. V., Brahmakumar, M., Sudha, J. D., and Menon, A. R. (2017). Studies on natural rubber containing kaolin modified with hexamethylenediamine derivative of phosphorylated cashew nut shell liquid prepolymer. *Appl. Clay Sci.* 141, 171–179. doi: 10.1016/j.clay.2017.02.034
- Tahereh, G., Masoud, S. N., and Shokufeh, V. (2016). Investigation of the electrochemical hydrogen storage and photocatalytic properties of CoAl₂O₄ pigment: green synthesis and characterization. *Int. J. Hydrogen Ener.* 41, 9418–9426. doi: 10.1016/j.ijhydene.2016.03.144
- Tielens, F., Calatayud, M., Franco, R., Recio, J. M., Pérez-Ramírez, J., and Minot, C. (2006). Periodic DFT study of the structural and electronic properties of bulk CoAl₂O₄ spinel. *J. Phys. Chem. B* 110, 988–995. doi: 10.1021/jp0533751
- Tirsoaga, A., Visinescu, D., Jurca, B., Ianculescu, A., and Carp, O. (2011). Eco-friendly combustion-based synthesis of metal aluminates MAl₂O₄ (M = Ni, Co). *J. Nanopart. Res.* 13, 6397–6408. doi: 10.1007/s11051-011-0392-1
- Vesely, D., Kalendov, A., and Kalend, P. (2010). A study of diatomite and calcined kaoline properties in anticorrosion protective coatings. *Prog. Org. Coat.* 68, 173–179. doi: 10.1016/j.porgcoat.2010.02.007
- Wang, C., Liu, S. M., Liu, L. H., and Bai, X. (2006). Synthesis of cobalt-aluminate spinels via glycine chelated precursors. *Mater. Chem. Phys.* 96, 361–370. doi: 10.1016/j.matchemphys.2005.07.066
- Xi, X. L., Nie, Z. R., Ma, L. W., Xu, X. Y., and Zuo, E. Y. (2012). Synthesis and characterization of ultrafine Co₂AlO₄ pigment by freeze-drying. *Powder Technol.* 226, 114–116. doi: 10.1016/j.powtec.2012.04.029
- Yang, Y., Li, L. L., and Li, W. K. (2013). Plasmon absorption of Au-in-CoAl₂O₄ linear nanopeapod chains. *J. Phys. Chem. C* 117, 14142–14148. doi: 10.1021/jp403150h
- Yeo, C. H. (2011). *Stability and Collapse Mechanisms of Unreinforced and Forepole-Reinforced Tunnel Headings*, Ph.D. thesis national university of Singapore, Singapore.
- Yoneda, M., Gotoh, K., Nakanishi, M., Fujii, T., and Nomura, T. (2018). Influence of aluminum source on the color tone of cobalt blue pigment. *Powder Technol.* 323, 574–580. doi: 10.1016/j.powtec.2016.06.021
- Zayat, M., and Levy, D. (2000). Blue CoAl₂O₄ particles prepared by the sol-gel and citrate-gel methods. *Chem. Mater.* 12, 2763–2769. doi: 10.1021/cm001061z

- Zha, W. W., Zhou, Z. H., Zhao, D. L., and Feng, S. J. (2016). Positive effects of Al³⁺ partially substituted by Co²⁺ cations on the catalytic performance of Co_{1-x}Al_{2-x}O₄ (x = 0-0.2) for methane combustion. *J. Sol-Gel Sci. Techn.* 78, 144–150. doi: 10.1007/s10971-015-3910-2
- Zhang, A., Mu, B., Wang, X., Wen, L., and Wang, A. (2018b). Formation and coloring mechanism of typical aluminosilicate clay minerals for CoAl₂O₄ hybrid pigment preparation. *Front. Chem.* 6:125. doi: 10.3389/fchem.2018.00125
- Zhang, A. J., Mu, B., Hui, A. P., and Wang, A. Q. (2018a). A facile approach to fabricate bright blue heat-resisting paint with self-cleaning ability based on CoAl₂O₄/kaoline hybrid pigment. *Appl. Clay Sci.* 160, 153–161. doi: 10.1016/j.clay.2017.12.004
- Zhang, A. J., Mu, B., Luo, Z. H., and Wang, A. Q. (2017). Bright blue halloysite/CoAl₂O₄ hybrid pigments: preparation, characterization and application in water-based painting. *Dyes Pigments* 139, 473–481. doi: 10.1016/j.dyepig.2016.12.055
- Zhang, C. L., He, Y., Li, F., Di, H. H., Zhang, L., and Zhan, Y. Q. (2016). h-BN decorated with Fe₃O₄ nanoparticles through mussel-inspired chemistry of dopamine for reinforcing anticorrosion performance of epoxy coatings. *J. Alloy. Compd.* 685, 743–751. doi: 10.1016/j.jallcom.2016.06.220
- Zhang, S. L., Liu, Q. F., Yang, Y. J., Wang, D., He, J. K., and Sun, L. Y. (2017). Preparation, morphology, and structure of kaolinites with various aspect ratios. *Appl. Clay Sci.* 147, 117–122. doi: 10.1016/j.clay.2017.07.014
- Zhou, S., Wu, L., Sun, J., and Shen, W. (2002). The change of the properties of acrylic-based polyurethane via addition of nano-silica. *Prog. Org. Coat.* 45, 33–42. doi: 10.1016/S0300-9440(02)00085-1
- Zhu, X. H., Li, H., Zhou, H., and Zhong, S. A. (2015). Fabrication and evaluation of protein imprinted polymer based on magnetic halloysite nanotubes. *RSC Adv.* 5, 66147–66154. doi: 10.1039/C5RA09740A
- Zou, J., and Zheng, W. (2016). TiO₂@CoTiO₃ complex green pigments with low cobalt content and tunable color properties. *Ceram. Int.* 42, 8198–8205. doi: 10.1016/j.ceramint.2016.02.029

Conflict of Interest Statement: The authors declare that the research was conducted in the absence of any commercial or financial relationships that could be construed as a potential conflict of interest.

Copyright © 2018 Zhang, Mu, Wang and Wang. This is an open-access article distributed under the terms of the Creative Commons Attribution License (CC BY). The use, distribution or reproduction in other forums is permitted, provided the original author(s) and the copyright owner(s) are credited and that the original publication in this journal is cited, in accordance with accepted academic practice. No use, distribution or reproduction is permitted which does not comply with these terms.



Formation and Coloring Mechanism of Typical Aluminosilicate Clay Minerals for CoAl_2O_4 Hybrid Pigment Preparation

Anjie Zhang^{1,2,3}, Bin Mu^{1*}, Xiaowen Wang^{1,2}, Lixin Wen³ and Aiqin Wang^{1*}

¹ Key Laboratory of Clay Mineral Applied Research of Gansu Province, Center of Eco-material and Green Chemistry, Lanzhou Institute of Chemical Physics, Chinese Academy of Sciences, Lanzhou, China, ² University of Chinese Academy of Sciences, Beijing, China, ³ Northwest Yongxin Coatings Limited Company, Lanzhou, China

OPEN ACCESS

Edited by:

Pu-Xian Gao,
University of Connecticut,
United States

Reviewed by:

Sibo Wang,
University of Connecticut,
United States
Kaixuan Bu,
Rutgers University, The State
University of New Jersey,
United States
Quansheng Liu,
Changchun University of Technology,
China

*Correspondence:

Bin Mu
mubin@licp.cas.cn
Aiqin Wang
aqwang@licp.cas.cn

Specialty section:

This article was submitted to
Green and Sustainable Chemistry,
a section of the journal
Frontiers in Chemistry

Received: 05 February 2018

Accepted: 03 April 2018

Published: 19 April 2018

Citation:

Zhang A, Mu B, Wang X, Wen L and
Wang A (2018) Formation and
Coloring Mechanism of Typical
Aluminosilicate Clay Minerals for
 CoAl_2O_4 Hybrid Pigment Preparation.
Front. Chem. 6:125.
doi: 10.3389/fchem.2018.00125

Different kinds of aluminosilicate minerals were employed to fabricate CoAl_2O_4 hybrid pigment for studying its formation and coloring mechanism. It revealed that the color of the obtained hybrid pigments was determined by the content of Al_2O_3 and lightness of clay minerals. The higher the Al_2O_3 content and the lightness of clay minerals, the better the color parameters of hybrid pigments. During the preparation of hybrid pigments, CoAl_2O_4 nanoparticles were confined to be loaded on the surface of the aluminosilicate minerals, which effectively prevented from the aggregation and the size increase of CoAl_2O_4 nanoparticles. What's more, aluminosilicate mineral might be an ideal natural aluminum source to compensate the aluminum loss due to the dissolution of $\text{Al}(\text{OH})_3$ at alkaline medium during precursor preparation, keeping an optimum molar ratio of $\text{Co}^{2+}/\text{Al}^{3+}$ for formation of spinel CoAl_2O_4 pigments in the process of high-temperature crystallization.

Keywords: CoAl_2O_4 , aluminosilicate minerals, hybrid pigments, formation mechanism, coloring mechanism

INTRODUCTION

AB_2O_4 spinel complex oxides usually are used as ceramic materials, inorganic pigments, magnetic materials, catalysts and gas-sensitive materials (Ren et al., 2014; Yoneda et al., 2016; Zou and Zheng, 2016; Álvarez-Docio et al., 2017; Chafi et al., 2017; Rani, 2017; Tang et al., 2017), the most famous one of them is cobalt aluminate (CoAl_2O_4). As a high-grade eco-friendly intense blue pigment, it can be applied in the fields of ceramics, plastics, paint, glass, and color TV tubes due to high refractive index, excellent chemical, and thermal stability (Mahé et al., 2008; Ryu et al., 2008; Tirsoaga et al., 2011; Merino et al., 2015; Soleimani-Gorgania et al., 2015). However, the high cost of CoAl_2O_4 pigments has severely restrained their wide applications because of the expensive cobalt compounds (De Souza et al., 2009; Gholizadeh and Malekzadeh, 2017; Zhang et al., 2017). In addition, the traditional method for preparation of cobalt blue pigment was involved in the calcination of CoO and Al_2O_3 at above $1,300^\circ\text{C}$ for a long time (Armijo, 1969; Salavati-Niasari et al., 2009; Sale, 2015; He et al., 2017; Zhang et al., 2017), which was obviously time-consuming. Therefore, it is urgent to develop a strategy to prepare the low-cost cobalt blue pigment with perfect color property in order to realize its wide applications.

Incorporation of non-toxic and low-cost elements may be an efficient method to decrease the use of Co element. Torkian et al. synthesized $\text{Co}_x\text{Mg}_{1-x}\text{Al}_2\text{O}_4$ nanopigment based on the substitution

of Co²⁺ using Mg²⁺ via combustion method (Torkian et al., 2013). Khattab et al. also synthesized Co_xMg_{1-x}Al₂O₄ blue pigment after replacing of Co²⁺ with Mg²⁺ during the calcination process (Khattab et al., 2017), and Sedghi prepared Co_xZn_{1-x}Al₂O₄ nano-pigments by gel combustion method (Sedghi et al., 2014). It suggests that the doping technology using the matched metal ions can enhance the color properties as well as decrease the cost of cobalt blue. However, the decrease in the cost of cobalt blue is limited by the substitution of Co²⁺ using other metal ions. What's more, the agglomeration and crystal grain growth of cobalt blue nanoparticles still remain during calcining process.

Recently, many inorganic substrates are employed to construct the eco-friendly high-grade inorganic hybrid pigment (Mousavand et al., 2006; Zhang et al., 2015; Meng et al., 2016; Mishra et al., 2017; Tian et al., 2017). Due to the abundance in nature, low-cost, non-toxic and unique structure features, clay minerals can be served as a promising substrate for loading of the inorganic nanoparticles (Wang et al., 2011; Todorova et al., 2014; Mu and Wang, 2015; Ezzatahmedi et al., 2017; Intachai et al., 2017). Therefore, our groups have prepared cobalt blue hybrid pigments after incorporating of attapulgite, halloysite (Hal), montmorillonite (Mt), etc., via co-precipitation method followed by a calcination process (Mu et al., 2015; Zhang et al., 2017). It has confirmed that the introduction of clay minerals dramatically decreases the cost of pigment, as well as improves the aggregation of cobalt blue nanoparticles. In addition, some components of clay minerals might enter into tetrahedral or octahedral positions of CoAl₂O₄ spinel structure to substitute Co²⁺ or Al³⁺, which have an obvious effect on the color properties of cobalt blue. However, the relevant formation and coloring mechanism of the CoAl₂O₄/clay mineral hybrid pigments was still not clear. Therefore, several of typical aluminosilicate minerals were selected to construct the CoAl₂O₄/aluminosilicate clay mineral hybrid pigments to study its relevant formation and coloring mechanism in this study, the involved clay minerals included Hal, Mt, kaoline (Kaol), andalusite (And), dickite (Dic), mullite (M47 and M70, the number is indicator of the Al₂O₃ content). The effect of the different aluminosilicate clay minerals on the color parameters of hybrid pigment was studied in detail, and the possible formation and coloring mechanism of the hybrid pigments was proposed. It is expected to provide guidance for preparation of low-cost and high-grade cobalt blue with the perfect color properties.

EXPERIMENTAL

Materials

Hal and And were obtained from Zhengzhou Jinyangguang Ceramics Co., Ltd. (HeNan, China). Mt, Dic, M47 and M70 were obtained from Yixian Kaolin Development Co., Ltd. (HeBei, China), Qingdao Yuzhou chemical Co., Ltd. (ShanDong, China), Huakang Non-Metallic Minerals Processing Plants (HeBei, China), respectively. Kaol was purchased from Longyan Kaolin Co., Ltd. (FuJian, China). In order to analyze the compositions of aluminosilicate minerals using X-ray fluorescence, the

aluminosilicate minerals were firstly crushed and purified by 4% HCl (wt%) to remove carbonates, and then the purified clay minerals were filtered by passing through a 200-mesh sieve. The composition of the involved aluminosilicate minerals is summarized in **Table 1**. Co(NO₃)₂·6H₂O and Al(NO₃)₃·9H₂O were purchased from Shanghai Reagent Factory (Shanghai, China). NaOH, HCl, and anhydrous ethanol were obtained by China National Medicines Co., Ltd.

Preparation of CoAl₂O₄/Aluminosilicate Clay Mineral Hybrid Pigment

The CoAl₂O₄/aluminosilicate clay mineral hybrid pigments were fabricated according to the similar procedure reported in our previous study (Zhang et al., 2017). Co(NO₃)₂·6H₂O (0.01 mol), Al(NO₃)₃·9H₂O (0.02 mol), and 1.090 g of aluminosilicate clay mineral (60 wt% of CoAl₂O₄) were added into water (50 mL) and magnetically stirred at 150 rpm for 1 h. And then the pH value of the reaction system was adjusted to 10 using 3 M NaOH aqueous solution and stirred for 2 h at room temperature. The obtained solid products were collected by centrifugation, and washed more than five times using water before being dried at 60°C for 10 h. Finally, it was calcined at 1,100°C for 2 h with a rate of 10°C/min from room temperature to 1,100°C, and the as-prepared hybrid pigments were abbreviated to Kaol-HP, Hal-HP, Mt-HP, M47-HP, M70-HP, And-HP, and Dic-HP corresponding to different clay minerals, respectively. As a control, cobalt blue pigments without clay minerals also were fabricated by the same procedures, and the productions were labeled to CoAl₂O₄-900, CoAl₂O₄-1000, CoAl₂O₄-1100, and CoAl₂O₄-1200 according to the calcining temperatures, respectively. In additional, different clay minerals were also calcined at 1,100°C and defined as Kaol-1100, Hal-1100, Mt-1100, M47-1100, M70-1100 And-1100, and Dic-1100, respectively.

Characterization

The morphology was measured using transmission electron microscopy (TEM, JEM-1200EX/S, JEOL). The structure and composition was analyzed using Fourier Transform infrared (FTIR, Thermo Nicolet NEXUS TM, Madison, USA). The X'pert PRO diffractometer ($\lambda = 1.54060\text{\AA}$) was used to analysis the XRD patterns of the sample with a scan step size of 0.02° per second. Raman spectra were recorded using the microprobe on a

TABLE 1 | Chemical composition of different clay minerals after acid treatment.

Clay minerals	Al ₂ O ₃ (%)	Na ₂ O (%)	MgO (%)	CaO (%)	SiO ₂ (%)	K ₂ O (%)	Fe ₂ O ₃ (%)	TiO ₂ (%)
Hal	29.49	0	0.39	0.08	41.15	0.61	1.71	–
Kaol	54.2	0.014	0.45	0.32	23.5	3.3	0.67	1.36
Mt	22	–	–	–	64.6	5.24	6.03	1.34
Dic	26.2	–	–	0.24	54.1	0.49	0.26	–
And	56.5	–	–	0.37	38.7	1.18	1.39	1.38
M47	49.1	–	–	0.92	42.8	0.96	2.38	3.07
M70	64.6	–	–	0.99	25.5	1.17	2.1	1.02

Labram HR Evolution Raman spectrometer (Horiba). The Color-Eye automatic differential colorimeter (X-Rite, Ci 7800) was used to study the color properties of the as-prepared pigments by the Commission Internationale de l'Éclairage (CIE) 1976 L^* , a^* , b^* colorimetric method. L^* is the lightness axis (0 for black and 100 for white). The parameters of a^* (negative values for green and positive values for red) and b^* (negative values for blue and positive values for yellow) denote the hue or color dimensions.

RESULTS AND DISCUSSION

Characterization of Kaol-HP

Figure S1 (see ESI) gives the CIE parameters of Kaol-HP calcined at different temperatures. It is observed that the L^* value of hybrid pigments firstly increases with the increase of the calcining temperatures, and then it decreases as the temperature is above 1,100°C. The same change trend is also observed from the value of b^* of Kaol-HP, but the color of CoAl₂O₄ pigments without Kaol is different compared with that of Kaol-HP prepared under the same conditions. In order to obtain the blue color, the calcining temperature for preparation of CoAl₂O₄ pigments without Kaol must be above 1,200°C (Figure S2, see ESI), but its color properties ($L^* = 37.41$, $a^* = -0.52$, $b^* = -41.14$) are poor compared with Kaol-HP prepared at 1,100°C ($L^* = 48.11$, $a^* = 2.64$, $b^* = -63.75$). Thus these two samples are selected to investigate the effect of introduction of clay minerals on the structure and properties of pigments. However, the L^* value of Kaol-HP decreases when the temperature increases to 1,200°C, which might be due to the crystal phase transition and the collapse of Kaol structure (Juneja et al., 2010; Yeo, 2011; Zhang et al., 2017).

Figure 1A presents the FTIR spectra of the raw Kaol, Kaol calcined at 1,100°C, Kaol-HP, and CoAl₂O₄ calcined at 1,200°C. As depicted in the FTIR spectrum of the raw Kaol, the band at 3,684 and 3,651 cm⁻¹ are assigned to stretching vibrations of Al-OH (Saikia and Parthasarathy, 2010). The bands at 3,440 and 1,636 cm⁻¹ are assigned to the physisorbed water on the surface of Kaol and the bending vibration of H-O-H, respectively. The IR peaks at 911 cm⁻¹ can be ascribed to the Al-Al-OH vibration of the clay sheet, while the bands located at 1,114, 1,096, 1,032, and 471 cm⁻¹ are related to Si-O-Si of the clay tetrahedron sheets (Jafari and Hassanzadeh-Tabrizi, 2014). After being calcined at 1,100°C, the typical absorption bands of Kaol at 3,651, 3,684, and 911 cm⁻¹ disappear due to the dehydroxylation of Kaol during calcination. After incorporating of CoAl₂O₄ nanoparticles, the characteristic absorption bands of CoAl₂O₄ at 668, 557, and 509 cm⁻¹ were clearly observed, which correspond to the stretching vibration of Al-O of AlO₆ and Co-O of CoO₄ (Chapskaya et al., 2005), respectively. Furthermore, these characteristic adsorption bands also can be found in the FTIR spectrum of CoAl₂O₄ pigments.

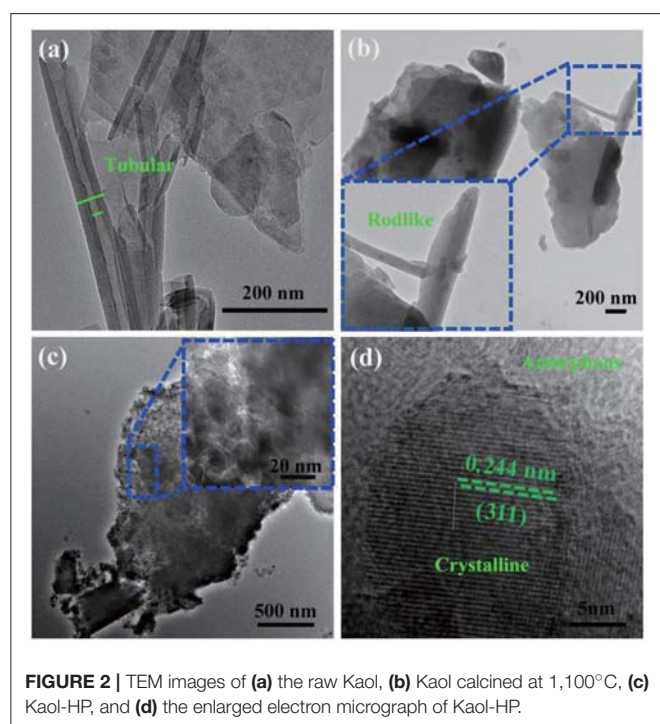
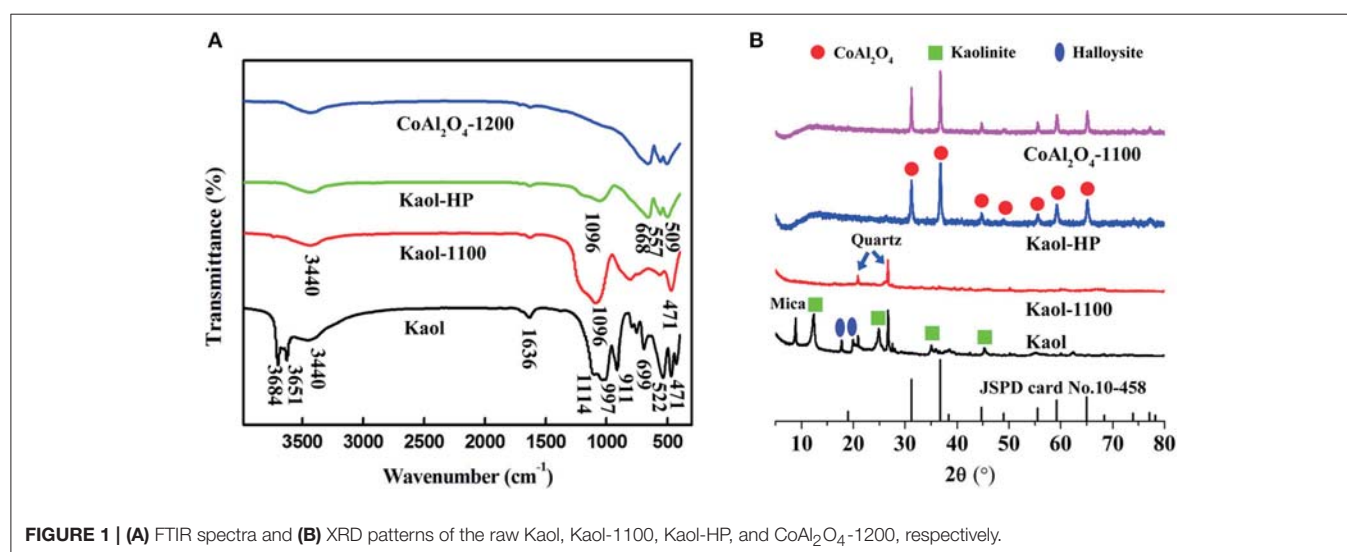
Figure 1B exhibits the XRD patterns of the raw Kaol, Kaol calcined at 1,100°C, Kaol-HP, and CoAl₂O₄ calcined at 1,200°C. The raw Kaol presents well-defined reflections at $2\theta = 12$ and 25° , which are typical characteristic peaks of kaolinite (Panda et al., 2010; Konduri and Fatehi, 2017). The diffraction peak

of mica is observed at $2\theta = 8.9^\circ$ while the ones located at $2\theta = 18.3$ and 20.2° are attributed to the diffraction peaks of Hal. It indicates that the raw Kaol is associated with Hal, quartz and mica. When Kaol is calcined at 1,100°C, the typical diffraction peaks of Kaol, Hal, and mica disappear, and only the diffraction peaks of quartz remain. As for Kaol-HP, it is obvious that the typical diffraction peaks of Kaol vanish accompanied with the presence of some new diffraction peaks, which are assigned to spinel CoAl₂O₄. According to JCPD card No. 10-458, the diffraction peaks located at $2\theta = 31.1$, 36.8, 44.8, 49.0, 55.5, 59.2, 65.2° correspond to (220), (311), (400), (331), (422), (511), and (440) of CoAl₂O₄, respectively (Abaide et al., 2015). In order to study the effect of calcining temperatures and incorporating of clay minerals on the sizes of CoAl₂O₄, the crystallite size is also calculated using Sherrer relation according to XRD patterns of all samples (including hybrid pigments prepared using Kaol at different temperatures, see Figure S3) (Equation 1):

$$D = \frac{0.89 \times \lambda}{B \times \cos \theta} \quad (1)$$

where D is the crystallite size, λ is the wavelength (Cu Ka), θ is the diffraction angle of the most intense diffraction peak (Zhang et al., 2018), B is the corrected half-width obtained using a quartz as reference. $B = B_m - B_s$, where B_m refers to the tested results and B_s was got by testing a reference substance. As shown in Table S1, it is clear that the crystallite sizes of CoAl₂O₄ increases with the increase of the calcining temperatures either hybrid pigments or CoAl₂O₄ pigments without Kaol. However, the crystallite sizes of the as-prepared hybrid pigments are smaller than that of CoAl₂O₄ pigments, suggesting that the introduction of clay minerals obviously prevents from the increase in size and the agglomeration of CoAl₂O₄ particles during calcining process.

Figure 2a provides the TEM image of Kaol, and it can be found that Kaol is a typical lamellar layered structure with a smooth surface, and some tubular morphology is also observed, which can be attributed to the associated tubular Hal. The length of Hal is around 0.2–2.0 μm while the external and inner diameters are about 50–80 and 20–50 nm, respectively. After being calcined at 1,100°C (**Figure 2b**), the lamellar morphology of Kaol remains while the tubular structure is transformed into rodlike one, which is possible related to the phase transformation of Hal. After introducing of CoAl₂O₄ nanoparticles, the surface of lamellar morphology becomes coarse due to the loading of CoAl₂O₄ nanoparticles. The CoAl₂O₄ nanoparticles with a diameter of about 10–20 nm are uniformly anchored on the surface of lamellar (**Figure 2c**). Furthermore, the selected area electron diffraction pattern of Kaol-HP calcined at 1,100°C also confirmed the formation of CoAl₂O₄ nanoparticles (Figure S4, see ESI) (Ouahdi et al., 2005; Mindru et al., 2010). In addition, **Figure 2d** gives an enlarged electron micrograph of **Figure 2c**, it provides a well-resolved lattice plane with an interplanar spacing of 0.244 nm, corresponding to [311] plane of the cubic $Fd\bar{3}m$ space group, which is identified on the basis of data from the standard CoAl₂O₄ database JCPD card no. 10-458 (Kim et al., 2012). The micrograph displays the coexistence of amorphous and crystalline phases, and the crystalline phase



might be attributed to the spinel CoAl₂O₄ while the amorphous one is related to silicate derived from Kaol (Cho and Kakihana, 1999).

Figure S5 depicts the EDX spectrum of Kaol-HP, and it can be found that Kaol-HP is mainly composed of Co, Al, O, and Si elements. Element mapping of Kaol-HP is illustrated in **Figure 3**, it is clear that Co element is uniformly distributed on the surface of lamellar, suggesting that the generated CoAl₂O₄ is well anchored on the surface of substrate. Furthermore, other elements also present the uniform distribution. By contrast, the edge color of Si element is obscure, which can be attributed to

the fact that the edge thickness of the silicate substrate is thin. However, the value of Co/Al decreases from 0.49 to 0.37 to 0.31 with the change of the selected area from boundary to center of Kaol-HP (**Table 2**), which indicates the loading content of CoAl₂O₄ in the edge reign is higher than the center of the silicate substrate. Based on the above analysis, it suggests that Kaol-HP has been successfully prepared.

Effect of Different Aluminosilicate Clay Minerals and Coloring Mechanism

In our previous study (Zhang et al., 2017), it has been confirmed that the introduction of clay minerals, especially aluminosilicate mineral of Hal, was in favor of decreasing the formation temperature of spinel-type CoAl₂O₄, and enhancing the color properties of CoAl₂O₄ pigment. In order to investigate the effect of the different aluminosilicate minerals on the color properties of hybrid pigments, several of representative aluminosilicate minerals were selected to prepare CoAl₂O₄ hybrid pigments including Hal, And, Kaol, Mt, Dic, M47, and M70.

The XRD patterns of the different aluminosilicate minerals are provided in **Figure 4**. Hal is a 1:1 aluminosilicate mineral with the empirical formula Al₂Si₂O₅(OH)₄, the typical diffraction peaks of Hal are observed at $2\theta = 12.3, 18.3, 20.2, 24.8^\circ$, and the diffraction peaks of quartz are located at $2\theta = 20.8, 26.7,$ and 36.6° (**Figure 4A**) (Philip et al., 2017). **Figure 4B** gives XRD pattern of Mt, its characteristic diffraction peaks are located at $2\theta = 5.9, 19.7,$ and 35.1° , while the diffraction peaks at $2\theta = 12.5$ and 17.5° are attributed to illite (Wang et al., 2016; Liang et al., 2017). Dic is a kind of layered silicate mineral, and pertains to 1:1 type of Kaol subgroup. As shown in **Figure 4C**, the characteristic diffraction peaks between 34 and 39° can be observed, which are assigned to (200), (131), (006), and (133) of Dic, respectively (Zheng et al., 2011). **Figures 4D–F** depicted the XRD patterns of M47, M70, and And. Mullite is an artificial material, which is synthesized using natural raw materials during 1,100–1,600°C, such as And, kyanite, etc. (Xu et al., 2017; Yuan et al., 2017).

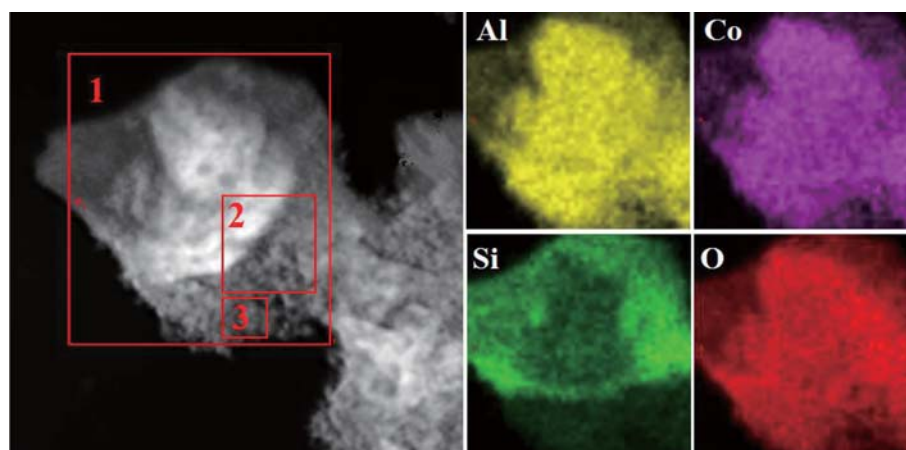


FIGURE 3 | Element mapping of Kaol-HP.

TABLE 2 | The element content of the different selection areas of Kaol-HP.

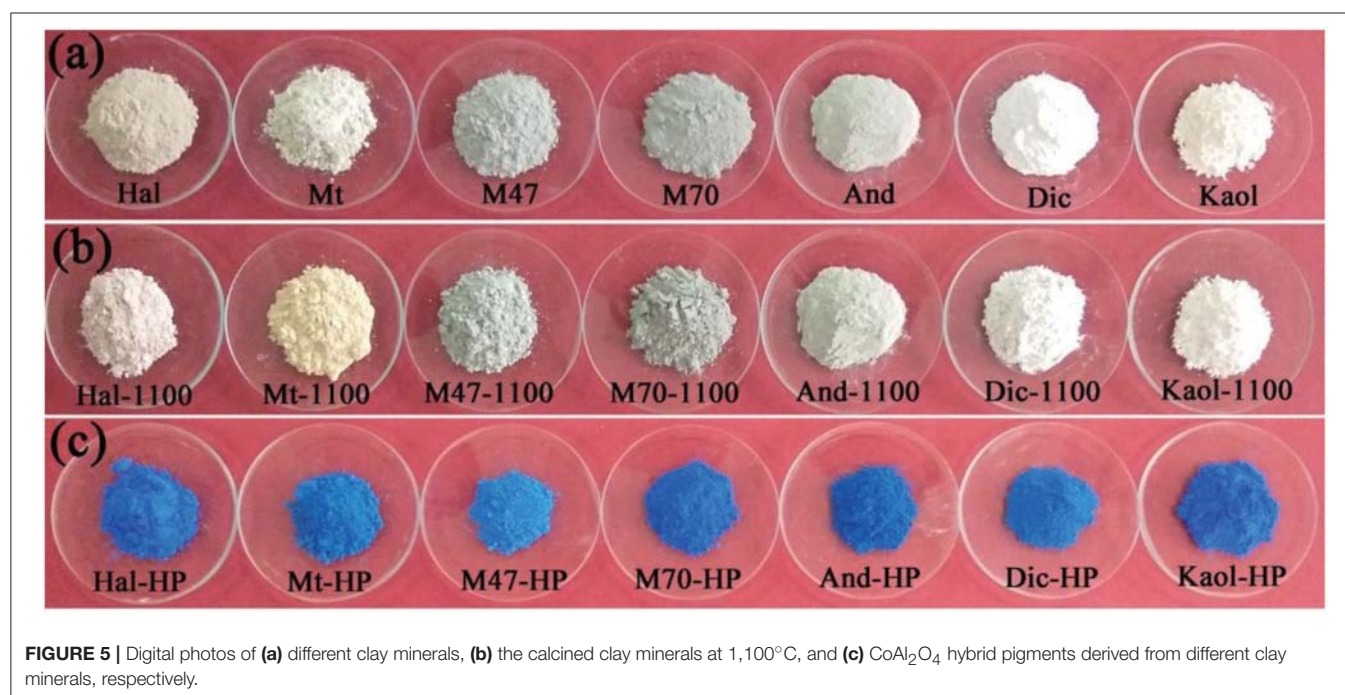
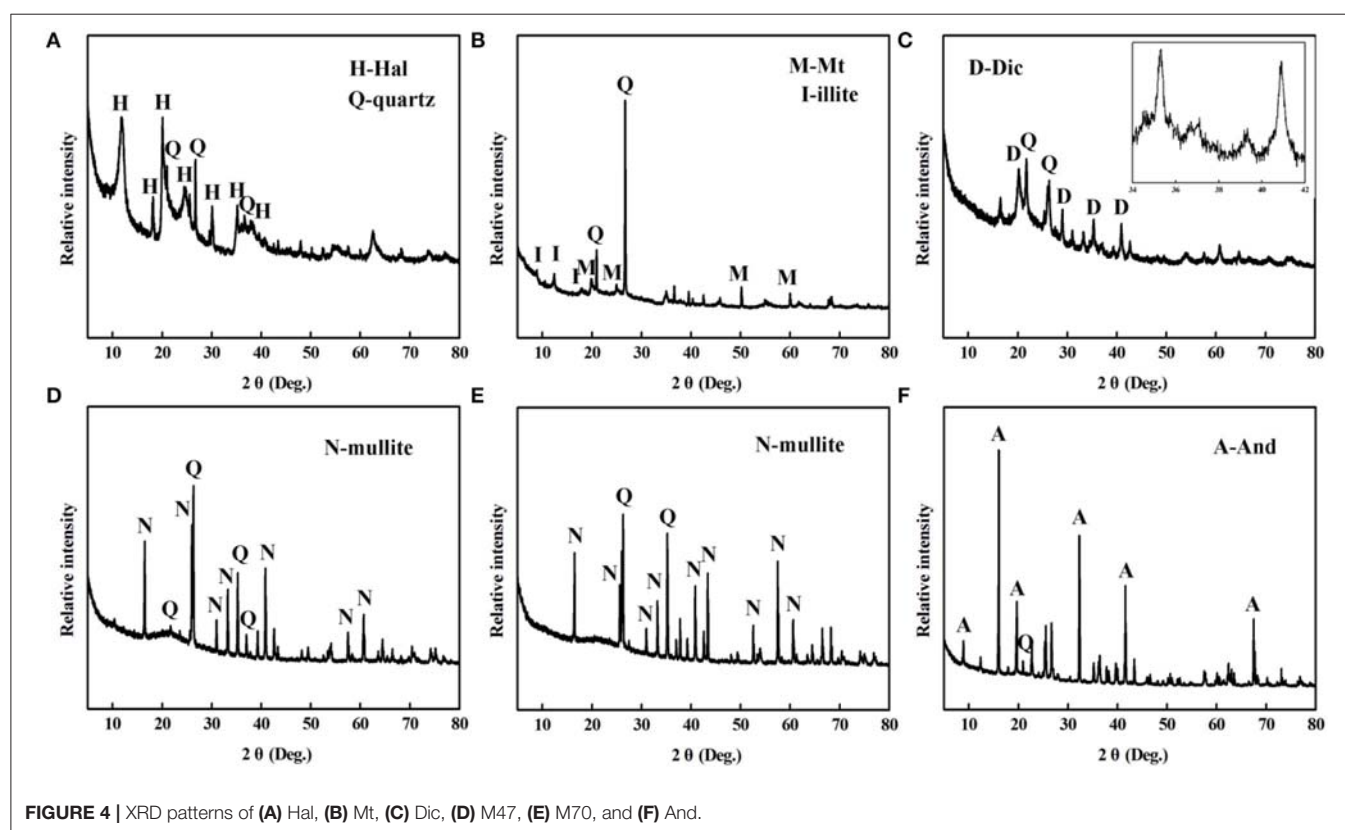
Element	Atomic (%)		
	No. 1	No. 2	No. 3
O	67	63.61	51.21
Na	0.95	0.90	0.47
Al	17.01	21.06	31.55
Si	9.49	6.17	1.35
K	0.35	0.22	0
Co	5.18	8.01	15.39
Co/Al	0.31	0.37	0.49
Total	100	100	100

Figure 5 shows the digital photos of the raw aluminosilicate clay minerals, the calcined aluminosilicate clay minerals at 1,100°C and CoAl₂O₄ hybrid pigments derived from different aluminosilicate clay minerals, respectively. It is obvious that different clay minerals present different colors. Dic and Kaol are white, Hal and Mt are light brown, while M47, M70, and And are gray. After being calcined at 1,100°C (Figure 5b), Kaol and Dic are white, Mt is yellowish-brown, Hal was light pink, and the others (M47, M70, and And) are gray. The digital photos of the as-prepared hybrid pigments are exhibited in Figure 5c, it is found that all hybrid pigments present typical blue, but there are differences among different hybrid pigments. By contrast, the color of Kaol-HP is optimal, which is also consistent with their color parameters (Table 3). Kaol-HP exhibits the maximum b^* and C^* values, followed by M70-HP, M47-HP, Hal-HP, respectively, while Mt-HP and And-HP indicate the worst lightness (L^*). It suggests that the colors of the hybrid pigments might be related to the types and compositions of aluminosilicate clay minerals.

As shown in Table 1, the main compositions of the involved aluminosilicate clay minerals are Al₂O₃ and SiO₂. Therefore, the relationship between the content of Al₂O₃ or SiO₂ and the color

parameters of hybrid pigments are investigated, and Figure 6 gives the relationship between the CIE parameters of CoAl₂O₄ hybrid pigments and the content of Al₂O₃ and SiO₂ of different aluminosilicate clay minerals, while Table S2 summarizes the content of Al₂O₃ and SiO₂ of the clay minerals and the CIE of hybrid pigments. As a whole, the value of a^* of hybrid pigments increases with the increase in the content of Al₂O₃, but the b^* value becomes more negative. It indicates the blue color of hybrid pigments become deeper with the increase in the Al₂O₃ content. However, the b^* value is more positive with the increase in the content of SiO₂, indicating a poor blue color. Therefore, Al₂O₃ and SiO₂ of aluminosilicate clay minerals plays an important role in adjusting the color of CoAl₂O₄ hybrid pigments, but the ultimate color properties of hybrid pigments result from the synergy of various compositions of aluminosilicate clay minerals, besides their colors. In order to prove above proposal, Al₂O₃ and SiO₂ with different added amounts were employed to fabricate hybrid pigments without clay minerals, respectively. As shown in Figure 7, the b^* value of hybrid pigments prepared using Al₂O₃ gradually decreases with the increase in the added amounts of Al₂O₃ (more negative). On the contrary, the b^* value of hybrid pigments derived from SiO₂ increases with the increase in the amount of SiO₂ (more positive), which might be attributed to the formation of cobalt silicate (Llusar et al., 2001). This variation trend is also in agreement with the results of Figures 6A,B.

In addition, the pH value of the reaction system is crucial to cobalt-aluminum double hydroxides (Co/Al DH) (Zhang et al., 2017), the excess OH⁻ affects the molar ratio of Co/Al in the ultimate CoAl₂O₄ due to the dissolution loss of Al in alkaline medium, which directly determines the color properties of pigments. In order to prove this effect, HCl was added into the centrifugate after the co-precipitation reaction, it can clearly observe the white precipitate upon the addition of HCl (1.0 M), and the precipitate is confirmed to be Al(OH)₃ using FTIR technique (Figure S6, see ESI) (Kamaraj and Vasudevan, 2016). In addition, the higher the pH values of the reaction, the more



the contents of white precipitate (Figure S6, see ESI). When the pH value of reaction system is above 10, the generated Al(OH)₃ will partially dissolve and the molar ratio of Co²⁺/Al³⁺ is <2,

which can be confirmed by the EDX of CoAl₂O₄ in the absence of clay minerals during preparation. As shown in Figure S7, the value of Co/Al of CoAl₂O₄ in the absence of clay minerals

is about 0.62, and thus the Al loss is about 20% due to the dissolution of Al(OH)₃ at alkaline medium during preparation of precursor. Therefore, the incorporation of aluminosilicate clay

mineral may be an ideal natural aluminum sources to compensate the aluminum loss due to the dissolution of Al(OH)₃ at alkaline medium during preparation of precursor, keeping an optimum molar ratio of Co²⁺/Al³⁺ for formation of spinel CoAl₂O₄ pigment. It can be inferred that the Al originated from clay minerals about 20% might be participated in reaction and enter into the octahedral positions of CoAl₂O₄ spinel structure to form CoAl₂O₄-silicate solid solution (Tang et al., 2018). This is also can be confirmed by the production derived from Co²⁺ salt and Kaol in the absence of Al³⁺ salt, which is prepared using the same procedure with Kaol-HP. As shown in Figure S8, the XRD pattern of the product presents the characteristic diffraction peaks of CoAl₂O₄ suggesting that Kaol can be served as an aluminum source to form CoAl₂O₄. The evolution process might be depicted by the following process (Figure 8) (Zhong et al., 1999; Cava et al., 2006).

TABLE 3 | CIE parameters of the different CoAl₂O₄ hybrid pigment.

Hybrid pigments	L*	a*	b*	C*
Hal-HP	54.60	-4.30	-50.10	50.28
Kaol-HP	48.11	2.64	-63.75	63.80
Mt-HP	29.66	-13.97	-43.33	45.53
Dic-HP	49.14	-8.27	-47.63	48.34
And-HP	30.26	-10.41	-54.69	55.67
M47-HP	40.69	-14.65	-52.43	54.44
M70-HP	33.53	-1.63	-58.45	58.47

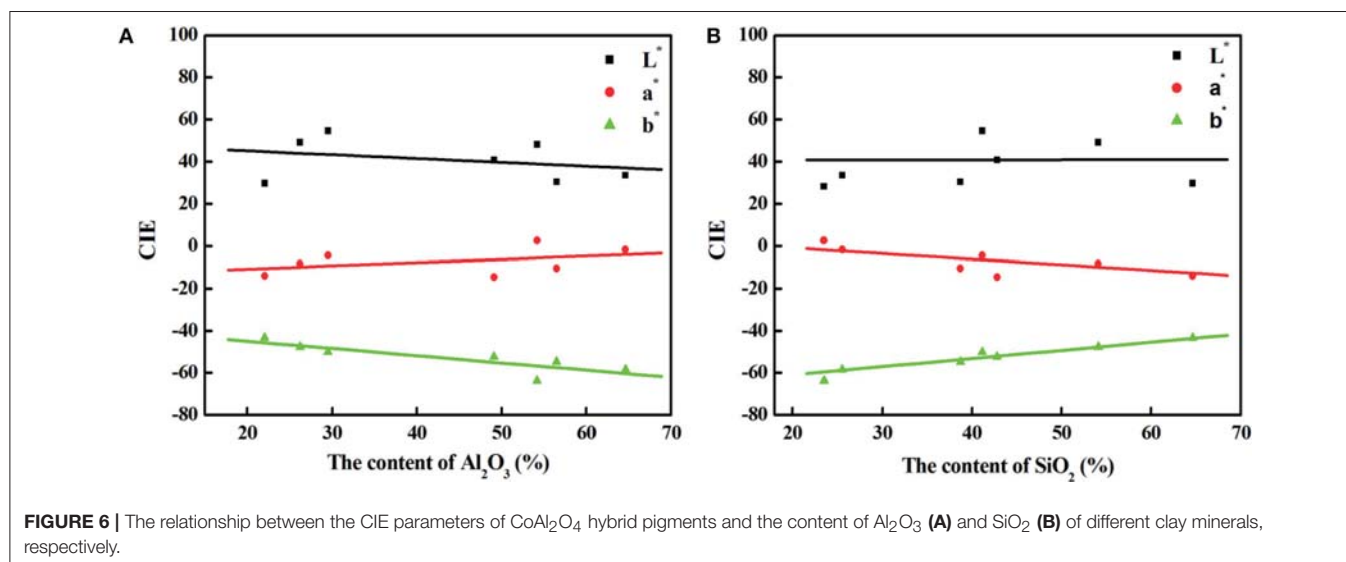


FIGURE 6 | The relationship between the CIE parameters of CoAl₂O₄ hybrid pigments and the content of Al₂O₃ (A) and SiO₂ (B) of different clay minerals, respectively.

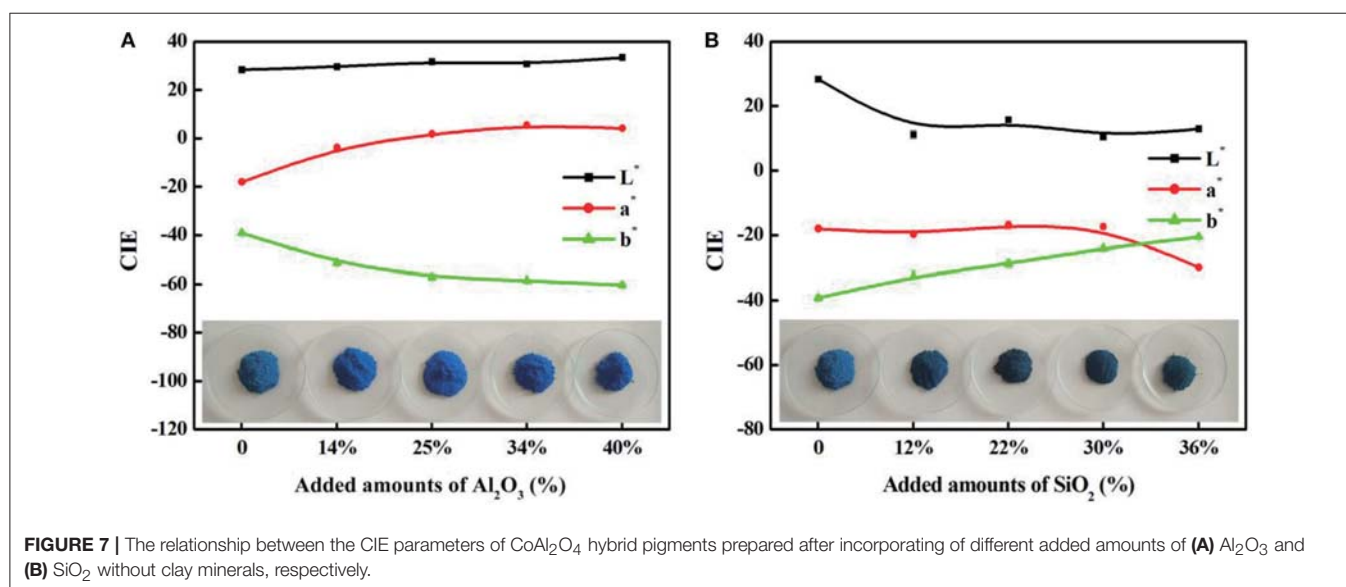
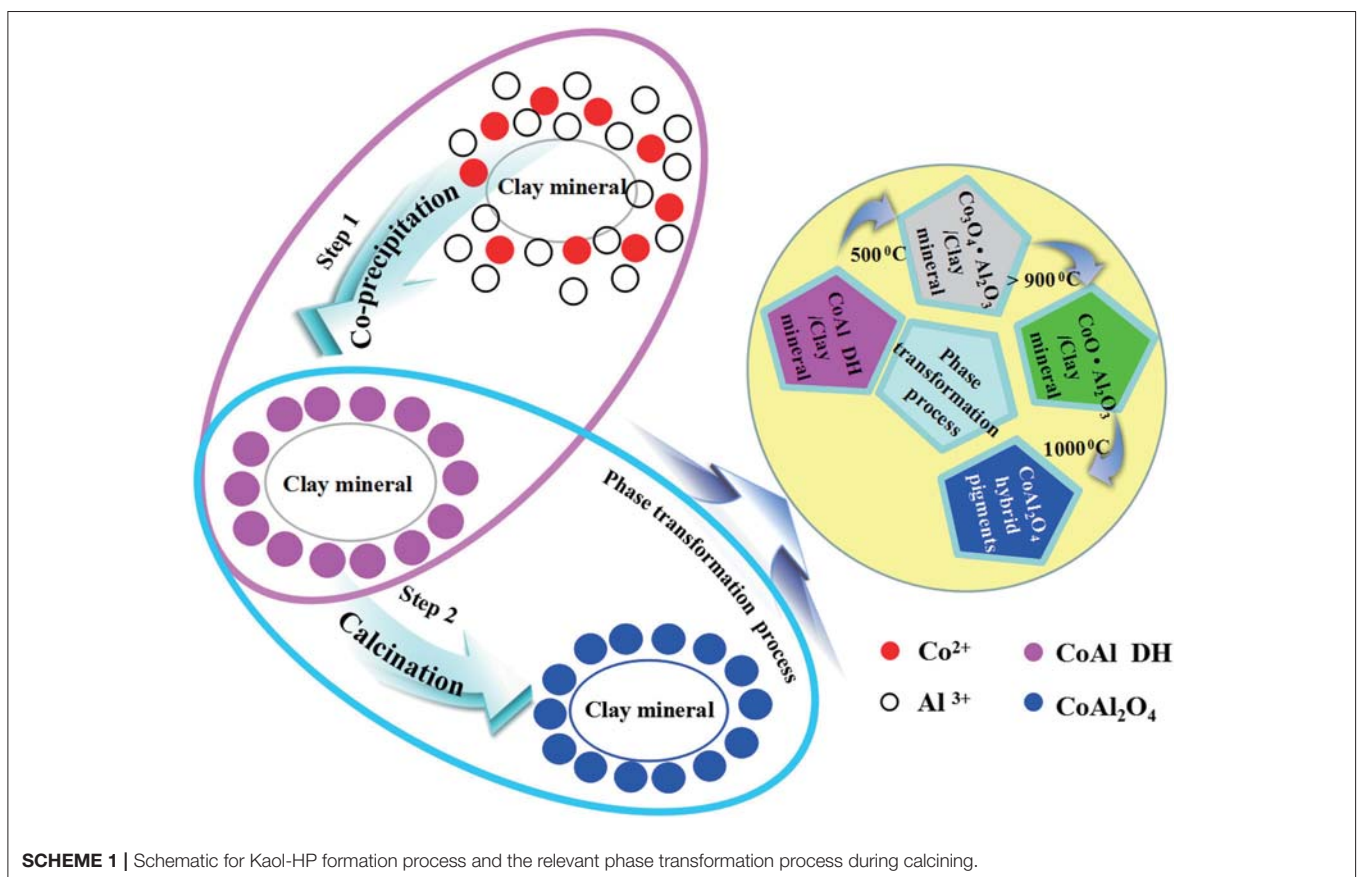
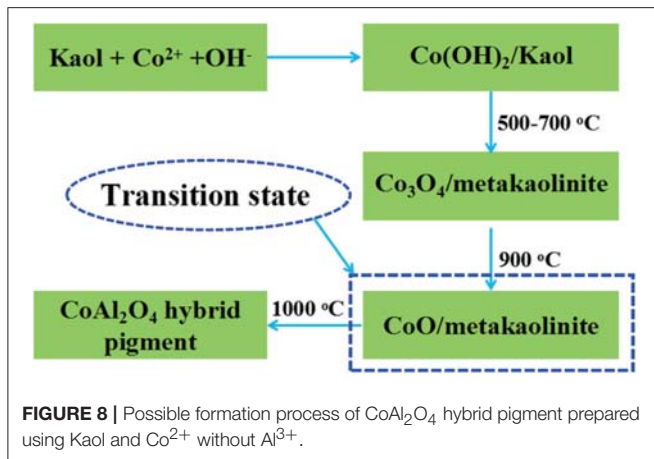


FIGURE 7 | The relationship between the CIE parameters of CoAl₂O₄ hybrid pigments prepared after incorporating of different added amounts of (A) Al₂O₃ and (B) SiO₂ without clay minerals, respectively.

Formation Mechanism of CoAl₂O₄ Hybrid Pigments

Based on the above results, the possible formation mechanism of CoAl₂O₄ hybrid pigments was proposed (Scheme 1). During the co-precipitation reaction, the Co²⁺ and Al³⁺ were firstly adsorbed on the surface of clay minerals due to the electrostatic interaction and ion exchange between metal ions and clay minerals, and then Co²⁺ and Al³⁺ were transformed into the hydroxides and deposited on the surface of clay mineral after

introducing of OH⁻. Due to the difference in the solubility constant of Al(OH)₃ and Co(OH)₂, Al³⁺ was firstly began to precipitate at lower pH, and then Co²⁺ was transformed into Co(OH)₂ at higher pH (Loganathan et al., 1977; He and Becker, 1997; Matjie et al., 2003; Akdemir et al., 2011). When the pH of reaction system was above 10, Co²⁺ almost precipitated completely, but Al(OH)₃ partially dissolved to form AlO₂⁻. As a result, the molar ratio of Co²⁺/Al³⁺ is <2. (Lavrenčič Štangar et al., 2003; Carta et al., 2005; Xu et al., 2008; Tielens et al., 2009; Kurajica et al., 2012). Therefore, CoAl DH was decomposed to form amorphous Co₃O₄ phase at around 400–500°C accompanied with the presence of highly amorphous Al₂O₃ once heating. With the increase in the calcining temperature (500–700°C), the amorphous Co₃O₄ was transformed into the spinel-type Co₃O₄ while Kaol was turned into metakaolinite (2SiO₂·Al₂O₃) (Yu et al., 2009; Duan et al., 2011), and Co₃O₄ was then progressively transformed into CoAl₂O₄ phase above 900°C, thus the content of spinel CoAl₂O₄ phase gradually increased with the vanishing of Co₃O₄ phase as the calcining temperature was above 1,000°C (Zayat and Levy, 2000; Duan et al., 2011; Álvarez-Docio et al., 2017; Zhang et al., 2018). In addition, metakaolinite was firstly transformed into spinel SiAl₂O₅ and amorphous SiO₂, and then the spinel SiAl₂O₅ changed into amorphous SiO₂ and low-order crystalline α-Al₂O₃ above 1,000°C (Chen et al., 2000; Ribeiro et al., 2005; Veselý et al., 2010; Wu et al., 2017). In fact, the thermal reduction of Co³⁺ to



Co²⁺ was simultaneous with the diffusion and reorganization of Co²⁺ and Al³⁺ ions derived from the precursor and clay minerals during this process.

It is well-known that the mass transfer process was the controlling rate step during CoAl₂O₄ preparation (Gabrovska et al., 2014). Therefore, the aluminosilicate clay minerals induced the anchoring of CoAl DH on their surface preventing from the free aggregations of CoAl DH, which could effectively decrease mass transfer resistance to reduce the time and calcining temperature for formation of spinel CoAl₂O₄. In addition, it was in favor of controlling the size and particle size distribution of CoAl₂O₄ nanoparticles during calcination process. What's more, Al³⁺ derived from aluminosilicate clay mineral also participated in the CoAl₂O₄ crystallization by the diffusion from substrate to compensate the aluminum loss during the co-precipitation reaction (Wang et al., 2006; Álvarez-Docio et al., 2017). Therefore, it may explain why the bright blue CoAl₂O₄ hybrid pigments could be obtained at 1,100°C for 2 h, but the traditional solid phase method for preparation of CoAl₂O₄ must be conducted at high temperature (>1,200°C) for a long time (Ji et al., 2000; Lorite et al., 2012). Especially, the hybrid pigments derived from the 1:1 style aluminosilicate clay minerals presented high CIE parameters. Due to the higher affinity of CoO to Al₂O₃ than SiO₂, and the CoO was easily arrived to the interphase of α-Al₂O₃ originating from aluminosilicate clay mineral to generate CoAl₂O₄ (Ahmed et al., 2012). For 2:1 style aluminosilicate clay minerals, the aluminosilicate clay minerals transformed into amorphous SiO₂ and α-Al₂O₃ at high temperature, and the content of SiO₂ is much higher than that of α-Al₂O₃. CoO might react with partially SiO₂ to form the CoSiO₃, which led to poor color properties of hybrid pigment. In order to prove above proposal, XRD patterns of Kaol-HP and Mt-HP are compared (Figure S9), it is clear that the CoSiO₃ (JCPD card no. 72-1508) occurs in Mt-HP accompanied with SiO₂ (JCPD card no. 86-0680), but they cannot be found in XRD pattern of Kaol-HP.

CONCLUSIONS

In summary, different aluminosilicate clay minerals were employed to prepare the CoAl₂O₄ hybrid pigment with different

color properties. It was found that the more content of Al₂O₃, the better color properties of hybrid pigment (higher lightness and blue), suggesting that the rich-aluminum silicate mineral was appropriate for preparation of bright blue cobalt blue pigment. The aluminosilicate clay mineral was served as a carrier to load CoAl₂O₄ nanoparticles, preventing from the aggregation and controlling the size of CoAl₂O₄ nanoparticles during calcining process. What's more, it was an ideal natural aluminum sources to compensate the aluminum loss due to the dissolution of Al(OH)₃ at alkaline medium during preparation of precursor, keeping an optimum molar ratio of Co²⁺/Al³⁺ for formation of spinel CoAl₂O₄ pigments during high-temperature crystallization. Therefore, this study may provide a feasible strategy not only to develop low-cost and bright blue cobalt blue pigments, but also to control the color properties of cobalt blue by adjusting the types of clay minerals to meet the personalized demand in the practice application.

AUTHOR CONTRIBUTIONS

AZ and XW contribute to the experiment process, data analysis, and paper preparation. BM and AW are mainly responsible for the design of experiment, data analysis and paper revision. LW contributes to the samples characterization.

ACKNOWLEDGMENTS

The authors are grateful for financial support of Regional Key Project of the Science and Technology Service (STS) of the Chinese Academy of Sciences [(2016) No. 70], the Youth Innovation Promotion Association of CAS (2017458), Major Science and Technology Projects of Lanzhou (2017-2-3), the Funds for Creative Research Groups of Gansu, China (No. 17JR5RA306) and the fifth 333 project of Jiangsu Province of China (No. BRA2017259 and BRA2016244).

SUPPLEMENTARY MATERIAL

The Supplementary Material for this article can be found online at: <https://www.frontiersin.org/articles/10.3389/fchem.2018.00125/full#supplementary-material>

REFERENCES

- Abaide, E. R., Anchieta, C. G., Foletto, V. S., Reinehr, B., Nunes, L. F., Kuhn, R. C., et al. (2015). Production of copper and cobalt aluminate spinels and their application as supports for inulinase immobilization. *Mat. Res.* 18, 1062–1069. doi: 10.1590/1516-1439.031415
- Ahmed, N. A., Abdel-Fatah, H. T. M., and Youssef, E. A. (2012). Corrosion studies on tailored Zn-Co aluminate/kaolin core-shell pigments in alkyd based paints. *Prog. Org. Coat.* 73, 76–87. doi: 10.1016/j.porgcoat.2011.09.003
- Akdemir, S., Ozel, E., and Suvaci, E. (2011). Solubility of blue CoAl₂O₄ ceramic pigments in water and diethylene glycol media. *Ceram. Int.* 37, 863–870. doi: 10.1016/j.ceramint.2010.10.031
- Álvarez-Docio, C. M., Reinoso, J. J., Del Campo, A., and Fernández, J. F. (2017). 2D particles forming a nanostructured shell: a step forward cool NIR reflectivity for CoAl₂O₄ pigments. *Dyes Pigments* 137, 1–11. doi: 10.1016/j.dyepig.2016.09.061
- Armijo, J. S. (1969). The kinetics and mechanism of solid-state spinel formation-review and critique. *Oxid. Met.* 1, 171–198. doi: 10.1007/BF00603514
- Carta, G., Casarin, M., Habra, N., and Zanella, P. (2005). MOCVD deposition of CoAl₂O₄ films. *Electrochim. Acta* 50, 4592–4599. doi: 10.1016/j.electacta.2004.10.094
- Cava, S., Tebcherani, S. M., Pianaro, S. A., Paskocimas, C. A., Longo, E., and Varela, J. A. (2006). Structural and spectroscopic analysis of γ-Al₂O₃ to α-Al₂O₃-CoAl₂O₄ phase transition. *Mater. chem. phys.* 97, 102–108. doi: 10.1016/j.matchemphys.2005.07.057
- Chafi, M. S., Ghasemi, B., and Arabi, A. M. (2017). Solution combustion synthesis (SCS) of chrome alumina as a high temperature pink pigment. *Int. J. Appl. Ceram. Tec.* 15, 203–209. doi: 10.1111/ijac.12770
- Chapskaya, A. Y., Radishevskaya, N. I., Kasatskii, N. G., Lepakova, O. K., Naiborodenko, Y. S., and Vereshchagin, V. V. (2005). The effect of composition

- and synthesis conditions on the structure of cobalt-bearing pigments of the spinel type. *Glass Ceram.* 62, 388–390. doi: 10.1007/s10717-006-0016-x
- Chen, C. Y., Lan, C. S., and Tuan, W. H. (2000). Microstructural evolution of mullite during the sintering of kaolin powder compacts. *Ceram. Int.* 26, 715–720. doi: 10.1016/S0272-8842(00)00009-2
- Cho, W. S., and Kakihana, M. (1999). Crystallization of ceramic pigment CoAl₂O₄ nanocrystals from Co-Al metal organic precursor. *J. Alloys Compd.* 287, 87–90. doi: 10.1016/S0925-8388(99)00059-6
- De Souza, L. K. C., Zamian, J. R., Da Rocha Filho, G. N., Soledadeb, L. E. B., Dos Santos, I. M. G., Souza, A. G., et al. (2009). Blue pigments based on Co_xZn_{1-x}Al₂O₄ spinels synthesized by the polymeric precursor method. *Dyes Pigments* 81, 187–192. doi: 10.1016/j.dyepig.2008.09.017
- Duan, X., Pan, M., Yu, F., and Yuan, D. R. (2011). Synthesis, structure and optical properties of CoAl₂O₄ spinel nanocrystals. *J. Alloy. Compd.* 509, 1079–1083. doi: 10.1016/j.jallcom.2010.09.199
- Ezzatahmedi, N., Ayoko, G. A., Millar, G. J., Speight, R., Yan, C., Li, J. H., et al. (2017). Clay-supported nanoscale zero-valent iron composite materials for the remediation of contaminated aqueous solutions: a review. *Chem. Eng. J.* 312, 336–350. doi: 10.1016/j.cej.2016.11.154
- Gabrovská, M. V., Crisan, D., Stanica, N., and Kardjieva, R. (2014). Co-Al layered double hydroxides as precursors of ceramic pigment CoAl₂O₄. Part I: phase composition. *Rev. Roum. Chim.* 59, 445–450.
- Gholizadeh, A., and Malekzadeh, A. (2017). Structural and redox features of La_{0.7}Bi_{0.3}Mn_{1-x}Co_xO₃ nanoperovskites for ethane combustion and CO oxidation. *Int. J. Appl. Ceram. Tec.* 14, 404–412. doi: 10.1111/ijac.12650
- He, T., and Becker, K. D. (1997). An optical *in-situ* study of a reacting spinel crystal. *Solid State Ionics* 101, 337–342. doi: 10.1016/S0167-2738(97)84050-7
- He, Y., Cao, Y., Liao, H. L., and Wang, J. A. (2017). Preparation of porous cobalt aluminate and its chromogenic mechanism. *Powder Technol.* 324, 95–101. doi: 10.1016/j.powtec.2017.08.056
- Intachai, S., Suppasso, C., Klinrisuk, S., Khaorapapong, N., and Ogawa, M. (2017). The possible doping of Al³⁺ and F⁻ modification onto CdS in montmorillonite. *Colloid Surf. A Physicochem. Eng. Asp.* 522, 133–139. doi: 10.1016/j.colsurfa.2017.02.044
- Jafari, M., and Hassanzadeh-Tabrizi, S. A. (2014). Preparation of CoAl₂O₄ nanoblue pigment via polyacrylamide gel method. *Powder Technol.* 266, 236–239. doi: 10.1016/j.powtec.2014.06.018
- Ji, L., Lin, J., and Zeng, H. C. (2000). Metal-support interactions in Co/Al₂O₃ catalysts: a comparative study on reactivity of support. *J. Phys. Chem. B* 104, 1783–1790. doi: 10.1021/jp993400l
- Juneja, A., Hegde, A., Lee, F. H., and Yeo, C. H. (2010). Centrifuge modelling of tunnel face reinforcement using forepoling. *Tunn. Undergr. Space Tech.* 25, 377–381. doi: 10.1016/j.tust.2010.01.013
- Kamaraj, A., and Vasudevan, S. (2016). Facile one-pot electrosynthesis of Al(OH)₃-kinetics and equilibrium modeling for adsorption of 2,4,5-trichlorophenoxyacetic acid from aqueous solution. *New J. Chem.* 40, 2249–2258. doi: 10.1039/C5NJ02407B
- Khattab, R. M., Sadek, H. E. H., and Gaber, A. A. (2017). Synthesis of Co_xMg_{1-x}Al₂O₄ nanospinel pigments by microwave combustion method. *Ceram. Int.* 43, 234–243. doi: 10.1016/j.ceramint.2016.09.144
- Kim, J. H., Son, B. R., Yoon, D. H., Hwang, K. T., Noh, H. G., Cho, W. S., et al. (2012). Characterization of blue CoAl₂O₄ nano-pigment synthesized by ultrasonic hydrothermal method. *Ceram. Int.* 38, 5707–5712. doi: 10.1016/j.ceramint.2012.04.015
- Konduri, M. K. R., and Fatehi, P. (2017). Dispersion of kaolin particles with carboxymethylated xylan. *Appl. Clay Sci.* 137, 183–191. doi: 10.1016/j.clay.2016.12.027
- Kurajica, S., Popović, J., Tkalčec, E., Gržeta, B., and Mandić, V. (2012). The effect of annealing temperature on the structure and optical properties of sol-gel derived nanocrystalline cobalt aluminate spinel. *Mater. Chem. Phys.* 135, 587–593. doi: 10.1016/j.matchemphys.2012.05.030
- Lavrenčić Štanger, U., Orel, B., and Krajnc, M. (2003). Preparation and spectroscopic characterization of blue CoAl₂O₄ coatings. *J. Sol Gel sci. Technol.* 26, 771–775. doi: 10.1023/A:1020770810027
- Liang, H., Wang, Z. Q., Liao, L. M., Chen, L., Li, Z., and Feng, J. (2017). High performance photocatalysts: montmorillonite supported-nano TiO₂ composites. *Optik* 136, 44–51. doi: 10.1016/j.ijleo.2017.02.018
- Llusar, M., Forés, A., Badenes, J. A., Calbo, J., Tena, M. A., and Monrós, G. (2001). Colour analysis of some cobalt-based blue pigments. *J. Eur. Ceram. Soc.* 21, 1121–1130. doi: 10.1016/S0955-2219(00)00295-8
- Loganathan, P., Burau, R. G., and Fuerstenau, D. W. (1977). Influence of pH on the sorption of Co²⁺, Zn²⁺ and Ca²⁺ by a hydrous manganese oxide. *Soil Sci. Soc. Am. J.* 41, 57–62. doi: 10.2136/sssaj1977.03615995004100010020x
- Lorite, I., Campo, A., Romero, J. J., and Fernández, J. F. (2012). Isolated nanoparticle Raman spectroscopy. *J. Raman Spectrosc.* 43, 889–894. doi: 10.1002/jrs.3112
- Mahé, M., Heintz, J., Rödel, J., and Reynnders, P. (2008). Cracking of titania nanocrystalline coatings. *J. Eur. Ceram. Soc.* 28, 2003–2010. doi: 10.1016/j.jeurceramsoc.2008.02.002
- Matjie, R. H., Mdeleeni, M. M., and Scurrall, M. S. (2003). Extraction of cobalt (II) from an ammonium nitrate-containing leach liquor by an ammonium salt of di (2-ethylhexyl) phosphoric acid. *Miner. Eng.* 16, 1013–1017. doi: 10.1016/S0892-6875(03)00265-6
- Meng, K., Gao, S., Wu, L., Wang, G., Liu, X., Chen, G., et al. (2016). Two-dimensional organic-inorganic hybrid perovskite photonic films. *Nano Lett.* 16, 4166–4173. doi: 10.1021/acs.nanolett.6b01046
- Merino, M. C. G., Estrella, A. L., Rodriguez, M. E., and Vázquez, P. (2015). Combustion syntheses of CoAl₂O₄ powders using different fuels. *Prog. Mater. Sci.* 8, 519–525. doi: 10.1016/j.mspro.2015.04.104
- Mindru, I., Marinescu, G., Gingasu, D., Patron, L., Ghica, C., and Giurginca, M. (2010). Blue CoAl₂O₄ spinel via complexation method. *Mater. Chem. Phys.* 122, 491–497. doi: 10.1016/j.matchemphys.2010.03.032
- Mishra, A., Mehta, A., Sharma, M., and Basu, S. (2017). Enhanced heterogeneous photodegradation of VOC and dye using microwave synthesized TiO₂/Clay nanocomposites: a comparison study of different type of clays. *J. Alloy. Compd.* 694, 574–580. doi: 10.1016/j.jallcom.2016.10.036
- Mousavand, T., Takami, S., Umetsu, M., Ohara, S., and Adschiri, T. (2006). Supercritical hydrothermal synthesis of organic-inorganic hybrid nanoparticles. *J. Mater. Sci.* 41, 1445–1448. doi: 10.1007/s10853-006-7458-y
- Mu, B., and Wang, A. Q. (2015). One-pot fabrication of multifunctional superparamagnetic attapulgite/Fe₃O₄/polyaniline nanocomposites served as adsorbent and catalyst support. *J. Mater. Chem. A* 3, 281–289. doi: 10.1039/C4TA05367B
- Mu, B., Wang, Q., and Wang, A. Q. (2015). Effect of different clay minerals and calcination temperature on the morphology and color of clay/CoAl₂O₄ hybrid pigments. *RSC Adv.* 5, 102674–102681. doi: 10.1039/C5RA19955G
- Ouahdi, N., Guillemet, S., Demai, J. J., Durand, B., Er Rakhho, L., Moussa, R., et al. (2005). Investigation of the reactivity of AlCl₃ and CoCl₂ toward molten alkali-metal nitrates in order to synthesize CoAl₂O₄. *Mater. Lett.* 59, 334–340. doi: 10.1016/j.matlet.2004.10.013
- Panda, A. K., Mishra, B. G., Mishra, D. K., and Singha, R. K. (2010). Effect of sulphuric acid treatment on the physico-chemical characteristics of kaolin clay. *Colloid Surf. A Physicochem. Eng. Asp.* 363, 98–104. doi: 10.1016/j.colsurfa.2010.04.022
- Philip, A., Lihavainen, J., Keinänen, M., and Pakkanen, T. T. (2017). Gold nanoparticle decorated halloysite nanotubes-selective catalysts for benzyl alcohol oxidation. *Appl. Clay Sci.* 143, 80–88. doi: 10.1016/j.clay.2017.03.015
- Rani, G. (2017). Annealing effect on the structural, optical and thermoluminescent properties of ZnAl₂O₄:Cr³⁺. *Powder Technol.* 312, 354–359. doi: 10.1016/j.powtec.2017.02.040
- Ren, Z., Botu, V., Wang, S., Meng, Y., Song, W., Guo, Y., et al. (2014). Monolithically integrated spinel M_xCo_{3-x}O₄ (M=Co, Ni, Zn) nanoarray catalysts: scalable synthesis and cation manipulation for tunable low-temperature CH₄ and CO oxidation. *Angew. Chem. Int. Edit.* 53, 7223–7227. doi: 10.1002/anie.201403461
- Ribeiro, M. J., Tulyagavov, D. U., Ferreira, J. M., and Labrincha, J. A. (2005). High temperature mullite dissolution in ceramic bodies derived from Al-rich sludge. *J. Eur. Ceram. Soc.* 25, 703–710. doi: 10.1016/j.jeurceramsoc.2004.03.028
- Ryu, Y. C., Kim, T. G., Seo, G., Park, J. H., Suh, C. S., Park, S., et al. (2008). Effect of substrate on the phase transformation of TiO₂ in pearlescent pigment. *J. Ind. Eng. Chem.* 14, 213–218. doi: 10.1016/j.jiec.2007.11.004
- Saikia, B. J., and Parthasarathy, G. (2010). Fourier transform infrared spectroscopic characterization of kaolinite from Assam and Meghalaya, Northeastern India. *J. Mod. Phys.* 1, 206–210. doi: 10.4236/jmp.2010.14031

- Salavati-Niasari, M., Khansari, A., and Davar, F. (2009). Synthesis and characterization of Co₃O₄ nanoparticles by thermal treatment process. *J. Clust. Sci.* 362, 4937–4942. doi: 10.1016/j.jca.2009.07.023
- Sale, S. (2015). Relationship between gel rheology and specific surface area of nano-sized CoAl₂O₄ powder manufactured by autoignition technique. *Mater. Lett.* 139, 498–500. doi: 10.1016/j.matlet.2014.10.118
- Sedghi, A., Alimohammadi, M., and Zadeh, M. C. (2014). Structure and properties of Co_xZn_{1-x}Al₂O₄ nano-pigments fabricated by gel combustion method. *Ceram. Silikáty* 58, 145–150.
- Soleimani-Gorgania, A., Ghaharib, M., and Peymannia, M. (2015). *In-situ* production of nano-CoAl₂O₄ on a ceramic surface by ink-jet printing. *J. Eur. Ceram. Soc.* 35, 779–786. doi: 10.1016/j.jeurceramsoc.2014.08.047
- Tang, W. X., Ren, Z., Lu, X. X., Wang, S. B., Guo, Y. B., Hoang, S., et al. (2017). Scalable integration of highly uniform Mn_xCo_{3-x}O₄ nano-sheet array onto ceramic monolithic substrates for low temperature propane oxidation. *ChemCatChem* 9, 4112–4119. doi: 10.1002/cctc.201700795
- Tang, Y., Wu, C., Song, Y., Zheng, Y., and Zhao, K. (2018). Effects of colouration mechanism and stability of CoAl₂O₄ ceramic pigments sintered on substrates. *Ceram. Int.* 44, 1019–1025. doi: 10.1016/j.ceramint.2017.10.038
- Tian, G. Y., Wang, W. B., Wang, D. D., Wang, Q., and Wang, A. Q. (2017). Novel environment friendly inorganic red pigments based on attapulgite. *Powder Technol.* 315, 60–67. doi: 10.1016/j.powtec.2017.03.044
- Tielens, F., Calatayud, M., Franco, R., Recio, J. M., Pérez-Ramírez, J., and Minot, C. (2009). Theoretical investigation of the inversion parameter in Co_{3-s}Al_sO₄ (s = 0–3) spinel structures. *Solid State Ionics* 180, 1011–1016. doi: 10.1016/j.ssi.2009.03.023
- Tirsoaga, A., Visinescu, D., Jurca, B., Ianculescu, A., and Carp, O. (2011). Eco-friendly combustion-based synthesis of metal aluminates MAl₂O₄ (M = Ni, Co). *J. Nanopart. Res.* 13, 6397–6408. doi: 10.1007/s11051-011-0392-1
- Todorova, N., Giannakopoulou, T., Karapati, S., Petridis, D., Vaimakis, T., and Trapalis, C. (2014). Composite TiO₂/clays materials for photocatalytic NO_x oxidation. *Appl. Surf. Sci.* 319, 113–120. doi: 10.1016/j.apsusc.2014.07.020
- Torkian, L., Daghighi, M., and Boorboor, Z. (2013). Simple and efficient route for synthesis of spinel nanopigments. *J. Chem.* 2013, 1–6. doi: 10.1155/2013/694531
- Vesely, D., Kalendova, A., and Kalenda, P. A. (2010). Study of diatomite and calcined kaoline properties in anticorrosion protective coatings. *Prog. Org. Coat.* 68, 173–179. doi: 10.1016/j.porgcoat.2010.02.007
- Wang, C., Liu, S. M., Liu, L. H., and Bai, X. (2006). Synthesis of cobalt-aluminate spinels via glycine chelated precursors. *Mater. Chem. Phys.* 96, 361–370. doi: 10.1016/j.matchemphys.2005.07.066
- Wang, G. F., Wang, S., Sun, W., Sun, Z. M., and Zheng, S. L. (2016). Synthesis of a novel illite@carbon nanocomposite adsorbent for removal of Cr (VI) from wastewater. *J. Environ. Sci.* 57, 62–71. doi: 10.1016/j.jes.2016.10.017
- Wang, R. J., Jiang, G. H., Ding, Y. W., Wang, Y., Sun, X. K., Wang, X. H., et al. (2011). Photocatalytic activity of heterostructures based on TiO₂ and halloysite nanotubes. *Appl. Mater. Inter.* 3, 4154–4158. doi: 10.1021/am201020q
- Wu, J. F., Hu, C., Xu, X. H., and Zhang, Y. F. (2017). Preparation and performance study of Mullite/Al₂O₃ composite ceramics for solar thermal transmission pipeline. *Int. J. Appl. Ceram. Tec.* 13, 1017–1023. doi: 10.1111/ijac.12584
- Xu, X. H., Li, J. W., Wu, J. F., Tang, Z. H., Chen, L. L., Li, Y., et al. (2017). Preparation and thermal shock resistance of corundum-mullite composite ceramics from andalusite. *Ceram. Int.* 43, 1762–1767. doi: 10.1016/j.ceramint.2016.10.116
- Xu, X. H., Qin, X. F., Jiang, F. X., Li, X. L., Chen, Y., and Gehring, G. A. (2008). The dopant concentration and annealing temperature dependence of ferromagnetism in Co-doped ZnO thin films. *Appl. Surf. Sci.* 254, 4956–4960. doi: 10.1016/j.apsusc.2008.01.164
- Yeo, C. H. (2011). *Stability and Collapse Mechanisms of Unreinforced and Forepole-Reinforced Tunnel Headings*. Ph.D. thesis, National University of Singapore, Singapore.
- Yoneda, M., Gotoh, K., Nakanishi, M., Fujii, T., and Nomura, T. (2016). Influence of aluminum source on the color tone of cobalt blue pigment. *Powder Technol.* 323, 574–580. doi: 10.1016/j.powtec.2016.06.021
- Yu, F., Yang, J., Ma, J., Du, J., and Zhou, Y. Q. (2009). Preparation of nanosized CoAl₂O₄ powders by sol-gel and sol-gel-hydrothermal methods. *J. Alloy. Compd.* 468, 443–446. doi: 10.1016/j.jallcom.2008.01.018
- Yuan, L., Ma, B. Y., Zhu, Q., Zhang, X. D., Zhang, H., and Yu, J. K. (2017). Preparation and properties of mullite-bonded porous fibrous mullite ceramics by an epoxy resin gel-casting process. *Ceram. Int.* 43, 5478–5483. doi: 10.1016/j.ceramint.2017.01.062
- Zayat, M., and Levy, D. (2000). Blue CoAl₂O₄ particles prepared by the sol-gel and citrate-gel methods. *Chem. Mater.* 12, 2763–2769. doi: 10.1021/cm001061z
- Zhang, A. J., Mu, B., Li, H. M., An, X. C., and Wang, A. Q. (2018). Cobalt blue hybrid pigment doped with magnesium derived from sepiolite. *Appl. Clay Sci.* 157, 111–120. doi: 10.1016/j.clay.2018.02.032
- Zhang, A. J., Mu, B., and Wang, A. Q. (2017). Bright blue halloysite/CoAl₂O₄ hybrid pigments: preparation, characterization and application in water-based painting. *Dyes Pigments* 139, 473–481. doi: 10.1016/j.dyepig.2016.12.055
- Zhang, Y., Wang, W. B., Mu, B., Wang, Q., and Wang, A. Q. (2015). Effect of grinding time on fabricating a stable methylene blue/palygorskite hybrid nanocomposite. *Powder Technol.* 280, 173–179. doi: 10.1016/j.powtec.2015.04.046
- Zheng, Q. M., Liu, Q. F., Shen, Q., Wu, Z. G., and Zhang, Y. M. (2011). The mineralogical characteristics and genesis of the dickite in Taiyuan formation in Southeastern Shanxi. *Proc. Eng.* 26, 898–901. doi: 10.1016/j.proeng.2011.11.2253
- Zhong, Z. Y., Mastai, Y., Koltypin, Y., Zhao, Y. M., and Gedanken, A. (1999). Sonochemical coating of nanosized nickel on alumina microspheres and the interaction between the nickel and nickel oxide with the substrate. *Chem. Mater.* 11, 2350–2359. doi: 10.1021/cm981005m
- Zou, J., and Zheng, W. (2016). TiO₂@CoTiO₃ complex green pigments with low cobalt content and tunable color properties. *Ceram. Int.* 42, 8198–8205. doi: 10.1016/j.ceramint.2016.02.029

Conflict of Interest Statement: The authors declare that the research was conducted in the absence of any commercial or financial relationships that could be construed as a potential conflict of interest.

The reviewer SW and handling Editor declared their shared affiliation.

Copyright © 2018 Zhang, Mu, Wang, Wen and Wang. This is an open-access article distributed under the terms of the Creative Commons Attribution License (CC BY). The use, distribution or reproduction in other forums is permitted, provided the original author(s) and the copyright owner are credited and that the original publication in this journal is cited, in accordance with accepted academic practice. No use, distribution or reproduction is permitted which does not comply with these terms.



Fabrication of an AMC/MMT Fluorescence Composite for its Detection of Cr(VI) in Water

Yanke Wei¹, Lefu Mei^{1*}, Rui Li², Meng Liu¹, Guocheng Lv^{1*}, Jianle Weng¹, Libing Liao^{1*}, Zhaohui Li^{1,3} and Lin Lu²

¹ Beijing Key Laboratory of Materials Utilization of Nonmetallic Minerals and Solid Wastes, National Laboratory of Mineral Materials, School of Materials Science and Technology, China University of Geosciences, Beijing, China, ² State Grid Corporation of China, Beijing, China, ³ Geosciences Department, University of Wisconsin—Parkside, Kenosha, WI, United States

OPEN ACCESS

Edited by:

Wenbo Wang,
Lanzhou Institute of Chemical Physics
(CAS), China

Reviewed by:

Liang Bian,
Southwest University of Science and
Technology, China
Runliang Zhu,
Guangzhou Institute of Geochemistry
(CAS), China

*Correspondence:

Lefu Mei
mlf@cugb.edu.cn
Guocheng Lv
guochenglv@cugb.edu.cn
Libing Liao
clayl@cugb.edu.cn

Specialty section:

This article was submitted to
Green and Sustainable Chemistry,
a section of the journal
Frontiers in Chemistry

Received: 07 June 2018

Accepted: 30 July 2018

Published: 21 August 2018

Citation:

Wei Y, Mei L, Li R, Liu M, Lv G,
Weng J, Liao L, Li Z and Lu L (2018)
Fabrication of an AMC/MMT
Fluorescence Composite for its
Detection of Cr(VI) in Water.
Front. Chem. 6:367.
doi: 10.3389/fchem.2018.00367

Hexavalent chromium species, Cr(VI), which can activate teratogenic processes, disturb DNA synthesis and induce mutagenic changes resulting in malignant tumors. The detection and quantification of Cr(VI) is very necessary. One of the rapid and simple methods for contaminant analysis is fluorescence detection using organic dye molecules. Its application is limited owing to concentration quenching due to aggregation of fluorescent molecules. In this study, we successfully intercalated 7-amino-4-methylcoumarin (AMC) into the interlayer space of montmorillonite (MMT), significantly inhibited fluorescence quenching. Due to enhanced fluorescence property, the composite was fabricated into a film with chitosan to detect Cr(VI) in water. Cr(VI) can be detected in aqueous solution by instruments excellent, ranging from 0.005 to 100 mM with a detection limit of 5 μM.

Keywords: AMC/MMT composite, fluorescence, quenching, detection, hexavalent chromium

INTRODUCTION

Due to the high toxicity of heavy metals and bioaccumulation in human body through the food chain, will bring human health and environmental great issue. Cr is one of the most serious contaminants among various heavy metals (Soewu et al., 2014; Wu et al., 2015a; Širić et al., 2017). While Cr(III) is an essential micronutrient, Cr(VI) is toxic (Weibel et al., 2016). Cr(VI) is mainly produced by electroplating, leather tanning, and textile dyeing (Dehghani et al., 2016; Omorogie et al., 2016). Cr(VI) is the most virulent form (Miretzky and Cirelli, 2010) of Cr, which is a highly toxic agent and act as carcinogens, mutagens, and teratogens in biological systems (Hlihor et al., 2017; Mullick et al., 2017). The carcinogenic and toxicity of Cr(VI) is based on its oxidation states like the most transition metals (Yusof and Malek, 2009; Kumar et al., 2017). An effective, simple and low-cost method for detecting Cr(VI) is needed (Babu and Gupta, 2008; Wang G. et al., 2017). The classic methods for detecting Cr(VI) include electrochemical method, atomic absorption method and liquid chromatography (Anthemidis et al., 2002; De Ruiter et al., 2008). These methods are credible. However, the processes are complicated. Due to its sensitivity, fluorescence spectroscopy has become one of the most increasingly used techniques (Wang et al., 2015; Li and Wei, 2017). The sensors made of organic or inorganic materials show great promise in detection, lighting, and other application (Rao et al., 2014).

Montmorillonite is a typical phyllosilicate of the smectite group of clay minerals (Ismadji et al., 2016; Xu et al., 2016). It consists of two layers of silicon tetrahedron (T) and the middle layer of aluminum octahedron (O) (Bekri-Abbes and Srasra, 2016; Scholtzová et al., 2016; Wang W. et al., 2017). Because of the isomorphous replacement of Al^{3+} by Mg^{2+} and Fe^{2+} in the octahedral sites and Si^{4+} by Al^{3+} in the tetrahedral sites, TOT layers are negative electric charge, balanced by the cations such as Ca^{2+} and Na^{+} intercalate into the layers (Dominijanni and Manassero, 2012; Wu et al., 2016; Zhou et al., 2016). Luminescent materials of small organic molecules are easily modified and chemically purified to have wider emission spectrum coverage (Wu et al., 2015b; Tian et al., 2017). However, when they are applied in solid devices, stabilize and enhance their luminous intensity is crucial. Although several methods of assembling materials have been developed (Zhang et al., 2005), they often suffer from phase separation, agminated organic small molecules (Wei et al., 2016; De Sa et al., 2017). Clay minerals were rarely used as base materials for the organic-inorganic composite preparation for luminescence and fluorescence applications.

This research focused on the fabrication of a fluorescence material for Cr(VI) detection. To prevent quenching, the photoactive organic dye AMC was interposed into the interlining of MMT for maximal dye separation and minimum agminated (Yu et al., 2013, 2014). The AMC/MMT was fabricated in a film with chitosan. Quenching of fluorescence was used various solutions to be evaluated. The response of AMC/MMT composites in Cr(VI) was excellent, ranging from 0.005 to 100 mM.

MATERIALS AND METHODS

Materials

The montmorillonite was bought from Ningcheng, Inner Mongolia, China. Its CEC (Cation Exchange Capacity) was 9.8 $mmol_c/10g$ which used Na^{+} as the staple commutable cation

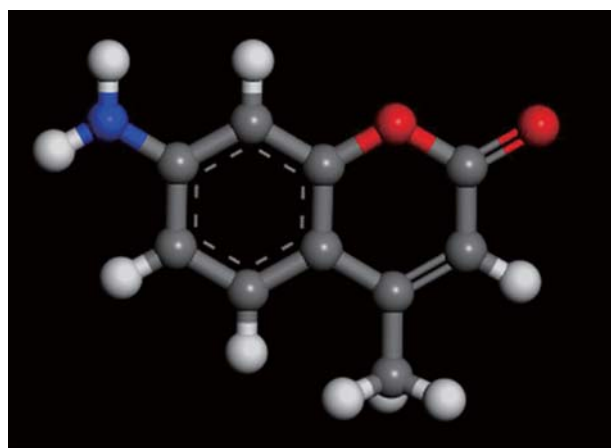


FIGURE 1 | Molecular structure of AMC studied. The all strains, C, gray; N, blue; O, red; H, white.

exchange. The specific external surface area was 78 m^2/g . AMC was purchased from Aladdin. The molecular structure (Nowakowska et al., 2001) of AMC is presented in **Figure 1**. The potassium dichromate Cr(VI), chitosan, and other reagents were purchased from various manufactures that were all of analytical grade. Deionized water was used as a solvent.

Preparation of AMC/MMT

The effect of initial AMC concentrations on a performance of fluorescence were tested, 50 mL the original concentrations of AMC in water for 20, 50, 100, 200, 500, and 800 mg/L were blended with 0.25 g of MMT in every 100 mL centrifugal tube after shaking at 200 rotations per minute at indoor temperature for 8 h, respectively. The admixtures were centrifuged at 7,500 rotations per minute for 2 min. Afterwards, removing the supernatant, then at 60°C were dried the residues and pulverized the residues to powder as raw materials. This type of product was used for the AMC/MMT.

Preparation of the Chitosan Film (AMF) for Cr(VI) Detection in Water

The chitosan film was prepared as follows: 0.25 g chitosan, 8 mL 0.1 M NaOH solution, 0.1 g AMC/MMT powder and two drops of 1 g/mL Polyvinyl Alcohol (PVA) solution were appended. The

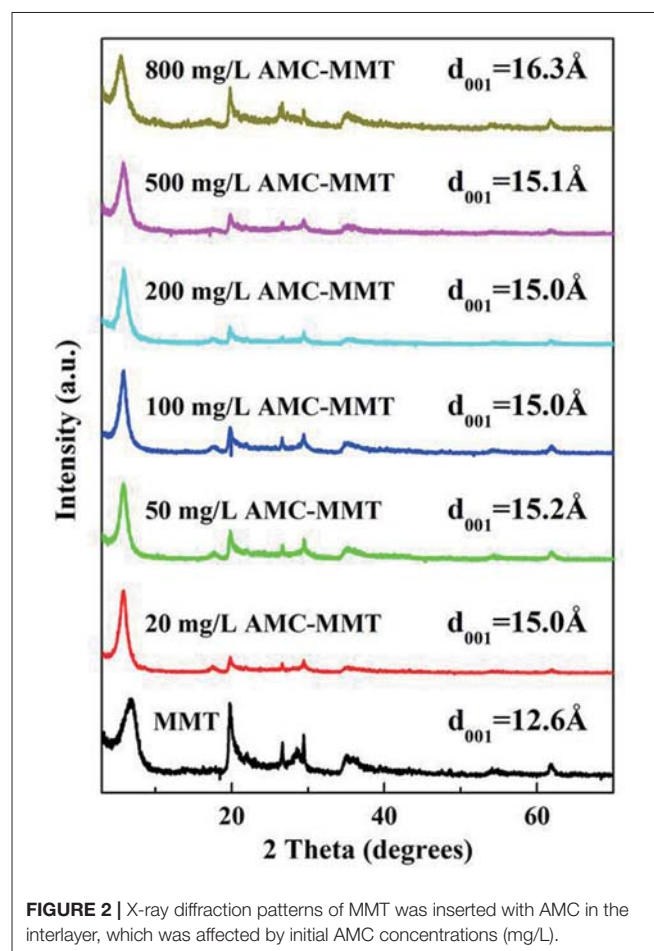


FIGURE 2 | X-ray diffraction patterns of MMT was inserted with AMC in the interlayer, which was affected by initial AMC concentrations (mg/L).

admixture was whipped for 30 min and then poured into a mold and air dried.

The followed solutions at a concentration of 0.1 M were originally screened for quenching of fluorescence in AMF: Al^{3+} , Ca^{2+} , Ba^{2+} , Cr(VI) , CTAB, K^+ , Na^+ , Ni^{3+} , Pb^{2+} , Fe^{3+} , Imidazole, $\text{C}_2\text{H}_5\text{OH}$. Afterwards, they were dropped onto the AMF. Then, the fluorescence degrees were measured using a fluorescence spectrophotometer (Hitachi, F4600).

In order to estimate the Cr(VI) range of response, different concentrations of Cr(VI) solution were dropped onto the AMF. The Cr(VI) of original concentrations were the ranged of $5\ \mu\text{M}$ to 100 mM.

Pictures of the AMF after in contact with Cr(VI) solutions were already obvious demonstration quenching of fluorescence effect by Cr(VI) and then measure the florescence intensions of AMF by fluorescence spectrophotometer (Hitachi, F4600).

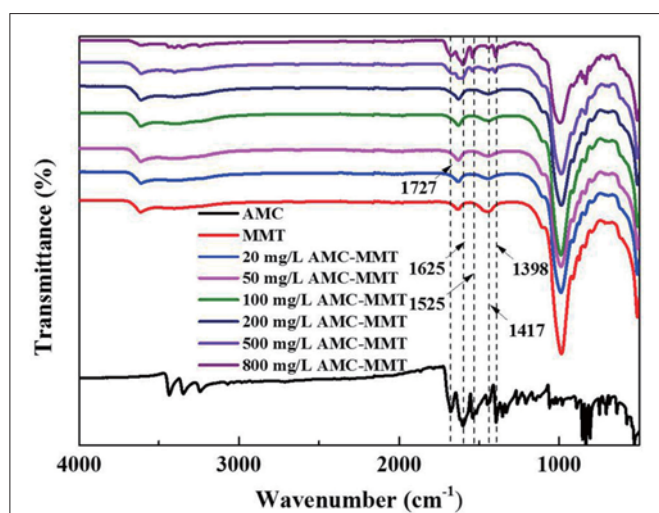


FIGURE 3 | FTIR spectra of AMC, and MMT with different amounts of AMC adsorption.

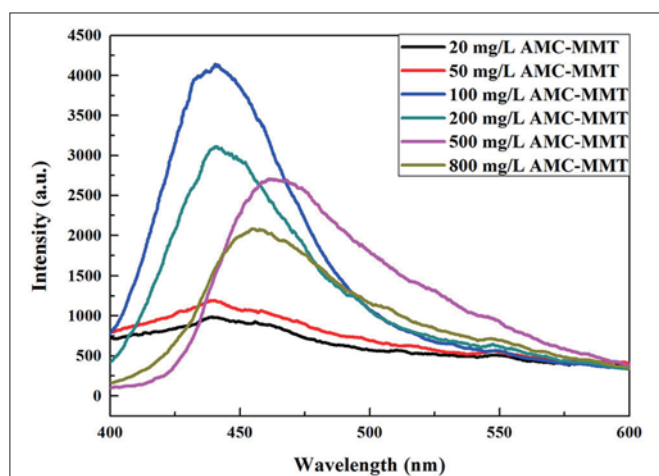


FIGURE 4 | Fluorescence spectra of AMC/MMT was Influenced by initial concentrations of AMC.

Instrumental Analyses

Powder X-Ray Diffraction (XRD) was performed by a Rigaku D/max-IIIa diffractometer (Tokyo, Japan) with a Ni-filtered Cu K α radiation at 40 kV and 40 mA. Prototypes were scanned the range of 3° to 70° at 8° per minute with a pace of 0.01° to research the particular changes in d_{001} separation distance of MMT as a function of original AMC concentrations. The changing of peak position proved the intercalation of AMC into the MMT was succeeded. The gallery heights were deduced from the (001) reflection of the composites using the Bragg's equation.

Fourier Transform Infrared Spectroscopy (FTIR) spectra were acquired on a Perkin Elmer Spectrum 100 Spectrometer. The spectra were obtained from $4,000$ to $500\ \text{cm}^{-1}$ by adding 256 scans in the resolution ratio of $4\ \text{cm}^{-1}$.

Photoluminescence emission (PL) spectrum was obtained on a fluorescence spectrophotometer (Hitachi, F4600) at the scope of 400–600 nm with a photomultiplier tube handled at 800 volt. A 150 watt xenon lamp was served as the pumping source, at an excitation wavelength of 340 nm (Zamojć et al., 2015). The emission and excitation slits size were 5 nm and scan speed was setting at 240 nm per min.

Molecular mimicry was performed at the standard module “Forcite” of Materials Studio 6.0 software to research the structure of AMC in the interval of MMT. The unit lattice parameters were setted at $a = 1.55\ \text{nm}$, $b = 1.79\ \text{nm}$, $c = 1.25\ \text{nm}$, $\alpha = \gamma = 90^\circ$, and $\beta = 99^\circ$. A suite of $2 \times 2 \times 1$ supercells were constructed of the interlayer spacing setting at 1.63 nm. Every circulation consisted of 10^6 steps, repeating three cycles.

RESULTS AND DISCUSSION

The MMT Was Intercalated With AMC

The idea that interlayer cation was Na^+ with a monolayer hydration was confirmed because the d_{001} value of pure MMT was $12.6\ \text{Å}$. The d_{001} spacing progressively increased from 12.6 to $16.3\ \text{Å}$ with the initial AMC concentration increased (Figure 2),

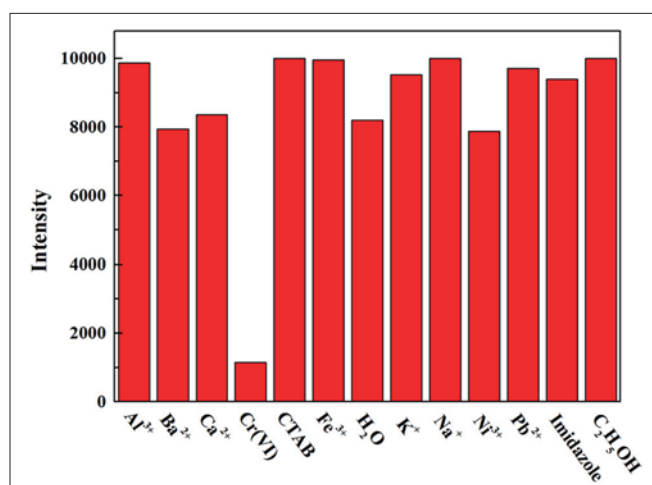
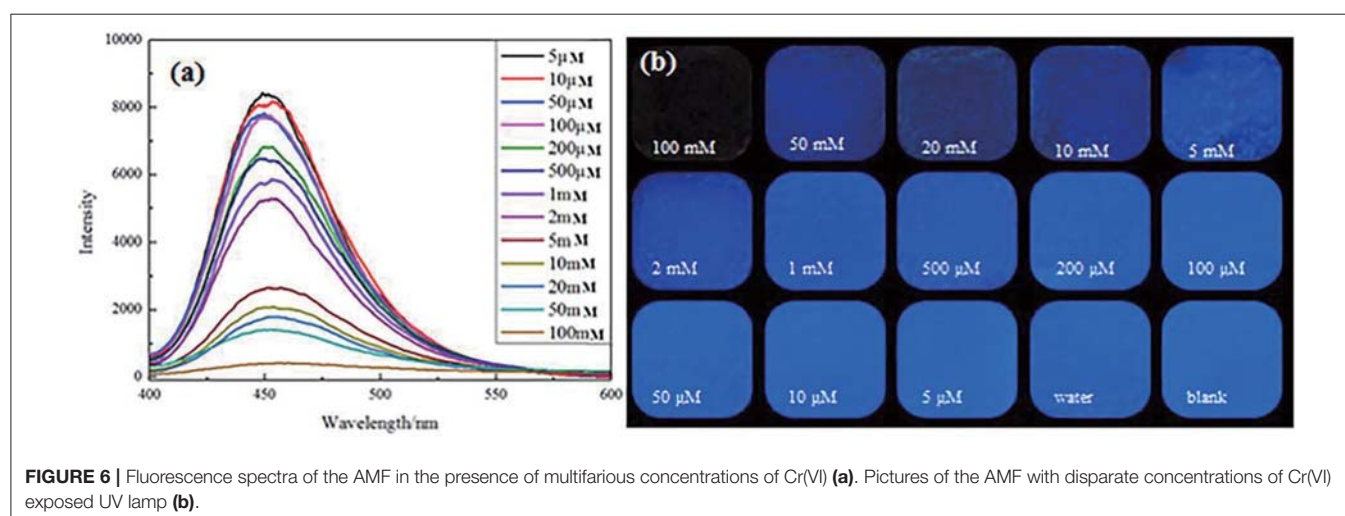


FIGURE 5 | Fluorescence intensity of the AMF in response to a variety of aqueous solutions at a concentration of 0.1 M.



suggesting AMC molecules insert the portion between the interlayer space of MMT.

FTIR Spectra of AMC/MMT

FTIR spectra of MMT adsorbed with different amounts of AMC displayed both bands of raw MMT and AMC (Figure 3). The bands between 1,400 and 1,650 cm^{-1} were allocated to C-C stretching vibrations in aromatic and hetero aromatic compounds (Talbi et al., 1998; Krishnakumar and Xavier, 2005). Therefore, the bands observed at 1,727, 1,695, 1,625, 1,566, 1,525, 1,475, 1,446, 1,417, 1,398, 1,390 cm^{-1} in FTIR spectra were allocated to C-C stretching vibrations of AMC (Arivazhagana et al., 2010). The characteristic peaks of AMC appeared in FTIR spectra of AMC/MMT, as shown in the dotted line (Figure 3), indicating that AMC had been loaded onto MMT.

Luminescence Properties of AMC/MMT

AMC powder was hardly used as a luminescent material just because the lack of strong luminescence (Wang et al., 2012), causing by concentration quenching (Wu et al., 2015b). The luminous intensity increased significantly after the intercalation of AMC into the interlayer of MMT, which reason was AMC was uniformly dispersed on MMT, inhibiting its aggregation. The highest spectral intensity was found by AMC/MMT at 100 mg/L, which was an initial concentration (Figure 4).

The Fluorescent Detection of Cr(VI) in Aqueous Phase by AMF

The AMF was screened for response to various solutes (Figure 5). The fluorescence response to Cr(VI) was very significant when the test solute with an initial concentration of 0.1 M, while others were not obvious, indicating the high selectivity of AMF for Cr(VI).

The mechanism of photoluminescence (PL) quenching of AFM was further investigated when the aqueous solution contains Cr(VI). Most importantly, an apparent decrease

in fluorescence intensity was observed while the Cr(VI) concentration was increasing over the whole concentration ranges from 0.005 to 100 mM (Figure 6a). A full PL quenching process can be observed visually at a Cr(VI) concentration of 1 mM. The images of AMF with addition of Cr(VI) that exposed ultraviolet light showed a consistent tendency (Figure 6b).

Mechanism Analysis

Molecular mimicry was performed at the standard module “Forcite” of Materials Studio 6.0 software to research the structure of AMC between the interval of MMT. The interlayer spacing of MMT was directly influenced by the interlayer arrangement of AMC and the amount of AMC intercalation, this, on the other hand, would play an significant role in understanding the system structure and interaction forces (Krauss et al., 2011; Wang et al., 2011; Tournassat et al., 2016). The interlayer condition of AMC interpolation MMT with different quantities was qualitatively simulated, and the initial states were represented by a, c, and e; and b, d, and f represent the states after simulation (a stands for low concentration; c stands for medium concentration; and e stands for higher concentration; Figure 7). The concentration quenching could be effectively avoid by AMC intercalation MMT and it could also significantly improve luminous intensity, lifespan, and stability notably owing to the stronger interaction forces between AMC molecules and MMT sheet (Yan et al., 2010a,b; Liu et al., 2014).

CONCLUSIONS

In this research, an organic dye (AMC) was resoundingly intercalated into the interlayer space of MMT, resulting in observably inhibition in quenching of fluorescence. The composite was fabricated into a film with chitosan to detect Cr(VI) in water with its enhanced fluorescent property. Cr(VI) can be detected in aqueous solution by instruments

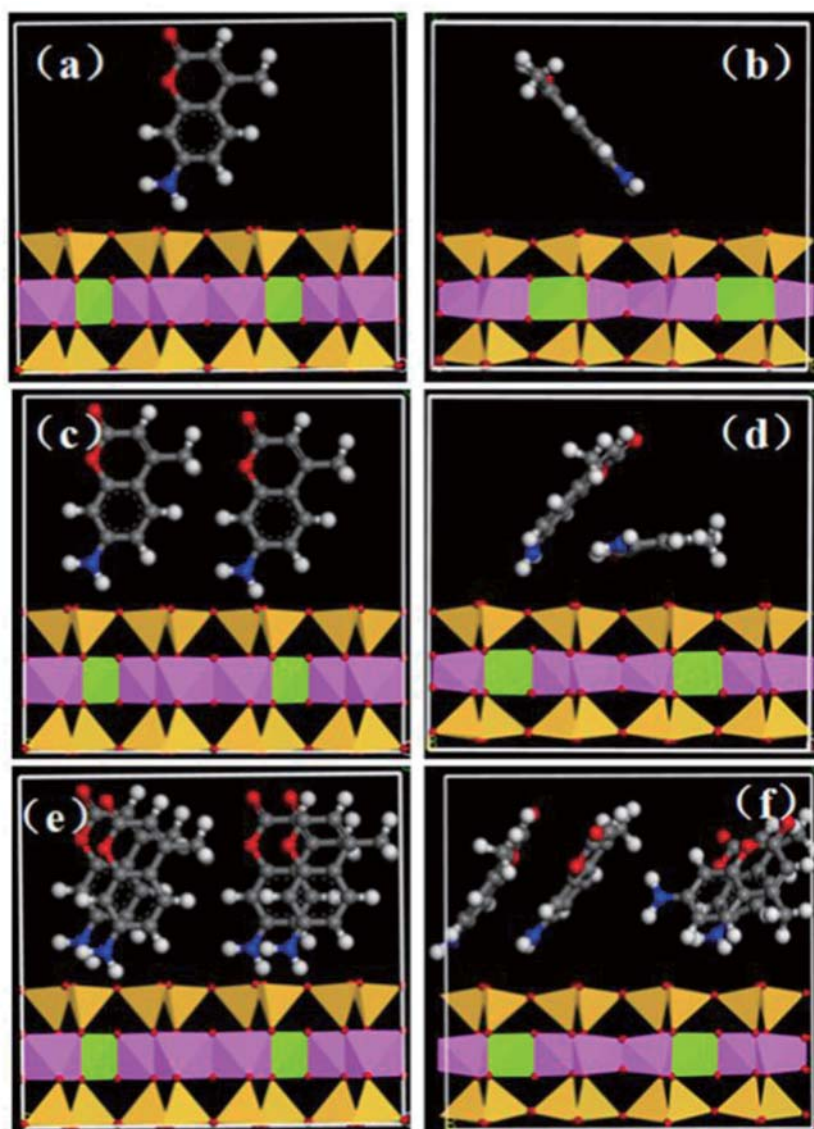


FIGURE 7 | Dynamic simulation of molecular interposition AMC into MMT at a different angle on account of the electric density and AMC loading distinction. The initial states were represented by **a**, **c**, and **e**; and **b**, **d**, and **f** represent the states after simulation: **a** stands for low concentration, **c** stands for medium concentration and **e** stands for higher concentration. The all strains, Mg, green; Al, pink; Si, yellow; C, gray; N, blue; O, red; H, white.

ranging from 0.005 to 100 mM with a detection limit of $5 \mu\text{M}$.

AUTHOR CONTRIBUTIONS

YW and LM conceived the project. LM, GL, and LibL designed and performed the experiments. RL, ML, JW, and LinL analyzed the data. YW, ZL, and LM wrote the manuscript.

FUNDING

This research was supported by National Natural Science Foundation of China (grant number: 51604248), the National Key R&D Program of China (grant number: 2017YFB0310704), and Fundamental Research Funds for the Central Universities (grant numbers: 2652017335, 2652017338 and 2652017366).

REFERENCES

- Anthemidis, A. N., Zachariadis, G. A., Kougoulis, J. S., and Stratis, J. A. (2002). Flame atomic absorption spectrometric determination of chromium (VI) by on-line preconcentration system using a PTFE packed column. *Talanta* 57, 15–22. doi: 10.1016/S0039-9140(01)00676-2
- Arivazhagana, M., Sambathkumar, K., and Jeyavijayanc, S. (2010). Density functional theory study of FTIR and FT-Raman spectra of 7-acetoxy-4-methyl coumarin. *Indian J. Pure Appl. Phys.* 48, 716–722. doi: 10.13140/RG.2.1.4538.7361
- Babu, B. V., and Gupta, S. (2008). Adsorption of Cr (VI) using activated neem leaves: kinetic studies. *Adsorption* 14, 85–92. doi: 10.1007/s10450-007-9057-x
- Bekri-Abbes, I., and Srasra, E. (2016). Effect of mechanochemical treatment on structure and electrical properties of montmorillonite. *J. Alloys Compd.* 671, 34–42. doi: 10.1016/j.jallcom.2016.02.048
- De Rooter, G., Gupta, T., and Van Der Boom, M. E. (2008). Selective optical recognition and quantification of parts per million levels of Cr⁶⁺ in aqueous and organic media by immobilized polypyridyl complexes on glass. *J. Am. Chem. Soc.* 130, 2744–2745. doi: 10.1021/ja7110527
- De Sa, A., Moura, I., Abreu, A. S., Oliveira, M., Ferreira, M. F., and Machado, A. V. (2017). High fluorescent water soluble CdTe quantum dots—a promising system for light harvesting applications. *J. Nanopart. Res.* 19:180. doi: 10.1007/s11051-017-3872-0
- Dehghani, M. H., Sanaei, D., Ali, I., and Bhatnagar, A. (2016). Removal of chromium (VI) from aqueous solution using treated waste newspaper as a low-cost adsorbent: kinetic modeling and isotherm studies. *J. Mol. Liq.* 215, 671–679. doi: 10.1016/j.molliq.2015.12.057
- Dominijanni, A., and Manassero, M. (2012). Modelling the swelling and osmotic properties of clay soils. Part II: the physical approach. *Int. J. Eng. Sci.* 51, 51–73. doi: 10.1016/j.ijengsci.2011.11.001
- Hlihor, R. M., Figueiredo, H., Tavares, T., and Gavrilescu, M. (2017). Biosorption potential of dead and living *Arthrobacter viscosus* biomass in the removal of Cr (VI): batch and column studies. *Process Safe. Environ. Prot.* 108, 44–56. doi: 10.1016/j.psep.2016.06.016
- Ismadji, S., Tong, D. S., Soetaredjo, F. E., Ayucitra, A., Yu, W. H., and Zhou, C. H. (2016). Bentonite hydrochar composite for removal of ammonium from Koi fish tank. *Appl. Clay Sci.* 119, 146–154. doi: 10.1016/j.clay.2015.08.022
- Kraus, T. N., Barrera, E., Lohmüller, T., Spatz, J. P., and Dosch, H. (2011). Growth mechanisms of phthalocyanine nanowires induced by Au nanoparticle templates. *Phys. Chem. Chem. Phys.* 13, 5940–5944. doi: 10.1039/C0CP02191A
- Krishnakumar, V., and Xavier, R. J. (2005). Density functional theory calculations and vibrational spectra of 3, 5-dibromopyridine and 3, 5-dichloro-2, 4, 6-trifluoropyridine. *Spectrochim. Acta Part A Mol. Biomol. Spectrosc.* 61, 253–260. doi: 10.1016/j.saa.2004.03.038
- Kumar, R., Kim, S. J., Kim, K. H., Lee, S. H., Park, H. S., and Jeon, B. H. (2017). Removal of hazardous hexavalent chromium from aqueous phase using zirconium oxide-immobilized alginate beads. *Appl. Geochem.* 88, 113–121. doi: 10.1016/j.apgeochem.2017.04.002
- Li, C., and Wei, C. (2017). DNA-templated silver nanocluster as a label-free fluorescent probe for the highly sensitive and selective detection of mercury ions. *Sens. Actuat. B Chem.* 242, 563–568. doi: 10.1016/j.snb.2016.11.091
- Liu, M., Wang, T., Ma, H., Fu, Y., Hu, K., and Guan, C. (2014). Assembly of luminescent ordered multilayer thin-films based on oppositely-charged MMT and magnetic NiFe-LDHs nanosheets with ultra-long lifetimes. *Sci. Rep.* 4:7147. doi: 10.1038/srep07147
- Miretzky, P., and Cirelli, A. F. (2010). Cr (VI) and Cr (III) removal from aqueous solution by raw and modified lignocellulosic materials: a review. *J. Hazard. Mater.* 180, 1–19. doi: 10.1016/j.jhazmat.2010.04.060
- Mullick, A., Moullick, S., and Bhattacharjee, S. (2017). Removal of hexavalent chromium from aqueous solutions by low-cost rice husk-based activated carbon: kinetic and thermodynamic studies. *Indian Chem. Eng.* 60, 58–71. doi: 10.1080/00194506.2017.1288173
- Nowakowska, M., Smoluch, M., and Sendor, D. (2001). The effect of cyclodextrins on the photochemical stability of 7-amino-4-methylcoumarin in aqueous solution. *J. Incl. Phenom. Macrocycl. Chem.* 40, 213–219. doi: 10.1023/A:1011820513256
- Omorogie, M. O., Babalola, J. O., Unuabonah, E. I., Song, W., and Gong, J. R. (2016). Efficient chromium abstraction from aqueous solution using a low-cost biosorbent: *nauclea diderrichii* seed biomass waste. *J. Saudi Chem. Soc.* 20, 49–57. doi: 10.1016/j.jscs.2012.09.017
- Rao, K. V., Jain, A., and George, S. J. (2014). Organic-inorganic light-harvesting scaffolds for luminescent hybrids. *J. Mater. Chem. C* 2, 3055–3064. doi: 10.1039/C3TC31729C
- Scholtzová, E., Madejová, J., and Tunega, D. (2016). Structural and spectroscopic characterization of montmorillonite intercalated with n-butylammonium cations (n= 1–4)—Modeling and experimental study. *Clays Clay Miner.* 64, 401–412. doi: 10.1346/CCMN.2016.0640404
- Širić, I., Kasap, A., Bedeković, D., and Falandysz, J. (2017). Lead, cadmium and mercury contents and bioaccumulation potential of wild edible saprophytic and ectomycorrhizal mushrooms, Croatia. *J. Environ. Health Part B* 52, 156–165. doi: 10.1080/03601234.2017.1261538
- Soewu, D. A., Agbolade, O. M., Oladunjoye, R. Y., and Ayodele, I. A. (2014). Bioaccumulation of heavy metals in cane rat (*Thryonomys swinderianus*) in Ogun State, Nigeria. *J. Toxicol. Environ. Health Sci.* 6, 154–160. doi: 10.5897/JTEHS2014.0310
- Talbi, H., Humbert, B., and Billaud, D. (1998). FTIR and Raman spectroscopic investigations on the redox behaviour of poly (5-cyanoindole) in acidic aqueous solutions. *Spectrochim. Acta A Mol. Biomol. Spectr.* 54, 1879–1893. doi: 10.1016/S1386-1425(98)00146-2
- Tian, G., Wang, W., Wang, D., Wang, Q., and Wang, A. (2017). Novel environment friendly inorganic red pigments based on attapulgite. *Powder Technol.* 315, 60–67. doi: 10.1016/j.powtec.2017.03.044
- Tournassat, C., Bourg, I. C., Holmboe, M., Sposito, G., and Steefel, C. I. (2016). Molecular dynamics simulations of anion exclusion in clay interlayer nanopores. *Clays Clay Miner.* 64, 374–388. doi: 10.1346/CCMN.2016.0640403
- Wang, F. X., Liu, Y. D., and Pan, G. B. (2011). Vapor growth and photoconductivity of single-crystal nickel-phthalocyanine nanorods. *Mater. Lett.* 65, 933–936. doi: 10.1016/j.matlet.2010.12.012
- Wang, G., Wang, S., Sun, W., Sun, Z., and Zheng, S. (2017). Synthesis of a novel illite@ carbon nanocomposite adsorbent for removal of Cr (VI) from wastewater. *J. Environ. Sci.* 57, 62–71. doi: 10.1016/j.jes.2016.10.017
- Wang, J., Hu, Y., Deng, R., Xu, W., Liu, S., Liang, R., et al. (2012). Construction of multifunctional photonic crystal microcapsules with tunable shell structures by combining microfluidic and controlled photopolymerization. *Lab. Chip* 12, 2795–2798. doi: 10.1039/C2LC40419B
- Wang, M., He, L., Xu, W., Wang, X., and Yin, Y. (2015). Magnetic assembly and field-tuning of ellipsoidal-nanoparticle-based colloidal photonic crystals. *Angew. Chem. Int. Edn.* 54, 7077–7081. doi: 10.1002/anie.201501782
- Wang, W., Tian, G., Zong, L., Zhou, Y., Kang, Y., Wang, Q., et al. (2017). From illite/smectite clay to mesoporous silicate adsorbent for efficient removal of chlortetracycline from water. *J. Environ. Sci.* 51, 31–43. doi: 10.1016/j.jes.2016.09.008
- Wei, X., Hao, T., Xu, Y., Lu, K., Li, H., Yan, Y., et al. (2016). Facile polymerizable surfactant inspired synthesis of fluorescent molecularly imprinted composite sensor via aqueous CdTe quantum dots for highly selective detection of λ -cyhalothrin. *Sens. Actuat. B Chem.* 224, 315–324. doi: 10.1016/j.snb.2015.10.048
- Weibel, G., Waber, H. N., Eggenberger, U., and Mäder, U. K. (2016). Influence of sample matrix on the alkaline extraction of Cr (VI) in soils and industrial materials. *Environ. Earth Sci.* 75:548. doi: 10.1007/s12665-015-5236-3
- Wu, L., Liao, L., Lv, G., and Qin, F. (2015a). Stability and pH-independence of nano-zero-valent iron intercalated montmorillonite and its application on Cr (VI) removal. *J. Contam. Hydrol.* 179, 1–9. doi: 10.1016/j.jconhyd.2015.05.001
- Wu, L., Lv, G., Liu, M., Li, Z., Liao, L., and Pan, C. (2015b). Adjusting the layer charges of host phyllosilicates to prevent luminescence

- quenching of fluorescence dyes. *J. Phys. Chem. C* 119, 22625–22631. doi: 10.1021/acs.jpcc.5b07243
- Wu, L. M., Tong, D. S., Li, C. S., Ji, S. F., Lin, C. X., Yang, H. M., et al. (2016). Insight into formation of montmorillonite-hydrochar nanocomposite under hydrothermal conditions. *Appl. Clay Sci.* 119, 116–125. doi: 10.1016/j.clay.2015.06.015
- Xu, W., Mu, B., and Wang, A. (2016). From adsorbents to electrode materials: facile hydrothermal synthesis of montmorillonite/polyaniline/metal oxide (hydroxide) composites. *New J. Chem.* 40, 2687–2695. doi: 10.1039/C5NJ03734D
- Yan, D., Lu, J., Chen, L., Qin, S., Ma, J., Wei, M., et al. (2010a). A strategy to the ordered assembly of functional small cations with layered double hydroxides for luminescent ultra-thin films. *Chem. Commun.* 46, 5912–5914. doi: 10.1039/C0CC00522C
- Yan, D., Lu, J., Ma, J., Wei, M., Wang, X., Evans, D. G., et al. (2010b). Anionic poly (p-phenylenevinylene)/layered double hydroxide ordered ultrathin films with multiple quantum well structure: a combined experimental and theoretical study. *Langmuir* 26, 7007–7014. doi: 10.1021/la904228b
- Yu, W. H., Li, N., Tong, D. S., Zhou, C. H., Lin, C. X. C., and Xu, C. Y. (2013). Adsorption of proteins and nucleic acids on clay minerals and their interactions: a review. *Appl. Clay Sci.* 80–81, 443–452. doi: 10.1016/j.clay.2013.06.003
- Yu, W. H., Ren, Q. Q., Tong, D. S., Zhou, C. H., and Wang, H. (2014). Clean production of CTAB-montmorillonite: formation mechanism and swelling behavior in xylene. *Appl. Clay Sci.* 97–98, 222–234. doi: 10.1016/j.clay.2014.06.007
- Yusof, A. M., and Malek, N. A. (2009). Removal of Cr (VI) and As (V) from aqueous solutions by HDTMA-modified zeolite Y. *J. Hazard. Mater.* 162, 1019–1024. doi: 10.1016/j.jhazmat.2008.05.134
- Zamojć, K., Wiczak, W., Zaborowski, B., Jacewicz, D., and Chmurzynski, L. (2015). Fluorescence quenching of 7-amino-4-methylcoumarin by different TEMPO derivatives. *Spectrochim. Acta Part A Mol. Biomol. Spectrosc.* 136, 1875–1880. doi: 10.1016/j.saa.2014.10.102
- Zhang, H., Wang, C., Li, M., Ji, X., Zhang, J., and Yang, B. (2005). Fluorescent nanocrystal– polymer composites from aqueous nanocrystals: methods without ligand exchange. *Chem. Mater.* 17, 4783–4788. doi: 10.1021/cm050260l
- Zhou, C. H., Zhao, L. Z., Wang, A. Q., Chen, T. H., and He, H. P. (2016). Current fundamental and applied research into clay minerals in China. *Appl. Clay Sci.* 119, 3–7. doi: 10.1016/j.clay.2015.07.043

Conflict of Interest Statement: The authors declare that the research was conducted in the absence of any commercial or financial relationships that could be construed as a potential conflict of interest.

Copyright © 2018 Wei, Mei, Li, Liu, Lv, Weng, Liao, Li and Lu. This is an open-access article distributed under the terms of the Creative Commons Attribution License (CC BY). The use, distribution or reproduction in other forums is permitted, provided the original author(s) and the copyright owner(s) are credited and that the original publication in this journal is cited, in accordance with accepted academic practice. No use, distribution or reproduction is permitted which does not comply with these terms.



Molecular Structure and Decomposition Kinetics of Kaolinite/Alkylamine Intercalation Compounds

Yi Zhou^{1,2}, Qinghe Liu¹, Peijie Xu¹, Hongfei Cheng^{1,3*} and Qinfu Liu¹

¹ School of Geoscience and Surveying Engineering, China University of Mining & Technology, Beijing, China, ² Department of Chemical and Biomolecular Engineering and Polymer Program, Institute of Materials Science, University of Connecticut, Storrs, CT, United States, ³ School of Environmental Science and Engineering, Chang'an University, Xi'an, China

OPEN ACCESS

Edited by:

Steve Suib,
University of Connecticut,
United States

Reviewed by:

Haibo Liu,
Hefei University, China
Runliang Zhu,
Guangzhou Institute of Geochemistry
(CAS), China
Junping Zhang,
Lanzhou Institute of Chemical Physics
(CAS), China
Xuan Dou,
Northwestern University, United States
Ping Zhang,
Nanchang University, China

*Correspondence:

Hongfei Cheng
h.cheng@cumtb.edu.cn

Specialty section:

This article was submitted to
Green and Sustainable Chemistry,
a section of the journal
Frontiers in Chemistry

Received: 22 May 2018

Accepted: 09 July 2018

Published: 27 July 2018

Citation:

Zhou Y, Liu Q, Xu P, Cheng H and
Liu Q (2018) Molecular Structure and
Decomposition Kinetics of
Kaolinite/Alkylamine Intercalation
Compounds. *Front. Chem.* 6:310.
doi: 10.3389/fchem.2018.00310

Although the development of clay/polymer nanocomposites and their applications have attracted much attention in recent years, a thorough understanding of the structure and the decomposition mechanism of clay/polymer nanocomposites is still lacking. In this research, the intercalation of kaolinite (Kaol) with different alkylamines were investigated by X-ray diffraction (XRD), Fourier-transform infrared spectroscopy (FTIR), and thermogravimetry and differential scanning calorimetry (TG-DSC). The results showed that the intercalation of Kaol/methanol compound with hexylamine (HA), dodecylamine (DA), and octadecylamine (OA) led to the expansion of the interlayer distance and resulted in the dominant basal diffraction at 2.86, 4.08, and 5.66 nm. The alky chains of HA, DA, and OA are tilted toward the Kaol surface in bilayer with an inclination angle of $\sim 40^\circ$. The most probable mechanism function, activation energy E , and pre-exponential factor A were obtained by mutual authentication using KAS and Ozawa methods, iterative and Satava integral method. The average activation energy E of the three intercalation compounds are 104.44, 130.80, and 154.59 kJ mol⁻¹, respectively. It shows a positive correlation with the alkyl chain length. The pre-exponential factor A was estimated to be 1.09×10^{15} , 1.15×10^8 , and 4.17×10^{21} s⁻¹, respectively. The optimized mechanism function for the decomposition of alkylamine is $G(\alpha) = [(1-\alpha)^{-1/3} - 1]^2$.

Keywords: kaolinite, alkylamine, intercalation, structural model, decomposition

INTRODUCTION

Design and fabrication of clay/polymer nanocomposites have attracted high interest from both the scientific and engineering communities (Cheng et al., 2017). A wide variety of clay/polymer nanocomposites have been developed and are being used in widespread application (Gogoi and Raidongia, 2017). Pre-intercalating clays followed by the incorporation of polymers into clay minerals layer is a widely adopted approach for the preparation of clay/polymer nanocomposites (Li et al., 2009; Zare et al., 2017). While being intercalated within inorganic clay layers, organic polymer chains naturally reduce their structural mobility and some of them assume a highly organized conformation within the layered structure.

In nature, kaolinite (Kaol) is a type of clay mineral with a 1:1 dioctahedral aluminum silicate layered structure (Brindley and Robinson, 1945). The layers in Kaol are held together by hydrogen bonds, dipole-dipole interactions, and van der Waals forces (Brindley et al., 1967). However, only a limited number of highly polar organic species including urea (Makó et al., 2009), dimethyl sulfoxide (Costanzo and Giesse, 1986), formamide (Frost et al., 2000a), hydrazine (Cruz and Franco, 2000), and potassium acetate (Frost et al., 2000b) were successfully intercalated into the gallery of Kaol. The intercalation of small molecules into Kaol layers causes an increase in the basal spacing, and can be used as a preliminary expansion step for subsequent insertion of large-sized, non-reactive species by the displacement of the pre-intercalated small molecules (Cheng et al., 2015). For example, based on the previous reports, a Kaol/methanol intercalation compound can be an effective intermediate for further intercalation reaction with ethylene glycol (Hirseman et al., 2011), hexylamine (Matusik et al., 2012), *n*-alkylamines (Gardolinski and Lagaly, 2005), and quaternary ammonium salts (Cheng et al., 2016). In addition, the majority of guest molecules are difficult to be inserted into the interlayer space, one of the reasons is the strong hydrogen bonds, another is that there is no exchangeable ions in the Kaol structure.

Although clay/polymer nanocomposites have been well developed in recent years, to synthesize new clay/organic nanocomposites for potential application still presents a big challenge (Kotal and Bhowmick, 2015). In order to settle this problem, it is really an urgent matter to figure out the nano-scale process of kaolinite intercalation and make a thorough inquiry to the mechanism of decomposition with modern technology and analytical tools. Thermal analysis and kinetic calculation of clay/polymer intercalation compounds can help characterize the decomposition processes and provide scientific basis for control over intercalation reactions (Zhang et al., 2015). The kinetic parameters of the decomposition reaction kinetics process, such as the activation energy, pre-exponential, reaction orders, and rate constant were assessed with the data from clay/polymer thermograms. In this study, the intercalation of Kaol with various alkylamines was investigated. Additionally, the intercalation process and the decomposition mechanism was systematically investigated.

EXPERIMENTAL

Materials

Kaolin used in this study was exploited from Zhangjiakou, China. The main mineral composition is a well ordered kaolinite (95% in mass). It was ground to pass a 325-mesh sieve (particles that measure <44 μm) before intercalation. Alkylamine hexylamine (HA, 99%), dodecylamine (DA, Chemically Pure), and octadecylamine (OA, Chemically Pure) were purchased from Nanjing Shuguang Chemical Company, China. Dimethyl sulfoxide (DMSO, Analytical Reagent), methanol (MeOH, Analytical Reagent), and toluene (99%) were received from Xilong Chemical Company, China, and used as received without further purification. The chemical formula and structural formula of HA, DA, and OA are shown in **Table 1**.

Synthesis of Intercalation Compounds

First, Kaol/DMSO intercalation compound was prepared by dispersing 20.0 g Kaol into a mixture of 36.0 g DMSO and 4.0 g water. The mixture was stirred in a water-bath for 2 h at 95°C, and then the suspension was separated by centrifugation with ethanol. Second, the Kaol/DMSO intercalation compound was used as a precursor for further reaction with MeOH. MeOH was added to the pre-intercalated Kaol and the reaction mixture was stirred for 10 days, with MeOH being replaced each day with a same amount of fresh MeOH. The precipitate in the mixture was separated by centrifugation and dried in an oven at 60°C for 12 h to obtain Kaol/MeOH intercalation compounds. Finally, 2 g Kaol/MeOH intercalation compound was mixed with 30.0 mL HA, DA, or OA methanol solutions (1 mol/L) by stirring at ambient temperature, respectively. The dispersions were centrifuged after reaction for 24 h. The sediments were washed three times with toluene to remove the excessive HA, DA, or OA. The samples were dried at room temperature for 12 h and ground into powders with an agate mortar (Komori et al., 1999). The resulting compounds are labeled as Kaolpi/HA (pi as pre-intercalated), Kaolpi/DA, and Kaolpi/OA.

Characterization


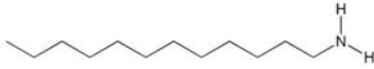
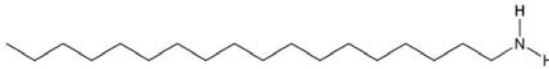
The XRD patterns were recorded on a Rigaku D/max 2500PC X-ray diffractometer with Cu Kα ($\lambda = 1.54178 \text{ \AA}$) radiation operating at 40 kV and 150 mA. The randomly oriented specimens samples were scanned in the 2θ range between 1 and 20° at a speed of 2° min⁻¹. A Thermo Fisher Nicolet 6700 spectrophotometer were used to recorded the FTIR spectra within the range of 4,000~400 cm⁻¹. The TG-DSC analyses were performed with a Mettler-Toledo TG-DSC I/1600 HT simultaneous thermal analyzer under nitrogen atmosphere. Twenty milligrams of sample was placed in an alumina crucible and heated from 30 to 1,100°C with a series of heating rates at 4, 6, 8, 10°C min⁻¹.

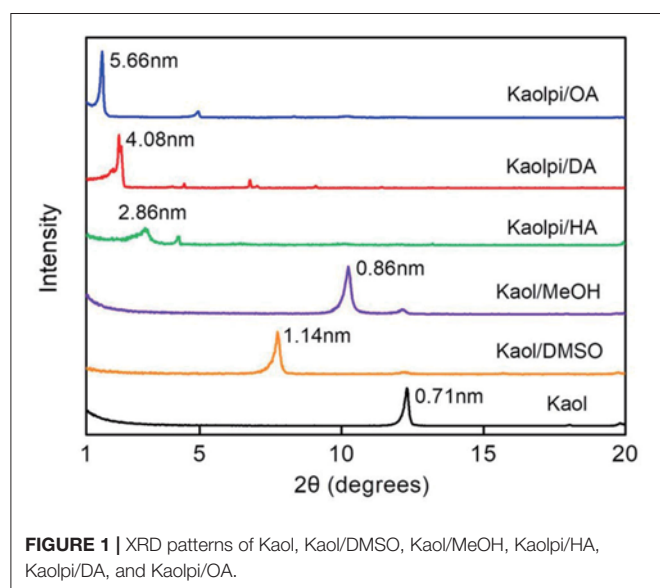
RESULTS AND DISCUSSION

XRD Characterization

The XRD patterns of the pristine Kaol and its intercalation compounds are shown in **Figure 1**. The pattern of the pristine Kaol displays a well-ordered layered structure with a basal spacing [$d_{(001)}$] of 0.71 nm. This value matches well with the standard ICDD reference pattern 14-0164 [kaolinite, Al₂Si₂O₅(OH)₄]. Upon being treated with DMSO, a new basal reflection peak appeared at 1.14 nm, indicating that DMSO was successfully inserted into Kaol interlayers. After the Kaol/DMSO intercalation compound was treated with MeOH, the 1.14 nm (001) reflection characteristic of Kaol/DMSO intercalation compound was shifted to 0.86 nm. It was reported by Matusik et al. (2012) that Kaol/DMSO/MeOH compound was dried at 110°C, the reflection with $d = 1.12 \text{ nm}$ disappeared and a broad reflection with maximum at 0.95 nm was observed. Based on the chemical formula Al₂Si₂O₅(OH)_{3.20}(OCH₃)_{0.80} of Kaol/DMSO intercalation compound which has been calculated according to the basis of CHNS analysis, it showed that about 1/3 of the inner surface OH groups were replaced by methoxy groups, and

TABLE 1 | Chemical and structural formula of HA, DA, and OA.

Chemicals	Chemical formula	Structural formula
Hexylamine (HA)	C ₆ H ₁₅ N	
Dodecylamine (DA)	C ₁₂ H ₂₇ N	
Octadecylamine (OA)	C ₁₈ H ₃₉ N	



this observation also suggests the formation of a Kaol/MeOH intercalation compound (Tunney and Detellier, 1996; Cheng et al., 2015). The XRD patterns also show that the Kaol/MeOH compounds intercalated with HA, DA, and OA expands the structure along the *c*-axis, leading to a large interlayer distance of 2.86, 4.08, and 5.66 nm, respectively. The lengths of HA, DA, and OA molecular chains are 1.56, 2.51, and 3.65 nm, respectively (McNulty et al., 2011, 2014). Overall, the interlayer distance of the Kaol/alkylamine intercalation compounds increased with the alkyl chain length of the alkylamines, but the alkylamine molecule is not a single layer or bilayer structure which is perpendicular to the Kaol surface.

FTIR Spectra

FTIR spectroscopy has been widely used in the characterization of intercalation compounds (Ledoux and White, 1964; Frost et al., 2000; Cheng et al., 2012). The FTIR spectra of the original Kaol, Kaolpi/HA, Kaolpi/DA, and Kaolpi/OA intercalation compounds are shown in **Figure 2**. The characteristic bands at 432, 470, and 541 cm⁻¹ (**Figure 2B**) belong to the deformation mode of Si-O, Si-O-Si, and Al-O-Si. The other bands at 1,009, 1,031,

and 1,114 cm⁻¹ (**Figure 2C**) are assigned to the stretching vibrations of Si-O-Si in the layer of Kaol. Comparing Kaol and its intercalation compounds spectra, the position of the bands have no apparent variation, which indicates that this stretching vibrations bands are not affected by the intercalated molecules.

The bands at 912 and 938 cm⁻¹ (**Figure 2C**) belong to the OH deformation of inner hydroxyl groups and inner-surface hydroxyl groups. There are four obvious hydroxyl stretching bands at 3,694, 3,669, 3,652, and 3,620 cm⁻¹ (**Figure 2D**) in the spectrum of the original Kaol, the bands at 3,694, 3,669, and 3,652 cm⁻¹ are caused by the inner-surface hydroxyl groups while the one at 3,620 cm⁻¹ results from the inner hydroxyl groups (Farmer, 1964; Ledoux and White, 1964; Giese and Datta, 1973). After the intercalation of alkylamine molecules, some bands were weakened due to the change of the interactions with neighboring atoms. The shift to 3,697 cm⁻¹ and the decrease of the intensity of the band at 3,694 cm⁻¹ indicates that numerous hydroxyl groups in Kaol participated and formed hydrogen bonds with the amine groups in the alkylamine molecules (Caglar, 2012; Caglar et al., 2013; Zhang et al., 2015).

The presence of interlayer alkylamine molecules was detected on the FTIR spectrum by the new peaks, which are shown in **Figures 2A,E**. For the intercalation compounds, some obvious characteristic peaks such as the band at 1,388 and 1,468 cm⁻¹ belong to the C-H bending mode of -CH₃ and -CH₂, respectively. A new vibration band at 3,334 cm⁻¹ was observed which is due to the stretching mode of the N-H stretching vibration (Griffiths and De Haseth, 2007; Zhang et al., 2018). The new vibration band at 2,956 cm⁻¹ was observed and usually assigned to the C-H asymmetric stretching band of the terminal methyl groups (Cheng et al., 2016). The two vibration bands at 2,919 and 2,851 cm⁻¹ are usually assigned to the symmetric and asymmetric stretching vibrations of the -(CH₂)_n- (Venkataraman and Vasudevan, 2001). The intensity of the bands increases gradually which means more alkylamine carbon atoms has been inserted into Kaol interlayers. Furthermore, the volatility of alkylamines will decrease with the increase of carbon chain, so the stability of the corresponding Kaol intercalation compounds will gradually increase with larger alkylamine molecular mass (Wang et al., 2010).

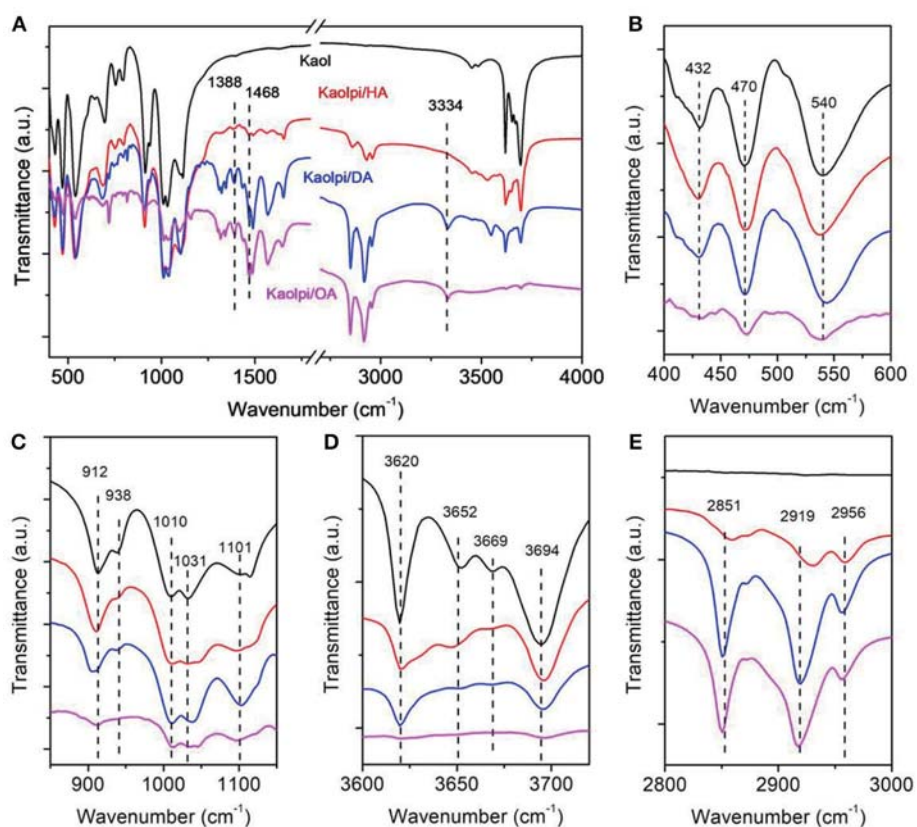


FIGURE 2 | Infrared spectra of Kaol, Kaolpi/HA, Kaolpi/DA, Kaolpi/OA.

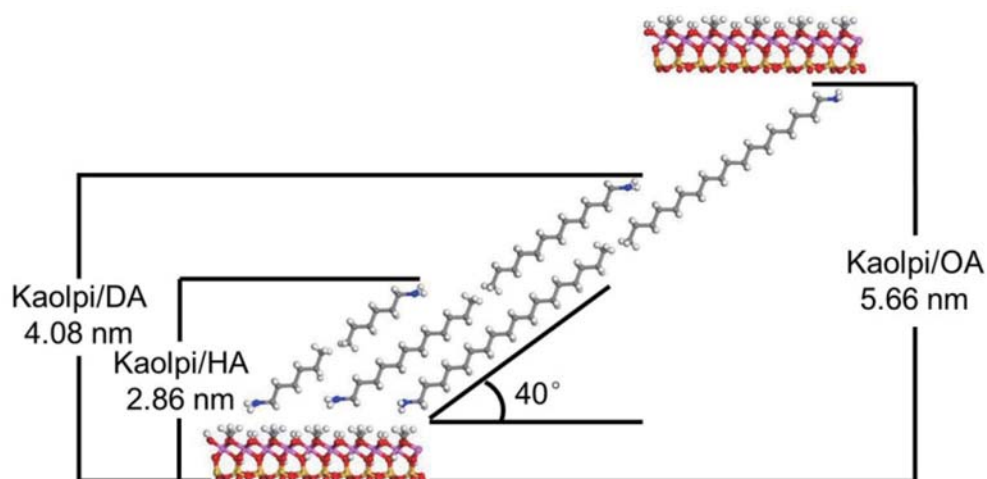


FIGURE 3 | The most possible structural model for the kaolinite/alkylamine intercalation compounds.

Structural Model of Kaol/Alkylamine Intercalation Compounds

The arrangement of intercalated molecules is the foundation for experimental analysis of the Kaol/alkylamine intercalation

compound structure. According to Lagaly (1981), the montmorillonite-quaternary ammonium salt intercalation compounds structural models can be divided into three categories: (a) monolayers: short chain alkylamine ions; (b)

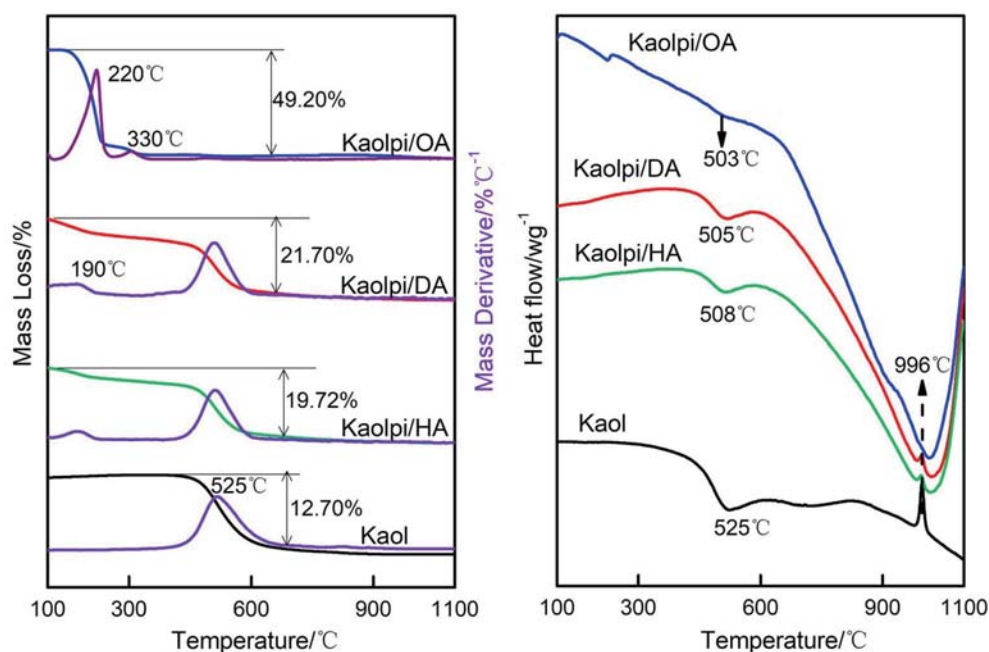


FIGURE 4 | TG-DSC curves for Kaol, Kaolpi/OA, Kaolpi/DA, Kaolpi/HA.

bilayers: long-chain quaternary ammonium ions; (c) three-layers: kinked alkyl chains in highly charged clay minerals. Beneke and Lagaly (1982) further proposed different structure of the intercalated alkylamine molecules based on the XRD, which are summarized as follows: (a) the alkyl chains in the interlayer space are tilted to the (001) crystal plane; (b) the alkyl chains are arranged in bilayers. Brindley and Moll (1965) described that the intercalated molecules are tilted to the silicate sheets in a single layer, whereas the angle is about 65° to (001) crystal plane. If the interacting molecules are uniformly attached to all silicate surfaces by the active hydroxyl groups, an “end to end” organization in pairs with some longitudinal displacement is suggested. The incline angle is in accord with the possible close packing manner between the silicate oxygen surfaces and the terminal hydroxyl groups and the degree of close packing of chain molecules among themselves.

The alkyl molecules are hard to intercalate directly the original Kaol layers since it lacks exchangeable ions in interlayer space of Kaol. Valid precursors are essential when the alkylamine molecules insert into the interlayer of Kaol. It was reported that the alkyl trimethyl ammonium chloride chain forms a tilted bilayer in the interlayer of Kaol and the angle of tilt is $\sim 36^\circ$ after calculation (Kuroda et al., 2011). Yuan et al. (2013) pointed out that the structural arrangement of the quaternary ammonium salt molecules in the interlayer of Kaol tilted bilayer and the angle of tilt is $\sim 38.4^\circ$. Gardolinski and Lagaly (2005) proposed that the alkyl chains in the interlayers are fully stretched and oriented perpendicular to the Kaol surface by bilayer. Therefore, from analyzing the length of HA, DA, and OA molecules chain, the conclusion can be drawn that

the basal spacing after intercalation is not sufficient to allow the alkyl chain entering by vertical and bilayer manner. It can be seen by further analyzing the XRD results that the alkyl chains of HA, DA, and OA are tilted to the Kaol surface in bilayer and the incline angle of the alkyl chains are about 39.9 , 39.9 , 41.1° , respectively. In addition, due to the hydroxyl bond between inner-surface hydroxyl in Kaol and amine groups in alkylamine molecules, the most possible structural model for the Kaol/alkylamine intercalation compounds is shown in Figure 3.

Thermal Analysis

The TG-DSC analysis results of Kaol and its intercalation compounds are shown in Figure 4. The main mass loss of Kaol is the one between 400 and 600°C with the maximum loss rate at 525°C attributed to the loss of water because of the dehydroxylation of the crystal lattice, resulting in the formation of meta-kaolinite (Toussaint et al., 1963; Criado et al., 1984; Sperinck et al., 2011). This loss corresponds to about 12.7% of the total mass which is extremely close to the theoretical reference (13.9%). By comparing the TG-DSC curves of the original Kaol, two main mass loss steps are observed in that of Kaolpi/OA, Kaolpi/DA, and Kaolpi/HA intercalation compounds. The first one occurred between 150 and 350°C , which is due to the decomposition of the intercalated alkylamine molecules (Yuan et al., 2013). The second one occurred at about 500°C is due to the dehydroxylation of the de-intercalated Kaol. For Kaolpi/OA, some OA were intercalated into the silicate interlayer space to form a stable intercalation, which can be proved by XRD pattern. Some molecules are entangled within each other due to the long chain or a clamp in the nanoscrolls that cannot be fully removed

TABLE 2 | E of Kaol/alkylamine intercalation compounds with different α calculated by KAS, Ozawa, and iteration methods.

	α	$E/(KJ \cdot mol^{-1})$			
		KAS	Ozawa	$\ln[\beta/h(x)T^2]-1/T$	$\ln[\beta/H(x)]-1/T$
Kaolpi/HA	0.1	74.92	77.76	75.17	75.18
	0.2	77.35	80.19	77.61	77.62
	0.3	85.44	88.00	85.69	85.69
	0.4	100.23	102.16	100.45	100.45
	0.5	113.52	114.89	113.72	113.72
	0.6	116.15	117.49	116.35	116.35
	0.7	122.54	123.66	122.74	122.74
	0.8	126.32	127.38	126.52	126.52
	0.9	121.48	122.91	121.69	121.70
Kaolpi/DA	0.1	109.36	109.81	109.51	109.51
	0.2	116.52	116.77	116.67	116.67
	0.3	104.95	105.96	105.12	105.13
	0.4	111.42	112.29	111.59	111.59
	0.5	120.44	121.05	120.61	120.61
	0.6	136.10	136.12	136.26	136.26
	0.7	178.68	176.79	178.81	178.80
	0.8	151.39	151.24	151.56	151.56
	0.9	146.88	147.24	147.07	147.06
Kaolpi/OA	0.1	105.52	108.44	105.81	105.81
	0.2	113.12	115.78	113.40	113.40
	0.3	134.68	136.43	134.92	134.92
	0.4	179.42	179.37	179.62	179.63
	0.5	178.76	178.98	178.98	178.99
	0.6	182.19	182.38	182.42	182.42
	0.7	183.42	183.66	183.64	183.64
	0.8	155.85	157.54	156.11	156.11
	0.9	156.15	157.92	156.43	156.43

(Li et al., 2015; Liu et al., 2016). At 220°C, the distinct mass loss is due to the decomposition of the coated or unbonded OA, while the mass loss at 330°C is attributed to the decomposition of intercalated OA. The exothermic peak at 996°C is result from the recrystallization of Kaol.

By comparing the TG-DSC curves of the original Kaol and Kaol/alkylamine intercalation compounds (Kaolpi/HA, Kaolpi/DA, Kaolpi/OA), one can observe: (a) it has different mass loss steps, as well as a significant difference in the mass losses between Kaolpi/OA and the other two intercalation compounds (Kaolpi/HA, Kaolpi/DA). The mass loss for the decomposition of Kaolpi/HA and Kaolpi/DA were about 20%, but the amount of the two mass losses for Kaolpi/OA is about 50%. This could be owing to a larger amount of OA was intercalated into the silicate interlayer space than that HA and DA (Wang et al., 2017). (b) Dehydroxylation temperature of the intercalation compounds was lower than that of the original Kaol by about 20°C. This is because the intercalation molecules expanded the interlayer spacing, weakened the hydrogen bonds between Kaol

layers, bringing about a more facile dehydroxylation from Kaol surface. Therefore, the crystallinity of Kaol sharply decreased after intercalation, which can be confirmed by XRD and IR (below 800 cm^{-1}). This result is consistent with the conclusion of some other reports that the temperature of dehydroxylation was determined by the crystallinity of Kaol (Yeskis et al., 1985; Gabor et al., 1995; Sahnoune et al., 2012).

Decomposition Reaction Kinetics

The degradation kinetics of the Kaol/alkylamine intercalation compound were investigated by thermogravimetry techniques. The kinetic parameters (activation energy E and the pre-exponential factor A) of degradation process were calculated on the basic of KAS and Ozawa methods (Kissinger, 1957; Škvára and Šesták, 1975). The thermal degradation mechanism of the Kaol/alkylamine intercalation compound was studied with Satava integral method (Xie et al., 2001; Gao et al., 2005; Zhang et al., 2015).

According to the reaction theory, the non-isothermal decomposition kinetic formula is usually expressed as follows:

$$\frac{d\alpha}{dt} = k \cdot f(\alpha) \quad (1)$$

where α is the extent of conversion rate of B(s) at time t , $f(\alpha)$ is the reaction mechanism function, and k is the reaction rate constant. k obeys the following equation:

$$k = A \exp\left(-\frac{E}{RT}\right) \quad (2)$$

where A , E , R , T are pre-exponential factor (s^{-1}), apparent activation energy ($J \cdot mol^{-1}$), universal gas constant ($8.314 J \cdot mol^{-1} K^{-1}$), and the temperature of the mass loss (K). Combining Equations (1) and (2) gives the following equation:

$$\frac{d\alpha}{dt} = A \exp\left(-\frac{E}{RT}\right) f(\alpha) \quad (3)$$

If the temperature of the sample is controlled at a constant heating rate ($\beta = dT/dt$), the reaction rate can be defined as follows:

$$\frac{d\alpha}{dt} = \frac{A}{\beta} \exp\left(-\frac{E}{RT}\right) f(\alpha) \quad (4)$$

After separating the variable, rearranging with integral or differential functions of Equation (4), KAS Equation (5), and Ozawa Equation (6) can be computed as follows:

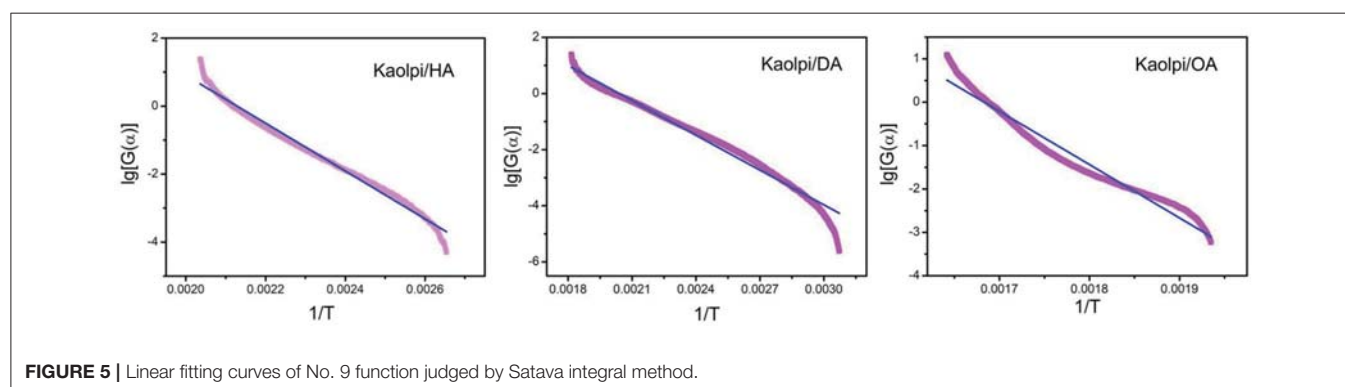
$$\ln \frac{\beta}{T^2} = \ln \frac{AR}{G(\alpha)E} - \frac{E}{RT} \quad (5)$$

$$\ln \beta = \ln \frac{0.00484AE}{G(\alpha)R} - \frac{1.0516E}{RT} \quad (6)$$

Where $G(\alpha)$ represents the integral function of conversion. Because of integral approximation, iterative methods were used

TABLE 3 | Selected kinetic mechanism functions judged by Satava integral method.

	Functions number	Integral functions	Goodness of fit (%)	E (kJ/mol)	LgA (s ⁻¹)
Kaolpi/HA	6	$\left[1 - (1 - \alpha)^{\frac{1}{3}}\right]^2$	93.95	107.15	11.17
	9	$\left[(1 - \alpha)^{-\frac{1}{3}} - 1\right]^2$	96.50	135.84	15.04
	10	$[-\ln(1 - \alpha)]^{\frac{1}{4}}$	95.92	15.02	1.90
	20	$[-\ln(1 - \alpha)]^4$	95.92	240.40	28.32
	28	$1 - (1 - \alpha)^{\frac{1}{4}}$	94.54	55.09	5.56
Kaolpi/DA	6	$\left[1 - (1 - \alpha)^{\frac{1}{3}}\right]^2$	92.18	61.61	5.75
	9	$\left[(1 - \alpha)^{-\frac{1}{3}} - 1\right]^2$	96.81	77.43	8.06
	10	$[-\ln(1 - \alpha)]^{\frac{1}{4}}$	95.03	8.60	1.34
	20	$[-\ln(1 - \alpha)]^4$	95.03	137.62	15.80
	28	$1 - (1 - \alpha)^{\frac{1}{4}}$	95.03	31.64	2.89
Kaolpi/OA	6	$\left[1 - (1 - \alpha)^{\frac{1}{3}}\right]^2$	94.51	179.10	14.96
	9	$\left[(1 - \alpha)^{-\frac{1}{3}} - 1\right]^2$	96.41	208.90	21.61
	10	$[-\ln(1 - \alpha)]^{\frac{1}{4}}$	95.35	26.07	2.31
	20	$[-\ln(1 - \alpha)]^4$	95.35	367.05	38.56
	28	$1 - (1 - \alpha)^{\frac{1}{4}}$	94.89	92.90	7.48

**FIGURE 5** | Linear fitting curves of No. 9 function judged by Satava integral method.**TABLE 4** | Kinetic mechanism functions of Kaol/alkylamine intercalation compounds.

Samples	E/kJ mol ⁻¹	A/s ⁻¹	Kinetic mechanism function
Kaolpi/HA	104.44	1.09×10^{15}	$\frac{d\alpha}{dt} = 1.64 \times 10^{14} \times (1 - \alpha)^{\frac{4}{3}} \left[(1 - \alpha)^{-\frac{1}{3}} - 1 \right]^{-1} \times \exp\left(-\frac{1.26 \times 10^4}{T}\right)$
Kaolpi/DA	130.80	1.15×10^8	$\frac{d\alpha}{dt} = 1.73 \times 10^7 \times (1 - \alpha)^{\frac{4}{3}} \left[(1 - \alpha)^{-\frac{1}{3}} - 1 \right]^{-1} \times \exp\left(-\frac{1.57 \times 10^4}{T}\right)$
Kaolpi/OA	154.59	4.17×10^{21}	$\frac{d\alpha}{dt} = 6.26 \times 10^{20} \times (1 - \alpha)^{\frac{4}{3}} \left[(1 - \alpha)^{-\frac{1}{3}} - 1 \right]^{-1} \times \exp\left(-\frac{1.86 \times 10^4}{T}\right)$

to calculate E in order to avoid certain deviation. The functions of iterative methods are as follows:

$$\ln \frac{\beta}{h(x)T^2} = \ln \frac{AR}{G(\alpha)E} - \frac{E}{RT} \quad (7)$$

$$\ln \frac{\beta}{H(x)} = \ln \frac{0.00484AE}{G(\alpha)R} - \frac{1.0516E}{RT} \quad (8)$$

Set $x = E/RT$, the definition of $h(x)$ and $H(x)$ are:

$$h(x) = \frac{x^4 + 18x^3 + 88x^2 + 96x}{x^4 + 20x^3 + 120x^2 + 240x + 120} \quad (9)$$

$$H(x) = \frac{\exp(-x)h(x)/x^2}{0.00484\exp(-1.0516x)} \quad (10)$$

The iteration are as the following three steps:

- Set $h(x) = 1$ or $H(x) = 1$, calculate E_0 by least squares method according to the slope of the linear relationship $\ln\beta/T^2$ and $\ln\beta$ to $1/T$.
- E_0 and T at different α and β were substituted into $x = E/RT$ and then x was substituted into $h(x)$ and $H(x)$, the values were substituted into (7) and (8), calculate E_1 by least squares method according to the slope of the linear relationship $\ln[\beta/h(x)T^2]$ and $\ln[\beta/H(x)]$ to $1/T$.
- Replace E_0 with E_1 , repeat step (b) until $E_i - E_{i-1} < 0.1 \text{ kJ mol}^{-1}$. E_i is the exact value of the activation energy of the decomposition reaction.

The E -values of Kaol/alkylamine intercalation compounds were calculated by KAS, Ozawa, and iterative methods (Table 2). The calculated results obtained by KAS method were closer to the results from iterative methods, however, the results from Ozawa iterative method showed larger deviation to others. Therefore, the average E from iterative methods can be regarded as the activation energy of the decomposition reaction since they are an improvement over KAS and Ozawa methods. The average E of Kaolpi/HA, Kaolpi/DA, and Kaolpi/OA are 104.44, 130.80, and 154.59 kJ mol^{-1} . It can be seen that the average E among of Kaol/alkylamine compounds are positive correlation with the alkyl chain length. One of the reason is that the volatility weakens as the alkyl chain grows. Another reason is that the Kaolpi/OA possesses the best well-ordered intercalation structure which is the most difficult to de-intercalate. And these results can be confirmed by XRD patterns.

The functions and A of decomposition reaction mechanism was calculated by Satava methods, which was described as follow:

$$\lg G(\alpha) = \lg \frac{AE}{\beta R} - 2.315 - \frac{0.4567E}{RT} \quad (11)$$

Substitute α into every mechanism function $G(\alpha)$ to obtain the value of $\lg[G(\alpha)]$, linear fitting $\lg[G(\alpha)]$, and $1/T$ which corresponding to the heating rate, the function which has the largest fit can be determined as the most probable mechanism function. And the values of E and A can be obtained through the slope and intercept of a linear fitting curve.

As shown in Table 3, five mechanism functions with goodness of fit above 90% are chosen based on Satava integral formula. By comparing there five functions, No. 9 mechanism function $G(\alpha) = [(1-\alpha)^{-1/3} - 1]^2$ with goodness of fit about 97% can be regarded as the most probable mechanism function, and the linear fitting curves of No. 9 function has been shown in Figure 5. E and A are also in the normal range of decomposition

kinetics. The decomposition mechanism functions for the three Kaol/alkylamine intercalation compounds are given in Table 4.

CONCLUSIONS

The possible structure models and decomposition kinetics for Kaol/alkylamine intercalation compounds have been studied using XRD, FT-IR, and TG-DSC. The intercalation of Kaol/MeOH compound with HA, DA, and OA expands the interlayer spacing of Kaol along the c -axis, resulting in the dominant reflection appearing at 2.86, 4.08, and 5.66 nm, respectively. Moreover, the basal spacing after intercalation is not sufficient to allow the alky chain entering by vertical single and bilayer manner. It was concluded that the alky chains of HA, DA, and OA are tilted to the Kaol surface in bilayer and the inclination angle of the alky chains are $\sim 40^\circ$.

Based on the KAS, Ozawa, and iterative methods, the results of activation energy E of Kaol/alkylamine intercalation compounds were calculated. The average activation energy E of Kaolpi/HA, Kaolpi/DA, and Kaolpi/OA are 104.44, 130.80, and 154.59 kJ mol^{-1} . The average activation energy E among Kaol/alkylamine compounds have a positive correlation with the alkyl chain length. The optimized mechanism function of Kaol/alkylamine decomposition process was determined as a 3D diffusion with the integral function $G(\alpha) = [(1-\alpha)^{-1/3} - 1]^2$. This research is advantageous to better understand the decomposition mechanism of clay/organic nanocomposites in addition to provide an inspiration to synthesize new clay-based materials.

AUTHOR CONTRIBUTIONS

HC and QfL designed the experiment and revised the paper. YZ, QhL, and PX did the experiments and wrote the paper. YZ and QhL contributed equally to this work.

ACKNOWLEDGMENTS

Dr. Luyi Sun (Department of Chemical and Biomolecular Engineering and Polymer Program, Institute of Materials Science, University of Connecticut) is acknowledged for revising the paper. The authors gratefully acknowledge the financial support provided by the National Natural Science Foundation of China (41602171), the Beijing Natural Science Foundation (8164062) and the Yue Qi Young Scholar Project, China University of Mining & Technology, Beijing.

REFERENCES

- Beneke, K., and Lagaly, G. (1982). The brittle mica-like KNiAsO₄ and its organic derivatives. *Clay Miner.* 17, 175–183. doi: 10.1180/claymin.1982.017.2.02
- Brindley, G., and Moll, W. (1965). Complexes of natural and synthetic caumontmorillonites with fatty acids (CLAY-ORGANIC STUDIES-9). *Am. Mineral.* 50, 1355.
- Brindley, G. W., and Robinson, K. (1945). Structure of Kaolinite. *Nature* 156, 661–662. doi: 10.1038/156661b0

- Brindley, G. W., Sharp, J., Patterson, J., and Narahari, B. (1967). Kinetics and mechanism of dehydroxylation processes. I. Temperature and vapor pressure dependence of dehydroxylation of kaolinite. *Am. Mineral.* 52, 201.
- Caglar, B. (2012). Structural characterization of kaolinite-nicotinamide intercalation composite. *J. Mol. Struct.* 1020, 48–55. doi: 10.1016/j.molstruc.2012.03.061
- Caglar, B., Tabak, A., Afsin, B., and Eren, E. (2013). Covalent grafting of pyridine-2-methanol into kaolinite layers. *J. Mol. Struct.* 1032, 12–22. doi: 10.1016/j.molstruc.2012.08.004

- Cheng, H., Hou, X., Liu, Q., Li, X., and Frost, R. L. (2015). New insights into the molecular structure of kaolinite-methanol intercalation complexes. *Appl. Clay Sci.* 109–110, 55–63. doi: 10.1016/j.clay.2015.03.010
- Cheng, H., Liu, Q., Cui, X., Zhang, Q., Zhang, Z., and Frost, R. L. (2012). Mechanism of dehydroxylation temperature decrease and high temperature phase transition of coal-bearing strata kaolinite intercalated by potassium acetate. *J. Colloid Interface Sci.* 376, 47–56. doi: 10.1016/j.jcis.2012.02.065
- Cheng, H., Xu, P., Wang, D., and Frost, R. L. (2016). Thermal decomposition behavior and de-intercalation kinetics of kaolinite/quaternary ammonium salt complexes. *J. Therm. Anal. Calorim.* 126, 421–433. doi: 10.1007/s10973-016-5572-x
- Cheng, H., Zhou, Y., Feng, Y., Geng, W., Liu, Q., Guo, W., et al. (2017). electrokinetic energy conversion in self-assembled 2d nanofluidic channels with janus nanobuilding blocks. *Adv. Mater.* 29:1700177. doi: 10.1002/adma.201700177
- Costanzo, P., and Giesse, R. (1986). Ordered halloysite; dimethylsulfoxide intercalate. *Clays Clay Miner.* 34, 105–107. doi: 10.1346/CCMN.1986.0340115
- Criado, J., Ortega, A., Real, C., and Torres De Torres, E. (1984). Re-examination of the kinetics of the thermal dehydroxylation of kaolinite. *Clay Miner. Clay Miner.* 19, 653–661. doi: 10.1180/claymin.1984.019.4.11
- Cruz, M. D. R., and Franco, F. (2000). Thermal behavior of the kaolinite-hydrazine intercalation complex. *Clays Clay Miner.* 48, 63–67. doi: 10.1346/CCMN.2000.0480108
- Farmer, V. C. (1964). Infrared absorption of hydroxyl groups in kaolinite. *Science* 145, 1189–1190. doi: 10.1126/science.145.3637.1189
- Frost, R. L., Kristof, J., Horvath, E., and Klopogge, J. T. (2000a). Effect of water on the formamide-intercalation of kaolinite. *Spectrochim. Acta Part A Mol. Biomol. Spectrosc.* 56, 1711–1729. doi: 10.1016/S1386-1425(00)0224-9
- Frost, R. L., Kristof, J., Horvath, E., and Klopogge, J. T. (2000b). Rehydration and phase changes of potassium acetate-intercalated halloysite at 298 K. *J. Colloid Interface Sci.* 226, 318–327. doi: 10.1006/jcis.2000.06807
- Frost, R. L., Kristof, J., Horvath, E., and Klopogge, J. T. (2000c). Vibrational spectroscopy of formamide-intercalated kaolinites. *Spectrochim. Acta Part A Mol. Biomol. Spectrosc.* 56, 1191–1204. doi: 10.1016/S1386-1425(99)00221-8
- Gabor, M., Toth, M., Kristof, J., and Komaromi-Hiller, G. (1995). Thermal behavior and decomposition of intercalated kaolinite. *Clays Clay Miner.* 43, 223–228. doi: 10.1346/CCMN.1995.0430209
- Gao, P., Xiao, H., Wang, H., and Jin, Z. (2005). A study on the oxidation kinetics and mechanism of three-dimensional (3D) carbon fiber braid coated by gradient SiC. *Mater. Chem. Phys.* 93, 164–169. doi: 10.1016/j.matchemphys.2005.03.003
- Gardolinski, J. E. F. C., and Lagaly, G. (2005). Grafted organic derivatives of kaolinite: II. Intercalation of primary n-alkylamines and delamination. *Clay Miner.* 40, 547–556. doi: 10.1180/0009855054040191
- Giese, R., and Datta, P. (1973). Hydroxyl orientation in kaolinite, dickite, and nacrite. *Am. Mineral.* 58, 471–479.
- Gogoi, R. K., and Raidongia, K. (2017). Strategic shuffling of clay layers to imbue them with responsiveness. *Adv. Mater.* 29:1701164. doi: 10.1002/adma.201701164
- Griffiths, P. R., and De Haseth, J. A. (2007). *Fourier Transform Infrared Spectrometry*. New York, NY: John Wiley & Sons.
- Hirseman, D., Köster, T. K. J., Wack, J., Van Wüllen, L., Breu, J., and Senker, J. (2011). Covalent grafting to μ -hydroxy-capped surfaces? A kaolinite case study. *Chem. Mater.* 23, 3152–3158. doi: 10.1021/cm200235x
- Kissinger, H. E. (1957). Reaction kinetics in differential thermal analysis. *Anal. Chem.* 29, 1702–1706. doi: 10.1021/ac60131a045
- Komori, Y., Sugahara, Y., and Kuroda, K. (1999). Intercalation of alkylamines and water into kaolinite with methanol kaolinite as an intermediate. *Appl. Clay Sci.* 15, 241–252. doi: 10.1016/S0169-1317(99)00014-9
- Kotal, M., and Bhowmick, A. K. (2015). Polymer nanocomposites from modified clays: recent advances and challenges. *Prog. Polym. Sci.* 51, 127–187. doi: 10.1016/j.progpolymsci.2015.10.001
- Kuroda, Y., Ito, K., Itabashi, K., and Kuroda, K. (2011). One-Step exfoliation of kaolinites and their transformation into nanoscrolls. *Langmuir* 27, 2028–2035. doi: 10.1021/la1047134
- Lagaly, G. (1981). Characterization of clays by organic compounds. *Clay Miner.* 16, 1–21. doi: 10.1180/claymin.1981.016.1.01
- Ledoux, R. L., and White, J. L. (1964). Infrared study of the OH groups in expanded kaolinite. *Science* 143, 244–246. doi: 10.1126/science.143.3603.244
- Li, X., Liu, Q., Cheng, H., Zhang, S., and Frost, R. L. (2015). Mechanism of kaolinite sheets curling via the intercalation and delamination process. *J. Colloid Interface Sci.* 444, 74–80. doi: 10.1016/j.jcis.2014.12.039
- Li, Y., Sun, D., Pan, X., and Zhang, B. (2009). Kaolinite intercalation precursors. *Clays Clay Miner.* 57, 779–786. doi: 10.1346/CCMN.2009.0570610
- Liu, Q., Li, X., and Cheng, H. (2016). Insight into the self-adaptive deformation of kaolinite layers into nanoscrolls. *Appl. Clay Sci.* 124–125, 175–182. doi: 10.1016/j.clay.2016.02.015
- Makó, Kristóf, J., Horváth, E., and Vágvölgyi, V. (2009). Kaolinite-urea complexes obtained by mechanochemical and aqueous suspension techniques—A comparative study. *J. Colloid Interface Sci.* 330, 367–373. doi: 10.1016/j.jcis.2008.10.054
- Matusik, J., Gawel, A., and Bahrnowski, K. (2012). Grafting of methanol in dickite and intercalation of hexylamine. *Appl. Clay Sci.* 56, 63–67. doi: 10.1016/j.clay.2011.11.023
- McNulty, D., Buckley, D. N., and O'dwyer, C. (2011). Synthesis and characterization of layered vanadium oxide nanotubes for rechargeable lithium batteries. *ECS Trans.* 35, 237–245. doi: 10.1149/1.3654222
- McNulty, D., Buckley, D., and O'dwyer, C. (2014). Polycrystalline vanadium oxide nanorods: growth, structure and improved electrochemical response as a Li-ion battery cathode material. *J. Electrochem. Soc.* 161, A1321–A1329. doi: 10.1149/2.0601409jes
- Sahnoune, F., Saheb, N., Khmel, B., and Takkouk, Z. (2012). Thermal analysis of dehydroxylation of Algerian kaolinite. *J. Therm. Anal. Calorim.* 107, 1067–1072. doi: 10.1007/s10973-011-1622-6
- Škvára, F., and Šesták, J. (1975). Computer calculation of the mechanism and associated kinetic data using a non-isothermal integral method. *J. Therm. Anal. Calorim.* 8, 477–489. doi: 10.1007/BF01910127
- Sperinck, S., Raiteri, P., Marks, N., and Wright, K. (2011). Dehydroxylation of kaolinite to metakaolin—a molecular dynamics study. *J. Mater. Chem.* 21, 2118–2125. doi: 10.1039/C0JM01748E
- Toussaint, F., Fripiat, J. J., and Gastuche, M. C. (1963). Dehydroxylation of kaolinite. I. Kinetics. *J. Phys. Chem.* 67, 26–30. doi: 10.1021/j100795a007
- Tunney, J. J., and Detellier, C. (1996). Chemically modified kaolinite. Grafting of methoxy groups on the interlamellar aluminol surface of kaolinite. *J. Mater. Chem.* 6, 1679–1685. doi: 10.1039/jm9960601679
- Venkataraman, N. V., and Vasudevan, S. (2001). Conformation of methylene chains in an intercalated surfactant bilayer. *J. Phys. Chem. B* 105, 1805–1812. doi: 10.1021/jp002505h
- Wang, D., Liu, Q., Hou, D., Cheng, H., and Frost, R. L. (2017). The formation mechanism of organoammonium-kaolinite by solid-solid reaction. *Appl. Clay Sci.* 146, 195–200. doi: 10.1016/j.clay.2017.05.022
- Wang, L., Lal, V., Khalizov, A. F., and Zhang, R. (2010). Heterogeneous chemistry of alkylamines with sulfuric acid: implications for atmospheric formation of alkylammonium sulfates. *Environ. Sci. Technol.* 44, 2461–2465. doi: 10.1021/es9036868
- Xie, W., Gao, Z., Pan, W.-P., Hunter, D., Singh, A., and Vaia, R. (2001). Thermal degradation chemistry of alkyl quaternary ammonium montmorillonite. *Chem. Mater.* 13, 2979–2990. doi: 10.1021/cm010305s
- Yeskis, D., Van Groos, A. K., and Guggenheim, S. (1985). Dehydroxylation of kaolinite. *Am. Mineral.* 70, 1–2.
- Yuan, P., Tan, D., Annabi-Bergaya, F., Yan, W., Liu, D., and Liu, Z. (2013). From platy kaolinite to aluminosilicate nanoroll via one-step delamination of kaolinite: effect of the temperature of intercalation. *Appl. Clay Sci.* 83–84, 68–76. doi: 10.1016/j.clay.2013.08.027

- Zare, Y., Fasihi, M., and Rhee, K. Y. (2017). Efficiency of stress transfer between polymer matrix and nanoplatelets in clay/polymer nanocomposites. *Appl. Clay Sci.* 143, 265–272. doi: 10.1016/j.clay.2017.03.043
- Zhang, A., Mu, B., Wang, X., Wen, L., and Wang, A. (2018). Formation and coloring mechanism of typical aluminosilicate clay minerals for CoAl₂O₄ hybrid pigment preparation. *Front. Chem.* 6:125. doi: 10.3389/fchem.2018.00125
- Zhang, S., Ou, X., Qiang, Y., Niu, J., and Komarneni, S. (2015). Thermal decomposition behavior and decomposition mechanism of acetamide intercalated into kaolinite by thermoanalytical techniques. *Appl. Clay Sci.* 114, 309–314. doi: 10.1016/j.clay.2015.06.002

Conflict of Interest Statement: The authors declare that the research was conducted in the absence of any commercial or financial relationships that could be construed as a potential conflict of interest.

Copyright © 2018 Zhou, Liu, Xu, Cheng and Liu. This is an open-access article distributed under the terms of the Creative Commons Attribution License (CC BY). The use, distribution or reproduction in other forums is permitted, provided the original author(s) and the copyright owner(s) are credited and that the original publication in this journal is cited, in accordance with accepted academic practice. No use, distribution or reproduction is permitted which does not comply with these terms.



Z-Scheme Photocatalyst Constructed by Natural Attapulgite and Upconversion Rare Earth Materials for Desulfurization

Fengqin Wu, Xiazhang Li*, Haiguang Zhang, Shixiang Zuo and Chao Yao*

Advanced Catalysis and Green Manufacturing Collaborative Innovation Center, Changzhou University, Changzhou, China

OPEN ACCESS

Edited by:

Wenbo Wang,
Lanzhou Institute of Chemical Physics
(CAS), China

Reviewed by:

Jinxing Ma,
University of New South Wales,
Australia
Fenghua Liu,
Ningbo Institute of Industrial
Technology (CAS), China

*Correspondence:

Xiazhang Li
xiazhang@cczu.edu.cn
Chao Yao
yaochao@cczu.edu.cn

Specialty section:

This article was submitted to
Green and Sustainable Chemistry,
a section of the journal
Frontiers in Chemistry

Received: 25 June 2018

Accepted: 20 September 2018

Published: 05 October 2018

Citation:

Wu F, Li X, Zhang H, Zuo S and Yao C
(2018) Z-Scheme Photocatalyst
Constructed by Natural Attapulgite
and Upconversion Rare Earth
Materials for Desulfurization.
Front. Chem. 6:477.
doi: 10.3389/fchem.2018.00477

The Er³⁺:CeO₂/ATP (attapulgite) nanocomposites were prepared by a facile precipitation method. The samples were characterized by various measurements. XRD and TEM showed that Er³⁺:CeO₂ nanoparticles were well-crystallized and loaded on the surface of ATP. The visible light was converted into ultraviolet light by Er³⁺:CeO₂ as evidenced by upconversion photoluminance (PL) analysis. The mass ratio of Er³⁺:CeO₂ to ATP on the desulfurization efficiency was investigated. Results showed that the desulfurization rate reached 87% under 4 h visible light irradiation when the mass ratio was 4:10. The mechanism was put forward as follows. Er³⁺:CeO₂ and ATP formed Z-scheme heterostructure intermediated by oxygen vacancy, leading to the enhanced separation of photogenerated charges and preservation of high oxidation-reduction potential, both of which favored for the generation of radicals to oxidize sulfur species.

Keywords: attapulgite, upconversion, rare earth, Z scheme, photocatalyst

INTRODUCTION

Massive use of fuel has given rise to serious environmental problem including acid rain and atmospheric haze, since the combustion of sulfur compounds in fuels leads to the emission of pernicious SO_x. Therefore, it is imperative to develop new desulfurization technology to satisfy fuel purification (Liu et al., 2017; Zhang et al., 2018). The conventional hydrodesulfurization (HDS) has been extensively used in removing sulfur compound in fuel, which requires high temperature, pressure and expensive hydrogen (Wang et al., 2016; Zeng et al., 2017). Owing to the drawbacks of HDS for removing sulfur compound, many alternative strategies have been developed, including extractive desulfurization (Raj et al., 2017), oxidative desulfurization (Khodadadi Dizaji et al., 2018), biodesulfurization (Agarwal et al., 2016) and adsorption desulfurization (Yang et al., 2018). Among these strategies, oxidative desulfurization is considered as one of the promising strategy for deep desulfurization due to its cheap and efficient features. Particularly, photocatalytic oxidative desulfurization is deemed as a potential candidate. In our previous work, we have prepared attapulgite-CeO₂/MoS₂, CeO₂/attapulgite/g-C₃N₄ and BiP_{1-x}V_xO₄/attapulgite nanocomposites and found that the photocatalytic oxidative desulfurization rate reached as high as more than 90% under the irradiation of visible light (Li et al., 2016, 2017, 2018). As a natural clay material, attapulgite (ATP) has large specific surface area, superior adsorption performance and unique pore structure, which is widely used in catalyst support (Zhang et al., 2016b). Interestingly, the incorporation of Fe₂O₃ endows ATP with semiconductor property to some extent. Zhang et al. (Zhang et al., 2013, 2016a) sensitized ATP by taking advantage of eosine Y and CdS to generate

hydrogen from water. Li et al. (Ma et al., 2018) prepared CQDs/ATP nanocomposites with visible light response. However, ATP can only be stimulated by ultraviolet light which is accounted for 5% in solar light due to its wide band gap (Balaji et al., 2017).

The upconversion luminescence materials have attracted great attentions since they can absorb and upconvert long wave light with low-energy to short wave light with high-energy (Feng et al., 2013). In the general composition of upconversion luminescence material, the rare earth element has a rich 4f energy level enabling the electrons jump easily from high to low energy level. Among the rare earth family, Er^{3+} has abundant energy levels and higher upconversion luminescence efficiency, making it as a excellent candidate for the conversion from visible to UV light (Pickering et al., 2017). The Er^{3+} can be easily doped into the crystal lattice of CeO_2 along with the production of oxygen vacancy since the ion radius of Ce^{4+} is very close to Er^{3+} (Wu et al., 2014). Meanwhile, CeO_2 has high chemical stability and low phonon energy, making it suitable as matrix materials in upconversion. Han et al prepared upconversion Er, Yb- CeO_2 hollow spheres for improving the efficiency of dye-sensitized solar cells (Han et al., 2017). However, rare report has been put on the heterostructure constructed by rare earth doped upconversion luminescence materials (Bhethanabotla et al., 2016). Moreover, the decline of oxidation-reduction ability in traditional type heterostructure is non-negligible. It is worth noting that Z-type heterostructure causes the annihilation of photo-generated charges with lower reduction and oxidation potential, therefore leading to the preservation of high redox potential for the heterostructure (Šutka et al., 2018). Intriguingly, the self-generated oxygen vacancy has been proposed as mediator in the indirect Z-scheme with the absence of noble metals, such as Au, Ag, etc. For instance, Ding et al. (Ding et al., 2016) prepared $\text{BiO}_{1-x}\text{Br}/\text{Bi}_2\text{O}_2\text{CO}_3$ in which the oxygen vacancy of $\text{BiO}_{1-x}\text{Br}$ acted as the medium of transmission for electrons and the recombination center of photogenerated electrons and holes.

In this work, the Er doped CeO_2 upconversion luminescence oxide was immobilized on ATP. The doping fraction of Er^{3+} was adjusted to achieve the strongest emission of ultraviolet light to stimulate ATP. Meanwhile, $\text{CeO}_2:\text{Er}$ and ATP formed Z-type heterostructure intermediated by oxygen vacancy, which effectively preserved redox potential so as to improve the photocatalytic desulfurization activity of $\text{Er}^{3+}:\text{CeO}_2/\text{ATP}$.

EXPERIMENTAL SECTION

Materials

ATP powders were obtained from Xuyi, China. $\text{Ce}(\text{NO}_3)_3 \cdot 6\text{H}_2\text{O}$, $\text{Er}(\text{NO}_3)_3 \cdot 5\text{H}_2\text{O}$, hexamine ($\text{C}_2\text{H}_{12}\text{N}_4$, HMT), octane (C_8H_{18}), dibenzothiophene ($\text{C}_{12}\text{H}_8\text{S}$) and acetonitrile ($\text{C}_2\text{H}_3\text{N}$) were purchased from Sionpharm Chemical Reagent Co., Ltd. All reagents were analytical grade without further purification.

Synthesis of $\text{Er}^{3+}:\text{CeO}_2/\text{ATP}$

$\text{Er}^{3+}:\text{CeO}_2/\text{ATP}$ composites were synthesized via a one-step precipitation method. Typically, adequate amount of $\text{Ce}(\text{NO}_3)_3 \cdot 6\text{H}_2\text{O}$, $\text{Er}(\text{NO}_3)_3 \cdot 5\text{H}_2\text{O}$ and 1 g ATP were dissolved in

100 mL deionized water and mixed together, followed by adding excess HMT (molar ratio of HMT to $\text{Ce}(\text{NO}_3)_3$ was 5:1). The molar fraction of Er ($\text{Er}/\text{Ce}+\text{Er}$) was adjusted from 0.5 to 2.5%, and the mass ratio of $\text{Er}^{3+}:\text{CeO}_2$ to ATP was adjusted from 1:10 to 5:10. Then the mixture was heated in a water bath at 80°C for 2 h. After cooled down to room temperature, the precipitate was washed with deionized water for three times. Subsequently, the obtained solid was dried in vacuum at 80°C for 10 h, and finally calcined at 300°C for 2 h.

Materials Characterization

The powder X-ray diffraction (XRD) was performed with a D/max 2500PC diffractometer equipped with a $\text{Cu-K}\alpha$ radiation ($\lambda = 1.5406 \text{ \AA}$) at a scanning speed of 6° min^{-1} from 5 to 80° . The morphology was investigated with a JEM-2100 transmission electron microscope (TEM) operating at 200 kV. Raman spectra were collected with a Renishaw (UK) spectrometer with an Ar ion laser of 514 nm excitation. The ultraviolet visible (UV-Vis) spectra were acquired using a UV-2500 Shimadzu UV-Vis spectrophotometer. The photoluminescence (PL) spectra were collected with the PerkinElmer LS45 at room temperature. The X-ray photoelectron spectroscopy (XPS) was performed with a PHI 5300 equipped with $\text{K}\alpha$ in the condition of 284.6 eV for C 1s.

Photocatalytic Oxidative Desulfurization

The photocatalytic desulfurization performance of $\text{Er}^{3+}:\text{CeO}_2/\text{ATP}$ was carried out by degrading the model gasoline using a photocatalytic reaction apparatus (GHX-2) which was equipped with a 300 W xenon lamp. 0.4 g DBT was dissolved into 500 mL octane to acquire the model gasoline with sulfur compounds of 200 ppm. Then the model gasoline and catalysts were added into the photocatalytic reactor and kept 30 min with magnetic stirring to ensure adsorption equilibrium. Subsequently, simulated solar light using UV-cut off was irradiated during the reaction with the irradiation intensity of 30 W/cm^2 . The samples were collected twice an hour to satisfy the extraction process. The rest of sulfur content was measured by a sulfur determination device (THA2000S), and the desulfurization rate D was calculated based on the following formula:

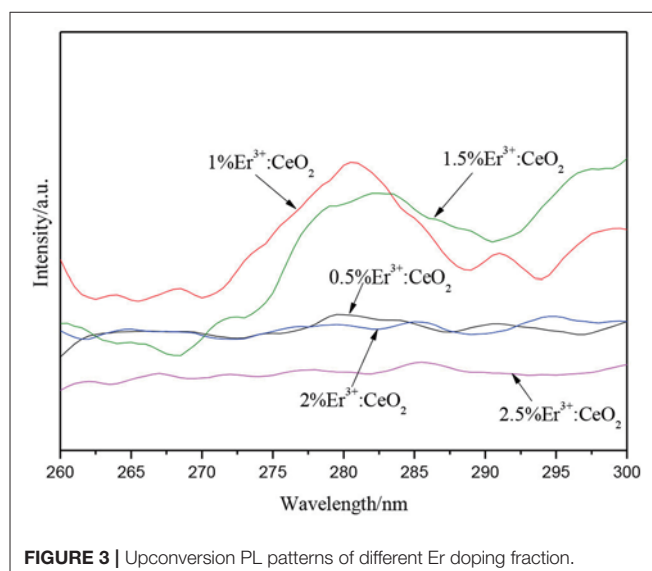
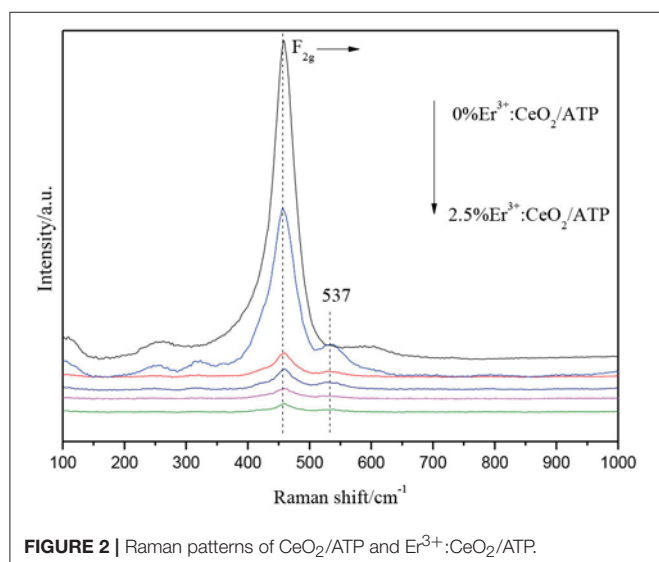
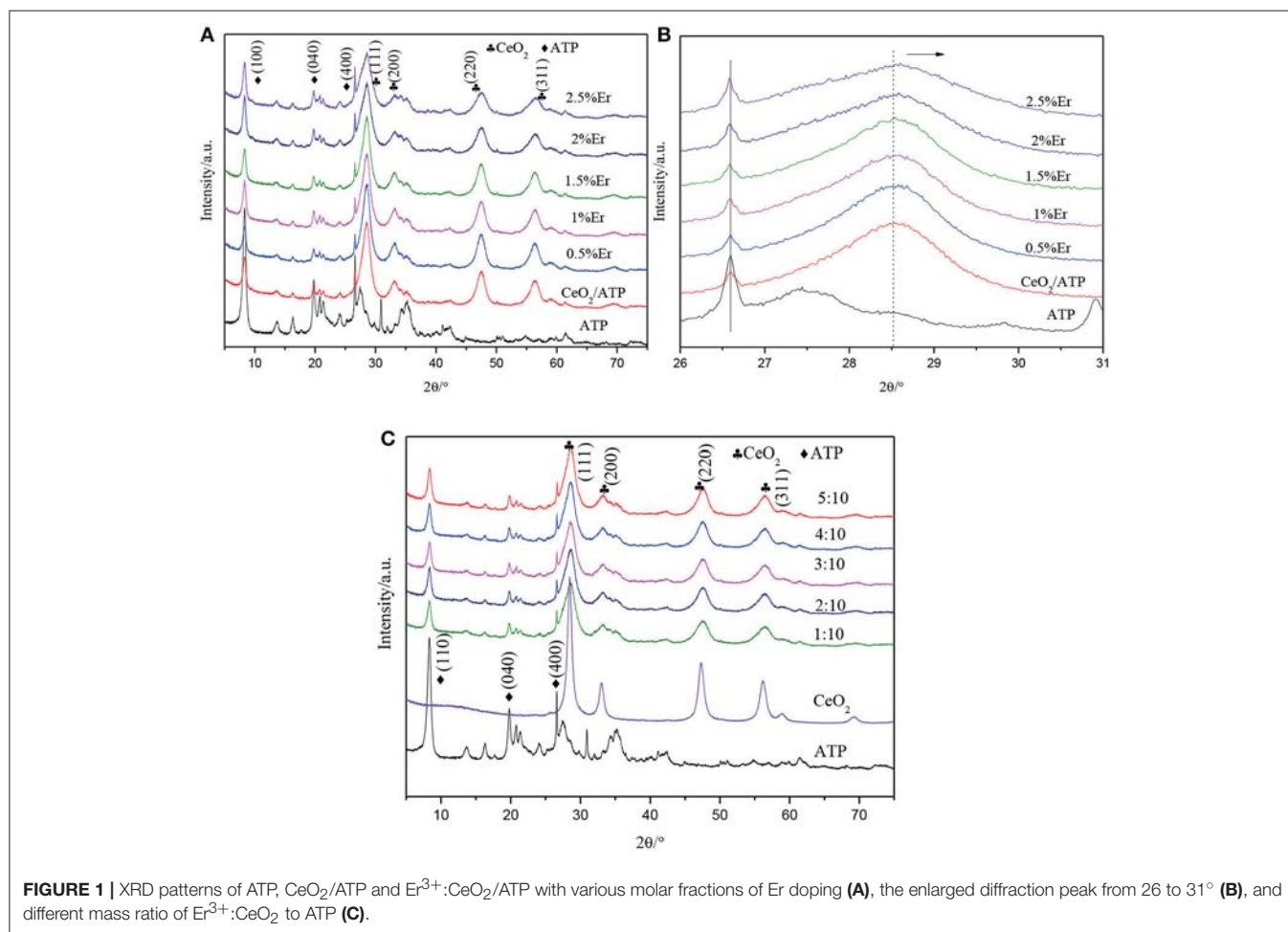
$$D = \left(1 - \frac{C}{C_0}\right) \times 100\%$$

where C_0 is the initial sulfur content of the model gasoline and C is the final sulfur content.

RESULTS AND DISCUSSIONS

XRD Analysis

Figure 1 shows the XRD patterns of ATP, CeO_2/ATP and $\text{Er}^{3+}:\text{CeO}_2/\text{ATP}$. In Figure 1A the characteristic peaks at 8.21 , 19.75 , and 26.54° correspond to the (110), (040), and (400) plane of pure ATP (Zhao et al., 2016). The characteristics at 28.55 , 33.07 , 47.48 , and 56.34° correspond to the (111), (200), (220), and (311) plane of CeO_2 (JCPDS 43-1002). However, there is no characteristic peak of Er in $\text{Er}^{3+}:\text{CeO}_2/\text{ATP}$ composites, which



may be due to the small doping amount of Er. In **Figure 1B**, the characteristic peak at 28.55° shows slight shift to higher Bragg angle, implying that the Er³⁺ dopant results in the lattice

contraction due to the fact that Er³⁺ (0.88 Å) replaced the Ce⁴⁺ (0.92 Å), subsequently leading to the lattice distortion and formation of oxygen vacancies (Li et al., 2012). **Figure 1C** shows

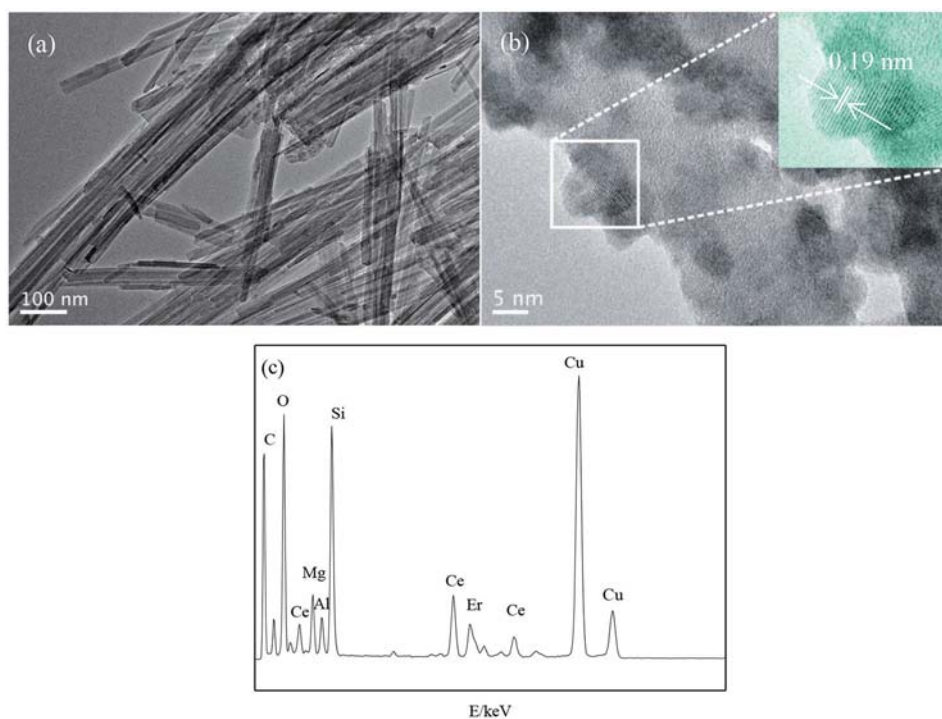


FIGURE 4 | TEM images of ATP (a), $\text{Er}^{3+}:\text{CeO}_2/\text{ATP}$ (b), and EDS of $\text{Er}^{3+}:\text{CeO}_2/\text{ATP}$ (c).

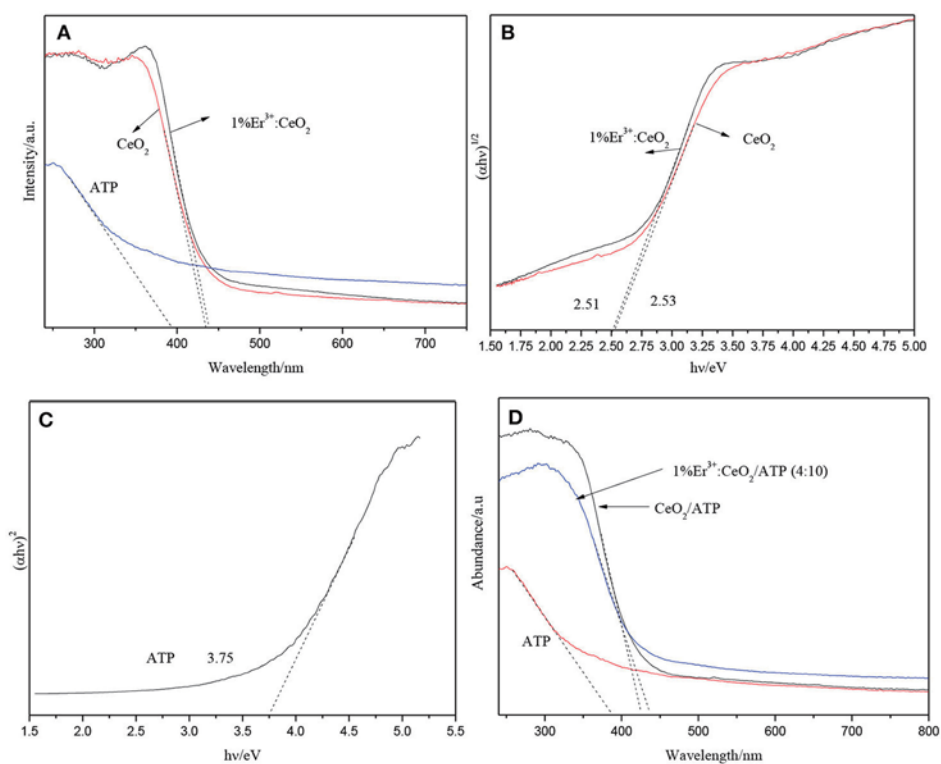


FIGURE 5 | UV-Vis patterns of ATP, CeO_2 , and $1\%\text{Er}^{3+}:\text{CeO}_2$ (A), the plots of transformed Kubelka-Munk function vs. light energy of CeO_2 , and $1\%\text{Er}^{3+}:\text{CeO}_2$ (B), the plots of transformed Kubelka-Munk function vs. light energy of ATP (C), and the UV-Vis patterns of ATP, CeO_2 , and $1\%\text{Er}^{3+}:\text{CeO}_2$ (4:10) (D).

the XRD patterns of different mass ratio of $\text{Er}^{3+}:\text{CeO}_2$ to ATP. With the increase of mass ratio, the characteristic peak intensity of ATP is gradually weakened whereas the intensity of CeO_2 is

strengthened without any change of peak position, suggesting the immobilization of $\text{Er}^{3+}:\text{CeO}_2$ on ATP.

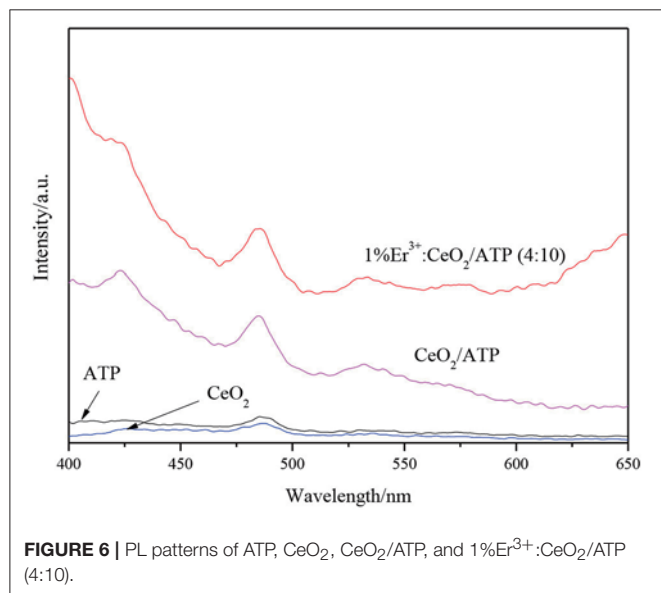


FIGURE 6 | PL patterns of ATP, CeO_2 , CeO_2/ATP , and $1\%\text{Er}^{3+}:\text{CeO}_2/\text{ATP}$ (4:10).

Raman Analysis

Figure 2 shows the Raman patterns of CeO_2/ATP and $\text{Er}^{3+}:\text{CeO}_2/\text{ATP}$. The peaks appearing in $454\text{--}459\text{ cm}^{-1}$ represent the F_{2g} vibration mode for cubic CeO_2 (Kumar and Kumar, 2017). Meanwhile, the peak intensity of F_{2g} is gradually decreased and the peak position is shifted to high wavenumber with the increase of Er, implying that Er is doped into CeO_2 lattice. The peaks located at 537 cm^{-1} can be attributed to the formation of oxygen vacancies (Mamontov et al., 2016), due to the fact that Er^{3+} replaces Ce^{4+} resulting in the transformation from Ce^{4+} to Ce^{3+} , subsequently oxygen vacancies are produced which is consistent with the results of XRD.

Optical Analysis

Figure 3 demonstrates the upconversion PL spectra of $\text{Er}^{3+}:\text{CeO}_2$ with different Er molar fraction. The upconversion luminescence was tested by the visible light of 488 nm as excitation light, while ultraviolet light was emitted near 281 nm, corresponding to the energy transfer from the $2\text{D}_{5/2}$ excited state to the $4\text{I}_{15/2}$ ground state. The upconversion luminescence intensity of $\text{Er}^{3+}:\text{CeO}_2$ is gradually increased below 1%, which

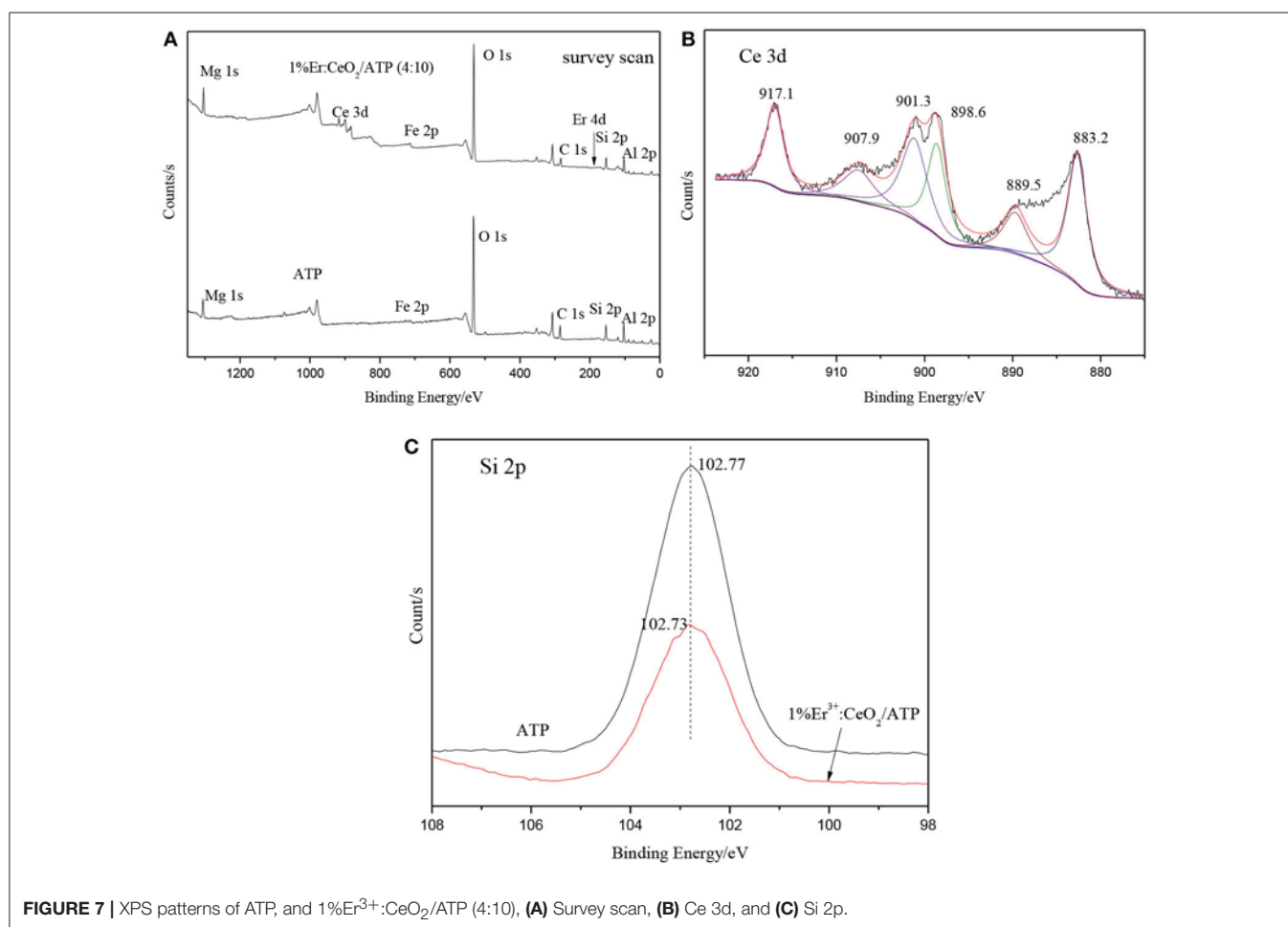


FIGURE 7 | XPS patterns of ATP, and $1\%\text{Er}^{3+}:\text{CeO}_2/\text{ATP}$ (4:10), (A) Survey scan, (B) Ce 3d, and (C) Si 2p.

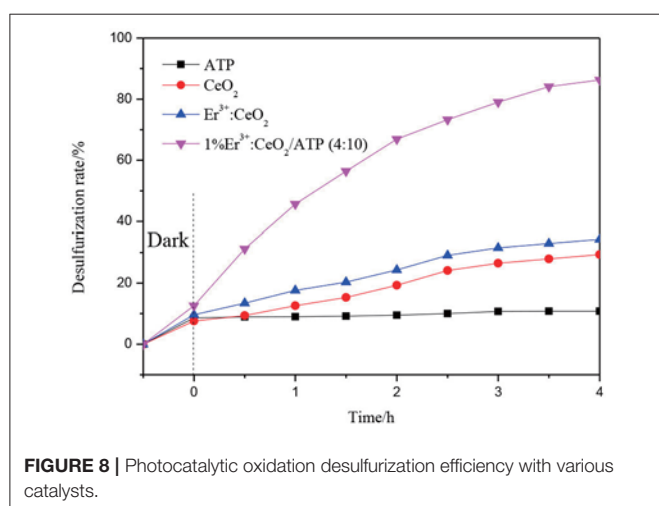


FIGURE 8 | Photocatalytic oxidation desulfurization efficiency with various catalysts.

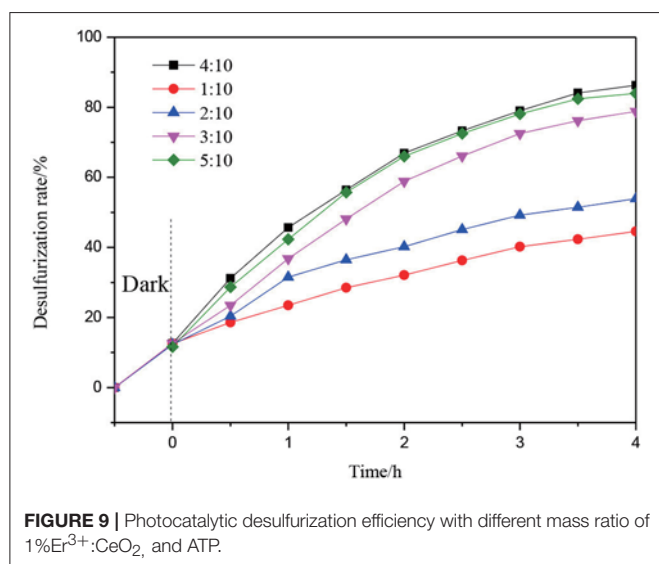


FIGURE 9 | Photocatalytic desulfurization efficiency with different mass ratio of 1%Er³⁺:CeO₂ and ATP.

reach strongest when the doping fraction is 1%. Afterwards, the upconversion luminescence intensity is obviously decreased when doping fraction is more than 1% due to the fact that the excessive doping of Er³⁺ shortens the distance and enhances the interaction among Er³⁺ ions, leading to the concentration quenching of the upconversion luminescence (Ramasamy et al., 2013). Therefore, the upconversion luminescence intensity is gradually decreased, and the doping fraction is optimized to be 1%.

TEM Analysis

Figure 4 shows the TEM results of ATP and Er³⁺:CeO₂/ATP. **Figure 4a** shows the pure ATP with a rod like structure having average diameter of 20–30 nm. **Figure 4b** shows the HRTEM image of 1% Er³⁺:CeO₂/ATP (4:10), and apparent nanoparticles are loaded on the surface of ATP. The inset lattice distance of CeO₂ is 0.19 nm corresponding to the (220) plane of CeO₂. Energy-dispersive spectroscopy (EDS) in **Figure 4c** displays Ce,

Er, Si, Fe, Mg, and Al elements, in which Si, Fe, Mg and Al are derived from ATP.

UV-Vis Analysis

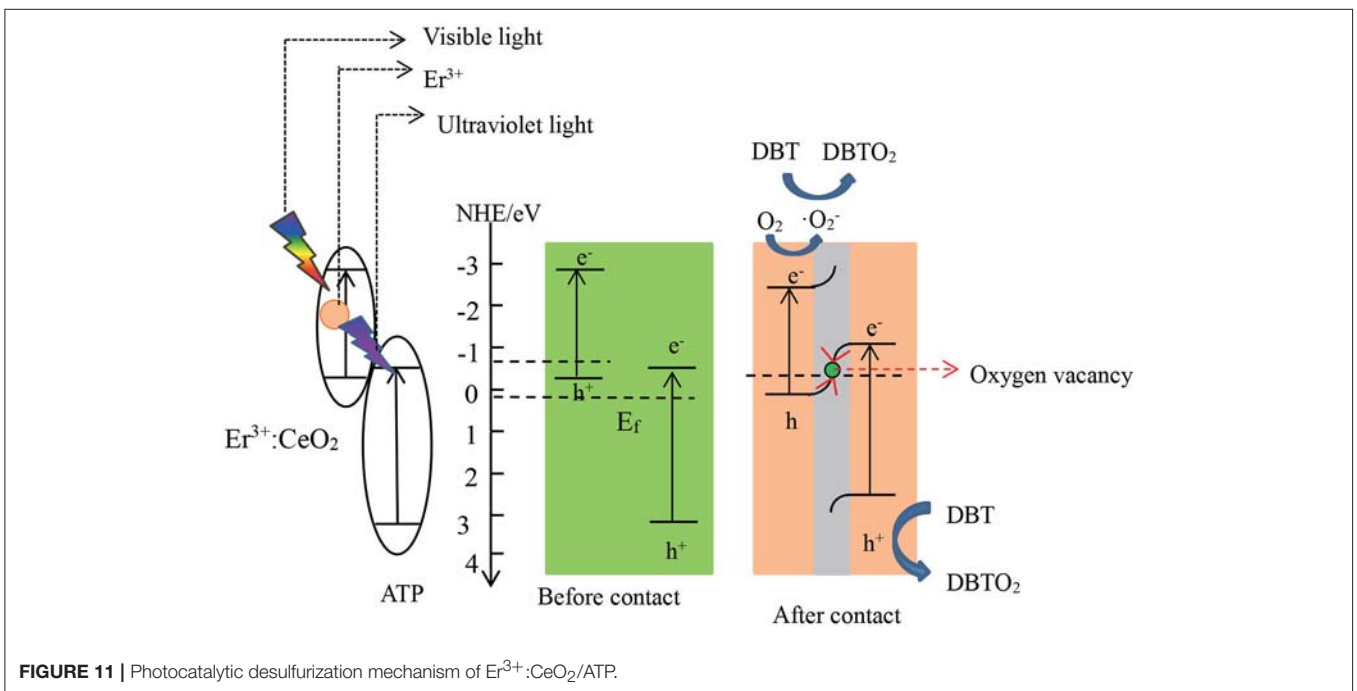
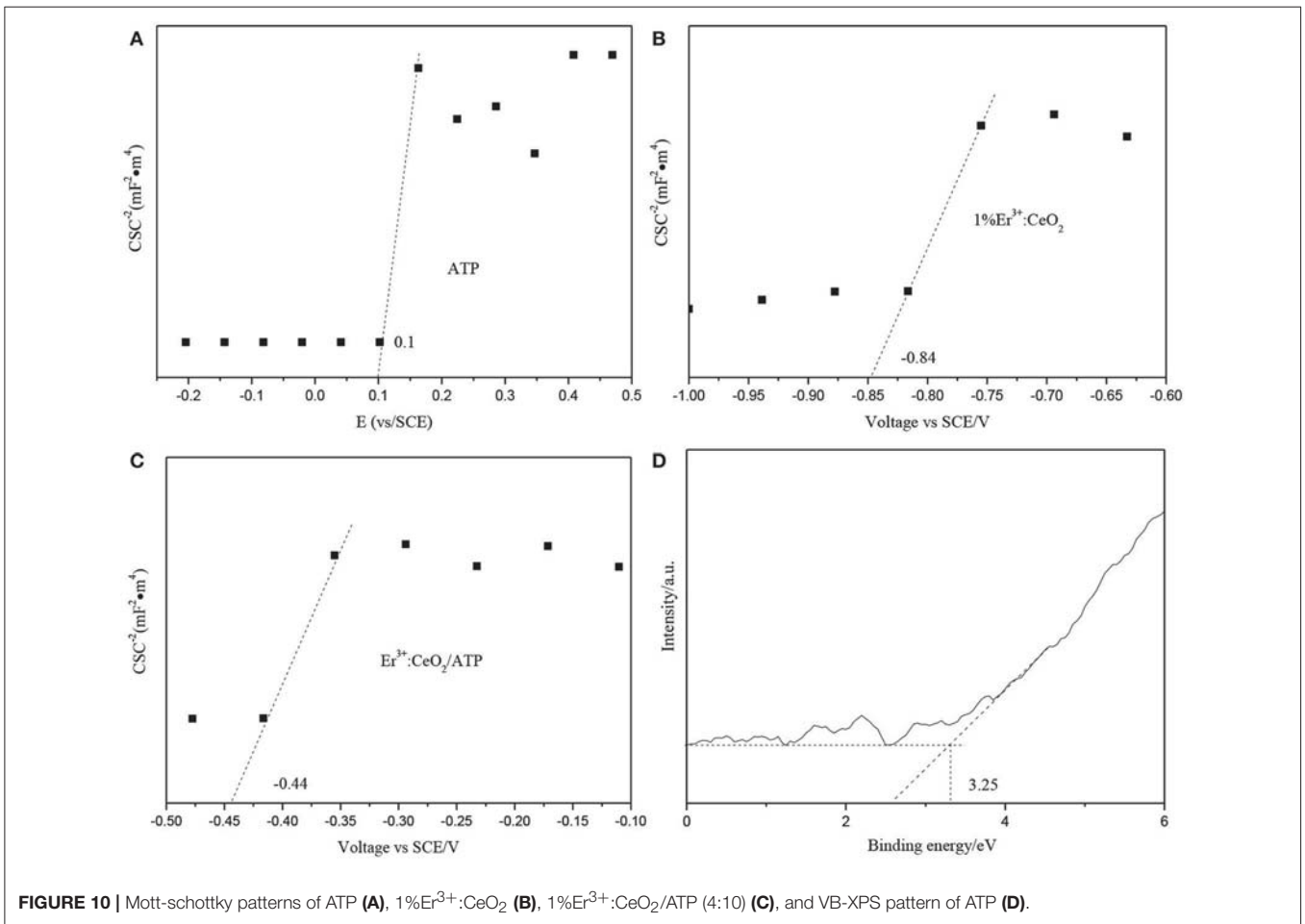
Figure 5A shows the UV-Vis image of CeO₂, ATP, and Er doping fraction for 1%. CeO₂ has a certain response to visible light, while the absorption edge of CeO₂ appears slightly red shift after doping of Er, which due to the fact that Er doping may change the band gap of the CeO₂. **Figure 5B** shows the plots of transformed Kubelka-Munk function vs. light energy of CeO₂ and 1% Er³⁺:CeO₂. The band gap of CeO₂ and 1% Er³⁺:CeO₂ is estimated to be 2.53 and 2.51 eV, respectively. As shown in **Figure 5C**, the band gap of ATP is estimated to be 3.75 eV, indicating ATP has ultraviolet response ability. It is reported that a semiconductor absorbs energy which is equal or larger than its band gap to produce photogenerated e⁻ and h⁺ (Zhuo et al., 2012). According to the results in **Figure 3**, the upconversion wavelength of 1% Er³⁺:CeO₂ locates at 281 nm corresponding to the band gap of 4.41 eV larger than the band gap of ATP with 3.75 eV. Therefore, ATP can be excited by the upconversion emission of 1% Er³⁺:CeO₂. **Figure 5D** shows the UV-Vis pattern of ATP, CeO₂/ATP and 1%Er³⁺:CeO₂/ATP. Compared with ATP, the absorption edge of CeO₂/ATP and 1% Er³⁺:CeO₂/ATP shows obviously red shift, which may favor for the photocatalytic performance.

PL Analysis

In order to investigate the recombination effect of photogenerated electrons and holes, PL analysis is performed under excitation of 300 nm. **Figure 6** shows the PL patterns of ATP, CeO₂, CeO₂/ATP and 1% Er³⁺:CeO₂/ATP (4:10). The emission peak of ATP is displayed, indicating that the photogenerated electrons and holes were recombined due to the fact that few Fe₂O₃ is stimulated to produce the photogenerated electrons and holes. Compared with pure ATP and CeO₂, the intensity of the emission peak of CeO₂/ATP and 1%Er³⁺:CeO₂/ATP (4:10) is significantly increased. In general, the intensity of the emission peak of PL is inversely proportional to the separation efficiency of the photogenerated charges. Obviously, the phenomenon described in the **Figure 6** violates the traditional law, which may be due to the unique Z-type heterostructure formed by Er³⁺:CeO₂ and ATP.

XPS Analysis

Figure 7 shows the XPS patterns of ATP and 1%Er³⁺:CeO₂/ATP (4:10). **Figure 7A** is the survey scan indicating the existence of Mg, Fe, Si, Al, Ce, Er, and C elements where Mg, Fe, Si, and Al are originated from ATP, Ce and Er are originated from Er³⁺:CeO₂. As shown in **Figure 7B**, the characteristic peaks of 883.2, 898.6, and 907.9 eV are ascribed to Ce³⁺ while the characteristic peaks of 889.5, 901.3, and 917.1 eV are ascribed to Ce⁴⁺, which is close to our previous result with respect to Ce 3d in CeO₂/ATP, (Li et al., 2017) indicating that the surface of CeO₂ contains oxygen vacancy. (Peng et al., 2017) The characteristic peak position of Si 2p in 1% Er³⁺:CeO₂/ATP (4:10) is lower than that of ATP shown in **Figure 7C**, due to the fact that the Si-O-Si bond may



be replaced by Si-O-Ce bond since the electronegativity of Ce is less than that of Si.

Photocatalytic Oxidation Desulfurization

The photocatalytic oxidation desulfurization is performed using various catalysts. As shown in **Figure 8**, the desulfurization rate is 10.8, 29.3, and 34.3% corresponding to ATP, CeO₂ and 1%Er³⁺:CeO₂ samples. Meanwhile, the photocatalytic oxidation desulfurization rate of 1%Er³⁺:CeO₂/ATP (4:10) reaches 87%. The 1%Er³⁺:CeO₂ and ATP may have synergy which accelerates the migration of photogenerated electrons and holes. Furthermore, a unique Z-type structure may form preserving the high redox potential, thus leads to the improved desulfurization performance.

Figure 9 shows the photocatalytic desulfurization performance with different mass ratios of 1%Er³⁺:CeO₂ and ATP. The desulfurization rate is enhanced gradually with the increase of the mass ratio. When the mass ratio is 4:10, the photocatalytic desulfurization rate of 1%Er³⁺:CeO₂/ATP reached 87% within 4 h, which may be due to the fact that with the content of 1%Er³⁺:CeO₂ increased, the concentration of oxygen vacancy is increased favoring for the transmission of charges. When the mass ratio is more than 4:10, the photocatalytic desulfurization rate is decreased, since the excess Er³⁺:CeO₂ nanoparticles may lead to aggregation restraining the exposure of surface active sites and destroying the balance of recombination of charges.

Photocatalytic Desulfurization Mechanism

The position of conduction band (CB), valence band (VB) and Fermi energy levels (E_f) of 1%Er³⁺:CeO₂ and ATP were calculated, respectively. **Figures 10A,B** show the Mott-schottky patterns of ATP and 1%Er³⁺:CeO₂, where the flat band potential (identical E_f) of ATP and 1%Er³⁺:CeO₂ is determined to be 0.1 and -0.84 eV, respectively. **Figure 10C** shows the Mott-schottky pattern of 1%Er³⁺:CeO₂/ATP (4:10) after contact, and the equilibrium E_f level is shifted to -0.44 eV located between that of Er³⁺:CeO₂ and ATP. **Figure 10D** shows the VB-XPS pattern of ATP, in which the VB value of ATP is determined to be 3.25 eV. In addition, the empirical formula of VB and CB is as follows (Obregon et al., 2016):

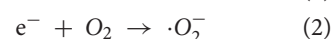
$$E_{VB} = X - E^e + \frac{1}{2}E_g$$

$$E_{CB} = E_{VB} - E_g$$

where E_{VB} and E_{CB} represent the VB and CB edge potential, respectively, X represents the electronegativity, E^e (about 4.5 eV) is the energy of free electrons on the hydrogen, and E_g is the band gap of the semiconductor. According to the above formula, the VB value for 1%Er³⁺:CeO₂ is calculated to be -0.42 eV. Since the E_g of ATP and 1%Er³⁺:CeO₂ is 3.75 and 2.51 eV by UV-Vis analysis in **Figure 5**, the corresponding CB for ATP and 1%Er³⁺:CeO₂ is -0.5 and -2.93 eV, respectively.

According to the above analysis, the photocatalytic desulfurization mechanism of 1%Er³⁺:CeO₂/ATP (4:10) is proposed as shown in **Figure 11**. After contact, free electrons

may flow from 1%Er³⁺:CeO₂ to ATP due to the disparity of E_f until they reach equilibrium, which forms an internal electric field, leading to the consumption and accumulation of free electrons (Huang et al., 2017). Simultaneously, the energy band edge of Er³⁺:CeO₂ is bended upward whereas the energy band edge of ATP is bended downward. Under visible light irradiation, the 1%Er³⁺:CeO₂ is stimulated to produce photogenerated e⁻ and h⁺ while Er³⁺ converts visible light to ultraviolet light. Subsequently, ATP is stimulated by the upconverted ultraviolet light to produce photogenerated e⁻ and h⁺. Then the downward band bending of ATP allows e⁻ flow to the oxygen vacancy in CeO₂ while the upward band bending of 1%Er³⁺:CeO₂ allows h⁺ flow to the oxygen vacancy which acted as the recombination center for the e⁻ and h⁺ (Ding et al., 2016). Finally, the photogenerated e⁻ in the CB of 1%Er³⁺:CeO₂ is preserved and reacts with O₂ to produce ·O₂⁻. Then, ·O₂⁻ and h⁺ in the VB of ATP synergistically oxidize DBT to DBTO₂ (Li et al., 2018). According to the above statement, the reaction equations are put forward as follows:



CONCLUSION

In this work, Er³⁺:CeO₂/ATP nanocomposites have been successfully prepared via a one-step precipitation method. Doping of Er not only alters the band gap of CeO₂, but also converts visible light to ultraviolet light and reach the strongest when the doping fraction of Er is 1%. Er³⁺:CeO₂ and ATP form Z-type heterostructure intermediated by oxygen vacancy, which promotes the transfer of photogenerated electrons and holes and preserves the charges with higher oxidation-reduction ability. The photocatalytic desulfurization rate reaches the highest 87% when the mass ratio of Er³⁺:CeO₂ and ATP is 4:10. This novel photocatalyst integrated by natural clay and rare earth upconversion may pave a new way for design of eco-friendly materials and beyond.

AUTHOR CONTRIBUTIONS

FW drafted the manuscript, XL made analysis and revision, HZ synthesized the samples and conducted desulfurization experiment, SZ characterized the samples, CY provided the idea and proposed the mechanism.

FUNDING

This work was supported by the National Science Foundation of China (51674043, 51702026), Jiangsu Key Laboratory of Advanced Catalytic Materials and Technology (BM2012110) and Priority Academic Program Development of Jiangsu Higher Education Institutions (PAPD).

REFERENCES

- Agarwal, M., Dikshit, P. K., Bhasarkar, J. B., Borah, A. J., and Moholkar, V. S. (2016). Physical insight into ultrasound-assisted biodesulfurization using free and immobilized cells of *Rhodococcus rhodochrous* MTCC 3552. *Chem. Eng. J.* 295, 254–267. doi: 10.1016/j.cej.2016.03.042
- Balaji, R., Kumar, S., Reddy, K. L., Sharma, V., Bhattacharyya, K., and Krishnan, V. (2017). Near-infrared driven photocatalytic performance of lanthanide-doped NaYF₄@CdS core-shell nanostructures with enhanced upconversion properties. *J. Alloys Compd.* 724, 481–491. doi: 10.1016/j.jallcom.2017.07.050
- Bhethanabotla, V. C., Russell, D. R., and Kuhn, J. N. (2016). Assessment of mechanisms for enhanced performance of Yb/Er/titania photocatalysts for organic degradation: part 2. Role of rare earth elements in the titania phase. *Appl. Catal. B Environ.* 202, 156–164. doi: 10.1016/j.apcatb.2016.09.008
- Ding, J., Dai, Z., Qin, F., Zhao, H., Zhao, S., and Chen, R. (2016). Z-scheme BiO_{1-x}Br/Bi₂O₃CO₃ photocatalyst with rich oxygen vacancy as electron mediator for highly efficient degradation of antibiotics. *Appl. Catal. B Environ.* 205, 281–291. doi: 10.1016/j.apcatb.2016.12.018
- Feng, W., Han, C., and Li, F. (2013). Upconversion-nanophosphor-based functional nanocomposites. *Adv. Mater.* 25, 5287–5303. doi: 10.1002/adma.201301946
- Han, G., Wang, M., Li, D., Bai, J., and Diao, G. (2017). Novel upconversion Er, Yb-CeO₂ hollow spheres as scattering layer materials for efficient dye-sensitized solar cells. *Solar Energy Mater. Solar Cells* 160, 54–59. doi: 10.1016/j.solmat.2016.10.021
- Huang, Z.-F., Song, J., Wang X., Pan, L., Li, K., Zhang, X., et al. (2017). Switching charge transfer of C₃N₄/W₁₈O₄₉ from type-II to Z-scheme by interfacial band bending for highly efficient photocatalytic hydrogen evolution. *Nano Energy* 40, 308–316. doi: 10.1016/j.nanoen.2017.08.032
- Khodadadi Dizaji, A., Mortaheb, H. R., and Mokhtarani, B. (2018). Complete oxidative desulfurization using graphene oxide-based phosphomolybdic acid catalyst: process optimization by two phase mass balance approach. *Chem. Eng. J.* 335, 362–372. doi: 10.1016/j.cej.2017.10.129
- Kumar, S., and Kumar, A. (2017). Enhanced photocatalytic activity of rGO-CeO₂ nanocomposites driven by sunlight. *Mater. Sci. Eng. B* 223, 98–108. doi: 10.1016/j.mseb.2017.06.006
- Li, X., Li, F., Lu, X., Zuo, S., Li, Z., Yao, C., et al. (2018). Microwave hydrothermal synthesis of BiP_{1-x}V_xO₄/attapulgite nanocomposite with efficient photocatalytic performance for deep desulfurization. *Powder Technol.* 327, 467–475. doi: 10.1016/j.powtec.2018.01.005
- Li, X., Ni, C., Yao, C., and Chen, Z. (2012). Development of attapulgite/Ce_{1-x}Zr_xO₂ nanocomposite as catalyst for the degradation of methylene blue. *Appl. Catal. B Environ.* 117–118, 118–124. doi: 10.1016/j.apcatb.2012.01.008
- Li, X., Zhang, Z., Yao, C., Lu, X., Zhao, X., and Ni, C. (2016). Attapulgite-CeO₂/MoS₂ ternary nanocomposite for photocatalytic oxidative desulfurization. *Appl. Surf. Sci.* 364, 589–596. doi: 10.1016/j.apsusc.2015.12.196
- Li, X., Zhu, W., Lu, X., Zuo, S., Yao, C., and Ni, C. (2017). Integrated nanostructures of CeO₂/attapulgite/g-C₃N₄ as efficient catalyst for photocatalytic desulfurization: mechanism, kinetics and influencing factors. *Chem. Eng. J.* 326, 87–98. doi: 10.1016/j.cej.2017.05.131
- Liu, R., Zhang, J., Xu, Z., Zhao, D., and Sun, S. (2017). Visible light photocatalytic oxidative desulfurization using Ti-MCM-41-loaded iron phthalocyanine combined with ionic liquid extraction. *J. Mater. Sci.* 53, 4927–4938. doi: 10.1007/s10853-017-1954-0
- Ma, S., Li, X., Lu, X., Zuo, S., Li, Z., and Yao, C. (2018). Carbon quantum dots/attapulgite nanocomposites with enhanced photocatalytic performance for desulfurization. *J. Mater. Sci. Mater. Electron.* 29, 2709–2715. doi: 10.1007/s10854-017-8197-3
- Mamontov, G. V., Grabchenko, M. V., Sobolev, V. I., Zaikovskii, V. I., and Vodyankina, O. V. (2016). Ethanol dehydrogenation over Ag-CeO₂/SiO₂ catalyst: role of Ag-CeO₂ interface. *Appl. Catal. A Gen.* 528, 161–167. doi: 10.1016/j.apcata.2016.10.005
- Obregón, S., Zhang, Y., and Colón, G. (2016). Cascade charge separation mechanism by ternary heterostructured BiPO₄/TiO₂/g-C₃N₄ photocatalyst. *Appl. Catal. B Environ.* 184, 96–103. doi: 10.1016/j.apcatb.2015.11.027
- Peng, R., Li, S., Sun, X., Ren, Q., Chen, L., Fu, M., et al. (2017). Size effect of Pt nanoparticles on the catalytic oxidation of toluene over Pt/CeO₂ catalysts. *Appl. Catal. B Environ.* 220, 462–470. doi: 10.1016/j.apcatb.2017.07.048
- Pickering, J. W., Bhethanabotla, V. R., and Kuhn, J. N. (2017). Assessment of mechanisms for enhanced performance of TiO₂/YAG:Yb³⁺,Er³⁺ composite photocatalysts for organic degradation. *Appl. Catal. B Environ.* 202, 147–155. doi: 10.1016/j.apcatb.2016.09.007
- Raj, J. J., Magaret, S., Pranesh, M., Lethesh, K. C., Devi, W. C., and Mutalib, M. I. A. (2017). Extractive desulfurization of model fuel oil using ester functionalized imidazolium ionic liquids. *Sep. Purif. Technol.* 196, 115–123. doi: 10.1016/j.seppur.2017.08.050
- Ramasamy, P., Chandra, P., Rhee, S. W., and Kim, J. (2013). Enhanced upconversion luminescence in NaGdF₄:Yb,Er nanocrystals by Fe³⁺ doping and their application in bioimaging. *Nanoscale* 5, 8711–8717. doi: 10.1039/c3nr01608k
- Šutka, A., Vanags, M., Joost, U., Šmits, K., Ruža, J., Ločs, J., et al. (2018). Aqueous synthesis of Z-scheme photocatalyst powders and thin-film photoanodes from earth abundant elements. *J. Environ. Chem. Eng.* 6, 2606–2615. doi: 10.1016/j.jece.2018.04.003
- Wang, L., Wang, W. Y., Mominou, N., Liu, L. X., and Li, S. Z. (2016). Ultra-deep desulfurization of gasoline through aqueous phase *in-situ* hydrogenation and photocatalytic oxidation. *Appl. Catal. B Environ.* 193, 180–188. doi: 10.1016/j.apcatb.2016.04.032
- Wu, H., Yang, Z., Liao, J., Lai, S., Qiu, J., Song, Z., et al. (2014). Upconversion luminescence properties of three-dimensional ordered macroporous CeO₂:Er³⁺,Yb³⁺. *J. Alloys Compd.* 586, 485–487. doi: 10.1016/j.jallcom.2013.10.124
- Yang, Y., Lv, G., Li, J., Guo, W., and Zhang, Y. (2018). Synthesis of ceria nanorods as adsorbent for the adsorption desulfurization of gasoline fuel. *J. Alloys Compd.* 747, 189–196. doi: 10.1016/j.jallcom.2018.03.026
- Zeng, X., Xiao, X., Li, Y., Chen, J., and Wang, H. (2017). Deep desulfurization of liquid fuels with molecular oxygen through graphene photocatalytic oxidation. *Appl. Catal. B Environ.* 209, 98–109. doi: 10.1016/j.apcatb.2017.02.077
- Zhang, G., Ren, J., Liu, B., Tian, M., Zhou, H., and Zhao, J. (2018). *In situ* hydrothermal preparation and photocatalytic desulfurization performance of metallophthalocyanine sensitized SnO₂. *Inorg. Chim. Acta* 471, 782–787. doi: 10.1016/j.ica.2017.12.025
- Zhang, G., Wang, H., Guo, S., Wang, J., and Liu, J. (2016b). Synthesis of Cu/TiO₂/organo-attapulgite fiber nanocomposite and its photocatalytic activity for degradation of acetone in air. *Appl. Surf. Sci.* 362, 257–264. doi: 10.1016/j.apsusc.2015.11.218
- Zhang, J., Chen, A., Wang, L., Li, X. A., and Huang, W. (2016a). Striving toward visible light photocatalytic water splitting based on natural silicate clay mineral: the interface modification of attapulgite at the atomic-molecular level. *ACS Sust. Chem. Eng.* 4, 4601–4607. doi: 10.1021/acssuschemeng.6b00716
- Zhang, J., He, R., and Liu, X. (2013). Efficient visible light driven photocatalytic hydrogen production from water using attapulgite clay sensitized by CdS nanoparticles. *Nanotechnology* 24:505401. doi: 10.1088/0957-4484/24/50/505401
- Zhao, H., Qiu, F., Yan, J., Wang, J., Li, X., and Yang, D. (2016). Preparation of economical and environmentally friendly graphene/palygorskite/TiO₂ composites and its application for the removal of methylene blue. *Appl. Clay Sci.* 121–122, 137–145. doi: 10.1016/j.clay.2015.12.009
- Zhuo, S., Shao, M., and Lee, S. T. (2012). Upconversion and downconversion fluorescent graphene quantum dots: ultrasonic preparation and photocatalysis. *ACS Nano* 6, 1059–1064. doi: 10.1021/nn2040395

Conflict of Interest Statement: The authors declare that the research was conducted in the absence of any commercial or financial relationships that could be construed as a potential conflict of interest.

Copyright © 2018 Wu, Li, Zhang, Zuo and Yao. This is an open-access article distributed under the terms of the Creative Commons Attribution License (CC BY). The use, distribution or reproduction in other forums is permitted, provided the original author(s) and the copyright owner(s) are credited and that the original publication in this journal is cited, in accordance with accepted academic practice. No use, distribution or reproduction is permitted which does not comply with these terms.



Enhanced Degradation of Rh 6G by Zero Valent Iron Loaded on Two Typical Clay Minerals With Different Structures Under Microwave Irradiation

Wenxiu Rao, Guocheng Lv*, Danyu Wang and Libing Liao*

Beijing Key Laboratory of Materials Utilization of Nonmetallic Minerals and Solid Wastes, National Laboratory of Mineral Materials, School of Materials Science and Technology, China University of Geosciences, Beijing, China

OPEN ACCESS

Edited by:

Wenbo Wang,
Lanzhou Institute of Chemical Physics
(CAS), China

Reviewed by:

Xiazhang Li,
Changzhou University, China
Cláudia Gomes Silva,
Universidade do Porto, Portugal
Priyabrat Mohapatra,
C. V. Raman College of Engineering,
India

*Correspondence:

Guocheng Lv
guochenglv@cugb.edu.cn
Libing Liao
clayl@cugb.edu.cn

Specialty section:

This article was submitted to
Green and Sustainable Chemistry,
a section of the journal
Frontiers in Chemistry

Received: 30 July 2018

Accepted: 14 September 2018

Published: 09 October 2018

Citation:

Rao W, Lv G, Wang D and Liao L
(2018) Enhanced Degradation of Rh
6G by Zero Valent Iron Loaded on
Two Typical Clay Minerals With
Different Structures Under Microwave
Irradiation. *Front. Chem.* 6:463.
doi: 10.3389/fchem.2018.00463

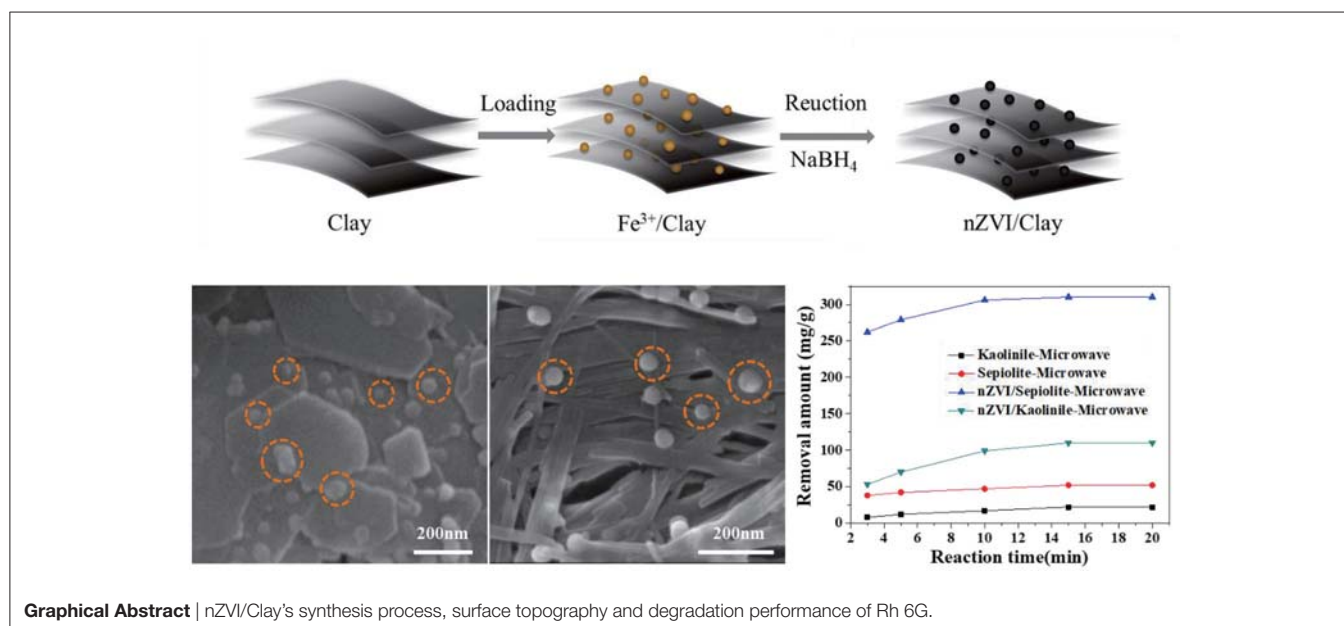
Nanoscale zero valent iron has been a widespread concern in various fields due to its large specific surface area and high reactivity. However, nanoscale zero valent iron (nZVI) is very likely to aggregate and be oxidized, which limit its wide application in industry. Most clay minerals have a large adsorption capacity of cations due to their negative charges and high specific surface areas. In the present work, nZVI was loaded onto two typical clay minerals: kaolinite and sepiolite, to inhibit its oxidation and aggregation. The composites were applied to degrade Rhodamine 6G (Rh 6G) under microwave irradiation. The effects of pH value and microwave power on degradation were studied. The results showed that the removal amount of Rh 6G by nZVI/kaolinite was 110 mg/g in 15 min, while it reached 300 mg/g by nZVI/sepiolite. The difference between these two composites was mostly determined by the structures of these two clay minerals.

Keywords: nanoscale zero valent iron, kaolinite, sepiolite, microwave, Fenton-like reaction

INTRODUCTION

About 80% of the textile wastewater comes from the textile printing and dyeing industry every year, which is an industrial sector with large water consumption and high discharge of wastewater (Liu et al., 2017). Printing and dyeing wastewaters have the characteristics of large water volume, high chroma and high pollutant concentration (Zhao et al., 2010). Textile processing wastewater contains a variety of contaminants. Direct discharge of the wastewater without treatment into rivers and lakes would cause serious pollution to environment and bring a serious threat to the survival of mankind (Kehinde and Aziz, 2016). However, the treatment of wastewater is extremely difficult, which made it necessary to develop new materials to process the wastewater (Liu et al., 2015).

Clay minerals are mainly composed of silicon, aluminum and magnesium. They are inexpensive and abundant in nature all over the world, and play an important role in environmental protection and the development of new mineral materials (Kelm et al., 2003). Clay minerals have complex pore structures and high specific surface areas (Steudel et al., 2009). We want to load nZVI on clay minerals' surface to make more sufficient contact with the solution. Kaolinite is a typical 1:1 layered structure, its lattice structure is very orderly, so there is basically no isomorphous substitution in its structure, resulting in poor swelling performance in water (Ezzatahmedi et al., 2017), sepiolite also can't spontaneously swell in water, therefore nZVI can only be supported on their surface.



Kaolinite can be used to adsorb many organic pollutants, due to its special layered structure, such as congo red dye (Vimonses et al., 2009), heavy metals (Matłok et al., 2015) and dipalmitoyl lecithin (Jr et al., 1975). Sepiolite is a common 2:1 chain layered type of clay mineral, composed of two layers of silicone tetrahedron and an intermediate layer of magnesium octahedron (Kaviratna, 1994). It can also adsorb numerous organic pollutants, such as reactive blue 221 (Alkan et al., 2007), 3-aminopropyltriethoxysilane (Demirbaş et al., 2007) and β -carotene (Sabah et al., 2007).

Fenton reaction of degradation of organic dyes attracted considerable attention in recent years (Cheng et al., 2008), using the catalytic power of Fe^{2+} to generate highly reactive hydroxyl radicals (HO^\bullet) to degrade organic dyes (Masomboon et al., 2010). However, Fenton reaction requires high concentrations of iron ions (Yoon et al., 2001) and an acidic reaction environment (Liu et al., 2013), greatly increasing the cost of degradation of organic dyes. Fenton-like reaction can degrade organic dyes using nZVI (Xu and Wang, 2013), which can solve the problems caused by Fenton reaction mentioned above. nZVI can degrade many organic pollutants due to its special properties, such as 2,4-dichlorophenol (Li et al., 2018), trichloroethylene (TCE) (Kim et al., 2010), methylene blue (Yang et al., 2015). However, due to the aggregation and oxidation of nZVI (Dong et al., 2017), the loading of nZVI onto clay minerals is expected to inhibit the aggregation and oxidation of nZVI.

It has been proven that microwave could accelerate the rate of catalytic reactions (Mochizuki et al., 2015; Bianchi et al., 2017). The aqueous solutions in the reaction systems can self-heat by absorbing microwaves (Zhang and Liao, 2017), and the reaction rate can be greatly improved.

In the present work, nZVI was loaded onto kaolinite and sepiolite, respectively, and used to degrade Rh 6G under microwave irradiation. It was found that the removal amount of

Rh 6G by nZVI/sepiolite was greater than that of nZVI/kaolinite. The loading amount of nZVI on sepiolite was almost three times as that on kaolinite, which was mainly determined by the structures of the clay minerals (**Graphical Abstract**).

EXPERIMENTAL

Materials

Iron (III) chloride hexahydrate ($\text{FeCl}_3 \cdot 6\text{H}_2\text{O}$) and sodium borohydride (NaBH_4) were purchased from Beijing Chemical Workstation. Rh 6G was from Aladdin. All the chemicals were of analytical grade. The sepiolite was obtained from Sigma Aldrich, its BET area and average pore size are $319.4 \text{ m}^2/\text{g}$ and 6.885 nm , respectively. The kaolinite was bought from China Kaolin Co, Ltd, its BET area and average pore size are $22 \text{ m}^2/\text{g}$ and 30.095 nm , respectively. All the chemicals and minerals were used without further purification. All of the solutions were formulated with distilled water.

Synthesis of nZVI/Kaolinite and nZVI/Sepiolite

100 mL distilled water, 5 g kaolinite (or sepiolite) and 10 g $\text{FeCl}_3 \cdot 6\text{H}_2\text{O}$ were added in a three-necked flask and stirred for 12 h to load Fe^{3+} on clay minerals. Then 8 g NaBH_4 was added, and stirred for another 30 min under the protection of nitrogen at room temperature. The suspension was centrifuged and washed with ethanol for three times. The solid part was then freeze-dried.

Rh 6G Removal Experiment

2,000 mg Rh 6G was dissolved in 500 mL distilled water and ultrasonic for 15 min to prepare 4,000 mg/L Rh 6G solution. In batch experiments, 0.1 g as prepared sample was added in 10 mL Rh 6G solution, then, the mixture was placed in a microwave oven to degrade Rh 6G for a certain time under different

microwave power. After the degradation, the mixture was centrifuged and the supernatant was filtered through 0.22 μm syringe filters before being taken to a UV-Vis spectrophotometer for the analysis of equilibrium concentrations. In the cycle test, the used nZVI/clay was reduced by NaBH_4 before the next trial. All experiments were run in duplicates.

Characterizations

The crystal diffraction data was determined by the X-ray diffractometer (Rigaku D/Max-IIIa X-ray diffractometer) with a $\text{CuK}\alpha$ -radiation at 30 kV and 20 mA operating conditions. Angle ranged from 3 to 70° and the speed was 8° min^{-1} with a scanning step length of 0.01°. Scanning electron microscopy (SEM) was used to record the surface morphology of the samples, carried out on a scanning electron microscope (JSM-IT300) with conditions at 30 kV and 10⁻⁴ Pa. The equilibrium concentration of Rh 6G was determined by a UV-Vis spectrophotometer (UV2400/PC), the value of the absorption coefficient at 525 nm. The surface compositions of samples were tested by an X-ray photoelectron spectrometer (K-Alpha), which can analyze the valence of elements in samples, especially valence state of iron element. The microwave network analyzer N5244A (Agilent) was used to analyze microwave absorption properties of flexible absorbing film. The frequency range was from 2 to 10 GHz. Automated gas sorption analyzer (Autosorb-iQ-2MP) was used to analyze the specific surface area of the samples. Zeta potential was recorded by nanoparticle size potential analyzer (Zetasizer Nano ZS90). The coaxial wire method was adopted for the analysis.

RESULTS AND DISCUSSION

The composites were synthesized by liquid phase reducing method. The structures of nZVI, kaolinite, sepiolite and the

composites were showed in **Figure 1**. The reflections at $2\theta = 12.38^\circ$ (**Figure 1A**), 7.58° (**Figure 1B**) corresponded to the (001) basal plane of kaolinite (JCPDS No. 89-6538) and the (001) basal plane of sepiolite (JCPDS No. 29-863), respectively. The diffraction peak at 44.7° is attributed to the (110) basal plane

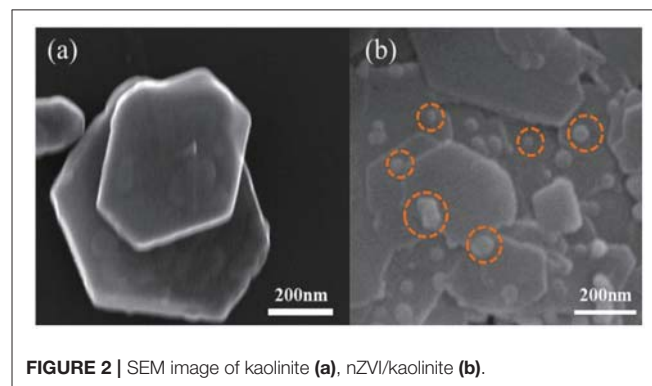


FIGURE 2 | SEM image of kaolinite (a), nZVI/kaolinite (b).

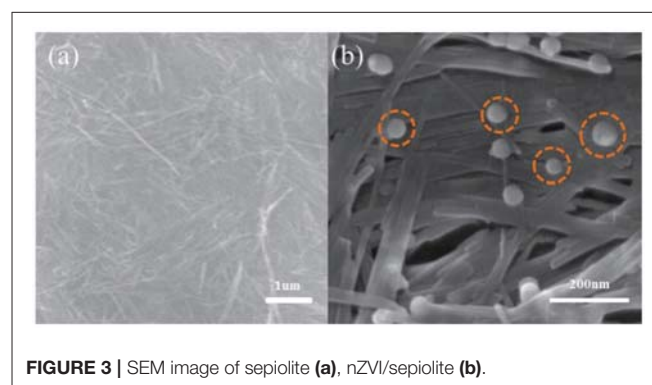


FIGURE 3 | SEM image of sepiolite (a), nZVI/sepiolite (b).

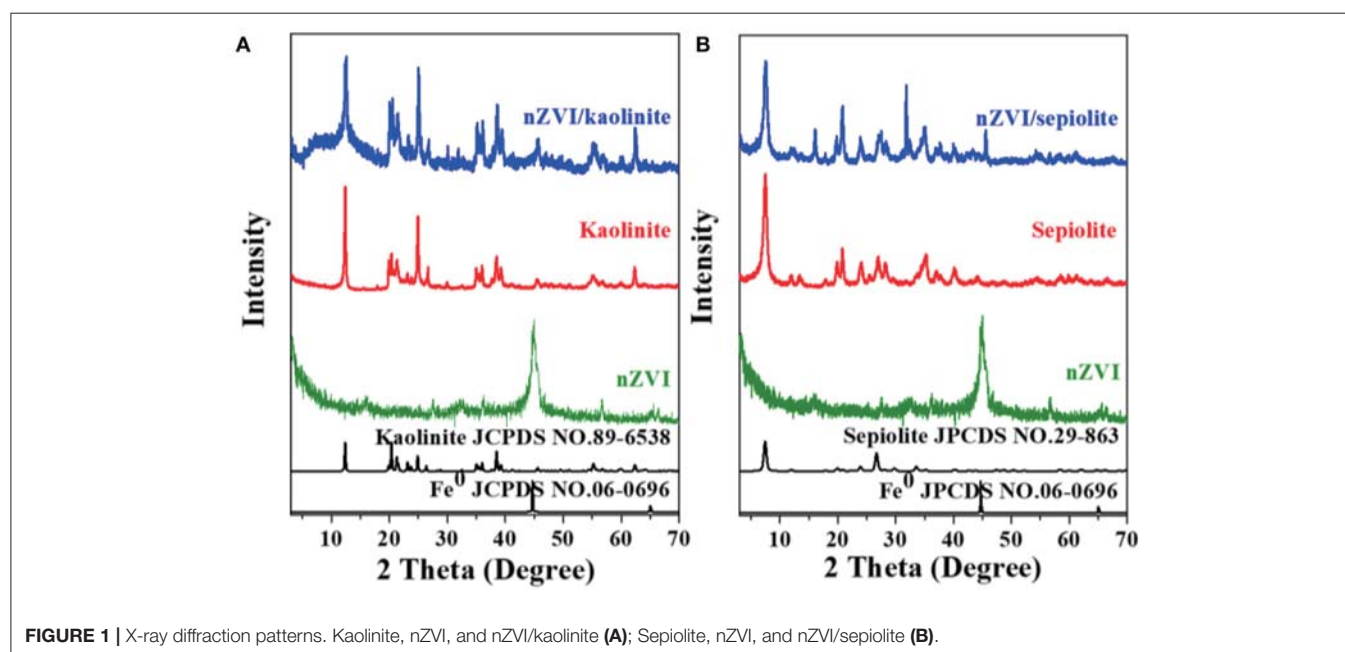


FIGURE 1 | X-ray diffraction patterns. Kaolinite, nZVI, and nZVI/kaolinite (A); Sepiolite, nZVI, and nZVI/sepiolite (B).

of Fe^0 (JCPDS No. 06-0696). No obvious characteristic peaks of iron oxides was founded in the nZVI/kaolinite or nZVI/sepiolite, indicating that nZVI was not oxidized or only a very small part was oxidized during the synthesis process. Besides, the patterns of the composites stayed almost the same before and after the loading, suggesting that the structures of clay minerals not yet destroyed, and nZVI is loaded on the surface of mineral material rather than intercalated in this study.

The SEM results in **Figures 2, 3** revealed the morphology of the minerals before and after the loading of nZVI. The lamellar

structure of kaolinite was observed clearly. nZVI particles were evenly distributed on the layers of kaolinite, within a size range of 25–35 nm, indicating that the loading of nZVI on kaolinite could suppress the aggregation of nZVI effectively.

While loading onto sepiolite, most of the nZVI particles were attached to the fibers within a size range of 20–45 nm.

Figure 4 showed the color changes of nZVI and nZVI/clay composites after dispersed in water for different amounts of time.

The color of materials changed to black after the addition of nZVI and nZVI/clay. As time went by, the color of both materials become lighter gradually due to the oxidation of nZVI. However, nZVI/clay showed a better resistance to oxidation than nZVI as the color of nZVI suspension changed from black to yellow completely after 72 h while the color of nZVI/clay suspension just started to turn yellow after the same time. It indicated that only a small portion of nZVI was oxidized after loading, which means that loading nZVI onto clay could effectively inhibit its oxidation.

The surface compositions of nZVI/kaolinite and nZVI/sepiolite and the valence state of Fe on its surface were analyzed by XPS technique. The survey spectrum of this sample was shown in **Figure 5A**, proving that the composites contains iron elements. The fine spectrum of Fe 2p of nZVI/kaolinite and nZVI/sepiolite contains four different peaks, as shown in **Figure 5B**. The peaks at binding energies of 705 and 720 eV could be assigned to the 2p_{3/2} and 2p_{1/2} peaks of Fe^0 in nZVI/sepiolite and nZVI/kaolinite. The other two peaks at binding energies of 713.5 and 726.5 eV could be attributed to the 2p_{3/2} and 2p_{1/2}

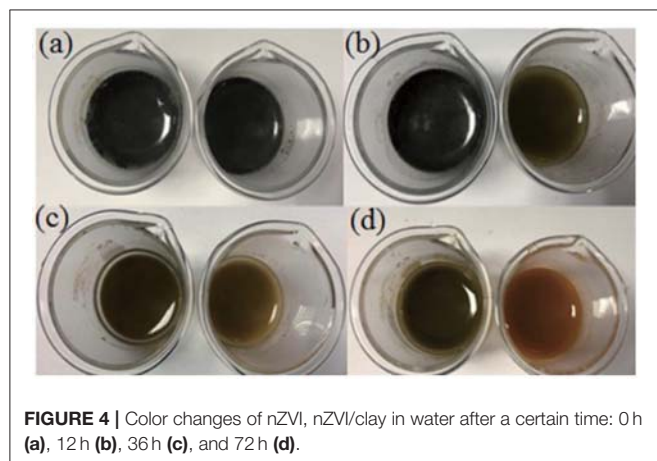


FIGURE 4 | Color changes of nZVI, nZVI/clay in water after a certain time: 0 h (a), 12 h (b), 36 h (c), and 72 h (d).

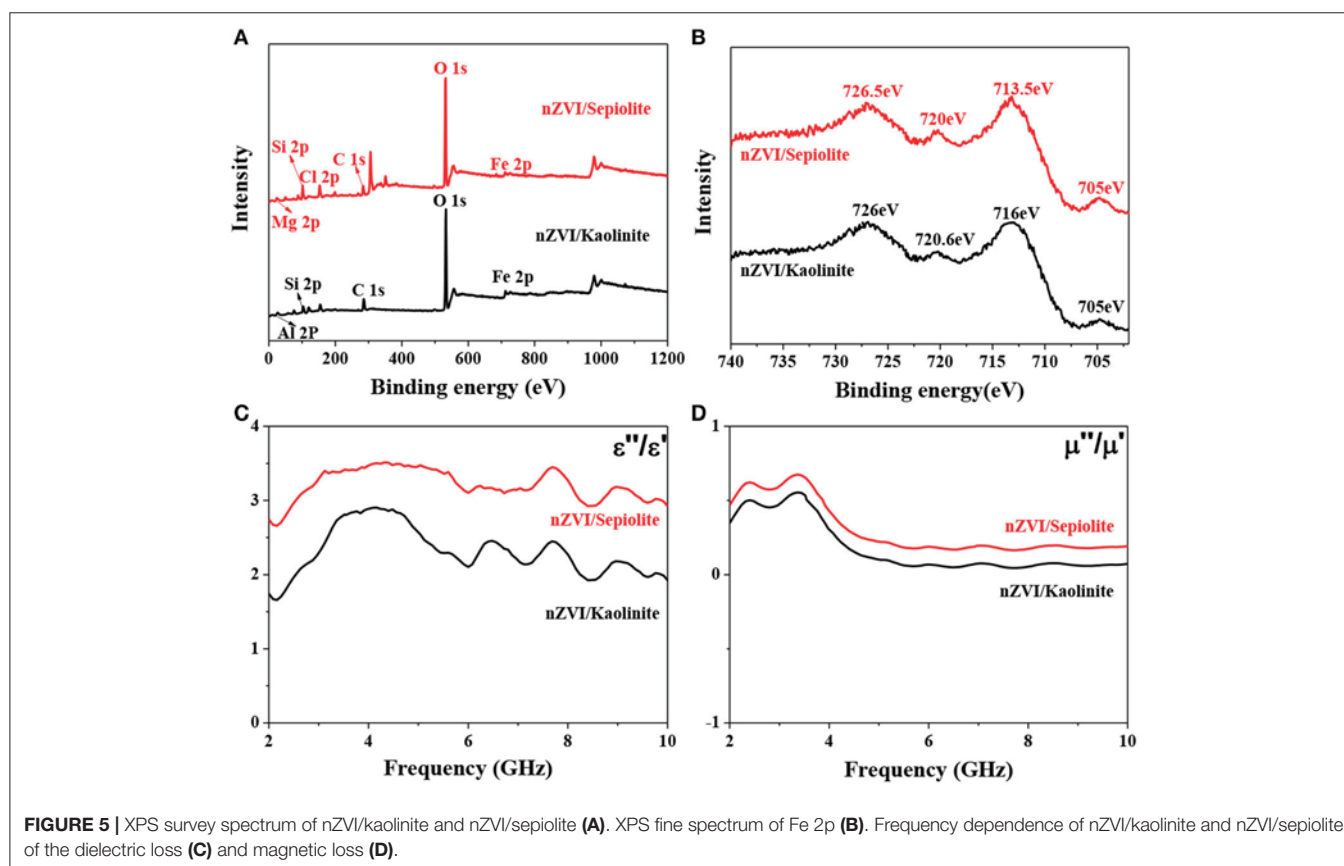


FIGURE 5 | XPS survey spectrum of nZVI/kaolinite and nZVI/sepiolite (A). XPS fine spectrum of Fe 2p (B). Frequency dependence of nZVI/kaolinite and nZVI/sepiolite of the dielectric loss (C) and magnetic loss (D).

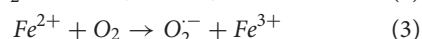
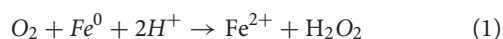
peaks of Fe (III) in nZVI/sepiolite while 716 and 726 eV in nZVI/kaolinite, indicating that a small part of Fe⁰ on the surface of the composite was oxidized to Fe (III).

The ability of a substance to absorb microwaves is mainly determined by its dielectric loss factor. A substance with a large dielectric loss factor usually has a strong ability to absorb microwaves. On the contrary, a material with a small dielectric loss factor has a weak ability to absorb microwaves. The dielectric loss ($\tan \delta \epsilon = \epsilon''/\epsilon'$) of nZVI/kaolinite and nZVI/sepiolite was analyzed by a microwave network analyzer (Figure 5C). The dielectric loss of nZVI/sepiolite was higher than that of nZVI/kaolinite from 2 to 10 GHz. In addition, good microwave absorption performance also relate to magnetic loss. The greater the magnetic loss, the better the microwave absorption performance. The magnetic loss ($\tan \delta \mu = \mu''/\mu'$) of nZVI/sepiolite was higher than that of nZVI/kaolinite from 2 to 10 GHz (Figure 5D). Therefore, nZVI/sepiolite had higher microwave absorption properties than those of nZVI/kaolinite.

Table 1 presented the chemical compositions of different materials. Kaolinite and sepiolite showed a slight difference in iron content. However, there was a significant difference in iron content between nZVI/kaolinite and nZVI/sepiolite, indicating different loadings of iron.

DEGRADATION OF RH 6G USING NZVI/KAOLINITE AND NZVI/SEPIOLITE

nZVI can effectively degrade organic dyes through the following Fenton-like reactions. Fe⁰ was gradually oxidized to Fe³⁺ and generated hydroxyl radicals (HO•) and superoxide radicals (O₂⁻), which were the main active ingredients for the degradation of Rh 6G.



The degradation ability of Rh 6G was reflected by the removal amount of Rh 6G under microwave irradiation by nZVI/kaolinite and nZVI/sepiolite. The effect of pH on the degradation rate of Rh 6G was shown in Figure 6A. Both nZVI/kaolinite and nZVI/sepiolite showed higher degradation ability under acidic conditions, indicating that acidic conditions are more suitable. It was because that, under alkaline conditions, the generation of HO• and O₂⁻ would be inhibited and Fe⁰ would react with OH⁻ to form iron hydroxide. Meanwhile, H₂O₂ would

decompose rapidly when pH > 7. The effect of microwave power on the degradation of Rh 6G by nZVI/kaolinite and nZVI/sepiolite was also investigated (Figure 6B). The removal amount of Rh 6G by nZVI/kaolinite and nZVI/sepiolite increases with the increase of microwave power, since the generation rate of HO• and O₂⁻ are proportional to the microwave power.

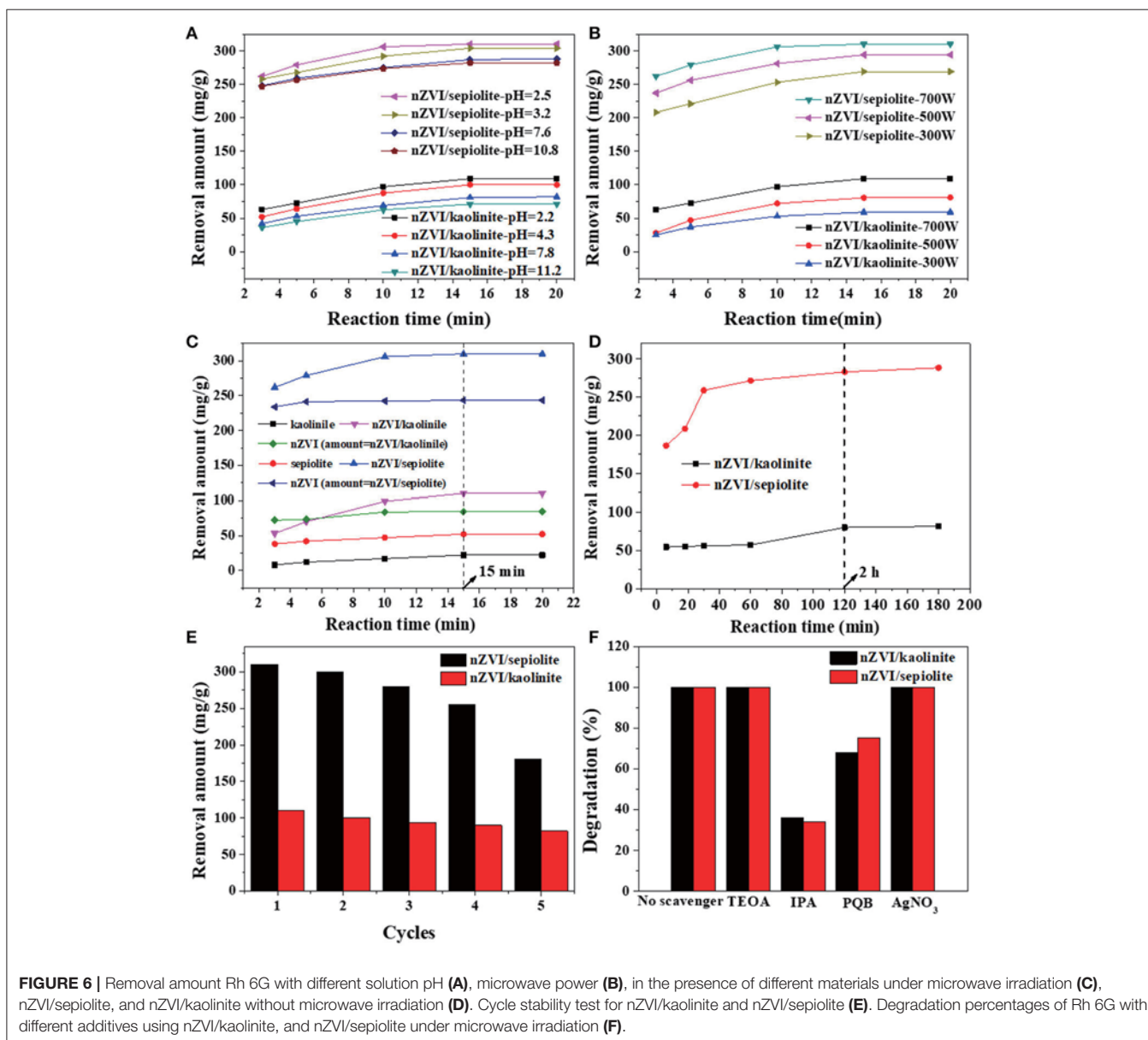
Figure 6C showed the degradation abilities of kaolinite, sepiolite, nZVI/kaolinite, nZVI/sepiolite and nZVI (same amount with nZVI/kaolinite or nZVI/sepiolite). The removal amounts of Rh 6G by nZVI/sepiolite, nZVI/kaolinite, sepiolite and kaolinite in 15 min were 300, 110, 52, and 22 mg/g, respectively. The removal amount of Rh 6G by nZVI/sepiolite was better than that of sepiolite and kaolinite adsorption and nZVI/kaolinite degradation. It was possibly caused by the iron content of the materials. We prepared the same amount of nZVI as nZVI/sepiolite and nZVI/kaolinite, whose removal amount of Rh 6G are 243 and 84 mg/g, respectively, indicating that loading nZVI on clay can increase the removal amount of Rh 6G. The higher the negative charge of the layer, the more favorable to adsorb cations. The zeta potentials of sepiolite and kaolinite are -17.4 mV and -11.2 mV, respectively. Therefore, more Fe³⁺ could be adsorbed onto sepiolite and be reduced to Fe⁰, which could generate more free radicals to degrade Rh 6G. In addition, the specific surface area of nZVI/sepiolite is higher than that of nZVI/kaolinite, which could provide more reactive sites for the reaction. What's more, compared with nZVI/kaolinite, the microwave absorption properties of nZVI/sepiolite were also stronger. Without microwave irradiation, the removal amounts of Rh 6G by nZVI/sepiolite and nZVI/kaolinite were 288 and 81 mg/g (Figure 6D), respectively. Although the removal amount of Rh 6G was not significantly improved in the presence of microwave, the equilibrium time decreased from 2 h (Figure 6D) to 15 min (Figure 6C) with the irradiation of the microwave, indicating the presence of microwave could greatly accelerate the reaction. Therefore, microwave is necessary in the process.

NaBH₄ was used to reduce the Fe³⁺ loaded on the used material to Fe⁰ for the recycle of the composites to investigate the recycling performance of the materials (Figure 6E). There was no significant change in the removal of Rh 6G after three cycles, suggesting that the composites could be reused for several times. We performed an inductively coupled plasma spectroscopy test to check iron leaching to the solution after each reaction, no iron leaching was found, indicating iron has good load stability on clay.

In order to prove the main active ingredient that degrades Rh 6G are HO• and O₂⁻, the same molar concentrations of indolepropionic acid (IPA), p-benzoquinone (PBQ), triethanolamine (TEOA) and silver nitrate (AgNO₃) were added to solutions during the reaction (Figure 6F). It is well-known that IPA is a typical hydroxyl radical inhibitor and PBQ is a typical superoxide radical inhibitor. The removal amount of Rh 6G dramatically dropped with the addition of these two inhibitors, which indicated that HO• and O₂⁻ were the main active ingredients for the degradation of Rh 6G by nZVI/clay composites.

TABLE 1 | Chemical composition of kaolinite, nZVI/kaolinite, sepiolite, and nZVI/sepiolite.

	Si	Al	Fe	K	Ti	Na	Ca	Mg
Kaolinite	21.65	18.93	0.347	0.637	0.323			
nZVI/Kaolinite	18.60	16.87	9.02	0.518	0.268			
Sepiolite	31.70	3.65	0.676	3.87		6.56	0.669	0.175
nZVI/Sepiolite	27.58	3.03	11.18		0.06	1.00	0.76	2.43



CONCLUSION

In summary, the aggregation and oxidation of nZVI can be effectively inhibited by loading nZVI on clay minerals. When the composites were used to degrade Rh 6G under microwave irradiation, nZVI/sepiolite exhibited better removal performance than nZVI/kaolinite, due to the difference in iron loading amount, which was caused by the difference in specific surface area and zeta potential. In addition, composites could be reused for several times after regeneration. With the addition of different types of scavengers, it was demonstrated that HO^\bullet and $\text{O}_2^{\cdot-}$ were the main active ingredients in the degradation of Rh 6G. It will be a very promising method for future use of nZVI by loading nZVI on clay minerals.

AUTHOR CONTRIBUTIONS

WR and GL conceived the project. GL and LL designed and performed the experiments. DW analyzed the data. WR and GL wrote the manuscript.

ACKNOWLEDGMENTS

This research was supported by the National Key R&D Program of China (2017YFB0310704, 2017YFE0107000), National Natural Science Foundation of China (51604248) and Fundamental Research Funds for the Central Universities (2652017338).

REFERENCES

- Alkan, M., Demirbaş, Ö., and Dogan, M. (2007). Adsorption kinetics and thermodynamics of an anionic dye onto sepiolite. *Microporous Mesoporous Mater.* 101, 388–396. doi: 10.1016/j.micromeso.2006.12.007
- Bianchi, C., Bonato, P., Dughiero, F., and Canu, P. (2017). Enhanced power density uniformity for microwave catalytic reactions adopting solid-state generators: comparison with magnetron technology. *Chem. Eng. Process. Process Int.* 120, 286–300. doi: 10.1016/j.cep.2017.07.006
- Cheng, M. M., Song, W. J., Ma, W. H., Chen, C. C., Zhao, J. C., Lin, J., et al. (2008). Catalytic activity of iron species in layered clays for photodegradation of organic dyes under visible irradiation. *Appl. Catal. B Environ.* 77, 355–363. doi: 10.1016/j.apcatb.2007.08.006
- Demirbaş, O., Alkan, M., Dogan, M., Turhan, Y., Namli, H., and Turan, P. (2007). Electrokinetic and adsorption properties of sepiolite modified by 3-aminopropyltriethoxysilane. *J. Hazard Mater.* 149, 650–656. doi: 10.1016/j.jhazmat.2007.04.036
- Dong, H. R., Zhang, C., Hou, K. J., Cheng, Y. J., Deng, J. M., Jiang, Z., et al. (2017). Removal of trichloroethylene by biochar supported nanoscale zero-valent iron in aqueous solution. *Sep. Purif. Technol.* 188, 188–196. doi: 10.1016/j.seppur.2017.07.033
- Ezzatahmedi, N., Ayoko, G. A., Millar, G. J., Speight, R., Yan, C., Li, J. H., et al. (2017). Clay-supported nanoscale zero-valent iron composite materials for the remediation of contaminated aqueous solutions: a review. *Chem. Eng. J.* 312, 336–350. doi: 10.1016/j.cej.2016.11.154
- Jr, W. E. W., Headley, L. C., and Weber, K. C. (1975). Dipalmitoyl lecithin surfactant adsorption by kaolin dust *in vitro*. *J. Colloid Interf. Sci.* 51, 535–537. doi: 10.1016/0021-9797(75)90152-6
- Kaviratna, H. (1994). Acid Hydrolysis of Octahedral Mg²⁺ sites in 2:1 layered silicates: an assessment of edge attack and gallery access mechanisms. *Clays Clay Miner.* 42, 717–723. doi: 10.1346/CCMN.1994.0420607
- Kehinde, F. O., and Aziz, H. A. (2016). Classical optimization of process variables in the treatment of real textile wastewater using clinoptilolite. *J. Environ. Chem. Eng.* 4, 1242–1247. doi: 10.1016/j.jece.2015.08.019
- Kelm, U., Sanhueza, V., and Guzman, C. (2003). Filtration and retention of mineral processing slurries with pumice and common clay: low-cost materials for environmental applications in the small-scale mining industry. *Appl. Clay Sci.* 24, 35–42. doi: 10.1016/j.clay.2003.07.004
- Kim, H., Hong, H. J., Jung, J., Kim, S. H., and Yang, J. W. (2010). Degradation of trichloroethylene (TCE) by nanoscale zero-valent iron (nZVI) immobilized in alginate bead. *J. Hazard Mater.* 176, 1038–1043. doi: 10.1016/j.jhazmat.2009.11.145
- Li, G., Xu, Q. Y., Jin, X. Y., Li, R. C., Dharmarajan, R., and Chen, Z. L. (2018). Enhanced adsorption and Fenton oxidation of 2,4-dichlorophenol in aqueous solution using organobentonite supported nZVI. *Sep. Purif. Technol.* 197, 401–406. doi: 10.1016/j.seppur.2018.01.032
- Liu, H. B., Gao, S. S., and Zhu, M. L., Chen, P., and Pan, D. (2015). Use of manganese/silicon tailing waste for coking wastewater treatment: evaluation of phenol and phenylamine removal efficiencies. *Water Air Soil Pollut.* 226, 1–9. doi: 10.1007/s11270-015-2303-z
- Liu, M., Shadbeigian, R., and Zhang, B. (2017). Does environmental regulation affect labor demand in China? Evidence from the textile printing and dyeing industry. *J. Environ. Econ. Manage.* 86, 277–294. doi: 10.1016/j.jeem.2017.05.008
- Liu, S. T., Huang, J., Ye, Y., Zhang, A. B., Pan, L., and Chen, X. G. (2013). Microwave enhanced fenton process for the removal of methylene blue from aqueous solution. *Chem. Eng. J.* 215–216, 586–590. doi: 10.1016/j.cej.2012.11.003
- Masomboon, N., Ratanatamskul, C., and Lu, M. C. (2010). Mineralization of 2,6-dimethylaniline by photoelectro-fenton process. *Appl. Catal. A Gen.* 384, 128–135. doi: 10.1016/j.apcata.2010.06.012
- Matłok, M., Petrus, R., and Warchol, J. K. (2015). Equilibrium study of heavy metals adsorption on Kaolin. *Ind. Eng. Chem. Res.* 54, 6975–6984. doi: 10.1021/acs.iecr.5b00880
- Mochizuki, D., Sasaki, R., Maitani, M. M., Okamoto, M., Suzuki, E., and Wada, Y. (2015). Catalytic reactions enhanced under microwave-induced local thermal non-equilibrium in a core-shell, carbon-filled zeolite@zeolite. *J. Catal.* 323, 1–9. doi: 10.1016/j.jcat.2014.12.003
- Sabah, E., Cinar, M., and Celik, M. S. (2007). Decolorization of vegetable oils: adsorption mechanism of β -carotene on acid-activated sepiolite. *Food Chem.* 100, 1661–1668. doi: 10.1016/j.foodchem.2005.12.052
- Steudel, A., Batenburg, L. F., Fischer, H. R., Weidler, P. G., and Emmerich, K. (2009). Alteration of non-swelling clay minerals and magadiite by acid activation. *Appl. Clay Sci.* 44, 95–104. doi: 10.1016/j.clay.2009.02.001
- Vimonses, V., Lei, S. M., Jin, B., Chow, C. W. K., and Saint, C. (2009). Adsorption of congo red by three Australian kaolins. *Appl. Clay Sci.* 43, 465–472. doi: 10.1016/j.clay.2008.11.008
- Xu, L., and Wang, J. (2013). Degradation of 4-chloro-3,5-dimethylphenol by a heterogeneous fenton-like reaction using nanoscale zero-valent iron catalysts. *Environ. Eng. Sci.* 30, 294–301. doi: 10.1089/ees.2012.0025
- Yang, B., Tian, Z., Zhang, L., Guo, Y. P., and Yan, S. Q. (2015). Enhanced heterogeneous fenton degradation of methylene blue by nanoscale zero valent iron (nZVI) assembled on magnetic Fe₃O₄/reduced graphene oxide. *J. Water Process Eng.* 5, 101–111. doi: 10.1016/j.jwpe.2015.01.006
- Yoon, J., Lee, Y., and Kim, S. (2001). Investigation of the reaction pathway of OH radicals produced by fenton oxidation in the conditions of wastewater treatment. *Water Sci. Technol.* 44, 15–21. doi: 10.2166/wst.2001.0242
- Zhang, Z., and Liao, X. (2017). Microwave design and analysis of a micromachined self-heating power sensor based on matching thermocouples. *J. Micromech. Microeng.* 27:085002. doi: 10.1088/1361-6439/aa780a
- Zhao, K., Zhao, G., Li, P., Gao, J., Lv, B., and Li, D. (2010). A novel method for photodegradation of high-chroma dye wastewater via electrochemical pre-oxidation. *Chemosphere* 80, 410–415. doi: 10.1016/j.chemosphere.2010.04.019

Conflict of Interest Statement: The authors declare that the research was conducted in the absence of any commercial or financial relationships that could be construed as a potential conflict of interest.

Copyright © 2018 Rao, Lv, Wang and Liao. This is an open-access article distributed under the terms of the Creative Commons Attribution License (CC BY). The use, distribution or reproduction in other forums is permitted, provided the original author(s) and the copyright owner(s) are credited and that the original publication in this journal is cited, in accordance with accepted academic practice. No use, distribution or reproduction is permitted which does not comply with these terms.



Effect of Natural Nanostructured Rods and Platelets on Mechanical and Water Resistance Properties of Alginate-Based Nanocomposites

Dajian Huang*, Zhuo Zhang, Zonghong Ma and Qiling Quan

School of Materials Science and Engineering, Lanzhou Jiaotong University, Lanzhou, China

A series of biopolymer-based nanocomposite films were prepared by incorporating natural one-dimensional (1D) palygorskite (PAL) nanorods, and two-dimensional (2D) montmorillonite (MMT) nanoplatelets into sodium alginate (SA) film by a simple solution casting method. The effect of different dimensions of nanoclays on the mechanical, water resistance, and light transmission properties of the SA/PAL or MMT nanocomposite films were studied. The field-emission scanning electron microscopy (FE-SEM) result showed that PAL can disperse better than MMT in the SA matrix in the case of the same addition amount. The incorporation of both PAL and MMT into the SA film can enhance the tensile strength (TS) and water resistance capability of the film. At a high content of nanoclays, the SA/PAL nanocomposite film shows relatively higher TS, and better water resistance than the SA/MMT nanocomposite film. The SA/MMT nanocomposite films have better light transmission than SA/PAL nanocomposite film at the same loading amount of nanoclays. These results demonstrated that 1D PAL nanorods are more suitable candidate of inorganic filler to improve the mechanical and water resistance properties of biopolymers/nanoclays nanocomposites.

Keywords: palygorskite, montmorillonite, bionanocomposite films, sodium alginate, mechanical strength, water resistance

OPEN ACCESS

Edited by:

Wenbo Wang,
Lanzhou Institute of Chemical Physics
(CAS), China

Reviewed by:

Yushan Liu,
Zhengzhou University, China
Yuqi Li,
Guilin University of Technology, China

*Correspondence:

Dajian Huang
huangdj2015@yeah.net

Specialty section:

This article was submitted to
Green and Sustainable Chemistry,
a section of the journal
Frontiers in Chemistry

Received: 29 June 2018

Accepted: 07 December 2018

Published: 19 December 2018

Citation:

Huang D, Zhang Z, Ma Z and Quan Q
(2018) Effect of Natural
Nanostructured Rods and Platelets on
Mechanical and Water Resistance
Properties of Alginate-Based
Nanocomposites.
Front. Chem. 6:635.
doi: 10.3389/fchem.2018.00635

INTRODUCTION

Over the past decades, the commodity plastics (i.e., polyethylene, polypropylene, and polyethylene terephthalate) as commonly used food packaging materials have played very important roles in human daily production. However, these plastic packaging materials are totally non-biodegradable, so their widespread use caused serious environmental pollution problems (Souza et al., 2017; Costa et al., 2018; Salama et al., 2018). Therefore, the development of biodegradable films using natural, non-toxic, and environment benign polymers such as polysaccharides, proteins, and lipids has drawn much more attention in both of academic and industrial areas (Mushi and Berglund, 2014; Wang and Jing, 2017; Youssef and El-Sayed, 2018). Among numerous biodegradable natural polymers, sodium alginate (SA) was especially concerned owing to its excellent biocompatibility, film-forming ability, and active functional groups (Shankar et al., 2016; Fabra et al., 2018). SA is an anionic natural biomacromolecule, which is composed of poly-b-1, 4-D-mannuronic acid (M units), and a 1, 4-L-glucuronic acid (G units) in different proportions by 1–4 linkages. It is extracted from marine algae or produced by bacteria, and so it has the advantages including abundance,

renewability, non-toxicity, water-solubility, biodegradability, and biocompatibility (Wang and Wang, 2010). However, the inherent hydrophilicity and brittleness of neat SA films limited their applications in film materials (Rhim, 2004; Zhang et al., 2017).

In order to overcome the drawbacks of neat SA films, a variety of nanoscale particles such as montmorillonite (MMT) (Tunç and Duman, 2010; Zlopasa et al., 2015), graphene oxide (Liu et al., 2017), and cellulose nanocrystals (Sirvio et al., 2014) have been incorporated into the SA matrix to fabricate a nanocomposite. Abdollahi et al. (2013) developed an alginate/MMT nanocomposite by a solvent casting method, and found that the mechanical properties of the alginate/MMT composites were enhanced significantly after the addition of MMT. However, MMT forms an agglomeration in the polymer matrix when its addition amount exceeds a certain value, which leads to the decrease of the mechanical properties of the film. It has been shown that MMT is a 2:1-type layered clay mineral with a sandwiched structure composed of two 2D platelets and interlayer cations (i.e., Na^+ , Ca^{2+} , Mg^{2+}). The strong hydrogen-bonding and electrostatic interaction, and van der Waals forces between two platelets make MMT difficult to be exfoliated and tend to be present in a form of agglomeration (Zhang et al., 2014; Block et al., 2015; Liu et al., 2016). In comparison, natural 1D rod-like nanoclays are easy to be dispersed as nanoscale size, and showed great potential to be used to develop polymer/nanoclays composites (Nikolic et al., 2017; Ajmal et al., 2018; Shankar et al., 2018; Zhang P. et al., 2018). It has been demonstrated that the dispersion of nanoclays in polymer matrix, and the comprehensive performance of the resultant polymer composites exhibited interesting dependence on the shape of fillers. Usually, rod-like nanoclays have a relatively smaller contact surface and weaker interaction amount rods, so that they could probably be dispersed in the polymer matrix well with less aggregation (Bilotti et al., 2009). Palygorskite (PAL) is a naturally available 1D nanorod-like silicate clay mineral (Deng et al., 2012; Zhang et al., 2018b). It consists of two double chains of the pyroxene-type $(\text{SiO}_3)^{2-}$ like amphibole $(\text{Si}_4\text{O}_{11})^{6-}$ running parallel to the fiber axis (Gard and Follett, 1968; Zhu et al., 2016; Zhang et al., 2018a). PAL is a potential filler to fabricate polymer composite due to its unique advantages, such as high aspect ratio, large specific surface area, good thermal stability, and high modulus (Huang et al., 2012; Ruiz-Hitzky et al., 2013; Ding et al., 2019). It has been confirmed that the incorporation of silylated PAL into the polyurethane matrix improved significantly the thermal stability and mechanical properties of polyurethane (Peng et al., 2011). In addition, 1D fibrous nanoclay has relatively higher density of silanol groups on its surface than 2D layered silicates, making it able to form more hydrogen bonds with hydrophilic biopolymers (Alcantara et al., 2014). So far, the studies on the comparison of 1D and 2D nanoclays in fabricating SA/nanoclays nanocomposites still received less attention.

In this paper, we have prepared a series of SA/nanoclays nanocomposite film using 1D PAL and 2D MMT as the inorganic ingredients, and studied the effect of different dimensions of nanoclays on the structure, organic/inorganic interface interaction and the mechanical, water resistance, light

transmission properties of the films. The potential of 1D PAL nanorods and 2D MMT for fabricating SA-based nanocomposite film was also assessed by a systematic comparative study.

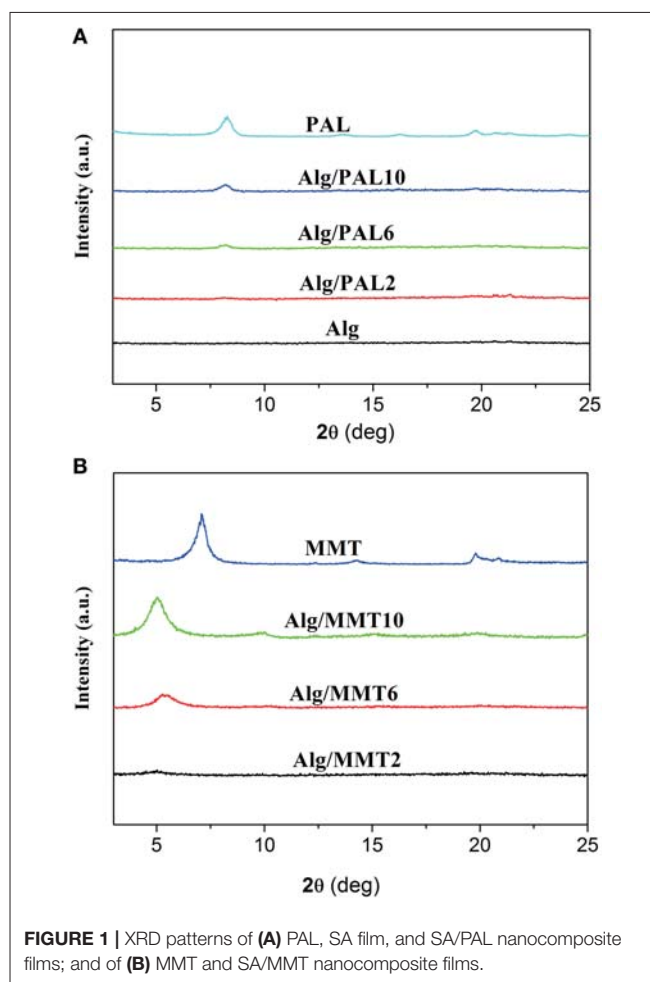
EXPERIMENT SECTION

Materials

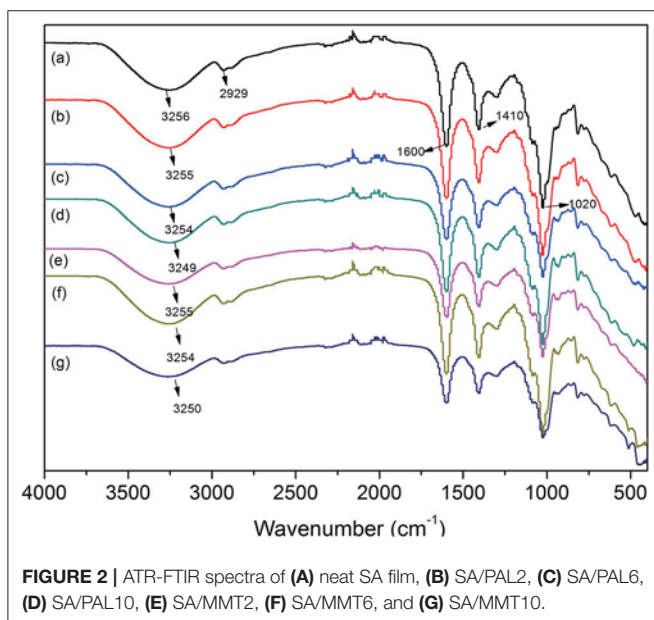
SA [characteristic viscosity of 1% aqueous solution at 20 °C $\geq 0.02 \text{ Pa}\cdot\text{s}$, mannuronic (M) acid/guluronic (G) acid ratio = 65/35, molecular weight $\approx 120,000 \text{ g/mol}$] was purchased from Sinopharm Chemical Reagent Co., Ltd. (Shanghai, China). Glycerol was obtained from Guangdong Guanghua Chemical Factory Co., Ltd. (Guangdong, China). MMT was purchased from Zhejiang Fenghong New Material Co., Ltd. (Zhengjiang, China). PAL was purchased from Changzhou Dingbang Clay Co., Ltd (Jiangsu, China).

Preparation of SA/PAL and SA/MMT Nanocomposite Films

The SA, SA/PAL, and SA/MMT films were prepared by a solution casting method. The aqueous solution containing 2 wt.% of SA were prepared by dissolving SA powder into distilled water under



mechanical stirring for 24 h. Then, glycerol (40 w/w% of the mass of SA) as a plasticizer was added into the SA solution, and the mixture was stirred continuously at 600 rpm to obtain a homogeneous solution. PAL or MMT dispersions (2 wt.%) were prepared by dispersing given amounts of clays in distilled water under mechanical agitation at 600 rpm for 1 h at room temperature. Afterward, the obtained mixture was dispersed with the aid of ultrasound equipment operating at 40 kHz for 10 min. The obtained dispersion of PAL or MMT was added to the SA solutions (the amount of clays is 2, 4, 6, 8, and 10 wt.% of the mass of SA) to form a precursor solution for film-forming. Then, the resultant mixture solutions were poured into the PS dishes (9 cm diameter) and evaporated at atmosphere for 72 h. After drying, the films were peeled off from the plate surface and then kept in a conditioning cabinet with the relative humidity (RH) of 53% for further treatments. The neat SA film was prepared according to a similar procedure without the addition of PAL or MMT.



Test of Mechanical Properties

The tensile performance of the film with length of 80 mm and width of 10 mm was studied using an AG-IS material testing machine (Shimadzu Co., Ltd., Japan). A 200 N load cell was used, and the strain rate was 10 mm/min. Samples were studied in each test and all tests occurred at room temperature. The averages of tensile strength and elongation at break of five specimens of each film were taken and presented.

Test of Moisture Uptake

The moisture uptake (MU) was measured by cutting the film samples into small pieces (2 × 2 cm). The samples were dried at 70°C for 24 h. After the samples were weighed (W_0), they were conditioned for 72 h at 76% RH (saturated NaCl solution) to ensure equilibrium of the moisture before reweighing (W_1).

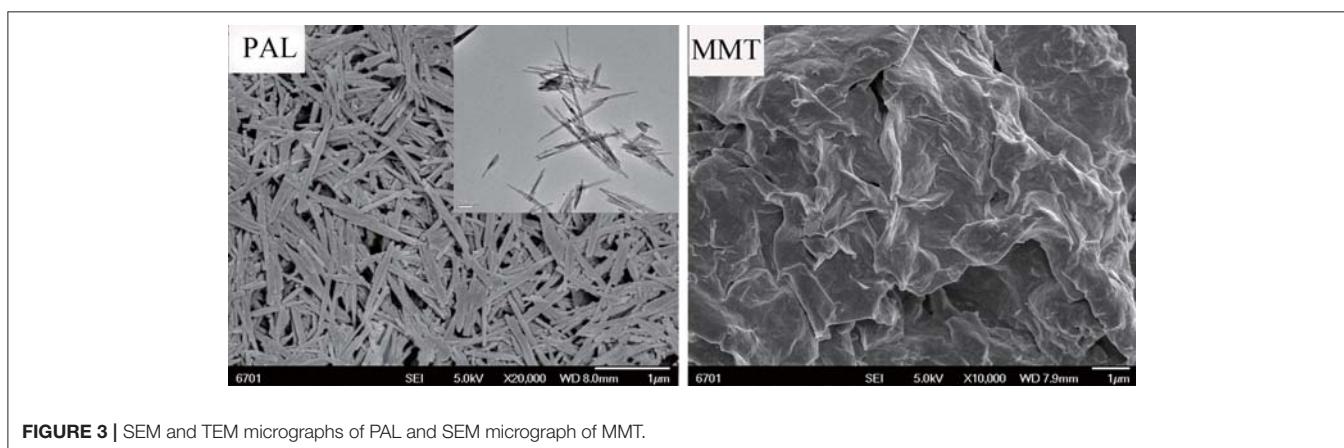
MU of the samples was calculated as follows:

$$\text{MU} = [W_1 - W_0]/W_0 \times 100\% \quad (1)$$

An average value of five replicates for each sample was taken.

Characterizations

The crystalline structure of samples was characterized with an X-ray diffractometer (Philips, X'pert PRO, The Netherlands), with the Cu K α radiation at 40 kV and 30 mA. The diffraction patterns were collected in reflection mode by scanning the 2θ range from 5° to 30°, with a scan speed of 6°/min. A FTIR Spectrophotometer (Thermo Nicolet, NEXUS 670, USA) was employed to record the Infrared spectra of films with the attenuated total reflectance (ATR) model in the range of 4,000–500 cm^{-1} . The surface morphology of samples was observed with a JEOL JSM-6701F microscope after the samples were coated with gold. The films for test were immersed in liquid nitrogen and cryo-fractured manually. TEM images of samples were taken with a TECNAIG2-F30 Transmission electron microscope (FEI, USA). Light transmission of films was measured with a UV-vis spectrophotometer [N4, INESA (Group) Co., Ltd, China] at selected wavelengths between 200 and 600 nm.



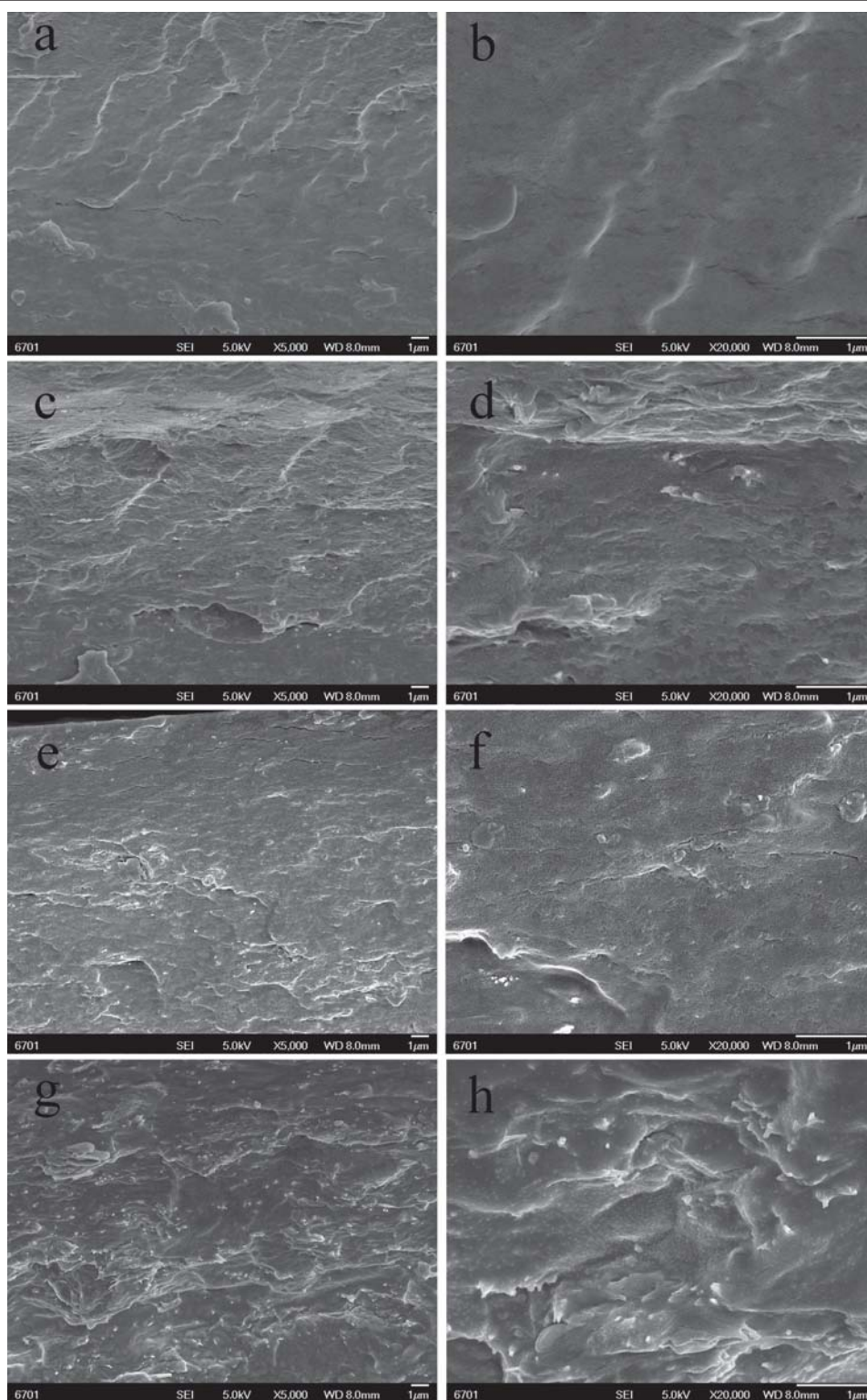


FIGURE 4 | SEM micrographs of the cross-sections of SA/PAL nanocomposite films: neat SA films (**A,B**), SA/PAL (4 wt.%) (**C,D**), SA/PAL (6 wt.%) (**E,F**), and SA/PAL (10 wt.%) (**G,H**).

RESULTS AND DISCUSSION

XRD Analysis

As shown in **Figure 1**, no sharp diffraction peaks were observed in the XRD patterns of SA/glycerol films (**Figure 1A**), indicating that neat SA film shows no crystalline state and the polymer chains are arranged randomly. The neat PAL showed the diffraction peak at $2\theta = 8.4^\circ$, ascribed to the characteristic reflection of (110) crystallographic plane (**Figure 1A**) (Xu et al., 2017). The diffraction peak of (110) plane of PAL ($2\theta = 8.4$) was observed in the XRD pattern of SA/PAL nanocomposite films. The position of (110) diffraction peak has not been changed, but the peak intensity increased with increasing the loading amount of PAL in the SA/PAL film. This result indicated that SA polymer chains cannot enter the tunnel to cause the change of the crystal structure of PAL, which is in good agreement with previous

reports (Peng et al., 2011; Huang et al., 2012). Different from smectite, PAL has a layer-chain structure in which the structure unit composed of continuous tetrahedrons and discontinuous octahedrons are very stable and cannot be intercalated or exfoliated, so the crystal structure, and morphology of PAL can remain well after forming nanocomposite.

The XRD patterns of MMT and the SA/MMT nanocomposite films with different loading amount of MMT are presented in **Figure 1B**. An intense diffraction peak at $2\theta = 7.06^\circ$ (basal spacing is 1.25 nm), ascribed to the characteristic reflection of (001) crystalline plane of MMT, was observed in the XRD pattern of MMT. The characteristic reflection of MMT has not been observed in the XRD pattern of SA/MMT when the content of MMT is 2 wt.%, indicating MMT was exfoliated after its composite with SA polymer chains at a relatively lower MMT loading amounts. When the loading amount of MMT increased

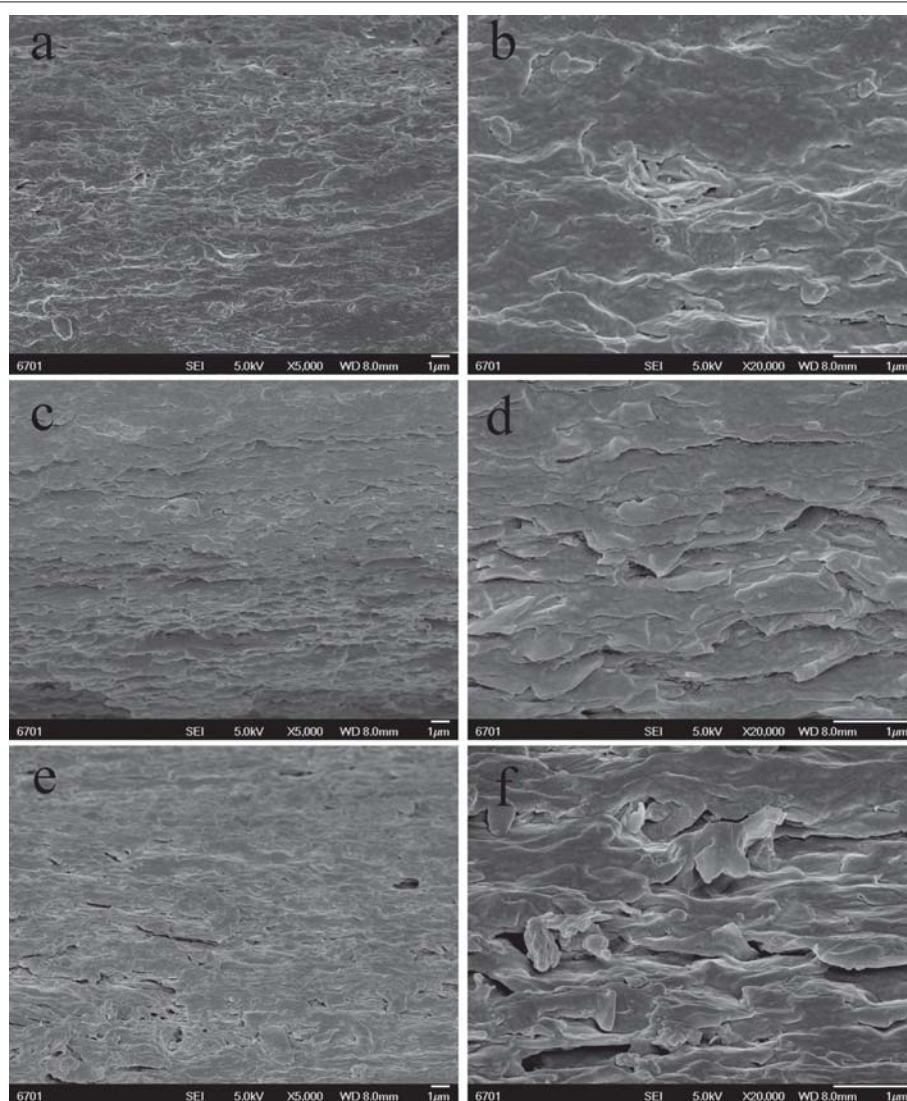
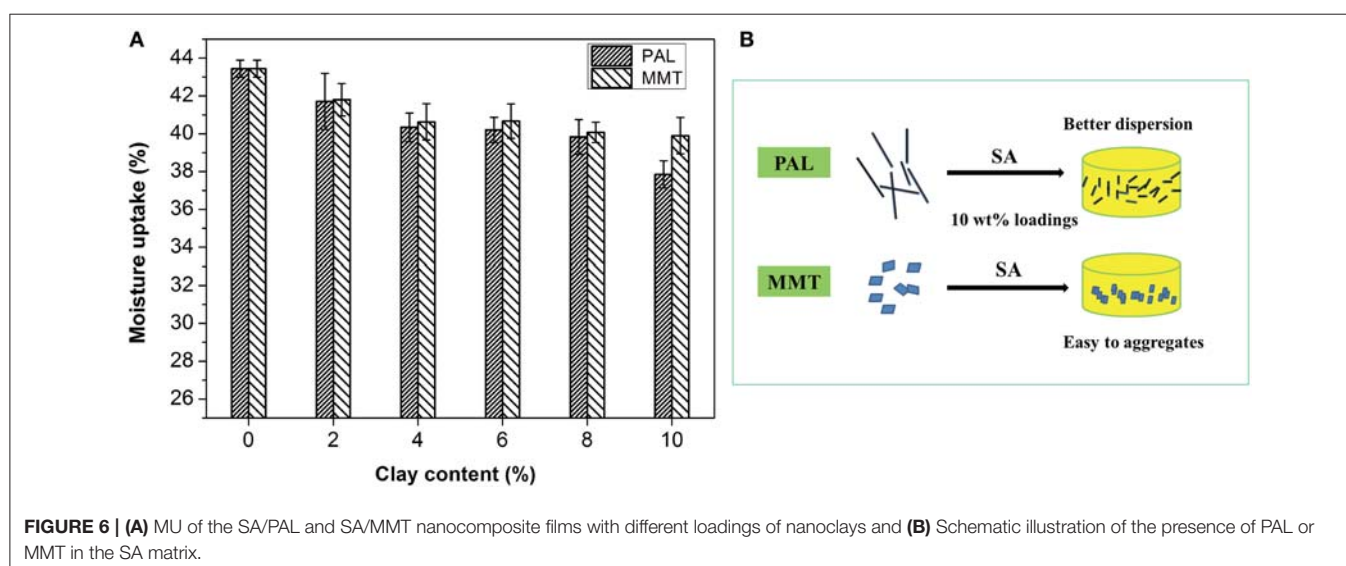


FIGURE 5 | SEM images of the surface of SA/MMT nanocomposite films: SA/MMT (2 wt.%) (**A,B**), SA/MMT (6 wt.%) (**C,D**), and SA/MMT (10 wt.%) (**E,F**).



to 6 and 10 wt.%, the diffraction peak of MMT shifted from 7.06° to 5.28° and 5.02° , respectively. These results indicated that some SA polymer chains were intercalated into the interlayer space of MMT (Majdzadeh-Ardakani and Nazari, 2010), forming an intercalated-exfoliated nanocomposite structure at relatively higher contents of MMT (Nagarajan et al., 2015).

FTIR Analysis

The incorporation of PAL or MMT into SA matrix was evaluated by ATR-FTIR analysis of films, because the vibrations and shifts of the FTIR absorption bands may reflect the interactions between SA and nanoclays. The ATR-FTIR spectra of the SA and SA/PAL or SA/MMT nanocomposite films are shown in **Figure 2**. As shown in **Figure 2A**, the absorption bands of neat SA film at $3,256$, $1,600$ and $1,410$, $1,020$ cm^{-1} can be attributed to the O-H stretching vibration, the COO symmetric, and asymmetric stretching vibration of carboxylate groups, and the C-O-C stretching vibration (Tezcan et al., 2012). After introducing PAL or MMT into the SA matrix, the absorption band at $3,256$ cm^{-1} shifted to low wavenumber region (**Figures 2B–G**), which confirmed there are strong interaction between SA and PAL or MMT, and the incorporation of PAL or MMT partially break the the hydrogen bonding between SA and glycerol, and formed new hydrogen bonding between SA chains and PAL or MMT (Huang et al., 2004; Liu M. et al., 2012). A similar tendency has also been observed in the CS/PVA/PAL composite film (Huang et al., 2012).

Micrographs of PAL, MMT, and Corresponding Composites

Figure 3 showed the SEM and TEM micrographs of PAL and the FESEM image of MMT used in this study. It can be seen from the SEM and TEM images of PAL that the PAL shows good rod-like shape with a diameter of $30\text{--}70$ nm, and a length of about $0.3\text{--}1.5$ μm . The rods are slightly aggregated together to form a loose bundle. The MMT exhibits a platelet-like shape, but most of

the lamellae of MMT stacked together without presence of single MMT layers.

The dispersion of the PAL or MMT in the SA matrix was also studied by SEM observation. The SEM images (magnifications $\times 5,000$ and $\times 20,000$) of the cross-section of SA/PAL nanocomposites with the PAL loading of 0, 2, 6, and 10 wt.% are shown in **Figure 4**, respectively. The fracture surface of neat SA film showed a glossy and ordered morphology, indicating the neat SA film has homogeneous microstructure, and the SA and glycerol are compatible very well. All the SA/PAL nanocomposites showed much rougher fractured surfaces in comparison with SA film. The bright dots observed in the SEM image of the nanocomposites indicated that the PAL rods embedded within the SA matrix very well. The number of the bright dots reflecting a well-dispersion of inorganic components increased with increasing the loading amount of PAL. The PAL has a well-dispersion in the SA matrix without obvious agglomeration, indicating a good compatibility between SA matrix and PAL. The well-dispersion of PAL in the SA matrix can be ascribed to the following reasons. First, the 1D nanorod-like feature of PAL and the relatively weaker interaction among rods allowed them easy to be dispersed in polymer matrix under the action of shear forces. Secondly, PAL can interact with SA via hydrogen bonding interactions, which is also helpful to strip effectively the crystal bundles as individually dispersed nanorods. In addition, the good compatibility between PAL and SA matrix also indicated a strong matrix-filler interfacial adhesion, which facilitates to enhance the mechanical properties of the resulting SA/PAL composite films.

Figure 5 showed the SEM micrographs of the cross-section of SA/MMT nanocomposite films with the MMT loading amounts of 2, 6, and 10 wt.% at different magnifications ($\times 5,000$ and $\times 20,000$). Compared with the neat SA film, the cross-section of SA/MMT nanocomposite films is more rough and uneven in varying degrees. The roughness degree of cross-section of SA/MMT films increased with increasing the loading amount of

MMT, owing to the platelet-shaped structure of MMT. It can be seen that the MMT platelets were directionally stacked and densely packed with SA matrix, forming a laminated structure (Figure 5D). When the loading amount of MMT increased to 10%, the cross-section of SA/MMT nanocomposite film becomes looser owing to the agglomeration of MMT in the SA matrix, which may have a negative impact on the performance of the composites. From Figures 4, 5 it can be seen that PAL has relatively better dispersion than MMT in the SA matrix at high loading amounts (6 and 10 wt.%). This behavior may be because that the interactions among PAL rods are relatively weaker than the interaction between the nanoplatelets of MMT (Lu et al., 2005; Liu M. X. et al., 2012).

Moisture Uptake (MU)

MU capability of the SA/PAL and SA/MMT was measured to study the effect of the nanoclays on the water-resistant properties of the SA films. As shown in Figure 6A, The MU of neat SA film was higher than that of SA/PAL and SA/MMT nanocomposites, indicating that the introduction of PAL or MMT can inhibit the penetration of water molecules into the film, and decrease the MU of the nanocomposite films (Almasi et al., 2010). This reduction of MU is because that PAL and MMT are able to form hydrogen bonding networks with SA matrix, increase the surface roughness of film, and block the diffusion pathway of water molecules, which decreased the water sensitivity of the nanocomposites (Wu et al., 2009; Almasi et al., 2010; Bidsorkhi et al., 2014). In addition, the hydrophilicity of PAL or MMT is weaker than that of neat SA matrix, so the incorporation of PAL or MMT is favorable to reduce the MU.

In comparison, the PAL has a relatively better effect than MMT on reducing the MU of SA film. The total MU of SA film reduced about 12.9% after the incorporation of 10 wt.% PAL, which was higher than that of SA/MMT10 (MU only reduced 8.1%). This can be attributed to the fact that PAL has a better dispersion than MMT in the SA matrix at high loadings of nanoclays (see Figure 6B). The good dispersion of PAL nanorod in SA matrix enable it to form more stable and dense hydrogen bond networks with the hydroxyl groups of SA than MMT (little agglomeration in SA matrix) at the same loading amounts. In addition, SA/MMT nanocomposites had a relatively looser surface structure than SA/PAL nanocomposites at the sample loading amount of 10 wt.%, which enable them to absorb easily more water molecules.

Mechanical Performance of SA/PAL and SA/MMT Nanocomposites

The effect of PAL and MMT addition on mechanical properties of SA film was studied by a tensile testing experiment. As shown in Figure 7A, the addition of PAL or MMT has great influence on the tensile strength of nanocomposites. The tensile strength (TS) of SA/PAL nanocomposites increased by 84.56% (from 13.67 to 25.23 MPa) with an increase of PAL loading amount from 0 to 10 wt.%. This obvious improvement of TS of SA/PAL can be ascribed to the homogenous dispersion of PAL in SA matrix and the strong hydrogen bonding interaction between the silanol groups of PAL and the -OH or -COOH groups of SA.

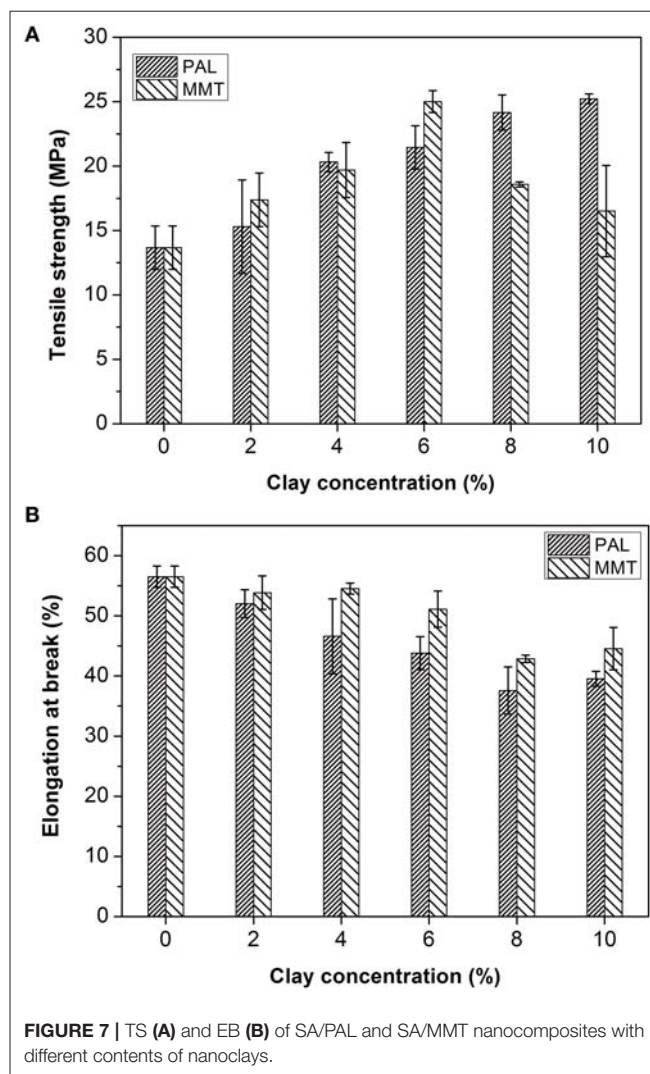


FIGURE 7 | TS (A) and EB (B) of SA/PAL and SA/MMT nanocomposites with different contents of nanoclays.

In addition, the high aspect ratio of PAL was also favorable to the stress transfer when the film was subject to be stretched. The similar results were observed in other PAL nanorod-reinforced polymers (Chen et al., 2012; Liu et al., 2014).

The TS of SA/MMT increased initially, reached the optimal value at the MMT content of 6 wt.%, and then decreased with the increase of addition amounts of MMT. The TS of nanocomposite films increased by 82.96% in contrast to the SA films. The TS of nanocomposites decreased when the MMT loading amount is larger than 6 wt.%. This tendency is ascribed to the aggregation of MMT in the SA matrix, as confirmed by SEM and XRD analysis results. The similar behavior was also observed by previous research result that the tensile strength of gelatin/MMT films decreased after adding 5% of MMT due to a loss in the quality of MMT dispersion in the gelatin matrix (Flaker et al., 2015).

Figure 7B showed the elongation at breakage (EB) of SA film, SA/PAL, and SA/MMT nanocomposite films. The EB of nanocomposites showed a decreasing trend with the increase of the loading amounts of PAL or MMT. This reduction of EB of

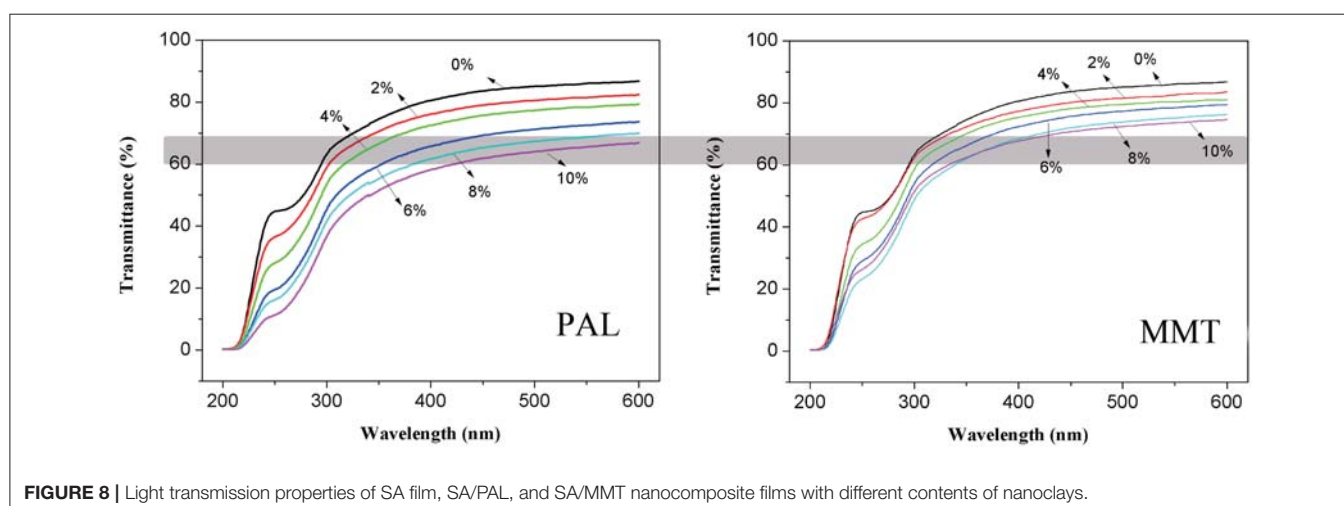


FIGURE 8 | Light transmission properties of SA film, SA/PAL, and SA/MMT nanocomposite films with different contents of nanoclays.

SA/PAL and SA/MMT nanocomposite films can be attributed to the fact that the inclusion of rigid clay restricted the motion of SA molecular chains in the matrix. Peng et al. (2011) confirmed that the EB of the waterborne polyurethane/PAL nanocomposite decreased with the increase of PAL loading amount. Slavutsky et al. (2014) also proved the EB of brea gum/MMT composites decreased with increasing the MMT content.

Light Transmission and Transparency

The light transmission of neat SA film, SA/PAL, and SA/MMT nanocomposite films as a function of wavelength is shown in **Figure 8**. The transmittance of SA film is about 87% at 600 nm (visible region), but it decreased slightly with the increase of PAL or MMT contents. This decrease was possibly related to the presence of PAL or MMT nanoparticles, because light would be absorbed partly by clay nanoparticles, leading to the decrease of energy of transmitted light. This result is similar to the previous findings that the light transmittance of pure polyimide film at 800 nm sharply decreased by incorporating 7 wt.% of PAL (An et al., 2008). Slavutsky et al. (2014) also found that the light transmission of brea gum/MMT composite films decreased after incorporation of MMT.

In addition, the light transmittance of SA/PAL nanocomposites is slightly lower than that of SA/MMT nanocomposites at the same addition amount. The light transmittance of the nanocomposites with addition of 10 wt.% PAL and 10 wt.% MMT at 600 nm was about 67 and 75%, respectively. This result may be due to the diameter of PAL nanorods (50–100 nm) is higher than the thickness of MMT nanoplatelets (about 1 nm) (Ge et al., 2015). Thus, the PAL obstructed the transmission of light more significantly than MMT.

REFERENCES

Abdollahi, M., Alboofetileh, M., Rezaei, M., and Behrooz, R. (2013). Comparing physico-mechanical and thermal properties of alginate nanocomposite films

CONCLUSIONS

The effects of 1D PAL nanorods and 2D MMT nanoplatelets on the mechanical, water resistance, and light transmission properties of the SA/PAL and SA/MMT nanocomposites were studied by a comparative study. It was revealed that PAL can enhance the mechanical and water resistance properties of SA/PAL nanocomposites better than MMT, because the 1D PAL has better dispersion than 2D MMT in the SA matrix at the same loading amounts. As a result of it, the TS of SA film increased sharply by 84.56% (from 13.67 to 25.23 MPa) after incorporation of 10 wt.% PAL, which is better than the TS of SA/MMT nanocomposite. In addition, the effect of PAL on the reduction of MU was more significant than that of MMT. Therefore, the 1D PAL nanorods are more suitable candidate of nanofillers to fabricate biopolymer-based nanocomposite films than MMT, and this study would lay a foundation to the design and preparation of new types of environment-friendly packing film materials.

AUTHOR CONTRIBUTIONS

DH and ZZ conceived and designed the experiments; ZM performed the experiments; DH, ZM, and ZZ analyzed the data; QQ contributed reagents, materials, and analysis tools; DH wrote the paper.

ACKNOWLEDGMENTS

The authors would like to thank the funding of the Science and Technology Support Project of National Natural Science Foundation of the Gansu Province (No. 1506RJZA068).

reinforced with organic and/or inorganic nanofillers. *Food Hydrocoll.* 32, 416–424. doi: 10.1016/j.foodhyd.2013.02.006

Ajmal, A. W., Masood, F., and Yasin, T. (2018). Influence of sepiolite on thermal, mechanical and biodegradation

- properties of poly-3-hydroxybutyrate-co-3-hydroxyvalerate nano composites. *Appl. Clay Sci.* 156, 11–19. doi: 10.1016/j.clay.2018.0.1010
- Alcantara, A. C. S., Darder, M., Aranda, P., and Ruiz-Hitzky, E. (2014). Polysaccharide-fibrous clay bionanocomposites. *Appl. Clay Sci.* 96, 2–8. doi: 10.1016/j.clay.2014.02.018
- Almasi, H., Ghanbarzadeh, B., and Entezami, A. A. (2010). Physicochemical properties of starch-CMC-nanoclay biodegradable films. *Int. J. Biol. Macromol.* 46, 1–5. doi: 10.1016/j.ijbiomac.2009.10.001
- An, L., Pan, Y., Shen, X., Lu, H., and Yang, Y. (2008). Rod-like attapulgite/polyimide nanocomposites with simultaneously improved strength, toughness, thermal stability and related mechanisms. *J. Mater. Chem.* 18, 4928–4941. doi: 10.1039/b805849k
- Bidsorkhi, H. C., Soheilnoghaddam, M., Pour, R. H., Adelnia, H., and Mohamad, Z. (2014). Mechanical, thermal, and flammability properties of ethylene-vinyl acetate (EVA)/sepiolite nanocomposites. *Polym. Test.* 37, 117–122. doi: 10.1016/j.polymertesting.2014.05.007
- Bilotti, E., Zhang, R., Deng, H., Quero, F., Fischer, H. R., and Peijs, T. (2009). Sepiolite needle-like clay for PA6 nanocomposites: an alternative to layered silicates? *Compos. Sci. Technol.* 69, 2587–2595. doi: 10.1016/j.compscitech.2009.07.016
- Block, K. A., Trusiak, A., Katz, A., Alimova, A., Wei, H., Gottlieb, P., et al. (2015). Exfoliation and intercalation of montmorillonite by small peptides. *Appl. Clay Sci.* 107, 173–181. doi: 10.1016/j.clay.2015.01.021
- Chen, L., Liu, K., Jin, T. X., Chen, F., and Fu, Q. (2012). Rod like attapulgite/poly(ethylene terephthalate) nanocomposites with chemical bonding between the polymer chain and the filler. *eXPRESS Polym. Lett.* 6, 629–638. doi: 10.3144/expresspolymlett.2012.67
- Costa, M. J., Marques, A. M., Pastrana, L. M., Teixeira, J. A., Sillankorva, S. M., and Cerqueira, M. A. (2018). Physicochemical properties of alginate-based films: effect of ionic crosslinking and mannuronic and guluronic acid ratio. *Food Hydrocoll.* 81, 442–448. doi: 10.1016/j.foodhyd.2018.03.014
- Deng, Y., Wang, L., Hu, X., Liu, B., Wei, Z., Yang, S., et al. (2012). Highly efficient removal of tannic acid from aqueous solution by chitosan-coated attapulgite. *Chem. Eng. J.* 181–182, 300–306. doi: 10.1016/j.cej.2011.11.082
- Ding, J. J., Huang, D. J., Wang, W. B., Wang, Q., and Wang, A. Q. (2019). Effect of removing coloring metal ions from the natural brick-red palygorskite on properties of alginate/palygorskite nanocomposite film. *Int. J. Biol. Macromol.* 122, 684–694. doi: 10.1016/j.ijbiomac.2018.10.218
- Fabra, M. J., Falcó, I., Randazzo, W., Sánchez, G., and López-Rubio, A. (2018). Antiviral and antioxidant properties of active alginate edible films containing phenolic extracts. *Food Hydrocoll.* 81, 96–103. doi: 10.1016/j.foodhyd.2018.02.026
- Flaker, C. H. C., Lourenco, R. V., Bittante A. M. Q. B., and Sobral, P. J. A. (2015). Gelatin-based nanocomposite films: a study on montmorillonite dispersion methods and concentration. *J. Food Eng.* 167, 65–70. doi: 10.1016/j.jfoodeng.2014.11.009
- Gard, J. A., and Follett, E. A. C. (1968). A structural scheme for palygorskite. *Clay Miner.* 7, 367–370. doi: 10.1180/claymin.1968.007.3.10
- Ge, L., Li, X., Zhang, R., Yang, T., Ye, X., Li, D., et al. (2015). Development and characterization of dialdehyde xanthan gum crosslinked gelatin based edible films incorporated with amino-functionalized montmorillonite. *Food Hydrocoll.* 51, 129–135. doi: 10.1016/j.foodhyd.2015.04.029
- Huang, D. J., Wang, W. B., Xu, J. X., and Wang, A. Q. (2012). Mechanical and water resistance properties of chitosan/poly(vinyl alcohol) films reinforced with attapulgite dispersed by high-pressure homogenization. *Chem. Eng. J.* 210, 166–172. doi: 10.1016/j.cej.2012.08.096
- Huang, M. F., Yu, J. G., and Ma, X. F. (2004). Studies on the properties of Montmorillonite-reinforced thermoplastic starch composites. *Polymer* 45, 7017–7023. doi: 10.1016/j.polymer.2004.07.068
- Liu, M., Pu, M., and Ma, H. (2012). Preparation, structure and thermal properties of polylactide/sepiolite nanocomposites with and without organic modifiers. *Compos. Sci. Technol.* 72, 1508–1514. doi: 10.1016/j.compscitech.2012.05.017
- Liu, M. X., Li, W. D., Rong, J. H., and Zhou, C. R. (2012). Novel polymer nanocomposite hydrogel with natural clay nanotubes. *Colloid Polym. Sci.* 290, 895–905. doi: 10.1007/s00396-012-2588-z
- Liu, P., Du, P. C., Zhu, L. X., Wu, Z. H., Wang, H. M., Chen, M., et al. (2014). Attapulgite/polylactide nanocomposites: effect of polymer brush length. *Mater. Lett.* 117, 214–216. doi: 10.1016/j.matlet.2013.12.015
- Liu, S., Cai, P., Li, X., Chen, L., Li, L., and Li, B. (2016). Effect of film multi-scale structure on the water vapor permeability in hydroxypropyl starch (HPS)/Na-MMT nanocomposites. *Carbohydr. Polym.* 154, 186–193. doi: 10.1016/j.carbpol.2016.08.006
- Liu, S., Li, Y., and Li, L. (2017). Enhanced stability and mechanical strength of sodium alginate composite films. *Carbohydr. Polym.* 160, 62–70. doi: 10.1016/j.carbpol.2016.12.048
- Lu, H. B., Shen, H. B., Song, Z. L., Shing, K. S., Tao, W., and Nutt, S. (2005). Rod-like silicate-epoxy nanocomposites. *Macromol. Rapid Commun.* 26, 1445–1450. doi: 10.1002/marc.200500360
- Majdzadeh-Ardakani, K., and Nazari, B. (2010). Improving the mechanical properties of thermoplastic starch/poly(vinyl alcohol)/clay nanocomposites. *Compos. Sci. Technol.* 70, 1557–1563. doi: 10.1016/j.compscitech.2010.05.022
- Mushi, N. E., and Berglund, L. A. (2014). Nanostructured biocomposite films of high toughness based on native chitin nanofibers and chitosan. *Front. Chem.* 2:99. doi: 10.3389/fchem.2014.00099
- Nagarajan, M., Benjakul, S., Prodpran, T., and Songtipya, P. (2015). Effects of pHs on properties of bio-nanocomposite based on tilapia skin gelatin and Cloisite Na⁺. *Int. J. Biol. Macromol.* 75, 388–397. doi: 10.1016/j.ijbiomac.2015.01.034
- Nikolic, M. S., Petrovic, R., Veljovic, D., Cosovic, V., Stankovic, N., and Djonlagic, J. (2017). Effect of sepiolite organomodification on the performance of PCL/sepiolite nanocomposites. *Eur. Polym. J.* 97, 198–209. doi: 10.1016/j.eurpolymj.2017.10.010
- Peng, L., Zhou, L., Li, Y., Pan, F., and Zhang, S. (2011). Synthesis and properties of waterborne polyurethane/attapulgite nanocomposites. *Compos. Sci. Technol.* 71, 1280–1285. doi: 10.1016/j.compscitech.2011.04.012
- Rhim, J. (2004). Physical and mechanical properties of water resistant sodium alginate films. *LWT Food Sci. Technol.* 37, 323–330. doi: 10.1016/j.lwt.2003.09.008
- Ruiz-Hitzky, E., Darder, M., Fernandes, F. M., Wicklein, B., Alcántara, A. C., and Aranda, P. (2013). Fibrous clays based bionanocomposites. *Prog. Polym. Sci.* 38, 1392–1414. doi: 10.1016/j.progpolymsci.2013.05.004
- Salama, H. E., Abdel Aziz, M. S., and Sabaa, M. W. (2018). Novel biodegradable and antibacterial edible films based on alginate and chitosan biguanidine hydrochloride. *Int. J. Biol. Macromol.* 116, 443–450. doi: 10.1016/j.ijbiomac.2018.04.183
- Shankar, S., Kasapis, S., and Rhim, J. (2018). Alginate-based nanocomposite films reinforced with halloysite nanotubes functionalized by alkali treatment and zinc oxide nanoparticles. *Int. J. Biol. Macromol.* 118, 1824–1832. doi: 10.1016/j.ijbiomac.2018.07.026
- Shankar, S., Wang, L., and Rhim, J. (2016). Preparations and characterization of alginate/silver composite films: effect of types of silver particles. *Carbohydr. Polym.* 146, 208–216. doi: 10.1016/j.carbpol.2016.03.026
- Sirvio, J. A., Kolehmainen, A., Liimatainen, H., Niinimäki, J., and Hormi, O. E. (2014). Biocomposite cellulose-alginate films: promising packaging materials. *Food Chem.* 151, 343–351. doi: 10.1016/j.foodchem.2013.11.037
- Slavutsky, A. M., Bertuzzi, M. A., Armada, M., Garcia, M. G., and Ochoa, N. A. (2014). Preparation and characterization of montmorillonite/brea gum nanocomposites films. *Food Hydrocoll.* 35, 270–278. doi: 10.1016/j.foodhyd.2013.06.008
- Souza, V. G. L., Fernando, A. L., Pires, J. R. A., Rodrigues, P. F., Lopes, A. A. S., and Fernandes, F. M. B. (2017). Physical properties of chitosan films incorporated with natural antioxidants. *Int. Crop Prod.* 107, 565–572. doi: 10.1016/j.indcrop.2017.04.056
- Tezcan, F., Gunister, E., Ozen, G., and Erim, F. B. (2012). Biocomposite films based on alginate and organically modified clay. *Int. J. Biol. Macromol.* 50, 1165–1168. doi: 10.1016/j.ijbiomac.2012.01.006
- Tunç, S., and Duman, O. (2010). Preparation and characterization of biodegradable methyl cellulose/montmorillonite nanocomposite films. *Appl. Clay Sci.* 48, 414–424. doi: 10.1016/j.clay.2010.01.016
- Wang, S., and Jing, Y. (2017). Effects of formation and penetration properties of biodegradable montmorillonite/chitosan nanocomposite film on the barrier of package paper. *Appl. Clay Sci.* 138, 74–80. doi: 10.1016/j.clay.2016.12.037
- Wang, W. B., and Wang, A. Q. (2010). Synthesis and swelling properties of pH-sensitive semi-IPN superabsorbent hydrogels based on sodium alginate-g-poly

- (sodium acrylate) and polyvinylpyrrolidone. *Carbohydr. Polym.* 80, 1028–1036. doi: 10.1016/j.carbpol.2010.01.020
- Wu, H., Liu, C., Chen, J., Chang, P. R., Chen, Y., and Anderson, D. P. (2009). Structure and properties of starch/alpha-zirconium phosphate nanocomposite films. *Carbohydr. Polym.* 77, 358–364. doi: 10.1016/j.carbpol.2009.01.002
- Xu, J. X., Wang, W. B., and Wang, A. Q. (2017). Stable formamide/palygorskite nanostructure hybrid material fortified by high-pressure homogenization. *Powder Technol.* 318, 1–7. doi: 10.1016/j.powtec.2017.05.032
- Youssef, A. M., and El-Sayed, S. M. (2018). Bionanocomposites materials for food packaging applications: concepts and future outlook. *Carbohydr. Polym.* 193, 19–27. doi: 10.1016/j.carbpol.2018.03.088
- Zhang, N., Xu, J., Gao, X., Fu, X., and Zheng, D. (2017). Factors affecting water resistance of alginate/gellan blend films on paper cups for hot drinks. *Carbohydr. Polym.* 156, 435–442. doi: 10.1016/j.carbpol.2016.08.101
- Zhang, P., Tian, N., Zhang, J., and Wang, A. (2018). Effects of modification of palygorskite on superamphiphobicity and microstructure of palygorskite@fluorinated polysiloxane superamphiphobic coatings. *Appl. Clay Sci.* 160, 144–152. doi: 10.1016/j.clay.2018.01.015
- Zhang, Y., Zhu, W., Lu, Y., Gao, Z., and Gu, J. (2014). Nano-scale blocking mechanism of MMT and its effects on the properties of polyisocyanate-modified soybean protein adhesive. *Ind. Crop. Prod.* 57, 35–42. doi: 10.1016/j.indcrop.2014.03.027
- Zhang, Z. F., Wang, W. B., Mu, B., and Wang, A. Q. (2018a). Thiourea-induced change of structure and color of brick-red palygorskite. *Clay Clay Miner.* 66, 403–414. doi: 10.1346/CCMN.2018.064099
- Zhang, Z. F., Wang, W. B., Tian, G. Y., Wang, Q., and Wang, A. Q. (2018b). Solvothermal evolution of red palygorskite in dimethyl sulfoxide/water. *Appl. Clay Sci.* 159, 16–24. doi: 10.1016/j.clay.2017.06.014
- Zhu, L., Guo, J., and Liu, P. (2016). Effects of length and organic modification of attapulgite nanorods on attapulgite/polystyrene nanocomposite via *in-situ* radical bulk polymerization. *Appl. Clay Sci.* 119, 87–95. doi: 10.1016/j.clay.2015.06.029
- Zlopasa, J., Norder, B., Koenders, E. A. B., and Picken, S. J. (2015). Origin of highly ordered sodium alginate/montmorillonite bionanocomposites. *Macromolecules* 48, 1204–1209. doi: 10.1021/ma502147m

Conflict of Interest Statement: The authors declare that the research was conducted in the absence of any commercial or financial relationships that could be construed as a potential conflict of interest.

Copyright © 2018 Huang, Zhang, Ma and Quan. This is an open-access article distributed under the terms of the Creative Commons Attribution License (CC BY). The use, distribution or reproduction in other forums is permitted, provided the original author(s) and the copyright owner(s) are credited and that the original publication in this journal is cited, in accordance with accepted academic practice. No use, distribution or reproduction is permitted which does not comply with these terms.



Novel Design of Eco-Friendly Super Elastomer Materials With Optimized Hard Segments Micro-Structure: Toward Next-Generation High-Performance Tires

Xuan Qin¹, Jiadong Wang¹, Bingyong Han², Bo Wang¹, Lixin Mao¹ and Liqun Zhang^{1,3,4*}

¹ State Key Laboratory of Organic-Inorganic Composites, Beijing University of Chemical Technology, Beijing, China, ² State Key Lab Chemical Resource Engineering, Beijing University of Chemical Technology, Beijing, China, ³ Engineering Research Center of Elastomer Materials on Energy Conservation and Resources, Beijing University of Chemical Technology, Beijing, China, ⁴ Beijing Advanced Innovation Center for Soft Matter Science and Engineering, Beijing University of Chemical Technology, Beijing, China

OPEN ACCESS

Edited by:

Wenbo Wang,
Lanzhou Institute of Chemical Physics
(CAS), China

Reviewed by:

Guocheng Lv,
China University of Geosciences,
China

Aiwei Tang,

Beijing Jiaotong University, China
Guang-Sheng Wang,
Beihang University, China

*Correspondence:

Liqun Zhang
Zhanglq@mail.buct.edu.cn

Specialty section:

This article was submitted to
Green and Sustainable Chemistry,
a section of the journal
Frontiers in Chemistry

Received: 24 May 2018

Accepted: 04 June 2018

Published: 20 July 2018

Citation:

Qin X, Wang J, Han B, Wang B, Mao L
and Zhang L (2018) Novel Design of
Eco-Friendly Super Elastomer
Materials With Optimized Hard
Segments Micro-Structure: Toward
Next-Generation High-Performance
Tires. *Front. Chem.* 6:240.
doi: 10.3389/fchem.2018.00240

Recently, sustainable development has become a significant concern globally, and the energy crisis is one of the top priorities. From the perspective of the industrial application of polymeric materials, rubber tires are critically important in our daily lives. However, the energy consumption of tires can reach 6% of the world's total energy consumption per annum. Meanwhile, it is calculated that around 5% of carbon dioxide comes from the emission of tire rolling due to energy consumption. To overcome these severe energy and environmental challenges, designing and developing a high-performance fuel-saving tire is of paramount significance. Herein, a next-generation, eco-friendly super elastomer material based on macromolecular assembly technology has been fabricated. Hydroxyl-terminated solution-polymerized styrene-butadiene rubber (HTSSBR) with high vinyl contents prepared by anionic polymerization is used as flexible soft segments to obtain excellent wet skid resistance. Furthermore, highly symmetrical 1,5-naphthalene diisocyanate (NDI), different proportions of chain extender, and the cross-linking agent with moderate molecular length are selected as rigid hard segments to achieve simultaneous high heat resistance. Through this approach, a homogeneous network supported by uniformly distributed hard segment nanoparticles is formed because soft segments with equal length are chemically end-linked by the hard segments. This super elastomer material exhibits excellent wear resistance and low rolling resistance. More importantly, the wear resistance, rolling resistance, and wet-skid resistance are reduced by 85.4, 42.3, and 20.8%, respectively, compared to the elastomeric material conventionally used for tire. By taking advantage of this excellent comprehensive service performance, the long-standing challenge of the "magic triangle" plaguing the rubber tire industry for almost 100 years is resolved. It is anticipated that this newly designed and fabricated elastomeric material tailored for tires will become the next generation product, which could exhibit high potential for significantly cutting the fuel consumption and reducing the emission of carbon dioxide.

Keywords: super elastomer, eco-friendly material, green tire, magic triangle, chain extender, cross-linking agent

INTRODUCTION

Wheels are one of the greatest inventions in the history of human civilization and have led to significant improvements in work efficiency and liberation of productive force. The entire world mounts on wheels and advances at full speed. Tires are the only vital functional components of vehicles with direct contact with the ground, and play the crucial roles of supporting vehicle load, transferring power, braking, shock absorption, and maintaining and changing driving direction. Since rubber tires were invented, they have undergone several technical and theoretical advances; meanwhile, the rapid development of the automotive industry and highways requires tires to be one of the polymer products with maximum yield and at the highest technological level. Nevertheless, social development and environmental problems such as the increasing energy consumption, increase in safety accidents, and a vast quantity of tire waste due to the short service life give rise to a higher requirement for the development of the tire industry.

In 1980, the concept of sustainable development was explicitly proposed by “The World Conservation Strategy” (U-Nations, 1980), which has attracted extensive worldwide concern and attention in recent years. “Fossil fuel depletion” and “pollutant emissions and global warming” are the two issues that should be considered by the “sustainable energy development system” (Hammond, 2004). Owing to the rapid development of the global economy, the large use of fossil energy results in the increase of greenhouse gas emissions, sea level rise, extreme weather change, a sharp decline of biological species, and a serious threat to the environment for human survival. Therefore, the improvement in the utilization efficiency of fossil energy has become the problem that is faced and needs to be solved by the whole world. Data from the European Union indicates that transportation energy consumption accounts for more than 20% of the world’s total energy consumption in the past 5 years and the fuel consumption of tires is 20–30% of that of the automobiles. Eighteen percent of the global carbon dioxide emissions are related to traffic and 24% of the carbon dioxide emissions of road vehicles are related to tires. To comply with the development trend of fuel-efficiency and safe tires with high performance, the European Union released the world-noted legislation of “Tire Labelling Regulation” in 2009 (EU, 2009). This leads to the classification of the rolling resistance and wet-skid resistance of tires. It is estimated that decreasing rolling resistance of tires by 20% leads to a 5% reduction in fuel consumption and using B-level green tires can save 20 billion liters of gasoline and reduce 50 million tons of carbon dioxide emissions every year.

At present, the rubber composites used for manufacturing pneumatic tires are prepared via vulcanization by mixing more than 10 kinds of raw materials. Therefore, the energy consumption of rubber processing is very high. Large amounts of carbon disulfide, non-methane hydrocarbons, and other organic waste are produced during the production process, and the addition of strong carcinogens (e.g., aromatic hydrocarbon oil) is required. Moreover, the constant discharge of heavy metals and dusts due to surface abrasion of rubber tires causes an adverse impact on the environment. Eighty percent of PM₁₀

of the cities in the UK comes from traffic, and more than 10,000 death cases can be attributed to cardiopulmonary disease caused by PM₁₀ (Karl, 2012). Furthermore, waste rubber tires cannot be recycled effectively. About 40 million tires are discarded in the UK annually (Mavroulidou et al., 2006), and the accumulation of waste tires provides a breeding place for mosquitoes and increases the risk of infectious disease outbreaks (Jang et al., 1998). Regarding the structure of tires, pneumatic tires still control the tire market. However, they suffer from the shortcomings of poor impact and puncture resistance. There is a risk of leakage or even blow-out during use, which may even lead to major accidents with loss and death. The data shows that there were 921 traffic accidents caused by tire fault in the UK in 2015, including 17 deaths and 147 serious injuries (UNECE, 2012).

The energy consumption and carbon dioxide emissions of the tire are related to the rolling resistance, whereas safety is correlated with the wet-skid resistance and solid particle pollution is affected by their wear resistance (Heinz and Grosch, 2007). These three properties are called the “magic triangle.” Traditional rubber composites are approaching a bottleneck to overcome the problem of the “magic triangle,” which restricts the development of high-performance tires.

As we reported elsewhere (Qin et al., 2018), polyurethane elastomer materials, with nano-particles chemically end-linked, have remarkably low dynamic hysteresis loss. The polyurethane features the presence of the urethane group $\left(\begin{array}{c} \text{H} \quad \text{O} \\ | \quad || \\ -\text{N}-\text{C}-\text{O}- \end{array} \right)$ on the macromolecular chain with a more or less frequency (Cooper and Tobolsky, 1967), which is a versatile copolymer consisting of alternating flexible soft segments and rigid hard segments (Liff et al., 2007; Jiang et al., 2015). Compared to traditional rubber composite materials, polyurethane has better wear resistance, relatively high tear strength and elongation, wide hardness range, low rolling resistance, large carrying capacity, and excellent oil and chemical resistance (Fu et al., 2016). The manufacturing process of polyurethane is simple, which leads to less consumption of environmental pollutants and the emission of waste water and gas. Besides, modified polyurethane can be made biodegradable, and hence, the recovery would be easier than that of rubber. Moreover, airless tires made from polyurethane have better safety performance and their service life is four times than that of ordinary rubber tires. The application of polyurethane in retread tires can not only reduce energy consumption but also achieve the goal of recycling development (Chiou and Schoen, 2002), which has a tremendous strategic significance of popularization. However, the undesirable wet traction, which has bearing on the glass transition temperature of the material, and poor heat resistance (Yoshida et al., 2017), which goes hand in hand with the structure of the material itself, of the preexisting polyurethane materials, bring up the inconvenience in driving security and preclude the possibility for its practical usage in the situation of high-speed and heavy-loading tires as well. Once these disadvantages are overcome, polyurethane elastomer is not only the ideal material to manufacture “green tires,” but also the best choice for realizing “green manufacturing” of tires.

To address this challenge, we put forward a new thought (Qin et al., 2018): we replace polyester polyols and polyether polyols of the soft segments of existing polyurethane materials with hydroxyl-terminated solution-polymerized styrene-butadiene rubber (HTSSBR) of designed and optimized molecule structure. HTSSBR exhibits a glass transition temperature that can be easily adjusted in a wide temperature range, and HTSSBR with relatively high levels of 1,2-butadiene and low levels of styrene possessed glass transition temperature of $-25\sim-15^{\circ}\text{C}$ measured by DSC. The polyurethane elastomer material with this structural designed HTSSBR acting as soft segments reveals a higher $\tan \delta$ at 0°C than those of traditional materials, which means a better wet-skid resistance. Hard segments chemically link the end of equal length HTSSBR molecular chains to form a network of uniform and tunable distribution of nano-reinforcing units in the polymer matrix, which minimizes the nano-scale frictions, and the $\tan \delta$ at 60°C is unusually low which means a lower rolling resistance. Meanwhile, in order to ensure the stability at very high temperature, high heat-resistant 1,5-naphthalene diisocyanate (NDI) is programmed to synthesize the innovative polyurethane elastomer material, because the low thermal conductivity of polymer may cause heat accumulation. The birth of eco-friendly next generation super elastomer material with a concurrent excellent performance of wet-skid resistance, wear resistance, rolling resistance, and dynamic mechanical properties, is indeed something to celebrate.

The properties of the super elastomer material are intensively influenced by the micro-structures. The chain extender and cross-linking agent are essential parts of the elastomer, which will determine the perfect degree of their network. Therefore, we regulated the hard segment micro-structure, principally about the ratio of chain extender and cross-linking agent of the elastomers. The effects of micro-structure change on its macroscopic properties were systematically studied by FT-IR, $^1\text{H-NMR}$, XRD, TEM, DSC, TGA, TMA, DMA, and other characterization methods. The sketch of the molecular structure of this super elastomer was shown in **Figure 1**.

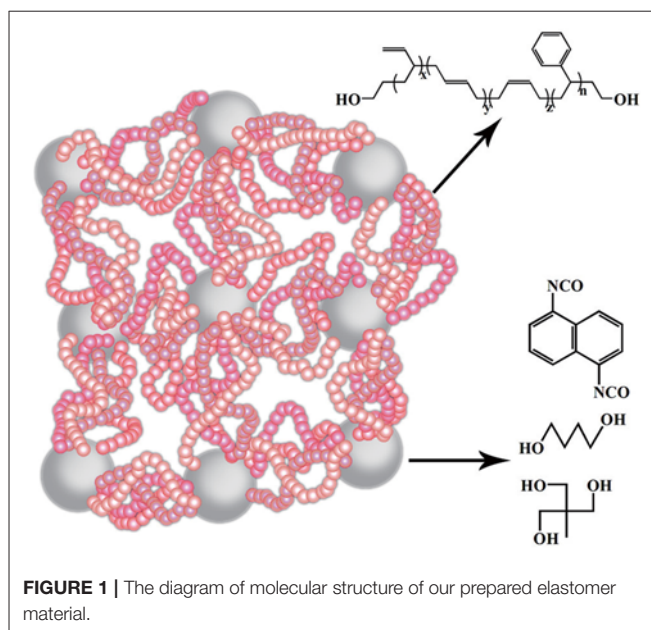
EXPERIMENTAL

Reagents and Materials

Butadiene (polymerization grade) was produced by Beijing Yanshan Petrochemical Co., China; styrene was purchased from Beijing Chemical reagents, China; THF (AR), cyclohexane (AR), and ethanol (AR) were supplied by Beijing Chemical Works, China; butyl lithium (CP) and lithium (AR) were provided by Baling Petrochemical Corp, China. NDI (AR) was supported by TCI; BDO and TMP (AR) were produced by Adamas.

Preparation of HTSSBR

Through anionic polymerization, the hydroxyl-terminated solution-polymerized styrene butadiene rubber (HTSSBR) was synthesized using self-made dilithium anionic initiator. Considering that the anionic polymerization is highly sensitive to impurities, it is necessary to purify all the instruments and reagents. To guarantee that the polymerization was suitable,



the entire reaction system was cleaned with reactive-polymer and high-purity nitrogen several times. The dilithium anionic initiator was synthesized as follows. A 1:1 (volume ratio) mixture of isoprene and cyclohexane was introduced by dripping slowly into a tetrahydrofuran solution of lithium flask protected by argon gas; the reaction was carried out at the temperature of 0°C for 6 h. After settling for 24 h, the brownish red transparent initiator solution was obtained by filtering. Next, butadiene, styrene, cyclohexane, and tetrahydrofuran were successively added into a 2 L reactor which had been thoroughly washed and purified by butyl lithium, followed by adding self-made dilithium anionic initiator. The polymerization progress lasted for 8 h at the temperature of 50°C . Then, the polymer was end-capped with ethylene oxide under stirring. After 24 h, the reaction was terminated by ethanol.

Preparation of HTSSBR-PU

The synthesis of HTSSBR-PU was achieved by a two-step method. In the first step, the prepolymer was prepared by reacting NDI and HTSSBR at 80°C under the nitrogen atmosphere. In the second step, extender 1,4-butanediol (BDO), cross-linking agent trimethylolpropane (TMP) and the prepolymer were mixed up under high-speed stirring at 65°C for 6–8 min. At last, the sample was cast into a specific metal mold and then cured at 105°C for 24 h.

Materials Characterization

The molecular weight of HTSSBR was characterized by GPC (Waters 1525). The molecular structure was measured using $^1\text{H NMR}$ (Bruker AV600) and FT-IR (Nicolet 8700). The micro-structure of the elastomer was measured by TEM (Hitachi JEM-3010). X-ray diffraction (XRD) with $\text{Cu-K}\alpha$ radiation ($\lambda = 0.154 \text{ nm}$) was performed on a Bruker D8 ADVANCE. The

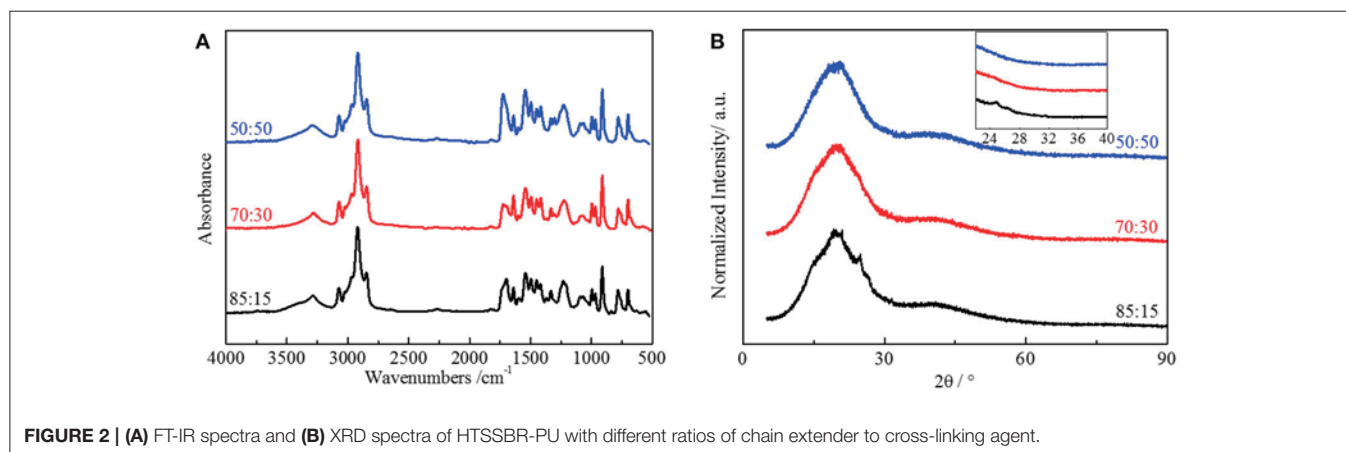


FIGURE 2 | (A) FT-IR spectra and **(B)** XRD spectra of HTSSBR-PU with different ratios of chain extender to cross-linking agent.

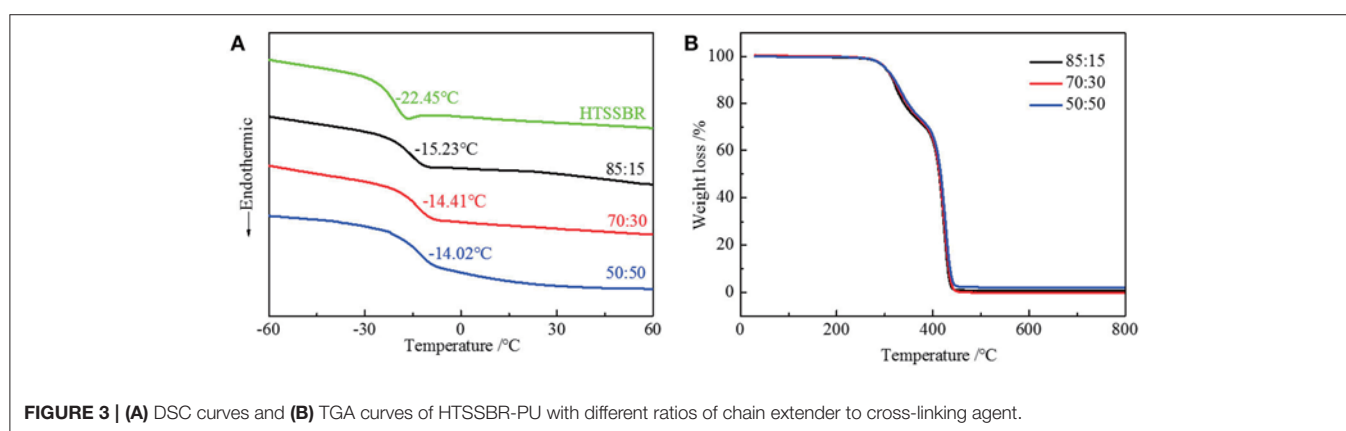


FIGURE 3 | (A) DSC curves and **(B)** TGA curves of HTSSBR-PU with different ratios of chain extender to cross-linking agent.

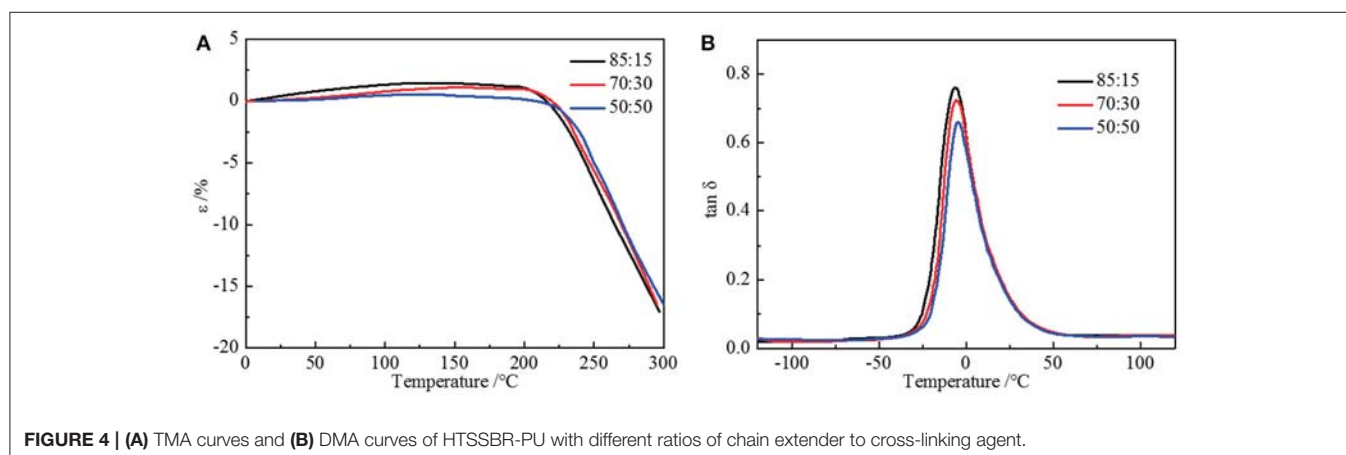


FIGURE 4 | (A) TMA curves and **(B)** DMA curves of HTSSBR-PU with different ratios of chain extender to cross-linking agent.

thermal properties were tested by TGA (Mettler-Toledo), DSC (Mettler-Toledo STARE), TMA (TA Q800), and DMA (TA Q800). The mechanical performances of the elastomer were conducted by the universal testing machine (LRX Plus/LLOYD LRX/MTS CMT4104), Akron abrasion tester (MINGZHU MZ-4061) and a friction coefficient tester (LEIYUN BM-III). The detailed information of material characterizations is offered in the Supplementary Materials.

RESULTS AND DISCUSSION

HTSSBR was successfully synthesized via anionic polymerization. By analyzing ¹H NMR and FT-IR spectroscopy, the content of 1,2-butadiene, 1,4-butadiene and styrene were 61.56%, 14.69 and 23.75%, respectively. The glass transition temperature is -22.47°C as expected. The molecular weight is ~3,000 and with a narrow distribution.

TABLE 1 | The comparison between SSBR composites and our prepared super elastomer material on mechanical properties.

	SSBR composites ^{a)}	HTSSBR-PU
Tensile strength /MPa	16.1	22.3 (+38.5%)
Elongation at break/%	365	481 (+31.8%)
Tensile stress at 300%/MPa	12.9	15.1 (+17.1%)
Tear strength /kN·m ⁻¹	40.6	45.8 (+12.8%)
Compression heat build-up/°C	20.9	16.2 (−22.5%)
Akron abrasion loss /mm ³	74.0	10.8 (−85.4%)
60°C tan δ(strain 7%, frequency 10 Hz)	0.130	0.075 (−42.3%)
Pendulum-type friction coefficient	24	29 (+20.8%)

^{a)} Formulas of contrast sample SSBR composites are shown as follows: SSBR 96.3, BR 30.0, Silica 70.0, Bis [3-(triethoxysilyl)propyl] tetrasulfide (TESPT) 6.3, Stearic acid (SA) 2.0, ZnO 3.5, N-tert-Butyl-2-benzothiazolesulfenamide (TBBS) 2.0, diphenyl guanidine(DPG) 2.0, N-1,3-dimethylbutyl-N'-phenyl-p-phenylenediamine (Antioxidant 4020) 1.0, S 1.7.

To demonstrate our thought, we emphasized polyurethane materials using HTSSBR as soft segments with different ratio of cross-linking agent and chain extender. The chemical content of the elastomer is a critical factor for the performance of the material. FT-IR spectroscopy (**Figure 2A**) was used to support that the synthesis progress was successful. The sample is designated as A:B, where A and B denote the mass percentages of chain extender and cross-linking agent, respectively. Taking the sample 50:50 as an example, the broad absorption at 3,290 cm⁻¹ corresponds to the N-H bonding. The absorptions from 1,740 to 1,700 cm⁻¹ correspond to the stretching vibration of C=O. The absorption at 2,280–2,255 cm⁻¹, the witness of –NCO, indicates the complete reaction of NDI. There is redshift of the absorption peaks of N-H and C=O, attributed to the hydrogen bonded amino group and the carbonyl group. By using peak-fitting software and imitating procedure by the Levenberg-Marquardt algorithm, hydrogen bonding degree calculated by peak areas is summarized. Degrees of ordered and disordered hydrogen bonding, and the total degree of hydrogen bonding decrease with the increasing content of the cross-linking agent (And and Painter, 2007). In this system of polyurethane, the soft segment made up of styrene and butadiene does not include strong electronegativity elements, making the hydrogen bonding only form between the hard segments (Harthcock, 1989; Król, 2007). The decrease of microtacticity of hard segments, which is lowered by the trifunctional trimethylolpropane, is the main reason for the reduction of hydrogen bonding. Compared with the difunctional 1,4-butanediol, the structure formed by TMP is more rigid and irregular, making the hydrogen bonding harder to form. The degree of ordered and disordered hydrogen bonding both decreases from 52.39 to 45.41% and from 22.64 to 18.30% respectively, resulting in the total degree of hydrogen bonding decreasing from 74.03 to 63.71%. The crystallization property of hard segments in the material, which is also associated with the molecular structure, is also influenced by the reduction of hydrogen bonding degree. X-ray diffraction (XRD) was performed to explore the crystallization of the elastomer (**Figure 2B**). There are dispersing diffraction peaks and a sharp diffraction peak ($2\theta \approx 20^\circ$). The dispersing diffraction peak is formed due to the long-range disorder of the elastomer, and

**FIGURE 5** | The schematic diagram of the rolling resistance test machine (RSS II model).

the sharp diffraction peak is formed by the short-range ordered crystal area. The shape of the dispersing diffraction peaks is almost identical, whereas the strength of sharp hard segment diffraction peak decreases and the degree of crystallization decreases from 7.27 to 1.22% with the ratio of chain extender to cross-linking agent reduces. As the main content of hard segment, NDI is a kind of isocyanate with good symmetry, which benefits from the regular structure of molecular chains and allows the hard phase to have crystallization. Crystallization formed by hard segment units is short range order, and the whole elastomer remains long range disorder. As a tri-functionality cross-link agent, TMP is not as symmetrical as BDO. This influences the formation of short-range order and partly long-range order structure, so the degree of crystallization will decrease with the accretion of TMP (Seefried and Critchfield, 2010).

Due to the difference in polarity between the soft and the hard segments, the micro-phase separation and chemically end-linked nanoparticles are generated uniformly through the self-assembly progress. The thermal and mechanical properties are mainly supported by the hard segment nanoparticles; therefore, it is of vital importance to study the effect of

the structure of hard segment. The thermal properties were acquired through thermogravimetric analysis and differential scanning calorimetry. Glass transition temperature (**Figure 3A**) of HTSSBR is -22.45°C , and glass transition temperature increases as the ratio of chain extender to cross-linking agent reduces. As described in the theoretical formula of glass transition temperature:

$$T_{gx} = T_g + K_x \rho$$

where T_{gx} is the glass transition temperature of the cross-linked polymer, T_g is the glass transition temperature of the origin polymer, K_x is the characteristic constant, and ρ is the cross-linking density. As the cross-linking density increases, the glass transition temperature of the cross-linked polymer will rise correspondingly. Adding more cross-linking agent into the system increases the chemical cross-linking density, and the mobility of molecular chains is restricted by the three-dimensional network restricts, which will raise the glass transition temperature. The thermal decomposition progress (**Figure 3B**) of PU is composed of two-stages, including hard segment and soft segment dissociation (Petrović et al., 2010), successively. The amount of final residual carbon is almost equal. The weight loss rate of two stages is the same as the weight ratio of the hard and soft segment, which indicates the complete reaction as well. The initial thermal decomposition temperature is about 300°C . The changing ratios of chain extender to cross-linking agent have little effect on the two-stage weight loss. The decomposition is mainly caused by chemical bond rupture, while the network structures formed by TMP and BDO have a slight influence on chemical bonds, so the thermal destruction temperature increases slightly. Thermomechanical analysis (TMA) was applied to further investigate the thermal properties of the elastomer. The softening temperature is defined as the critical temperature when the elastomer having a reduction in thickness which leads to a sudden decline in modulus (Lee and Ko, 1993). The softening temperature and expansivity were measured (**Figure 4A**). The disentanglement of hard segment is relieved by cross-linking structure at high temperature, which raises the softening temperature. At the same time, with the content of cross-link agent increasing, the deformation is more restricted by the network structure with temperature increases. By comparing with our previous work, the increase of the hard segment content has more effect on softening temperature than that of the ratio of the cross-linking agents to the chain extender. The explanation is as follows: these two factors both contribute to the cross-linking points of the structure. The difference is that hard segment, as physical cross-linking points, mainly forms the well-defined micro-phase separation due to hydrogen bonding and polarity of hard and soft segment, however cross-linking agents have mainly impacted the hard segment phase and have no direct correlation with micro-phase separation. Additionally, the hardness of the elastomer is slightly influenced by the changing the ratio of the chain extender to the cross-linking agent, which varies from 70 to 73. In a micro structure, the hardness of the partial area is increased by the network structure formed by tri-functional cross-linking agent. As analyzed earlier, the

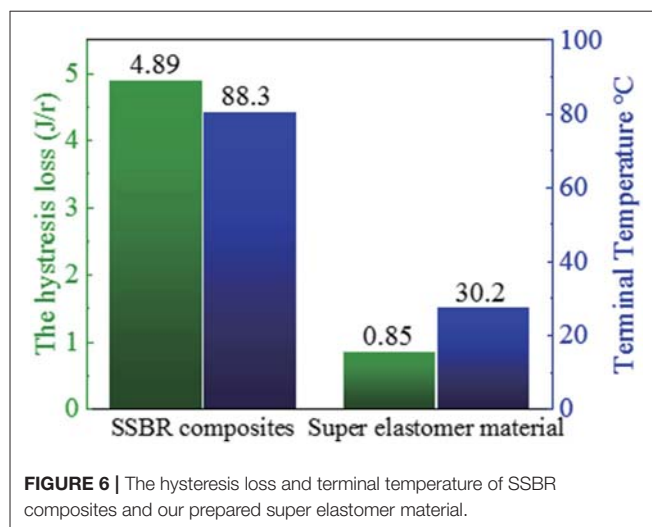


FIGURE 6 | The hysteresis loss and terminal temperature of SSBR composites and our prepared super elastomer material.

macro properties are mildly affected by the cross-link in hard segment phase, so there is a slight increase in hardness. Dynamic mechanical analyzer (**Figure 4B**) was used to test the mechanical properties of the elastomer (Dong and Cooper, 1971). The area of loss peaks is reduced as the ratio of chain extender to cross-linking agent decreases. The $\tan \delta$ 0°C , which is also known as the wet-skid resistance, is influenced by change of cross-linking density. The increase in cross-linking density limits the mobility of molecular chain between cross-link points, which will reduce the loss of energy, resulting in the decrease of peak area. The temperature of the loss peak moves to high temperature, as evidenced in DSC.

The above performances of HTSSBR with different ratios of chain extender and cross-linking agents completely match the requirement of a tire material (Prisacariu, 2011). Comparison between the sample with relatively better performances and SSBR composites are made to highlight the excellent mechanical properties. The general mechanical properties comparison are given in **Table 1**. The tensile strength is 22.3 MPa, compared with SSBR composites (16.1 MPa), an increase of 38.5%. The elongation at break is 481%, while the elongation of SSBR composites is 365%. Moreover, the wear resistance of HTSSBR is much better, with Akron abrasion loss at 10.8 mm^{-3} , while the Akron abrasion loss of SSBR composites is 74 mm^{-3} , which is much larger than Akron abrasion loss of HTSSBR. Tires with better wear resistance means less weight loss at work and longer service life, which can not only save the cost but also protect the environment. The exceptional wear resistance of the elastomer makes it an environmental-friendly material. In comparison with HTSSBR and SSBR composites, our PU elastomer shows apparent improvement in mechanical properties. However, before this elastomer comes to practical application, there are still several properties to be discussed. Hysteresis loss, which is also called dynamic energy loss, is one of the most important properties of dynamic elastomers products. As usual, the hysteresis loss dissipates in the form of heat, so it is known as rolling resistance. The dynamic energy loss of tires (Futamura, 1991), turning into heat accumulation, will raise

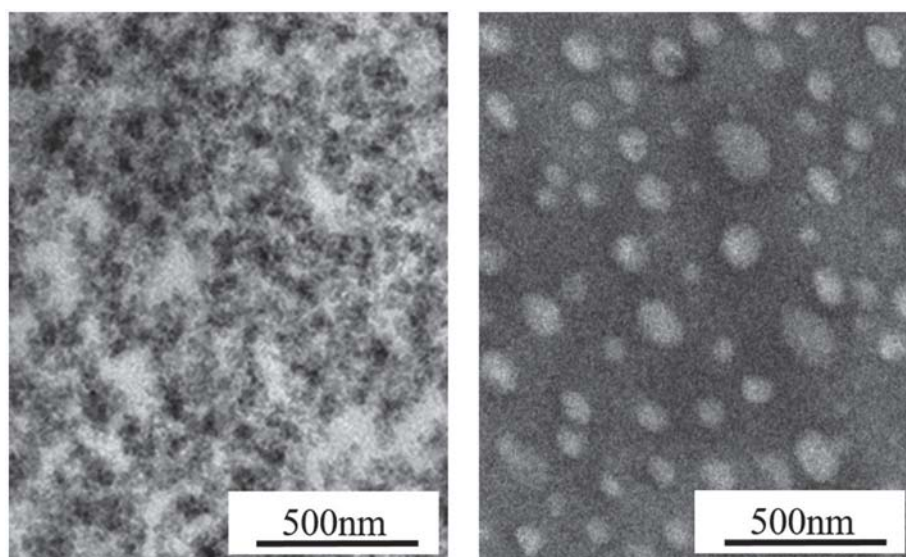


FIGURE 7 | TEM images of SSBR composites and HTSSBR-PU.

the working temperature of the tires, which could affect the mechanical properties of the tire and have a potential safety hazard. At the same time, rolling resistance determines the fuel assumption of tires. Therefore, it is of great importance to develop tires with low dynamic energy loss. In order to reflect the property of the HTSSBR-PU, a comparison between HTSSBR-PU and conventionally SBR composites used for tire used was invested to discuss the mechanical performance of the HTSSBR-PU. Based on the theory of the viscoelasticity of elastomer, a machine (RSS-II model, **Figure 5**) was designed to measure the rolling resistance. The dynamic energy loss can be measured by the viscoelasticity response of the elastomer in the rotating progress of the material sampler on the roller. The dynamic strain and stress (Willett, 1973) given as $\varepsilon(t) = \varepsilon_a \sin(\omega t - \delta)$ and $\sigma(t) = \sigma_a \sin \omega t$, respectively. The energy loss under a specific controlled energy cycle is give as follows

$$H = \int_0^{2\pi/\omega} \sigma(t) \frac{d\varepsilon(t)}{dt} dt = \pi \varepsilon_a \sigma_a \sin \delta \approx \pi \varepsilon_a \sigma_a \tan \delta$$

where ω is the frequency, ε_a is the amplitude of strain, σ_a is the amplitude of stress, δ is the phase difference between stress and strain, and $\tan \delta$ is the loss factor. After the test cycling (**Figure 6**), the hysteresis loss of HTSSBR-PU is measured to be 0.85 J/r, which is significantly lower than the hysteresis loss of the SBR composites (4.89 J/r). Due to the heat accumulation caused by the dynamic energy loss, the temperature rise of HTSSBR-PU is 30.2°C, but the temperature rise of SBR composites incredibly reached 88.3°C. To simulate the reality viscoelastic response relation with alternating stress of the materials under the working conditions, DMA with the strain ε at 7% and the frequency at 10 Hz was performed. The 60°C $\tan \delta$ of the SBR composites (0.130) is larger than the 60°C $\tan \delta$ of HTSSBR-PU, which could further prove that the latter have

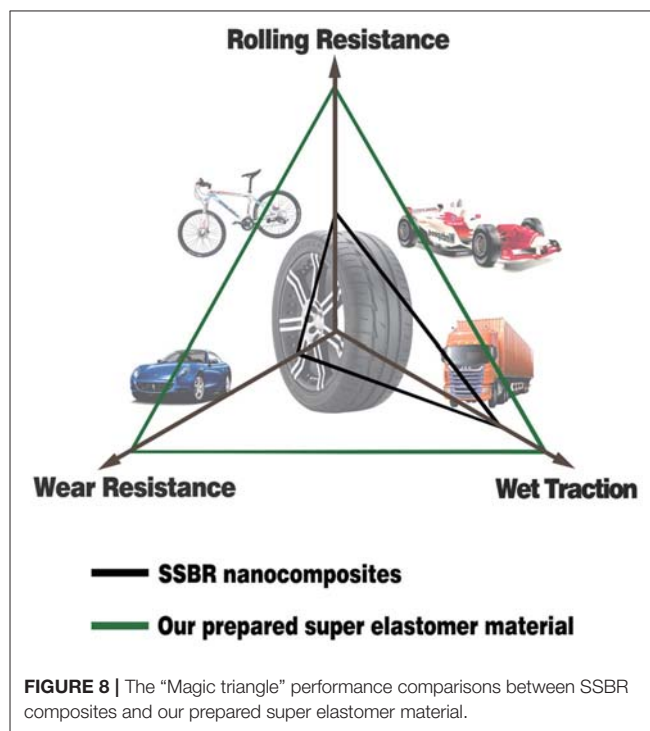


FIGURE 8 | The "Magic triangle" performance comparisons between SBR composites and our prepared super elastomer material.

lower rolling resistance. In addition, the pendulum-type friction coefficient reflects that the HTSSBR-PU lost less energy during the friction process, illustrating the low rolling resistance of HTSSBR-PU. As **Figure 7** shows, the microstructure of SBR composites is uneven due to the severe conglomerating of silica nanoparticles, while homogeneous phase separation in HTSSBR-PU is generated by the self-assembly progress of soft and hard segments. At the molecular level, the viscoelasticity

of the SSBR composites is mainly based on the polymer blend of SSBR/BR, the size, and distribution of nano-particles. The vulcanization and the nano-particles provide the essential chemical cross-linking points, but there will be the problem of combination between the particles and the polymer and uneven distribution of polymer and filler. The system of HTSSBR-PU is totally different in these aspects; the synergy of the network is supported by the soft segment with uniformly dispersed molecular weight and the even distribution of physical cross-link points provided by the micro-phase separation (Chen and Hsu, 1990; Cho et al., 2013), which leads to noticeable diminution of hysteresis loss and decrease of heat accumulation. The well-performed rolling resistance can also obviously reduce fuel consumption, which effectively reduces the carbon emission. Additionally, the molding process of HTSSBR-PU, which does without mixing and vulcanization, is much more straightforward and more efficient than the preparation technology of SSBR composites. To highlight our super elastomer material more intuitively, “Magic triangle” performance comparisons with SSBR composites are expressed in **Figure 8**. The markedly enlarged “Magic triangle” area elucidated that our super elastomer has the highest comprehensive performance. It is now well-established that our super elastomer is a kind of advanced material with fantastic performance and inestimable application prospects.

CONCLUSIONS

In conclusion, we designed and synthesized a super elastomer material by combing the HTSSBR and NDI, and the properties influenced by the ratio of chain extender and cross-link agent are discussed in particular detail. The excellent mechanical properties of the elastomer are provided by the micro-phase separation structure and hard segment nanoparticles, and the structure of hard segments are influenced by the chain

extender and cross-link agent. As the content of cross-link agent increases, the short-range order structures are affected and the degree of crystallization decreases. The tri-functional TMP raises the cross-link density of the hard segment, which increases the softening temperature and reduces the expansivity. The network structure in the hard segment has a light impact on the micro-phase separation and heat resistance of the material. Compared with commercial SSBR composites, the super elastomer material has advantages in most aspects, especially the excellent rolling resistance and wear resistance, which help to decrease the carbon dioxide emission. Our prepared elastomer material perfectly matches the requirement of “green tire,” and it provides a new idea for further development excellent energy-saving and eco-friendly advanced elastomers.

AUTHOR CONTRIBUTIONS

XQ, JW, and BW contribute to the experiment process, samples characterization, data analysis, and paper preparation. BH, LM, and LZ are mainly responsible for the design of experiment, data analysis and paper revision.

ACKNOWLEDGMENTS

This research is financially supported by the National 973 Basic Research Program of China 2015CB654700 (2015CB654704) and the Major Program (51790500).

SUPPLEMENTARY MATERIAL

The Supplementary Material for this article can be found online at: <https://www.frontiersin.org/articles/10.3389/fchem.2018.00240/full#supplementary-material>

REFERENCES

- And, J. M., and Painter, P. (2007). A Comparison of hydrogen bonding and order in a polyurethane and poly(urethane-urea) and their blends with poly(ethylene glycol). *Macromolecules* 40, 1546–1554. doi: 10.1021/ma0626362
- Chen, S. A., and Hsu, J. S. (1990). Polyurethane anionomers. II. Phase inversion and its effect on physical properties. *Polymer* 28, 1515–1532.
- Chiou, B. S., and Schoen, P. E. (2002). Effects of crosslinking on thermal and mechanical properties of polyurethanes. *J. Appl. Polymer Sci.* 83, 212–223. doi: 10.1002/app.10056
- Cho, J. R., Lee, H. W., Jeong, W. B., Jeong, K. M., and Kim, K. W. (2013). Finite element estimation of hysteretic loss and rolling resistance of 3-D patterned tire. *Int. J. Mech. Mater. Design* 9, 355–366. doi: 10.1007/s10999-013-9225-y
- Cooper, S. L., and Tobolsky, A. V. (1967). Anomalous depression of rubbery modulus through crosslinking. *J. Appl. Polymer Sci.* 11, 1361–1369. doi: 10.1002/app.1967.070110801
- Dong, S. H., and Cooper, S. L. (1971). Dynamic mechanical properties of polyurethane block polymers. *Polymer Eng. Sci.* 11, 369–376. doi: 10.1002/pen.760110504
- EU. (2009). *Official Journal of the European Union* L342, 46–58
- Fu, G., Yuan, L., Liang, G., and Gu, A. (2016). Heat-resistant polyurethane film with great electrostatic dissipation capacity and very high thermally reversible self-healing efficiency based on multi-furan and liquid multi-maleimide polymers. *J. Mater. Chem. A* 4, 4232–4241. doi: 10.1039/C6TA00953K
- Futamura, S. (1991). Deformation index—concept for hysteretic energy-loss process. *Rubber Chem. Tech.* 64, 57–64. doi: 10.5254/1.3538540
- Hammond, G. P. (2004). Engineering sustainability: thermodynamics, energy systems and the environment. *Int. J. Energy Res.* 28, 613–639. doi: 10.1002/er.988
- Harthcock, M. A. (1989). Probing the complex hydrogen bonding structure of urethane block copolymers and various acid containing copolymers using infra-red spectroscopy. *Polymer* 30, 1234–1242. doi: 10.1016/0032-3861(89)90041-4
- Heinz, M., and Grosch, K. A. (2007). A laboratory method to comprehensively evaluate abrasion, traction and rolling resistance of tire tread compounds. *Rubber Chem. Technol.* 80, 580–607. doi: 10.5254/1.3548182
- Jang, J. W., Yoo, T. S., Oh, J. H., and Iwasaki, I. (1998). Discarded tire recycling practices in the United States, Japan and Korea. *Resour. Conserv. Recycl.* 22, 1–14. doi: 10.1016/S0921-3449(97)00041-4
- Jiang, L., Wu, J., Nedolisa, C., Saiani, A., and Assender, H. E. (2015). Phase separation and crystallization in high hard block content polyurethane thin films. *Macromolecules* 48, 5358–5366. doi: 10.1021/acs.macromol.5b01083
- Karl, S. (2012). *How Dangerous is Rubber Dust?* Available online at: <http://www.abc.net.au/science/articles/2012/07/31/3554997.htm>.

- Król, P. (2007). Synthesis methods, chemical structures and phase structures of linear polyurethanes. Properties and applications of linear polyurethanes in polyurethane elastomers, copolymers and ionomers. *Prog. Mater. Sci.* 52, 915–1015. doi: 10.1016/j.pmatsci.2006.11.001
- Lee, H. K., and Ko, S. W. (1993). Structure and thermal properties of polyether polyurethaneurea elastomers. *J. Appl. Polymer Sci.* 50, 1269–1280. doi: 10.1002/app.1993.070500718
- Liff, S. M., Kumar, N., and McKinley, G. H. (2007). High-performance elastomeric nanocomposites via solvent-exchange processing. *Nat. Mater.* 6, 76–83. doi: 10.1038/nmat1798
- Mavroulidou, M., Hughes, S. J., and Hellawell, E. E. (2006). A comparison of two interaction matrix coding techniques used in a gis-based tool for air quality assessment. *Global Nest* 49, 923–947. doi: 10.30955/gnj.000417
- Petrović, Z. S., Zavargo, Z., Flynn, J. H., and Macknight, W. J. (2010). Thermal degradation of segmented polyurethanes. *J. Appl. Polymer Sci.* 51, 1087–1095. doi: 10.1002/app.1994.070510615
- Prisacariu, C. (2011). Polyurethane elastomers: from morphology to mechanical aspects. 18, 2808–2814. doi: 10.1007/978-3-7091-514-6
- Qin, X., Han, B., Lu, J., Wang, Z., Sun, Z., Wang, D., et al. (2018). Rational design of advanced elastomer nanocomposites towards extremely energy-saving tires based on macromolecular assembly strategy. *Nano Energy* 48, 180–188. doi: 10.1016/j.nanoen.2018.03.038
- Seefried, Jr, C. G., Koleske, J. V., and Critchfield, F. E. (2010). Thermoplastic urethane elastomers. III. Effects of variations in isocyanate structure. *J. Appl. Polymer Sci.* 19, 3185–3191. doi: 10.1002/app.1975.070191204
- U-Nations (1980). *Environmental Policy and Law* 6: 102.
- UNECE (2012). *UNECE Regulation 64.02*. Available online at: <http://www.roadsafetyobservatory.com/KeyFacts/vehicles/tyres>.
- Willett, P. R. (1973). Hysteretic losses in rolling tires. *Rubber Chem. Technol.* 46, 425–441. doi: 10.5254/1.3542912
- Yoshida, S., Ejima, H., and Yoshie, N. (2017). Tough elastomers with superior self-recoverability induced by bioinspired multiphase design. *Adv. Funct. Mater.* 27:1701670. doi: 10.1002/adfm.201701670

Conflict of Interest Statement: The authors declare that the research was conducted in the absence of any commercial or financial relationships that could be construed as a potential conflict of interest.

Copyright © 2018 Qin, Wang, Han, Wang, Mao and Zhang. This is an open-access article distributed under the terms of the Creative Commons Attribution License (CC BY). The use, distribution or reproduction in other forums is permitted, provided the original author(s) and the copyright owner(s) are credited and that the original publication in this journal is cited, in accordance with accepted academic practice. No use, distribution or reproduction is permitted which does not comply with these terms.



Rietveld Structure Refinement of Cu-Trien Exchanged Nontronites

Xiaoli Wang¹ and Libing Liao^{2*}

¹ Institute of Mineralogy, TU Bergakademie Freiberg, Freiberg, Germany, ² Key Laboratory of Materials Utilization of Nonmetallic Minerals and Solid Wastes, National Laboratory of Mineral Materials, School of Materials Science and Technology, China University of Geosciences, Beijing, China

OPEN ACCESS

Edited by:

Wenbo Wang,
Lanzhou Institute of Chemical Physics
(CAS), China

Reviewed by:

Luyi Sun,
University of Connecticut,
United States
Jianxi Zhu,
Guangzhou Institute of Geochemistry
(CAS), China
Yunfei Xi,
Queensland University of Technology,
Australia

*Correspondence:

Libing Liao
Clayl@cugb.edu.cn

Specialty section:

This article was submitted to
Green and Sustainable Chemistry,
a section of the journal
Frontiers in Chemistry

Received: 27 July 2018

Accepted: 29 October 2018

Published: 20 November 2018

Citation:

Wang X and Liao L (2018) Rietveld
Structure Refinement of Cu-Trien
Exchanged Nontronites.
Front. Chem. 6:558.
doi: 10.3389/fchem.2018.00558

The Rietveld analysis of X-ray powder diffraction patterns is used widely for obtaining the structural information of clay minerals. However, the complex hydration behavior and the variability of interlayer contents are often considered difficult to be described correctly by a simple structure model. In the present work, the use of Cu-triethylenetetramine (Cu-trien)-exchanged nontronites has been proposed to simplify the interlayer structure. This method provides a potential to obtain the structural information of nontronites, for example, the layer charge density, occupancies of *cis*-octahedral sites, and the iron content by the Rietveld analysis from the X-ray powder diffraction patterns. The approach was demonstrated on three Cu-trien-exchanged nontronite samples. The Rietveld refinements were carried out first on the purified samples and the results showed a good peak fitting between measured and calculated patterns. The refined iron content and the occupancies of *cis*-octahedral sites are in general agreement with the reference data, which have been obtained from chemical and thermal analyses. The refinement of layer charge density showed lower values compared with the reference. It may be due to the assumption of temperature factor of Cu-trien in the interlayer. A raw sample with natural impurities was chosen to test the applicability of this method. The refinement pattern of the raw sample led to good agreement with the observed data. The results of the iron content and the occupancies of *cis*-octahedral sites showed the same tendency as purified samples. This study showed that this approach allows for obtaining some structural details of nontronites directly from X-ray powder diffraction patterns of Cu-trien-exchanged samples.

Keywords: nontronites, Rietveld refinement, Cu-triethylenetetramine, crystal structure, X-ray powder diffraction

INTRODUCTION

Nontronite is the iron-rich dioctahedral smectite. The dominant cation in the tetrahedral sheet is Si⁴⁺, which can be substituted by Al³⁺ commonly (Manceau et al., 2000a). The octahedral sheet contains predominantly Fe³⁺, partially Al³⁺, and a minor amount of Mg²⁺. Only two-thirds of the octahedral positions are occupied by cations in dioctahedral smectites. In general, octahedral sheet shows two different configurations, that is, *cis*- and *trans*-octahedron that relate to the disposition of hydroxyl groups. In the *cis*-octahedron, the OH groups are on the same side, whereas in the *trans*-octahedron, the OH groups are on the opposite side. Tsipursky and Drits (1984) found that natural dioctahedral smectites may cover a wide range of *cis*-vacant (*cv*) and *trans*-vacant (*tv*) proportions. Based on the oblique-texture electron diffraction and X-ray diffraction analyses,

Besson et al. (1983) and Tsipursky and Drits (1984) demonstrated that for Fe-rich dioctahedral smectites, *cis*-octahedral positions were occupied and *trans*-octahedral sites were vacant. In general, nontronites show turbostratic stacking disorder (Biscoe and Warren, 1942) due to the weak bonds between the 2:1 layers (Moore and Reynolds, 1997). This kind of disorder can be described when the layers rotate or translate randomly to each other along the c^* direction (Moore and Reynolds, 1997). This kind of structural defect leads to non-Bragg diffraction effects and restricts the applicability of the conventional Rietveld method (Bish, 1993) to smectite. Several attempts of the Rietveld refinement have been done on turbostratically disordered structure (Taylor and Matulis, 1994; Viani et al., 2002; Gournis et al., 2008). However, these authors assumed more or less the ordered structure models, but not a real turbostratically disordered structure. The BGMN software can describe turbostratic disorder features of the diffraction patterns successfully by using the structure model containing a single-layer approach (Ufer et al., 2004). This method allowed an acceptable quantification of the smectite content in bentonites (Ufer et al., 2008). Later, it was applied for the Rietveld refinement of illite-smectite mixed-layer minerals (Ufer et al., 2012). However, this approach cannot handle the complex hydration behavior in the interlayer (Sato et al., 1992, 1996; Ferrage et al., 2005b).

Sposito et al. (1999) concluded the hydration shells of the cations like Na^+ and K^+ and the results indicated a tendency of inhomogeneous distribution in the interlayer of montmorillonite. Ferrage et al. (2005a,b) showed the hydration behavior of the smectites and the configuration of the interlayer to be complex and varying. It seems that the correct description of the interlayer configuration is another difficulty for the Rietveld analysis of nontronites, except for the turbostratically disordered structure. Therefore, a defined and stable occupancy of the interlayer space, which is independent of humidity, may

provide a potential for the modeling of such modified interlayer structures. In general, the intercalation of ethylene glycol (EG) in smectites is used for the characterization of smectites and vermiculites (MacEwan and Wilson, 1984). However, EG is not sufficiently stable for long-time measurements. The Cu-triethylenetetramine (Cu-trien) is a kind of stable complex and used routinely in the determination of the cation exchange capacity (CEC) (Meier and Kahr, 1999). The high selectivity of the index cation $[\text{Cu}(\text{trien})]^{2+}$ makes the exchange with the interlayer content fast and complete (Bergaya et al., 2006). Kaufhold et al. (2011) investigated the swelling capacity of Cu-trien-exchanged smectites and concluded that the Cu-trien-exchanged smectites showed constant d_{001} spacing and without significant water uptake. It may offer a chance to obtain information on the layer charge density by refining the occupancy of the Cu-trien complex in the interlayer spacing.

The current work applied X-ray diffraction analysis to the Cu-trien-exchanged nontronites by using the Rietveld method. The main objectives of this study are given as follows: (I) to investigate if some structural details of nontronites such as the layer charge density, iron content, and the occupancies of the *trans*- and *cis*- octahedral sites can be obtained directly from the X-ray diffraction patterns of purified samples and (II) to test the applicability of this method to raw nontronite samples with natural impurities.

MATERIALS AND METHODS

Sample Preparation

Two of the studied samples are from Uley Mine, South Australia (NAu-1 and NAu-2, Source Clays Repository) (Keeling et al., 2000). The other one is Washington nontronite (NWa). Keeling et al. (2000) found that both NAu-1 and NAu-2 showed high purity. This was also proved by primary X-ray diffraction analysis of samples. Thus, no further chemical treatment was

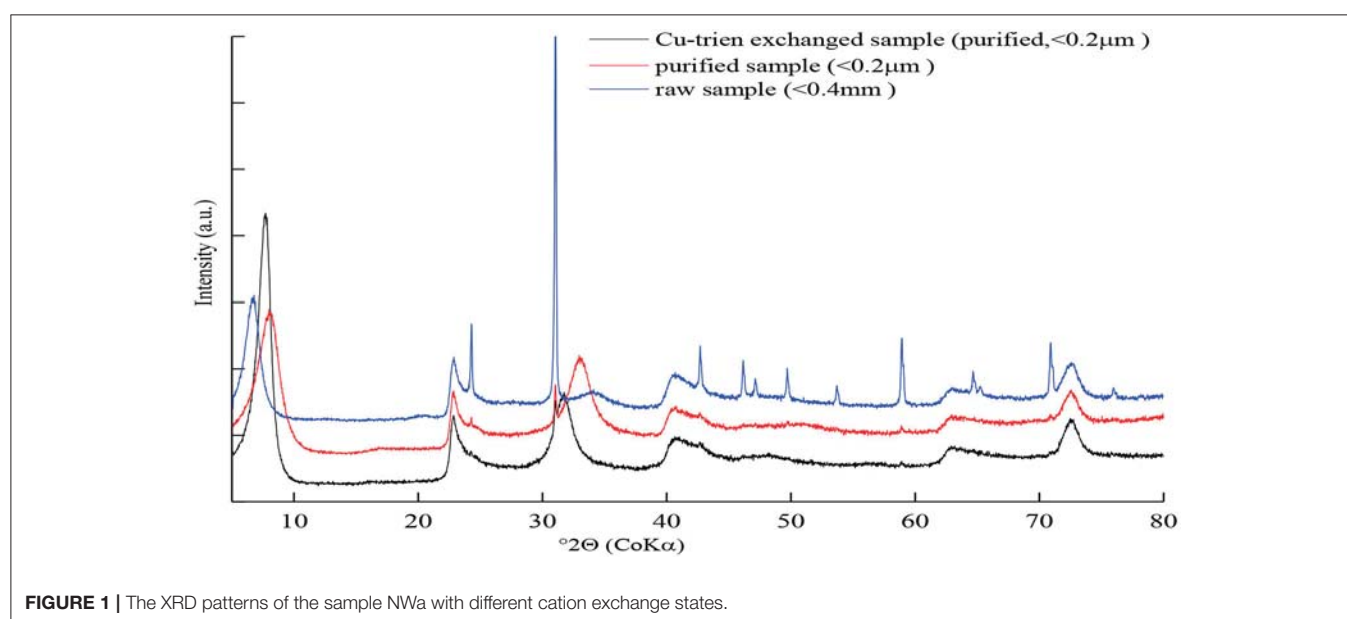


FIGURE 1 | The XRD patterns of the sample NWa with different cation exchange states.

performed for samples, N Au-1 and N Au-2, to remove impurities like carbonite, iron oxides, or organic matter. In contrast, sample N Wa contained amounts of quartz and trace amounts of goethite (Figure 1 and Table 5). Due to the large size, quartz can be easily removed from samples by the particle size separation process. The common method for the dissolution of iron oxides is described by Mehra and Jackson (1960). However, Manceau et al. (2000a,b) found that more than 99% octahedral Fe³⁺ was reduced to Fe²⁺ after the removal of iron oxides by using this method. Also, the layer charge may also change during the reduction processes (Carrado et al., 2006). Therefore, this procedure was not applied on this sample to avoid the destruction of the structure. To get the enrichment of nontronites, the particle-size separation of the <0.2 μm fraction from sodium-saturated samples was necessary. The excess salts were removed by dialysis and the <0.2 μm fraction was obtained by centrifugation. Then, the purified samples (<0.2 μm) were exchanged with Cu-trien complex: 0.8 g purified samples (<0.2 μm) were suspended in 100 ml 0.1 M Cu-trien solution. After shaking for 24 h, the suspension was centrifuged and washed with deionized water. Then, 100 ml of fresh Cu-trien solution was added into the centrifuge tube and shaken for 3 h again to ensure the exchange reaction was completed. After washing, the dispersion was dialyzed to remove excess salts and then dried at room temperature.

The chemical composition of Cu-trien-exchanged nontronite samples (Table 1) was calculated from the analysis of XRF (Table 2) using the method described by Köster (1977) (Table 1). The XRF measurement was performed on a MagiX PRO XRF-spectrometer (stimulation power: 3.2 KW) in the Institute of Geosciences, the Johannes Gutenberg University, Mainz. Sample N Au-2 showed higher iron content and lower aluminum content compared with sample N Au-1 (Table 1). The result is in good agreement with the study of Keeling et al. (2000). The other sample, N Wa, showed significantly lower iron content and higher aluminum than N Au-1 and N Au-2 (Table 1). The layer charge density was determined by the alkyl ammonium

method (AAM) (Lagaly and Weiss, 1976; Olis et al., 1990; Lagaly, 1991, 1994). The occupancies of *cis*- and *trans*-octahedral sites were calculated by fitting the derivative thermogravimetry (dTG) curves, which provided the information of the dehydroxylation temperature (Drits et al., 1995, 1998). The results showed that almost all *cis*-octahedral sites were occupied (Table 1) and the octahedral sheets were dominated by *trans*-vacant structure. The occupancy of iron cations in the octahedral sites was obtained by dividing the octahedral iron content by the octahedral occupancy (Table 1). The structural information obtained from the chemical and thermal analyses was used as independent references to evaluate the Rietveld refinements.

X-ray Powder Diffraction Analysis

The X-ray powder diffraction patterns of nontronites were collected by using a URD 6 (Seifert, CoK α radiation) diffractometer with a secondary beam graphite monochromator, a 0.2-mm detector slit, and an automatic divergence slit (15-mm irradiated length). The measurements were performed from 5° to 80° 2 θ , with a step width of 0.03° 2 θ and 3–5 s/step. The patterns were analyzed by the Analyze RayfleX v.2.352 software. The dried samples (<0.2 μm) were ground in an agate mortar by hand and filled into the sample holder by using a side-loading technique. To reduce the influence of the preferred orientation on X-ray powder diffraction patterns, a specific method for sample preparation was applied. The powders passed through a sieve with 100-μm mesh to destroy the aggregates, which had formed during the previous drying process and formed a rough surface.

Rietveld Refinements

The program BGMN (Bergmann et al., 1998) was applied for the Rietveld refinement. The single-layer approach (Ufer et al., 2004) was used to describe the turbostratically disordered structure of nontronites. A standard cell was elongated 10 times in the stacking direction and filled only by one single 2:1 layer (Ufer et al., 2004). The atomic coordinates of the 2:1 layers of

TABLE 1 | Structural formulae and properties of nontronite samples (<0.2 μm fraction).

Samples	Chemical composition /FU	Layer charge density [eq/FU]	Iron content per cation position	Occupancy of <i>cis</i> -octahedral sites
N Au-1	Cu _{0.18} ²⁺ (Al _{0.21} Fe _{1.83} ³⁺) [(Si _{3.51} Al _{0.49}) O ₁₀ (OH) ₂]	0.37*	0.897	1
N Au-2	Cu _{0.12} ²⁺ (Al _{0.04} Fe _{1.94} ³⁺) [(Si _{3.81} Al _{0.19}) O ₁₀ (OH) ₂]	0.25**	0.980	1
N Wa	Cu _{0.17} ²⁺ (Al _{0.43} Fe _{1.46} ³⁺ Mg _{0.21}) [(Si _{3.58} Al _{0.42}) O ₁₀ (OH) ₂]	0.34*	0.695	0.955

*Layer charge density according to Lagaly (1994).

**Mean layer charge density according to Olis et al. (1990).

TABLE 2 | XRF analysis of the Cu-trien-exchanged nontronites (< 0.2 μm).

Oxides/%	SiO ₂	Al ₂ O ₃	Fe ₂ O ₃ (t)	MnO	MgO	CaO	Na ₂ O	TiO ₂	P ₂ O ₅	CuO	LOI
N Au1	52.04	8.78	36.08	0.01	0.00	0.03	0.00	0.03	0.00	4.56	17.46
N Au2	56.44	2.91	38.14	0.00	0.01	0.05	0.00	0.05	0.00	3.58	15.86
N Wa	56.33	10.46	27.86	0.02	2.00	0.03	0.00	0.72	0.03	3.60	19.4

nontronites were taken from the Manceau et al. (2000a) study and recalculated for an orthogonal unit cell (Table 3). The positions of the atoms were kept constant during the refinement. The start value for the lattice constant b was set at 0.906 nm and refined with the limits ranging from 0.90 to 0.93 nm, and the lattice constant a was connected to b setting as $a = b / \sqrt{3}$ due to the assumption of the hexagonal layer symmetry (Manceau et al., 2000a). The start value of lattice constant c of Cu-trien-exchanged nontronites was set at 1.31 nm and refined with the limitation between 1.29 and 1.36 nm (Kaufhold et al., 2011). The atomic structure of the Cu-trien complex was derived from the Keramidias and Rentzeperis (1992) study. The Cu-trien molecule was placed in the middle of the interlayer and rotated parallel to the TOT layer. During the refinement, the atomic positions were kept fixed. The lattice constants were set as $a = 0.7362$ nm, $b = 1.4708$ nm, and $c = 1.5551$ nm (Keramidas and Rentzeperis, 1992). According to the study of Szczerba and Ufer (2018), the temperature factor of Cu-trien cation in the interlayer was set at 0.3 nm^2 , which should be significantly higher than the atoms in other positions.

The occupancy of the Cu-trien complex in the interlayer P (Cu_{trien}) and the iron occupation in the octahedral position P (Fe) were refined. The layer charge density was presented by the parameter P (Cu_{trien}). Despite the nontronites being known to prefer the *trans*-vacant octahedral configuration, both *cis*- and *trans*-vacant sites are considered. The *cis*-site occupancy P (*cis*-sites) was tried to be refined for checking this precondition. The scaling factor and the peak-broadening parameters were refined. The correction function for the preferred orientation was introduced and refined during the refinement. The zero-point shift correction and the sample displacement error were refined as nonstructural parameters.

RESULTS AND DISCUSSION

Rietveld Refinement on Purified Cu-Trien-Exchanged Samples

The X-ray diffraction patterns of sample NWA with different treatments are shown in Figure 1. The patterns of the raw and purified Na-saturated sample displayed asymmetric and broad 001 reflection (Figure 1), which indicated complex hydration states and inhomogeneous layer charge distribution in the interlayer (Ferrage et al., 2005b, 2007). Thus, such a peak profile is difficult to be simulated by a simple structure model. After exchanging the interlayer contents with the Cu-trien, the intensity of the 001 reflection was enhanced and well-defined (Figure 1). This method makes the description of the interlayer structure much easier and provides a probability to obtain the layer charge density by refining the occupancy of the Cu-trien complex in the interlayer.

The refinement of the sample NAu-1 showed a good agreement between the measured and calculated patterns and gave reasonable results for the iron content and the *cis*-octahedral sites occupancies (Table 4). The value of R_{wp} was 6.79% (Figure 2). The refined value of P (Fe) = 0.86(8) agreed with the chemical data within the estimated confidence interval

TABLE 3 | Atomic coordinates of the orthogonalized unit cell for nontronite recalculated from Manceau et al. (2000a).

	x	y	z
T1	0.63	0.329	0.78
T2	0	0.329	0.22
M1	0.316	0.333	0.5
M2	0.316	0	0.5
O1	0.63	0.688	0.613
O2	0.64	0.5	0.822
O3	0.375	0.736	0.845
O4	0.003	0.313	0.387
O5	0.97	0.5	0.179
O6	0.26	0.74	0.156
O7	0.683	0	0.611
O8	0.944	0	0.389
Na1	0.646	0	0.892
Na2	0	0	0.108
T1	0.63	0.671	0.78
T2	0	0.671	0.22
M1	0.316	0.667	0.5
O1	0.63	0.312	0.613
O3	0.375	0.264	0.845
O4	0.003	0.687	0.387
O6	0.26	0.26	0.156
T1	0.13	0.829	0.78
T2	0.5	0.829	0.22
M1	0.816	0.833	0.5
M2	0.816	0.5	0.5
O1	0.13	0.188	0.613
O2	0.14	0	0.822
O3	0.875	0.236	0.845
O4	0.503	0.813	0.387
O5	0.47	0	0.179
O6	0.76	0.24	0.156
O7	0.183	0.5	0.611
O8	0.444	0.5	0.389
Na1	0.146	0.5	0.892
Na2	0.5	0.5	0.108
T1	0.13	0.171	0.78
T2	0.5	0.171	0.22
M1	0.816	0.167	0.5
O1	0.13	0.812	0.613
O3	0.875	0.764	0.845
O4	0.503	0.187	0.387
O6	0.76	0.76	0.156

Space group = $C1/m1$, $a = 0.523$ nm; $b = 0.906$ nm; $c = 0.967$ nm.

"M" indicates the cations Al^{3+} , Mg^{2+} , and Fe^{3+} in the octahedral sites.

"T" indicates the cations Si^{4+} and Al^{3+} in the tetrahedral sites.

(Table 4). The *cis*-octahedral site occupancy P (*cis*-sites) = 0.97(2) was close to the expected value of 1. On the contrary, the occupancy of Cu-trien in the interlayer P (Cu_{trien}) = 0.312(5) was underestimated compared with the value 0.37 obtained by the AAM method (Table 4).

The refinement of NAu-2 resulted in satisfactory results. The R_{wp} value was 6.09%. The iron content P (Fe) = 0.91(7) was near

TABLE 4 | The refinement results of the purified nontronite samples (<0.2 μm).

	Start value	Refinement limits	Nau-1		Nau-2		Nwa	
			Reference values	Refinement result $R_{wp} = 6.79\%$ $R_{exp} = 2.63\%$	Reference values	Refinement result $R_{wp} = 6.09\%$ $R_{exp} = 2.63\%$	Reference values	Refinement result $R_{wp} = 9.95\%$ $R_{exp} = 2.68\%$
Contents/wt. %								
Nontronite/[3σ]				100		100		99.4(2)
Quartz/[3σ]								0.1(2)
Goethite/[3σ]								0.5(6)
Lattice parameter								
<i>b</i> (nm)/[3σ]	0.906	0.90-0.93		0.914(1)		0.9101(2)		0.9072(2)
Structure parameters								
P(Fe)/[3σ]	0.4	0-1	0.897	0.86(8)	0.980	0.91(7)	0.695	0.65(9)
P(<i>cis</i> -sites)/[3σ]	0.5	0-1	1	0.97(2)	1	1	0.995	1
Layer charge density	0.2	0-0.4	0.37	0.312(5)	0.25	0.238(4)	0.34	0.310(6)
P(Cu _{trien})/[3σ]								
Preferred orientation/(correction factor in <00>, deviation from random orientation)	0			1.37(2)		1.23(2)		1.81(3)

Reference values: P (Fe) from chemical analysis, P(*cis*-sites) from thermal analysis, P(Cu-trien) from layer charge density determined by the AAM method.

TABLE 5 | Comparison of the refinement results for purified and raw Washington nontronite.

	Start value	Refinement limits	Reference values		Purified sample (<0.2 μm)	Raw sample (<0.4 mm)
					$R_{wp} = 9.95\%$ $R_{exp} = 2.68\%$	$R_{wp} = 8.72\%$ $R_{exp} = 3.51\%$
Contents [mass %]						
Smectite/[3σ]					99.4(2)	79.3(4)
Quartz/[3σ]					0.1(2)	17.0(3)
Goethite/[3σ]					0.5(6)	3.7(3)
Structure parameters						
P(Fe)/[3σ]		0.4	0-1	0.695	0.65(9)	0.63(9)
P(<i>cis</i> -sites)/[3σ]		0.5	0-1	0.995	1	1
Layer charge density P(Cu _{trien})/[3σ]		0.2	0-0.4	0.34	0.310(6)	0.355(4)
Preferred orientation/(correction factor in <00>, deviation from random orientation)		0			1.81(3)	1.23(4)

Reference values: P(Fe) from chemical analysis, P(*cis*-sites) from thermal analysis, P(Cu-trien) from layer charge density determined by the AAM method.

the value 0.980 as calculated from the structural formula. The refined values of P (Cu_{trien}) = 0.238(4) and P (*cis*-sites) = 1 were in good agreement with the reference data (Table 4).

The refinement of the sample Nwa got the R_{wp} value of 9.95% (Figure 2). Mismatches of two main profiles were present at the 21–26° 2θ 02; 11 band and 30–33° 2θ 003 reflection. The high-measured intensities may be related to the high-preferred orientation (Table 4), which could not be compensated completely by the correction model. Alternatively, it may be considered that this sample has comparably low iron and high aluminum content in the octahedral sites. The coordinates derived from the Manceau et al. (2000a) study may not fit

perfectly for such Al-rich varieties. The refined iron content P(Fe) = 0.65(9) was in agreement with the value of 0.695 (in the estimated confidence interval). The refined parameter P (*cis*-sites) = 1 was as expected from the results of the thermal analysis. The refined P (Cu_{trien}) = 0.310(6) was lower compared with the value of 0.34 as determined by the AAM method (Table 4).

The obtained results showed that the refined *cis*-site occupancies and the iron content for purified samples were found to be comparatively consistent with the references. A tendency for underestimation of the layer charge density was observed. It may relate to the assumed values of the temperature factor. Despite the temperature factor of Cu-trien

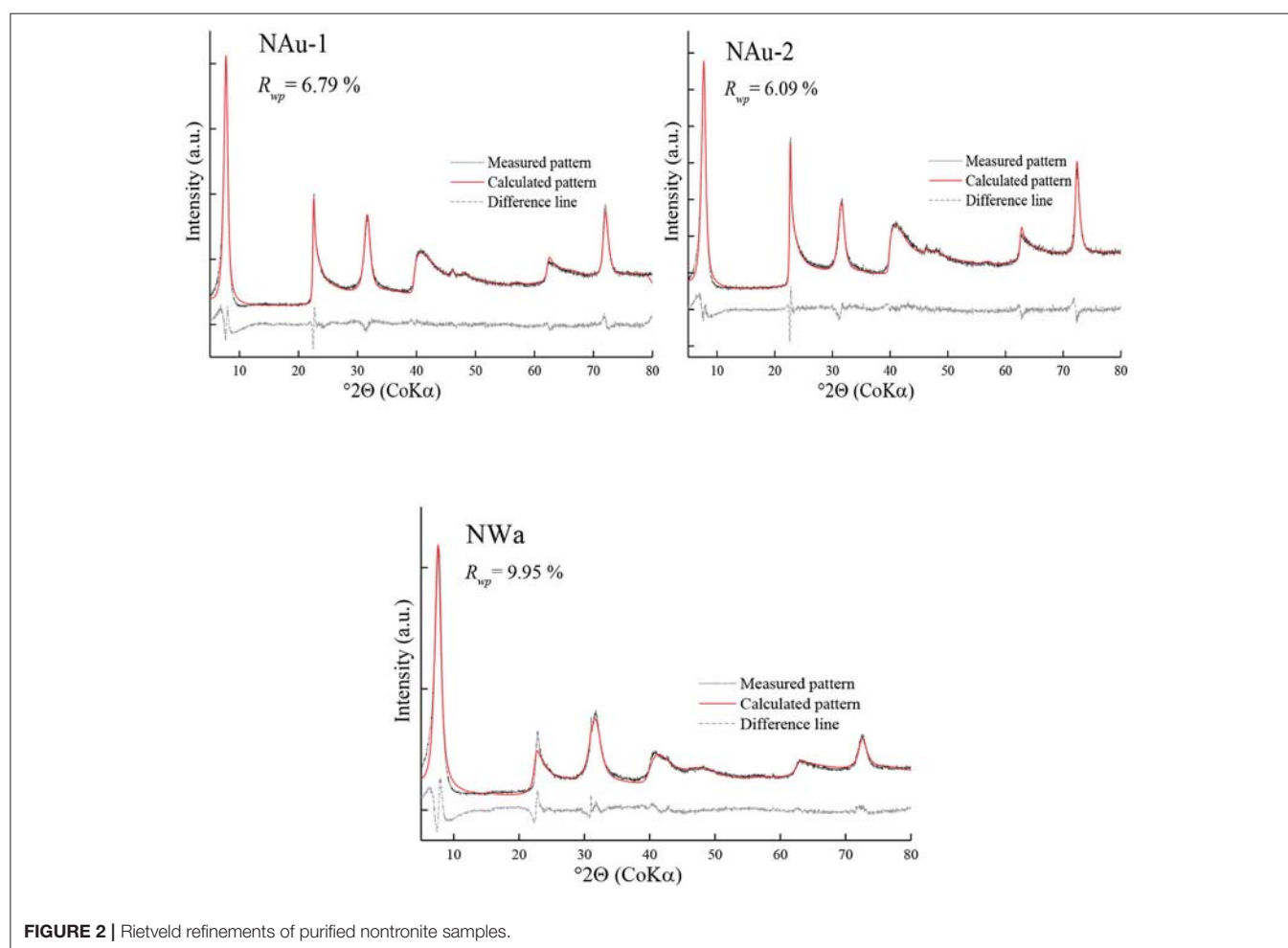


FIGURE 2 | Rietveld refinements of purified nontronite samples.

in the interlayer already having been enhanced according to Szczerba and Ufer (2018), there is still room for improvement if the temperature factor could be estimated independently, which, however, is hard to substantiate. The misfit of 001 reflection may be caused by the sample roughness, which can make deviation of peak profiles and intensities at a very low angle.

Rietveld Refinement of Raw Sample

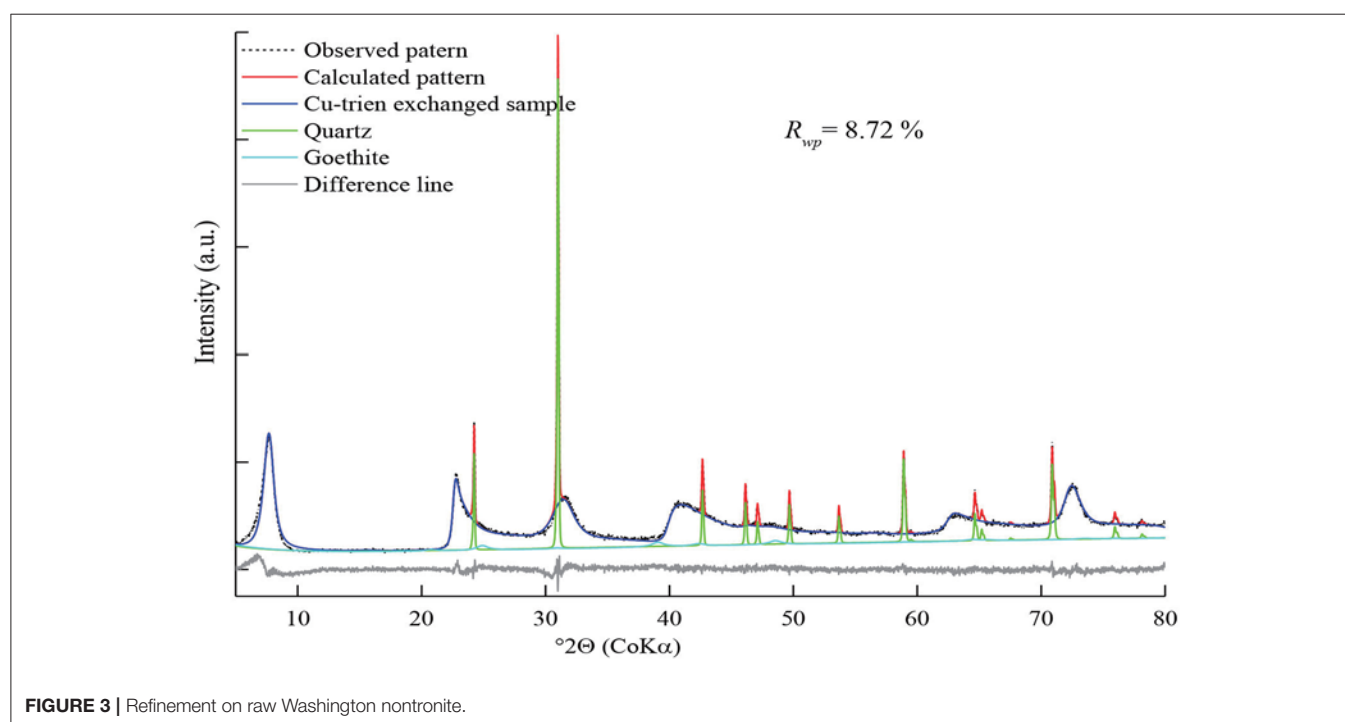
The feasibility of the structural model was tested in a raw nontronite sample with natural impurities. As the Washington bulk nontronite (sample N W a) was the only one containing significant impurities, it was chosen as a representative example in this study. This raw sample was exchanged with the Cu-trien complex directly without purification and particle size-separation process.

The calculated pattern was fitted satisfactorily with the observed data (Figure 3). The intensity of 02; 11 band was enhanced and matched much better than the purified sample. This might be related to the low preferred orientation (Table 5). Generally, the bulk sample had bigger particle size and less

aggregation than the purified sample, which may lead to lower preferred orientation (Table 5).

The measured pattern was covered with a large number of quartz reflections and small broadened peaks of goethite. The contents of the quartz and goethite were estimated as 17.0(3) and 3.7(3)% (Table 5). The R_{wp} value of raw N W a sample decreased to 8.72%, while the refinement result of the purified sample was 9.95% (Table 5). The refined value of *cis*-octahedral site occupancy $P(cis\text{-sites}) = 1$ was in good agreement with the value of 0.995, which came from the thermal analysis (Table 1). The refined iron content $P(Fe) = 0.63(9)$ was lower than the value of 0.695 calculated from the structural formula. However, it displayed the same tendency for the purified sample (Table 5). The refinement result of $P(Cu\text{-trien}) = 0.355(4)$ was slightly higher than the reference; by contrast, the refined value for the purified sample was lower than the reference (Table 5).

The refinement result of raw nontronite samples showed that the refined *cis*-octahedral site occupancies and iron content led to the same trends as the purified sample. However, the refined value of the layer charge density resulted in a reverse tendency to that of the purified sample (Table 5). This may further confirm the previous discussion: the selected coordinates may not work



satisfactorily for this specific sample with lower iron-content and higher aluminum-content nontronites (Tables 4, 5). The atomic coordinates applied to all samples were chosen identically (derived by Manceau et al., 2000a); however, such a choice might be a kind of simplification or compromise.

SUMMARY AND CONCLUSIONS

The Rietveld refinements of purified Cu-trien-exchanged nontronites led to comparatively reasonable results. The refined values of the iron content and the *cis*-octahedral sites were highly consistent with the references obtained from the chemical and thermal analyses. However, the refined layer charge density showed a tendency for underestimation. It may be attributed to the uncertainty of the temperature factor of Cu-trien in the interlayer. The test of the structural model on the raw Washington nontronite showed good agreement between calculated and measured patterns. The refinement results showed similar tendency for the iron content and occupancies of *cis*-octahedral sites, but an uncertain difference of layer charge densities between the raw and purified samples. It may be a consequence of the simplification of the atomic coordinates. However, the models should be applied to more nontronite samples with different iron contents in further research so as provide evidence for this presumption.

The results of this work show that the current structure model works better for nontronites with high iron content than those with low iron content. The structure information such as the layer charge density, iron content, and occupancies of *cis*-octahedral sites can be obtained directly from X-ray diffraction patterns by

the Rietveld method. This study may offer a potential for refining more structural parameters of nontronites by using this novel approach. The temperature factor of the interlayer species should be considered seriously since the occupancy of the atoms in the interlayer is related to this parameter. On the other hand, further developments should also focus on the optimization of the atomic positions, which may cover nontronite variabilities.

AUTHOR CONTRIBUTIONS

XW performed the experiments, derived the models, interpreted the data and wrote manuscript. LL supervised development of this work, helped in data interpretation and manuscript evaluation, and acted as corresponding author.

ACKNOWLEDGMENTS

This research was supported by the National Key R&D Program of China (2017YFB0310704). The authors are very grateful to Dr. Reinhard Kleeberg (TU Bergakademie Freiberg) for his helpful suggestions and corrections for the manuscript. We would like to thank Dr. Kristian Ufer (Bundesanstalt für Geowissenschaften und Rohstoffe, BGR) for his assistance in the structural model creation. We are delighted to thank Dr. Katja Emmerich and Dr. Annett Steudel (Karlsruhe Institute of Technology, KIT) for their support in the laboratory for the measurement of layer charge density and the assistance in the thermal analysis. We would like to thank Prof. Dr. Gerhard Heide (TU Bergakademie Freiberg) for all the support during this work.

REFERENCES

- Bergaya, F., Lagaly, G., and Vayer, M. (2006). "Cation and anion exchange," in *Handbook of Clay Science, Vol. 1*, eds F. Bergaya, B. K. G. Theng, and G. Lagaly (Clay Science), 988–995. doi: 10.1016/S1572-4352(05)01036-6
- Bergmann, J., Friedel, P., and Kleeberg, R. (1998). BGMN – a new fundamental parameters based Rietveld program for laboratory X-ray sources; it's use in quantitative analysis and structure investigations. *CPD Newsl. Commis. Powder Diffract. Int Union Crystallogr.* 20, 5–8.
- Besson, G., Bookin, A. S., Dainyak, L. G., Rautureau, M., Tsipursky, S. I., Tchoubar, C., et al. (1983). Use of diffraction and Mössbauer methods for the structural and crystallochemical characterisation of nontronites. *J. Appl. Crystallogr.* 16, 374–383. doi: 10.1107/S0021889883010651
- Biscoe, J., and Warren, B. E. (1942). An X-ray study of carbon black. *J. Appl. Phys.* 13, 364–371. doi: 10.1063/1.1714879
- Bish, D. L. (1993). "Studies of clays and clay minerals using X-ray powder diffraction and the Rietveld method," in *CMS Workshop, Lectures 5, Computer Applications to X-ray Powder Diffraction Analysis of Clay Minerals*, eds J. R. Walker and R. C. Reynolds Jr. (Boulder, CO: The Clay Minerals Society), 79–112.
- Carrado, K. A., Decarreau, A., Petit, S., Bergaya, F., and Lagaly, G. (2006). Synthetic clay minerals and purification of natural clays. *Dev. Clay Sci.* 1, 115–139. doi: 10.1016/S1572-4352(05)01004-4
- Drits, V. A., Besson, G., and Muller, F. (1995). An improved model for structural transformations of heat-treated aluminous dioctahedral 2:1 layer silicates. *Clays Clay Miner.* 43, 718–731. doi: 10.1346/CCMN.1995.0430608
- Drits, V. A., Lindgreen, H., Salyn, A. L., Ylagan, R., and McCarty, D. K. (1998). Semiquantitative determination of trans-vacant and cis-vacant 2:1 layers in illites and illite-smectites by thermal analysis and X-ray diffraction. *Am. Mineral.* 83, 1188–1198. doi: 10.2138/am-1998-11-1207
- Ferrage, E., Lanson, B., Malikova, N., Planon, A., Sakharov, B. A., and Drits, V. A. (2005a). New insights on the distribution of interlayer water in bi-hydrated smectite from X-ray diffraction profile modeling of 001 reflections. *Chem. Mater.* 17, 3499–3512. doi: 10.2138/am.2005.1776
- Ferrage, E., Lanson, B., Sakharov, B. A., and Drits, V. A. (2005b). Investigation of smectite hydration properties by modeling experimental X-ray diffraction pattern. Part I. Montmorillonite hydration properties. *Am. Mineral.* 90, 1358–1374. doi: 10.1021/cm047995v
- Ferrage, E., Lanson, B., Sakharov, B. A., Geoffroy, N., Jacquot, E., and Drits, V. A. (2007). Investigation of dioctahedral smectite hydration properties by modeling of X-ray diffraction profiles: influence of layer charge and charge location. *Am. Mineral.* 92, 1731–1743. doi: 10.2138/am.2007.2273
- Gournis, D., Lappas, A., Karakassides, M. A., Többsen, D., and Moukarika, A. (2008). A neutron diffraction study of alkali cation migration in montmorillonites. *Phys. Chem. Miner.* 35, 49–58. doi: 10.1007/s00269-007-0197-z
- Kaufhold, S., Dohrmann, R., Ufer, K., Kleeberg, R., and Stanjek, H. (2011). Termination of swelling capacity of smectites by Cu-trien exchange. *Clay Miner.* 46, 411–420. doi: 10.1180/claymin.2011.046.3.411
- Keeling, J. L., Raven, M. D., and Gates, W. P. (2000). Geology and characterization of two hydrothermal nontronites from weathered metamorphic rocks at Uley graphite mine, South Australia. *Clays Clay Miner.* 48, 537–548. doi: 10.1346/CCMN.2000.0480506
- Keramidas, K. G., and Rentzeperis, P. I. (1992). The crystal structure of triethylenetetramine copper(II) fluorophosphate, Cu(trien)(PF₆)₂. *Zeitschrift für Kristallographie* 201, 171–176.
- Köster, H. M. (1977). Die Berechnung kristallchemischer Strukturformeln von 2:1 Schichtsilikaten unter Berücksichtigung der gemessenen Zwischenschichtladungen und Kationenumtauschkapazitäten, sowie der Darstellung der Ladungsverteilung in der Strukturmittels Dreieckskoordinaten. *Clay Miner.* 12, 45–54. doi: 10.1180/claymin.1977.012.1.03
- Lagaly, G. (1991). *Erkennung und Identifizierung von Tonmineralen mit organischen Stoffen*. eds H. Tributh and G. Lagaly (Gießen: DTTG), 86–130.
- Lagaly, G. (1994). "Layer charge determination by alkylammonium ions," in *CMS Workshop, Lectures 6, Layer Charge Characteristics of 2:1 Silicate Clay Minerals*, ed A. R. Mermut (Aurora, CO: The Clay Minerals Society), 1–46.
- Lagaly, G., and Weiss, A. (1976). "The layer charge of smectitic layer silicates," in *Proceedings of the International Clay Conference (Mexico)*, 157–172.
- MacEwan, D. M. C., and Wilson, M. J. (1984). "Interlayer and intercalation complexes of clay minerals," in *Crystal Structures of Clay Minerals and Their x-ray Identification*, eds G. W. Brindley, and G. Brown (London: Mineralogical Society), 197–248.
- Manceau, A., Lanson, B., Drits, V. A., Chateigner, D., Gates, W. P., Wu, J., et al. (2000a). Oxidation-reduction mechanism of iron in dioctahedral smectites. I. Crystal chemistry of oxidized reference nontronites. *Am. Mineral.* 85, 133–152. doi: 10.2138/am-2000-0114
- Manceau, A., Lanson, B., Drits, V. A., Chateigner, D., Gates, W. P., Wu, J., et al. (2000b). Oxidation-reduction mechanism of iron in dioctahedral smectites. II. Crystal chemistry of reduced Garfield nontronite. *Am. Mineral.* 85, 153–172. doi: 10.2138/am-2000-0115
- Mehra, O. P., and Jackson, M. L. (1960). "Iron oxide removal from soils and clays by a dithionite-citrate-system buffered with sodium bicarbonate," in *7th National Conference on Clays and Clay Minerals*, ed A. Swineford (Washington, DC: Pergamon Press), 317–327.
- Meier, L. P., and Kahr, G. (1999). Determination of the cation exchange capacity (CEC) of clay minerals using the complexes of copper (II) ion with triethylenetetramine and tetraethylenepentamine. *Clays Clay Miner.* 47, 386–388. doi: 10.1346/CCMN.1999.0470315
- Moore, D. M., and Reynolds, R. C. Jr. (1997). *X-ray Diffraction and the Identification and Analysis of Clay Minerals*. New York, NY: Oxford University Press, 335–339.
- Olis, A. C., Malla, P. B., and Douglas, L. A. (1990). The rapid estimation of the layer charges of 2:1 expanding clays from a single alkylammonium ion expansion. *Clay Miner.* 25, 39–50. doi: 10.1180/claymin.1990.025.1.05
- Sato, T., Murakami, T., and Watanabe, T. (1996). Change in layer charge of smectites and smectitelayers in illite/smectite during diagenetic alteration. *Clays Clay Miner.* 44, 460–469. doi: 10.1346/CCMN.1996.0440403
- Sato, T., Watanabe, T., and Otsuka, R. (1992). Effects of layer charge, charge location, and energy change on expansion properties of dioctahedral smectites. *Clays Clay Miner.* 40, 103–113. doi: 10.1346/CCMN.1992.0400111
- Sposito, G., Skipper, N. T., Sutton, R., Park, S., Soper, A. K., and Greathous, J. A. (1999). Surface geochemistry of the clay minerals. *Proc. Natl. Acad. Sci. USA.* 96, 3358–3364. doi: 10.1073/pnas.96.7.3358
- Szczerba, M., and Ufer, K. (2018). New model of ethylene glycol intercalate in smectites for XRD modelling. *Appl. Clay Sci.* 153, 113–123. doi: 10.1016/j.clay.2017.12.010
- Taylor, J. C., and Matulis, C. E. (1994). A new method for Rietveld clay analysis: part 1. Use of a universally measured standard profile for Rietveld quantification of montmorillonites. *Powder Diffract.* 9, 119–123. doi: 10.1017/S0885715600014093
- Tsipursky, S. I., and Drits, V. A. (1984). The distribution of octahedral cations in the 2:1 layers of dioctahedral smectites studied by oblique-texture electron diffraction. *Clay Miner.* 19, 177–193. doi: 10.1180/claymin.1984.019.2.05
- Ufer, K., Kleeberg, R., Bergmann, J., and Dohrmann, R. (2012). Rietveld refinement of disordered illite-smectite mixed-layer structures by a recursive algorithm – II: powder-pattern refinement and quantitative phase analysis. *Clays Clay Miner.* 60, 535–552. doi: 10.1346/CCMN.2012.0600508
- Ufer, K., Roth, G., Kleeberg, R., Stanjek, H., Dohrmann, R., and Bergmann, J. (2004). Description of X-ray powder pattern of turbostratically disordered layer structures with a Rietveld compatible approach. *Z. Kristallogr.* 219, 519–527. doi: 10.1524/zkri.219.9.519.44039
- Ufer, K., Stanjek, H., Roth, G., Kleeberg, R., Dohrmann, R., and Kaufhold, S. (2008). Quantitative phase analysis of bentonites by the Rietveld method. *Clays Clay Miner.* 56, 272–282. doi: 10.1346/CCMN.2008.0560210
- Viani, A., Gualtieri, A. F., and Artioli, G. (2002). The nature of disorder in montmorillonite by simulation of X-ray powder patterns. *Am. Mineral.* 87, 966–975. doi: 10.2138/am-2002-0720

Conflict of Interest Statement: The authors declare that the research was conducted in the absence of any commercial or financial relationships that could be construed as a potential conflict of interest.

Copyright © 2018 Wang and Liao. This is an open-access article distributed under the terms of the Creative Commons Attribution License (CC BY). The use, distribution or reproduction in other forums is permitted, provided the original author(s) and the copyright owner(s) are credited and that the original publication in this journal is cited, in accordance with accepted academic practice. No use, distribution or reproduction is permitted which does not comply with these terms.

Advantages of publishing in Frontiers



OPEN ACCESS

Articles are free to read for greatest visibility and readership



FAST PUBLICATION

Around 90 days from submission to decision



HIGH QUALITY PEER-REVIEW

Rigorous, collaborative, and constructive peer-review



TRANSPARENT PEER-REVIEW

Editors and reviewers acknowledged by name on published articles

Frontiers

Avenue du Tribunal-Fédéral 34
1005 Lausanne | Switzerland

Visit us: www.frontiersin.org

Contact us: info@frontiersin.org | +41 21 510 17 00



REPRODUCIBILITY OF RESEARCH

Support open data and methods to enhance research reproducibility



DIGITAL PUBLISHING

Articles designed for optimal readership across devices



FOLLOW US

[@frontiersin](https://twitter.com/frontiersin)



IMPACT METRICS

Advanced article metrics track visibility across digital media



EXTENSIVE PROMOTION

Marketing and promotion of impactful research



LOOP RESEARCH NETWORK

Our network increases your article's readership